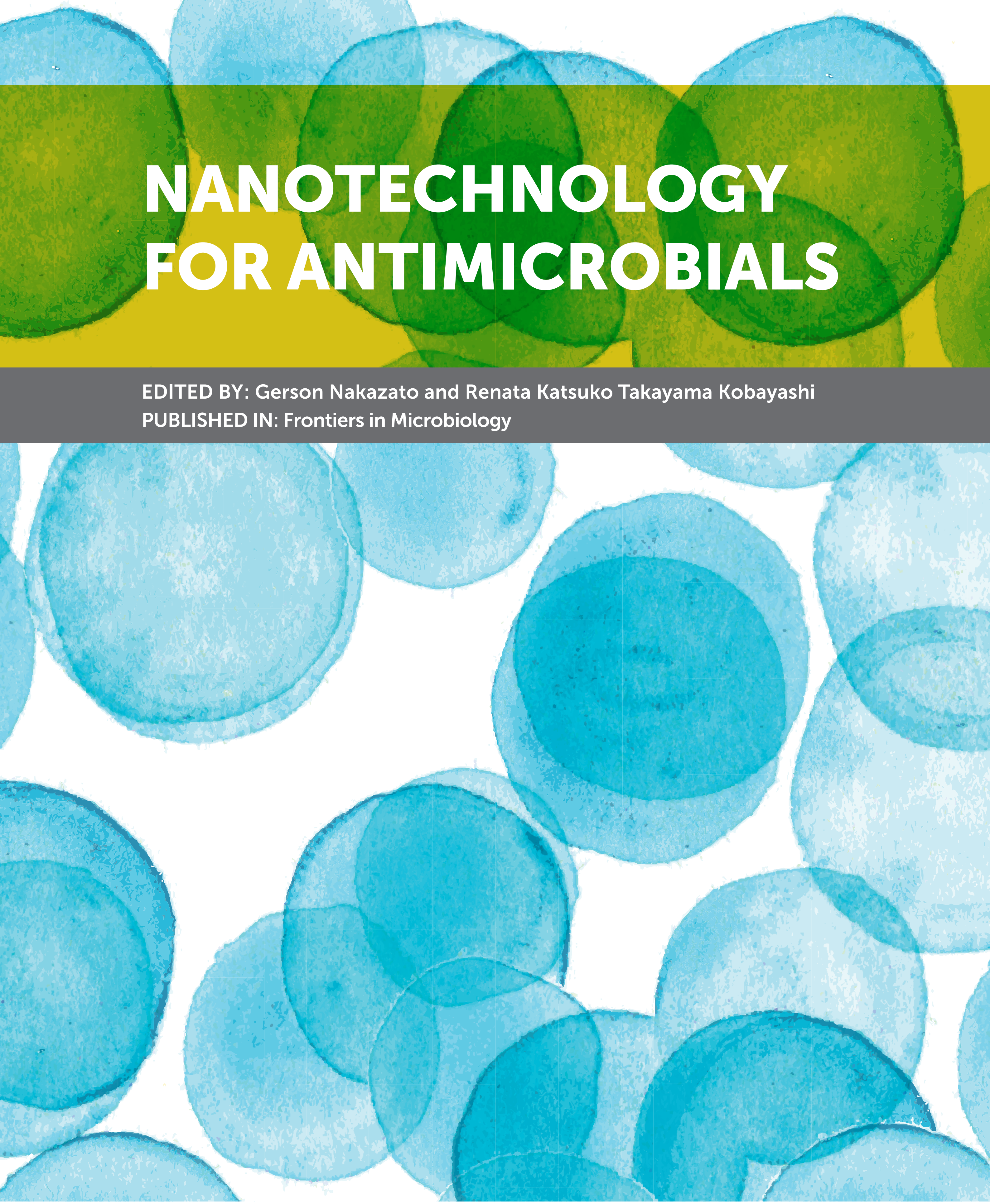

NANOTECHNOLOGY FOR ANTIMICROBIALS

EDITED BY: Gerson Nakazato and Renata Katsuko Takayama Kobayashi
PUBLISHED IN: Frontiers in Microbiology

frontiers Research Topics

ISSN 1664-8714
ISBN 978-2-88963-972-4
DOI 10.3389/978-2-88963-972-4

About Frontiers

Frontiers is more than just an open-access publisher of scholarly articles: it is a pioneering approach to the world of academia, radically improving the way scholarly research is managed. The grand vision of Frontiers is a world where all people have an equal opportunity to seek, share and generate knowledge. Frontiers provides immediate and permanent online open access to all its publications, but this alone is not enough to realize our grand goals.

Frontiers Journal Series

The Frontiers Journal Series is a multi-tier and interdisciplinary set of open-access, online journals, promising a paradigm shift from the current review, selection and dissemination processes in academic publishing. All Frontiers journals are driven by researchers for researchers; therefore, they constitute a service to the scholarly community. At the same time, the Frontiers Journal Series operates on a revolutionary invention, the tiered publishing system, initially addressing specific communities of scholars, and gradually climbing up to broader public understanding, thus serving the interests of the lay society, too.

Dedication to Quality

Each Frontiers article is a landmark of the highest quality, thanks to genuinely collaborative interactions between authors and review editors, who include some of the world's best academicians. Research must be certified by peers before entering a stream of knowledge that may eventually reach the public - and shape society; therefore, Frontiers only applies the most rigorous and unbiased reviews.
Frontiers revolutionizes research publishing by freely delivering the most outstanding research, evaluated with no bias from both the academic and social point of view. By applying the most advanced information technologies, Frontiers is catapulting scholarly publishing into a new generation.

What are Frontiers Research Topics?

Frontiers Research Topics are very popular trademarks of the Frontiers Journals Series: they are collections of at least ten articles, all centered on a particular subject. With their unique mix of varied contributions from Original Research to Review Articles, Frontiers Research Topics unify the most influential researchers, the latest key findings and historical advances in a hot research area! Find out more on how to host your own Frontiers Research Topic or contribute to one as an author by contacting the Frontiers Editorial Office: researchtopics@frontiersin.org

NANOTECHNOLOGY FOR ANTIMICROBIALS

Topic Editors:
Gerson Nakazato, State University of Londrina, Brazil
Renata Katsuko Takayama Kobayashi, State University of Londrina, Brazil

Citation: Nakazato, G., Kobayashi, R. K. T., eds. (2020). Nanotechnology for Antimicrobials. Lausanne: Frontiers Media SA. doi: 10.3389/978-2-88963-972-4

Table of Contents

frontiers in Microbiology

EDITORIAL
published: 09 July 2020
doi: 10.3389/fmicb.2020.01421

Editorial: Nanotechnology for Antimicrobials

Renata K. T. Kobayashi and Gerson Nakazato**

Department of Microbiology, Center of Biological Sciences, State University of Londrina, Londrina, Brazil

Keywords: nanoparticles, drug delivery, microbial pathogens, therapy, disease prevention, synthesis, resistance

OPEN ACCESS

Edited by:
Bingyun Li,
West Virginia University, United States

Reviewed by:
Hai Liang,
National Institutes of Health (NIH),
United States

****Correspondence:***
Renata K. T. Kobayashi
kobayashirkt@uel.br
Gerson Nakazato
gnakazato@uel.br

Specialty section:
This article was submitted to
Antimicrobials, Resistance and
Chemotherapy,
a section of the journal
Frontiers in Microbiology

Received: *09 April 2020*
Accepted: *02 June 2020*
Published: *09 July 2020*

Citation:
Kobayashi RKT and Nakazato G
(2020) Editorial: Nanotechnology for
Antimicrobials.
Front. Microbiol. 11:1421.
doi: 10.3389/fmicb.2020.01421

Editorial on the Research Topic

Nanotechnology for Antimicrobials

Nanotechnology has presented many advantages and benefits in science and industrial process. Nanoparticles have special characteristics that optimize the biological, physical, and chemistry properties being studied for many aims. The use of nanoparticles resulted in great evidences in Microbiology including antimicrobial activity against bacteria, fungi, virus, and protozoa. In this Research Topic, different nanoparticles and their strategies showed efficient antimicrobial effects with potential applications to control infections and biological contaminations. All articles showed the antimicrobial activity of these nanoparticles, direct or indirectly, against pathogenic microorganisms that cause severe infections, including those multidrug-resistant to the conventional antimicrobials.

The global spread of multidrug-resistant (MDR) microbial pathogens is currently considered one of the principal threats to global public health according to the World Health Organization (WHO) and it is estimated that unless action is taken, the number of deaths worldwide could increase to 10 million each year by 2050. Although the emergence of antimicrobial resistant bacteria is a natural process, this process can be accelerated by the non-rational use of antimicrobials, inadequate surveillance, and the insufficiently controlled regulation of antibiotics use in clinical medicine and in the livestock industry.

In view of the emergence of MDR microorganisms associated with scarcity in the discovery of new antibiotics, new anti-infectious strategies, need to be increasingly explored. In this Research Topic new effective strategies are showed as: metallic, biominerals and selenium nanoparticles with antimicrobial action (Basera et al.; Gunti et al.; Lakshmeesha et al.; Masum et al.; Nagaraj and Samiappan; Santos et al.), metallic nanoparticles that inhibited the biofilms formation (Fonseca et al.), magnetic nanoconjugate antibiotics that improved the antimicrobial action (Armenia et al.; Chen et al.), prebiotics in nanoparticles to better the antibacterial properties of probiotics (Hong et al.), antimicrobial peptides and bacteriophages nanoencapsulated in liposomes for prolonged delivery (Cinquerrui et al.; Zambom et al.).

All articles in this Research Topic proved the antimicrobial action of the respective compounds against pathogenic bacteria or fungi and some of them were effective against *Clostridium difficile*, Methicillin-resistant *Staphylococcus aureus* (MRSA) and Vancomycin-resistant *Enterococcus* (VRE) that are part of the threat list considered the most alarming antibiotic-resistant microorganisms according to the Centers for Disease Control and Prevention (CDC).

Nagaraj and Samiappan performed the biomimetization of Hydroxyapatite (HA) with *Azadirachta indica* (AI) and the preparation of HA-AI composite which showed potent antibacterial activity against *Staphylococcus aureus* ATCC 700699, which strain is Methicillin resistant (MRSA), resistant to Oxacillin and shows reduced Vancomycin susceptibility. Armenia et al. also tested magnetic nanoconjugated teicoplanin (NP-TEICO) against MRSA and Vancomycin-resistant *Enterococcus* (VRE). Both MRSA and VRE are classified as serious threat according to CDC, since they are resistant to the antimicrobials usually prescribed to combat these species, which can make it difficult to treat serious infections in hospitalized or community patients, highlighting the importance of developing new antimicrobials against these pathogens.

Chen et al. developed a sporicidal and antimicrobial vancomycin-loaded spore targeting iron oxide nanoparticle (van-IONP) that selectively binds to *C. difficile* spores. This microorganism is classified as urgent threat by CDC once it is a major cause of healthcare-acquired life-threatening diarrhea associated with the rising use of antibiotics, which is responsible to substantial mortality around the world. Van-IONP can target and completely cover spore surfaces. They not only successfully delayed the germination of the spores but also inhibited of vegetative cell outgrowth. This delivery therapy showed advantages over traditional therapeutics in treating *C. difficile* infection.

The articles published in this Research Topic approached some specific aspects about antimicrobial activity of nanoparticles in different fields (human medicine, veterinary, and foods). Nagaraj and Samiappan showed that the biomimetization of hydroxyapatite has an interesting anti-inflammatory potential property over lipopolysaccharide (bacterial endotoxin from Gram-negative) besides the antibacterial activity with a potential application in dentistry and orthopedic. Often inflammatory reactions are very important for treatment of infections because in this case the lipopolysaccharide causes septic shock in patients, leading to death.

Drug delivery strategy has been studied to optimize the antimicrobial activity using different carriers and actives. Many drug delivery models are similar to cancer treatment including the use of nanocarriers. Zambom et al. performed a drug delivery strategy using nanoliposomes with Histatin 5 inhibiting the growth of *Candida albicans*. Already Cinquerrui et al. used nanoliposomes encapsulated phages like a "Trojan Horse." Nanocarriers conjugated with antibiotics using magnetic nanoparticles were also suggested by Armenia et al. as potential application to infections sites.

Syntheses of different types of nanoparticles were also approached in some studies of this Research Topic. The biological synthesis was well-performed in some articles resulting in metallic nanoparticles with antimicrobial properties. Lakshmeesha et al. showed that the zinc oxide nanoparticles biosynthesized using a flower bud extract reduced the production of mycotoxins of *Fusarium graminearum* suggesting the use of these nanoparticles as a potential antifungal in agriculture and food industry. The pythofabrication of selenium nanoparticles using fruit extract was performed by Gunti et al. and these nanoparticles showed antimicrobial, antioxidant, and biocompatibility properties. Biogenic silver nanoparticles have been an interesting alternative as antibacterial as demonstrated (Basera et al.). Santos et al. also got great results using biogenic nanosilver in the treatment of *Corynebacterium pseudotuberculosis* infections in small ruminants. In this last study, the results *in vivo* indicate that biogenic nanosilver can be applied as an alternative in the treatment of infections in Veterinary field. These studies revealed that the antimicrobial properties of biogenic nanoparticles depend on the source of reducing agent as well as active molecules.

Some bacterial strains are able to protect themselves against antimicrobials by resistance mechanisms or bacterial structure. Spore forming is a classic example of bacterial structure of resistance. Still, the sporicidal effect of vancomycin-loaded nanoparticles against *Clostridium* was demonstrated by Chen et al. in this Research Topic. Masum et al. using biogenic silver nanoparticles managed to disturb biofilm formation and swarming ability. Another study about biofilm inhibition was performed by Fonseca et al., in this case using nanocomposite of silver-doped ZnO and AgO nanocrystals to control biofilm formation in eggshell. Structural and inhibition biofilms have been studied in Microbiology and Pathogenesis mainly for some materials such as medical devices. These biofilms are difficult to eliminate or remove in the surfaces. In this case, these nanoparticles prevented the biofilm formation suggesting a potential use in materials.

Another way to control infections is the probiotics, prebiotics and symbiotics including the application of nanoparticles. Hong et al. described pullulan nanoparticles as prebiotics enhancing the antibacterial effect of *Lactobacillus* against *Listeria monocytogenes*. This study indicates that some nanoparticles can act on microbiome interacting positively with other bacteria on prevent of infections.

The results of these studies demonstrated the importance of Nanotechnology for infection control in different field even as model studies for antimicrobial activity. The nanoparticles synthesized biologically ("green nanoparticles") and biocompatible present in some articles corroborate with the concerns about safety and ecology in the use of these antimicrobials. Many applications and products using nanoparticles can be generated from this Research Topic.

Future perspectives revolve around new strategies and development of products to prevent, control and treat microbial infections in humans and other animals, including viral infection, as seen in the actual pandemic scenario.

AUTHOR CONTRIBUTIONS

All authors listed have made a substantial, direct and intellectual contribution to the work, and approved it for publication.

FUNDING

This work was supported in part by the National Council for Scientific and Technological Development – CNPq (313305/2019-6) to RK and (315435/2018-6) to GN.

ACKNOWLEDGMENTS

We would like to thank the Marcelly C. Gonçalves for the English language edition. The editorial guidance and the suggestions of Dr. Rustam Aminov for handling this Research Topic were highly appreciated.

Conflict of Interest: The authors declare that the research was conducted in the absence of any commercial or financial relationships that could be construed as a potential conflict of interest.

frontiers in Microbiology

ORIGINAL RESEARCH
published: 12 September 2018
doi: 10.3389/fmicb.2018.02172

Nanoencapsulation of Bacteriophages in Liposomes Prepared Using Microfluidic Hydrodynamic Flow Focusing

Salvatore Cinquerrui[1], Francesco Mancuso[1], Goran T. Vladisavljević[1], Saskia E. Bakker[2] and Danish J. Malik[1]*

[1] Chemical Engineering Department, Loughborough University, Loughborough, United Kingdom, [2] Advanced Bioimaging Research Technology Platform, University of Warwick, Coventry, United Kingdom

OPEN ACCESS

Edited by:
Renata Katsuko Takayama Kobayashi,
Universidade Estadual de Londrina,
Brazil

Reviewed by:
Gustavo Bueno Gregoracci,
Federal University of São Paulo, Brazil
Katarzyna Małgorzata
Danis-Włodarczyk,
The Ohio State University,
United States

***Correspondence:**
Danish J. Malik
d.j.malik@lboro.ac.uk

Specialty section:
This article was submitted to
Antimicrobials, Resistance and
Chemotherapy,
a section of the journal
Frontiers in Microbiology

Received: 23 June 2018
Accepted: 23 August 2018
Published: 12 September 2018

Citation:
Cinquerrui S, Mancuso F, Vladisavljević GT, Bakker SE and Malik DJ (2018) Nanoencapsulation of Bacteriophages in Liposomes Prepared Using Microfluidic Hydrodynamic Flow Focusing. Front. Microbiol. 9:2172. doi: 10.3389/fmicb.2018.02172

Increasing antibiotic resistance in pathogenic microorganisms has led to renewed interest in bacteriophage therapy in both humans and animals. A "Trojan Horse" approach utilizing liposome encapsulated phages may facilitate access to phagocytic cells infected with intracellular pathogens residing therein, e.g., to treat infections caused by *Mycobacterium tuberculosis, Listeria, Salmonella,* and *Staphylococcus* sp. Additionally, liposome encapsulated phages may adhere to and diffuse within mucosa harboring resistant bacteria which are challenges in treating respiratory and gastrointestinal infections. Orally delivered phages tend to have short residence times in the gastrointestinal tract due to clinical symptoms such as diarrhea; this may be addressed through mucoadhesion of liposomes. In the present study we have evaluated the use of a microfluidic based technique for the encapsulation of bacteriophages in liposomes having mean sizes between 100 and 300 nm. Encapsulation of two model phages was undertaken, an *Escherichia coli* T3 podovirus (size ∼65 nm) and a myovirus *Staphylococcus aureus* phage K (capsid head ∼80 nm and phage tail length ∼200 nm). The yield of encapsulated T3 phages was 10^9 PFU/ml and for phage K was much lower at 10^5 PFU/ml. The encapsulation yield for *E. coli* T3 phages was affected by aggregation of T3 phages. *S. aureus* phage K was found to interact with the liposome lipid bilayer resulting in large numbers of phages bound to the outside of the formed liposomes instead of being trapped inside them. We were able to inactivate the liposome bound *S. aureus* K phages whilst retaining the activity of the encapsulated phages in order to estimate the yield of microfluidic encapsulation of large tailed phages. Previous published studies on phage encapsulation in liposomes may have overestimated the yield of encapsulated tailed phages. This overestimation may affect the efficacy of phage dose delivered at the site of infection. Externally bound phages would be inactivated in the stomach acid resulting in low doses of phages delivered at the site of infection further downstream in the gastrointestinal tract.

Keywords: bacteriophage therapy, *E. coli*, intracellular infections, liposome fabrication, microfluidics, nanoencapsulation, *S. aureus*

INTRODUCTION

The widespread inappropriate use of antibiotics in both humans (clinical medicine) and animals (livestock industry) worldwide has led to an acceleration in the emergence and global spread of multidrug antibiotic resistant bacterial clones (Morgan et al., 2011). The problem of antibiotic resistance is a complex one requiring global coordination for antibiotic stewardship to preserve the efficacy of current treatments. In much of the world outside Europe and North America, lifesaving antibiotics are sold without a prescription or oversight by health professionals (Laxminarayan et al., 2013). In the period between 1940 and 1962, 20 new classes of antibiotics were introduced to the market; however, since 1962, there has been a discovery void with only two new classes reaching this stage (Coates et al., 2011). The speed of development of resistance has been faster than the rate of discovery (Kelly et al., 2016). The substantial public health threat from antibiotic resistance includes jeopardizing effectiveness of treatments in modern medicine from minor elective surgeries to cancer therapy.

The ESKAPE pathogens (*Enterococcus faecium, Staphylococcus aureus, Klebsiella pneumoniae, Acinetobacter baumannii, Pseudomonas aeruginosa*, and *Enterobacter* species) represent a key group of commonly occurring Multi-Drug Resistant organisms at the heart of the antibiotic resistance crisis (Schooley et al., 2017). Initiatives to develop new therapeutic approaches with novel mechanisms of activity against MDR bacterial pathogens include the potential use of lytic bacteriophages (Summers, 2001; Czaplewski et al., 2016). Lytic bacteriophages (phages) are viruses that infect and kill bacteria, and they represent a promising approach to targeting bacterial infections in a treatment known as phage therapy (Alisky et al., 1998; Abedon, 2009; Abedon et al., 2011; Allen et al., 2014). The specificity of bacteriophages and their potential role in maintaining healthy microbiota makes them an attractive alternative to employing antibiotics. Technical advances are reducing the cost, processing and sequencing times of next-generation sequencing (NGS), thereby allowing rapid culture independent identification of disease causing bacteria (Toma et al., 2014). These developments increase the opportunities for using narrow spectrum antibiotics where the infection causing bacterial agent is known, thereby opening-up the possibility of employing phages for therapeutic purposes (Malik et al., 2017). A number of recent studies in animals and humans have been carried out to investigate the clinical safety and therapeutic or prophylactic efficacy of phages against *P. aeruginosa, S. aureus, A. baumannii, Escherichia coli,* and *Salmonella enteritidis* (Wright et al., 2009; Lim et al., 2012; Sarker et al., 2016; Schooley et al., 2017).

Limitations regarding the broad utility of phage therapy for the treatment of bacterial infections include narrow host ranges of individual phages and bacterial host resistance leading to phage resistant mutant. There is some debate as to whether bacteriophages would be able to diffuse across eukaryotic cell membranes killing intracellular bacteria infecting macrophages and other eukaryotic cells. Some recent *in vitro* studies have shown free phage entry into macrophages and other non-phagocytic eukaryotic cells however, the mechanisms of entry remain unclear (Nieth et al., 2015b; Zhang et al., 2017). Intracellular phage entry into eukaryotic cells has been explained to occur either through phagocytosis of phage infected bacteria or via bacterial induced endocytosis (Finlay, 1997). Important multi-drug resistant intracellular pathogens include those causing chlamydia, salmonella, staphylococcal, and mycobacterial infections, as well as infections due to *Brucella abortus*, *Burkholderia cenocepacia*, *K. pneumoniae*, *Legionella pneumophilia,* and *Listeria monocytogenes* (Nieth et al., 2015a; Singla et al., 2016b). Use of phage cocktails permits broadening of the host range whilst judicious selection of phages making-up the cocktail targeting different receptors tends to reduce the risk of resistance arising in host bacteria due to random mutations (Tanji et al., 2005; Denou et al., 2009; Yen et al., 2017). In chronic infections phage treatment may be compromised by the adaptive host immune response (anti-phage antibodies) leading to clearance of delivered phages lowering the phage titer at the site of infection resulting in poor efficacy of phage therapy (Dabrowska et al., 2005). Another considerable challenge is associated with accessibility of phages to a wide range of pathogenic bacteria residing within mucosa and biofilms including highly resistant strains of *Bordetella pertussis* (whooping cough), *E. coli* (diarrheas, meningitis, urinary tract infections), *Helicobacter pylori* (ulcers, gastritis), *Neisseria gonorrhoea* (gonorrhoea), *Neisseria meningitidis* (meningitis), *P. aeruginosa* (infections in people suffering from cystic fibrosis), *S. aureus* (wound associated infections e.g., diabetic foot ulcers), streptococci (meningitis, otitis media, pharyngitis, scarlet fever), etc.

Encapsulation of phages in liposomes may address some of the challenges associated with the development of effective phage therapy discussed above. Liposomes are composed of phospholipids, which self-assemble and self-enclose to form spheres of lipid bilayers with an inner aqueous core which may be designed to contain therapeutic agents such as phages. Liposomes may aid in shielding phages from the action of the reticuloendothelial system thereby increasing the length of time of circulation of phages instead of having to find long-circulating mutant phage strains (Merril et al., 1996). A previous study demonstrated that non-virulent *Mycobacterium smegmatis* and *Mycobacterium avium* transiently infected with the lytic phage TM4 were able to deliver the phage into *Mycobacterium tuberculosis* infected macrophages in a "Trojan Horse" approach (Broxmeyer et al., 2002). In a similar manner, liposome encapsulated phages may permit phage access to intracellular pathogens for the treatment of serious infections, such as those caused by *M. tuberculosis*, *S. aureus,* and *E. coli* (Nieth et al., 2015b).

Liposomes have been used to encapsulate a vast variety of cargos, like hydrophilic and hydrophobic drugs, proteins, living cells, nanoparticles, quantum dots, plasmid DNAs (Pattni et al., 2015). Ideally, liposome encapsulation techniques should allow full control over liposome formulation composition (e.g., for regulatory safety compliance) as well as control over vesicle size and size distribution which are important factors as they affect the encapsulated dose as well as *in vivo* circulation times and pharmacokinetics of the encapsulated active ingredient and its biodistribution (Sawant and Torchilin, 2012b). The liposome production process needs to be scalable and have a low environmental impact (Torchilin, 2005). Since their discovery in the 60s, several methods for the preparation of liposomes have been developed (Sawant and Torchilin, 2012a). However, classical techniques (e.g., thin film hydration, sonication, solvent dispersion, detergent removal, dilution) as well as sophisticated/innovative ones (e.g., use of supercritical fluids) do not completely fulfill the requirements for an ideal encapsulation process and lack adequate control over liposome production. The choice of the manufacturing technique is constrained by specific requirements and is quite often a compromise. Recently, microfluidic approaches have been used to address some of the constraints of other liposome production methods (van Swaay and deMello, 2013). Microfluidic devices offer many advantages over traditional liposome fabrication methods, such as control over the average size of liposomes, narrow particle size distribution, portability, integration and automation possibilities, and small reagent consumption thereby allowing rapid screening of formulations and production parameters. Liposome size and size distribution affect crucial characteristics including cargo release profile, loading capacity, biodegradation rate, biodistribution, and liposome stability over time.

There are relatively few published studies on phage encapsulation in liposomes (Nieth et al., 2015a; Singla et al., 2015, 2016a,b; Chibber et al., 2017; Leung et al., 2018). Recent animal studies in chickens have shown that liposome encapsulated *Salmonella* phages were significantly more stable upon exposure to stomach acid and showed longer intestinal retention times in comparison with free phages and this resulted in better treatment outcomes (Colom et al., 2015). Liposome encapsulated *K. pneumoniae* phage delivered via intraperitoneal injection remained in the systemic circulation of mice longer than the corresponding free phages (Singla et al., 2015). Liposomal nanoparticles (NPs) may be able to penetrate deep into the intestinal mucosa to reach infection sites, thereby improving the efficacy of phage therapy by targeting pathogenic bacteria residing in these difficult to access niches (Takeuchi et al., 2005). The residence time of NPs has been found to be longer compared to larger particles. For instance, chitosan coated sub-micron liposomes showed longer residence times in the GI tract than larger multilamellar vesicles attributed to their high penetration ability into the mucosa (Takeuchi et al., 2005; Thirawong et al., 2008).

The aim of this study was to investigate the use of a novel co-flow microfluidic glass capillary device for the encapsulation of bacteriophages in sub-micron sized liposomes. Previous studies have typically employed a thin-film hydration method for liposome preparation which does not afford precise control over the resulting liposome size and phage encapsulation. The effects of lipid composition, phage titer and experimental procedures related to encapsulation of two model phages, an *E. coli* T3 podovirus and a myovirus *Staphylococcus* phage K, have been investigated.

MATERIALS AND METHODS

Bacteria and Phage Strain and Propagation

Bacterial host strains used were *S. aureus* ATCC 19685 and *E. coli* ATCC 11303 strain B. Both strains were sourced from LGC standards, United Kingdom (UK). *S. aureus* bacteriophage K ATCC 1985-B1 (family *Myoviridae*) and *E. coli* bacteriophage ATCC® 11303-B3 (family *Podoviridae*, T3) were also sourced from LGC standards, UK.

S. aureus bacterial host strain and phage were propagated in liquid culture using Brain Heart Infusion (BHI, Oxoid, UK). Luria Broth (LB, Oxoid, UK) was used to grow *E. coli.* For *S. aureus* phage propagation, a single colony from a streaked overnight culture on a BHI agar plate was used to inoculate fresh BHI broth and left shaking overnight at 37°C. The culture was diluted to O.D. 0.05 and regrown to log phase between 0.2 and 0.3 O.D. ($\lambda = 600$ nm) for all phage work. To evaluate actual MOI a 10 μl sample was withdrawn and serially diluted to measure the CFU/ml of the sample at the point prior of addition of a known quantity of phage. Previously, growth curves were measured where both the O.D. and corresponding CFU/ml measurements were obtained under identical growth conditions; the measurements were reliably repeatable (data not shown). The correspondence between growth curve CFU/ml and O.D. values gave us confidence that using O.D. values between 0.2 and 0.3 for both *S. aureus* and *E. coli* corresponded to $\sim 10^8$ CFU/ml prior to phage addition. At this point bacteriophages of known titer were added to the culture at a multiplicity of infection (MOI) of ∼0.01. Once the culture had cleared (∼6 h later) the lysate was centrifuged at 2,000 *g* for 15 min at 4°C and the supernatant filtered using a 0.22 μm pore size in-line syringe filter (Millipore, USA). Hundred kilo Daltons of MWCO tangential flow ultrafiltration cassettes (Merck Millipore, UK) were used for exchange of lysate media with SM buffer (50 mM of Tris-HCl, pH of 7.5, 100 mM NaCl, 10mM $MgSO_4$, all chemicals purchased from Fisher Scientific, UK) and if needed to concentrate the phage titer. All phage samples were stored in SM buffer at 4°C until further use.

To titer the phage samples, phage solutions were serially diluted and spotted (six replicates) on a double layer agar plate (Adams, 1959). The plate was dried near a flame and then incubated overnight at 37°C. On the following day plaques were counted to determine the phage titer and expressed as plaque forming units PFU ml $^{-1}$.

Reagent Chemicals

Phospholipid DSPC (1,2-distearoyl-sn-glycero-3-phosphocholine) was purchased in dry powder form from BACHEM (Bubendorf, Switzerland) and was used without any further purification. Cholesterol ≥99%, Chloroform anhydrous ≥99%, Isopropanol anhydrous 99.5%, and Triton X-100 were purchased from Sigma-Aldrich, UK. Ethanol 99.5% (extra dry) was purchased from Fisher Scientific, UK.

Co-flow Microfluidic Device Fabrication

The co-flow microfluidic (MF) device used for liposome formation was fabricated in-house following the procedure reported earlier (Vladisavljevic et al., 2014). The main body of the MF device consisted of two coaxial borosilicate glass capillaries glued onto a microscope glass slide. To assemble the device, a round tapered-end borosilicate glass capillary (Intracel, Royston, UK) with a 1 mm outer diameter, 0.58 mm inner diameter, and 100–200 μm orifice diameter was inserted halfway into an outer square glass capillary (1 mm inner dimension, AIT Glass, Rockaway, US) and aligned (see **Figure 1**). A P-97 Flaming/Brown micropipette puller (Sutter Instrument Co., USA) was used to produce a sharp capillary tip of about 20 μm in diameter. The orifice size of inner capillary was then increased by sanding the tip against sand paper until the orifice with a required size and smooth rim was obtained. The orifice size was controlled using a Narishige's MF-830 microforge microscope (Intracel Ltd., Stephenson, UK). Two syringe needles (BD Precisionglide®, Sigma–Aldrich, O.D. 0.9 mm) and PTFE tubing (I.D. 0.8 mm) were used to deliver the organic phase and the aqueous phage solution.

Generation of Liposomes

Liposomes were produced using the MF device described above (**Figure 1**) and the method of direct co-flow alcohol injection (Vladisavljevic et al., 2014). Lipid solutions (with different DSPC:cholesterol ratios) were prepared by dissolution of lipids in chloroform in a round bottom flask. The lipids were dried using a rotary evaporator for 2 h to obtain a thin film, and subsequently further dried overnight under vacuum. Isopropanol (IPA) was used to solubilize the film of lipids to a final concentration of 10 mg ml^{-1}. The organic lipid solution and the aqueous buffer solution were delivered, respectively, through the inner tapered round capillary and the outer square capillary by means of Vici Model M6 microfluidic pumps (Valco Instruments Co. Inc.,). The flow rates of the organic phase, Q_o and the aqueous phase, Q_a were adjusted to control the degree of hydrodynamic focusing and the width of the central stream, thus controlling the IPA/buffer micromixing process. The flow rate ratio ($FRR = Q_a:Q_o$) between the outer aqueous phase and the inner organic phase of 2:1 was used. The MF device was immersed in a water bath and allowed to reach thermal steady state under experimental conditions to ensure the experiments were performed under constant temperature. The IPA solution was filtered through 0.1 μm PVDF syringe filters (Fisher Scientific, UK) prior to pumping through the MF device. Liposomes were collected in sterile glass vials (Fisher Scientific, UK).

Nanoencapsulation of Bacteriophage in Vesicles

Bacteriophages were encapsulated in liposomes as per the procedure outlined above. Purified concentrated bacteriophages in SM buffer were prepared at titers >10^{11} PFU/ml. This concentrated phage stock was diluted to the appropriate working concentration by mixing with SM buffer prior to use in the MF device if lower concentrations of phage were used for encapsulation (working concentrations were varied as needed in the range 10^{9}-10^{10} PFU/ml). The aqueous phage solution was delivered through the outer capillary, while the organic lipid solution was injected through the inner capillary.

Determination of Encapsulated Bacteriophage K Titers

Separation of Free *S. aureus* Phage K From Liposome Suspensions

The *S. aureus* phage K product stream collected from the MF device containing a mixture of free and encapsulated phages was dialyzed (Visking Dialysis Membranes, Molecular Weight Cut-off 3,500 Da) overnight against SM buffer (pH 7.5) to remove residual isopropanol. Free K phages were separated from liposomes using a 0.22 μm MidGee hoop ultrafiltration hollow fiber tangential flow cartridge with a 1 ml hold-up volume (GE Healthcare, UK). The membrane flux was 2 l/m^2.h and run for 8 h until no further change in retentate phage titer was recorded. The liposomes were retained in the retentate and free phage removed in the permeate.

Removal of Liposome Bound *S. aureus* Phage K

To evaluate the binding of free K phages to liposomes, empty liposomes (formulation described previously) at a concentration of 10^{10} liposomes/ml were gently mixed with phage K solution (final concentration in liposome solution ~10^{10} PFU/ml). The total volume was 1 ml. The empty liposomes were left in contact with K phages for 15 min at either 4, 25, or 37°C to allow the phages to adsorb to the liposomes. Liposomes were separated from unbound free phages by centrifugation at 13,000 g for 3 min and phage titer in the supernatant was measured using double overlay plaque assay technique.

To evaluate the inactivation of liposome bound phages, empty liposomes were left in contact with K phages for 15 min at 37°C to allow the phages to adsorb to the liposomes (as described above). The solution was then dialyzed against SM buffer (pH 2.75) for 60 min. The solution was subsequently neutralized with NaOH (0.1 M) followed by measurement of the phage titer by double overlay plaque assay technique. All phages were rendered unviable.

Inactivation of phage K adsorbed to the liposome bilayer membrane was undertaken to evaluate the encapsulated phage K titer. Liposomes containing K phages were exposed to pH 2.75 to inactivate the liposome adsorbed phages. Phage K were prepared in a pH 5.5 SM buffer and were encapsulated using the microfluidic device as per the procedure described above. The lower pH of the buffer was used to reduce the proton concentration gradient and therefore the proton flux across the membrane to minimize pH change within the liposome compartment (Deamer, 1987). Encapsulation at pH 7.5 was found to result in complete inactivation of phage K in the liposomes exposed to pH 2.75 hence lowering of the internal pH to pH 5.5 was undertaken which resulted in viable phage recovery. Phage K titer was stable over a period of 24 h in pH 5.5 buffered solution. Phage K was completely inactivated (10 log reduction) at pH 4 (data not shown).

Free phage K (titer ~10^{10} PFU/ml) was dialyzed against SM buffer (pH 2.75) for 60 min. The solution was subsequently neutralized with NaOH (0.1 M) followed by measurement of the

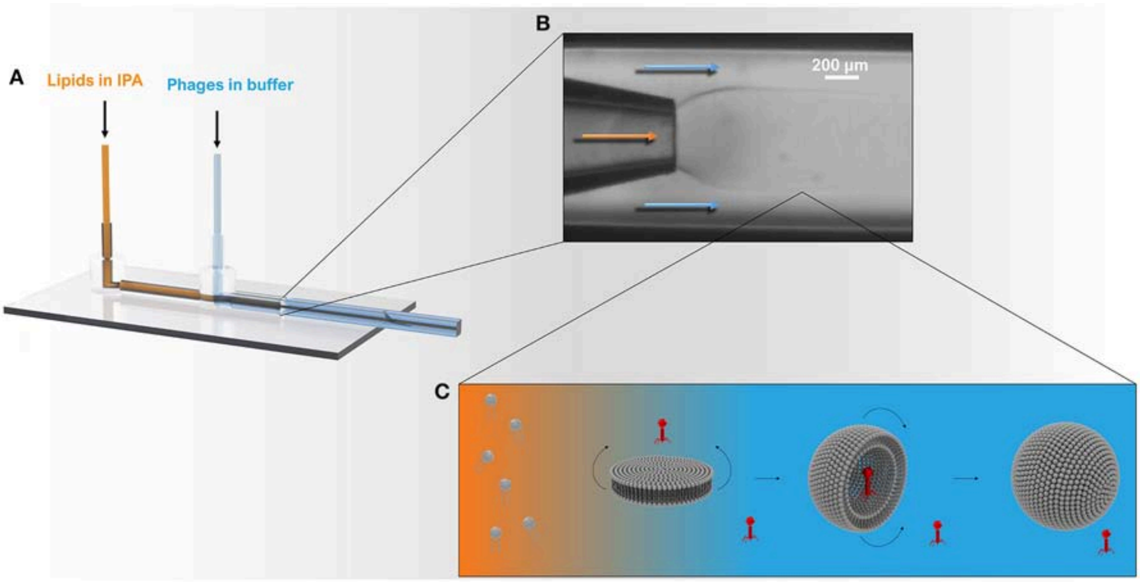

FIGURE 1 | Schematic showing the microcapillary micromixing device for the production of liposomes. **(A)** 3D model of the co-axial glass capillary device. Solutions were pumped using two microfluidic pumps using a total flow rate of ∼1 ml h^{-1} and a flow rate ratio (FRR) of aqueous to organic phase (Q_a:Q_o) of 2:1. **(B)** The round capillary was inserted into a square capillary that delivered the aqueous phase containing phages. The internal round capillary delivered the lipid dissolved in IPA solution. **(C)** Once the organic phase mixes with the aqueous phase, the phospholipids experience a highly polar environment that leads to self-assembly of lipids into bilayer discs. The latter grow in the radial direction by collision with other discs or through addition of phospholipid molecules from solution. When the disc bending energy is overcome by the energy gain when the edge around the bilayer disc is removed, the planar bilayer closes upon itself resulting in a spherical structure entrapping the surrounding solution and any phages in the vicinity of the bilayer.

phage titer by double overlay plaque assay technique. All free phages were rendered unviable.

The liposome samples containing encapsulated phages was dialyzed against SM buffer (pH 2.75) for 60 min, subsequently neutralized with NaOH (0.1 M) followed by measurement of the phage titer by double overlay plaque assay technique to ensure that all remaining free phages were rendered unviable. The pH in the dialysis bag was measured and attained at pH 2.75 within 30 min. Encapsulated phages were then released by disrupting the liposomes with Triton X-100 according to a previously described protocol (Patra et al., 1998). The final concentration of both Triton X-100 and $(NH_4)_2SO_4$ in the liposomal dispersion was 5 mM. The sample was left in a water bath at 40°C for 1 h and the phage titer after disruption of the liposomes was assessed by plaque assay. We found that at 40°C there was no change in phage titer for both phage K and T3 phages (data not shown).

Determination of Encapsulated Bacteriophage T3 Titers

Separation of Free *E. coli* T3 Phages From Liposome Suspensions

E. coli T3 bacteriophages were encapsulated in liposomes as per the procedure outlined above. The titer of phages in the liposome collection vial was evaluated to give an indication of the inactivation of T3 phages due to exposure to IPA. Free T3 phages were separated from liposomes by centrifugation at 9,000 × *g* for 5 min. The liposome pellet was resuspended in SM buffer at pH 7.5, this procedure was repeated three times to remove free T3 phages and titer of phages measured. Encapsulated phages were then released by disrupting the liposomes with Triton X-100 according to a previously described protocol.

To evaluate the effect of phage T3 titer on encapsulation yield, three different initial titers of phage T3 (10^9, 10^{10}, 10^{11} PFU/ml) were used for encapsulation. The process of encapsulation was identical to the method described above. Following separation of free phages from liposomes by centrifugation (details above), encapsulated T3 phages were released by disrupting the liposomes with Triton X-100 (described above) and encapsulated phage titer was assessed by plaque assay.

Characterization

Liposome Size and Size Distribution

A NanoSight LM10 (Malvern Instruments Ltd., UK) using nanoparticle tracking analysis (NTA) was used to determine the average size and size distribution of both liposomes and bacteriophages. NTA measurements were performed in a sample chamber equipped with a 640 nm laser to track the NPs. Typically, a 10 µl aliquot was taken from each sample and diluted 10^2-10^3 fold in order to achieve a particle concentration of 10^7-10^{10} particles ml^{-1}. The sample was injected into the sample chamber using a sterile syringe and sample flow was maintained through the chamber until all air bubbles were removed. The temperature was registered with a thermometer (RTD Pt100, OMEGA, UK) and temperature correction was carried out. The software used for capturing and analyzing the data was NTA 3.0 (Malvern Instruments Ltd., UK). Data for each sample was captured over a period of 60 s and each measurement was repeated five times. The focus was set to achieve a uniform perfect spherical particle view. Before capturing the video, the camera had to set-up to ensure all the particles in the sample were clearly visible with no more than the 20% saturation. The single gain mode was used throughout the whole measurement process. Statistical analysis was carried out using the NTA software.

Cryo-Transmission Electron Microscopy (Cryo-TEM)

An 8 μl aliquot of sample was pipetted onto a carbon coated copper grid (HC300Cu, Holey Carbon film on Copper 300 mesh, EM Resolutions, UK). Excess liquid was blotted away with filter paper (Whatman number 1) and the grid was plunge-frozen in a liquid mixture of ethane/propane cooled by liquid nitrogen. The sample was then kept at liquid nitrogen temperatures throughout the analysis. TEM images were taken on a JEOL 2200FS TEM at 200 keV using a Gatan K2 Summit and Gatan 914 cryo-holder.

RESULTS

Increasing the concentration of added cholesterol in the liposome formulation resulted in an increase in the liposome mean size and broadening of the size distribution (**Figure 2A**). NTA measurements indicated that the mean size of the liposomes increased with the amount of added cholesterol from 134 ± 13 nm for pure DSPC, to 206 ± 28 nm for a DSPC:cholesterol molar ratio of 5:1 and finally 301 ± 32 nm for a DSPC:cholesterol molar ratio of 1:1.

The morphology and size of phage T3 (*Podoviridae* family; phage dimensions ∼65 nm) and phage K (*Myoviridae* family, capsid head ∼80 nm and phage tail length ∼200 nm) were visualized using cryo-TEM (**Figure 3**). Concentrated purified phages in SM buffer were initially prepared at high phage titers of $\sim 10^{10}$ PFU ml^{-1} on the premise that there would be an increasing likelihood of phage encapsulation in liposomes resulting in higher phage encapsulation yield, but high phage titers promoted phage aggregation. Phage aggregation into larger clusters was observed for T3 at relatively low phage concentrations, as low as 10^7 PFU ml^{-1}. However, phage K showed noticeable aggregation only when phage titers were $\sim 10^{10}$ PFU ml^{-1} (**Figure 3**). T3 phages were more susceptible to aggregation due to the compact shape of their tail-free heads. Phage K began to aggregate only at high concentrations due to steric hindrance imposed by the long tails of these phages.

The clusters of both phages were found to be stable at high phage concentrations irrespective of ionic strength of the solution, since the presence of various salts at different concentrations did not affect the size of the clusters (data not shown). Dilution of phages resulted in a reduction in the average cluster size suggesting the aggregation process was reversible (**Figure 3**). The average size of phage clusters is dictated by the dynamic equilibrium between the rate of aggregation due to attractive Van der Waals forces acting between the phages and the rate of disaggregation due to their thermal motion. The rate of phage aggregation increases with an increasing rate of phage collisions in the solution, which is proportional to the phage concentration. Therefore, phages in more concentrated solutions are more prone to aggregation. The size of the aggregates formed at high phage concentrations was similar to the average size of the liposomes formed using the microfluidic device thereby limiting the likelihood of phage encapsulation in the formed liposomes. We found increasing the T3 phage titer did not yield correspondingly higher titers of encapsulated phages in liposomes (discussed later).

The morphology and structure of the liposome-encapsulated phages were visualized using cryo-TEM (**Figure 4**). The liposomes were typically found to be unilamellar with a high proportion of empty liposomes and large numbers of unencapsulated phages (**Figure S1**). Unilamellar vesicles are usually prepared using significant energy inputs supplied by sonication or extrusion through a membrane at high pressure. Here, unilamellar vesicles were formed using a low energy method. The thickness of the bilayer membrane on cryo-TEM images is 4–5 nm, which corresponds to the thickness of the DSPC bilayer ∼4.2 nm estimated from small angle neutron and X-ray scattering data (Kučerka et al., 2011).

Due to the relatively large head and long tail, phage K were found encapsulated only in large liposomes (∼500 nm or bigger) which were formed using DSPC:cholesterol molar ratio of 5:1. Encapsulated liposomes contained typically one and sometimes two phages per liposome (**Figure 4A**). Verification of the encapsulation of phage K within the liposome was achieved through tilting of the sample during observation using tomography and reconstruction of the three dimensional structure of the liposome encapsulated phage (tomography reconstruction and extended looped video provided as **Supplementary Materials**). The tomography image shows layer-by-layer reconstruction of phage K located within the liposome. Multiple phage K tails were observed to frequently interact with the lipid bilayer and bind to the outside wall of the fully formed liposomes as well as lipid bilayer fragments (**Figures 4B,C**). Schematic representations of encapsulated and externally bound phages are also shown (**Figures 4A.1–C.1**).

Liposome suspensions containing encapsulated phage K prepared using the formulation with a DSPC:cholesterol molar ratio of 5:1 were tittered for free phages before [sample mean 2.1×10^7 PFU/ml, 95% Confidence Interval (CI) 1.1×10^7-3.2×10^7 PFU/ml] and after disruption of the liposomes (sample mean 4×10^7 PFU/ml, 95% CI 2.1×10^7-5.9×10^7 PFU/ml) following treatment with Triton X-100 to disrupt the liposomes (**Figure 5A**). Disruption of the liposomes did not result in a statistically significant change in measured phage titers ($p = 0.068$). The phages remained viable following treatment with Triton X-100 (this was also the case for T3 phages, data not shown). Liposome suspensions containing free and encapsulated K phages were then exposed to pH 2.75 to inactivate free and liposome bound phages. Acid exposure of liposomes (containing K phages at pH 5.5) resulted in a significant reduction in phage titer (sample mean 2.6×10^4 PFU/ml, 95% CI 1.3×10^4-4×10^4 PFU/ml). Acid exposed liposomes were subsequently disrupted with Triton X-100 to release any viable K phages remaining inside the liposomes. Disruption of liposomes resulted in a significant

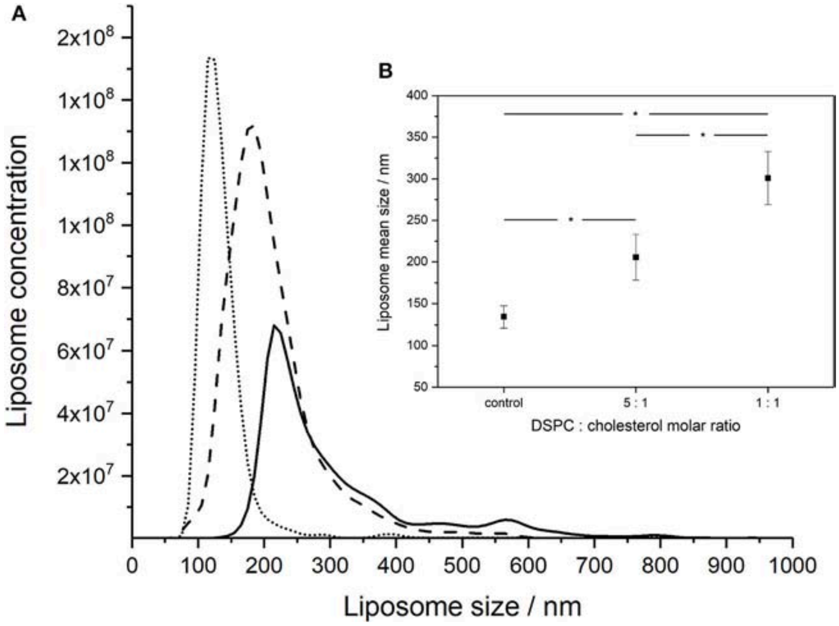

FIGURE 2 | NanoSight measurements of the size distributions of liposomes formed using different DSPC:cholesterol molar ratios: **(A)** DSPC only (dotted line), 5:1 DSPC:cholesterol molar ratio (dashed line), and 1:1 DSPC:cholesterol molar ratio (solid line). Liposomes were prepared at room temperature (~20°C) using aqueous to organic phase volumetric flow rate ratio FRR of 2:1 and the total volumetric flow rate of ~1 ml h^{-1}. **(B)** Inset showing average mean sizes, error bars indicate one standard deviation. *Indicates significance ($p < 0.05$) using 2-sample *t*-test.

increase in phage titer (sample mean 2.4×10^5 PFU/ml, 95% CI 1.8×10^5-3×10^5 PFU/ml). The 95% CI for the increase in phage titer upon liposome disruption was 1.5×10^5-2.7×10^5 PFU/ml which is indicative of the yield of encapsulated phage K in the liposomes. It was not possible to quantify the loss (if any) in titer of encapsulated phage K due to acid exposure. When the same experiment was carried out with the pH inside the liposomes kept at pH 7.5 and liposomes subsequently exposed to pH 2.75, no viable phages were recovered. Encapsulating phage K using a pH 5.5 buffer allowed us to have a lower pH inside the liposome which reduced the pH gradient across the liposome membrane bilayer to less than ΔpH 3 and hence reduced the driving force for proton flux (Deamer, 1987). A reverse of this approach has been used previously to load liposomes with drugs in response to transmembrane pH gradients (Mayer et al., 1990). The reduction in phage titer following acid exposure to pH 2.75 may be attributed to inactivation of both free phages and phages externally bound to the liposomes which was confirmed separately (**Figure 5C**).

Empty liposomes prepared using the formulation with a DSPC:cholesterol molar ratio of 5:1 were gently mixed with free phage K for 15 min at 4, 25, and 37°C. A considerable amount of phages adsorbed to the outer surface of empty liposomes resulting in a significant decrease in phage titer of the supernatant for all investigated temperatures (**Figure 5B**). Exposure to pH 2.75 of the K phages bound to empty liposomes resulted in no recovery of viable phages (**Figure 5C**), suggesting that K phages bound to the outside of the liposomes were not protected from acid exposure and were inactivated. In addition, free phages present in solution without the presence of any liposomes were also completely inactivated after exposure to pH 2.75 (**Figure 5C**). On the other hand, phages truly encapsulated in liposomes were able to withstand acid exposure. This procedure provided a means of discriminating between free phages, phages externally bound to liposomes and phages actually encapsulated within the liposomes.

The encapsulation process resulted in a significant reduction in phage T3 titer upon exposure to IPA during the liposome formation process (**Figure 6A**). The phage titer fell from 2.4×10^9 PFU/ml (95% CI 1.1×10^9-3.7×10^9 PFU/ml) to 8.7×10^7 PFU/ml (95% CI 4.5×10^7-1.3×10^8 PFU/ml). Removal of free phages by centrifugation and resuspension in SM buffer resulted in phage T3 titer reduction from 8.7×10^7 to 2.1×10^7 PFU/ml (95% CI 1.3×10^7-2.8×10^7 PFU/ml). Disruption of the liposomes with Triton X-100 resulted in a significant increase in phage titer to 8.1×10^7 PFU/ml (95% CI 3.1×10^7-1.3×10^8 PFU/ml) (**Figure 6A**). The difference in means was 6.1×10^7 PFU/ml (95% CI 1×10^7-1.1×10^8 PFU/ml) which is an estimation of the phage T3 encapsulation yield.

Increasing free phage T3 titers used in the MF device for encapsulation from $\sim 10^9$ to $\sim 10^{10}$ PFU/ml resulted in a significant increase in encapsulated phage yield from 8.1×10^7 PFU/ml (95% CI 3.1×10^7-1.3×10^8 PFU/ml) to 3.5×10^9 PFU/ml (95% CI 1.9×10^9-5.2×10^9 PFU/ml) (**Figure 6B**). Increasing the free phage T3 titers further to $\sim 10^{11}$ PFU/ml resulted in a lower encapsulated phage yield with sample mean falling to 1.5×10^9 PFU/ml (95% CI 7.5×10^7-2.8×10^9 PFU/ml)

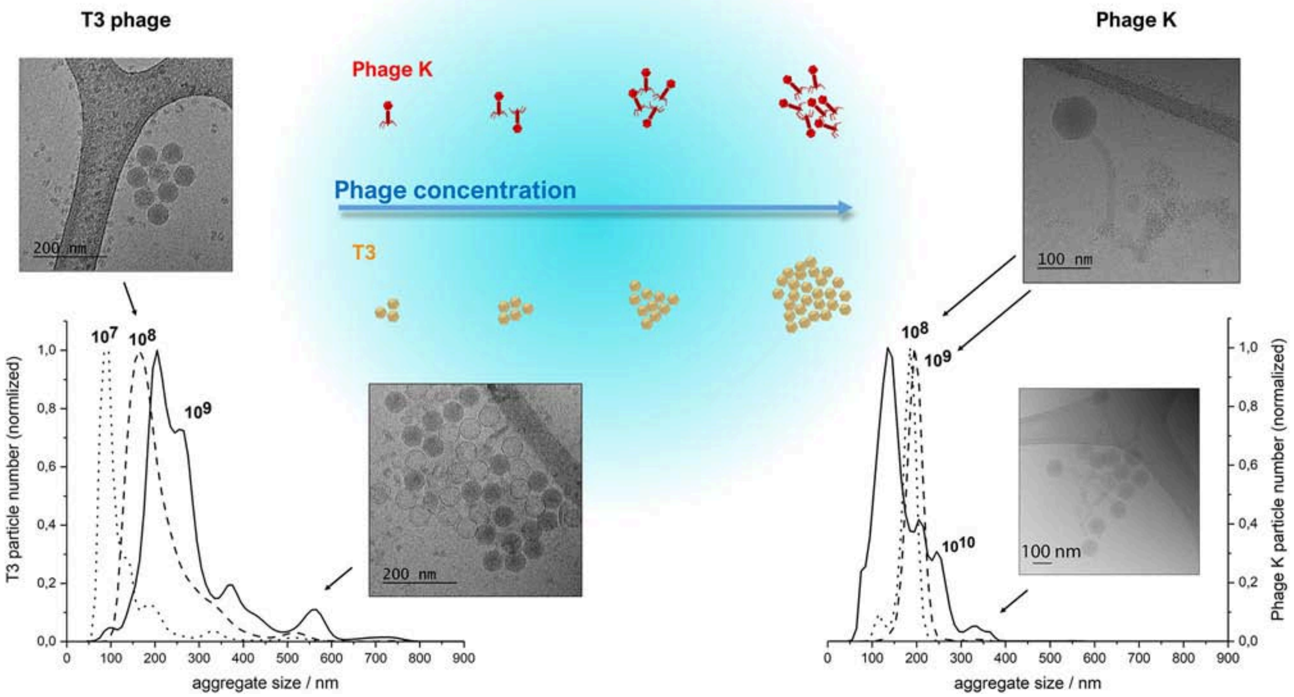

FIGURE 3 | NanoSight NTA measurements of size distributions of purified T3 phage (left) and phage K (right), respectively, at 10^7, 10^8, 10^9 and 10^8, 10^9, 10^{10} PFU/ml**.** Insets show CryoTEM images of observed phage aggregates and the schematized depiction of phage cluster sizes as a function of phage titer. Some heads on the lower CryoTEM images are transparent (empty), probably due to denaturation of DNA during encapsulation or loss of DNA during CryoTEM imaging.

(**Figure 6B**). The encapsulated phage yield was lower for the sample prepared using higher phage titer of $\sim 10^{11}$ PFU/ml compared with $\sim 10^{10}$ PFU/ml.

DISCUSSION

Micromixing of the lipid-containing organic phase with the aqueous buffer resulted in self-assembly of lipid bilayers in the collection channel of the MF device. This process is driven by hydrophobic effects in order to minimize entropically unfavorable interactions between the hydrophobic acyl chains and the surrounding aqueous buffer phase (Carugo et al., 2016). The lipid-in-alcohol stream was sheathed by a coaxial aqueous stream resulting in hydrodynamic flow focusing of the core fluid (Vladisavljevic et al., 2014). Microfluidic flow focusing permitted mixing of the two phases under low Reynolds number flow conditions (Re ∼1) and diffusion dominated mass transfer (Peclet number <1) resulting in controlled production of nanoscale liposomes (Jahn et al., 2004). A 3D geometry of the MF device allowed radially symmetric interdiffusion of IPA-solvated lipids, alcohol, and water across the alcohol-water interface which offers advantages including low polydispersity and higher production rates (Hood et al., 2014). The cross-sectional area of the core solution may be tuned by adjusting the orifice size of the injection capillary and the FRR of the outer (aqueous) and inner (organic) phases (Jahn et al., 2010). At low Reynolds and Peclet numbers used in this work laminar flow conditions prevailed in the downstream capillary and liposome formation was dominated by diffusion rather than advection. The microfluidic micromixing process allowed predictable and repeatable mixing across fluid interfaces and the continuous synthesis of liposomes of narrow size distributions and controlled size which could be modulated by controlling FRR, the total flow rate and composition of the lipids. The addition of cholesterol makes the assembled bilayers more rigid and therefore, more energy and time is required for their closure (Sawant and Torchilin, 2012a). Liposome formation in microchannels at low temperatures has been shown to result in larger liposomes compared with those produced under identical conditions albeit at higher temperatures (Wi et al., 2012). Increasing the proportion of organic phase to aqueous phase results in a shallower lipid concentration gradient and has previously been shown to result in larger liposomes for the same formulation (Jahn et al., 2010; Leung et al., 2018). We employed a FRR of 2:1 and a low total flow rate of ~ 1 ml h^{-1} which resulted in liposome sizes of the same order as those reported elsewhere under similar hydrodynamic conditions (Wi et al., 2012; Carugo et al., 2016; Leung et al., 2018).

Evidence of disc-like non-equilibrium lipid aggregates in a region close to the immediate mixing zone of the two phases

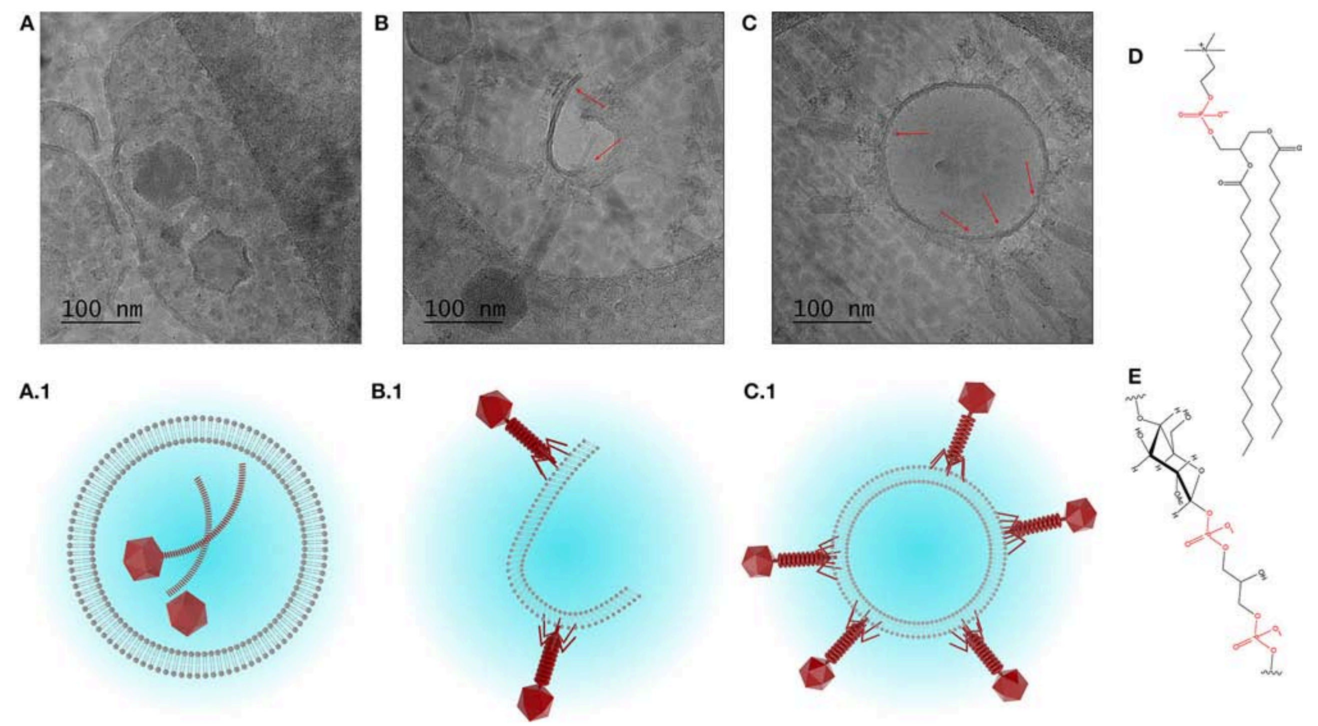

FIGURE 4 | Cryo-TEM images showing **(A)** encapsulation of phage K, and **(B,C)** interaction between phage K tails and the outer leaflet of the bilayer membrane of formed liposomes (DSPC:cholesterol molar ratio was 5:1), some tails look contracted. **(A1–C1)** Schematized depiction showing encapsulation of phage K within the liposome (favored outcome) and interaction of phage K with the outer surface of unilamellar liposome membrane and lipid bilayer (unfavorable outcome). **(D)** Chemical structure of DSPC and **(E)** chemical structure of teichoic acid (phosphate groups highlighted in red).

in a microfluidic channel was recently shown using cryo-ultramicrotomy and cryo-SEM (Jahn et al., 2013). Time is needed for lipid molecules to diffuse and aggregate; the concentration gradient of alcohol has a significant effect on the liposome formation process with gentle gradients (low FRR) favoring large liposome formation (Jahn et al., 2013). The closure of lipid bilayers may incidentally trap any bacteriophages in the vicinity of the enclosing lipid membrane and the number of phages encapsulated per vesicle is dictated by Poisson statistics. Parabolic velocity profile in pressure driven laminar flows results in the velocity decreasing toward the capillary wall which affects axial and radial concentration profiles and the distribution of liposome sizes formed. A number of factors may be responsible for the observed polydispersity of the liposomes formed (**Figure 2**). The rate of mass transfer of the lipids is affected by the velocity distribution along and across the channel resulting in variations in mixing times across and along the microcapillary affecting the size distribution of the liposomes formed. Our intention in this work was not to study these effects which have been considered in detail elsewhere (Fernandez-Puente et al., 1994; Zook and Vreeland, 2010; Carugo et al., 2016).

A number of previous studies have noted albeit briefly that encapsulation of phages in liposomes prepared using either the thin film hydration method or microfluidic micromixing resulted in empty liposomes and noted that phages were attached to the outside of the liposomes (Colom et al., 2015; Nieth et al., 2015a; Leung et al., 2018). However, to the best of our knowledge none of these studies went further to quantify and decouple the proportion of phages truly encapsulated in the liposomes and those that were externally bound to the lipid membranes. Previous studies have used high titers of phages (10^{10}-10^{11} PFU ml^{-1}) in order to achieve high reported yields of what are thought to be "encapsulated phages" (Colom et al., 2015; Chadha et al., 2017; Leung et al., 2018). However, consideration needs to be given to phage aggregation, which is more significant at higher phage concentrations. The resulting phage clusters may be too big to be physically encapsulated within formed liposomes. We found increasing the phage T3 titer from 10^9 to 10^{10} PFU ml^{-1} initially increased the encapsulated phage yield. Increasing the phage titer further to 10^{11} PFU ml^{-1} resulted in lowering of the phage T3 encapsulation yield (**Figure 6B**). This may be attributed to the formation of large phage T3 aggregates at high phage titers that are either too big to encapsulate in the liposomes or diffuse too slowly and are not in the vicinity of closing bilayers and therefore are not trapped in the liposomes (**Figure 3**). Other studies have reported phage aggregation and formation of cluster rosettes (Serwer et al., 2007; Bourdin et al., 2014). Methods for dispersion of phage aggregates may help in this regard (Szermer-Olearnik et al., 2017).

Our results suggest that the actual encapsulation yield of *S. aureus* K phages inside the liposomes may be considerably overestimated unless externally bound phages are accounted

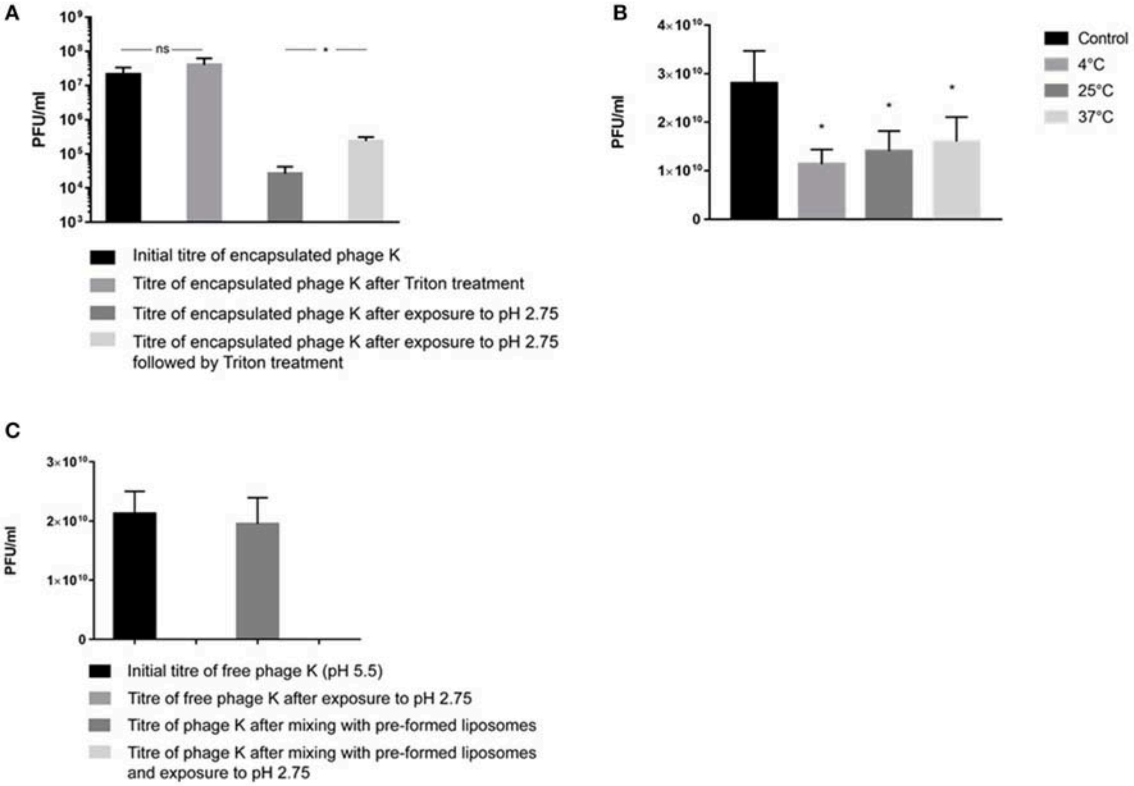

FIGURE 5 | (A) *S. aureus* phage K encapsulation in DSPC:cholesterol liposomes. Phages were encapsulated at FRR of 2:1 at room temperature. Phage titer of liposome encapsulated phages prior to and after acid exposure at pH 2.75 (with and without Triton X-100 disruption). *Indicates significance ($p < 0.05$) using 2-sample *t*-test. **(B)** The titer of free phages in the supernatant before and after incubation with empty liposomes at 4, 25, and 37°C for 15 min. After incubation, liposomes were separated by centrifugation at 13,000 × *g* for 3 min and the phage titer in the supernatant was measured. The difference in the titer occurred due to phage adsorption onto the outer leaflet of bilayer membranes. The maximum phage adsorption was observed at 4°C, which caused the highest phage titer reduction in the supernatant at 4°C. The adsorption was still highly significant at 37°C. *Indicates significance ($p < 0.05$) using 2-sample *t*-test of each sample compared with controls. **(C)** pH stability for free (non-encapsulated) phage K exposed to pH 2.75 and free phage K incubated with pre-made empty liposomes for 15 min at 37°C and subsequently dialyzed at pH 2.75 for 60 min. Error bars represent one standard deviation.

for. *S. aureus* phage K may bind to the lipid bilayers due to electrostatic interactions between negatively charged phosphate groups on the phospholipid head (shown in red in **Figure 4D**) and positively charged residues on the tail fibers of the phages. This interaction resembles a reversible interaction between phages and their hosts via wall teichoic acids, e.g., glycopolymers present in Gram-positive bacterial cell membranes (**Figure 4E**) (Xia et al., 2011). The reported encapsulation efficiencies have ranged between 40 and 80% which for large tailed phages may be attributed to phages externally bound to the lipid bilayers (Colom et al., 2015; Chadha et al., 2017; Leung et al., 2018). The adsorption process is reversible leading to a dynamic equilibrium between bound and unbound phages (Baptista et al., 2008; Xia et al., 2011). In a previous study, a 60 min exposure of liposome encapsulated *Salmonella* phages (prepared using thin film hydration technique) to simulated gastric fluid (pH 2.8) resulted in a significant reduction in phage titer (by 4–5 orders of magnitude) which mirrors the results reported here (**Figure 5A**) (Colom et al., 2015). In an effort to minimize acid induced phage inactivation within the internal liposome compartment we reduced the transmembrane pH gradient between the liposome core and the external solution to minimize proton permeability across the DSPC-cholesterol lipid membrane (Biloti et al., 2003). Phage encapsulated liposomes exposed to pH 2.75 showed a significant fall in phage titer to 10^4 PFU ml^{-1} with a statistically significant increase of ~1 log in phage K titer upon liposome disruption with Triton X-100 indicating that some or perhaps all encapsulated phages survived the acid treatment. The encapsulated phage K titer was however quite low $\sim 10^5$ PFU ml^{-1}. Following liposome formation external phages may subsequently bind to the outer liposome membrane. Cryo-TEM images suggested that only one or two phages were encapsulated in each liposome. A 1 log increase in phage titer upon liposome disruption suggests that removal of free phages and inactivation of bound phages followed by disruption of the liposomes provides a means for evaluating the titer of encapsulated phages.

We only observed phage K bound to the outside of the formed liposomes and not when they were encapsulated inside the aqueous core. This may be due to the rate of

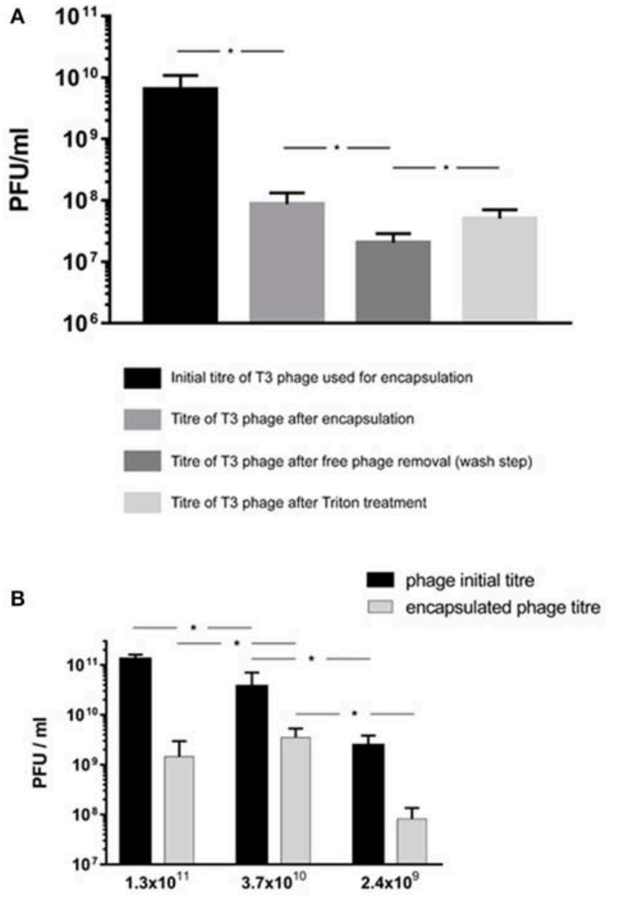

FIGURE 6 | *E. coli* T3 phage encapsulation in DSPC:cholesterol liposomes. T3 phages were encapsulated at FRR of 2:1 at room temperature. Free phages were separated by centrifugation for 10 min at 13,000 × g and re-suspended in SM buffer, the process was repeated three times to remove unencapsulated phages. Liposomes were disrupted with Triton X-100 and phage titer assessed by plaque assay. **(A)** Phage T3 titers following encapsulation, after removal of unencapsulated free phages (following three wash steps) and after liposome disruption with Triton X-100. **(B)** Phage encapsulation yield using different initial phage titers and after encapsulation, free phage removal by centrifugation (as above) and then liposome disruption with Triton X-100. *Indicates significance ($p < 0.05$) using 2-sample *t*-test.

formation of liposomes being much faster than the rate of interaction of phage K with the formed bilayer structures. The considerably faster interdiffusion of small molecules e.g., IPA and water may result in liposome formation in a zone close to the organic-aqueous interface. We hypothesize that due to their considerably larger size and hence much slower diffusion, phages may not be able to get near the vicinity of a large majority of rapidly forming bilayer discs in time to be encapsulated when the bilayers close resulting in low phage encapsulation yield. Aggregation of phages even at low phage titers compounds this effect making it problematic. Future efforts need to consider strategies to overcome these inherent difficulties if microfluidic approaches are to be successfully employed to encapsulate large entities such as bacteriophages in nanostructured materials.

CONCLUSIONS

We have demonstrated the controlled microfluidic production of liposomes with a mean size in the range of 100–300 nm. The size of the liposomes may be controlled by incorporating different amounts of cholesterol in a formulation containing the phospholipid DSPC and regulating the hydrodynamic conditions within the microfluidic micromixing device, in particular the FRR of aqueous to organic phases. We show that the yield of T3 encapsulated phages may be adversely affected by aggregation which limited the maximum attainable yield of encapsulated T3 phages ∼10^9 PFU/ml. *S. aureus* phage K was found to adsorb to the external lipid membranes resulting in large numbers of phages bound to the outside of the formed liposome instead of being trapped inside them. We developed a method that permitted inactivation of liposome-bound K phages whilst retaining the activity of phages encapsulated within the liposomes. This allowed estimation of the encapsulated phage K yield which was found to be low ∼10^5 PFU/ml. Inactivation of encapsulated phage K due to acid exposure cannot be ruled out and needs further work. Previous studies on tailed phage encapsulation in liposomes may therefore have overestimated the yield of encapsulated phages which may affect the efficacy of phage dose delivered at the site of infection. In the case of treatment of gastrointestinal infections externally bound phages may be inactivated due to the stomach acidity.

AUTHOR CONTRIBUTIONS

SC, DM, and FM wrote the methodology. SC and DM conceived the research, performed the formal analysis, executed the investigation and wrote the original draft of the manuscript. SB carried out the CryoTEM microscopy. DM organized the project administration and funding. DM, GV, and SB reviewed and edited the manuscript. DM and GV oversaw the supervision and resources.

ACKNOWLEDGMENTS

The authors would like to acknowledge EPSRC support for this work (Grant no. EP/M027341/1) Tackling Antimicrobial Resistance: An Interdisciplinary Approach. We acknowledge the University of Warwick Advanced Bioimaging Research Technology Platform supported by BBSRC ALERT14 award BB/M01228X/1.

SUPPLEMENTARY MATERIAL

The Supplementary Material for this article can be found online at: https://www.frontiersin.org/articles/10.3389/fmicb.2018.02172/full#supplementary-material

Figure S1 | Cryo-TEM images showing non-encapsulated *S. aureus* phage K and *E. Coli* T3 phages and empty unilamellar liposomes. **(a)** Phage K (yellow arrow) and a unilamellar liposome (red arrow) **(b)** T3 phages (yellow arrows), some of them with empty heads and unilamellar liposomes (red arrows). Images presented for formulation (DSPC:cholesterol molar ratio was 5:1), FRR 2:1.

Video S1 | Visualization of *S. aureus* phage K encapsulation in liposomes by Cryo-TEM tomography - extended video.

Video S2 | Visualization of *S. aureus* phage K encapsulation in liposomes by Cryo-TEM and tomography reconstruction.

REFERENCES

Abedon, S. T. (2009). Kinetics of phage-mediated biocontrol of bacteria. *Foodborne Pathog. Dis.* 6, 807–815. doi: 10.1089/fpd.2008.0242

Abedon, S. T., Kuhl, S. J., Blasdel, B. G., and Kutter, E. M. (2011). Phage treatment of human infections. *Bacteriophage* 1, 66–85. doi: 10.4161/bact.1.2.15845

Adams, M. H. (1959). *Bacteriophages*. New York, NY: Inter-Science Publishers.

Alisky, J., Iczkowski, K., Rapoport, A., and Troitsky, N. (1998). Bacteriophages show promise as antimicrobial agents. *J. Infect.* 36, 5–15. doi: 10.1016/S0163-4453(98)92874-2

Allen, H. K., Trachsel, J., Looft, T., and Casey, T. A. (2014). Finding alternatives to antibiotics. *Ann. N. Y. Acad. Sci.* 1323, 91–100. doi: 10.1111/nyas.12468

Baptista, C., Santos, M. A., and São-José, C. (2008). Phage SPP1 reversible adsorption to *Bacillus subtilis* cell wall teichoic acids accelerates virus recognition of membrane receptor YueB. *J. Bacteriol.* 190, 4989–4996. doi: 10.1128/JB.00349-08

Biloti, D. N., Santana, M. H. A., and Pessine, F. B. T. (2003). Lipid membrane with low proton permeability. *Biochim. Biophys. Acta* 1611, 1–4. doi: 10.1016/S0005-2736(03)00035-X

Bourdin, G., Schmitt, B., Guy, L. M., Germond, J. E., Zuber, S., Michot, L., et al. (2014). Amplification and purification of T4-Like *Escherichia coli* phages for phage therapy: from laboratory to pilot scale. *Appl. Environ. Microbiol.* 80, 1469–1476. doi: 10.1128/AEM.03357-13

Broxmeyer, L., Sosnowska, D., Miltner, E., Chacón, O., Wagner, D., McGarvey, J., et al. (2002). Killing of *Mycobacterium avium* and *Mycobacterium tuberculosis* by a Mycobacteriophage delivered by a nonvirulent Mycobacterium: a model for phage therapy of intracellular bacterial pathogens. *J. Infect. Dis.* 186, 1155–1160. doi: 10.1086/343812

Carugo, D., Bottaro, E., Owen, J., Stride, E., and Nastruzzi, C. (2016). Liposome production by microfluidics: potential and limiting factors. *Sci. Rep.* 6:25876. doi: 10.1038/srep25876

Chadha, P., Katare, O. P., and Chhibber, S. (2017). Liposome loaded phage cocktail: enhanced therapeutic potential in resolving *Klebsiella pneumoniae* mediated burn wound infections. *Burns* 43, 1532–1543. doi: 10.1016/j.burns.2017.03.029

Chibber, S., Shukla, A., and Kaur, S. (2017). Tansferosomal phage cocktail is an effective treatment against methicillin-resistant *Staphylococcus aureus*-mediated skin and soft tissue infections. *Antimicrob. Agents Chemother.* 61, 1–9. doi: 10.1128/AAC.02146-16

Coates, A. R., Halls, G., and Hu, Y. (2011). Novel classes of antibiotics or more of the same? *Br. J. Pharmacol.* 163, 184–194. doi: 10.1111/j.1476-5381.2011.01250.x

Colom, J., Cano-Sarabia, M., Otero, J., Cortés, P., Maspoch, D., and Llagostera, M. (2015). Liposome-encapsulated bacteriophages for enhanced oral phage therapy against *Salmonella* spp. *Appl. Environ. Microbiol.* 81, 4841–4849. doi: 10.1128/AEM.00812-15

Czaplewski, L., Bax, R., Clokie, M., Dawson, M., Fairhead, H., Fischetti, V. A., et al. (2016). Alternatives to antibiotics — a pipeline portfolio review. *Lancet Infect. Dis.* 16, 239–251. doi: 10.1016/S1473-3099(15)00466-1

Dabrowska, K., Switała-Jelen, K., Opolski, A., Weber-Dabrowska, B., and Gorski, A. (2005). A review: bacteriophage penetration in vertebrates. *J. Appl. Microbiol.* 98, 7–13. doi: 10.1111/j.1365-2672.2004.02422.x

Deamer, D. W. (1987). Proton permeation of lipid bilayers. *J. Bioenerg. Biomembr.* 19, 457–479.

Denou, E., Bruttin, A., Barretto, C., Ngom-Bru, C., Brüssow, H., and Zuber, S. (2009). T4 phages against *Escherichia coli* diarrhea: potential and problems. *Virology* 388, 21–30. doi: 10.1016/j.virol.2009.03.009

Fernandez-Puente, L., Bivas, I., Mitov, M. D., and Méléard, P. (1994). Temperature and chain length effects on bending elasticity of phosphatidylcholine bilayers. *Europhys. Lett.* 28, 181–186. doi: 10.1209/0295-5075/28/3/005

Finlay, B. B. (1997). Exploitation of mammalian host cell functions by bacterial pathogens. *Science* 276, 718–725. doi: 10.1126/science.276.5313.718

Hood, R. R., DeVoe, D. L., Atencia, J., Vreeland, W. N., and Omiatek, D. M. (2014). A facile route to the synthesis of monodisperse nanoscale liposomes using 3D microfluidic hydrodynamic focusing in a concentric capillary array. *Lab Chip* 14, 2403–2409. doi: 10.1039/C4LC00334A

Jahn, A., Lucas, F., Wepf, R. A., and Dittrich, P. S. (2013). Freezing continuous-flow self-assembly in a microfluidic device: toward imaging of liposome formation. *Langmuir* 29, 1717–1723. doi: 10.1021/la303675g

Jahn, A., Stavis, S. M., Hong, J. S., Vreeland, W. N., Devoe, D. L., and Gaitan, M. (2010). Microfluidic mixing and the formation of nanoscale lipid vesicles. *ACS Nano* 4, 2077–2087. doi: 10.1021/nn901676x

Jahn, A., Vreeland, W. N., Gaitan, M., and Locascio, L. E. (2004). Controlled vesicle self-assembly in microfluidic channels with hydrodynamic focusing. *J. Am. Chem. Soc.* 126, 2674–2675. doi: 10.1021/ja0318030

Kelly, R., Zoubiane, G., Walsh, D., Ward, R., and Goossens, H. (2016). Public funding for research on antibacterial resistance in the JPIAMR countries, the European Commission, and related European Union agencies: a systematic observational analysis. *Lancet Infect. Dis.* 16, 431–440. doi: 10.1016/S1473-3099(15)00350-3

Kučerka, N., Nieh, M. P., and Katsaras, J. (2011). Fluid phase lipid areas and bilayer thicknesses of commonly used phosphatidylcholines as a function of temperature. *Biochim. Biophys. Acta Biomembr.* 1808, 2761–2771. doi: 10.1016/j.bbamem.2011.07.022

Laxminarayan, R., Duse, A., Wattal, C., Zaidi, A. K. M., Wertheim, H. F. L., Sumpradit, N., et al. (2013). Antibiotic resistance-the need for global solutions. *Lancet Infect. Dis.* 13, 1057–1098. doi: 10.1016/S1473-3099(13)70318-9

Leung, S. S. Y., Morales, S., Britton, W., Kutter, E., and Chan, H. K. (2018). Microfluidic-assisted bacteriophage encapsulation into liposomes. *Int. J. Pharm.* 545, 176–182. doi: 10.1016/j.ijpharm.2018.04.063

Lim, T. H., Kim, M. S., Lee, D. H., Lee, Y. N., Park, J. K., Youn, H. N., et al. (2012). Use of bacteriophage for biological control of *Salmonella enteritidis* infection in chicken. *Res. Vet. Sci.* 93, 1173–1178. doi: 10.1016/j.rvsc.2012.06.004

Malik, D. J., Sokolov, I. J., Vinner, G. K., Mancuso, F., Cinquerrui, S., Vladisavljevic, G. T., et al. (2017). Formulation, stabilisation and encapsulation of bacteriophage for phage therapy. *Adv. Colloid Interface Sci.* 249, 100–133. doi: 10.1016/j.cis.2017.05.014

Mayer, L. D., Tai, L. C. L., Bally, M. B., Mitilenes, G. N., Ginsberg, R. S., and Cullis, P. R. (1990). Characterization of liposomal systems containing doxorubicin entrapped in response to pH gradients. *Biochim. Biophys. Acta.* 1025, 143–151. doi: 10.1016/0005-2736(90)90091-2

Merril, C. R., Biswas, B., Carlton, R., Jensen, N. C., Creed, G. J., Zullo, S., et al. (1996). Long-circulating bacteriophage as antibacterial agents. *Proc. Natl. Acad. Sci. U.S.A.* 93, 3188–3192. doi: 10.1073/pnas.93.8.3188

Morgan, D. J., Okeke, I. N., Laxminarayan, R., Perencevich, E. N., and Weisenberg, S. (2011). Non-prescription antimicrobial use worldwide: a systematic review. *Lancet Infect. Dis.* 11, 692–701. doi: 10.1016/S1473-3099(11)70054-8

Nieth, A., Verseux, C., Barnert, S., Süss, R., and Römer, W. (2015a). A first step toward liposome-mediated intracellular bacteriophage therapy. *Expert Opin. Drug Deliv.* 12, 1411–1424. doi: 10.1517/17425247.2015.1043125

Nieth, A., Verseux, C., and Römer, W. (2015b). A question of attire: dressing up bacteriophage therapy for the battle against antibiotic-resistant intracellular bacteria. *Springer Sci. Rev.* 3, 1–11. doi: 10.1007/s40362-014-0027-x

Patra, S. K., Alonso, A., and Gon, F. M. (1998). Detergent solubilisation of phospholipid bilayers in the gel state: the role of polar and hydrophobic forces. *Biochim. Biophys. Acta* 1373, 112–118. doi: 10.1016/S0005-2736(98)00095-9

Pattni, B. S., Chupin, V. V., and Torchilin, V. P. (2015). New developments in liposomal drug delivery. *Chem. Rev.* 115, 10938–10966. doi: 10.1021/acs.chemrev.5b00046

Sarker, S. A., Sultana, S., Reuteler, G., Moine, D., Descombes, P., Charton, F., et al. (2016). Oral phage therapy of acute bacterial diarrhea with two coliphage preparations: a randomized trial in children from Bangladesh. *EBioMed.* 4, 124–137. doi: 10.1016/j.ebiom.2015.12.023

Sawant, R. R., and Torchilin, V. P. (2012a). Challenges in development of targeted liposomal therapeutics. *AAPS J.* 14, 303–315. doi: 10.1208/s12248-012-9330-0

Sawant, R. R., and Torchilin, V. P. (2012b). Multifunctional nanocarriers and intracellular drug delivery. *Curr. Opin. Solid State Mater. Sci.* 16, 269–275. doi: 10.1016/j.cossms.2012.09.001

Schooley, R. T., Biswas, B., Gill, J. J., Hernandez-Morales, A., Lancaster, J., Lessor, L., et al. (2017). Development and use of personalized bacteriophage-based therapeutic cocktails to treat a patient with a disseminated resistant *Acinetobacter baumannii* infection. *Antimicrob. Agents Chemother.* 61, 1–14. doi: 10.1128/AAC.00954-17

Serwer, P., Hayes, S. J., Lieman, K., and Griess, G. A. (2007). *In situ* fluorescence microscopy of bacteriophage aggregates. *J. Microsc.* 228, 309–321. doi: 10.1111/j.1365-2818.2007.01855.x

Singla, S., Harjai, K., Katare, O. P., and Chhibber, S. (2015). Bacteriophage-loaded nanostructured lipid carrier: improved pharmacokinetics mediates effective resolution of *Klebsiella pneumoniae*-induced lobar pneumonia. *J. Infect. Dis.* 212, 325–334. doi: 10.1093/infdis/jiv029

Singla, S., Harjai, K., Katare, O. P., and Chhibber, S. (2016a). Encapsulation of bacteriophage in liposome accentuates its entry in to macrophage and shields it from neutralizing antibodies. *PLoS ONE* 11:e0153777. doi: 10.1371/journal.pone.0153777

Singla, S., Harjai, K., Raza, K., Wadhwa, S., Katare, O. P., and Chhibber, S. (2016b). Phospholipid vesicles encapsulated bacteriophage: a novel approach to enhance phage biodistribution. *J. Virol. Methods* 236, 68–76. doi: 10.1016/j.jviromet.2016.07.002

Summers, W. C. (2001). Bacteriophage therapy. *Annu. Rev. Microbiol.* 55, 437–451. doi: 10.1146/annurev.micro.55.1.437

Szermer-Olearnik, B., Drab, M., Makosa, M., Zembala, M., Barbasz, J., Dabrowska, K., et al. (2017). Aggregation/dispersion transitions of T4 phage triggered by environmental ion availability. *J. Nanobiotechnol.* 15, 1–15. doi: 10.1186/s12951-017-0266-5

Takeuchi, H., Matsui, Y., Sugihara, H., Yamamoto, H., and Kawashima, Y. (2005). Effectiveness of submicron-sized, chitosan-coated liposomes in oral administration of peptide drugs. *Int. J. Pharm.* 303, 160–170. doi: 10.1016/j.ijpharm.2005.06.028

Tanji, Y., Shimada, T., Fukudomi, H., Miyanaga, K., Nakai, Y., and Unno, H. (2005). Therapeutic use of phage cocktail for controlling *Escherichia coli* O157:H7 in gastrointestinal tract of mice. *J. Biosci. Bioeng.* 100, 280–287. doi: 10.1263/jbb.100.280

Thirawong, N., Thongborisute, J., Takeuchi, H., and Sriamornsak, P. (2008). Improved intestinal absorption of calcitonin by mucoadhesive delivery of novel pectin-liposome nanocomplexes. *J. Control. Release* 125, 236–245. doi: 10.1016/j.jconrel.2007.10.023

Toma, I., Siegel, M. O., Keiser, J., Yakovleva, A., Kim, A., Davenport, L., et al. (2014). Single-molecule long-read 16S sequencing to characterize the lung microbiome from mechanically ventilated patients with suspected pneumonia. *J. Clin. Microbiol.* 52, 3913–3921. doi: 10.1128/JCM.01678-14

Torchilin, V. P. (2005). Recent advances with liposomes as pharmaceutical carriers. *Nat. Rev. Drug Discov.* 4, 145–160. doi: 10.1038/nrd1632

van Swaay, D., and deMello, A. (2013). Microfluidic methods for forming liposomes. *Lab Chip* 13, 752–767. doi: 10.1039/c2lc41121k

Vladisavljevic, G. T., Laouini, A., Charcosset, C., Fessi, H., Bandulasena, H. C. H., and Holdich, R. G. (2014). Production of liposomes using microengineered membrane and co-flow microfluidic device. *Colloids Surf. A Physicochem. Eng. Asp.* 458, 168–177. doi: 10.1016/j.colsurfa.2014.03.016

Wi, R., Oh, Y., Chae, C., and Kim, D. H. (2012). Formation of liposome by microfluidic flow focusing and its application in gene delivery. *Korea Aust. Rheol. J.* 24, 129–135. doi: 10.1007/s13367-012-0015-0

Wright, A., Hawkins, C. H., Änggård, E. E., and Harper, D. R. (2009). A controlled clinical trial of a therapeutic bacteriophage preparation in chronic otitis due to antibiotic-resistant *Pseudomonas aeruginosa*; a preliminary report of efficacy. *Clin. Otolaryngol.* 34, 349–357. doi: 10.1111/j.1749-4486.2009.01973.x

Xia, G., Corrigan, R. M., Winstel, V., Goerke, C., Gründling, A., and Peschel, A. (2011). Wall teichoic acid-dependent adsorption of staphylococcal siphovirus and myovirus. *J. Bacteriol.* 193, 4006–4009. doi: 10.1128/JB.01412-10

Yen, M., Cairns, L. S., Camilli, A., Zuckerman, J. N., Rombo, L., Fisch, A., et al. (2017). A cocktail of three virulent bacteriophages prevents *Vibrio cholerae* infection in animal models. *Nat. Commun.* 8, 14187. doi: 10.1038/ncomms14187

Zhang, L., Sun, L., Wei, R., Gao, Q., He, T., Xu, C., et al. (2017). Intracellular *Staphylococcus aureus* control by virulent bacteriophages within MAC-T bovine mammary epithelial cells. *Antimicrob. Agents Chemother.* 61, e01990-16. doi: 10.1128/AAC.01990-16

Zook, J. M., and Vreeland, W. N. (2010). Effects of temperature, acyl chain length, and flow-rate ratio on liposome formation and size in a microfluidic hydrodynamic focusing device. *Soft Matter* 6:1352. doi: 10.1039/b923299k

Conflict of Interest Statement: The authors declare that the research was conducted in the absence of any commercial or financial relationships that could be construed as a potential conflict of interest.

frontiers
in Microbiology

ORIGINAL RESEARCH
published: 17 October 2018
doi: 10.3389/fmicb.2018.02270

Magnetic Nanoconjugated Teicoplanin: A Novel Tool for Bacterial Infection Site Targeting

Ilaria Armenia, Giorgia Letizia Marcone, Francesca Berini, Viviana Teresa Orlandi, Cristina Pirrone, Eleonora Martegani, Rosalba Gornati, Giovanni Bernardini and Flavia Marinelli*

Department of Biotechnology and Life Sciences, University of Insubria, Varese, Italy

Nanoconjugated antibiotics can be regarded as next-generation drugs as they possess remarkable potential to overcome multidrug resistance in pathogenic bacteria. Iron oxide nanoparticles (IONPs) have been extensively used in the biomedical field because of their biocompatibility and magnetic properties. More recently, IONPs have been investigated as potential nanocarriers for antibiotics to be magnetically directed to/recovered from infection sites. Here, we conjugated the "last-resort" glycopeptide antibiotic teicoplanin to IONPs after surface functionalization with (3-aminopropyl) triethoxysilane (APTES). Classical microbiological methods and fluorescence and electron microscopy analysis were used to compare antimicrobial activity and surface interactions of naked IONPs, amino-functionalized NPs (NP-APTES), and nanoconjugated teicoplanin (NP-TEICO) with non-conjugated teicoplanin. As bacterial models, differently resistant strains of three Gram-positive bacteria (*Staphylococcus aureus*, *Enterococcus faecalis,* and *Bacillus subtilis*) and a Gram-negative representative (*Escherichia coli*) were used. The results indicated that teicoplanin conjugation conferred a valuable and prolonged antimicrobial activity to IONPs toward Gram-positive bacteria. No antimicrobial activity was detected using NP-TEICO toward the Gram-negative *E. coli.* Although IONPs and NP-APTES showed only insignificant antimicrobial activity in comparison to NP-TEICO, our data indicate that they might establish diverse interaction patterns at bacterial surfaces. Sensitivity of bacteria to NPs varied according to the surface provided by the bacteria and it was species specific. In addition, conjugation of teicoplanin improved the cytocompatibility of IONPs toward two human cell lines. Finally, NP-TEICO inhibited the formation of *S. aureus* biofilm, conserving the activity of non-conjugated teicoplanin versus planktonic cells and improving it toward adherent cells.

Keywords: antibiotic resistance, iron oxide nanoparticles, glycopeptide antibiotics, antimicrobial activity, teicoplanin, *Staphylococcus aureus* biofilm

Edited by:
Bingyun Li,
West Virginia University, United States

Reviewed by:
Fintan Thomas Moriarty,
AO Research Institute, Switzerland
Shuilin Wu,
Tianjin University, China

****Correspondence:***
Flavia Marinelli
flavia.marinelli@uninsubria.it

Specialty section:
This article was submitted to Antimicrobials, Resistance and Chemotherapy, a section of the journal Frontiers in Microbiology

Received: *29 June 2018*
Accepted: *05 September 2018*
Published: *17 October 2018*

Citation:
Armenia I, Marcone GL, Berini F, Orlandi VT, Pirrone C, Martegani E, Gornati R, Bernardini G and Marinelli F (2018) Magnetic Nanoconjugated Teicoplanin: A Novel Tool for Bacterial Infection Site Targeting. Front. Microbiol. 9:2270. doi: 10.3389/fmicb.2018.02270

INTRODUCTION

According to a recent survey of the World Health Organization (WHO, 2017), antibiotic resistance represents one of the greatest threats to global health today and contributes significantly to longer hospital permanence, higher medical costs, and increased mortality. At least 700,000 people die annually because of infections caused by resistant bacteria. This number is predicted to increase up to 10 million by 2050 and is consequentially associated with a social and economic burden. This public health threat is exacerbated by the paucity of novel antibiotics expected to enter clinical use in the near future (Fedorenko et al., 2015). A corollary to acute illness is the increased number of chronic bacterial infections due to the prevalence of biofilm colonization (Arciola et al., 2018). Currently, medical device-related infections account for more than 60% of all the hospital-acquired infections in the United States (Weiner et al., 2016). Biofilms are complex, three-dimensional bacterial communities living in a self-produced extracellular matrix. The biofilm-forming bacteria survive better than their free-living (planktonic) counterparts in hostile environments; they are 10 to 100 times less susceptible to antimicrobial agents and are protected against the host immune system, making the treatment of these infections quite challenging (Davis, 2003; Venkatesan et al., 2015).

One promising approach in the field of antimicrobial therapy is the use of nanotechnology-tailored agents for preventing and treating infections caused by resistant bacteria. Unique and well-defined features distinguish nanoparticles (NPs) from their bulk counterparts, such as large surface area-to-volume ratio and dimensions that are comparable to those of biomolecules, effectively providing a platform with a high number of functional sites and possible interactions with bacterial cells and biofilms. Of all the NPs tested for antimicrobial activity thus far, silver NPs (AgNPs) have been studied most intensively (Natan and Banin, 2017). Although researchers have widely agreed that the broad-spectrum antibacterial activity of AgNPs can be predominantly ascribed to the release of Ag ions, AgNPs demonstrate unique properties because they adhere to the bacterial surface, altering membrane properties and thus delivering Ag ions more effectively to the bacterial cytoplasm and membrane (Durán et al., 2016). Consequently, the antibacterial effect of AgNPs is observed at concentrations with a 10-fold lower magnitude than those used for bulk Ag ions. The antibacterial activity of AgNPs is reported to be mediated by a multiplicity of still-not-completely understood mechanisms following their interaction with the bacterial surface, which act in parallel (i.e., oxidative stress, membrane depolarization, and protein and DNA interaction), thus explaining why bacterial resistance does not easily arise (Hajipour et al., 2012; Natan and Banin, 2017; Baranwal et al., 2018). Very recent studies (Xiang et al., 2017; Xie et al., 2017, 2018) show that the antibacterial activity of AgNPs may be successfully exploited in preparing nanocomposite materials to be used as antibacterial coatings of titanium-based metallic implants and poly(ether ether ketone) medical devices, which are both widely employed in dentistry and orthopedic applications. Entrapping AgNPs in graphene oxide nanosheets wrapped with a thin layer of collagen (Xie et al., 2017), in hybrid polydopamine/graphene oxide coatings (Xie et al., 2018), or in biocompatible polymers such as poly(lactic-*co*-glycolic) acid (Xiang et al., 2017) endows medical implants with a long-lasting self-antibacterial activity. *In vivo* studies using these innovative coatings in animal models confirm that combining the unique properties of different nanomaterials prevents bacterial infection and provides a good cytocompatibility of the medical devices (Xie et al., 2017, 2018).

A synergic, but as yet less exploited strategy when developing nano-based antimicrobial agents involves using NPs as nanocarriers for antibiotics, taking advantage of the high surface-to-volume ratio platform that they offer for attaching a large number of molecules. The advantages of using NPs in this way depend on the nature of both the NPs and the drugs under consideration, as recently reviewed (Natan and Banin, 2017). These advantages might include (i) protecting the nanoconjugated drug from degradation and oxidation; (ii) increasing drug solubility, antimicrobial activity, and biodistribution; (iii) delivering the antibiotic to the site of the infection; and (iv) enhancing drug penetration into biofilms, facilitating the killing of encased bacteria. As antibiotic nanocarriers, iron oxide nanoparticles (IONPs) have recently attracted increased interest thanks to their unique magnetic properties (Dinali et al., 2017). In fact, IONPs can be guided by an external magnetic field to a targeted organ/biofilm and specifically localized at the site of infection (Wu et al., 2015; Stepien et al., 2018). In addition, IONPs are easily produced and functionalized, and they possess a high drug-loading capacity, low cell toxicity, and high biocompatibility (Ali et al., 2016; Dinali et al., 2017). In the last decade, relatively few studies have investigated the potential of surface-modified IONPs as antibacterial agents in depth. Core-shell Fe_3O_4-AgNPs were tested as antimicrobial agents against Gram-positive and Gram-negative bacteria where the silver shell was responsible for antimicrobial action (Chudasama et al., 2009). Biocompatible polyvinyl alcohol-coated IONPs were used in biomedical applications and reported to be active against *Staphylococcus aureus* in a dose-dependent manner (Tran et al., 2010). Similarly, chitosan-coated IONPs were shown to have a higher antimicrobial activity than naked IONPs due to the positive surface potential, which interacted better with negatively charged bacterial cell surfaces (Arakha et al., 2015a). According to other authors (Huang et al., 2010; Ebrahiminezhad et al., 2014), IONP surface functionalization with (3-aminopropyl) triethoxysilane (APTES) elicited an antimicrobial effect by creating a high density of amino groups, which could interact with negatively charged sites on the bacterial cells through electrostatic interactions. The well-developed surface chemistry of IONPs made it possible to incorporate a variety of commonly used antibiotics such as the β-lactam amoxicillin, penicillin, and ampicillin, the aminoglycoside streptomycin, and the glycopeptide vancomycin (Chifiriuc et al., 2013; Grumezescu et al., 2014; Hussein-Al-Ali et al., 2014; El Zowalaty et al., 2015; Wang et al., 2017), providing evidence that biocompatible magnetic NPs might enable site-specific antibiotic delivery. Vancomycin-carrying, folic acid-tagged chitosan NPs were successfully used to deliver vancomycin to bacterial cells (Chakraborty et al., 2010, 2012), and vancomycin-modified mesoporous silica NPs were used for selective recognition and killing of Gram-positive bacteria over macrophage-like cells (Qi et al., 2013). An alternative use of IONPs functionalized with vancomycin – an antibiotic that binds to bacterial cell walls – was to apply them as ligands for the affinity capture of a wide range of bacteria from biological samples, including Gram-positive bacteria such as *S. aureus* and Gram-negative bacteria such as *Escherichia coli* (Gu et al., 2003; Lin et al., 2005; Kell et al., 2008). Because of the magnetic properties of vancomycin-functionalized IONPs, vancomycin-captured bacteria can be magnetically separated and concentrated from large volumes into much smaller volumes, allowing bacterial analysis and detection based on, for example, genomic DNA (Kell et al., 2008; Zhu et al., 2015).

In this work, we employed IONPs as carriers of the lipoglycopeptide antibiotic teicoplanin, which has been used in clinical practice since 1988 in Europe and 1998 in Japan. Teicoplanin is considered a drug of "last resort" for treating severe infections by multiresistant Gram-positive pathogens, including the methicillin-resistant *S. aureus* (MRSA) and the anaerobe *Clostridioides difficile* (Marcone et al., 2018). Teicoplanin is a complex molecule with a peptide core of seven aromatic amino acids tailored with sugar residues, chlorine atoms, methyl groups, and a lipid chain. It forms five specific hydrogen bonds with the D-alanyl-D-alanine terminus of the peptidoglycan precursors of the bacterial cell wall, blocking its synthesis and consequently causing cell lysis (Binda et al., 2014). The antibacterial spectrum of teicoplanin activity against Gram-positive bacteria is similar to that of vancomycin, but teicoplanin shows an increased potency, particularly against some resistant clinical isolates belonging to *Staphylococcus*, *Streptococcus,* and *Enterococcus* genera (Van Bambeke, 2006). In addition, teicoplanin is active on vancomycin-resistant enterococci with VanB-phenotype (Van Bambeke, 2006; Binda et al., 2014). The superior antimicrobial potency of the lipoglycopeptide teicoplanin in comparison to the glycopeptide vancomycin is due to the *in vivo* membrane anchoring of the hydrophobic tail of teicoplanin, which strengthens the bond to membrane-localized peptidoglycan precursors and promotes synergic back-to-back dimerization of antibiotic molecules (Allen and Nicas, 2003; Treviño et al., 2014). In addition, lipidation seems to represent the key functional difference between vancomycin and teicoplanin, which is related to their differing abilities of inducing glycopeptide antibiotic resistance response in enterococci and actinomycetes (Dong et al., 2002; Binda et al., 2018). To the best of our knowledge, this is the first study exploring the feasibility of conjugating teicoplanin to IONPs and testing the potential of nanoconjugated teicoplanin as a promising tool for treating bacterial infections caused by resistant bacteria.

MATERIALS AND METHODS

Materials

All chemical reagents, including acetonitrile (CH_3CN), ammonium formate ($HCOONH_4$), ammonium hydroxide (NH_4OH), APTES, boric acid (H_3BO_3), crystal violet ($C_{25}N_3H_{30}Cl$), 2′,7′-dichlorodihydrofluorescein (DCFH-DA), *N*-(3-dimethylaminopropyl)-*N*′-ethylcarbodiimide hydrochloride (EDC), ethanol (C_2H_6O), ferric nitrate [$Fe(NO_3)_3 \times 9H_2O$], formaldehyde (CH_2O), glutaraldehyde ($C_5H_8O_2$), iron dichloride ($FeCl_2 \times 4H_2O$), iron trichloride ($FeCl_3 \times 6H_2O$), *N*-hydroxysuccinimide (NHS), nitric acid (HNO_3), osmium tetroxide (OsO_4), phosphate-buffered saline (PBS), sodium cacodylate ($C_2H_7AsO_2$), sodium chloride (NaCl), sodium hydroxide (NaOH), sodium 2-(*N*-morpholino)ethanesulfonic acid hemisodium salt (MES), and teicoplanin, were purchased from Sigma-Aldrich, Milan, Italy. The LIVE/DEAD BacLight fluorescence assay kit was purchased by Thermo Fisher Scientific, Monza, Italy. Epon-Araldite 812 was purchased from Electron Microscopy Sciences, Hatfield, PA, United States. All the chemical reagents were used without additional purification.

Microbial Strains and Culture Conditions

Escherichia coli ATCC 35218, *Bacillus subtilis* ATCC 6633, *S. aureus* ATCC 6538P (methicillin susceptible *S. aureus*, MSSA), *S. aureus* ATCC 43300 (MRSA), *Enterococcus faecalis* ATCC 29212, and *E. faecalis* ATCC 51299 (VanB phenotype) were obtained from the American Type Culture Collection (ATCC). *E. faecalis* 9160188401-EF-34 (VanA phenotype) is a clinical isolate, which was kindly provided by Laboratorio Microbiologia Clinica – Ospedale di Circolo, Varese, Italy. *E. coli* and *B. subtilis* were propagated overnight in Luria Bertani medium (LB, 2% tryptone, 2% yeast extract, and 1% NaCl), and the *S. aureus* and *E. faecalis* strains in Müller Hinton broth 2 (MHB2, 0.3% beef infusion solids, 1.75% casein hydrolysate, and 0.15% starch) with continuous shaking at 200 rpm and 37°C. For exponential growth, overnight cultures were transferred to fresh medium: inocula were prepared to start the cultures with an optical density at 600 nm ($OD_{600\ nm}$) of 0.1 in the final medium. For long-term preservation, bacterial cultures were stored at −20°C in 20% glycerol. Media were acquired from Sigma-Aldrich, Milan, Italy, unless otherwise stated.

Synthesis of the IONPs

Iron oxide (Fe_2O_3) NPs were synthesized using the coprecipitation method reported by Balzaretti et al. (2017). Briefly, under vigorous stirring for 30 min, 8.89 g of $FeCl_3 \times 6H_2O$ and 3.28 g $FeCl_2 \times 4H_2O$ were mixed in 380 mL of water, while slowly adding 1.5 mL of HCl (37%) dropwise into the solution to completely dissolve the salts. Following this step, 25 mL of NH_4OH (25%) was added. Particles were washed several times with Milli-Q water and 40 mL of 2 M HNO_3 was added and heated at 90°C for 5 min. Then, particles were separated by a magnet from the reaction mixture; subsequently, 60 mL of 0.34 M solution of $Fe(NO_3)_3 \times 9H_2O$ was added. The suspension was heated at 90°C for 30 min. The supernatant was removed and IONPs were collected by a magnet, suspended in Milli-Q water, and left in dialysis overnight. IONPs were stored at 4°C.

Functionalization With APTES

To prepare functionalized IONPs, a standard protocol (Balzaretti et al., 2017) was followed: a 1.5 M solution of APTES in ethanol was added to 150 mg of IONPs and stirred for 1 h at room temperature. Then, the temperature was increased to 90°C and the solution was stirred for an additional hour. The amino-modified IONPs (NP-APTES) were collected by a magnet, washed several times, and suspended in Milli-Q water.

Teicoplanin Conjugation to NP-APTES

To prepare teicoplanin-conjugated NPs (NP-TEICO), a solution containing teicoplanin (500 μg), 13 mM EDC, and 26 mM NHS was prepared and added to the NP-APTES (4 mg/mL) dispersed in 30 mM MES buffer at pH 6.0 in a final volume of 1 mL. The reaction was mixed for 6 h at room temperature. NP-TEICO were washed twice and resuspended in fresh 30 mM MES buffer at pH 6.0.

Characterization of NPs

The shape, size, and size distribution of IONPs, NP-APTES, and NP-TEICO were investigated by transmission electron microscopy (TEM) using a JEOL 1010 electron microscope (Tokyo, Japan). Samples for TEM were dispersed in Milli-Q water on carbon-coated copper grids and dried at room temperature. The hydrodynamic diameter size and polydispersity index (PDI) of IONPs, NP-APTES, and NP-TEICO were measured in 0.9% NaCl. Zeta potential was measured on samples diluted in 1 mM KCl at 25°C. Measurements were performed at 25°C using a 90 Plus Particle Size Analyzer (Brookhaven Instruments Corporation, NY, United States).

HPLC Analysis

Teicoplanin was measured by HPLC according to the method previously reported in Taurino et al. (2011). HPLC analyses were performed on a 5-μm particle size Symmetry C18 (VWR International LCC, Radnor, PA, United States) column (4.6 mm × 250 mm). The column was eluted at a 1 mL/min flow rate with a 30-min linear gradient from 15 to 65% of Phase B, followed by 10 min with 100% Phase B. For Phase A we used a 32 mM $HCOONH_4$, pH 7.0:CH_3CN 90:10 (v/v) mixture, and for Phase B a 32 mM $HCOONH_4$, pH 7.0:CH_3CN 30:70 (v/v) mixture. Chromatography was performed with a model 1100 HPLC system (Elite Lachrom Hitachi LLC, VWR, Milan, Italy) and UV detection was at 236 nm.

Agar Diffusion Test

Antimicrobial activities of IONPs, NP-APTES, and NP-TEICO were tested against *E. coli* ATCC 35218, *B. subtilis* ATCC 6633, and *S. aureus* ATCC 6538P by employing an agar diffusion assay (Finn, 1959). Briefly, bacterial cultures were grown in MHB2 until an $OD_{600\ nm}$ of 0.4 was reached and then used to prepare agar plates containing Müller-Hinton Agar (MHA). 10 μL of IONPs, NP-APTES, NP-TEICO (4 mg/mL loaded with 500 μg/mL of teicoplanin in the case of NP-TEICO), and of teicoplanin (500 μg/mL) in 30 mM MES buffer, pH 6.0, were loaded manually onto the inoculated plates. The plates were incubated at 37°C for 24 h. The diameters of the zones of bacterial growth inhibition surrounding the droplets were measured.

Determination of Minimum Inhibitory Concentration and Minimum Bactericidal Concentration

Minimum inhibitory concentrations (MICs) of non-conjugated and nanoconjugated teicoplanin were determined toward *B. subtilis*, *S. aureus,* and *E. faecalis* strains by applying the broth dilution method using MHB2, as recommended by the Clinical and Laboratory Standards Institute guidelines (CLSI, 2018). About 5×10^5 exponentially growing bacterial cells were inoculated into MHB2 containing increasing concentrations of teicoplanin and NP-TEICO in 30 mM MES buffer, pH 6.0, and shaken for 16–20 h at 37°C. NP-TEICO concentrations to be added were calculated considering the amount of teicoplanin loaded onto IONPs (nanoconjugated teicoplanin) under the reaction conditions described above. MICs were the minimal concentrations of nanoconjugated and non-conjugated teicoplanin at which no turbidity could be detected.

To evaluate the minimum bactericidal concentrations (MBCs), 100 μL of bacterial cultures used for the MIC test were plated onto MHA and incubated at 37°C for 24 h. MBCs were the minimal concentrations of nanoconjugated and non-conjugated teicoplanin at which no growth could be detected. The tolerance level of each tested bacterial strain toward nanoconjugated and non-conjugated teicoplanin was determined according to May et al. (1998) using the following formula: Tolerance = MBC/MIC.

Growth Kinetic Analysis

Growth kinetics of *B. subtilis* ATCC 6633, *S. aureus* ATCC 6538P, and *E. coli* ATCC 35218 populations were followed by measuring $OD_{600\ nm}$ using an UV-Vis V-560 Spectrophotometer (JASCO, MD, United States) at regular time intervals. Preinocula were prepared from overnight cultures in LB or MHB2 at 37°C and at 200 rpm. Experiments were conducted in 50-mL tubes containing a final volume of 10 mL of LB or MHB2 added after 1 h of growth from inocula with equivalent volumes of IONPs, NP-APTES, and NP-TEICO preparations (4 mg/mL) previously resuspended in 30 mM MES buffer, pH 6.0, or with the teicoplanin control solution (500 μg/mL).

Viability Assay

Viable counts (expressed as colony-forming units per mL, CFU/mL) were estimated by employing the plate count technique. For CFU measurement, a standard volume (10 μL) of undiluted or serially diluted samples collected from stationary phase cultures on treatment with teicoplanin, IONPs, NP-APTES, and NP-TEICO, as reported above, were plated on nutrient agar. Plates were incubated for 24 h at 37°C to evaluate the viable cells.

Fluorescence Microscopy Analysis

To investigate the effect of IONPs, NP-APTES, and NP-TEICO on bacterial cells, the LIVE/DEAD BacLight fluorescence assay was used (L7007, Molecular probes, Thermo Fisher Scientific). Following the manufacturer's protocol, bacteria were cultivated overnight at 37°C and agitated at 200 rpm, appropriately diluted, and treated for 5 h with 4 mg/mL of IONPs, NP-APTES, and NP-TEICO and teicoplanin (500 μg/mL). From these cultures, 10 mL of each bacterial solution was centrifuged at 7000 rpm for 15 min. The supernatants were discarded and the pellets were suspended in saline solution (0.9%). The samples were incubated at room temperature for 1 h (mixing every 15 min) and then washed twice with saline solution. Finally, the pellets were resuspended in an equal volume of saline solution (0.9%). Then, 3 μL of dye mixture was added to each 1 mL of the prepared bacterial samples and incubated in the dark for 15 min after properly mixing the bacterial suspensions. Fluorescence images were taken by trapping 5 μL of stained bacterial samples between a slide and a cover slip. For imaging the samples, an optical microscope with appropriate filters was employed (Axiophot; Carl Zeiss, Milan, Italy). ImageJ (Schneider et al., 2012) was used to quantify total fluorescence intensity of the bacteria. Intensities were expressed as percentage (%) relative to the saturation fluorescence within the field; red and green fluorescence stains corresponded to live or dead bacteria, respectively (Borcherding et al., 2014; Arakha et al., 2015a,b).

Transmission Electron Microscopy Analysis

The interaction pattern of NPs with bacteria was also studied by TEM. After 5 h of exposure to 4 mg/mL IONPs, NP-APTES, NP-TEICO, or teicoplanin (500 μg/mL), pellets were washed with PBS and fixed in Karnovsky solution (4% formaldehyde, 2% glutaraldehyde, 0.1 M sodium cacodylate, pH 7.2) overnight at 4°C. The samples were washed three times with 0.1 M sodium cacodylate for 10 min and postfixed in the dark for 1 h with 1% osmium tetroxide in 0.1 M sodium cacodylate buffer, pH 7.2, at room temperature. After dehydration with a series of ethyl alcohol, the samples were embedded in an Epon-Araldite 812 1:1 mixture. Thin sections (90 nm), obtained with a Pabisch Top-Ultra ultramicrotome (Emme 3 S.r.l., Milan, Italy), were observed with a Morgagni electron microscope (Philips, Eindhoven, Netherlands) operated at 80 keV.

Biofilm Assay

S. aureus ATCC 6538P cultures, grown overnight in LB, were diluted in fresh medium to reach a cell density of 10^7 CFU/mL and dispensed in 24-well plates, adding increasing concentrations of nanoconjugated or non-conjugated teicoplanin (2.5, 5, and 10 μg/mL) and of naked IONPs or NP-APTES (20, 40, and 80 μg/mL). The amounts of NPs to be added took into account the teicoplanin loaded on NPs under the reaction conditions described above. Following incubation at 37°C for 24 h, the adherent biomass was quantified by crystal violet (CV) staining. Biofilms were stained with CV 0.1% for 20 min, washed twice with PBS, and air dried overnight at room temperature; the CV was then dissolved in 33% acetic acid for 10 min. The amount of solubilized dye was spectrophotometrically measured at 595 nm (Infinite 200 PRO; TECAN, Männedorf, Switzerland). To assess the effect of teicoplanin and of NP preparations on the cell viability of planktonic and adherent cell subpopulations, cells from the planktonic phase were collected and adherent cells were recovered by scraping the wells and then suspended in 1 mL of phosphate buffer. Cultures were diluted and CFU were estimated by plate counting in MHA plates. Viable counts of planktonic cells were expressed as CFU/mL and adherent cells as CFU per well (CFU/well).

To test the effect of teicoplanin and NP preparations on biofilm dispersal, biofilms were prepared as indicated previously and incubated at 37°C for 48 h before adding nanoconjugated or non-conjugated teicoplanin (5, 25, and 50 μg/mL) and naked IONPs or NP-APTES (40, 200, and 400 μg/mL). Following 24-h incubation at 37°C, biofilm biomass was evaluated by CV staining and the cell viability of adherent and planktonic cells was estimated by applying the viable count technique, as previously described.

Cell Cultures

Two different cell lines were used to evaluate NP-TEICO *in vitro* cytotoxicity: a tumor model SKOV-3 cell line from ovarian adenocarcinoma and a non-tumor cell line, hASCs (human adipose-derived stem cells). SKOV-3 cells were cultured as reported in the literature (Cappellini et al., 2015). hASCs were isolated and cultured as previously reported (Palombella et al., 2017).

Cytotoxicity Test

Cell cytotoxicity was determined by measuring ATP content using the RealTime-Glo^{TM} MT Cell Viability Assay (Promega, Milan, Italy) according to the manufacturer's instructions. Briefly, 500 cells were plated in 96-well plates in 200 μL of cell medium (RPMI for SKOV-3 and DMEM/DMEM F12 1:1 for hASC). After 24 h, the cells were exposed to increasing concentrations of nanoconjugated or non-conjugated teicoplanin or to the corresponding concentrations of NPs (considering the teicoplanin loaded per mg of NPs) and then a solution 2× the substrate and NanoLuc® Enzyme were added. The cells were incubated at 37°C and in 5% CO_2-humidified atmosphere, and luminescence was read every 24 h using the Infinite F200 plate reader (Tecan Group, Männedorf, Switzerland).

Statistics

All experiments were repeated at least three times on separate dates. Mean and standard deviation (SD) calculations were performed using Microsoft Excel 2003 (Microsoft Corporation, Redmond, WA, United States). Data were analyzed by means of one-way analysis of variance (Origin_7.0 SR0; Origin lab Corporation, Northampton, MA, United States). Significant effects of treatments were estimated ($p < 0.05$, $p < 0.01$, and $p < 0.0001$).

RESULTS

Characterization of Synthetized NPs

Numerous methods for synthesizing IONPs have been reported in the literature (Wu et al., 2015). In this study, we used the coprecipitation method previously optimized by Balzaretti et al. (2017), by which IONPs with good stability and size distribution and no tendency to aggregation could be produced. We confirmed that the NPs obtained had a spherical shape and an average diameter of 10.5 ± 4 nm, as shown by TEM micrograph (**Figures 1A,D**). The functionalization protocol, used to introduce amino groups on the IONPs (**Figure 2**), led to an insignificant increase in the diameter of NP-APTES, which was 10.6 ± 3.6 nm (**Figures 1B,E**). Teicoplanin was conjugated by following a slightly modified protocol, which was previously used for enzyme conjugation (Armenia et al., 2017): carboxylic groups

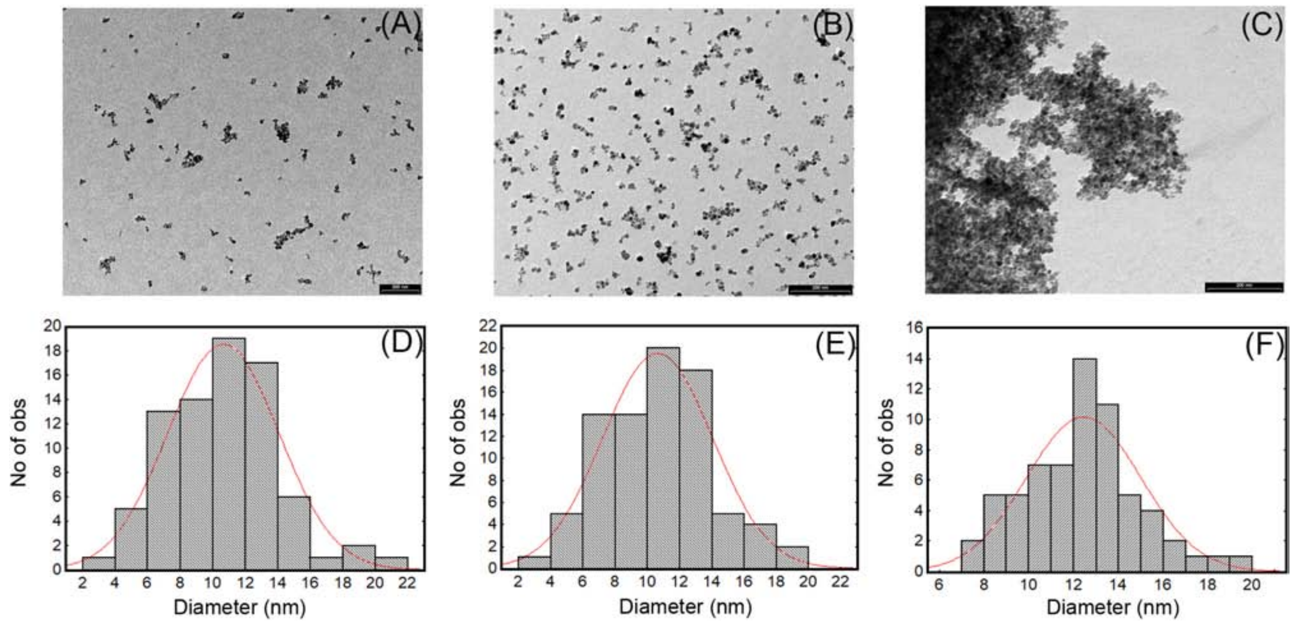

FIGURE 1 | TEM images and size distribution of IONPs **(A,D)**, NP-APTES **(B,E)**, and NP-TEICO **(C,F)**.

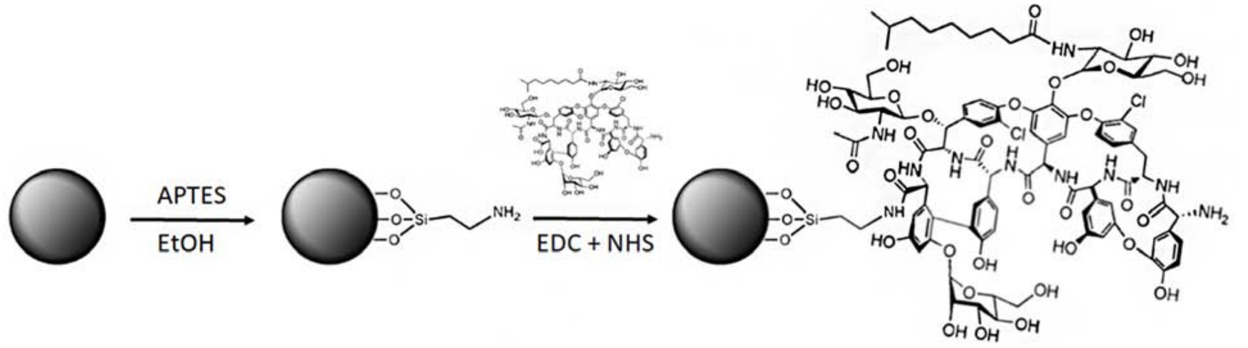

FIGURE 2 | Synthetic route for teicoplanin conjugation to IONPs (not in scale). The first step is functionalization of the IONPs with APTES, followed by the conjugation of teicoplanin by covalent bonding of the terminal carboxylic groups of the antibiotic molecules with the amino groups of NP-APTES via EDC/NHS cross-linking.

of teicoplanin molecules reacted with the amino groups on the surface of NP-APTES after EDC/NHS antibiotic activation (see below, **Figure 2**). Teicoplanin conjugation led to a more irregular shape of the particles and a slight tendency to aggregation. It is known that correctly conformed teicoplanin molecules tend to dimerize back-to-back in aqueous solutions and that dimerization plays an important role in their biological activity (Treviño et al., 2014). However, this phenomenon was not strong as no NP precipitation occurred. NP-TEICO had an average diameter of 13.6 nm (**Figures 1C,F**).

Transmission electron microscopy observations were complemented by measuring dynamic light scattering (DLS) of the hydrodynamic size of IONPs (**Table 1**); their diameter was estimated to be 14.2 ± 0.5 nm with an average size distribution (PDI) of 0.127, indicating a slight polydispersity typical for the coprecipitation synthesis (Wu et al., 2015). For NP-APTES, an increase in the hydrodynamic diameter (26.8 ± 0.2 nm) due to the presence of the APTES shell around the NP core was registered. The hydrodynamic diameter of NP-TEICO was much larger (568.2 ± 0.6 nm) (**Table 1**), probably due to aggregate formation in the medium used for DLS analysis and to the effect of the glycopeptide side chains and their tendency to dimerize, which might slow down particle diffusion and increase their apparent size (Szpak et al., 2013; **Table 1**). The difference in NP sizes measured by DLS versus TEM is generally attributed to the formation of extra hydrate layers in aqueous solutions (De Palma et al., 2007; Gonçalves et al., 2017). In addition, antibiotic shells conjugated to NPs are usually not sufficiently electron dense to be visible under the electron microscope. The measurement of zeta potential (**Table 1**) showed that the superficial charge of

TABLE 1 | Physical parameters of synthesized IONPs, NP-APTES, and NP-TEICO.

	Baseline	Polydispersity	Diameter (nm)	Conductance (μS)	Mobility	Z potential (mV)
IONPs	9.9	0.127	14.2 ± 0.5	421	1.5	11.0 ± 0.8
NP-APTES	9	0.18	26.8 ± 0.2	373	1.9	22.5 ± 0.5
NP-TEICO	9	0.189	568.2 ± 0.6	400	1	12.8 ± 0.6

NP-APTES was twofold higher than for IONPs, that is, 22.5 ± 0.2 versus 11 ± 0.8 mV, due to the presence of the amino groups of APTES. A reduction in the surface charge was indeed observed after teicoplanin conjugation: NP-TEICO zeta potential was 12.8 ± 0.6 mV, indicating that NP-APTES were successfully loaded with teicoplanin.

Preparation of NP-TEICO

Teicoplanin was conjugated to NP-APTES using standard EDC/NHS chemistry: EDC reacted with the carboxylic group of the antibiotic, forming an active O-acylisourea intermediate that could be displaced by the nucleophilic attack of the amino groups present on the NP-APTES surface (**Figure 2**; Hermanson, 2013). Different reaction conditions (reaction medium, EDC/NHS ratio, teicoplanin concentration, time, and temperature of reaction) were explored to improve teicoplanin conjugation on NP-APTES. The quantity of teicoplanin bound to the surface of NP-APTES was estimated by subtracting the unreacted teicoplanin present in the supernatant from the added total antibiotic amount. Teicoplanin was quantified by reverse-phase HPLC as previously reported (Taurino et al., 2011). First trails in water, PBS, and MES buffer indicated that the latter, at pH 6.0, was the most preferable medium for the conjugation reaction (data not shown). As reported in **Table 2**, HPLC analyses confirmed that under the best experimental conditions tested so far, that is, 4 mg/mL of NP-APTES in 30 mM MES buffer, pH 6.0, 13 mM EDC, 26 mM NHS, 500 μg/mL of teicoplanin, the teicoplanin conjugation yield was approximately 90%. Under these conditions, more than 100 μg of teicoplanin was loaded per mg of NP-APTES.

TABLE 2 | Reaction conditions tested for teicoplanin conjugation to NP-APTES via EDC/NHS chemistry in 30 mM MES, pH 6.0.

Teicoplanin (μg/mL)	EDC (mM)	NHS (mM)	Temperature (°C)	Time (h)	Yield (%)
100	26	13	4	2	10 ± 0.7
100	26	13	4	4	10 ± 1.5
100	26	13	4	6	12 ± 1.0
100	26	13	25	2	25 ± 0.5
100	26	13	25	4	30 ± 0.4
100	26	13	25	6	65 ± 0.8
100	13	26	25	2	70 ± 1.7
100	13	26	25	4	85 ± 1.4
50	13	26	25	6	100 ± 1.2
100	13	26	25	6	100 ± 0.7
500	13	26	25	6	90 ± 0.9
1000	13	26	25	6	50 ± 0.5

NP-APTES were used at a concentration of 4 mg/mL. Conjugation yield was calculated by estimating the amount of residual teicoplanin in the reaction medium by HPLC.

NP-TEICO prepared in this way remained chemically stable when stored at pHs ranging from 5.5 to 7.1 and temperatures from −20 to 25°C. Under these conditions, release of teicoplanin from NP-TEICO was measured by HPLC analysis of incubation buffer; 100% of the antibiotic remained fully attached to NPs for 1 week and decreased by approximately 10% in 1 month (data not shown). Consistently, the antimicrobial activity of NP-TEICO – measured by the antimicrobial susceptibility test versus *S. aureus* ATCC 6538P and *B. subtilis* ATCC 6633 (see below) – was also maintained. After 3 weeks, NP-TEICO maintained from 70 to 90% of its initial antimicrobial activity. Under the same conditions, a water solution of teicoplanin (500 μg/mL) maintained 90% of its initial antimicrobial activity.

Antimicrobial Activity of NP-TEICO

Antibacterial activity of NP-TEICO was initially investigated by comparing the growth inhibitory effects of two commonly used representative species of Gram-positive bacteria, that is, *S. aureus* ATCC 6538P and *B. subtilis* ATCC 6633, and the Gram-negative *E. coli* ATCC 35218, using an agar diffusion assay. **Figure 3** reveals that NP-TEICO inhibited the growth of *S. aureus* and

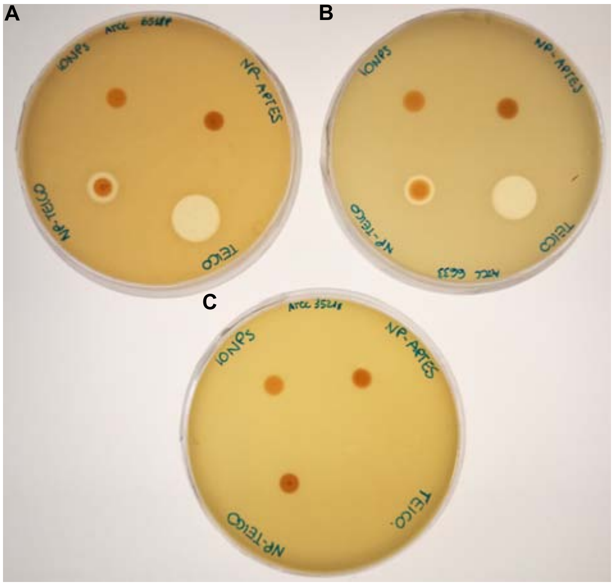

FIGURE 3 | Agar diffusion assay for measuring the antimicrobial activity of IONPs, NP-APTES, NP-TEICO, and non-conjugated teicoplanin versus the two Gram-positive bacteria *S. aureus* ATCC 6538P **(A)** and *B. subtilis* ATCC 6633 **(B)**, and versus the Gram-negative *E. coli* ATCC 35218 **(C)**.

B. subtilis, whereas no inhibition halos were observed for *E. coli,* thus demonstrating that NP-TEICO maintained the typical activity and spectrum of action of teicoplanin. Sizes of inhibition halos for the nanoconjugated teicoplanin were not comparable with the ones determined by the non-conjugated teicoplanin, as expected, considering the probably slower diffusion rate of NP-loaded antibiotic in agar medium. Conversely, IONPs and NP-APTES did not show any inhibition halos toward either the Gram-positive or the Gram-negative bacteria. These data indicate that the antimicrobial activity measured by the agar diffusion assay was conferred to NP-TEICO by the conjugation of the antibiotic and that it was not an intrinsic feature of IONPs.

Table 3 reports the MICs of nanoconjugated and non-conjugated teicoplanin toward clinically relevant strains of *S. aureus* and *E. faecalis*. Although the potency of nanoconjugated teicoplanin was slightly reduced in comparison with the non-conjugated antibiotic, NP-TEICO maintained a valuable antibiotic activity against MRSA and on vancomycin-resistant *E. faecalis* with a VanB phenotype. MICs and MBCs, and consequently the tolerance levels of NP-TEICO toward *B. subtilis, S. aureus,* and *E. faecalis,* showed the same trend as those measured for non-conjugated teicoplanin. NP-TEICO and non-conjugated teicoplanin were inactive toward the Gram-negative *E. coli* and toward the vancomycin- and teicoplanin-resistant *E. faecalis* clinical isolate with a VanA phenotype (Van Bambeke, 2006; Binda et al., 2014).

Effects of NPs on Bacterial Growth Kinetics and Cell Viability

As the antimicrobial activity of IONPs and their derivatives is a matter of intensive debate (Auffan et al., 2008; Chatterjee et al., 2011; Borcherding et al., 2014; Arakha et al., 2015a; Ansari et al., 2017), we further investigated the effects of IONPs, NP-APTES, and NP-TEICO on bacterial cell viability, by adding our NP preparations at the log phase of the growth kinetics of *S. aureus* ATCC 6538P, *B. subtilis* ATCC 6633, and *E. coli* ATCC 35218 populations. Cultures with no added NP or to which only teicoplanin was added were used as negative and positive controls. **Figure 4** indicates that the three bacterial species responded differently to NP interaction. *S. aureus* growth kinetics (**Figure 4A**) were dramatically affected by the addition of NP preparations and, as expected, by the treatment with teicoplanin. Albeit with a slightly different kinetics, cell density appeared equally reduced by two-thirds on 5 h of incubation. Indeed, NP-TEICO and non-conjugated teicoplanin drastically reduced the population growth of *B. subtilis,* whereas the effects of IONPs and NP-APTES were clearly less relevant (**Figure 4B**). Finally, teicoplanin was completely inactive toward the Gram-negative *E. coli*, whereas the addition of IONPs, NP-APTES, and NP-TEICO halved the population growth in a comparable mode (**Figure 4C**).

Significantly, CFU measurements at the end of the growth kinetics reported in **Figure 5** clearly indicate that exposure of Gram-positive bacteria to teicoplanin and NP-TEICO cleared the bacteria population, confirming the comparable antibiotic activity of the nanoconjugated versus the non-conjugated antibiotic (**Figure 5**). As expected, teicoplanin and NP-TEICO were ineffective against *E. coli* cells, which conforms to the antimicrobial spectrum of the antibiotic. In addition, exposure to IONPs and NP-APTES was not bactericidal for any of the tested strains as the cells survived quite well, and in some cases (*E. coli*) even better than the untreated cultures. Thus, we can conclude that NP-TEICO retained an antibiotic activity that was comparable to that of the non-conjugated teicoplanin, whereas IONPs and NP-APTES showed a species-specific transient interaction with bacterial cells, which slowed down population growth but did not kill bacterial cells. This phenomenon merits further investigation.

Interaction Patterns of NPs With Bacterial Cells

To shed light on the interaction pattern at the IONPs-, NP-APTES- and NP-TEICO-bacteria interfaces, we investigated the effect of adding NP on bacterial cell integrity by using the

TABLE 3 | Comparison of MICs, MBCs, and tolerance levels between non-conjugated and nanoconjugated teicoplanin.

	MIC (μg/mL)		MBC (μg/mL)		Tolerance level	
	Non-conjugated teicoplanin	**Nanoconjugated teicoplanin**	**Non-conjugated teicoplanin**	**Nanoconjugated teicoplanin**	**Non-conjugated teicoplanin**	**Nanoconjugated teicoplanin**
B. subtilis ATCC 6633	2	2	>128	>128	>64	>64
S. aureus ATCC 6538P (MSSA)	1	2	128	128	128	64
S. aureus ATCC 43300 (MRSA)	0.5	2	64	>128	128	>64
E. faecalis ATCC 29212	0.5	1	32	32	64	32
E. faecalis ATCC 51299 (VanB)	0.5	2	64	>128	128	>64
E. faecalis 9160188401-EF-34 (VanA)	>128	>128	>128	>128	–	–
E. coli ATCC 35218	>128	>128	>128	>128	–	–

The values represent the average of the data from three independent experiments.

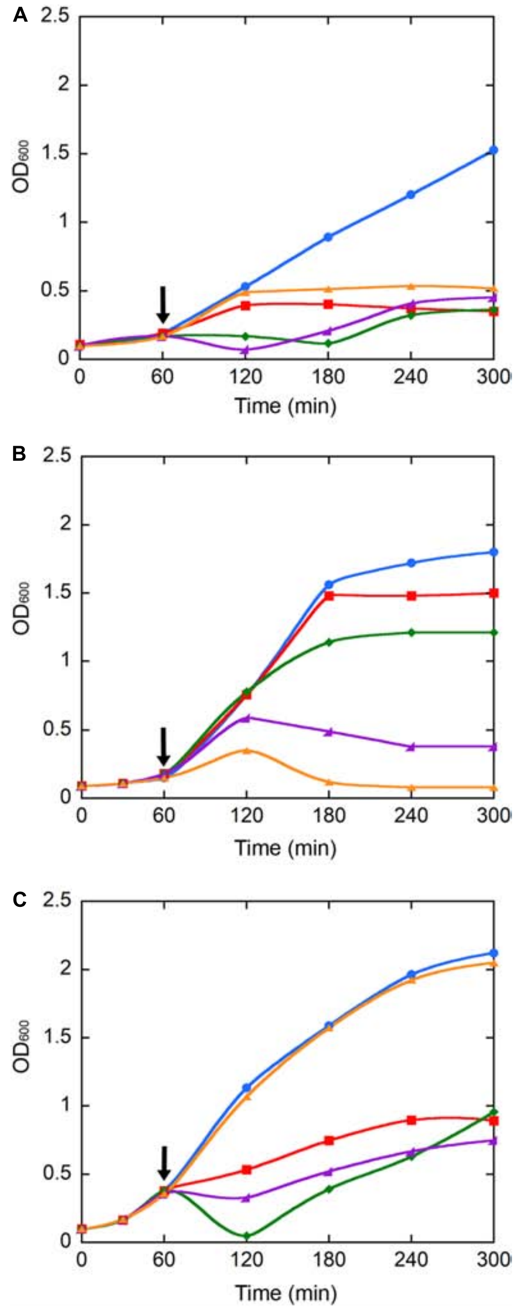

FIGURE 4 | Population growth kinetics of *S. aureus* ATCC 6538P **(A)**, *B. subtilis* ATCC 6633 **(B)**, and *E. coli* ATCC 35218 **(C)** exposed to teicoplanin (orange), IONPs (red), NP-APTES (green), and NP-TEICO (violet). Cultures without any addition (blue) were used as controls. Growth was recorded for 5 h. Black arrows indicate the addition (after 1 h of growth) of NP preparations and of teicoplanin to the bacterial populations. Triplicate experiments were conducted for each condition: standard errors were lower than 5%.

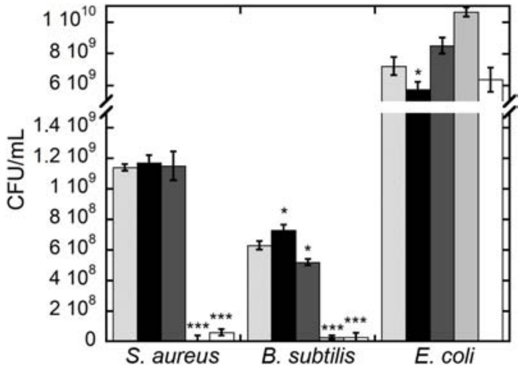

FIGURE 5 | Bacterial cell viability of *S. aureus* ATCC 6538P, *B. subtilis* ATCC 6633, and *E. coli* ATCC 35218 measured as CFUs after 5-h growth (see **Figure 4**) in the presence of IONPs (black bar), NP-APTES (gray bar), NP-TEICO (light gray bar), and teicoplanin (white bar) compared to the untreated control populations (lined bar). Triplicate experiments were conducted for each condition, and the error bars represent the standard errors. One-way ANOVA analyses, $^{*}p < 0.05$ and $^{***}p < 0.0001$.

LIVE/DEAD BacLight fluorescence assay. According to the assay principle and as shown in **Figure 6**, viable cells having an intact cell membrane were stained green by the Syto9 fluorescence dye, whereas non-viable cells with deformed cell membranes were stained red by propidium iodide fluorescence dye (Arakha et al., 2015a). As shown in **Figures 6A–C**, untreated cells of *S. aureus* ATCC 6538P, *B. subtilis* ATCC 6633, and *E. coli* ATCC 35218 exhibited green fluorescence, indicating the presence of 99% viable cells. **Figures 6D–L** show that both Gram-positive and Gram-negative bacteria tended to aggregate on NPs when present. In the presence of IONPs and NP-APTES, the *S. aureus* population exhibited almost 90% of green viable cells (**Figures 6D,G**), whereas more than 50% cells turned to red fluorescence on exposure to NP-TEICO (**Figure 6J**). On the other hand, the *B. subtilis* population exposed to IONPs (**Figures 6E,H**) exhibited the presence of 75% green viable cells, whereas the 95% of *B. subtilis* cells treated with NP-TEICO were red (**Figure 6K**), indicating that nanoconjugated teicoplanin caused a severe loss of membrane integrity and cell viability. Control populations of *S. aureus* and *B. subtilis* treated with non-conjugated teicoplanin exhibited 98% of red non-viable cells (**Figures 6M,N**). In the presence of IONPs, NP-APTES, NP-TEICO, and teicoplanin, the fraction of red fluorescent *E. coli* cells was insignificant compared to untreated cells (**Figures 6F,I,L,O**). Once again, these observations confirm that the three bacterial species responded as expected to nanoconjugated and non-conjugated teicoplanin antibiotic action. They also suggest that naked IONPs and NP-APTES interacted with the different bacteria in a species-specific mode, likely depending on the diverse bacterial surface composition, as already suggested by other authors (Huang et al., 2010; Ebrahiminezhad et al., 2014; Arakha et al., 2015a; Dinali et al., 2017).

Transmission electron microscopy images (**Figures 7A,D,G,J,M**) indicated that the exposure of *S. aureus* ATCC 6538P cells to IONPs, NP-APTES, NP-TEICO, and teicoplanin significantly altered cell morphology in comparison to the untreated cells. IONPs, NP-APTES, and, to a significantly greater extent, NP-TEICO interacted with the cell wall of this Gram-positive species. In the presence of NP-APTES,

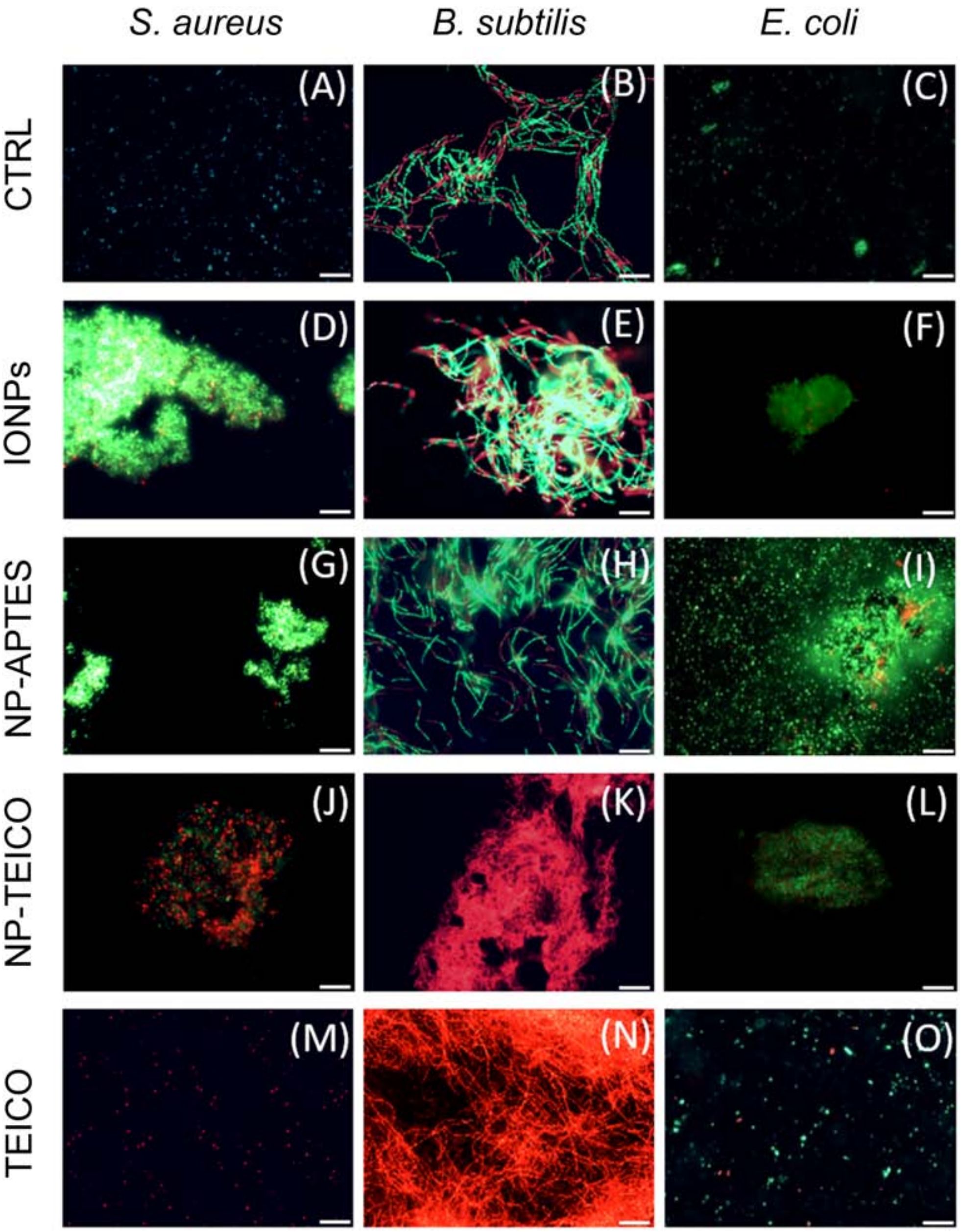

FIGURE 6 | Fluorescence microscopy images of live and dead cells of *S. aureus* ATCC 6538P [first column on the left: **(A,D,G,J,M)**], *B. subtilis* ATCC 6633 [middle column: **(B,E,H,K,N)**], and *E. coli* ATCC 35218 [column on the right: **(C,F,I,L,O)**] in the absence and presence of different NP preparations and of teicoplanin. **(A–C)** untreated cells; **(D–F)** cells treated with IONPs; **(G–I)** cells treated with NP-APTES; **(J–L)** cells treated with NP-TEICO; **(M–O)** cells treated with teicoplanin. Scale bar: 12 μm.

NP-TEICO, and teicoplanin, an increasing percentage of cells without cell walls, so-called ghost cells, became detectable (**Figures 8A,B**). Lysed cells, too, which presented damage in cell walls with cytoplasmic content leaking out, were visible within NP-APTES- and NP-TEICO-treated cells (**Figures 8A,C**). Furthermore, in the presence of NP-APTES and NP-TEICO, intracellular spherical membrane-layered, mesosome-like structures could be detected inside the cells (**Figures 8A,B**). Mesosomes were previously described by other authors (Shimoda et al., 1995; Hartmann et al., 2010), as a consequence of cell membrane damage in *S. aureus* cells treated with antimicrobial peptides such as defensins and gramicidin S.

Conversely, most of the *B. subtilis* ATCC 6633 cells (**Figures 7B,E,H**) exposed to IONPs and NP-APTES showed the same morphology as untreated cells, with undamaged structures, although a few dead or dying cells were detected, characterized by a rough surface and by an interrupted cell membrane. Indeed,

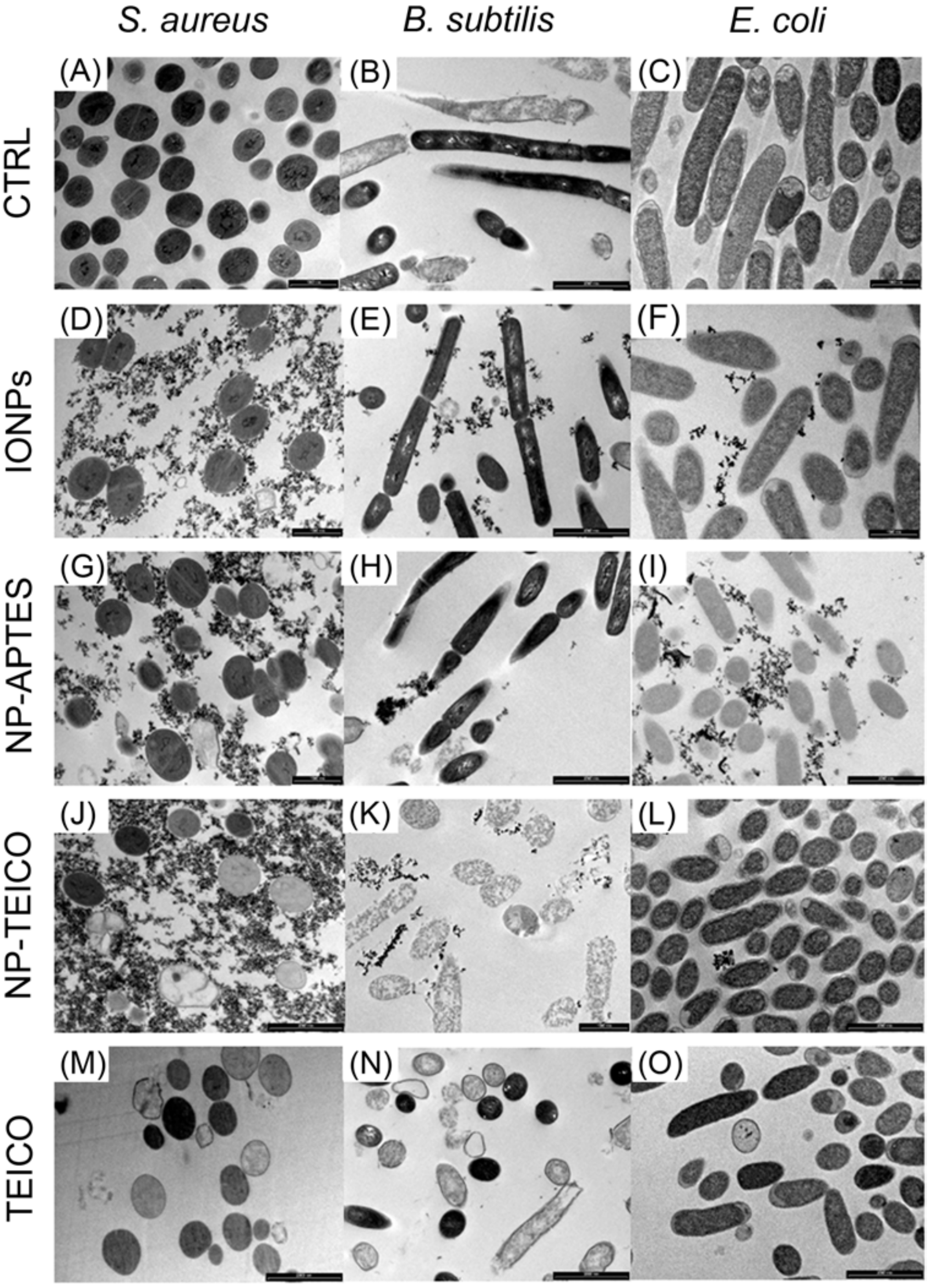

FIGURE 7 | TEM images of *S. aureus* ATCC 6538P [first column on the left: **(A,D,G,J,M)**], *B. subtilis* ATCC 6633 [middle column: **(B,E,H,K,N)**], and *E. coli* ATCC 35218 [column on the right: **(C,F,I,L,O)**] cells in the absence and presence of different NP preparations and of teicoplanin. **(A–C)** untreated cells; **(D–F)** cells treated with IONPs; **(G–I)** cells exposed to NP-APTES; **(J–L)** cells exposed to NP-TEICO; **(M–O)** cells treated with teicoplanin. Scale bars: 1 μm.

the effect of NP-TEICO and teicoplanin on cell integrity was dramatic (**Figures 7K,N**). Cells treated with NP-TEICO and teicoplanin lost their envelope integrity as a consequence of the antibiotic action (**Figures 8D,E**).

No specific alteration in cell morphology was observed in NP- or antibiotic-treated cells of *E. coli* in comparison to the untreated ones (**Figures 7C,F,I,L,O**). Interestingly, in this case, IONPs and, to a much greater extent, NP-APTES tended to stick to the microorganism envelope, whereas the presence of NP-TEICO impeded this interaction. This observation seems to confirm the occurrence of an unspecific electrostatic interaction between positively charged NP-APTES and the negatively charged external cell membrane of this Gram-negative strain, which was previously suggested by other authors (Kell et al., 2008;

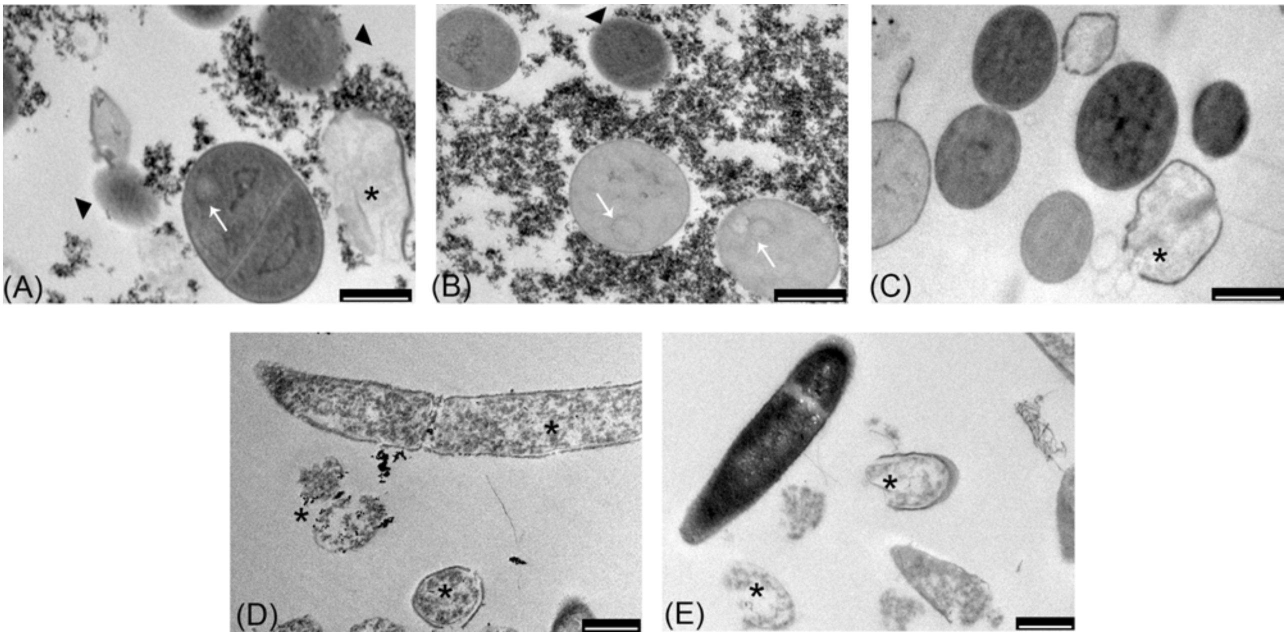

FIGURE 8 | TEM images of *S. aureus* ATCC 6538P **(A–C)** exposed to NP-APTES **(A)**, NP-TEICO **(B)**, teicoplanin **(C)**, and *B. subtilis* ATCC 6633 **(D,E)** exposed to NP-TEICO **(D)** and teicoplanin **(E)**. Scale bar: 500 nm. ▶indicates ghost cells; *indicates lysed cells; white arrows indicate mesosome-like structures.

Huang et al., 2010; Ebrahiminezhad et al., 2014; Arakha et al., 2015a; Dinali et al., 2017).

Effect of NPs on *S. aureus* Biofilm

Because of the clinical relevance of biofilm infections, the effect of our NP preparations was tested on *S. aureus* ATCC 6538P biofilm formation and eradication. As shown in **Figure 9A**, non-conjugated teicoplanin and nanoconjugated teicoplanin inhibited significantly the biofilm formation at a concentration of 2.5 μg/mL ($p = 8.03 \times 10^{-5}$) and 5 μg/mL ($p = 0.002$), respectively. No inhibitory effect on biofilm formation was observed after adding IONPs or NP-APTES in comparison to the untreated condition. In the same experimental setting, investigating the effect of IONPs, NP-APTES, NP-TEICO, and teicoplanin on the bacterial viability of adherent and planktonic cell subpopulations gave further information. It was confirmed that IONPs and NP-APTES did not influence the viability of the two subpopulations. Conversely, nanoconjugated and non-conjugated teicoplanin inhibited in a dose-dependent manner the cell viability of both planktonic (**Figure 9B**) and adherent (**Figure 9C**) cells. Teicoplanin at 5 μg/mL caused the decrease of approximately 5 log units in the survival of planktonic cells in comparison to the untreated control cells, whereas the NP-TEICO addition showed a comparable antimicrobial effect at the highest tested concentration of nanoconjugated teicoplanin corresponding to 10 μg/mL (**Figure 9B**). Increasing concentrations of non-conjugated teicoplanin caused a reduction of 2–3 log units in the survival of adherent cells, whereas, notably, the effect of nanoconjugated teicoplanin toward adherent cells was more pronounced (a reduction of 5 log units) than that of non-conjugated teicoplanin at 10 μg/mL and it was statistically significant ($p = 0.010$) (**Figure 9C**). Conversely, neither non-conjugated teicoplanin nor nanoconjugated teicoplanin showed any dispersal effect on 48-h-old biofilms (data not shown), as expected, taking into account that this glycopeptide antibiotic inhibits cell wall synthesis in exponentially growing bacterial cells and is not active on bacterial cells entering into the stationary phase (Binda et al., 2014; Marcone et al., 2018).

Cytotoxicity of NP-TEICO

Cytotoxicity of NP-TEICO was evaluated using two different human cell lines, the well-established immortalized tumor cell line (SKOV-3) (Cappellini et al., 2015) and primary mesenchymal stem cells extracted from human adipose tissue, which are particularly sensitive to nanomaterials (Palombella et al., 2017). Results shown in **Figure 10** indicate that teicoplanin did not exert any effect on the cell viability of either of the human cell lines at any of the tested concentrations. Conversely, both SKOV-3 cells and hASC responded to the exposure of IONPs and NP-TEICO in a concentration-dependent manner. No significant decrease in cell viability was observed after adding nanoconjugated teicoplanin in the range of teicoplanin antibacterial MICs (0.78 μg/mL) (**Figures 10A,B**). The corresponding amounts of carrying NPs did not influence cell viability significantly (**Figures 10A,B**). At a concentration threefold higher than the antibacterial MICs of NP-TEICO (6 μg/mL), the effects of nanoconjugated teicoplanin and of the carrier NPs significantly differed from that of the free antibiotic. Naked IONPs reduced cell viability by more than 60% (after 24 h of exposure) to 50% (after 96 h) in SKOV-3 cells (**Figure 10C**), and by 50% (after 24 h) to 70% (after 96 h) in hASC (**Figure 10D**). NP-TEICO were less cytotoxic, reducing cell viability by 40% (after 24 h) to 20% (after

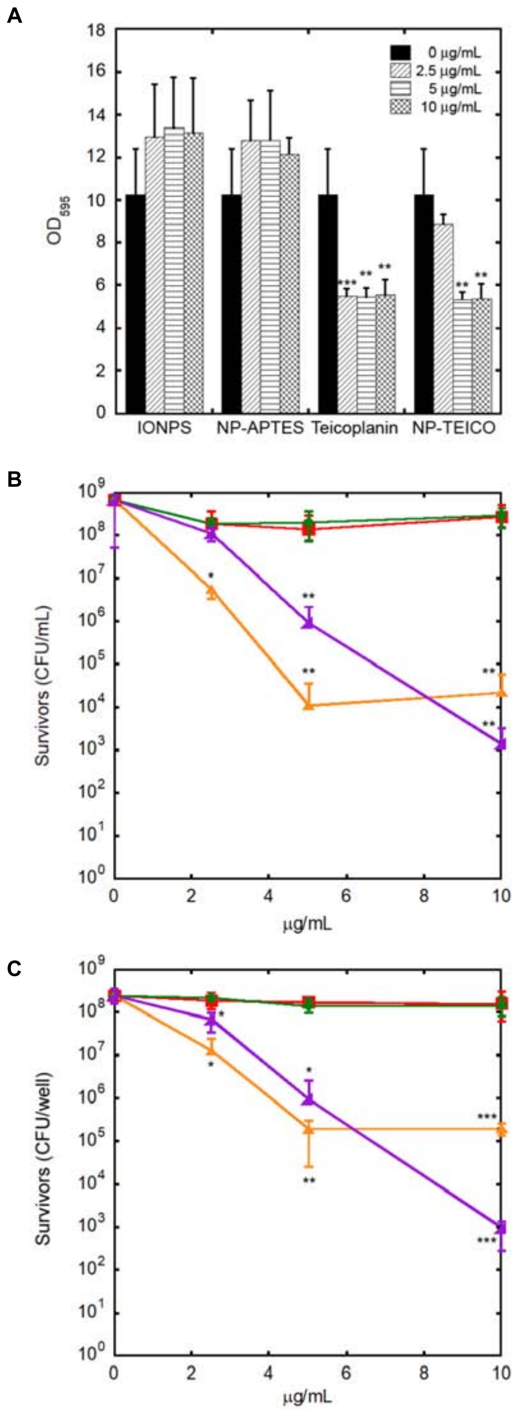

FIGURE 9 | Effect of increasing concentrations of teicoplanin, NP-TEICO, IONPs, and NP-APTES on *S. aureus* ATCC 6538P biofilm formation. In the case of NP preparations, the amounts to be added were defined considering the teicoplanin loaded on IONPs under the conditions defined in the Materials and Methods. Effect on adherent biomass following crystal violet staining **(A)**. Effect on planktonic **(B)** and adherent **(C)** cells exposed to teicoplanin (orange), IONPs (red), NP-APTES (green), and NP-TEICO (violet) on viability assay. The values are expressed as mean ± SD of three independent experiments. One-way ANOVA analyses, $^*p < 0.05$, $^{**}p < 0.01$, and $^{***}p < 0.0001$.

96 h) in SKOV-3 cells (**Figure 10C**) and by less than 30% (after 24 h) to 20% (after 96 h) in hASC (**Figure 10D**). Interestingly, conjugation of antibiotic molecules to IONPs surface tended to reduce their intrinsic cytotoxicity, as already reported by other authors who demonstrated that covering the NP surface shields toxicity and improves biocompatibility (Javed et al., 2017; Xiang et al., 2017; Xie et al., 2017, 2018).

DISCUSSION

In the era of antibiotic resistance, the lipoglycopeptide teicoplanin is an extremely important antibiotic used for the prophylaxis and treatment of serious infections caused by Gram-positive bacteria, including MRSA and *E. faecalis* (Van Bambeke, 2006; Marcone et al., 2018). It is used to treat endocarditis, bacteremia, and bone and joint infections. Because of its efficacy and safety, it is used in pediatrics, too. Its spectrum of antibacterial action is similar to that of the previously discovered glycopeptide vancomycin, but teicoplanin has several advantages over vancomycin in the treatment of serious infections: longer half-life, lower nephrotoxicity and ototoxicity, and lack of requirement for serum assays in treated patients. Because of its better stability *in vivo*, it can be administered once a day or with an alternate daily dosage and by intravenous bolus or by intramuscular injection. Oral administration of teicoplanin has also been demonstrated to be effective in the treatment of pseudomembranous colitis and *C. difficile*-associated diarrhea. In addition, teicoplanin is active on some of the vancomycin-resistant enterococci, which are increasingly spreading in hospitals (Binda et al., 2014).

Notwithstanding these important features, to the best of our knowledge, this is the first report of using teicoplanin to functionalize NPs. The teicoplanin molecule has an addressable functional group (the N-terminal carboxylic group of the heptapeptide chain) that we used to covalently bind the amino-activated IONPs. Although there are few published data on optimizing the fabrication of nanoconjugated antibiotics onto IONPs (Lin et al., 2005; Hussein-Al-Ali et al., 2014; Zhu et al., 2015; Dinali et al., 2017), we succeeded in anchoring more than 100 μg of teicoplanin per mg of NP-APTES in this work. The antimicrobial potency of nanoconjugated teicoplanin was slightly lower than that of the non-conjugated counterpart, particularly toward resistant clinical isolates, but NP-TEICO conserved the teicoplanin antimicrobial spectrum of activity toward Gram-positive bacteria and it was particularly active in controlling *S. aureus* biofilm formation. The external membrane of Gram-negative bacteria covering the peptidoglycan layer remained highly impenetrable to both NP-TEICO and teicoplanin, impeding their interaction with the molecular target (Binda et al., 2014). One of the positive features of NP-TEICO prepared in this way was that the formulation maintained chemical stability and antimicrobial activity for at least 1 month. This aspect is relevant, considering that one main advantage of using magnetic antibiotic nanocarriers *in vivo* could be that they can be recovered and recycled after single uses, reducing local dose administration and potential side effects and decreasing the risk of selective

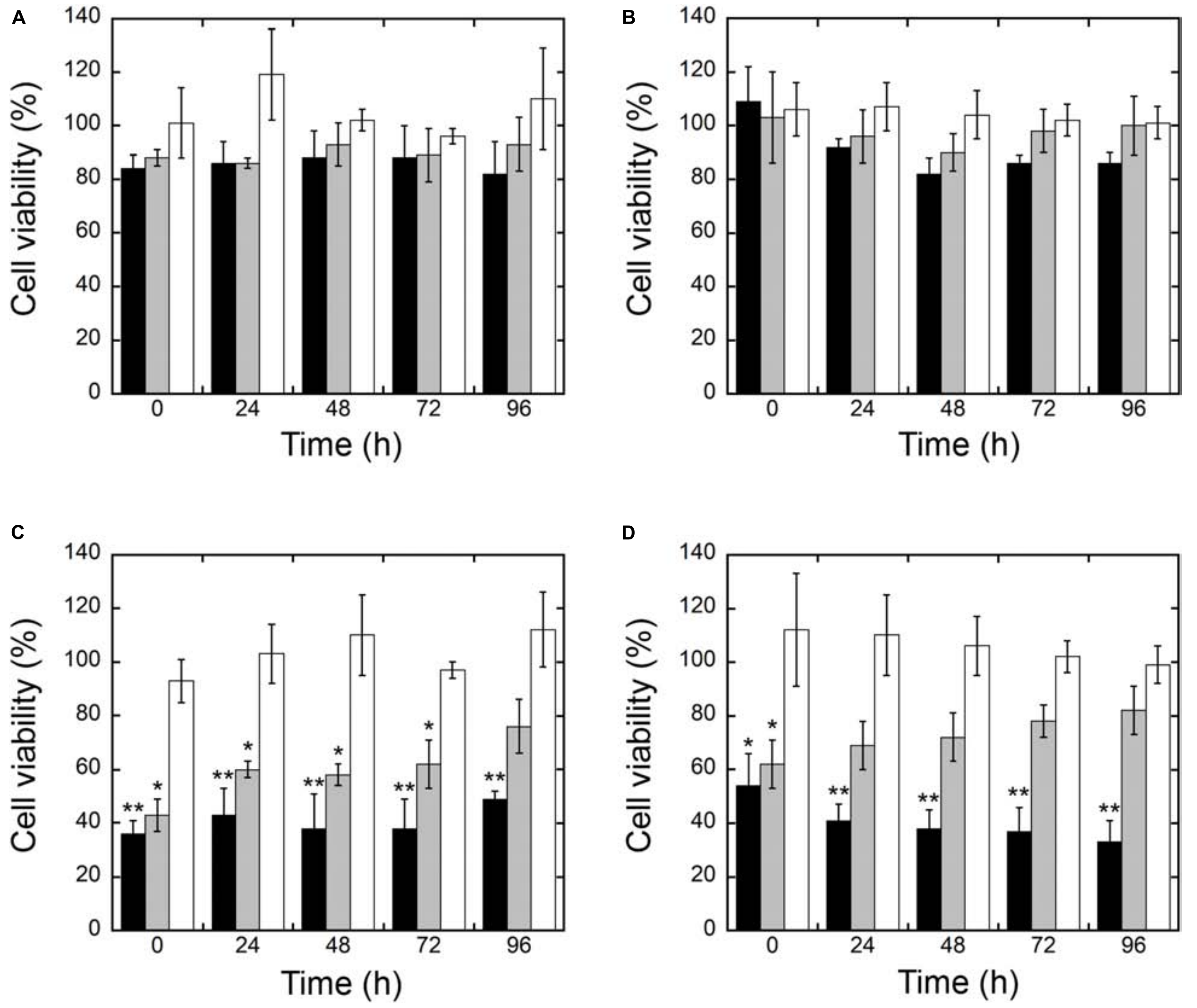

FIGURE 10 | Cell viability of SKOV 3 **(A,C)** and hASC **(B,D)** after different times of exposure to IONPs (black), NP-TEICO (gray), and teicoplanin (white). Cell viability is expressed as a percentage of viable cells compared to the untreated sample, set as 100%. Here, 0.78 μg/mL of non-conjugated or nanoconjugated teicoplanin or 6.24 μg/mL of carrying NPs were added in **(A,B)**; 6 μg/mL of non-conjugated or nanoconjugated teicoplanin or 48 μg/mL of carrying NPs were added in **(C,D)**. In the case of NP preparations, the amounts to be added were defined considering the teicoplanin loaded on IONPs under the conditions defined in the Materials and Methods. The values are expressed as mean ± SD of three independent experiments. One-way ANOVA analyses, $^{*}p < 0.05$ and $^{**}p < 0.01$.

pressure on resistant strains. In addition, their targeted delivery to the site of infection/biofilm by using an external magnetic field might increase their *in situ* concentration, potentiating their local efficacy. For this reason, we consider the fact that NP-TEICO inhibited *S. aureus* biofilm formation, conserving the activity of non-conjugated teicoplanin versus the planktonic cells and improving it toward the adherent cells, to be promising. Different non-specific interactions such as electrostatic, hydrophobic, and van der Waal interactions are responsible for adhesion of bacteria on any material surfaces creating biofilms. Thus, it is possible that NP-TEICO anti-biofilm activity is potentiated (in comparison to the non-conjugated antibiotic) by intercepting these non-specific interactions, although in our experiments IONPs and NP-APTES had no effect on biofilm formation.

Unfortunately, *S. aureus* has dramatically re-emerged as a clinically relevant pathogen due to its resistance to antibiotics and the increased use of indwelling clinical devices. Millions of indwelling medical devices are implanted every year, and *S. aureus* is the major culprit for infections and failure of these devices (Arciola et al., 2018). *S. aureus* biofilms are also implicated in chronic wound infections such as diabetic foot ulcers, venous stasis ulcers, and pressure sores, which are quite resistant to antibiotic treatments. Teicoplanin carried by magnetically driven NPs can more easily reach deep tissue infections, which are difficult to treat using topical antibiotics due to the poor tissue penetration, and better penetrate the diffusion barriers that biofilms produce.

In the last decade, a certain level of intrinsic antimicrobial and cytotoxicity activity has been controversially attributed to the IONPs themselves. Although IONPs and NP-APTES have shown some antibacterial effect against diverse Gram-positive and Gram-negative bacteria, the real extent of this phenomenon and the underlying mechanism has hitherto not been well understood (Baranwal et al., 2018). Ansari et al. (2017) reported a dose-dependent antibacterial activity of IONPs against *Bacillus cereus* and *Klebsiella pneumoniae.* In contrast, Auffan et al. (2008) indicated that chemically stable IONPs were not toxic to *E. coli* at 700 mg/L, whereas Chatterjee et al. (2011) reported a dose-dependent effect on *E. coli* cells. Borcherding et al. (2014) showed that IONPs had a positive effect in promoting the growth of *Pseudomonas aeruginosa.* Arakha et al. (2015a) published an illuminating study and demonstrated, by combining a complete set of microbiological and biophysical methods, that IONPs did not show any significant antimicrobial activity toward *B. subtilis* and *E. coli*. Coating IONPs with positively charged chitosan, instead, conferred them with an increased so-called antimicrobial propensity against *B. subtilis* and *E. coli,* which depends on the interfacial interaction between NPs and bacterial surfaces (Arakha et al., 2015a,b).

In the present work, we compared the antimicrobial activity of NP-TEICO with that shown by IONPs and NP-APTES by using a set of methods (agar diffusion assay, BacLight fluorescence assay, bacterial growth kinetics, CFU measurement, and TEM observations) comparable to those previously used by Arakha et al. (2015a,b). Thus, we could conclude that the antibiotic activity of nanoconjugated and non-conjugated teicoplanin differed dramatically from the phenomenon described as antimicrobial propensity, which is based on an electrostatic attraction between cationic NPs and anionic bacterial cell surfaces (Arakha et al., 2015a,b). Electrostatic attraction promotes unspecific adhesion of NPs onto the cell wall of Gram-positive bacteria and the external cell membrane of the Gram-negative bacteria (Qi et al., 2013; Baranwal et al., 2018). This adhesion likely represents the mechanism by which IONPs and, to a greater extent, the positively charged NP-APTES impaired the growth of *S. aureus*, *B. subtilis,* and *E. coli* in our experiments of bacterial growth kinetics. This interfacial effect was transient and reversible, differing from the specific killing activity of teicoplanin and NP-TEICO toward the Gram-positive bacteria. Nevertheless, TEM observations suggested that we cannot completely rule out that cell adhesion of IONPs and of NP-APTES might provoke cytosolic shrinkage and cell membrane detachment (and eventually cell rupture), as observed in *S. aureus* and, with a lower frequency, in *B. subtilis*. In any case, this phenomenon was again sporadic, probably depending on surface composition and on the physiological state of single bacterial cells, as indicated by Dinali et al. (2017).

Although IONPs have been increasingly proposed for a wide range of biomedical applications, such as drug delivery, magnetic resonance imaging, thermal ablation therapy, and treatment of iron-deficient anemia, our understanding of their interaction with animal cells and animal models is still relatively limited (Natan and Banin, 2017; Feng et al., 2018). Recent studies showed that physicochemical properties, including particle size, PDI, surface charge, oxidation state of iron, and different surface coatings, greatly influence their biological effect *in vitro* and *in vivo* (Feng et al., 2018; Wang et al., 2018). Among the super magnetic NPs, IONPs were generally preferred because they are less toxic than those based on nickel and cobalt (Gornati et al., 2016). However, it was recently demonstrated that IONPs can enter eukaryotic cells not only by endocytosis, but also by diffusion through the plasma membrane, gaining direct access to the cytoplasm (Zanella et al., 2017). In addition, the intrinsic catalase-like activity of IONPs might antagonize the accumulation of toxic reactive oxygen species they have induced and thereby modulate the extent of cellular oxidative stress, autophagic activity, and programmed cell death (Wang et al., 2018). In this complex framework, a complete evaluation of the cytocompatibility of our NP-TEICO preparation *in vitro* and *in vivo* systems lies outside the scope of this work, although it would represent a future interesting extension of the study. Here, we demonstrated that at the concentrations that encompass the teicoplanin antibacterial MIC values, teicoplanin coating of IONPs reduced their intrinsic cytotoxicity toward two human cell lines, thus improving their potential biocompatibility. Further intensive *in vitro* and *in vivo* investigations are needed to develop an NP-TEICO-based drug formulation that could be administered systemically or topically to treat deep tissue infections and/or cover medical devices to prevent biofilm formation. Our results indicate that combining synergistically the unique properties of different nanomaterials would represent a good strategy, in this way providing a novel route to prevent and treat bacterial infections and, at the same time, reduce the intrinsic cytotoxicity of NPs, as already indicated by other authors (Xiang et al., 2017; Xie et al., 2017, 2018).

AUTHOR CONTRIBUTIONS

IA, GM, GB, and FM conceived the experiments, interpreted the results, and wrote the manuscript. IA developed and produced the NPs and performed the characterization. IA, FB, and GM conducted and interpreted the experiments on the microbiological activity of NPs. VO and EM conducted and analyzed the experiments on biofilms. CP and RG performed the microscopical observations and cell cytotoxicity tests and analyzed the results. All authors reviewed and approved the final manuscript.

FUNDING

This work was supported by public grants "Fondo di Ateneo per la Ricerca" 2016, 2017 to FM, GM, RG, and GB.

ACKNOWLEDGMENTS

We are grateful to Consorzio Interuniversitario per le Biotecnologie for supporting congress participation of FB. IA is a Ph.D. student of the "Biotechnology, Biosciences and Surgical Technology" course at Università degli Studi dell'Insubria. EM is a Ph.D. student of the "Life Science and Biotechnology" course at Università degli Studi dell'Insubria.

REFERENCES

Ali, A., Zafar, H., Zia, M., ul Haq, I., Phull, A. R., Ali, J. S., et al. (2016). Synthesis, characterization, applications, and challenges of iron oxide nanoparticles. *Nanotechnol. Sci. Appl.* 9, 49–67. doi: 10.2147/NSA.S99986

Allen, N. E., and Nicas, T. I. (2003). Mechanism of action of oritavancin and related glycopeptide antibiotics. *FEMS Microbiol. Rev.* 26, 511–532. doi: 10.1111/j.1574-6976.2003.tb00628.x

Ansari, S. A., Oves, M., Satar, R., Khan, A., Ahmad, S. I., Jafri, M. A., et al. (2017). Antibacterial activity of iron oxide nanoparticles synthesized by co-precipitation technology against *Bacillus cereus* and *Klebsiella pneumoniae*. *Polish J. Chem. Technol.* 4, 110–115. doi: 10.1515/pjct-2017-0076

Arakha, M., Pal, S., Samantarrai, D., Panigrahi, T. K., Mallick, B. C., Pramanik, K., et al. (2015a). Antimicrobial activity of iron oxide nanoparticle upon modulation of nanoparticle-bacteria interface. *Sci. Rep.* 5:14813. doi: 10.1038/srep14813

Arakha, M., Saleem, M., Mallick, B. C., and Jha, S. (2015b). The effects of interfacial potential on antimicrobial propensity of ZnO nanoparticle. *Sci. Rep.* 5:9578. doi: 10.1038/srep09578

Arciola, C. R., Campoccia, D., and Montanaro, L. (2018). Implant infections: adhesion, biofilm formation and immune evasion. *Nat. Rev. Microbiol.* 16, 397–409. doi: 10.1038/s41579-018-0019-y

Armenia, I., Balzaretti, R., Pirrone, C., Allegretti, C., D'Arrigo, P., Valentino, M., et al. (2017). L-aspartate oxidase magnetic nanoparticles: synthesis, characterization and L-aspartate bioconversion. *RSC Adv.* 7, 21136–21143. doi: 10.1039/C7RA00384F

Auffan, M., Achouak, W., Rose, J., Roncato, M. A., Chanéac, C., Waite, D. T., et al. (2008). Relation between the redox state of iron-based nanoparticles and their cytotoxicity toward *Escherichia coli*. *Environ. Sci. Technol.* 42, 6730–6735. doi: 10.1021/es800086f

Balzaretti, R., Meder, F., Monopoli, M. P., Boselli, L., Armenia, I., Pollegioni, L., et al. (2017). Synthesis, characterization and programmable toxicity of iron oxide nanoparticles conjugated with D-amino acid oxidase. *RSC Adv.* 7, 1439–1442. doi: 10.1039/c6ra25349k

Baranwal, A., Srivastava, A., Kumar, P., Bajpai, V. K., Maurya, P. K., and Chandra, P. (2018). Prospects of nanostructure materials and their composites as antimicrobial agents. *Front. Microbiol.* 9:422. doi: 10.3389/fmicb.2018.00422

Binda, E., Cappelletti, P., Marinelli, F., and Marcone, G. L. (2018). Specificity of induction of glycopeptide antibiotic resistance in the producing actinomycetes. *Antibiotics* 7:E36. doi: 10.3390/antibiotics7020036

Binda, E., Marinelli, F., and Marcone, G. L. (2014). Old and new glycopeptide antibiotics: action and resistance. *Antibiotics* 3, 572–594. doi: 10.3390/antibiotics3040572

Borcherding, J., Baltrusaitis, J., Chen, H., Stebounova, L., Wu, C. M., Rubasinghege, G., et al. (2014). Iron oxide nanoparticles induce *Pseudomonas aeruginosa* growth, induce biofilm formation, and inhibit antimicrobial peptide function. *Environ. Sci. Nano* 1, 123–132. doi: 10.1039/C3EN00029J

Cappellini, F., Recordati, C., Maglie, M., De Pollegioni, L., Rossi, F., Daturi, M., et al. (2015). New synthesis and biodistribution of the D-amino acid oxidase-magnetic nanoparticle system. *Future Sci. OA* 1, FS067. doi: 10.4155/Fso.15.67

Chakraborty, S. P., Sahu, S. K., Mahapatra, S. K., Santra, S., Bal, M., Roy, S., et al. (2010). Nanoconjugated vancomycin: new opportunities for the development of anti-VRSA agents. *Nanotechnol.* 21, 105103–105111. doi: 10.1088/0957-4484/21/10/105103

Chakraborty, S. P., Sahu, S. K., Pramanik, P., and Roy, S. (2012). In vitro antimicrobial activity of nanoconjugated vancomycin against drug resistant *Staphylococcus aureus*. *Int. J. Pharm.* 436, 659–676. doi: 10.1016/j.ijpharm.2012.07.033

Chatterjee, S., Bandyopadhyay, A., and Sarkar, K. (2011). Effect of iron oxide and gold nanoparticles on bacterial growth leading towards biological application. *J. Nanobiotechnol.* 9, 34–40. doi: 10.1186/1477-3155-9-34

Chifiriuc, M. C., Grumezescu, A. M., Andronescu, E., Ficai, A., Cotar, A. I., Grumezescu, V., et al. (2013). Water dispersible magnetite nanoparticles influence the efficacy of antibiotics against planktonic and biofilm embedded *Enterococcus faecalis* cells. *Anaerobe* 22, 14–19. doi: 10.1016/j.anaerobe.2013.04.013

Chudasama, B., Vala, A. K., Andhariya, N., Upadhyay, R. V., and Mehta, R. V. (2009). Enhanced antibacterial activity of bifunctional Fe3O4-Ag core-shell nanostructures. *Nano Res.* 2, 955–965. doi: 10.1007/s12274-009-9098-4

CLSI (2018). *Performance Standards for Antimicrobial Susceptibility Testing*, 28th Edn. Wayne, PA: Clinical and Laboratory Standards Institute.

Davis, D. (2003). Understandng biofilm resistance to antibacterial agents. *Nat. Rev. Drug Discov.* 2, 114–122. doi: 10.1038/nrd1008

De Palma, R., Peeters, S., Van Bael, M. J., Van Den Rul, H., Bonroy, K., Laureyn, W., et al. (2007). Silane ligand exchange to make hydrophobic superparamagnetic nanoparticles water-dispersible. *Chem. Mater.* 19, 1821–1831. doi: 10.1021/cm0628000

Dinali, R., Ebrahiminezhad, A., Manley-Harris, M., Ghasemi, Y., and Berenjian, A. (2017). Iron oxide nanoparticles in modern microbiology and biotechnology. *Crit. Rev. Microbiol.* 43, 493–507. doi: 10.1080/1040841X.2016.1267708

Dong, S. D., Oberthür, M., Losey, H. C., Anderson, J. W., Eggert, U. S., Peczuh, M. W., et al. (2002). The structural basis for induction of VanB resistance. *J. Am. Chem. Soc.* 124, 9064–9065. doi: 10.1021/ja026342h

Durán, N., Durán, M., de Jesus, M. B., Seabra, A. B., Fávaro, W. J., and Nakazato, G. (2016). Silver nanoparticles: a new view on mechanistic aspects on antimicrobial activity. *Nanomedicine* 12, 789–799. doi: 10.1016/j.nano.2015.11.01

Ebrahiminezhad, A., Rasoul-Amini, S., Davaran, S., Barar, J., and Ghasemi, Y. (2014). Impacts of iron oxide nanoparticles on the invasion power of *Listeria monocytogenes*. *Curr. Nanosci.* 10, 382–388. doi: 10.2174/15734137113096660109

El Zowalaty, M. E., Hussein-Al-Ali, S. H., Husseiny, M. I., Geilich, B. M., Webster, T. J., and Hussein, M. Z. (2015). The ability of streptomycin-loaded chitosan-coated magnetic nanocomposites to possess antimicrobial and antituberculosis activities. *Int. J. Nanomedicine* 10, 3269–3274. doi: 10.2147/IJN.S74469

Fedorenko, V., Genilloud, O., Horbal, L., Marcone, G. L., Marinelli, F., Paitan, Y., et al. (2015). Antibacterial discovery and development: from gene to product and back. *Biomed. Res. Int.* 2015:591349. doi: 10.1155/2015/591349

Feng, Q., Liu, Y., Huang, J., Chen, K., Huang, J., and Xiao, K. (2018). Uptake, distribution, clearance, and toxicity of iron oxide nanoparticles with different sizes and coatings. *Sci. Rep.* 8:2082. doi: 10.1038/s41598-018-19628-z

Finn, R. K. (1959). Theory of agar diffusion methods for bioassay. *Anal. Chem.* 31, 975–977. doi: 10.1021/ac60150a040

Gonçalves, L. C., Seabra, A. B., Pelegrino, M. T., de Araujo, D. R., Bernardes, J. S., and Haddad, P. S. (2017). Superparamagnetic iron oxide nanoparticles dispersed in pluronic F127 hydrogel: potential uses in topical applications. *RSC Adv.* 7, 14496–14503. doi: 10.1039/C6RA28633J

Gornati, R., Pedretti, E., Rossi, F., Cappellini, F., Zanella, M., Olivato, I., et al. (2016). Fe, Co and Ni nanoparticle toxicity evaluated on SKOV-3 and U87 cell lines. *J. Appl. Toxicol.* 36, 385–393. doi: 10.1002/jat.3220

Grumezescu, A. M., Gesta, M. C., Holban, A. M., Grumezescu, V., Vasile, B. S., Mogoanta, L., et al. (2014). Biocompatible Fe3O4 increases the efficacy of amoxicillin delivery against Gram-positive and Gram-negative bacteria. *Molecules* 19, 5013–5027. doi: 10.3390/molecules19045013

Gu, H., Ho, P. L., Tsang, K. W. T., Yu, C. W., and Xu, B. (2003). Using biofunctional magnetic nanoparticles to capture Gram-negative bacteria at an ultra-low concentration. *Chem. Commun.* 7, 1966–1967. doi: 10.1039/b305421g

Hajipour, M. J., Fromm, K. M., Akbar Ashkarran, A., Jimenez de Aberasturi, D., Larramendi, I. R., de Rojo, T., et al. (2012). Antibacterial properties of nanoparticles. *Trends Biotechnol.* 30, 499–511. doi: 10.1016/j.tibtech.2012.06.004

Hartmann, M., Berditsch, M., Hawecker, J., Ardakani, M. F., Gerthsen, D., and Ulrich, A. S. (2010). Damage of the bacterial cell envelope by antimicrobial peptides gramicidin S and PGLa as revealed by transmission and scanning electron microscopy. *Antimicrob. Agents Chemother.* 54, 3132–3142. doi: 10.1128/AAC.00124-10

Hermanson, G. T. (2013). "Zero-Length Crosslinkers," in *Bioconjugate Techniques*, 3rd Edn, eds J. Audet and M. Preap (London, UK: Academic Press), 259–268. doi: 10.1016/B978-0-12-382239-0.00004-2

Huang, Y. F., Wang, Y. F., and Yan, X. P. (2010). Amine-functionalized magnetic nanoparticles for rapid capture and removal of bacterial pathogens. *Environ. Sci. Technol.* 44, 7908–7913. doi: 10.1021/es102285n

Hussein-Al-Ali, S. H., El Zowalaty, M. E., Hussein, M. Z., Geilich, B. M., and Webster, T. J. (2014). Synthesis, characterization, and antimicrobial activity of an ampicillin-conjugated magnetic nanoantibiotic for medical applications. *Int. J. Nanomedicine* 9, 3801–3814. doi: 10.2147/IJN.S61143

Javed, Y., Akhtar, K., Anwar, H., and Jamil, Y. (2017). MRI based on iron oxide nanoparticles contrast agents: effect of oxidation state and architecture. *J. Nanopart. Res.* 19:366. doi: 10.1007/s11051-017-4045-x

Kell, A. J., Stewart, G., Ryan, S., Peytavi, R., Boissinot, M., Huletsky, A., et al. (2008). Vancomycin-modified nanoparticles for efficient targeting and preconcentration of Gram-positive and Gram-negative bacteria. *ACS* 2, 1777–1788. doi: 10.1021/nn700183g

Lin, Y. S., Tsai, P. J., Weng, M. F., and Chen, Y. C. (2005). Affinity capture using vancomycin-bound magnetic nanoparticles for the MALDI-MS analysis of bacteria. *Anal. Chem.* 77, 1753–1760. doi: 10.1021/ac048990k

Marcone, G. L., Binda, E., Berini, F., and Marinelli, F. (2018). Old and new glycopeptide antibiotics: from product to gene and back in the post-genomic era. *Biotechnol. Adv.* 36, 534–554. doi: 10.1016/j.biotechadv.2018.02.009

May, J., Shannon, K., King, A., and French, G. (1998). Glycopeptide tolerance in *Staphylococcus aureus*. *J. Antimicrob. Chemother.* 42, 189–197. doi: 10.1093/jac/42.2.189

Natan, M., and Banin, E. (2017). From Nano to Micro: using nanotechnology to combat microorganisms and their multidrug resistance. *FEMS Microbiol. Rev.* 41, 302–322. doi: 10.1093/femsre/fux003

Palombella, S., Pirrone, C., Rossi, F., Armenia, I., Cherubino, M., Valdatta, L., et al. (2017). Effects of metal micro and nano-particles on hASCs: an in vitro model. *Nanomaterials* 7:E212. doi: 10.3390/nano7080212

Qi, G., Li, L., Yu, F., and Wang, H. (2013). Vancomycin-modified mesoporous silica nanoparticles for selective recognition and killing of pathogenic Gram-positive bacteria over macrophage-like cells. *ACS Appl. Mater. Interfaces* 5, 10874–10881. doi: 10.1021/am403940d

Schneider, C. A., Rasband, W. S., and Eliceiri, K. W. (2012). NIH Image to ImageJ: 25 years of image analysis. *Nat. Methods* 9, 671–675.

Shimoda, M., Ohki, K., Shimamoto, Y., and Kohashi, O. (1995). Morphology of defensin-treated *Staphylococcus aureus*. *Infect. Immun.* 63, 2886–2891.

Stepien, G., Moros, M., Pérez-Hernández, M., Monge, M., Gutiérrez, L., Fratila, R. M., et al. (2018). Effect of surface chemistry and associated protein corona on the long-term biodegradation of iron oxide nanoparticles in vivo. *ACS Appl. Mater. Interfaces* 10, 4548–4560. doi: 10.1021/acsami.7b18648

Szpak, A., Kania, G., Skórka, T., Tokarz, W., Zapotoczny, S., and Nowakowska, M. (2013). Stable aqueous dispersion of superparamagnetic iron oxide nanoparticles protected by charged chitosan derivatives. *J. Nanoparticle Res.* 15, 1372–1382. doi: 10.1007/s11051-012-1372-9

Taurino, C., Frattini, L., Marcone, G. L., Gastaldo, L., and Marinelli, F. (2011). Actinoplanes teichomyceticus ATCC 31121 as a cell factory for producing teicoplanin. *Microb. Cell Fact.* 10, 82–94. doi: 10.1186/1475-2859-10-82

Tran, N., Mir, A., Mallik, D., Sinha, A., Nayar, S., and Webster, T. J. (2010). Bactericidal effect of iron oxide nanoparticles on Staphylococcus aureus. *Int. J. Nanomedicine* 5, 277–283. doi: 10.2147/IJN.S9220

Treviño, J., Bayón, C., Ardá, A., Marinelli, F., Gandolfi, R., Molinari, F., et al. (2014). New insights into glycopeptide antibiotic binding to cell wall precursors using SPR and NMR spectroscopy. *Chemistry* 20, 7363–7372. doi: 10.1002/chem.201303310

Van Bambeke, F. (2006). Glycopeptides and glycodepsipeptides in clinical development: a comparative review of their antibacterial spectrum, pharmacokinetics and clinical efficacy. *Curr. Opin. Investig. Drug* 7, 740–749.

Venkatesan, N., Perumal, G., and Doble, M. (2015). Bacterial resistance in biofilm-associated bacteria. *Future Microbiol.* 10, 1743–1750. doi: 10.2217/fmb.15.69

Wang, C., Zhang, K., Zhou, Z., Li, Q., Shao, L., Hao, R. Z., et al. (2017). Vancomycin-modified Fe3O4@SiO2@Ag microflowers as effective antimicrobial agents. *Int. J. Nanomedicine* 12, 3077–3094.

Wang, L., Wang, Z., Li, X., Zhang, Y., Yin, M., Li, J., et al. (2018). Deciphering active biocompatibility of iron oxide nanoparticles from their intrinsic antagonism. *Nano Res.* 11, 2746–2755. doi: 10.1007/s12274-017-1905-8

Weiner, L. M., Webb, A. K., Limbago, B., Dudeck, M. A., Patel, J., Kallen, A. J., et al. (2016). Antimicrobial-resistant pathogens associated with healthcare-associated infections: summary of data reported to the National Healthcare Safety Network at the Centers for Disease Control and Prevention, 2011-2014. *Infect. Control Hosp. Epidemiol.* 37, 1288–1301. doi: 10.1017/ice.2016.174

WHO (2017). *Antibacterial Agents in Clinical Development: an Analysis of the Antibacterial Clinical Development Pipeline, Including Tuberculosis*. Geneva: World Health Organization.

Wu, W., Wu, Z., Yu, T., Jiang, C., and Kim, W. S. (2015). Recent progress on magnetic iron oxide nanoparticles: synthesis, surface functional strategies and biomedical applications. *Sci. Technol. Adv. Mater.* 16:023501. doi: 10.1088/1468-6996/16/2/023501

Xiang, Y., Li, J., Liu, X., Cui, Z., Yang, X., Yeung, K. W. K., et al. (2017). Construction of poly(lactic-co-glycolic acid)/ZnO nanorods/Ag nanoparticles hybrid coating on Ti implants for enhanced antibacterial activity and biocompatibility. *Mater. Sci. Eng. C* 79, 629–637. doi: 10.1016/j.msec.2017.05.115

Xie, X., Mao, C., Liu, X., Tan, L., Cui, Z., Yang, X., et al. (2018). Tuning the bandgap of photo-sensitive polydopamine/Ag3PO4/graphene oxide coating for rapid, noninvasive disinfection of implants. *ACS Cent. Sci.* 4, 724–738. doi: 10.1021/acscentsci.8b00177

Xie, X., Mao, C., Liu, X., Zhang, Y., Cui, Z., Yang, X., et al. (2017). Synergistic bacteria killing through photodynamic and physical actions of graphene oxide/Ag/collagen coating. *ACS Appl. Mater. Interfaces* 9, 26417–26428. doi: 10.1021/acsami.7b06702

Zanella, D., Bossi, E., Gornati, R., Bastos, C., Faria, N., and Bernardini, G. (2017). Iron oxide nanoparticles can cross plasma membranes. *Sci. Rep.* 7:11413. doi: 10.1038/s41598-017-11535-z

Zhu, M., Liu, W., Liu, H., Liao, Y., Wei, J., Zhou, X., et al. (2015). Construction of Fe3O4/vancomycin/PEG magnetic nanocarrier for highly efficient pathogen enrichment and gene sensing. *ACS Appl. Mater. Interfaces* 7, 12873–12881. doi: 10.1021/acsami.5b02374

Conflict of Interest Statement: The authors declare that the research was conducted in the absence of any commercial or financial relationships that could be construed as a potential conflict of interest.

frontiers in Microbiology

ORIGINAL RESEARCH
published: 06 February 2019
doi: 10.3389/fmicb.2019.00142

Pullulan Nanoparticles as Prebiotics Enhance the Antibacterial Properties of *Lactobacillus plantarum* Through the Induction of Mild Stress in Probiotics

Liang Hong*[1]*, Whee-Soo Kim*[1]*, Sang-Mok Lee*[1]*, Sang-Kee Kang*[2]*, Yun-Jaie Choi*[1,3]** and Chong-Su Cho*[1,3]

[1] Department of Agricultural Biotechnology, Seoul National University, Seoul, South Korea, [2] Institutes of Green-bio Science & Technology, Seoul National University, Pyeongchang, South Korea, [3] Research Institute of Agriculture and Life Sciences, Seoul National University, Seoul, South Korea

Edited by:
Gerson Nakazato,
State University of Londrina, Brazil

Reviewed by:
Paola Sperandeo,
University of Milan, Italy
César de la Fuente,
Massachusetts Institute of Technology, United States

***Correspondence:**
Yun-Jaie Choi
cyjcow@snu.ac.kr
Chong-Su Cho
chocs@snu.ac.kr

Specialty section:
This article was submitted to Antimicrobials, Resistance and Chemotherapy, a section of the journal Frontiers in Microbiology

Received: *02 August 2018*
Accepted: *21 January 2019*
Published: *06 February 2019*

Citation:
Hong L, Kim W-S, Lee S-M, Kang S-K, Choi Y-J and Cho C-S (2019) Pullulan Nanoparticles as Prebiotics Enhance the Antibacterial Properties of Lactobacillus plantarum Through the Induction of Mild Stress in Probiotics.
Front. Microbiol. 10:142.
doi: 10.3389/fmicb.2019.00142

Synbiotics, which are the combination of probiotics and prebiotics, have recently attracted attention because of their synergistic net health benefits. Probiotics have been used as alternatives to antibiotics. Among the probiotics, *Lactobacillus plantarum* (LP) has shown strong antimicrobial activity against *Escherichia coli K99*, a major livestock pathogen. In this study, we aimed to investigate the antimicrobial activity of phthalyl pullulan nanoparticle (PPN)-treated LP. Interestingly, when PPNs were added to LP, the PPNs were internalized into the LP through an energy-dependent and galactose transporter-dependent mechanism. Additionally, more plantaricin, a natural antibacterial peptide, was secreted from PPN-treated LP than from untreated or pullulan-treated LP. Furthermore, antimicrobial activity against Gram-negative *Escherichia coli K99* and Gram-positive *Listeria monocytogenes* by PPN-treated LP was higher than those of untreated or pullulan-treated LP. It is thought that the enhanced antimicrobial properties of the PPN-treated LP are due to intracellular stimulation. Overall, this research provides a new method of producing plantaricin in LP through intracellular stimulation by internalized PPNs.

Keywords: probiotics, prebiotics, pullulan nanoparticles, internalization, plantaricin

INTRODUCTION

According to the World Health Organization (WHO), the use of antibiotics as growth promoters for livestock is a major cause of antibiotic resistance. Antibiotic resistance affects not only livestock health but also human health (World Health Organization, 2000). Therefore, finding alternatives to antibiotics and addressing drug resistance have become important issues for scientists (de la Fuente-Nunez et al., 2012; Allen et al., 2014). Recently, several studies have demonstrated the potential of probiotics are potential candidates as antibiotic alternatives due to their ability to inhibit bacterial colonization on the gut barrier or to directly kill pathogens through their secreted bacteriocins (Gillor et al., 2008). Therefore, there have been many attempts to increase the production of bacteriocins, including biological and physical methods. A biological engineering strategy as one of biological methods enhanced production of bacteriocins in probiotics with higher stability and good characteristics (Papagianni and Anastasiadou, 2009); however, the method is very complex, and consumers are increasingly concerned about genetically modified products. The physical methods used to optimize the production of bacteriocins include changing pH, temperature, pressure, oxygen content, and incubation time during probiotic culture (Arokiyamary and Sivakumaar.,2011). Interestingly, in our previous studies (Cui et al., 2018; Kim et al., 2018), pediocin production in *Pediococcus acidilactici* (PA) was markedly enhanced through intracellular stimulation by internalized inulin nanoparticles used as a synbiotic.

Among the probiotics, *Lactobacillus plantarum* (LP) is a versatile and abundant microorganism found in several environments ranging from food to animal gastrointestinal tracts (de Vries et al., 2006). It is also known that some strains of LP are capable of producing several natural antimicrobial substances, such as bacteriocins and organic acids (lactic acid and acetic acid), thereby inhibiting competitors in the same niche (Todorov et al., 2011; Reis et al., 2012). It was previously reported that LP 177 isolated from pig intestines exhibited strong antibacterial activity against *E. coli K99*, which can cause bacterial diarrhea in pigs (Yun, 2007; Seo, 2012).

Prebiotics used as non-digestible food additives beneficially affect the host by selectively stimulating the growth and/or activity of a limited number of microorganisms in the colon (Gibson and Roberfroid, 1995). Most prebiotics are inulin-based fructose oligomers or galacto-oligosaccharides (Kneifel, 2000). Among potential prebiotic compounds, pullulan has long been applied to food additives (Cheng et al., 2011). Pullulan is an α-1,6 linked polymer of maltotriose subunits and is secreted by the fungus *Aureobasidium pullulans* (Catley et al., 1986). Due to its high molecular weight and slow hydrolysis by α-amylase and glucoamylase, pullulan is considered to be a non-digestible carbohydrate (Leathers, 2003). It was previously reported that pullulan fermented by the microbiota can alter the composition of the intestinal microbiota (Sugawa-Katayama et al., 1994).

In recent years, many researchers have begun to synthesize and apply drug delivery systems based on pullulan-based self-assembled nanoparticles (Na et al., 2003; Jeong et al., 2006; Zhang et al., 2010). By contrast, our synthetic PPN application is not a drug or gene carrier but a new type of prebiotic.

One of the simplest ways to synthesize polymeric nanoparticles is the self-assembly of hydrophobically modified hydrophilic polymers. Self-assembled polymeric nanoparticles, consisting of a hydrophobic core and a hydrophilic shell, have been used as promising drug carriers because they can be rapidly internalized by mammalian cells after loading drugs into their hydrophobic cores (Zhang et al., 2008).

In this study, we are aimed to investigate the antimicrobial activities of phthalyl pullulan nanoparticle (PPN)-treated LP. We synthesized and characterized PPNs to develop a new type of prebiotic for LP. In addition, we checked whether the internalization of PPNs by LP led to enhanced antimicrobial activity by LP against Gram negative bacteria *Escherichia coli K99* and Gram positive bacteria *Listeria.monocytogenes* (LM) than LP or pullulan alone by antimicrobial assays. We further validated the mechanism of the antimicrobial activity of PPN-treated LP by the internalization of PPNs by LP.

MATERIALS AND METHODS

Materials

Pullulan used in this study was purchased from Shandong Freda Biotechnology Co., Ltd. (Shandong, China), and other chemicals were purchased from Sigma-Aldrich (St. Louis, MO, United States). Lysogeny broth (LB), LB agar, De Man, Rogosa and Sharpe agar (MRS) broth, MacConkey agar, and brain heart infusion (BHI) broth were purchased from BD Difco (Sparks, MD, United States) for bacterial culture.

Synthesis of PPNs

Phthalyl pullulan nanoparticles were synthesized according to a previously described method,(Na and Bae, 2002) with a slight modification. One gram of pullulan was dissolved in 10 ml of dimethyl formamide (DMF), and 0.1 mol-% dimethylaminopyridine per pullulan sugar residue was added to the solution as a catalyst., and then phthalic anhydride was added to the above solution at different molar ratios per pullulan, including 6:1 (phthalic anhydride: pullulan) (named PPN1), 9:1 (phthalic anhydride: pullulan) (named PPN2), and 12:1 (phthalic anhydride: pullulan) (named PPN3), to produce PPNs with different degrees of substitution of phthalic groups. The reaction was performed at 54°C for 48 h under nitrogen. The produced PPNs were dialyzed first in DMF to remove unreacted phthalic anhydride and then in distilled water at 4°C for 24 h to form self-assembled nanoparticles of phthalyl pullulan. The unreacted pullulan was removed after ultra-centrifugation of prepared PPNs. Finally, the PPNs were freeze-dried and stored at −20°C until use.

Characterization of PPNs

The content of the phthalyl groups in PPNs was confirmed by 600 MHz ^{1}H-nuclear magnetic resonance (NMR) spectroscopy (AVANCE 600, Bruker, Germany). The surface topography of PPNs was analyzed using a field-emission scanning electron microscope (FE-SEM) with SUPRA 55VP-SEM (Carl Zeiss, Oberkochen, Germany). The PPNs were mounted onto stubs with adhesive copper tape and coated with platinum under a vacuum using a coating chamber (CT 1500 HF, Oxford Instruments, Oxfordshire, United Kingdom). The sizes of the nanoparticles were measured with a dynamic light scattering (DLS) spectrophotometer (DLS-7000, Otsuka Electronics, Japan). The zeta potential of the nanoparticles was measured with an electrophoretic light scattering (ELS) spectrophotometer (ELS-8000, Otsuka Electronics, Japan).

Confirmation of Internalization of PPNs by LP

First, the fluorescence isothiocyanate (FITC)-labeled PPNs were prepared as follows. Five mg of FITC was mixed with 100 mg

PPNs or pullulan dissolved in 2 ml dimethyl sulfoxide (DMSO). After stirring for 4 h in an opaque tube at room temperature, the products were dialyzed against distilled water at 4°C for 24 h. Finally, FITC-labeled PPNs and pullulan were lyophilized and stored at −20°C until use.

To observe the internalization of PPNs and pullulan by probiotics, LP 177 (2.0×10^6 CFU/ml) was inoculated into 1 ml of MRS broth, treated with 0.5% (w/v) FITC-PPNs or FITC-pullulan, and incubated for 2 h at 37°C. The samples were then washed with PBS and analyzed by flow cytometry and confocal laser scanning microscopy (CLSM) (SP8X STED, Leica, Wetzlar, Germany). To confirm the internalization of nanoparticles into the probiotics, LP treated with FITC-PPN3 was observed by Z-section mode in CLSM.

To confirm the temperature-dependent internalization of nanoparticles, three separate cultures of LP were treated with 0.5% (w/v) FITC-PPN3 and incubated at 4, 20, and 37°C for 2 h. The samples were further washed with PBS and analyzed by flow cytometry and CLSM. To confirm further the transporter-dependent internalization of nanoparticles into probiotics, and glucose, galactose, fructose and PPN3 were used as blocking agents. LP (2.0×10^6 CFU/ml) was inoculated into 1 ml of PBS and pre-treated with 10% (w/v) glucose, galactose, fructose or PPN3 for 10 min at 37°C before treatment with 0.5% (w/v) FITC-PPN3. After 2 h of incubation at 37°C, the samples were washed three times with PBS, and the internalization of PPN3 was analyzed by flow cytometry and CLSM.

Bacterial Cultures

Escherichia coli (E. coli) K99 and *Listeria monocytogenes* (LM) were used as representative Gram-negative and Gram-positive pathogens, respectively. MRS, LB, and BHI broths were used for LP 177, *E. coli* K99, and LM, respectively. All bacteria cultures were incubated at 37°C in a shaking incubator (250 rpm) for 24 h prior to experimental procedures or stored at −70°C in 15% glycerol for further use.

Co-culture Assay and Agar Diffusion Test for Antimicrobial Ability

Antimicrobial activity of LP against *E. coli* and LM was determined using co-culture assays (Ditu et al., 2011) and agar diffusion tests (Driscoll et al., 2012), with some modifications. To compare the antimicrobial activity of LP against *E. coli* by co-culture assay, 2.0×10^6 CFU/ml of *E. coli* was co-cultured with 2.0×10^5 CFU/ml LP treated with or without 0.5% (w/v) PPNs or pullulan in MRS broth for 8 h at 37°C under aerobic conditions in a shaking incubator (250 rpm). The antimicrobial activity was determined by the survival rate of *E. coli*. The co-cultured samples were spread on MacConkey agar and incubated for 24 h at 37°C, and the number of *E. coli* colonies was counted. The antimicrobial activity of LP against LM was also determined by co-culture assay. LP and LM were co-cultured in BHI broth under similar conditions as described above. Finally, the co-cultured samples were spread on Oxford agar, and the number of LM colonies was counted.

The agar diffusion test was used to determine whether the cultured medium of LP treated with or without PPNs and pullulan was able to inhibit the growth of pathogens on an agar plate. First, 100 μl *E. coli* stock (2.0×10^8 CFU/ml) was spread onto LB agar. A paper disk was placed on the *E. coli*-spread plate, then 120 μl 8 h-cultured LP media of LP treated with or without (0.5% w/v) PPNs and pullulan was dropped onto the paper disk. After drying at room temperature, the plate was cultured overnight at 37°C. The zone of inhibition of *E. coli* growth was used as a direct measurement of antimicrobial activity. The same protocols were followed to test the inhibitory effect of LP treated with or without 0.5% (w/v) PPNs or pullulan on LM growth on BHI agar plates.

To confirm plantaricin activity, agar diffusion tests of LP against *E. coli* and LM were performed using the same protocols described above after the culture medium was treated with 1 mg/ml proteinase K and incubated at 37°C for 2 h, and then each culture supernatant was heated at 100°C for 30 min.

Analysis of the Growth Conditions of LP

After treatment of LP with or without PPNs or pullulan as described above, the growth characteristics of the LP were checked by measuring the pH of growth medium and viable cell counts at the indicated time points.

Protein Isolation and Identification by SDS–PAGE

Plantaricin was isolated and purified as described in a previous study(Song et al., 2014) with some modifications. Supernatants from the cocultured medium were stirred with ammonium sulfate (80% saturation) for 2 h at room temperature. The precipitated proteins, collected by centrifugation, was dissolved in citrate phosphate buffer (50 mM) and desalted by dialysis (1 kDa cut-off membrane, Spectrum Lab, United States). Proteins were lyophilized and stored at 4°C for further analyses.

Sodium dodecyl sulfate-polyacrylamide gel electrophoresis (SDS–PAGE) was used to observe the isolated plataricin.

Analysis of Stress Response and Plantaricin Genes by Quantitative Real-Time PCR

RNA extraction was performed using the TRIzol® Max™ Bacterial RNA Isolation Kit purchased from Thermo-Fisher Scientific Inc. (Waltham, MA, United States). Total RNA extraction was conducted according to the manufacturer's instructions. LP was treated with or without PPNs or pullulan as described above. After the isolation of RNA, cDNA was synthesized from 1 μg RNA using ReverTra Ace® qPCR RT Master Mix with gDNA Remover purchased from TOYOBO CO., LTD (Dojima, Osaka, Japan). Quantitative real-time PCR (qRT-PCR) was performed with SYBR qPCR Mix using one-step real-time PCR. The primers are listed in **Table 1**. Relative gene expression was calculated using the $-2\Delta\Delta$Ct method. The target gene expression was normalized to the relative expression of 16s rRNA as an internal control in each sample.

TABLE 1 | Primers used in this study.

Gene	Primer sequence (5′-3′)	Size (bp)
planS	F:GCCTTACCAGCGTAATGCCC R:CTGGTGATGCAATCGTTAGTTT	450
dnaK	F:ATTAACGGACATTCCAGCGG R:TTGGCCTTTTTGTTCTGCCG	600
dnaJ	F:GGAACGAATGGTGGCCCTTA R:CTAGACGCACCCACCACAAA	474

RESULTS

Synthesis and Characterization of PPNs

The reaction scheme of PPN synthesis is shown in **Figure 1**. The degree of substitution of phthalic moieties in pullulan was confirmed by ^{1}H-NMR spectroscopy (**Figure 2A**) and calculated by determining the ratio of phthalic acid protons (7.4–7.7 ppm) to sugar protons (C_1 position of α-1,6 and α-1,4 glycosidic bonds, 4.68 and 5.00 ppm, respectively) as described by Tao et al. (Tao et al., 2016). According to the degrees of substitution of phthalic acid, the PPNs were named as follows: PPN1 (DS: 30.90 mol. −%), PPN2 (DS: 50.45 mol. −%) and PPN3 (DS: 68.50 mol. −%). Using SEM, PPN3 (**Figure 2D**) was determined to be spherical and sized between 100 and 150 nm. The sizes of nanoparticles measured by DLS were 140.0, 108.9, and 82.1 nm for PPN1, PPN2, and PPN3, respectively (**Figure 2C**), indicating that the particles sizes decreased with an increase in the number of conjugated phthalic acid groups in pullulan. Furthermore, the surface charges of the PPNs, measured by ELS, were −38.09, −38.45, and −33.84 mV for PPN1, PPN2, and PPN3, respectively (**Figure 2B**). Due to the unreacted carboxyl groups in phthalic acid, the PPNs showed negative zeta potential.

Internalization of PPNs by LP

To confirm the internalization of PPNs by LP, PPNs were conjugated to fluorescence isothiocyanate (FITC). The internalization of FITC-PPNs by LP was analyzed by CLSM and quantified by fluorescence-activated cell sorting (FACS). It was observed by CLSM that FITC-PPNs and FITC-pullulan were able to enter LP after incubation at 37°C for 2 h (**Supplementary Figure S2A**). The internalization of PPNs into LP was not much different among the PPNs due to the not much differences of the particle sizes of the PPNs, although pullulan alone entered LP through a diffusion mechanism. To further confirm whether the PPNs were located at the

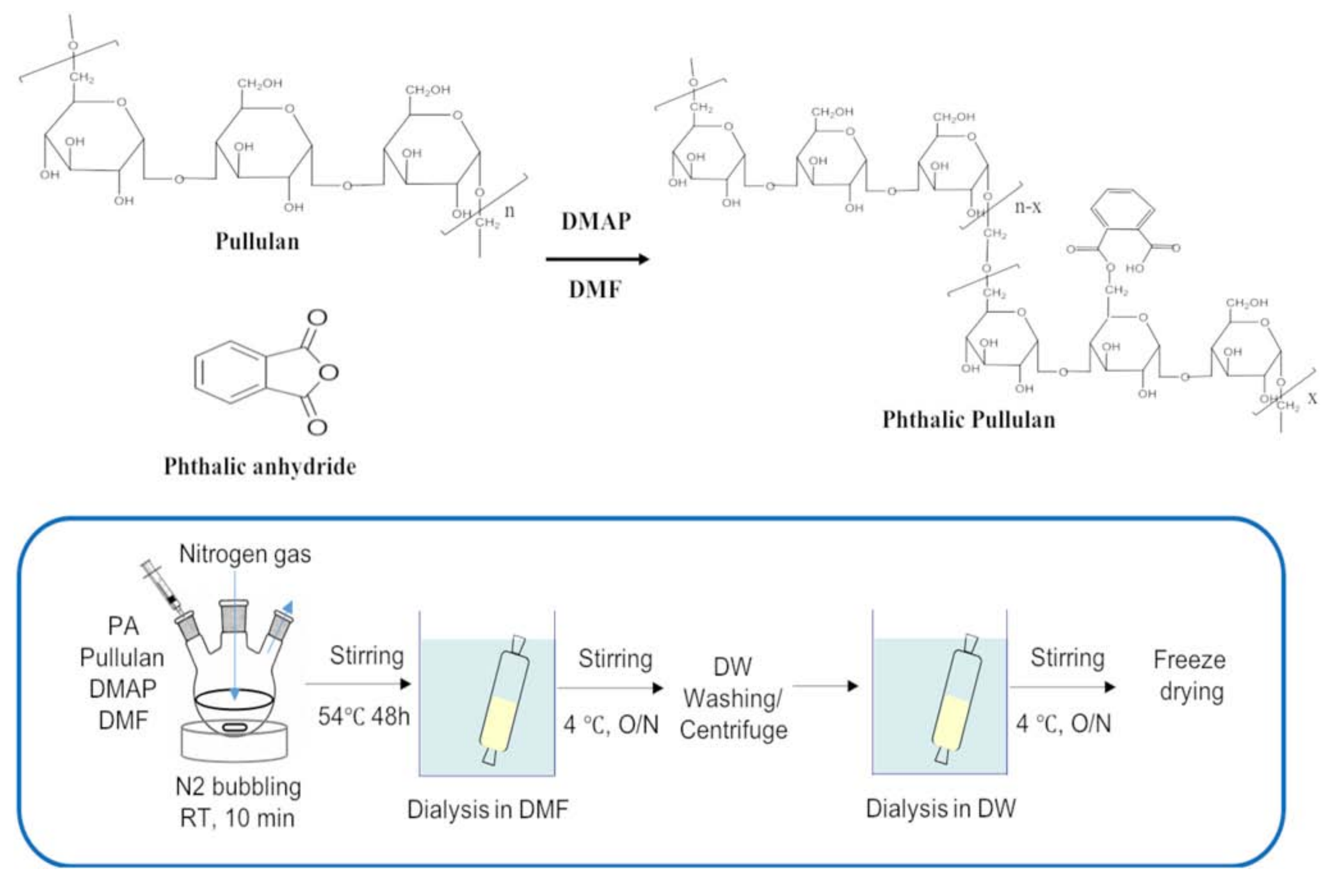

FIGURE 1 | Chemical reaction scheme for the synthesis of PPNs (PPNs: phthalyl pullulan nanoparticles).

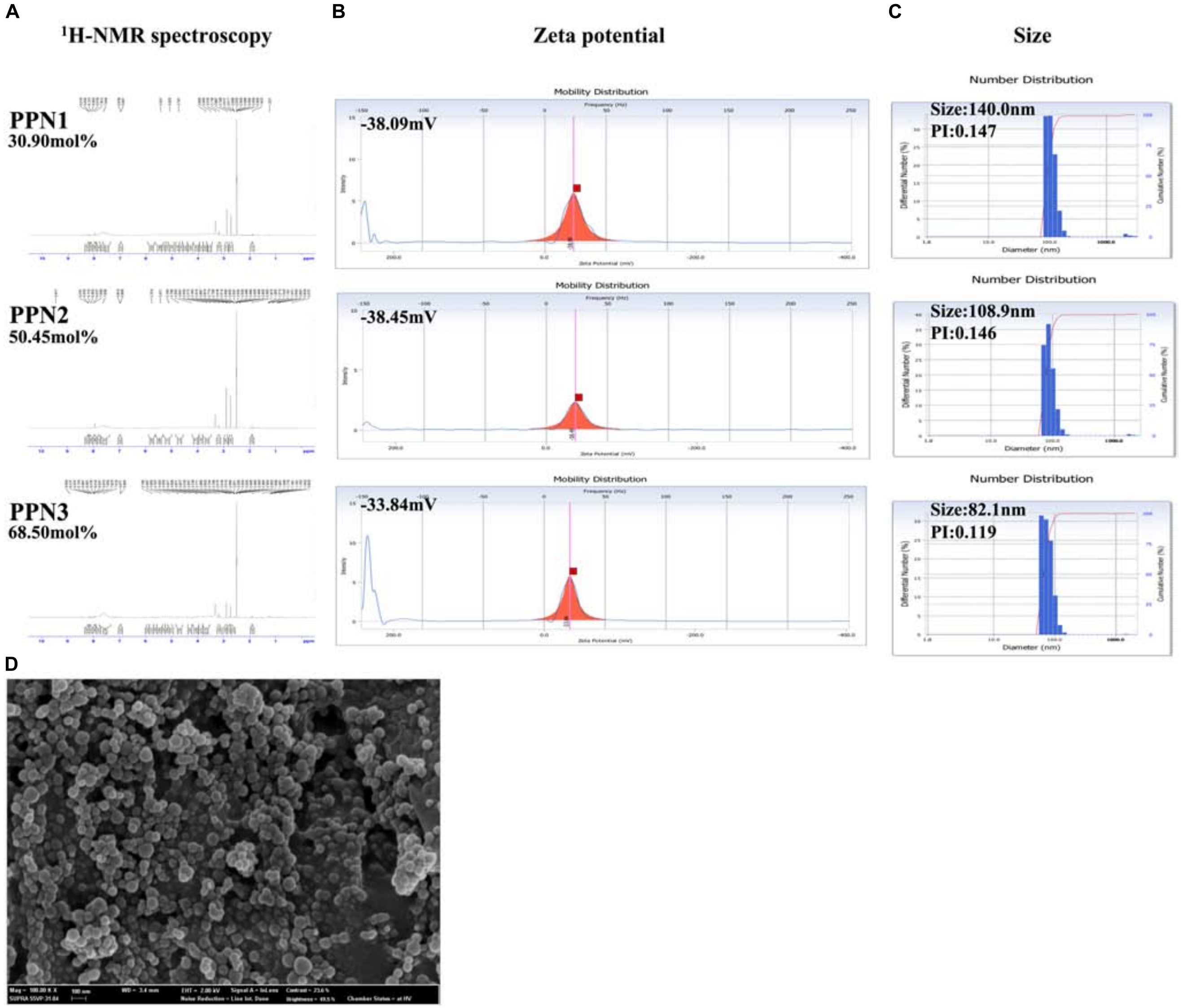

FIGURE 2 | Characteristics of PPNs. Calculation of mol.-% phthalic acid in PPNs by ^{1}H-NMR spectroscopy **(A)**. Measurement of the zeta potential of PPNs by ELS **(B)** and size by DLS **(C)**. Morphologies of PPNs observed by SEM **(D)**. Magnification: 100,00K, scale bar = 100 nm. (PPNs: phthalyl pullulan nanoparticles, H-NMR: nuclear magnetic resonance, ELS: electrophoretic light scattering, DLS: dynamic light scattering, SEM: scanning electron microscope).

cell surface or were internalized by LP, LP was treated with FITC-PPN3 and the location of FITC-PPN3 was identified by Z-section mode of CLSM. As shown in **Figure 3A**, the fluorescence intensity of FITC and DAPI was the highest at the center of LP, indicating the internalization of PPNs by LP. We also performed the experiment using a membrane binding dye (FM4-64) as a negative control. As shown in **Supplementary Figure S1A**, the fluorescence intensity of FITC was the highest at the center of LP, and confirmed that the FITC fluorescence appeared inside the bacteria (**Supplementary Figure S1B**).

Further studies were performed to determine the effect of incubation temperature and the role of sugar transporters in the internalization of PPNs by LP. To determine if the internalization of PPN3 by LP was temperature-dependent, LP was treated with FITC-PPN3 at 4°C, room temperature or 37°C for 2 h and subsequently analyzed by CLSM and FACS. The internalization of PPN3 by LP was highest at 37°C, suggesting that the internalization of PPN3 was energy-dependent (**Supplementary Figure S2B**). Furthermore, to determine whether the internalization of PPN3 was via a sugar transporter, LP was pre-treated with 10% (w/v) glucose, galactose, fructose, and PPN3, and then treated with 0.5% (w/v) FITC-PPN3 for 2 h. The internalization was then observed by CLSM and FACS (**Figure 3B**). The results showed that the internalization of PPN3 was predominantly dependent on the galactose transporter of LP because pre-treatment with galactose blocked approximately 40% of the

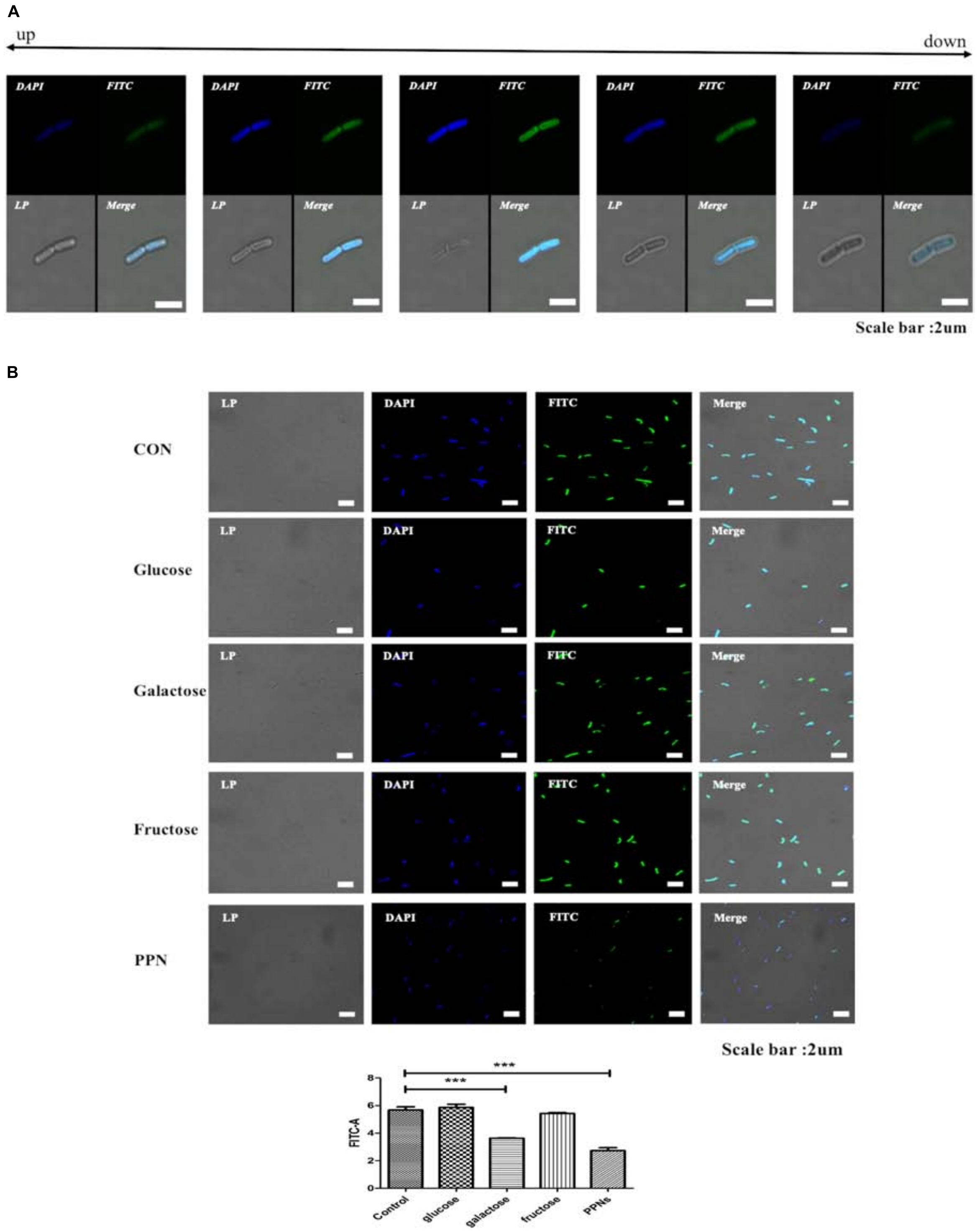

FIGURE 3 | Analysis of the internalization of PPNs by LP. FITC-PPNs are shown in green, and LP was stained blue with DAPI. The internalization of PPNs after 2 h of treatment was quantified by FACS and statistically analyzed. Z-section images show the internalization of corresponding PPNs into LP **(A)**. Analysis of the internalization of PPNs by LP depending on transporters **(B)**. LP, pre-incubated with 10% (w/v) glucose, fructose, galactose or PPN3 was treated with 0.5% (w/v) FITC-PPN3 for 2 h at 37°C, and internalization was observed by CLSM and FACS. Confocal and FACS data are representative of three independent experiments, and the average values are presented as the mean ± SEM of three independent FACS experiments in a bar chart. Statistical significance was analyzed between each group by one-way ANOVA and Tukey's *t*-test (***$p < 0.001$). Scale bar = 10 μm. (LP: *Lactobacillus plantarum,* PPN: phthalyl pullulan nanoparticle, CLSM: confocal laser scanning microscopy, FACS: fluorescence-activated cell sorting, FITC: fluorescein isothiocyanate, DAPI: 4′,6-diamidino-2-phenylindole).

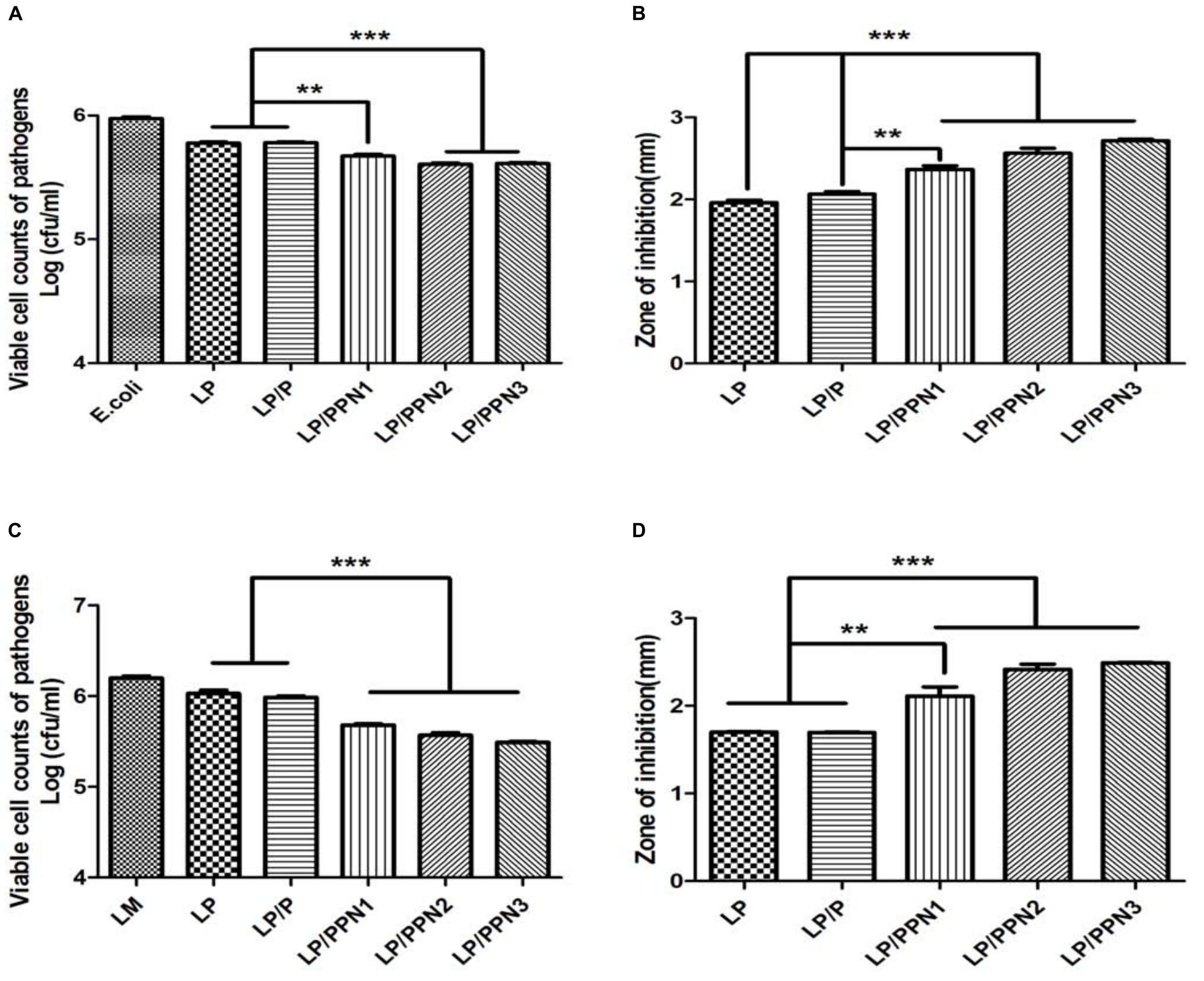

FIGURE 4 | Antimicrobial efficacy of LP/PPNs against *E. coli* and LM **(A-D).** LP treated with PPNs or pullulan were cultured with Gram-negative *E. coli* or Gram-positive LM, and the growth inhibition was calculated by CFU for *E. coli* **(A)** and LM **(C)**. Similarly, the diameters of the growth inhibition of *E. coli* **(B)** and LM **(D)** on LB and BHI agar plates, respectively, were measured. Data are presented as the mean ± SEM of three independent experiments. Statistical significance was analyzed between LP treated with P and LP treated with PPNs by one-way ANOVA and Tukey's *t*-test ($^{**}p < 0.01$ and $^{***}p < 0.001$). (LP: *Lactobacillus plantarum,* PPN: phthalyl pullulan nanoparticle, P: pullulan, CFU: colony forming unit, LM: *Listeria monocytogenes*, LB: lysogeny broth, BHI: brain heart infusion).

internalization of PPNs by LP. And it was found that the internalization of PPN3 was also blocked by pre-treatment of PPNs.

Effects of PPNs on Antimicrobial Activity

To evaluate whether the internalization of PPNs by LP affected its antimicrobial activity, LP was treated with three types of PPNs or pullulan itself. The antimicrobial activity of PPN-treated LP (LP/PPNs) was then tested against *E. coli* and LM and compared with that of untreated or pullulan-treated (LP/P) LP. The antimicrobial activity of the LP/PPNs groups was higher than that of untreated LP or LP/P against both *E. coli* and LM by co-culture assays (**Figures 4A,C**). Interestingly, stronger antimicrobial activity was observed when LP was treated with smaller nanoparticles. To determine whether the PPNs alone had antimicrobial activity, *E. coli* and LM were treated with PPNs. PPNs alone displayed no antimicrobial activity (data not shown), indicating that the antimicrobial activity must be derived from the internalization of the PPNs by LP. In addition, the antimicrobial activity of LP/PPNs against *E. coli* and LM was further evaluated by agar diffusion tests. The inhibition zone was relatively larger when LP was treated with smaller PPNs (**Figures 4B,D**), suggesting that the agar diffusion tests showed similar antimicrobial patterns of LP/PPNs against *E. coli* and LM.

To test whether LP exerts its antimicrobial activity via plantaricin, a natural peptide, we added proteinase K to the medium of LP during agar diffusion tests. The antimicrobial activity of the proteinase K-treated group was significantly

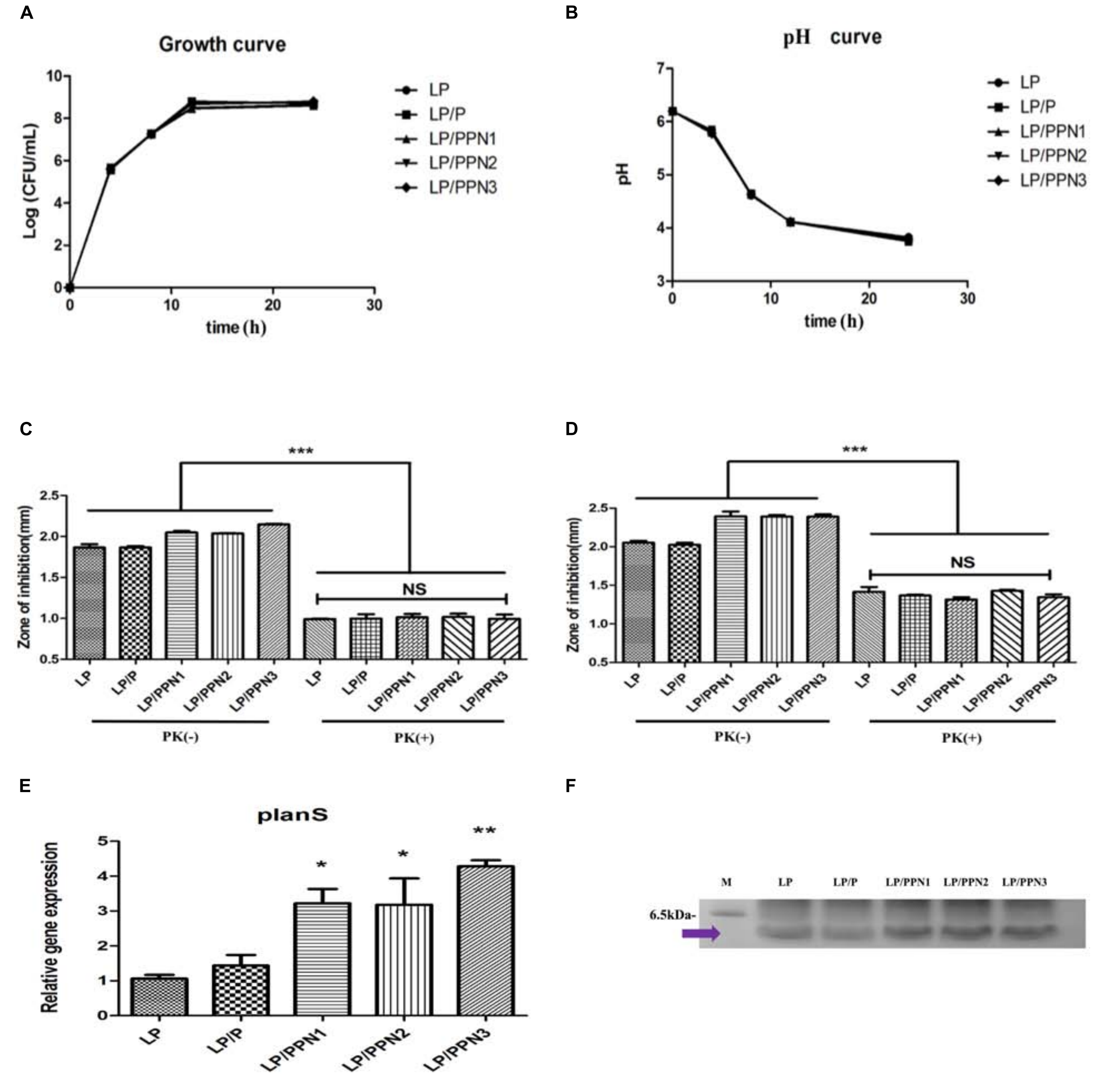

FIGURE 5 | Analysis the mechanism of enhanced antimicrobial ability. Measurement of the growth of LP **(A)** and pH of the culture medium **(B)** among LP groups with internalized PPNs or pullulan. Antimicrobial efficacy of LP/PPNs against *E. coli* **(C)** and LM **(D)** was measured after proteinase K treatment. Relative mRNA expression levels of *planS* compared with 16S rRNA expression levels **(E)**. The isolated plantaricin was determined by SDS–PAGE **(F)**. The full length gel is presented in **Supplementary Figure S4**. Data are presented as the mean ± SEM of three independent experiments. Statistical significance was analyzed between each group by one-way ANOVA and Tukey's *t*-test (*$p < 0.05$, **$p < 0.01$, and ***$p < 0.001$). (LP: *Lactobacillus plantarum,* PPN: phthalyl pullulan nanoparticle, P: pullulan, PK: proteinase K, LM: *Listeria monocytogenes*, SDS–PAGE: sodium dodecyl sulfate polyacrylamide gel electrophoresis).

reduced compared with the untreated group (**Figures 5C,D**), suggesting the degradation of plantaricin by proteinase K.

Effect of PPNs on Growth and Lactic Acid Production of LP

To test the growth of LP after treatment with PPNs or pullulan, cell colonies were counted at different time points (**Figure 5A**). The results showed no differences in LP growth with or without PPNs or pullulan treatment. The pH of the culture media of LP after treatment with PPNs or pullulan was also measured to evaluate lactic acid production. Consistent with the growth curve, the pH curve of the LP with or without PPNs or pullulan also showed no significant changes between the groups (**Figure 5B**). Therefore, the internalization of PPNs by LP had no negative effects on the growth of LP.

Effect of PPNs on Plantaricin Production by LP

To determine the variations in the production of plantaricin in LP by PPNs, the plantaricin from LP, LP/P, LP/PPNs was isolated and observed by SDS–PAGE. As results, we believed that molecular weight of isolated plantaricin was between from 2.5 to 6.5 kDa because it was already reported by Jimenez-Diaz et al. (1993). Also, the SDS–PAGE showed that LP/PPNs increased the production of plantaricin compared with the LP and LP/P groups under the same isolation conditions (**Figure 5F**).

Expression of Stress Response and Plantaricin Genes by Quantitative Real-Time PCR (qRT-PCR)

To evaluate production of plantaricin by PPN-treated LP at the mRNA level, the expression level of plantaricin mRNA in PPN-treated LP was compared with that of untreated LP using qRT-PCR. The plantaricin gene planS was selected, and 16s rRNA was used for normalization. After treatment with PPNs or pullulan for 8 h, the expression level of planS was higher in PPN-treated LP than in untreated or pullulan-treated LP (**Figure 5E**). The expression level of planS clearly demonstrated the enhanced antimicrobial activity of PPN-treated LP.

In our previous study, it was found that internalized inulin nanoparticles induced a stress response in PA (Cui et al., 2018; Kim et al., 2018). To verify whether similar behavior occurs in LP, the expression levels of genes related to heat shock proteins, dnaK and dnaJ, were determined. After treatment with PPNs or pullulan for 8 h, the expression levels of dnak and dnaJ were significantly higher in PPN-treated LP than those of untreated LP (**Figures 6A,B**). The results suggested that the internalization of PPNs by LP induced a stress response.

DISCUSSION

Many researchers have been interested in the use of probiotics as a promising alternative for synthetic antibiotics because synthetic antibiotics cannot only elicit negative side effects but, with improper use, can also lead to antibiotic-resistant bacteria (Witte, 1998). Prebiotics are generally defined as non-digestible compounds that stimulate the activity and/or growth of probiotics and other microorganisms in the gastrointestinal (GI) tract and have favorable effects on the health of the host (Gibson, 1999), which are often mediated by short chain fatty acids (SCFAs) derived from the metabolism of prebiotics by the gut microbiota (Gourbeyre et al., 2011).

In this study, we developed PPNs as a new formulation of prebiotics to increase the antimicrobial activity of probiotics. The PPNs were prepared by self-assembled nanoparticles after conjugation of hydrophobic phthalic anhydride to hydroxyl groups in pullulan through hydrophobic interactions. It is believed that the reaction occurs between the primary hydroxyl groups of the pullulan and the carboxylic acids of phthalic anhydride through esterification. Furthermore, increased conjugation of phthalic groups resulted in smaller PPN sizes due to the increased hydrophobic interactions among phthalic moieties in the PPNs.

A large number of researchers have been interested in how polymeric nanoparticles are internalized into mammalian cells through endocytosis (Oh and Park, 2014). Because polymeric nanoparticles can deliver therapeutic drugs to the necessary place of action (Zhang et al., 2010) and can be used to overcome cellular barriers when delivering hydrophobic drugs (Blanco et al., 2015); however, research on the internalization of polymeric nanoparticles by prokaryotes as a prebiotic, except for metal nanoparticles, is still in an early stage. Thus far, much of the research on prebiotics has focused on their fermentation

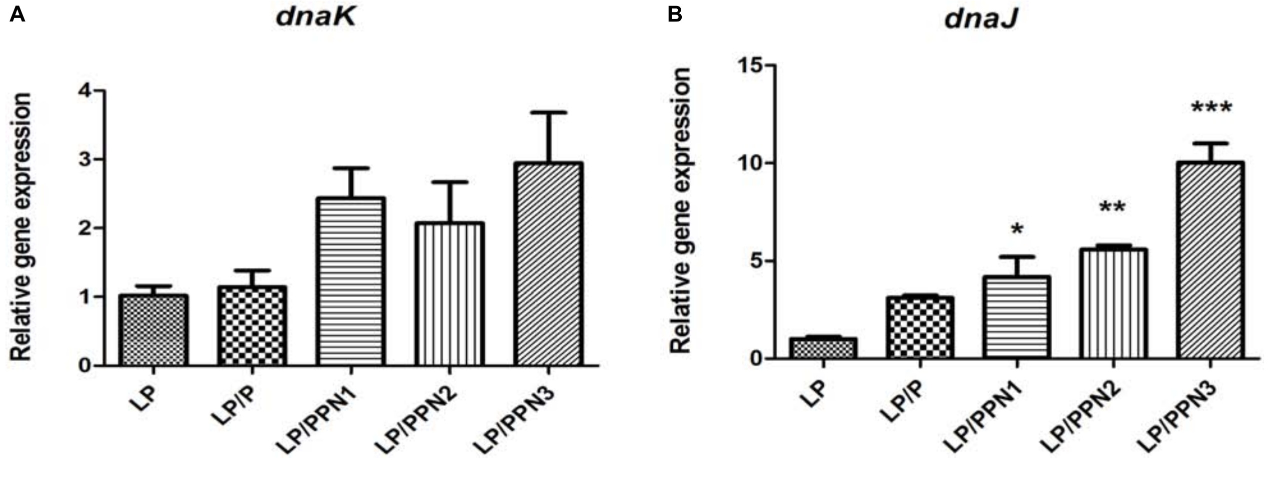

FIGURE 6 | Analysis of genes related to the stress response in LP treated with PPNs. The expression levels of *dnaK* **(A)** and *dnaJ* **(B)** relative to 16s rRNA was quantified by qRT-PCR. Data are presented as the mean ± SEM of three independent experiments. Statistical significance was analyzed between LP and other groups by one-way ANOVA and Tukey's *t*-test (*$p < 0.05$, **$p < 0.01$, and ***$p < 0.001$). (LP: *Lactobacillus plantarum,* PPN: phthalyl pullulan nanoparticle, P: pullulan*, dnaK*, *dnaJ*: heat shock proteins, qRT-PCR: quantitative real-time polymerase chain reaction).

by the microbiota (Slavin, 2013). Although the internalization of metal nanoparticles into pathogens occurs via electrostatic interactions (Sanyasi et al., 2016), we sought to develop polymeric nanoparticles as a prebiotic and to elucidate their internalization by probiotics. Interestingly, it is assumed that PPNs enter through galactose transporters on the cell surface of probiotics because pretreatment with galactose significantly decreased the internalization of PPN3 by LP, whereas glucose and fructose inhibited internalization to a lesser degree.

The other goal of our research was to evaluate the effect of prebiotics on the antimicrobial properties of probiotics. Many studies have described the antimicrobial properties of metal nanoparticles against pathogens due to their abrogation of bacterial growth by ionic interactions with the bacterial membrane (Sanyasi et al., 2016). However, metal nanoparticles can cause serious side effects in the host (Roy et al., 2003) and can inhibit both pathogens and beneficial microbes (Travan et al., 2009). Hence, the treatment of LP with PPNs enhanced its antimicrobial activity against both Gram-negative *E. coli* and Gram-positive *L. monocytogenes* compared to pullulan or LP alone although the effect of PPNs internalization in probiotics on observed antimicrobial activities was mild and PPNs did not show toxicity to the host. Particularly, LP/PPN3 showed the highest antimicrobial activity. The results indicated that the increased antimicrobial activity was dependent on the size of the PPNs taken up by LP. Moreover, we made starch and inulin nanoparticles using phthalic acid and the antibacterial activity of these nanoparticles was compared with PPNs (**Supplementary Figure S3**).

The advantages of probiotics as a food and feed additive have been mostly focused on their antimicrobial properties, suggesting that the enhancement of antimicrobial properties is of importance to probiotics researchers. Plantaricin is a natural peptide produced by LP and was reported to possess strong antimicrobial properties (Nes and Hole, 2000). In this study, treatment of LP with PPNs markedly increased the production of plantaricin, which was confirmed by the mRNA expression of planS. It is hypothesized that the internalization of PPNs directly affected the production of plantaricin. Therefore, we hypothesize that the internalization of PPNs by LP contributes to the enhanced antimicrobial properties of LP via increased expression of the plantaricin.

Notably, probiotics produce bacteriocins as their first defense mechanism (Cleveland et al., 2001; Castro et al., 2015). Several factors, such as culture pH, temperature, and pressure (Kalchayanand et al., 1998; Castro et al., 2015), affect the expression of bacteriocins by the upregulation of genes related to heat shock proteins (HSPs) (Bove et al., 2013) and the stress response. The mRNA expression levels of dnaK and dnaJ in PPN-treated LP were significantly higher than those of untreated LP. The results indicated that the internalization of PPNs by LP induced a mild intracellular stress response to stimulate antimicrobial activities without death of the host. Therefore, the internalization of PPNs by LP enhanced the expression of the plantaricin gene to activate the host's defense system. Further research is needed to determine the precise mechanism of the internalization of PPNs by LP.

Ultimately, polymeric nanoparticles as prebiotics can exert substantial effects on probiotics, which lead to the increased production of an antimicrobial peptide that is powerful against Gram-positive and Gram-negative pathogens. Therefore, our study shows a new way to produce antimicrobial peptides in probiotics through mild intracellular stimulation by the internalization of PPNs into probiotics, suggesting that PPNs have great promise as an alternative to synthetic antibiotics in veterinary, dairy, and human applications.

AUTHOR CONTRIBUTIONS

LH designed and performed the experiments, analyzed the data, and generated all the figures. LH wrote most of the manuscript. W-SK and S-ML discussed the results and corrected the manuscript. S-KK, Y-JC, and C-SC supervised the project.

FUNDING

This research was supported by the Basic Science Research Program through the National Research Foundation of Korea (NRF) funded by the Ministry of Education (No. 2016936920). LH, W-SK, and S-ML were supported by the Brain Korea 21 Plus program.

SUPPLEMENTARY MATERIAL

The Supplementary Material for this article can be found online at: https://www.frontiersin.org/articles/10.3389/fmicb.2019.00142/full#supplementary-material

FIGURE S1 | Analysis of the internalization of PPNs by LP. Confocal images and FACS analysis were performed after treatment of LP with 0.5% (w/v) FITC-PPNs for 2 h at 37°C. FITC-PPNs are shown in green, and membrane was stained red with FM4-64. Z-section showed that fluorescence intensity of FITC was highest at the center of LP (A). Confirmed that the FITC fluorescence appeared inside the bacteria (B). (LP: Lactobacillus plantarum, PPN: phthalyl pullulan nanoparticle, CLSM: confocal laser scanning microscopy, FACS: fluorescence-activated cell sorting, FITC: fluorescein isothiocyanate, FM4-64: N-(3-triethylammoniumpropyl)-4-(6-(4-(diethylamino) phenyl) hexatrienyl) pyridinium dibromide).

FIGURE S2 | Analysis of the internalization of PPNs by LP. Confocal images and FACS analysis were performed after treatment of LP with 0.5% (w/v) FITC-pullulan and FITC-PPNs for 2 h at 37°C. FITC-PPNs and FITC-pullulan are shown in green, and LP was stained blue with DAPI. The internalization of pullulan and PPNs after 2 h of treatment was quantified by FACS and statistically analyzed **(A)**. Next, LP was treated with 0.5% (w/v) FITC-PPN3 at different temperatures (4, 20, or 37°C) for 2 h **(B)**, and internalization was observed by CLSM and FACS. Confocal and FACS data are representative of three independent experiments, and the average values are presented as the mean ± SEM of three independent FACS experiments in a bar chart. Statistical significance was analyzed between each group by one-way ANOVA and Tukey's *t*-test ($^{***}p < 0.001$). Scale bar = 10 μm. (LP: *Lactobacillus plantarum,* PPN: phthalyl pullulan nanoparticle, CLSM: confocal laser scanning microscopy, FACS: fluorescence-activated cell sorting, FITC: fluorescein isothiocyanate, DAPI: 4′,6-diamidino-2-phenylindole).

FIGURE S3 | Antimicrobial efficacy of LP, LP/PSNs, LP/PINs, or LP/PPNs against *E. coli K99.* LP treated with different kinds of nanoparticles were cultured with Gram-negative *E. coli.* Statistical significance was analyzed between each group by one-way ANOVA and Tukey's t-test (***$p < 0.001$) (LP: *Lactobacillus plantarum,* PPN: phthalyl pullulan nanoparticle, PSN: phthalyl starch nanoparticle, PIN: phthalyl inulin nanoparticle, CFU: colony forming unit).

FIGURE S4 | The full length of SDS–PAGE gel. (M: marker, LP: *Lactobacillus plantarum,* PPN: phthalyl pullulan nanoparticle, P: pullulan, SDS–PAGE: sodium dodecyl sulfate polyacrylamide gel electrophoresis).

REFERENCES

Allen, H. K., Trachsel, J., Looft, T., and Casey, T. A. (2014). Finding alternatives to antibiotics. *Ann. N. Y. Acad. Sci.* 1323, 91–100. doi: 10.1111/nyas.12468

Blanco, E., Shen, H., and Ferrari, M. (2015). Principles of nanoparticle design for overcoming biological barriers to drug delivery. *Nat. Biotechnol.* 33, 941–951. doi: 10.1038/nbt.3330

Bove, P., Russo, P., Capozzi, V., Gallone, A., Spano, G., and Fiocco, D. (2013). Lactobacillus plantarum passage through an oro-gastro-intestinal tract simulator: carrier matrix effect and transcriptional analysis of genes associated to stress and probiosis. *Microbiol. Res.* 168, 351–359. doi: 10.1016/j.micres.2013.01.004

Castro, S. M., Kolomeytseva, M., Casquete, R., Silva, J., Saraiva, J. A., and Teixeira, P. (2015). Effect of high pressure on growth and bacteriocin production of *Pediococcus acidilactici* HA-6111-2. *High Press. Res.* 35, 405–418. doi: 10.1080/08957959.2015.1101095

Catley, B. J., Ramsay, A., and Servis, C. (1986). Observations on the structure of the fungal extracellular polysaccharide, pullulan. *Carbohydr. Res.* 153, 79–86. doi: 10.1016/S0008-6215(00)90197-6

Cheng, K. C., Demirci, A., and Catchmark, J. M. (2011). Pullulan: biosynthesis, production, and applications. *Appl. Microbiol. Biotechnol.* 92, 29–44. doi: 10.1007/s00253-011-3477-y

Cleveland, J., Montville, T. J., Nes, I. F., and Chikindas, M. L. (2001). Bacteriocins: safe, natural antimicrobials for food preservation. *Int. J. Food Microbiol.* 71, 1–20. doi: 10.1016/S0168-1605(01)00560-8

Cui, L. H., Yan, C. G., Li, H. S., Kim, W. S., Hong, L., Kang, S. K., et al. (2018). A new method of producing a natural antibacterial peptide by encapsulated probiotics internalized with inulin nanoparticles as prebiotics. *J. Microbiol. Biotechnol.* 28, 510–519. doi: 10.4014/jmb.1712.12008

de la Fuente-Nunez, C., Korolik, V., Bains, M., Nguyen, U., Breidenstein, E. B. M., Horsman, S., et al. (2012). Inhibition of bacterial biofilm formation and swarming motility by a small synthetic cationic peptide. *Antimicrob. Agents Chemother.* 56, 2696–2704. doi: 10.1128/AAC.00064-12

de Vries, M. C., Vaughan, E. E., Kleerebezem, M., and De Vos, W. M. (2006). Lactobacillus plantarum- survival, functional and potential probiotic properties in the human intestinal tract. *Int. Dairy J.* 16, 1018–1028. doi: 10.1016/j.idairyj.2005.09.003

Ditu, L. M., Chifiriuc, M. C., Bezirtzoglou, E., Voltsi, C., Bleotu, C., Pelinescu, D., et al. (2011). Modulation of virulence and antibiotic susceptibility of enteropathogenic *Escherichia coli* strains by *Enterococcus faecium* probiotic strain culture fractions. *Anaerobe* 17, 448–451. doi: 10.1016/j.anaerobe.2011.05.019

Driscoll, A. J., Bhat, N., Karron, R. A., O'brien, K. L., and Murdoch, D. R. (2012). Disk diffusion bioassays for the detection of antibiotic activity in body fluids: applications for the pneumonia etiology research for child health project. *Clin. Infect Dis.* 54(Suppl. 2), S159–S164. doi: 10.1093/cid/cir1061

Gibson, G. R. (1999). Dietary modulation of the human gut microflora using the prebiotics oligofructose and inulin. *J. Nutr.* 129, 1438s–1441s. doi: 10.1093/jn/129.7.1438S

Gibson, G. R., and Roberfroid, M. B. (1995). Dietary modulation of the human colonic microbiota – introducing the concept of prebiotics. *J. Nutr.* 125, 1401–1412. doi: 10.1093/jn/125.6.1401

Gillor, O., Etzion, A., and Riley, M. A. (2008). The dual role of bacteriocins as anti- and probiotics. *Appl. Microbiol. Biotechnol.* 81, 591–606. doi: 10.1007/s00253-008-1726-5

Gourbeyre, P., Denery, S., and Bodinier, M. (2011). Probiotics, prebiotics, and synbiotics: impact on the gut immune system and allergic reactions. *J. Leukoc. Biol.* 89, 685–695. doi: 10.1189/jlb.1109753

Jeong, Y. I., Na, H. S., Oh, J. S., Choi, K. C., Song, C. E., and Lee, H. C. (2006). Adriamycin release from self-assembling nanospheres of poly(DL-lactide-co-glycolide)-grafted pullulan. *Int. J. Pharm.* 322, 154–160. doi: 10.1016/j.ijpharm.2006.05.020

Jimenez-Diaz, R., Rios-Sanchez, R. M., Desmazeaud, M., Ruiz-Barba, J. L., and Piard, J. C. (1993). Plantaricins S and T, two new bacteriocins produced by *Lactobacillus plantarum* LPCO10 isolated from a green olive fermentation. *Appl. Environ. Microbiol.* 59, 1416–1424.

Kalchayanand, N., Sikes, A., Dunne, C. P., and Ray, B. (1998). Interaction of hydrostatic pressure, time and temperature of pressurization and pediocin AcH on inactivation of foodborne bacteria. *J. Food Protect.* 61, 425–431. doi: 10.4315/0362-028X-61.4.425

Kim, W. S., Lee, J. Y., Singh, B., Maharjan, S., Hong, L., Lee, S. M., et al. (2018). A new way of producing pediocin in *Pediococcus acidilactici* through intracellular stimulation by internalized inulin nanoparticles. *Sci. Rep.* 8:5878. doi: 10.1038/s41598-018-24227-z

Kneifel, W. (2000). *In vitro* growth behaviour of probiotic bacteria in culture media with carbohydrates of prebiotic importance. *Microb. Ecol. Health Dis.* 12, 27–34. doi: 10.1080/089106000435563

Leathers, T. D. (2003). Biotechnological production and applications of pullulan. *Appl. Microbiol. Biotechnol.* 62, 468–473. doi: 10.1007/s00253-003-1386-4

Na, K., and Bae, Y. H. (2002). Self-assembled hydrogel nanoparticles responsive to tumor extracellular pH from pullulan derivative/sulfonamide conjugate: characterization, aggregation, and adriamycin release in vitro. *Pharm. Res.* 19, 681–688. doi: 10.1023/A:1015370532543

Na, K., Lee, T. B., Park, K. H., Shin, E. K., Lee, Y. B., and Cho, H. K. (2003). Self-assembled nanoparticles of hydrophobically-modified polysaccharide bearing vitamin H as a targeted anti-cancer drug delivery system. *Eur. J. Pharm. Sci.* 18, 165–173. doi: 10.1016/S0928-0987(02)00257-9

Nes, I. F., and Hole, H. (2000). Class II antimicrobial peptides from lactic acid bacteria. *Biopolymers* 55, 50–61. doi: 10.1002/1097-0282(2000)55:1<50::AID-BIP50>3.0.CO;2-3

Oh, N., and Park, J. H. (2014). Endocytosis and exocytosis of nanoparticles in mammalian cells. *Int. J. Nanomed.* 9(Suppl. 1), 51–63. doi: 10.2147/IJN.S26592

Papagianni, M., and Anastasiadou, S. (2009). Pediocins: the bacteriocins of Pediococci. Sources, production, properties and applications. *Microb Cell Fact.* 8:3. doi: 10.1186/1475-2859-8-3

Reis, J. A., Paula, A. T., Casarotti, S. N., and Penna, A. L. B. (2012). Lactic acid bacteria antimicrobial compounds: characteristics and applications. *Food Eng. Rev.* 4, 124–140. doi: 10.1007/s12393-012-9051-2

Roy, S. R., Schiltz, A. M., Marotta, A., Shen, Y. Q., and Liu, A. H. (2003). Bacterial DNA in house and farm barn dust. *J. Aller. Clin. Immunol.* 112, 571–578. doi: 10.1016/S0091-6749(03)01863-3

Sanyasi, S., Majhi, R. K., Kumar, S., Mishra, M., Ghosh, A., Suar, M., et al. (2016). Polysaccharide-capped silver Nanoparticles inhibit biofilm formation and eliminate multi-drug-resistant bacteria by disrupting bacterial cytoskeleton with reduced cytotoxicity towards mammalian cells. *Sci. Rep.* 6:24929. doi: 10.1038/srep24929

Seo, H. H. (2012). *Selection and Characterization of LACTIC Acid Bacteria With Improved Antimicrobial Activity to Calf Diarrhea-Inducing Pathogen by Genome Shuffling*. Master's thesis, Seoul National University, Seoul.

Slavin, J. (2013). Fiber and prebiotics: mechanisms and health benefits. *Nutrients* 5, 1417–1435. doi: 10.3390/nu5041417

Song, D. F., Zhu, M. Y., and Gu, Q. (2014). Purification and characterization of plantaricin ZJ5, a new bacteriocin produced by *Lactobacillus plantarum* ZJ5. *PLoS One* 9:e105549. doi: 10.1371/journal.pone.0105549

Sugawa-Katayama, Y., Kondou, F., Mandai, T., and Yoneyama, M. (1994). Effect of pullulan, polydextrose and pectin on Cecal Microflora. *Oyo Toshitsu Kagaku* 41, 413–418.

Tao, X., Xie, Y., Zhang, Q., Qiu, X., Yuan, L., Wen, Y., et al. (2016). Cholesterol-modified amino-pullulan nanoparticles as a drug carrier: comparative study of cholesterol-modified carboxyethyl pullulan and pullulan nanoparticles. *Nanomaterials* 6:165. doi: 10.3390/nano6090165

Todorov, S. D., Prevost, H., Lebois, M., Dousset, X., Leblanc, J. G., and Franco, B. D. G. M. (2011). Bacteriocinogenic *Lactobacillus plantarum* ST16Pa isolated from papaya (Carica papaya) – From isolation to application: characterization of a bacteriocin. *Food Res. Int.* 44, 1351–1363. doi: 10.1016/j.foodres.2011.01.027

Travan, A., Pelillo, C., Donati, I., Marsich, E., Benincasa, M., Scarpa, T., et al. (2009). Non-cytotoxic silver nanoparticle-polysaccharide nanocomposites with antimicrobial activity. *Biomacromolecules* 10, 1429–1435. doi: 10.1021/bm900039x

Witte, W. (1998). Medical consequences of antibiotic use in agriculture. *Science* 279, 996–997. doi: 10.1126/science.279.5353.996

Yun, J. H. (2007). *Lactic Acid Bacteria Selection for Probiotics and Strain Improvement for Bacteriocin Production*. Master's thesis, Seoul National University, Seoul.

Zhang, H. Z., Li, X. M., Gao, F. P., Liu, L. R., Zhou, Z. M., and Zhang, Q. Q. (2010). Preparation of folate-modified pullulan acetate nanoparticles for tumor-targeted drug delivery. *Drug Delivery* 17, 48–57. doi: 10.3109/10717540903508979

Zhang, L. F., Chan, J. M., Gu, F. X., Rhee, J. W., Wang, A. Z., Radovic-Moreno, A. F., et al. (2008). Self-assembled lipid-polymer hybrid nanoparticles: a robust drug delivery platform. *ACS Nano* 2, 1696–1702. doi: 10.1021/nn800275r

Conflict of Interest Statement: The authors declare that the research was conducted in the absence of any commercial or financial relationships that could be construed as a potential conflict of interest.

frontiers
in Microbiology

ORIGINAL RESEARCH
published: 19 February 2019
doi: 10.3389/fmicb.2019.00217

Nanocomposite of Ag-Doped ZnO and AgO Nanocrystals as a Preventive Measure to Control Biofilm Formation in Eggshell and *Salmonella* spp. Entry Into Eggs

Belchiolina Beatriz Fonseca[1]*, Paula Luiza Alves Pereira Andrada Silva[1], Anielle Christine Almeida Silva[2], Noelio Oliveira Dantas[2], Aline Teodoro de Paula[2], Otavio Cintra Lemos Olivieri[1], Marcelo Emilio Beletti[3], Daise Aparecida Rossi[1] and Luiz Ricardo Goulart[4]

[1] School of Veterinary Medicine, Federal University of Uberlândia, Uberlândia, Brazil, [2] Physics Institute, Federal University of Alagoas, Maceió, Brazil, [3] Institute of Biomedical Sciences, Federal University of Uberlândia, Uberlândia, Brazil, [4] Institute of Biotechnology, Federal University of Uberlândia, Uberlândia, Brazil

Salmonella spp. is an important foodborne agent of salmonellosis, whose sources in humans often include products of avian origin. The control of this bacterium is difficult especially when *Salmonella* spp. is organized into biofilms. We hypothesized that the novel nanocomposites of ZnO nanocrystals doped with silver (Ag) and silver oxide (AgO) nanocrystals (ZnO:Ag-AgO) synthesized by the coprecipitation method could control or prevent the formation of *Salmonella* Enteritidis (SE) and *Salmonella* Heidelberg (SH) biofilm and its entry into turkey eggs. The diffraction characteristics of ZnO and AgO showed sizes of 28 and 30 nm, respectively. The Zn to Ag substitution into the ZnO crystalline structure was evidenced by the ionic radius of Ag+2 (1.26 Å), which is greater than Zn+2 (0.74 Å). For the SE analyses post-biofilm formation, the ZnO:Ag-AgO was not able to eliminate the biofilm, but the bacterial load was lower than that of the control group. Additionally, SE was able to infiltrate into the eggs and was found in both albumen and yolk. For the SH analyses applied onto the eggshells before biofilm formation, the ZnO:Ag-AgO treatment prevented biofilm formation, and although the bacterium infiltration into the eggs was observed in all treated groups, it was significantly smaller in ZnO:Ag-AgO pre-treated eggs, and SH could not reach the yolk. There was no difference in pore size between groups; therefore, the inhibition of biofilm formation and the prevention of bacterium entry into the egg were attributable to the use of ZnO:Ag-AgO, which was not influenced by the egg structure. Although the amount of Ag and Zn in the shell of the ZnO:Ag-AgO group was greater in relation to the control, this difference was not detected in the other egg components. In the search for new measures that are effective, safe and viable for controlling microorganisms in poultry farming, the application of a nanocomposite of Ag-doped ZnO and AgO nanocrystals appears as an alternative of great potential to prevent *Salmonella* sp biofilms in eggshells and other surfaces.

Keywords: disinfection, pore, preventive, nanocrystal, bacterium

Edited by:
Renata Katsuko Takayama Kobayashi,
State University of Londrina, Brazil

Reviewed by:
Ilana Kolodkin-Gal,
Weizmann Institute of Science, Israel
Yun Chen,
Zhejiang University, China

***Correspondence:**
Belchiolina Beatriz Fonseca
biafonseca@ufu.br

Specialty section:
This article was submitted to Antimicrobials, Resistance and Chemotherapy, a section of the journal Frontiers in Microbiology

Received: *17 November 2018*
Accepted: *25 January 2019*
Published: *19 February 2019*

Citation:
Fonseca BB, Silva PLAPA, Silva ACA, Dantas NO, de Paula AT, Olivieri OCL, Beletti ME, Rossi DA and Goulart LR (2019) Nanocomposite of Ag-Doped ZnO and AgO Nanocrystals as a Preventive Measure to Control Biofilm Formation in Eggshell and Salmonella spp. Entry Into Eggs. Front. Microbiol. 10:217. doi: 10.3389/fmicb.2019.00217

INTRODUCTION

The control of microorganisms is a primordial action for poultry production due to the potential risk of transmission of pathogenic organisms to humans and other animals throughout the entire food chain. Among the most important microorganisms, *Salmonella* spp. may be considered one of the most important foodborne agents in the European Union and the United States (Center for Disease Control CDC, 2016; EFSA, 2017) and may cause significant damage to the poultry industry as well as to public health. Importantly, products of avian origin represent 47% of salmonellosis sources in humans (Center for Disease Control CDC, 2016).

Control of the different serotypes of *Salmonella* spp. is required throughout the entire poultry production cycle. Embryonated eggs, equipment, facilities, vehicles and other materials involved in the process must undergo an efficient disinfection to control these microorganisms. Historically, formaldehyde has been chosen as one the main disinfectant agent of eggs, however, its use has been restricted (BRASIL, 2008), openning space to other disinfectants, such as the peracetic acid (PA).

Current research has sought alternatives for the effective biological control of avian products that are not only harmless to humans, other animals and the environment, but also easily applicable at a feasible cost. This scenario has introduced nanoparticles as a potential alternative biocidal agent, due to their ability to achieve intimate interactions with bacterial surfaces conferred by their small size, a property that results in a high surface-to-volume ratio, thus providing a high biocidal power (Allaker, 2010).

Zinc oxide (ZnO) nanocrystals (NCs) are a biocompatible materials, according to the U.S. Food and Drug Administration (FDA); therefore, in this work we investigated this nanocrystal doped with silver (Ag) and with silver oxide (AgO) nanocrystals. ZnO nanocrystals (NCs) exhibit many important characteristics, such as high catalytic activity, chemical and physical stability, as well as ultraviolet (UV) absorption (Tankhiwale and Bajpai, 2012). The doping technique is employed to produce defects aiming to increase the catalytic activity in ZnO NCs, and consequently, the ability to induce oxidative stress in bacteria, which is one of the main mechanisms of bactericidal action (Pati et al., 2014). The catalytic activity is a property that induces the generation of reactive oxygen species (ROS), leading to oxidative stress and bacterial death (Espitia et al., 2012). The mixing of NCs into nanocomposites (NC) can potentiate a certain physical property or the presence of two interesting physical properties. Thus, in the present work, we investigated the synergism of Ag-doped ZnO with AgO NCs in the bactericidal action.

In order to ensure survival in harsh environments, *Salmonella* spp., as well as other microorganisms, develop adaptation mechanisms, such as biofilm formation (Steenackers et al., 2012). Biofilm is the aggregation of sessile microorganisms on a surface, followed by self-production of extracellular matrix, composed of protein and exopolysaccharides (Donlan and Costerton, 2002; Martínez and Vadyvaloo, 2014). This mechanism confers to the bacteria capacities of persistence and survival in adverse environments, and especially, resistance to the action of biocides, since this physical barrier hinders the action of the disinfectant agent (Nikolaev and Plakunov, 2007; Tomihama et al., 2007; Flemming and Wingender, 2010). The formation of biofilms is a great concern given their ability to remain in environments, resisting sanitizers and antimicrobials, and give rise to a constant source of microorganisms, favoring pathogen propagation in production chains and, consequently, in foods (Schlisselberg and Yaron, 2013).

Nanocomposites consist of a mixture of different nanocrystals that may synergize and potentiate certain physical properties due to the combination of two interesting and complementary physical properties. Zinc oxide (ZnO) is generally recognized as safe (GRAS) by the U.S. Food and Drug Administration and may be used as food additives due to its antimicrobial properties. ZnO nanoparticles present pronounced antimicrobial activity due to their small size and high surface-to-volume ratio of nanoparticles, showing selective toxicity to bacteria and minimal effects on human cells (Reddy et al., 2007), most likely due to disruption of the bacterial membrane and oxidative stress (Xie et al., 2011; Espitia et al., 2012; Pati et al., 2014). Another important nanoparticle with significant antimicrobial effect is Silver Oxide (AgO). AgO has been used as cleaning and preservative agents due to its high catalytic activity and selectivity as catalyst in organic reactions, however, the antimicrobial activity of AgO nanoparticles against bacteria depends on their shape (Wang et al., 2010).

Considering the necessity and importance of controlling microorganisms, especially *Salmonella* spp. in relation to avian products, the present study aimed to verify the synergistic action of nanocomposites composed of Ag-doped ZnO containing AgO NCs (ZnO:Ag-AgO) on the control and prevention of *Salmonella* Enteritidis (SE) and *Salmonella* Heidelberg (SH) in biofilm formation in turkey embryonated eggshells, which present a rough surface with many pores that allow bacterial contamination during cleaning prior to consumption. Herein, we apply for the first time a nanocomposite as an antimicrobial agent on eggshells to prevent biofilm formation, which may have an important impact on the poultry industry.

MATERIALS AND METHODS

Synthesis and Characterization of the NCs of ZnO:Ag-AgO

The synthesis of the ZnO:Ag-AgO nanocrystals was performed at the "Laboratory of New Insulating and Semiconductor Materials (LNMIS)" at the Institute of Physics of the Federal University of Uberlândia. ZnO:Ag-AgO NCs were synthesized by the coprecipitation method, which is under a patent application (BR 10 2018 007714 7). The physical properties of the NCs were investigated by X-Ray Diffraction (XRD) and electronic scanning microscopy (SEM). XRD patterns were measured by a Shimadzu XRD-6000 diffractometer with a Cu-target radiation (λ = 0.154 nm). The SEM images and EDS results were obtained by scanning electron microscopy (SEM; Carl Zeiss SMT Ltd., EVO MA 15). All characterizations were performed at room temperature.

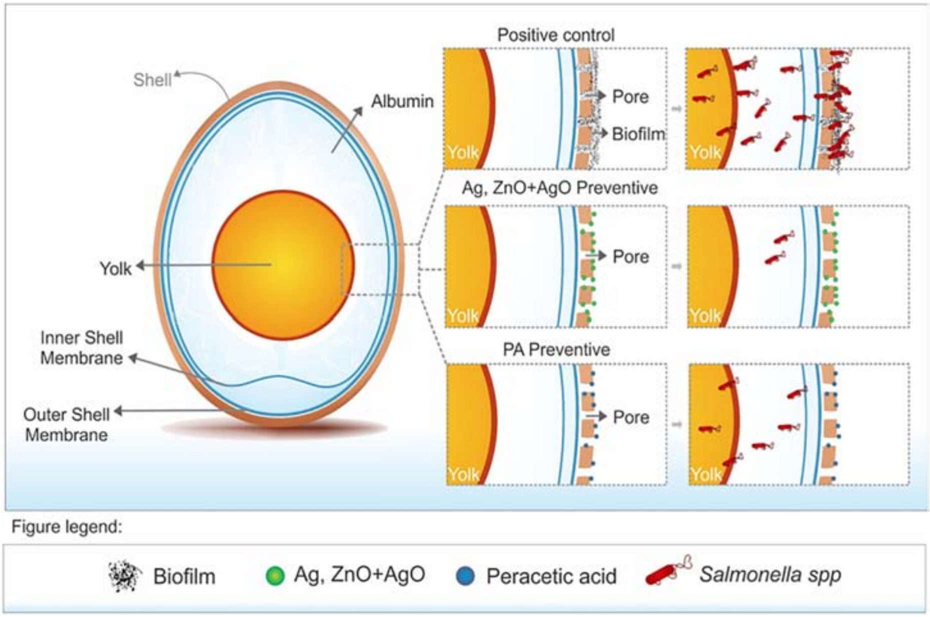

GRAPHICAL ABSTRACT | Preventive treatment with ZnO:Ag-AgO novel nanoscomposite nanocrystals prevented the SH biofilms formation and it was more efficient than peracetic acid to prevent the entry of bacteria into the eggs. The previous treatment with ZnO:Ag-AgO nanocomposite is a viable alternative to avoid the formation of biofilms and to diminish the bacterial load.

Evaluation of the Concentration of Ag-Doping for Inhibition of *Salmonella* spp.

The biological studies and eggs' incubation were performed, respectively, in the Laboratory of Molecular Epidemiology and Laboratory of Egg Incubation of the School of Veterinary Medicine at the Federal University of Uberlândia. To determine the activity of ZnO:Ag-AgO, we have used antibiograms according to Bauer et al. (1966), which consisted of inoculating a bacterial suspension (SE and SH) on Mueller Hinton agar plates, followed by the application of filter paper disks impregnated with 1.4 mg/mL of nanoparticles under three different dosages of Ag-doping (5, 9, and 11%). Sulfonamide disks (300 μg; LABORCLIN®) were used as a control. We incubated the plates for 20 h at 37°C. After incubation, the growth or inhibition pattern was analyzed around each disk, and the halos were measured for the determination of the inhibition spectrum.

Efficiency of ZnO:Ag-AgO NCs in the Elimination of SE and SH in Biofilm Formation in Eggshell and Entry Into Eggs

The eggs originated from a 35-week-old turkey breeder from an industrial poultry business. The SE strain used in the study was provided by the Instituto Oswaldo Cruz Foundation (FIOCRUZ) and the SH strain was isolated in our laboratory from broilers, where they were characterized and typed genetically.

The efficiency of the ZnO:Ag-AgO nanocomposite in the control of SE and SH biofilms was evaluated in eggs. As to SE, we divided 64 eggs into four groups, each group consisting of 16 eggs and each sample unit consisting of two eggs. For biofilm formation, three groups were submerged, separately two by two, in a 100 mL suspension of TSB containing 10^5 CFU/mL of SE, for a period of 24 h at 25°C. In the fourth group (negative control - NC), the eggs were also submerged for 24 h, but in sterile TSB. After this period (24 h) the eggs were washed three times in ultrapure water to remove free bacteria from the biofilms. The eggs were dried, after which the disinfectant treatments were applied: (i) ZnO:Ag-AgO: Spraying 1.4 mg of ZnO:Ag-AgO nanocomposite diluted in water per egg during 30 min; (ii) PA: Immersion in peracetic acid 2.5% (25,000 ppm) for 15 s; (iii) PC (positive control): Spray of ultrapure water, previously in contact with TSB containing Bacteria; and (iv) NC (negative control): Spray of ultrapure water, previously in contact with sterile TSB. After drying, the eggs were opened in laminar flow, separated aseptically into shell, albumen and yolk, and collected.

Bacterial Identification and Counting for SH and SE

We evaluated a total of 10 g of each sample unit both qualitatively and quantitatively. In the quantitative evaluation of the shell, a total of 10 g of the sample was added to 90 mL of 0.9% NaCl solution, thoroughly homogenized and submitted to serial dilutions for subsequent plating on TSA agar surface incubated at 37°C for 30 h for SE counting. At the same time, the presence and absence of SE in the shell, albumen and yolk were evaluated. A 10-gram sample of shell and 1 mL of albumen and yolk were added to 90 mL and 9 mL of peptone water (Isofar®), respectively, and separately. These samples were incubated for 24 h at 37°C; then a 1mL aliquot of this was inoculated into Rappaport (Oxoid®) culture medium and 1mL in Tetrathionate (Merck®) culture medium. After 24-h growth, both were depleted in XLD. Colonies with morphological characteristics of Salmonella were selected; three to five CFU per plate were submitted to a conventional PCR reaction for specie confirmation. As the eggs were only disinfected and not sterilized, another microarray PCR assay was performed to confirm serotypes. The multiplex ligation detection reaction (LDR) generated collections of DNA molecules. Such DNA molecules were subsequently amplified by means of a single pair of amplimers through a PCR. The PCR products were then sorted by hybridization by a low-density DNA microarray. Positive hybridization was detected using a biotin label incorporated in one of the PCR primers. Tubes were then inserted in the single-channel ATR03 array tube reader upon completion of the detection reaction, and images were acquired and interpreted via the software supplied by the manufacturer (Check-Points, Wageningen, Netherlands).

Efficiency of NCs of ZnO:Ag-AgO in Prevention of SH Biofilm Formation in Eggshell and Entry Into Eggs

The results of the SE experiments led us to make some modifications to the experiments on SH. To evaluate the efficiency of the nanoparticle in the control SH biofilms, the same methodology for bacteria inoculation and eggs analysis described above were used. However, two more groups were added: (i) ZnO:Ag-AgO pre (preventive treatment with ZnO:Ag-AgO): ZnO:Ag-AgO was applied twice, being approximately 1.4 mg/mL per egg in each application. A spray was performed 24 h before contact with the SH and another treatment 30 min after the biofilm formation and the removal of the free forms of the bacterium; (ii) ZnO:Ag-AgO post (treatment after biofilm formation with nanocomposite of ZnO:Ag-AgO): ZnO:Ag-AgO spray (1.4 mg per egg) was applied for 30 min after biofilm formation and removal of free forms of the bacteria; (iii) PA pre (preventive treatment) with peracetic acid: identical to NP pretreatment but using 25,000ppm of peracetic acid per egg; (vi) PA post (treatment after biofilm formation with peracetic acid): identical to treatment NP post but using 25,000ppm of peracetic acid per egg; (v) PC: Ultrapure water spray 24 h after biofilm formation; (vi) NC: Ultrapure water spray 24 h after immersion in sterile TSB. The same laboratorial experiments carried out for SE identification and quantification were conducted for SH.

Evaluation of Eggshell Pore Size

Considering the possibility that shell pore diameter may influence the nanocomposite treatments applied before and after SH contamination, we used confocal Raman microscopy. Images obtained from the equatorial region of the eggshells were evaluated by the program Gwyddion to obtain the figures with measurements of shell roughness height and pore diameter.

Scanning Electron Microscopy

The SH biofilm was evaluated by SEM, following the protocol described by Brown et al. (2014) with modifications. Biofilms formed in eggshells were fixed with 2.5% glutaraldehyde and 2.5% paraformaldehyde in 0.1 M buffer PBS (pH 7.4) overnight at 4°C. The fixed material was removed, and the samples were washed three times with PBS buffer. The eggshell was fixed again with 1% osmium tetroxide for 2 h and washed three times with PBS buffer. The eggshell was then dehydrated several times by using ethanol solutions at the following concentrations: 30, 40, 50, 60, 70, 80, and 90% and then three times at 100% for 20 min at each concentration. The samples were dried in Critical Drying Point (CPD; CPD 030, Baltec, Germany) using liquid carbon dioxide as the transition fluid. The samples were coated with a 20-nanometer-thick layer of gold (SCD 050, Baltec, Germany) and visualized on SEM (VP Zeiss Supra 55 SEM FEG operating at 5 kV).

Levels of the Ag and Zn in Egg Components

A total of three samples of albumen, yolk and eggshell from the NPpre and C (control -without nanoparticle) groups were analyzed to identify the presence of Ag and Zn, and thus to understand the invasiveness level of the nanoparticles in the eggs. A total of 1 g of each sample was muffled at 600°C for 3 h, then cooled in a desiccator to obtain the dry matter. The samples were then ground into a homogeneous powder form. Then 0.1 g of each sample was weighed and added to 6 ml of a nitro-perchloric solution, with the nitric and perchloric acid at the ratio of 8:1. During the digestion of the samples, there was a controlled variation of temperature: 15 min at 50°C, 15 min at 75°C, 30 min at 120°C, 40 min at 160°C and finally at 60 min at 210°C, to finally obtain approximately 5 ml of translucent extract. After cooling, 50 ml of water was added at 60°C and homogenized. The samples were filtered and submitted to Inductively Coupled Plasma Optical Emission Spectrometry (ICP-OES) and then the concentrations of Ag and Zn were quantified.

Statistical Analysis

The analyses were performed with the aid of the software GraphPad Prism, version 7.0. The quantitative biofilm formation tests performed on the eggshells were analyzed by the Kruskal–Wallis test followed by Dunn's multiple comparisons test. For the difference between percentages, the Chi-square test followed by the Fisher–Irwin tests of two-by-two was used. ANOVA and the Tukey test were employed to analyze the shell roughness height and the Ag and Zn amounts we used. The confidence level was 95% for all reports.

RESULTS

Characterization of ZnO:Ag-AgO Nanocomposites

The structural and morphological properties of the ZnO NCs and NC were investigated by XRD and electronic SEM, respectively.

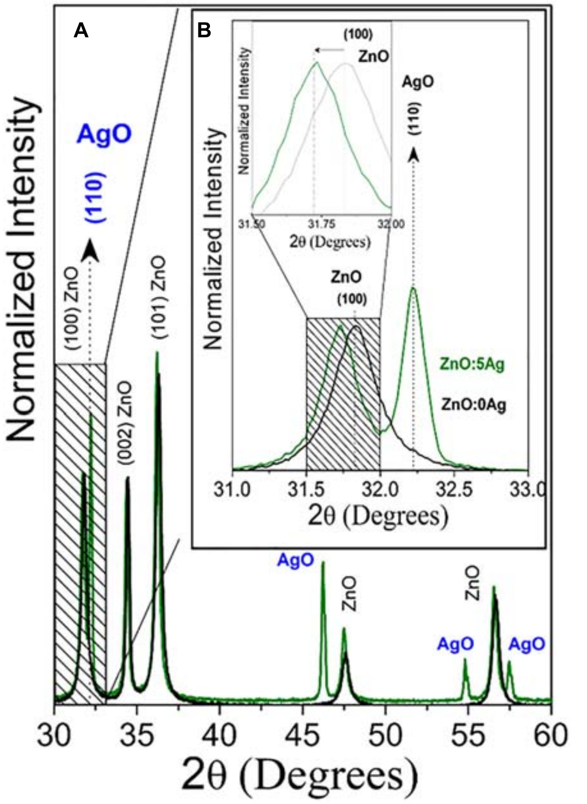

FIGURE 1 | (A) X-ray patterns of ZnO nanocrystals (black line) and nanocomposite (ZnO:5Ag; green line). **(B)** Amplification to investigate the alterations of the ZnO main peak due to the incorporation of Ag.

Figure 1 shows the XRD characteristic diffraction patterns of wurtzite ZnO nanocrystals (black line) and nanocomposite (green line). An amplification was performed to investigate the alterations of the ZnO main peak due to the incorporation of Ag. (**Figure 1B** inset). **Figure 1B** shows a shift to smaller angles relative to the ZnO peak (100), and this result confirms the substitutional incorporation of silver in place of zinc into the ZnO crystalline structure, since Ag^{+2} has an ionic radius (1.26 Å) greater than Zn^{+2} (0.74 Å) and the peak characteristic diffraction of AgO nanocrystals. The AgO NCs percentage formed was calculated by XRD patterns and obtained 49.36%. These results confirmed the formation of nanocomposite of Ag-doped ZnO with AgO nanocrystals.

Figure 2A shows SEM image of nanocomposite (ZnO:5Ag) confirming the rod-shaped Ag-doped ZnO nanocrystals with diameter of 73 nm and length of 140 nm, as well as the morphology of AgO NCs, which is a mixture of plates with a sphere. **Figure 2B** shows EDS results that confirmed the presence of Ag, Zn and O elements, which are the constituents of Ag-doped ZnO and AgO NCs in excellent agreement with XRD results (**Figure 1**). **Figure 2C** shows the quantitative elements in weight %. The elements C and Au consist of the substrate and metallization, respectively.

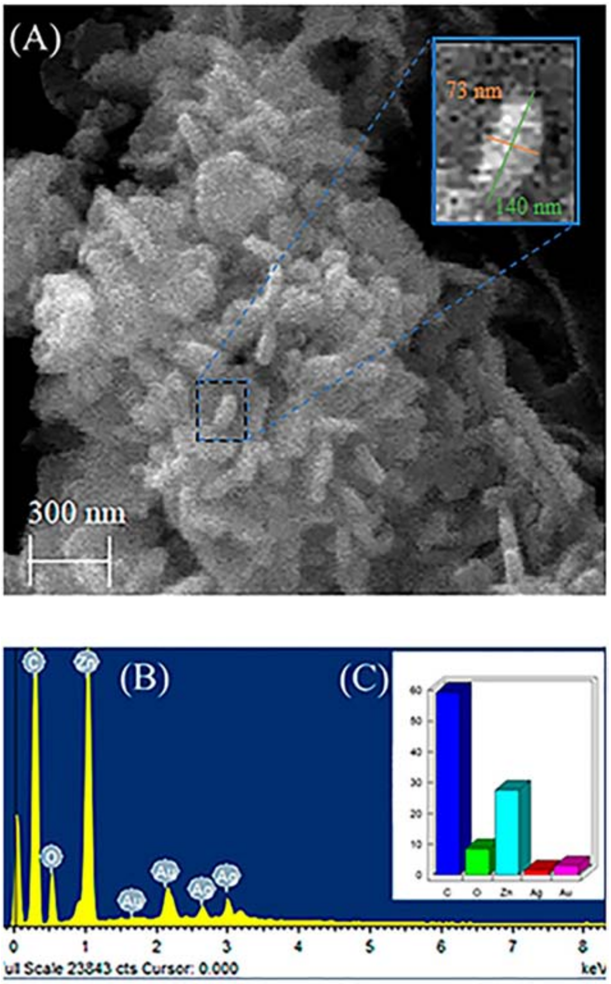

FIGURE 2 | (A) Scanning microscopy image of nanocomposite (ZnO:5Ag), **(B)** EDS results, and **(C)** Quantitative elements in weight%.

The antibiogram results showed that 5% Ag-doping was sufficient to inhibit SE and SH. Therefore, we have used this percentage of doping.

ZnO:Ag-AgO NCs Were Not Able to Decrease the Positivity of Biofilm Formation in Eggs but Reduced the Contaminant Load of SE

In the SE analyses, the biofilm was formed in all groups that were exposed to the bacterium. *Salmonella* was able to advance into the egg, being isolated in albumen and yolk. **Figure 3A** shows that there was no statistical difference between the percentages of contaminated eggs in eggshell, albumen or yolk among the ZnO:Ag-AgO, PA and PC groups. Nanocomposite of ZnO:Ag-AgO and PA were not efficient at decreasing the percentage of eggs positive for the presence of biofilm on their shells and the passage of the SE into the egg (**Figure 3A**). However, nanocomposite of ZnO:Ag-AgO and PA caused a

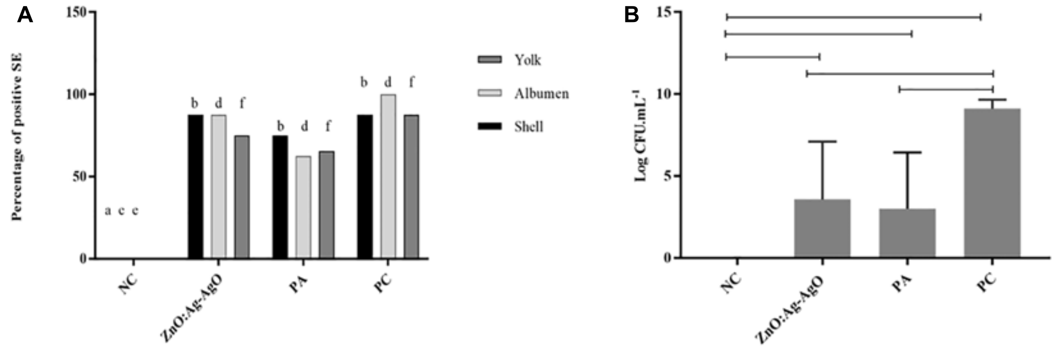

FIGURE 3 | Evaluation of the efficiency of ZnO:Ag-AgO in the manage the already formed SE biofilm. **(A)** Percentage of shell, albumen and yolk positive for SE submitted to different types of disinfection. Different letters represent statistical differences in the presence of SE in the shell (a,b), albumen (c,d) or yolk (e,f) of the eggs. NC: negative control; PA: Peracetic acid; PC: Positive control. **(B)** Bacterial load on SE biofilms formed in turkey eggs subjected to different types of disinfection. ZnO:Ag-AgO and PA caused a significant drop in the contaminant load on SE biofilms formed in turkey eggs. NC: negative control; PA: Peracetic acid; PC: Positive control.

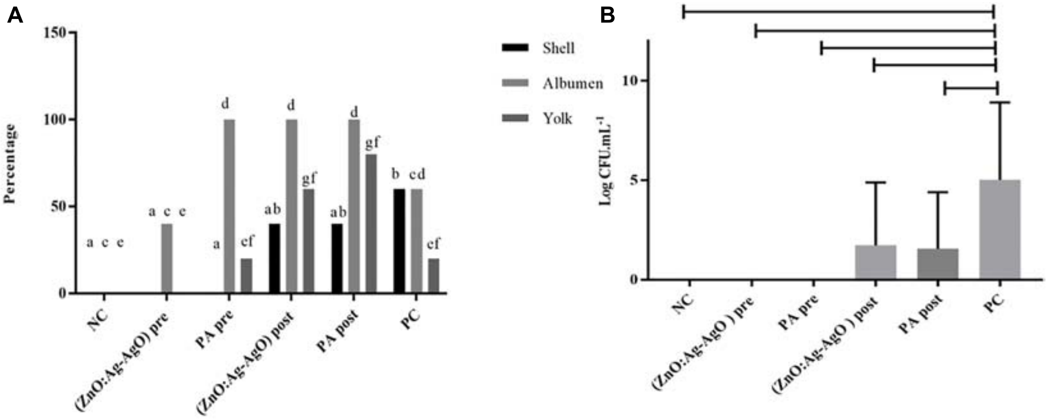

FIGURE 4 | Evaluation of the efficiency of ZnO:Ag-AgO in the manage the already formed SH and in the prevention of SH biofilm formation. **(A)** Percentage shell, albumen and yolk positive for SH submitted to different types of disinfection. Different letters represent statistical differences for the presence of SH in the shell (a,b), albumen (c,d) or yolk (e,f) of the eggs. (ZnO:Ag-AgO) pre and PA pre prevented the biofilm formation. (ZnO:Ag-AgO) pre: preventive treatment with nanocomposite of ZnO:Ag-AgO; PA pre: preventive treatment with peracetic acid; NC: negative control; (ZnO:Ag-AgO) post, treatment after biofilm formation with nanocomposite of ZnO:Ag-AgO; PA post: treatment after biofilm formation with peracetic acid; PC: Positive control. **(B)** Bacterial load on SH biofilms formed in eggshell subjected to different types of disinfection. (ZnO:Ag-AgO) pos and PA post caused a significant drop in the contaminant load on eggshell SH biofilms. (ZnO:Ag-AgO) pre and PA pre prevented the biofilm formation. (ZnO:Ag-AgO) pre: preventive treatment with nanocomposite of ZnO:Ag-AgO; PA pre: preventive treatment with peracetic acid; NC: negative control; (ZnO:Ag-AgO) post: treatment after biofilm formation with nanocomposite of ZnO:Ag-AgO; PA post: treatment after biofilm formation with peracetic acid; PC: Positive control.

significant drop in the contaminant load (**Figure 3B**). Compared to the PC group, the reduction caused in ZnO:Ag-AgO was 5.538 Log CFU.mL−1, whereas in PA it was 6.092 Log CFU.mL−1 (**Figure 3B**).

ZnO:Ag-AgO NCs Prevent SH Biofilm Formation in Eggshell and Decreased the Entrance of the Bacterium Into the Egg but Do Not Eliminate Previously Formed Biofilm

There was no biofilm formation in eggshell in both preventive treatments by means of ZnO:Ag-AgO and PA (denominated (ZnO:Ag-AgO) pre and PA pre, respectively (**Figure 4**). The passage of the bacterium into the eggs was noted in all treated groups, being smaller in ZnO:Ag-AgO pre (**Figure 4A**). In this group, the percentage of SH-positive albumin was lower than in the other treated groups and the bacteria did not reach the yolk (**Figure 4A**). Evaluating the efficiency of the SH biofilm inhibition of on eggshell, the nanocomposite of ZnO:Ag-AgO and peracetic acid post treatment caused a significant drop in the contaminant load (**Figure 4B**).

In order to verify whether the use of ZnO:Ag-AgO nanocomposite, either preventively or after the formation of biofilms, was influenced by eggshell pore size, we used Confocal Raman

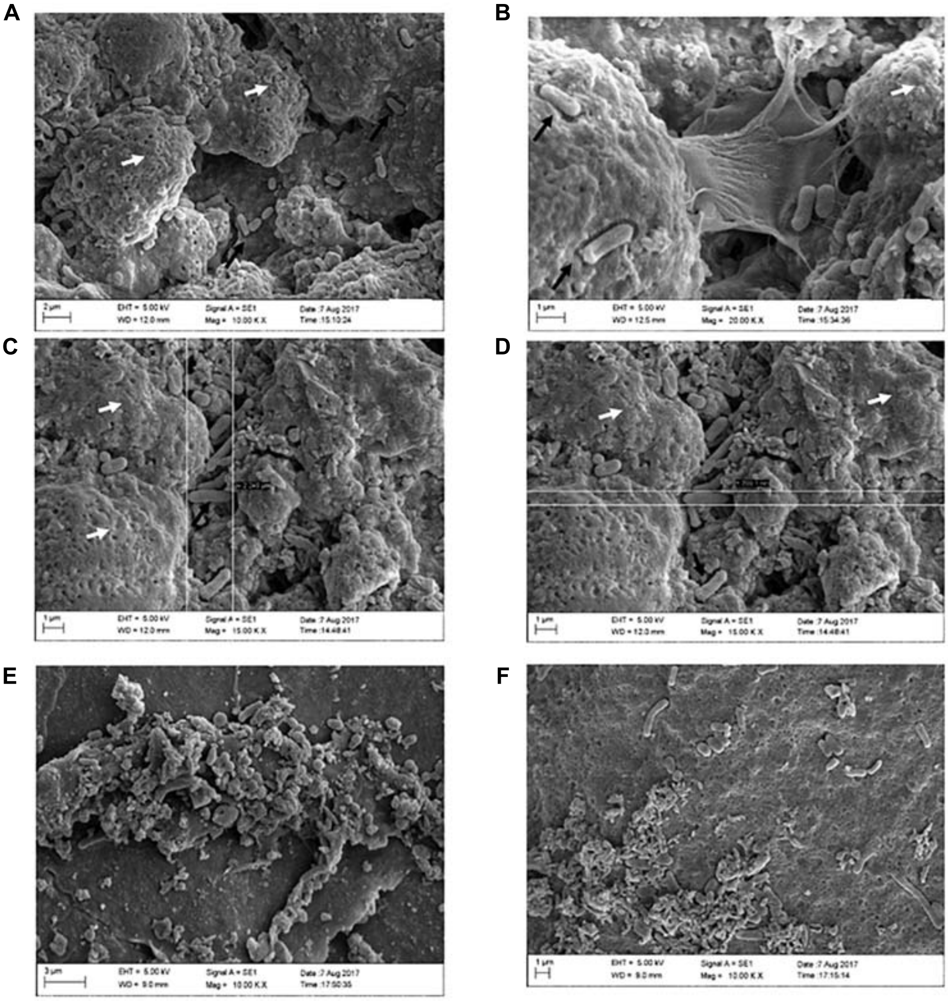

FIGURE 5 | Formation of SH biofilms on an eggshell in PC, (ZnO:Ag-AgO) pre and NC groups. **(A)** PC – Typical SE biofilm matrix formation (as seen on the white arrows), with invasion of bacteria as indicated by the black arrows. **(B)** PC – Biofilm of SH in stage of expansion, with visualization of the bacteria releasing the matrix. **(C)** PC – Biofilm of SH and presence of free bacteria on the surface. Length measurement (2,245 μm). **(D)** PC – Biofilm of SH and presence of free bacteria on the surface. Width measurement (703.1 nm). **(E)** (ZnO:Ag-AgO) pre – Structure similar to the SH biofilm matrix, however, it is unconfigured and bacteria are visualized in different formats. **(F)** NC – Group of cells in different formats verified near the unconfigured matrix.

Microscopy (**Supplementary Figure S1**). As expected, when we measured the size of the SH by SEM (**Figures 5B,C**), we realized that the eggshell pore size allows passage of SH into the eggs. There was no statistical difference in pore size between groups (**Table 1**).

Through SEM analyses, we can elucidate the conformation of SH biofilms in eggshells. In the group PC we observed characteristic formation of biofilm as well as free bacteria on the surface of these biofilms (**Figures 5A–D**). In groups (ZnO:Ag-AgO) pre, AP pre, and NC, we observed a sparsity of matrix that was incompatible with that presented by the group PC. We observed some bacteria in NC but detected no bacteria similar to PC in size and morphology (**Figures 5E,F**).

Small amounts of both matrix and other microorganisms were expected in the NC since the eggshells were not sterilized. Most of the bacteria found in the NC are probably environmental ones. Furthermore, in the eggshells we detected the presence of organic remnants, such as mucoproteins and other environmental substances, including nest material and suspended feed powder. However, our analysis detected greater differences between negative and positive groups in relation to the matrix formation, shape and bacterial amount. **Figure 5** strongly confirmed that the SH biofilm was not formed in the previously treated eggshell with ZnO:Ag-AgO.

TABLE 1 | Measurements of pore diameters in eggs submitted or not to different types of disinfection with nanoparticles.

	NC	(ZnO:Ag-AgO) post	(ZnO:Ag-AgO) pre
Pore diameters (μm)	4.032	4.095	4.536

There was not statistical difference in the eggs pore size.

TABLE 2 | Concentration of Ag and Zn (ppm) in shell, albumen or yolk of eggs treated with ZnO:Ag-AgO and NC.

	Shell NC	Shell ZnO:Ag-AgO	Albumen NC	Albumen ZnO:Ag-AgO	Yolk NC	Yolk ZnO:Ag-AgO
Ag	0,007a	0,100b	0,003a	0,010a	0.002a	0.001a
Zn	0.218a	0.797b	0.265a	0.232a	1.294c	1.295c

Different letters on the same line for same element means statistical difference.

Zn and Ag Ions Have Not Reached Into the Eggs Treated With ZnO:Ag-AgO NCs

As expected, the Ag and Zn, quantified by inductively Coupled Plasma Optical Emission Spectrometry (ICP-OES), showed a large presence of Ag on the shell treated with ZnO:Ag-AgO nanocomposite, but most important, Ag ions have not been detected in the albumen and yolk (**Table 2**). Zinc was detected in the shell, albumen and yolk samples. Although the amount of Ag and Zn in the shell of the ZnO:Ag-AgO group was statistically greater relative to the control, this difference was not observed in the other egg components (**Table 2**).

DISCUSSION

In the present work, we have demonstrated that a novel nanocomposite of Ag-doped ZnO and AgO nanocrystals has been successfully used as a preventive measure to control biofilm formation, and SE and SH infiltration into turkey eggs. This new nanocomposite has shown diffraction patterns of both ZnO and AgO, with respective sizes of 28 nm and 30nm. We have also confirmed the Ag doping with substitution of Zn by Ag into the ZnO crystalline structure, by demonstrating that the Ag+2 has an ionic radius (1.26 Å) greater than Zn+2 (0.74 Å). This doping strategy has increased the catalytic activity in ZnO NCs, improving its ability to induce oxidative stress in bacteria (Pati et al., 2014).

Salmonella control is a major concern for poultry producers in Brazil since the country is the largest exporter of poultry meat and eggs. The control of SH is quite difficult and highly prevalent in Brazil (Voss-Rech et al., 2015). In poultry products *Salmonella* spp. was the main cause of early warnings in the European Union between January 2017 and May 2018 (RASFF, 2018). It is possible that these bacteria remain in the farm environment as a biofilm form.

We have also used the ZnO:Ag-AgO to control the SE biofilms in eggs and its entry into albumen and yolk, but the nanocomposite was not able to eliminate previously formed biofilms, although has significantly reduced the bacterial load in the egg surface. The presence of *Salmonella* into eggs corroborates previous findings elsewhere (Gustin, 2003), in which *Salmonella* spp. is able to enter the egg contents after 24 h of contact with eggshells. However, we emphasize that the most important finding was the use of ZnO:Ag-AgO before SH biofilm formation, which not only protected from its formation, but also demonstrated that it has effectively blocked the bacterial entry into the albumen and yolk.

Eggshells present numerous pores that are sufficiently large to act as gateways for microorganisms (Cardoso et al., 2001; Silva, 2005). Considering that the shell pore diameter may be involved in the bacterial contamination and translocation into the egg, which may also facilitate the entry of nanocrystals, we have shown for the first time the pore size of turkey eggshells by Confocal Raman, and we also showed that toxic Ag ions did not reach the albumen and yolk, which was also successfully demonstrated by ICP-OES, demonstrating that no ions were internalized. Similar to Ag, higher Zn ion concentration was only observed at the eggshell surface treated with ZnO:Ag-AgO, demonstrating that although the ultra-small size of the ZnO:Ag-AgO NCs would easily allow their entry into the egg, they were not able to translocate to the inner side of eggs. We hypothesize that probably the surface charges of both eggshell and nanocrystals have favored the nanocrystals retention at the shell surface.

It is worth to note that microorganisms are highly resistant to disinfectants when structured as biofilms (Ziech et al., 2016). In general, disinfectants are not capable of eliminating the entire biofilm matrix, requiring further association with a mechanical processes to disturb the matrix structure and to expose the microorganisms to disinfectants (Maukonen et al., 2003; Srey et al., 2013). Although complete elimination has not occurred in the present study, the evaluated disinfectants significantly reduced the microbial load of the biofilm on treated eggs by 5 to 6 logs. Again, the similar performance between the ZnO:Ag-AgO and PA groups as control measures confirmed the potential of the ZnO:Ag-AgO nanocomposite, since the dose of PA used was much higher than the one recommended by the manufacturer. Several studies have shown full or partial efficiency of ZnO or AgO nanoparticles in inhibiting biofilm activity of different microorganisms in polystyrene wells or another material (Sinisa et al., 2015; Singh et al., 2016, 2018; Melo et al., 2017), but none has shown nanocrystals behavior in eggshells and their activity at the surface and within the egg components. Therefore, this is the first time an Ag-doped ZnO-AgO nanocomposite is successfully used as a preventive measure to protect eggs from *Salmonella* spp infection and biofilm formation.

Briefly, in our search for new effective, safe and viable measures to control microorganisms in the poultry farming, we have synthesized a novel nanocomposite that may become an alternative of great potential to effectively prevent *Salmonella* biofilm formation and infection of eggs. Moreover, since eggshells have a rough surface, we believe this in an excellent experimental model for biofilm formation, which reinforces its use on other surfaces. Besides its successful activity against the most important bacterial problem in the poultry industry, it is a harmless substance. Other studies should be performed to ascertain the best administration and control of other microorganisms.

AUTHOR CONTRIBUTIONS

BF and LG have developed and planned the project, analyzed and interpreted the data, and wrote the manuscript. AS and ND produced and characterized the nanoparticles. PS, AdP, DR, BF and OO performed microbiology and molecular assays. OO performed the ICP analyses. MB performed and analyzed the biofilm by SEM, and has partially contributed to the manuscript writing. All authors read and approved the final manuscript.

FUNDING

The publication of the manuscript will be paid by the Federal University of Uberlândia. The authors thank the Brazilian funding agencies, CNPq, CAPES, and FAPEMIG, for providing financial support to the National Institute of Science and Technology in Theranostics and Nanobiotechnology –INCT-Teranano (CNPq/CAPES/FAPEMIG, Grant # CNPq-465669/2014-0 and FAPEMIG-CBB-APQ-03613-17).

SUPPLEMENTARY MATERIAL

The Supplementary Material for this article can be found online at: https://www.frontiersin.org/articles/10.3389/fmicb.2019.00217/full#supplementary-material

FIGURE S1 | Image obtained in Raman confocal microscopy, presence of roughness and pores on turkey eggshells. The arrows in image **A** show the pores of the shell, while **B** depicts the eggshell dimensions in a 3D image.

REFERENCES

Allaker, R. P. J. (2010). The use of nanoparticles to control oral biofilm formation. *Dent. Res.* 89, 1175–1186. doi: 10.1177/0022034510377794

Bauer, A. W., Kirby, W. M. M., Sherris, J. C., and Turck, M. (1966). Antibiotic susceptibility testing by standardized single method. *Am. J. Clin Pathol.* 45, 493–496. doi: 10.1093/ajcp/45.4_ts.493

BRASIL (2008). *Resolução no 91, De 28 de Novembro de 2008. Agência Nacional de Vigilância Sanitária, Ministério da Saúde. Diário official da União. Brasilia 1 de dezembro de 2008*. Available in: http://bvsms.saude.gov.br/bvs/saudelegis/anvisa/2008/res0091_28_11_2008.html

Brown, H. L., Reuter, M., Salt, L. J., Cross, K. L., Betts, R. P., and Van Vliet, A. H. M. (2014). Chicken juice enhances surface attachment and biofilm formation of *Campylobacter jejuni*. *Appl. Environ. Microbiol.* 80, 7053–7060. doi: 10.1128/AEM.02614-14

Cardoso, A. L. S. P., Tessari, E. N. C., Castro, A. G. M., Kanashiro, A. M. I., and Gama, N. M. S. Q. (2001). Pesquisa de coliformes totais e coliformes fecais analisados em ovos comerciais no laboratório de patologia avícola de descalvado. *Arq. Inst. Bio.* 68, 19–22.

CDC (2016). Center for Disease Control. Making Food Safer to Eat: Reducing Contamination from the Farm to the Table. Available at: http://www.cdc.gov/vitalsigns/foodsafety/

Donlan, R. M., and Costerton, J. M. (2002). Biofilms: survival mechanisms of clinically relevant microorganisms. *Clin. Microbiol. Rev.* 15, 167–193. doi: 10.1128/CMR.15.2.167-193.2002

EFSA. (2017). The European Union summary report on trends and sources of zoonoses, zoonotic agents and food-borne outbreaks in 2016. *Eur. Food Saf. Authority J.* 15:5077.

Espitia, P. J. P., Soares, N. F. F., Coimbra, J. S. R., Andrade, N. J., Cruz, R. S., and Medeiros, E. A. A. (2012). Zinc oxide nanoparticles: synthesis, antimicrobial activity and food packaging applications. *Food. Bioprocess. Technol.* 5, 1447–1464. doi: 10.1007/s11947-012-0797-6

Flemming, H. C., and Wingender, J. (2010). The biofilm matrix. *Nat. Rev. Microbiol.* 8, 623–633. doi: 10.1038/nrmicro2415

Gustin, P. C. (2003). "Biossegurança no incubatório," in *Manejo da Incubação*, eds M. Macari and E. Gonzales (Campinas: Facta), 297–352.

Martínez, L. C., and Vadyvaloo, V. (2014). Mechanisms of post-transcriptional gene regulation in bacterial biofilms. *Front. Cell Infect. Microbiol.* 4:38. doi: 10.3389/fcimb.2014.00038

Maukonen, J., Mättö, J., Wirtanen, G., Raaska, L., Mattila-Sandholm, T., and Saarela, M. J. (2003). Methodologies for the characterization of microbes in industrial environments: a review. *J. Ind. Microbiol. Biotechnol.* 30, 327–356. doi: 10.1007/s10295-003-0056-y

Melo, R. T., Mendonça, E. P., Monteiro, G. P., Siqueira, M. C., Pereira, C. B., Peres, P. A. B. M., et al. (2017). Intrinsic and extrinsic aspects on Campylobacter jejuni biofilms. *Front. Microbiol.* 8:1332. doi: 10.3389/fmicb.2017.01332

Nikolaev, Y. A., and Plakunov, V. K. (2007). Biofilm city of microbes or an analogue of multicellular organisms. *Microbiology* 76, 149–163. doi: 10.1134/S0026261707020014

Pati, R., Mehta, R. K., Mohanty, S., Padhi, A., Sengupta, M., Vaseeharan, B., et al. (2014). Topical application of zinc oxide nanoparticles reduces bacterial skin infection in mice and exhibits antibacterial activity by inducing oxidative stress response and cell membrane disintegration in macrophages. *Nanomedicine* 10, 1195–1208. doi: 10.1016/j.nano.2014.02.012

RASFF (2018). *The Rapid Alert System for Food and Feed, Annual Report of European Comission*. Available at: https://webgate.ec.europa.eu/rasffwindow/portal/?event = searchResultList&S tartRow = 201.

Reddy, K. M., Feris, K., Bell, J., Wingett, D. G., Hanley, C., and Punnoose, A. (2007). Selective toxicity of zinc oxide nanoparticles to prokaryotic and eukaryotic systems. *Appl. Phys. Lett.* 90, 1–3. doi: 10.1063/1.2742324

Schlisselberg, D. B., and Yaron, S. (2013). The effects of stainless steel finish on *Salmonella* Typhimurium attachment biofilm formation and sensitivity to chlorine. *Food Microbiol.* 35, 65–72. doi: 10.1016/j.fm.2013.02.005

Silva, E. A. Jr. (2005). *Manual de Controle Higiênico Sanitário em Serviços de Alimentação*. São Paulo: Varela.

Singh, H., Du, H., Sing, P., and Yia, T. H. (2018). Extracellular synthesis of silver nanoparticles by *Pseudomonas* sp. THG-LS1.4 and their antimicrobial application. *J. Pharm. Anal.* 8, 258–264. doi: 10.1016/j.jpha.2018.04.004

Singh, P., Singh, H., Kim, Y. J., Mathiyalagan, R., Wang, C., and Yang, D. C. (2016). Extracellular synthesis of silver and gold nanoparticles by Sporosarcina koreensis DC4 and their biological applications. *Enzyme. Microb. Technol.* 86, 75–83. doi: 10.1016/j.enzmictec.2016.02.005

Sinisa, V., Elder, J., Medihala, P., Lawrence, J. R., Predicala, B., Zhang, H., et al. (2015). ZnO nanoparticles impose a panmetabolic toxic effect along with strong necrosis, inducing activation of the envelope stress response in *Salmonella enterica* Serovar enteritidis. *Antimicrob. Agents Chemother.* 59, 3317–3328. doi: 10.1128/AAC.00363-15

Srey, S., Jahid, I. K., and Ha, S. D. (2013). Biofilm formation in food industries: a food safety concern. *Food Control.* 31, 572–585. doi: 10.1016/j.foodcont.2012.12.001

Steenackers, H., Hermans, K., Vanderleyden, J., and Keersmaecker, S. C. (2012). *Salmonella* biofilms: an overview on occurrence, structure, regulation and eradication. *Food Res. Int.* 45, 502–531. doi: 10.1016/j.foodres.2011.01.038

Tankhiwale, R., and Bajpai, S. K. (2012). Preparation, characterization and antibacterial applications of ZnO-nanoparticles coated polyethylene films for food packaging. *Colloids. Surf. B. Biointerfaces* 90, 16–20. doi: 10.1016/j.colsurfb.2011.09.031

Tomihama, T., Nishi, Y., and Arai, K. J. (2007). Biofilm formation and resistance to bactericides of *Pseudomonas* syringae pv. theae. *Gen. Plant. Pathol.* 73, 193–196. doi: 10.1007/s10327-007-0006-z

Voss-Rech, D., Vaz, C. S. L., Alves, L., Coldebella, A., Leão, J. A., Rodrigues, D. P., et al. (2015). A temporal study of *Salmonella enterica* serotypes from broiler farms in Brazil. *Poult. Sci.* 94, 433–441. doi: 10.3382/ps/peu081

Wang, X., Wu, H. F., Kuang, Q., Huang, R. B., Xie, Z. X., and Zheng, L. S. (2010). Shape-dependent antibacterial activities of Ag2O polyhedral particles. *Langmuir* 26, 2774–2778. doi: 10.1021/la9028172

Xie, Y., He, Y., Irwin, P. L., Jin, T., and Shi, X. (2011). Antibacterial activity and mechanism of action of zinc oxide nanoparticles against *Campylobacter jejuni*. *Appl. Environ. Microbiol.* 77, 2325–2331. doi: 10.1128/AEM.02149-10

Ziech, R. E., Perin, A. P., Lampugnani, C., Sereno, M. J., Viana, C., and Soares, V. M. (2016). Biofilm-producing ability and tolerance to industrial sanitizers in *Salmonella* spp. isolated from Brazilian poultry processing plants. *Food Sci. Technol.* 68, 85–90. doi: 10.1016/j.lwt.2015.12.021

Conflict of Interest Statement: The authors declare that the research was conducted in the absence of any commercial or financial relationships that could be construed as a potential conflict of interest.

frontiers in Microbiology

ORIGINAL RESEARCH
published: 27 February 2019
doi: 10.3389/fmicb.2019.00282

Analytical Investigation of *Cymbopogon citratus* and Exploiting the Potential of Developed Silver Nanoparticle Against the Dominating Species of Pathogenic Bacteria

Priyanka Basera, Meeta Lavania*, Anil Agnihotri and Banwari Lal

The Energy and Resources Institute, New Delhi, India

Indian biodiversity is a hub for medicinal plants. Extensive research has been carried out to select plants with numerous properties which can be used for human welfare. Present research is about *Cymbopogon citratus*, an economically valuable medicinal plant. In this study *Cymbopogon citratus* was elected as a subject plant over the five selected plants (*Azadirachta indica*, *Plumeria obtuse*, *Sapindus mukorossi*, *Capsicum annuum* and *Phyllanthus emblica*) on the basis of antibacterial effect against dominating pathogenic species of gram positive (*Bacillus cereus, Bacillus licheniformis*) and gram negative (*Pseudomonas aeruginosa, Escherichia coli*) bacteria. Further, bioactive agents behind antibacterial potential of *Cymbopogon citratus* was analyzed using analytical method (Phyto-chemical, FTIR, NMR and GC-MS). Due to the broad antimicrobial spectrum, silver nanoparticles have turned into a noteworthy decision for the improvement of new medication. Therefore, this investigation further elaborated in the development of *Cymbopogon citratus* silver nano-particles (CNPs). Antibacterial potential of CNPs examine in a range of C_{25}–C_{150} (μg/ml) through minimum inhibitory concentration (MIC) and minimum bactericidal concentration (MBC) where, C_{25} (μg/ml) concentration of CNPs were recorded as the MIC for all bacterial species and C_{25} (μg/ml) and C_{50} (μg/ml) noted as the MBC for *Pseudomonas aeruginosa, Escherichia coli* and *Bacillus cereus, Bacillus licheniformis*, respectively. In agar disk diffusion assay of CNPs, maximum diameter of zone of inhibition was observed for C_{150} (μg/ml) concentration *Bacillus cereus* (20.12 ± 0.42), *Bacillus licheniformis* (22.34 ± 0.4), *Pseudomonas aeruginosa* (35.23 ± 0.46) and *Escherichia coli* (31.87 ± 0.24). Involvement of bioactive component as a reducing and capping agent can be confirmed through FTIR spectrum of CNPs. Moreover XRD, EDXRF and SEM showed crystalline and cuboidal nature of CNPs with ~35 nm sizes. Prominently, cytotoxic analysis was conducted to understand the toxic effect of CNPs. This research highlights the potential of CNPs due to the bioactive components present in *Cymbopogon citratus* extract: Polyphenols (phenol; 1584.56 ± 16.32 mg/L, Flavanoids) and mixture of terpenoids (Citral, Myrcene, Farnesol, β-myrcene and β –Pinene)

Keywords: *Cymbopogon citratus*, analytical analysis, *Cymbopogon citratus* silver nanoparticles, pathogenic species, minimum inhibitory concentration

OPEN ACCESS

Edited by:
Gerson Nakazato,
State University of Londrina, Brazil

Reviewed by:
M. Oves,
King Abdulaziz University,
Saudi Arabia
Amit Kumar Mandal,
Raiganj University, India

***Correspondence:**
Meeta Lavania
meetal@teri.res.in

Specialty section:
This article was submitted to
Antimicrobials, Resistance
and Chemotherapy,
a section of the journal
Frontiers in Microbiology

Received: *29 June 2018*
Accepted: *04 February 2019*
Published: *27 February 2019*

Citation:
Basera P, Lavania M, Agnihotri A and Lal B (2019) Analytical Investigation of Cymbopogon citratus and Exploiting the Potential of Developed Silver Nanoparticle Against the Dominating Species of Pathogenic Bacteria.
Front. Microbiol. 10:282.
doi: 10.3389/fmicb.2019.00282

INTRODUCTION

More than half of the world population use plants for their basic health needs. They are bestowed for humanity. From the millennia they have been used as a potent medicinal treatment against various kinds of diseases and ailment. Plant resides wide range of bioactive components/secondary metabolites viz Phenols, Tannins, Saponin, Steriods, Alkaloids, Flavanoids, Carbohydrates and Glycosides which are responsible for antimicrobial activity (Nascimento et al., 2000; Ewansiha et al., 2012; Chaudhary et al., 2017; Elish et al., 2017) therefore the discovery of extraction of bioactive components from plants have proved to be one of the important research for human kind. Due to the negative impact of chemically designed antimicrobial drugs as compared to natural drugs on human health and environment; treatment with natural constituents has increased potentially these days (Wu et al., 2013). Many reports cited numerous plants with antimicrobial activity; *C. citratus* is one of them commonly referred as lemon grass.

Cymbopogon *citratus* is an aromatic, perennial and economically valuable plant. Studies indicate that this plant have a strong lemon like aroma due to the presence of citral, which is a potent bioactive constituent having antimicrobial activity (Korenblum et al., 2013) and therefore in common language, *C. citratus* called by lemongrass. The component present in plant is conventionally used in variety of human therapy (Han and Parker, 2017). Traditionally aqueous extract of its dried leaves use to treat digestive disorders, diabetes, nervous disorders and cancer (Francisco et al., 2011). According Thangam et al., 2014 findings *C. citratus* polysaccharides has important role in turning off the genes that suppresses the tumor growth and act as a potent novel anti-cancer drugs. *C. citratus*is widely applicable in field of medicine, cosmetic (Perfumes, soap etc) and brewing (non-alcoholic like tea) (Ekpenyong et al., 2014). Because of the immense benefit to human kind, *C. citratus* has been used to conduct several of studies for investigation of its valuable potential.

Different physio-chemical methods have been opted for synthesizing nanoparticles with expensive cost and detrimental effects (Oves et al., 2013). Recently, production of plant nanoparticles is in high demand; due to the versatile nature of plant to be used as an antimicrobial agent. Attention of researchers has been diverted toward plants nanoparticle (PNPs) because of their eco-friendly and non-pathogenic nature. They have provided an environmentally suitable solution in bio-medicinal sector, as a green approach (Jain and Mehata, 2017; Oves et al., 2018). In general; a particle which range between 1 and 100 nm is referred to as nanoparticle (Baranwal et al., 2018). Due to the reduced size of synthesized nanoparticles, high surface to volume ratio was noticed by scientist which is a remarkable feature for obliterating bacterial density (Oves et al., 2017). For the production of nanoparticles noble metals like Silver (Ag), Gold (Au) and Platinum (Pt) have been used (Rai et al., 2015). Silver (Ag) used enormously among all metals, as researcher reported its use in broad sense as an anti-microbial agent like anti-bacterial, anti-fungal, anti-inflammatory, anti-cancerous and anti-viral (Goudarzi et al., 2016; Oves et al., 2017; Qayyum et al., 2017; Yugal et al., 2017). Therefore synthesizing silver nanoparticle through plant extract has been recognized as efficient biological approach in controlling the pathogenic microbes (Qayyum et al., 2017).

The study has focused on (i) Screening of potent plant from six different selected plants (*Azadirachta indica, Plumeria obtuse, Cymbopogon citratus*, *Sapindus mukorossi*, *Capsicum annuum* and *Phyllanthus emblica*) using antibacterial assay against dominating pathogenic gram positive (*Bacillus cereus, Bacillus licheniformis*) and gram negative (*Pseudomonas aeruginosa, Escherichia coli*) bacterial species.(ii) Characterization of bioactive components present in selected potent plant (*Cymbopogon citratus*) through phytochemical (qualitatively and quantitatively) and analytical (FTIR, NMR and GC-MS) analysis. (iii) Development of synthesized nanoparticles from *Cymbopogon citratus* referred as CNPs and further analyzed using FTIR, XRD, EDXRF, SEM, MIC/MBC and cyto-toxicity assay.

MATERIALS AND METHODS

Collection of Plant Material

Leaves of *A. indica, C. citrates*, and *P. obtuse* were collected from the institutional area of TERI-gram (Gurugram, India) in the month of June-July (2016). Seeds of *S. mukorossi, C. annuum,* and *P. emblica* obtained from raw fruits, commercially available. Study materials were stored at cold room (4°C) till further analysis.

Preparation of Plant Extracts

To prepare plant extract, leaves and raw fruits were first surface sterilized with distilled water followed by 70% ethanol (Merck Ltd) for removal of dust and unwanted particles. Seeds were obtained from raw fruits by removing the pulp and sterilized with 70% ethanol (Merck, Ltd). Sterilized plant material (leaves and seeds) were sun-dried and then powdered with mechanical grinder. For extraction, soxhlet method was opted, were methanol (Fisher Scientific, Ltd) served as a solvent. For each plant, different conditions such as ratio of solvent (ml): plant material (g) and time were optimized. Extracted samples were further concentrated using Rota-evaporator (Rotavac Heidolph).

Testing Microorganism

In the present study, for examining the antimicrobial activity; *B. cereus* (ATCC- BAA-512), *E. coli* (ATCC- 11775), *P. aeruginosa* (ATCC- 19429) and *B. licheniformis* (DSMZ-8059) bacteria were selected. For inoculum preparation loop full of bacterial culture from agar plates were transferred to Muller Hinton broth (HiMedia). Obtained bacterial suspension was incubated for 24 h at 37°C, further for antibacterial assay bacterial growth were adjusted to 0.5 MacFarland standard turbidity (Clinical and Laboratory Standards Institute [CLSI], 2012) approx 1.5×10^6 CFU/ml bacterial cultures.

Antibacterial Activity of Plant Extracts (Agar Disk-Diffusion)

For determination of antibacterial activity, agar disk-diffusion method was performed as per EUCAST (2019) Guidelines. Using Spread plate technique, Mueller-Hinton agar (HiMedia Laboratories Pvt. Ltd) plates were inoculated with selected microorganism. Sterile disk (6 mm diameter, HiMedia Laboratories Pvt., Ltd.) was dipped in different plant extracts (*Azadirachta indica, Plumeria obtuse, Cymbopogon citratus*, *Sapindu smukorossi*, *Capsicum annuum* and *Phyllanthus emblica*) solutions in selected concentration (100 μg/ml) made in methanol. Plates were incubated at 37°C for 24 h. The clear zone was noted in mm, which signifies the Zone of inhibition. From this investigation, *C. citratus* was selected for further examinations.

Qualitative and Quantitative Analysis of *C. citratus* Extract

Bioactive compounds present in *C. citratus* extract were assessed both qualitatively and quantitatively (TPC: Total phenolic compound). The standard protocols were used for determination of compounds such as carbohydrate, Saponin, Steroid, Phenols, Tannin, Flavonoids, Glycosides, Terpenoids, and Alkaloids (Ewansiha et al., 2012). Total phenolic content of the plant extract was determined through Folin-Ciocalteu reagent (Alhakmani et al., 2013).500 μl extract (1 mg/mL) mixed with 2 ml of 10% Follin-Coiocalteu (2N) (Sigma-Aldrich) and 4 ml of 7.5%$NaHCO_3$ (Sigma-Aldrich) solution. Mixture was incubated for 30 min at room temperature. Absorbance was measured at wavelength 765 nm. Standard curve (**Supplementary Figure S1**) was prepared using gallic acid. Total Phenolic content was expressed in mg/g of dry weight.

Analytical Investigation of *C. citratus* Extract

Fourier Transform Infrared Spectroscopy (FTIR)

Fourier transform infrared spectroscopy spectrum of *C. citratus* extract was obtained using FTIR spectrophotometer (Perkin Elmer). FTIR used for chemical identification as each molecule and chemical structure creates a unique spectra. The IR spectra were accounted in % transmittance. The wave number region for analysis was 4000–400 cm^{-1} (mid-infrared range.) with resolution of 0.15 cm^{-1} having 64 scans per spectrum.

Nuclear Magnetic Resonance (NMR)

Nuclear magnetic resonance spectroscopy was performed to obtain ^{1}H-NMR spectra of *C. citratus* extract, which was recorded using NMR (BrukerAvance III) spectrophotometer with operating frequency of 400 MHz at 289K temperature, the spectra obtained of 12 ppm width. To acquire high-quality spectra; sample run for 64 scans and chemical shifts were reported in parts per millions (ppm).

Gas Chromatography-Mass Spectrometry (GC-MS)

The extract of *C. citratus* was analyze using GC-MS (Agilent 5975C) equipped with DB-WAX capillary column. Helium was used as carrier gas. Temperature ranges between 230 and 325°C. Initially, column temperature was set at 70°C and further increased to 325°C. Dilute sample (1/50 in methanol) of 0.1 μl was used. The components were identified on the basis of their mass spectra using National Institute for Standards and Technology [NIST] Mass Spectrometry Data Center (2018) library data of GC-MS system.

Development, Characterization and Surface Analysis of *C. citratus* Silver Nano-Particle (CNPs)

Preparation of Silver Nano-Particle

The nanoparticle synthesized from *C. citratus* was mentioned as CNPs. Silver nanoparticle was prepared by mixing plant extract in ratio of 1:9 10 ml plant extract and 90 ml of 1 mM (AR grade $AgNO_3$, Sigma-Aldrich, India). This was incubated at 37°C for 24 h in dark condition. Colloidal suspension was obtained which was further centrifuged two times at 4000 rpm for 30 min; collected pellet was washed with distilled water with same condition for removal of any absorbed substances. The obtained nanoparticles were lyophilized and used as stock (Simon et al., 2017). From stock, working solution (in methanol) with varying range (C_{25}-C_{150}μg/ml) was prepared.

X-Ray Diffraction (XRD), Energy Dispersive X-Ray Fluorescence (EDXRF) and Fourier Transform Infrared Spectroscopy (FTIR) Analysis of CNPs

The prepared CNPs were characterized by; X-ray diffraction (XRD), energy dispersive X-ray fluorescence spectrometry (EDXRF) and Fourier transform infrared (FT-IR) spectroscopy. Analysis of lyophilized powder of synthesized CNPs was carried out in a Rigaku Mini-Flex II XRD machine to determine the phase crystallinity using Cu-κα radiation. XRD analysis was executed with in the 2θ scanning range of 3°–90° with speed 4.00 deg/min in continuous mode. The EDXRF was executed using DX-700HS spectrometer (Shimadzu) for the purity of silver. The XRF study has been carried out in Helium atmosphere, at suitable voltage and current intensity. FT-IR spectra were recorded over the range of 400–4000 cm^{-1} using a FT-IR Perkin Elmer spectrophotometer.

Scanning Electron Microscopy (SEM) of CNPs

Interactions between bacterial species and silver nanoparticle were studied by Scanning Electron Microscopy (Carl Zeiss) (Hayat, 2000). Under aseptic conditions sample was immersed 2 to 4 h in 2.5% glutaraldehyde solution. Primary washing was done by 0.1M phosphate buffer with pH 7.2 and dehydrated with ethanol solution in series of 10–100% followed by acetone. Samples were air dried overnight, which were further coated with thin layer of metal (gold and palladium).

Minimum Inhibitory Concentration (MIC) and Minimum Bactericidal Concentration (MBC) of CNPs

Minimum inhibitory concentration were performed using broth dilution technique, value which shows the 99.9% of bacterial inhibition after 24 h of incubation at 37°C were considered as a MIC. For determination of MBC a small portion of liquid was aliquots from the MIC wells and spread on agar plates for 24 h at 37°C, no visible bacterial growth after sub-culturing was considered as MBC (French, 2006). Under aseptic condition MIC was conducted using Muller Hinton broth (MHB) medium, purchased from HiMedia Laboratories Pvt Ltd. Potential of CNPs were tested in a range from 25 to 150 μg/ml placing with positive and negative controls. Positive control was a bacterial suspension in MHB broth whereas negative controls were wells containing only MHB and MHB with CNPs. Experiment was incubated for 24 h at 37°C, appearance of visible solution in treated wells with reference to positive and negative control reflected as the MIC value of CNPs against test organism.

Cytotoxicity Assay of *C. citratus* and CNPs

The cytotoxicity assay was performed according to Ishida et al. (2006). The RBCs suspension was treated with several concentrations of both plant extract and synthesized CNPs in range of 10–150 μg/ml for 48 h where Triton X-114 (Sigma-Aldrich), utilized as a marker for hemolysis. Incubation executed for 2 h at 37°C on experimental cells. The RBCs were centrifuged at 2000 for 10 min, and estimation of hemolysis was done by taking the supernatant part, using a spectrophotometer at 540 nm. The outcomes were communicated as the percentage of hemolysis cytotoxicity test was conducted at National Toxicology Institute, Pune, India.

Statistical Analysis

The experimental results were expressed as mean standard deviation of three replicates. Microsoft Excel 2010 statistical package was used for all analyses. The data were subjected to one-way analysis of variance

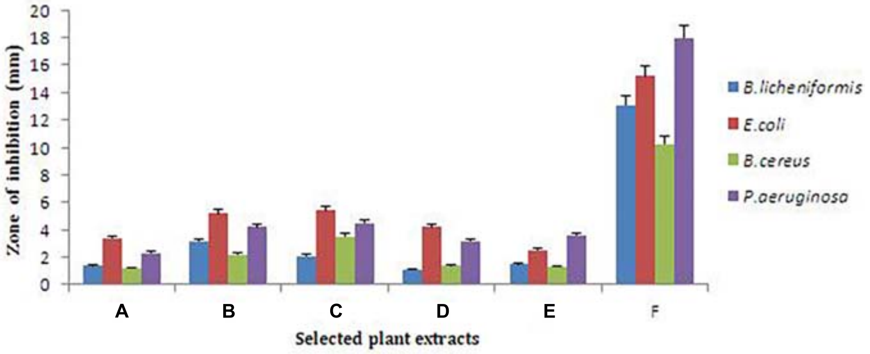

FIGURE 1 | Antibacterial activity depicted in various plant extracts A (*Phyllanthus emblica*), B (*Azadirachta indica*), C (*Capsicum annuum*), D (*Sapindus mukorossi*), E (*Plumeria obtuse*), F (*Cymbopogoncitratus*). *Cymbopogon citratus* displayed highest antibacterial activity. Mean values are significantly differ from each other according to statistical one way ANOVA ($P \leq 0.05$).

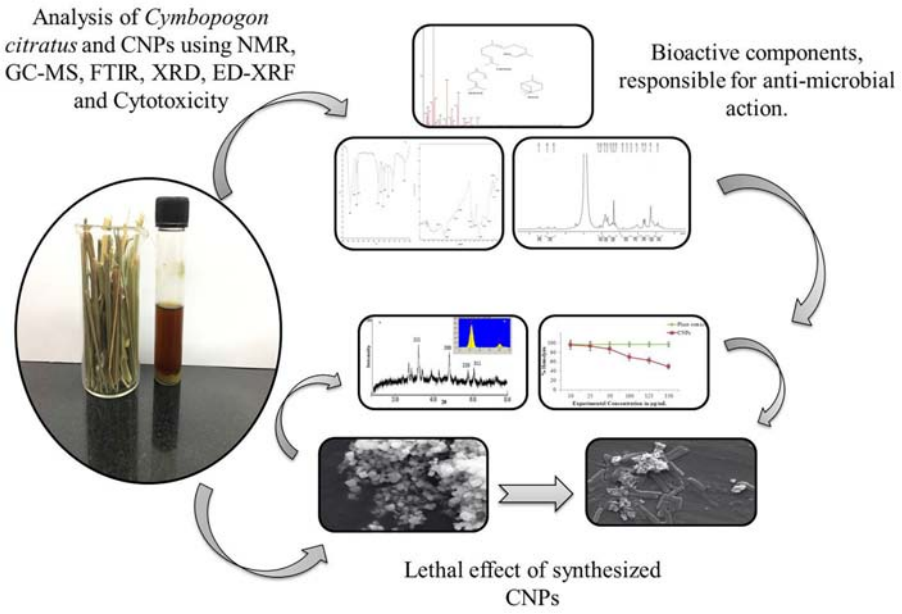

FIGURE 2 | Schematic representation of analytical analysis of *Cymbopogon citratus* and lethal effect of synthesized silver nano-particles (CNPs).

TABLE 1 | Qualitative analysis of phytochemical constituent present in *C. citratus* extract.

S. No.	Phytochemical test	Methanolic extract of *C. citratus*
1	Carbohydrates	+
2	Saponin	–
3	Steriod	+
4	Phenols	+++
5	Tannins	+
6	Flavanoid	++
7	Alkaloid	+
8	Terponoid	+++
9	Cardiac glycoside	+

"+++" Highly present; "+" moderate present; and "–" absent.

TABLE 2 | Quantitative analysis of phytochemical constituent present in *C. citratus* extract.

Phytochemical test	mg/ggallic acid equivalent
Total phenolic content (TPC)	1584.56 ± 16.32

±signify the Standard Deviation (SD) value.

(ANOVA) to determine the significant difference among variables. Difference was considered statistically significant at $p \leq 0.05$.

RESULTS AND DISCUSSION

Selection of Potent Plant on the Basis of Antibacterial Potential

Antimicrobial assay was performed to select the potent plant among the six selected plants. According to Ishida et al. (2006) plants inherent with medicinal properties which were studied for antimicrobial activities. Our finding signifies the importance of *C. citratus* among all selected plants; *C. citratus* gave the highest zone of inhibition against all the test microorganisms. The diameter of zone of inhibition recorded were 10.23 ± 0.08 for *B. cereus*, 13.1 ± 0.3 for *B. licheniformis*, 15.2 ± 0.5 for *E. coli* and 18.0 ± 0.12 for *P. aeruginosa* (**Figure 1** and **Supplementary Table S1**). Therefore, *C. citratus* selected and subjected for further analysis in order to identify its bioactive components responsible for its antibacterial nature and potential of synthesized silver nanoparticle against test microorganisms (**Figure 2**).

Qualitative and Quantitative Analysis

Previous reports of Matouschek and Stahl (1991), Chisowa et al. (1998), Negrelle and Gomes (2007), Aftab et al. (2011), and Lawal et al. (2017) on *C. citratus* suggested that geographical origin is responsible for variation in chemical composition of plant extract, though presence of sugar, steroid, phenols, tannins, alkaloid, flavanoid and terpenoid is well-known. Results of preliminary phytochemical screening confirmed the presence of similar chemical classes (**Table 1**). Existence of these chemicals in plant can act as bioactive components for plant, which are responsible for antimicrobial activity (Shah et al., 2011). Phenolic compounds are ubiquitous in nature and they exert several functions on plants such as such as plant growth, reproduction, development and disease resistance. These compounds were considered as the vital bioactive moiety for plant and produced by shikimate pathway (Lin et al., 2016). Several reports were suggesting that phenolic compound including terpenoid and flavonoid are anti-microbially bioactive components reside in plants (Parveen et al., 2010; Bhat et al., 2011; Voon et al., 2012; Wu et al., 2013). Quantitative finding of present research for the concentration of phenol was estimated to be 1584.56 ± 16.32 mg/g (**Table 2**). According to Mirghani et al. (2012) study, high amount of phenol is reported in *C. citratus*. Previously reported data on phenolic compounds including flavonoids validate that, these compounds contain polar hydroxyl groups which were responsible for antioxidants,

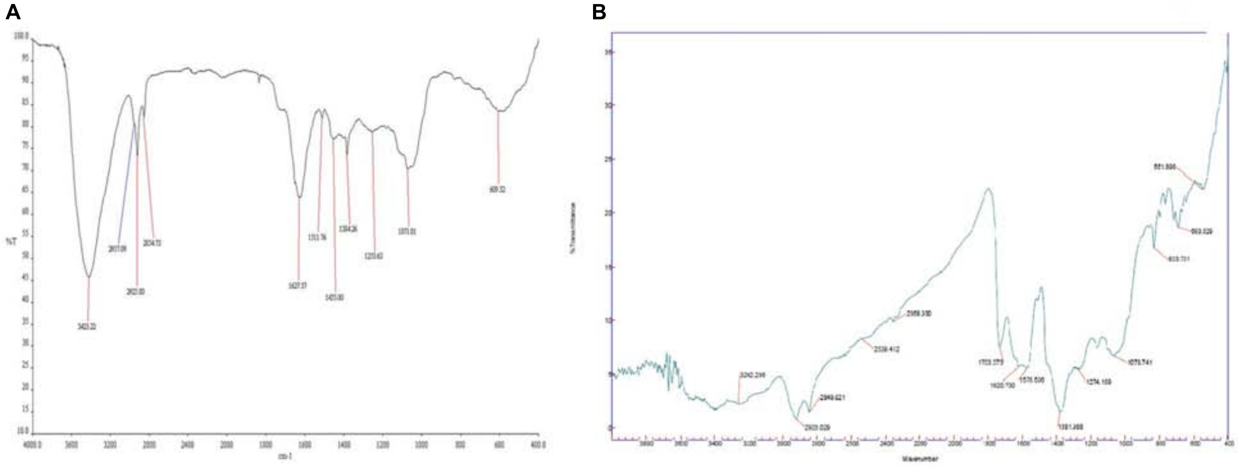

FIGURE 3 | (A) FTIR spectra of *Cymbopogon citratus* (methanolic extract), and **(B)** FTIR of CNPs.

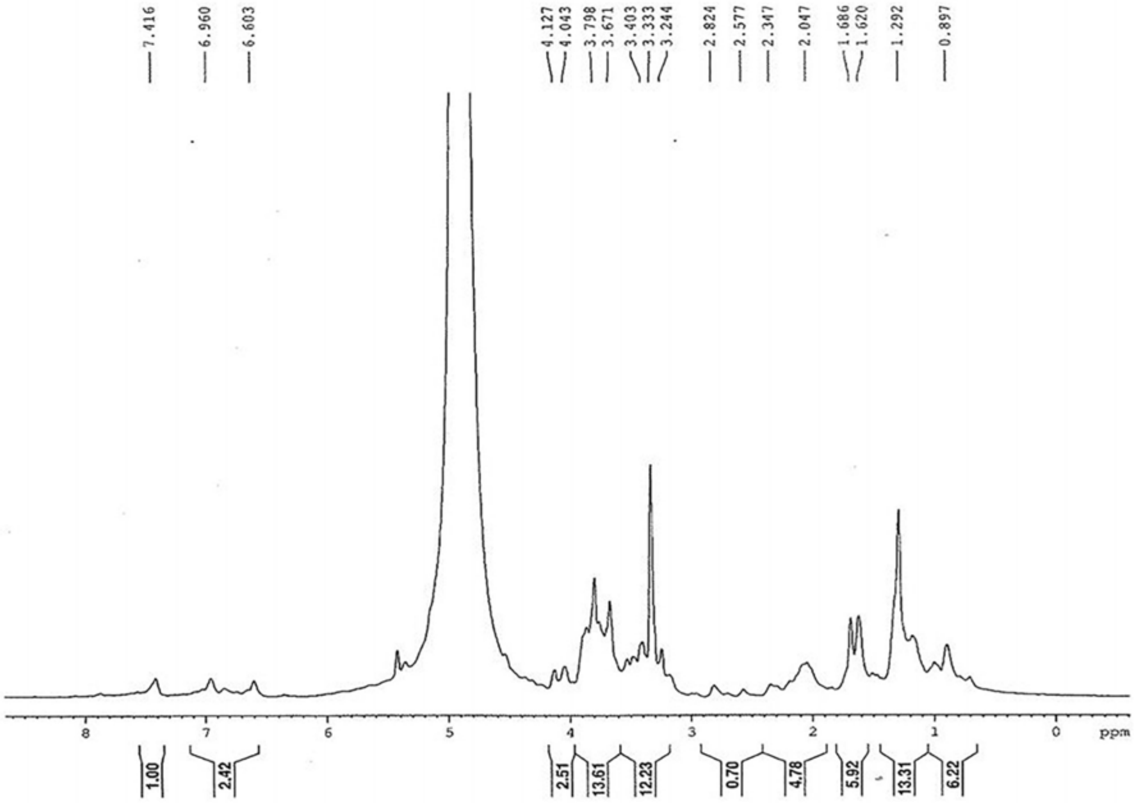

FIGURE 4 | ^{1}H-NMR spectrum of *Cymbopogon citratus* (methanolic extract).

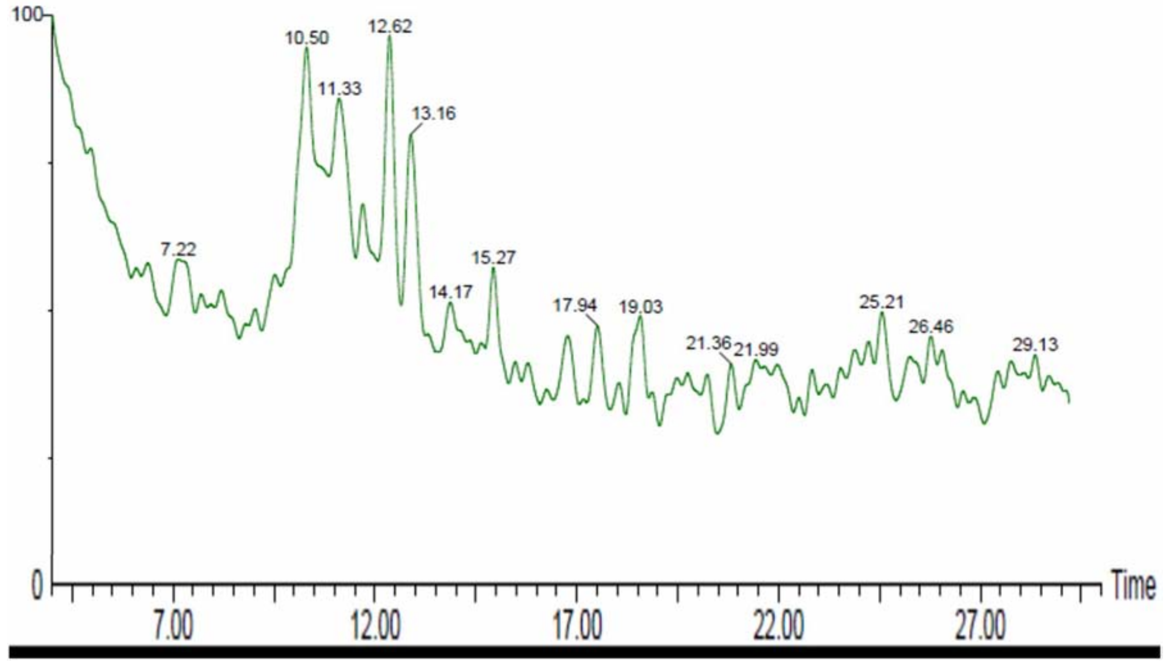

FIGURE 5 | GC-MS chromatogram obtained from *Cymbopogon citratus* (methanolic extract); depicted the molecule peak eluted at particular retention time.

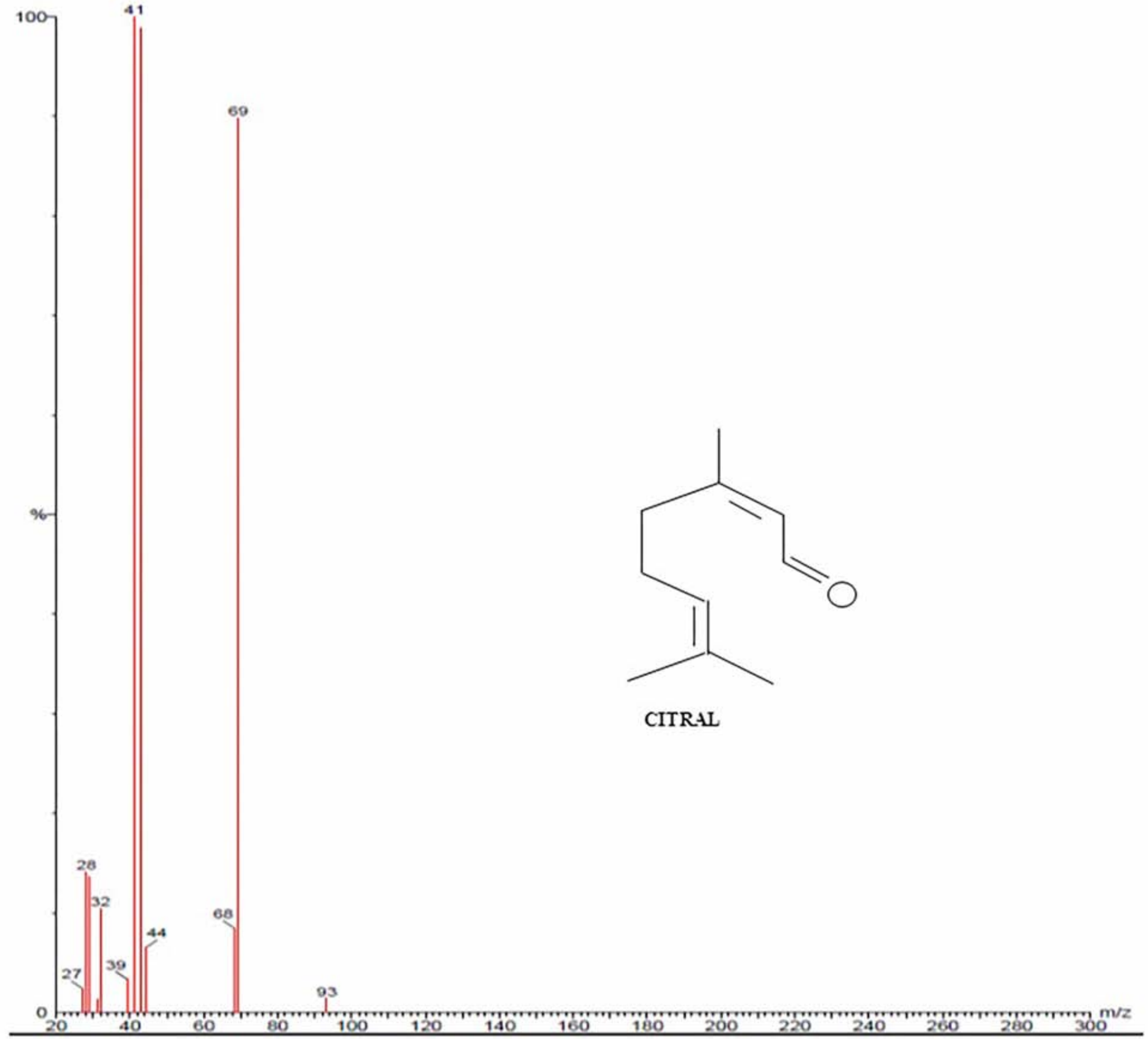

FIGURE 6 | Illustrated the fragmentation pattern of Citral molecule present in *Cymbopogon citratus* (methanolic extract).

free radical scavenger, anti-bacterial and anti-inflammatory actions (Cheel et al., 2005; Compean and Ynalvez, 2014; Pratiwi and Elin, 2016). Researcher additionally believed that inhibitory impact of bioactive component (terpenoids and phenols) is due to the interaction and disruption of enzymes and proteins useful for microbial metabolism (Ashraf et al., 2016).

Analytical Analysis

To obtain the reliable statistical data, analytical analysis of *C. citratus* was executed through FTIR, NMR and GC-MS; CNPs through XRD, EDXRF and FTIR. Further, comparative analysis of FTIR spectra of *C. citratus* and CNPs were illustrated.

FTIR Analysis of *C. citratus* and CNPs

For analyzing surface functional groups in plant extract and CNPs, FTIR technique was used as represented in **Figures 3A,B**. The spectra obtained for *C. citratus* (plant) extract and CNPs exhibited well defined spectral regions varied in the range of 400–4000 cm^{-1}. While comparing FTIR spectra of plant extract with CNPs, peaks of CNPs spectra observed at 693.529, 1070.741, 1381.988, 1620.7, 2849.921 and 2923.029 was found to be almost similar with minor shifts, indicates the role of plant extract as a capping agent to the silver nanoparticles (Ahmed and Ikram, 2015). According to Jain and Mehata (2017) plant extract contains the responsible agent for the reduction of silver ions into the formation of nanoparticles. Further, spectrum lying in range between 3600 and 3200 was assigned to -OH stretching of alcohol. The peaks in the region of 1700–1600 denotes the C = O and weak C = C stretching of aldehyde and ketone. C-H stretching of alkane was observed at 2923.029 (CNPs), 2925.80 (Plant extract) corresponding to an alkyl saturated aliphatic group. Peak at 2849.921 (CNPs), 2854.73 (Plant extract) related to symmetric

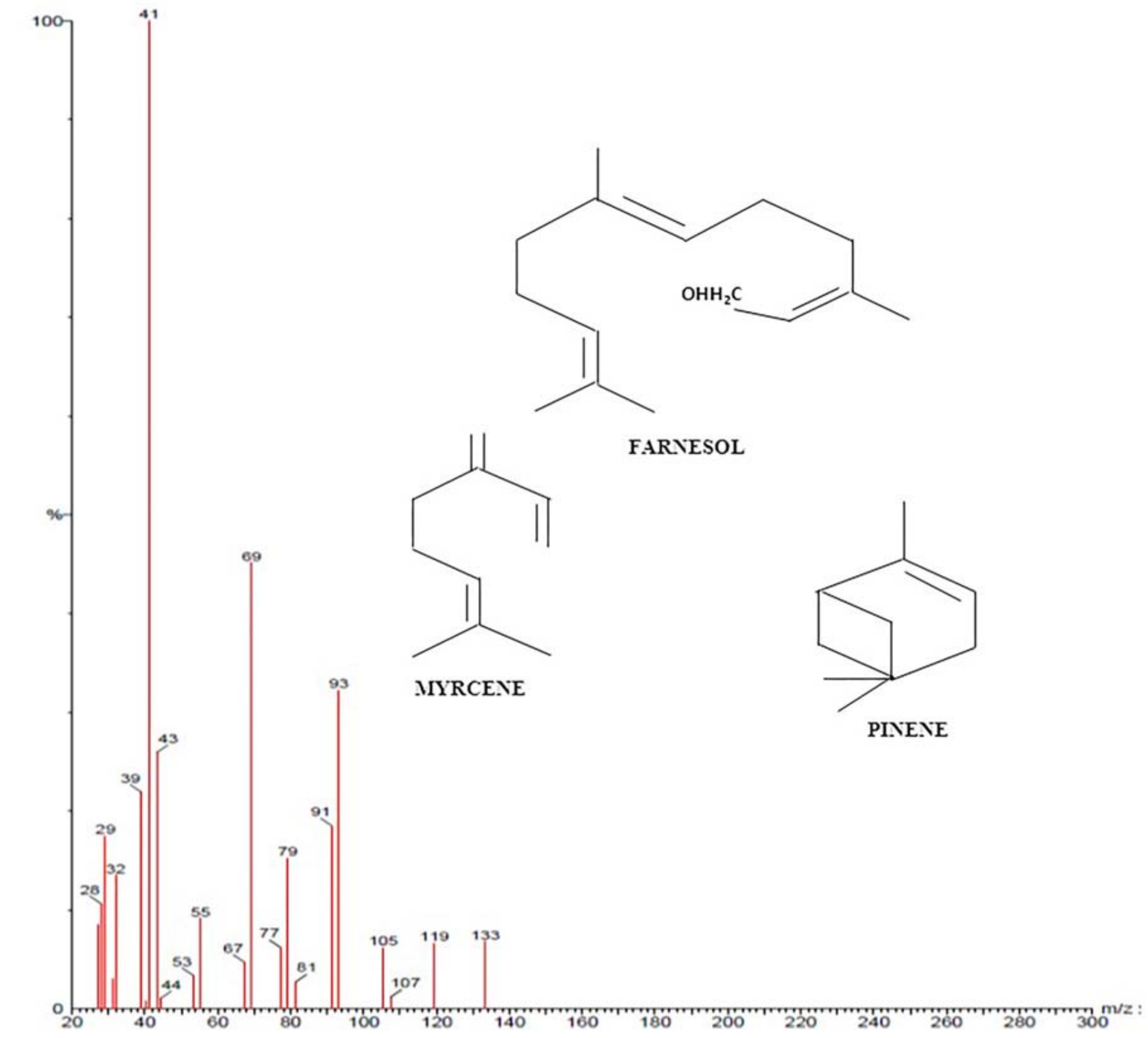

FIGURE 7 | Illustrated the fragmentation pattern of Farnesol, Myrcene, and Pinene molecule present in *Cymbopogon citratus* (methanolic extract).

and asymmetric stretching of CH_2, presence of similar carbon stretch was reported by Wany et al. (2014) and Jamuna et al. (2017). Observed spectra within 1400–1000 range correspond to N-H stretch of amines (1° and 2°) and C-O stretch (groups of polyphenols like flavanoid, terpenoids and polysaccharides) (Vankar and Shukla, 2012). The FTIR results confirmed the presence of –N-H, –OH, C = C, and C-H groups, which indicated that the plant extract containing the hydroxyl and amine groups that evidence the presence of flavonoids and terpenoids. Further, presence of flavonoids was responsible for reducing Ag^+ to Ag^0 and an amino group stabilized the synthesized nanoparticles (Balashanmugam and Kalaichelvan, 2015). Overall, biological agent resides in plants are responsible for capping and stabilizing the synthesized silver nanoparticles.

^{1}H-NMR Analysis of *C. citratus*

^{1}H-NMR is effective technique for metabolites study in plant extract, as it analyzes all the metabolites present in extract (Kim et al., 2010; Heyman and Meyer, 2012). **Figure 4** illustrated the ^{1}H-NMR spectrum of *C. citratus* extract. Chemical shift obtained from ^{1}H-NMR spectra can be due to proton on carbon or proton on Oxygen/Nitrogen. Chemical shift procured from proton on carbon is shown by signal at δ0.897,1.292 and 7.416 ppm which correspond to methyl, methylene and aromatic groups, respectively. The value range between δ 2–2.3 shows the presence of carbonyl group. Single range between δ4.043–7.416 and δ0.5–5 due to the shift for proton on Oxygen/Nitrogen which account for the presence of alcohol in the extract. Occurrence of allylic group in extract, is due to the shift acquired between δ 1.686–2.047. The Peak Fabrics obtained form NMR profile illustrated that *C. citratus* extract comprising of mixture of terpenoids and flavanoids.

GC-MS Analysis of *C. citratus*

GC-MS was performed to validate the data acquired from FTIR and NMR of *C. citratus*. GC-MS spectroscopy has

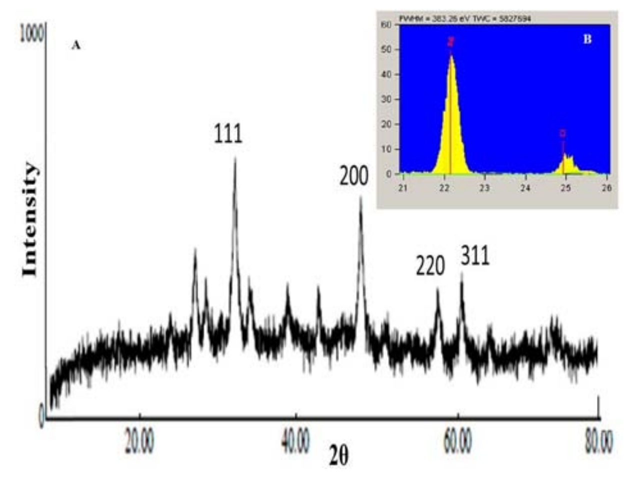

FIGURE 8 | (A) XRD and **(B)** EDXRF graphs depicted the crystalline nature of CNPs with ∼ 35 nm.

TABLE 3 | MIC and MBC values of CNPs synthesized from *C. citratus*.

S. No.	Test organism	Positive control	Negative control	MIC and MBC CNPs (μg/ml)	
				MIC	**MBC**
1	*Bacillus cereus*	+	–	25	50
2	*Bacillus licheniformis*	+	–	25	50
3	*Escherichia coli*	+	–	25	25
4	*Pseudomonas aeruginosa*	+	–	25	25

(–): Clear solution, (+): Turbidity.

been widely used as a powerful structural characterization technique. Analysis of *C. citratus* extract revealed the presence of α-citral in the sample showed by peak eluted at 10.50 min (**Figure 5**). By observing system library peaks eluted with retention time of 12.62 and 13.16, corresponds to myrcene and farnasol. The fragmentation patterns of the peaks and identified compounds of the plant were shown in **Figures 6**, **7**. By analyzing the fragmentation pattern of GC-MS divulged the existence of Citral, Myrcene, Farnesol, β-myrcene and β – Pinene with peaks at 29, 41, 69, 79, 93,105, and 119 m/z, respectively. Due to the hemolytic alpha and beta cleavage, citral shows peak at m/z 29, 69 (https://webbook.nist.gov/chemistry/) According to Nanjundaswamy et al. (2007), Kumar (2012), Madivoli et al. (2012), and Olorunnisola et al. (2014) bioactive component as elucidate above shows antibacterial effect. FTIR and NMR data indicated the presence of terpenoid and favanoids character of bioactive component, which was further proved by GC-MS data.

XRD and EDXRF of CNPs

XRD examination was executed to affirm the crystalline nature of the synthesized CNPs. **Figure 8A** delineated the XRD pattern of dried lyophized powder CNPs; four peaks 37.6°, 43.5°, 63.6° and 73.5° were obtained at 2θ, in the range of 20–80°. Braggs reflections obtained in this range clearly indicates that biosynthesized CNPs showed characteristic peaks which corresponds to the crystalline planes of face centered cubic structure, i.e., 111, 200, 220, and 311 (Oves et al., 2017; Qayyum et al., 2017). In addition, the weaker signals were recorded possibly due to components from the organic moieties present within the synthesized CNPs (Goudarzi et al., 2016). According to Zhang et al. (2016) size of silver nanoparticles lies between 2 and 100 nm. Nano-crystallite size can be calculated using Debye-Scherrer equation (Goudarzi et al., 2016; Jyoti et al., 2016):

$$D = \frac{K\lambda}{\beta Cos\theta}$$

Where D: Size of crystallites (nm), K: Crystallite shape factor (0.9), λ: X ray wavelength, β: Full width at half the maximum (FWHM) and θ: Braggs' angle. Using Debye-Scherrer equation it was observed that the size of CNPs were ∼35 nm.

For understanding the elemental composition present in CNPs, EDXRF analysis was conducted (Shameli et al., 2012). In the present investigation EDXRF of CNPs (**Figure 8B** and **Supplementary Figure S2**) revealed the presence of silver (Ag) and chloride (Cl) where, silver (Ag, 87.1%) as the major constituent element compared to chloride (Cl, 12.9%). EDXRF

TABLE 4 | Mean value of zone of inhibition of CNPs synthesized from *C. citratus* through agar disk-diffusion method.

Test organism	Zone of inhibition (mm)				
	CNPs (μg/ml)				
	$AgNO_3$ (25 μg/ml)	**C_{25}**	**C_{50}**	**C_{100}**	**C_{150}**
Bacillus cereus	0	1.41 ± 0.12	6.93 ± 0.08	12.23 ± 0.4	20.12 ± 0.42
Bacillus licheniformis	0	1.92 ± 0.07	7.52 ± 0.42	13.24 ± 0.12	22.34 ± 0.4
Escherichia coli	0	2.51 ± 0.44	8.12 ± 0.12	18.96 ± 0.46	31.87 ± 0.24
Pseudomonas aeruginosa	0	2.91 ± 0.12	9.12 ± 0.14	19.23 ± 0.24	35.23 ± 0.46

±: Standard Deviation (SD) and $C_{(25-150)}$: range of CNPs concentration and $AgNO_3$ (25 μg/ml): as a control. Mean values of each rows are significantly differ from each other according to statistical one way ANOVA ($P \leq 0.05$).

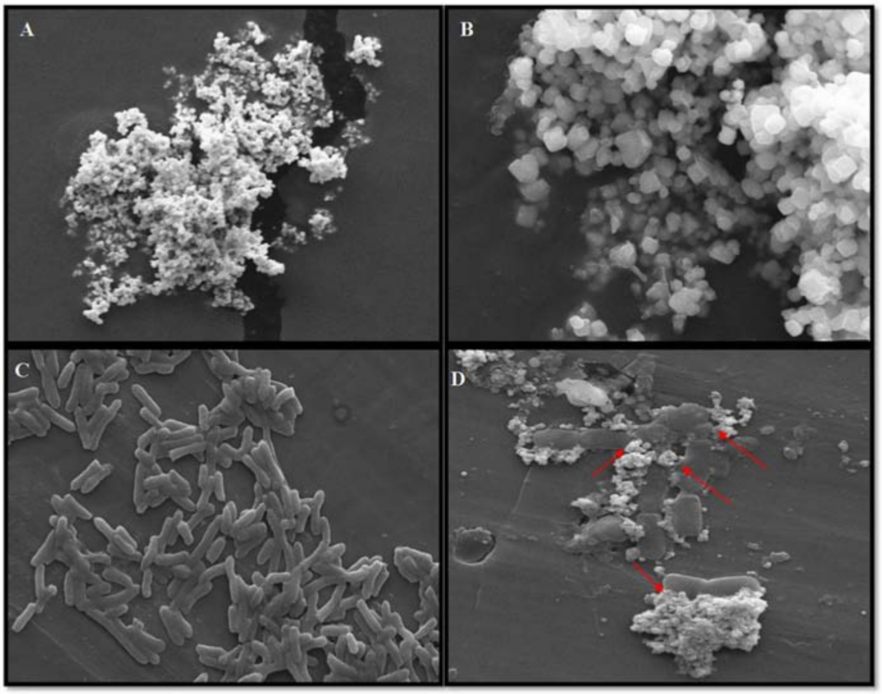

FIGURE 9 | (A) Scanning micrograph of CNPs (with bar of 2 μm). **(B)** Depicted cuboidal structure of CNPs (with bar of 1 μm). **(C)** Represented untreated bacterial population with intact cell membrane (with bar of 1 μm). **(D)** Detrimental effect of CNPs on bacterial cell membrane were observed marked by red arrows (with bar of 1 μm).

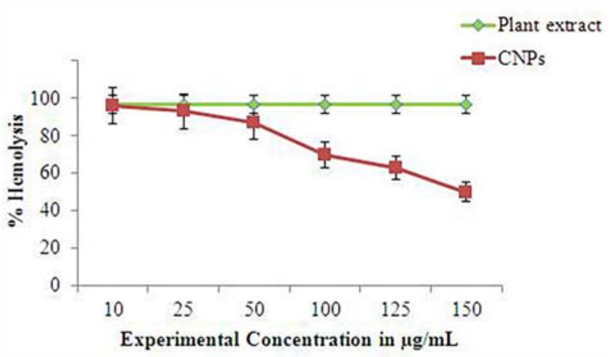

FIGURE 10 | Graph elucidated the cell cytotoxicity of CNPs in terms of percentage of hemolysis.

reading proved that the required phase of silver (Ag) was present in the CNPs.

Determination of Bactericidal Effect of *C. citratus* (CNPs) Through Antibacterial Assay and SEM Analysis

For the assessment of CNPs potential against test organisms; agar disk diffusion, minimum inhibitory concentration (MIC) and Minimum bactericidal concentration (MBC) techniques were performed. From the experimental range of CNPs (C_{25}- C_{150}μg/ml), C_{25} (μg/ml) concentration was determined to be the MIC for all bacterial species (*B. cereus, B. licheniformis, P. aeruginosa* and *E. coli*) while C_{25} μg/ml (*B. cereus, B. licheniformis)* and C_{50} μg/ml (*P. aeruginosa* and *E. coli*) as a MBC (**Table 3**). Investigation done by Hindumathy (2011) and Jafari et al. (2012) reported the MIC and MBC of *C. citratus* extract ranged between 50 and 150 mg/mL and 25 to 200 mg/mL, respectively. Tobramycin belongs to a class of drugs known as aminoglycoside antibiotics which is used to prevent or treat a wide variety of bacterial infections (especially related to eyes). According to Naik et al. (2010) investigation *B. cereus, E. coli,* and *P. aeruginosa* showed resistant behavior against tobramycin. While working on alkalinized *C. citratus* silver nano-particles Ajayi and Afolayan (2017) recorded the MIC values, ranged between 31.25 and 62.5 μg/ml and for antibiotic ciprofloxacin 31.25–15.63 μg/ml against *B. cereus, E. coli, E. faecalis, S. Flexneri.* Agar disk-diffusion data revealed that C_{150} (μg/ml) concentration expresses the maximum zone of inhibition (calculated in mm), for all bacterial species; *B. cereus* (20.12 ± 0.42), *B. licheniformis* (22.34 ± 0.4), *P. aeruginosa* (35.23 ± 0.46) and *E. coli* (31.87 ± 0.24) (**Table 4** and **Supplementary Figure S3**). According to Zulfa et al. (2016) report, illustrated the maximum zone of inhibition of *Cymbopogon citratus* extract against *B. Cereus* and *E. coli* was 12.00 ± 1.41 and 7.50 ± 0.71, respectively. While comparing the CNPs results with previous studies, effective results of CNPs were reflected.

Bactericidal profile of CNPs can be inspected by SEM studies, which is considered as the paramount technique for visual examination of bacterial interaction with synthesized nanoparticles as depicts in **Figure 9**. SEM images of CNPs illustrated the surface morphology in terms of size (20–40 nm) and shape (cuboidal) was represented in **Figures 9A,B**. Hong et al. (2016) illustrated the importance of cube shaped silver nanoparticles in antibacterial activity. Their study demonstrated that, while comparing the typical shaped silver particles that is nanosphere, nanocubes and nanowires; silver nanocube showed the strongest antibacterial activity as they can establish the close contact with bacteria due to the granulated shape and large surface area. **Figure 9C** represents untreated rod shape, diplo-bacillus intact bacteria with no sign of damage in cell wall. After treatment with CNPs, bacterial lysis was noticeably observed as marked with red arrows in **Figure 9D**. The capability of CNPs for antibacterial action is because of the diminished sizes of silver acting as capping agents with bioactive components present in plant extract. Researchers reported several approaches to describe the destructive nature of silver nanoparticles. Literature revealed that silver particles can interact with sulfur and phosphorous groups present in bacteria; continuous interaction causes the disruption of one of the most incumbent process, i.e., DNA replication which eventually ruptured the microbial structure and finally leads to the death of bacteria (Yugal et al., 2017). According to Xia et al. (2008) accretion of nanoparticles on bacteria showed the bactericidal effect, due to development of highly reactive species, i.e., ROS (Reactive oxygen species) which further leads to the formation of hydroxyl radicle and singlet oxygen species that disrupt the cell-wall and exterminated the bacteria (Lavakumar et al., 2015). Nevertheless, the factual operation behind lethality of silver nano-particle is not yet fully understood.

Cytotoxicity Assay

Cytotoxicity analysis provided the significance in identifying the lethality of synthesized silver nanoparticle. Though, plant based nanoparticles are trending subject among researchers due to its broad spectrum effect on microorganism (Ovais et al., 2016), but its toxicity need to be classified (Yugal et al., 2017). According to the present data of *C. citratus* extract and CNPs, revealed that CNPs has more efficacious effect in hemolytic action than *C. citratus* extract **Figure 10**. For the present experiment 10–150 g/ml range (Plant extract and CNPs) was used. Data exhibited that increasing the concentration of CNPs has negative effect on RBCs. Several factors are responsible for this significant higher rate of hemolytic action of CNPs, one possible explanation of hemolytic action on RBCs was considered to be the release of oxidative stress products which further damage the membrane and caused for lots of noxious effect such as morphological alterations and hemagglutination (Huang et al., 2016). Increased surface area of CNPs due to their nano size was an another explanation for toxicity, which generates pore in surface of RBC and finally leads to the death of cells. Hong et al. (2016) study illustrated that smaller AgNPs (silver nanoparticles) with larger surface area shows detrimental effects by damaging the entire cells, as they can developed the close contacts with bacterial cells. Whereas selected concentration range of plant extract has no reaction on experimental cells, Costa (2015) cited the extract of *C. citratus* act as a therapeutic agent due its innocuous and anti-inflammatory nature after oral and tropical administration (*in vivo*) in rats (as an experimental animal). Finding of Rao et al. (2009) also suggested the antigenotoxic and radioprotective potential of *C. citratus* extract.

CONCLUSION

Emerging resistant pathogenic species developed the interest in plant based nano-particles. In this study we demonstrated the elevated antimicrobial activity of synthesized *C. citratus* silver nanoparticles, i.e., CNPs against the gram positive (*B. cereus, B. licheniformis*) as well as gram negative (*P. aeruginosa, E. coli*) pathogenic species. Further Phytochemical, FTIR, NMR and GC-MS analysis helps to explore the bioactive components of *C. citratus* extract which helps in reduction of silver ion (Ag^{+1} to Ag^0) and act as an capping agent. Data obtained from XRD, EDXRF and SEM revealed the structural and chemical properties of CNPs. In addition, SEM images evidenced the physical interaction between the CNPs and bacteria which indicated the detrimental damages caused by CNPs by rupturing the bacterial membrane. Antibacterial assay was conducted to determine the MIC and MBC values against the test organism. Moreover, cell cytotoxicity findings revealed that increased concentration of CNPs over plant extract has lethal effect on cells. Taken all together, this investigation demonstrates the successfully synthesizes potentially active CNPs which can use as an effective bio-medical application against pathogenic species.

AUTHOR CONTRIBUTIONS

PB carried out all the experiments. PB and ML wrote the manuscript. ML critically reviewed and edited the manuscript. Financial support was provided by ML, AA, and BL.

ACKNOWLEDGMENTS

The authors want to acknowledge The Energy and Resources Institute (TERI), New Delhi providing research facilities. The authors would also like to acknowledge the support given by Garima Singh during the initial phases of this research.

SUPPLEMENTARY MATERIAL

The Supplementary Material for this article can be found online at: https://www.frontiersin.org/articles/10.3389/fmicb.2019.00282/full#supplementary-material

REFERENCES

Aftab, K., Ali, M. D., Aijaz, P., Beena, N., Gulza, H. J., and Sheikh, K. (2011). Determination of different trace and essential element in lemon grass samples by X-ray fluorescence spectroscopy technique. *Int. Food Res. J.* 18, 265–270.

Ahmed, S., and Ikram, S. (2015). Silver nanoparticles: one pot green synthesis using *Terminalia arjuna* extract for biological application. *J. Nanomed. Nanotechnol.* 6:4.

Ajayi, E., and Afolayan, A. (2017). Green synthesis, characterization and biological activities of silver nanoparticles from alkalinized *Cymbopogon citratus* Stapf. *Adv. Nat. Sci. Nanosci. Nanotechnol.* 8:015017. doi: 10.1088/2043-6254/aa5cf7

Ashraf, A., Sarfraz, R. A., Rashid, M. A., Mahmood, A., Shahid, M., and Noor, N. (2016). Chemical composition, antioxidant, antitumor, anticancer and cytotoxic effects of *Psidium guajava* leaf extracts. *Pharm. Biol.* 54, 1971–1981. doi: 10.3109/13880209.2015.1137604

Alhakmani, F., Kumar, S., and Khan, S. A. (2013). Estimation of total phenolic content, in-vitro antioxidant and anti-inflammatory activity of flowers of *Moringa oleifera*. *Asian Pac. J. Trop. Biomed.* 3, 623–627. doi: 10.1016/S2221-1691(13)60126-4

Balashanmugam, P., and Kalaichelvan, P. T. (2015). Biosynthesis characterization of silver nanoparticles using *Cassia roxburghii* DC. Aqueous extract, and coated on cotton cloth for effective antibacterial activity. *Int. J. Nanomed.* 1, 87–97. doi: 10.2147/IJN.S79984

Baranwal, A., Srivastava, A., Kumar, P., Bajpai, V. K., Maurya, P. K., and Chandra, P. (2018). Prospects of nano-structure materials and their composites as antimicrobial agents. *Front. Microbiol.* 9:422. doi: 10.3389/fmicb.2018.00422

Bhat, R., Ameran, S. B., Karim, A. A., and Liong, M. T. (2011). Quality attributes of star fruit (*Averrhoa carambola* L.) juice treated with ultraviolet radiation. *Food Chem.* 127, 641–644. doi: 10.1016/j.foodchem.2011.01.042

Chaudhary, S., Chandrashekar, K. S., Pai, K. S. R., Setty, M. M., Devkar, R. A., Reddy, N. D., et al. (2017).Screening of anticancer activity of selected medicinal plants indigenous to western ghats: *Argyreia nervosa*, *Memecylon malabaricum* and *Memecylo numbellatuma*, *Adv. Sci. Lett.* 23:784. doi: 10.1166/asl.2017.8510

Cheel, J., Theoduloz, C., Rodriäguez, J., and Hirschmann, G. S. (2005). Free radical scavengers and antioxidants from lemongrass (*Cymbopogon citratus* (DC.) Stapf). *J. Agric. Food Chem.*53, 2511–2517. doi: 10.1021/jf0479766

Chisowa, E. H., Hall, D. R., and Farman, D. I. (1998). Volatile constituents of the essential oil of *Cymbopogon citratus* stapf grown in Zambia. *Flavour Frag. J.* 13, 29–30. doi: 10.1002/(SICI)1099-1026(199801/02)13:1<29::AID-FFJ682>3.0.CO;2-S

Clinical and Laboratory Standards Institute [CLSI] (2012). *Methods for Dilution Antimicrobial Susceptibility Tests for Bacteria That Grow Aerobically; Approved Standard*, 9th Edn. Wayne, PA: CLSI.

Compean, K. L., and Ynalvez, R. A. (2014). Antimicrobial activity of plant secondary metabolites: a review. *J. Med. Plant Res.* 8, 204–213. doi: 10.3923/rjmp.2014.204.213

Costa, G. F. F. D. (2015). *Cymbopogon citratus and Its Polyphenols as Potential Phytotherapeutic Products: An In Vivo Approach*. Thesis, University of Coimbra, Coimbra.

Ekpenyong, C. E., Akpan, E. E., and Daniel, N. E. (2014). Phytochemical Constituents, therapeutic applications and toxicological profile of *Cymbopogon citrates* stapf (DC) leaf extract. *J. Pharmacogn. Phytochem.* 1, 133–141.

Elish, I. L., Botha, F. S., McGaw, L. J., and Eloff, J. N. (2017). The antibacterial activity of extracts of nine plant species with good activity against *Escherichia coli* against five other bacteria and cytotoxicity of extracts. *BMC Complement Altern. Med.* 17:133. doi: 10.1186/s12906-017-1645-z

EUCAST (2019). *EUCAST Disk Diffusion Test Methodology*. Available at: http://www.eucast.org/ast_of_bacteria/disk_diffusion_methodology

Ewansiha, J. U., Garba, S. A., Mawak, J. D., and andOyewole, O. A. (2012). Antimicrobial activity of *Cymbopogon Citrus* (Lemon Grass) and its phytochemical properties. *Front. Sci.* 2, 214–220. doi: 10.5923/j.fs.20120206.14

Francisco, V., Figueirinha, A., Neves, B. M., Rodríguez, C. G., Lopes, M. C., Cruz, M. T., et al. (2011). *Cymbopogon citratus* as source of new and safe anti-inflammatory drugs: bio-guided assay using lipopolysaccharide-stimulated macrophages. *J. Ethnopharmacol.* 133, 818–827. doi: 10.1016/j.jep.2010.11.018

French, G. L. (2006). Bactericidal agents in the treatment of MRSA infections-the potential role of daptomycin. *J. Antimicrob. Chemother.* 58, 1107–1117. doi: 10.1093/jac/dkl393

Goudarzi, M., Mir, N., Kamazani, M. M., Bagheri, S., and Niasari, M. S. (2016). Biosynthesis and characterization of silver nanoparticles prepared from two novel natural precursors by facile thermal decomposition methods. *Sci. Rep.* 6:32539. doi: 10.1038/srep32539

Han, X., and Parker, T. L. (2017). Lemongrass (*Cymbopogon flexuosus*) essential oil demonstrated anti-inflammatory effect in pre-inflamed human dermal fibroblasts. *Biochimie Open* 4, 107–111. doi: 10.1016/j.biopen.2017.03.004

Hayat, M. A. (ed.) (2000). *Principles and Techniques of Electron Microscopy: Biological Applications*, 4th Edn. Cambridge: Cambridge University Press, 1–80, 400–431.

Heyman, H. M., and Meyer, J. J. M. (2012). NMR-based metabolomics as a quality control tool for herbal products. *S. Afr. J. Bot.* 82, 21–32. doi: 10.1016/j.sajb.2012.04.001

Hindumathy, C. K. (2011) In vitro study of antibacterial activity of *Cymbopogon citratus*. *World Acad. Sci. Eng. Technol.* 74, 193–197.

Hong, X., Wen, J., Xiong, X., and Hu, Y. (2016). Shape effect on the antibacterial activity of silver nanoparticles synthesized via a microwave-assisted method. *Environ. Sci. Pollut. Res.* 23:4489. doi: 10.1007/s11356-015-5668-z

Huang, H., Lao, W., Cui, M., Liang, L., Lin, Y., Fang, Q., et al. (2016). An evaluation of blood compatibility of silver nanoparticles. *Sci. Rep.* 6:25518. doi: 10.1038/srep25518

Ishida, K., Mello, J. C. P. D., Cortez, D. A. G., Filho, B. P. D., Nakamura, T. U., and Nakamura, C. V. (2006). Influenced to tannins from *Stryphnodendron adstringens* on growth and virulence factors of *Candida albicans. J. Antimicrob. Chemother.* 58, 942–949. doi: 10.1093/jac/dkl377

Jafari, B., Ebadi, A., Aghdam, B. M., and Hassanzade, Z. (2012). Antibacterial activities of lemon grass methanol extract and essence on pathogenic bacteria. *Am.-Eur. J. Agric. Environ. Sci.* 12, 1042–1046.

Jain, S., and Mehata, M. S. (2017). Medicinal plant leaf extract and pure flavonoid mediated green synthesis of silver nanoparticles and their enhanced antibacterial property. *Sci. Rep.* 7:15867. doi: 10.1038/s41598-017-15724-8

Jamuna, S., Sakeena, S. M. S., Kumar, R. A., Shanmuganathan, G., Mozhi, S. S., and Devaraj, N. S. (2017). Potential antioxidant and cytoprotective effects of essential oil extracted from *Cymbopogon citratus*on OxLDL and H2O2 LDL induced human peripheral blood mononuclear cells (PBMC). *Food Sci. Hum. Wellness* 6, 60–69. doi: 10.1016/j.fshw.2017.02.001

Jyoti, K., Baunthiyal, M., and Singh, A. (2016). Characterization of silver nanoparticles synthesized using *Urtica dioica* Linn. Leaves and their synergistic effects with antibiotics. *J. Radiat. Res. Appl. Sci.* 9, 217–227. doi: 10.1016/j.jrras.2015.10.002

Kim, H. K., Choi, Y. H., and Verpoorte, R. (2010). NMR-based metabolomic analysis of plants. *Nat. Protoc.* 5, 536–549. doi: 10.1038/nprot.2009.237

Korenblum, E., Goulart, F. R. D. V., Rodrigues, I. D. A., Abreu, F., Lins, U., Alves, P. B., et al. (2013). Antimicrobial action and anti-corrosion effect against sulfate reducing bacteria by lemongrass (*Cymbopogon citratus*) essential oil ant its major component, the citral. *AMB Exp.* 3:44. doi: 10.1186/2191-0855-3-44

Kumar, A. K. (2012). Brief review on cyclopropane analogs: synthesis and their pharmacological applications. *Int. J. Pharm. Pharm. Sci.* 5:472.

Lavakumar, V., Masilamani, K., Ravichandiran, V., Venkateshan, N., Saigopal, D. V. R., Kumar, C. K. A., et al. (2015). Promising upshot of silver nanoparticles primed from *Gracilaria crassa* against bacterial pathogens *Chem. Cent. J.* 9:42. doi: 10.1186/s13065-015-0120-5

Lawal, O. A., Ogundajo, A. L., Avoseh, N. O., and Ogunwande, I. A. (2017). *Medicinal Spices and Vegetables from Africa*. Amsterdam: Elsevier Science.

Lin, D., Xiao, M., Zhao, J., Li, Z., Xing, B., Li, X., et al. (2016). An overview of plant phenolic compounds and their importance in human nutrition and management of type 2 diabetes. *Molecules* 21:1374. doi: 10.3390/molecules21101374

Madivoli, E. S., Gitu, L., and Gumba, E. (2012). Isolation and identification of essential oils from *Cymbopogan citratus* (stapf) Dc Using GC-MS and FT-IR. *Chem. Mater. Res.* 2:22.

Matouschek, B. K., and Stahl, B. E. (1991). Phyto chemical study of non-volatile substance from *Cymbopogon citratus* (D.C) Stapf (Poaceae). *Pharm. Acta Helv.* 66, 242–245.

Mirghani, M. E. S., Liyana, Y., and Praveen, J. (2012). Bioactivity analysis of lemon grass high amount of phenol is reported in (*Cymbopogon citratus*) essential oil. *Int. Food Res. J.* 19, 569–575.

Naik, M. I., Fomda, B. A., Jaykumar, E., and Bhat, J. A. (2010). Antibacterial activity of lemongrass (*Cymbopogon citratus*) oil against some selected pathogenic bacteria. *APJTM* 3, 535–538. doi: 10.1016/S1995-7645(10)60129-0

Nanjundaswamy, N., Satish, S., Lokanatha, K. M., Shashikanth, S., and Raveesha, K. A. (2007). Antibacterial activity of synthetic precursors of Podophyllotoxin. *Int. J. Biomed. Sci.* 3:472.

Nascimento, G. G. F., Locatelli, J., Freitas, P. C., and Silva, G. L. (2000). Antibacterial activity of plant extracts and phytochemicals on antibiotic resistant bacteria. *Braz. J. Microbiol.* 31:256. doi: 10.1590/S1517-83822000000400003

Negrelle, R. R. B., and Gomes, E. C. (2007) *Cymbopogon citratus* (D.C) Stapf: chemical composition and biological activites. *Rev. Bras. Plantas Med.* 9, 80–92.

National Institute for Standards and Technology [NIST] Mass Spectrometry Data Center (2018). "Mass spectra," in *NIST Chemistry WebBook, NIST Standard Reference Database Number 69*, eds P. J. Linstrom and W.G. Mallard (Gaithersburg, MD: National Institute of Standards and Technology), 20899. doi: 10.18434/T4D303

Olorunnisola, S. K., Asiyanbi, H. T., Hammed, A. M., and Simsek, S. (2014). Biological properties of lemongrass: an overview *IFRJ* 21, 455–462.

Ovais, M., Khalil, A. T., Raza, A., Khan, M. A., Ahmad, I., Islam, N. U., et al. (2016). Green synthesis of silver nanoparticles via plant extracts: beginning a new era in cancer theranostics. *Nanomedicine (Lond.)* 11, 3157–3177. doi: 10.2217/nnm-2016-0279

Oves, M., Aslam, M., Rauf, M. A., Qayyum, S., Qari, H. A., Khan, M. S., et al. (2018). Antimicrobial and anticancer activities of silver nanoparticles synthesized from the root hair extract of Phoenix dactylifera. *Mater. Sci. Eng.* 89, 429–443. doi: 10.1016/j.msec.2018.03.035

Oves, M., Khan, M. S., Zaidi, A., Ahmed, A. S., Ahmed, F., Ahmad, E., et al. (2013). Antibacterial and cytotoxic efficacy of extracellular silver nanoparticles biofabricated from chromium reducing Novel OS4 Strain of *Stenotrophomonas maltophilia*. *PLoS ONE* 8:e59140. doi: 10.1371/journal.pone.0059140

Oves, M., Qari, H. A., Felemban, N. M., Khan, M. Z., Rehan, Z. A., and Ismail, I. M. I. (2017). *Marinobacter lipolyticus* from red sea for lipase production and modulation of silver nanomaterials for anti-candidal activities. *IET Nanobiotechnol.* 11, 403–410. doi: 10.1049/iet-nbt.2016.0104

Parveen, M., Ghalib, R. M., Khanam, Z., Mehdi, S. H., and Ali, M. (2010). A novel antimicrobial agent from the leaves of *Peltophorum vogelianum* (Benth). *Nat. Prod. Res.* 24, 1268–1273. doi: 10.1080/14786410903387688

Pratiwi, W., and Elin, Y. S. (2016). The antibacterial activity of selected plants towards resistant bacteria isolated from clinical specimens. *Asian Pac. J. Trop. Biomed*. 6, 16–19. doi: 10.1016/j.apjtb.2015.08.003

Qayyum, S., Oves, M., and Khan, A. U. (2017). Obliteration of bacterial growth and biofilm through ROS generation by facilely synthesized green silver nanoparticles. *PLoS One* 12:e59140. doi: 10.1371/journal.pone.0181363

Rai, M., Ingle, A. P., Birla, S., Yadav, A., and Santos, C. A. D. (2015). Strategic role of selected noble metal nanoparticles in medicine. *Crit. Rev. Microbiol.* 42, 696–719. doi: 10.3109/1040841X.2015.1018131

Rao, B. S. S., Shanbhoge, R., Rao, B. N., Adiga, S. K., Upadhya, D., Aithal, B. K., et al. (2009). Preventive efficacy of hydroalcoholic extract of Cymbopogon citratus against radiation-induced DNA damage on V79 cells and free radical scavenging ability against radicals generated in vitro. *Hum. Exp. Toxicol.* 28, 195–202. doi: 10.1177/0960327109104822

Shah, G., Shri, R., Panchal, V., Sharma, N., Singh, B., and Mann, A. S. (2011).Scientific basis for the therapeutic use of *Cymbopogon citratus*, stapf (Lemon grass). *J. Adv. Pharm. Technol. Res.* 2, 3–8. doi: 10.4103/2231-4040.79796

Shameli, K., Ahmad, M. B., Mulla, E. A. J. A., Ibrahim, N. A., Shabanzadeh, P., Rustaiyan, A., et al. (2012). Green biosynthesis of silver nanoparticles using *Callicarpa maingayi* stem bark extraction. *Molecules*17, 8506–8517. doi: 10.3390/molecules17078506

Simon, J., Gupta, S. K., Shijitha, A. J., Lone, S. A., Limbu, B., Kumar, R. S., et al. (2017). Antibacterial activity of nano materials synthesized from plant extract against methicillin resistant *Staphylococcus aureus* (MRSA). *Int. J. Environ. Sci. Nat. Res.* 4, 555–645.

Thangam, R., Sathuvan, M., Poongodi, A., Sureshe, V., Pazhanichamye, K., Sivasubramanian, S., et al. (2014). Activation of intrinsic apoptotic signaling pathway in cancer cells by *Cymbopogon citratus* polysaccharide fractions *Carbohydr. Polym.* 107, 138–150. doi: 10.1016/j.carbpol.2014.02.039

Vankar, P. S., and Shukla, D. (2012). Biosynthesis of silver nanoparticles using lemon leaves extract and its application for antimicrobial finish on fabric. *Appl. Nanosci.* 2, 163–168. doi: 10.1007/s13204-011-0051-y

Voon, H. C., Bhat, R., and Rusul, G. (2012). Flower extracts and their essential oils as potential antimicrobial agents for food uses and pharmaceutical application. *Compr. Rev. Food Sci. Food. Saf.* 11, 34–55. doi: 10.1111/j.1541-4337.2011.00169.x

Wany, A., Kumar, A., Nallapeta, S., Jha, S., Nigam, V. K., and Pandey, D. M. (2014). Extraction and characterization of essential oil components based on geraniol and citronellol from Java citronella (*Cymbopogon winterianus* Jowitt). *J. Plant Growth Regul.* 73, 133–145. doi: 10.1007/s10725-013-9875-7

Wu, T., He, M., Zang, X., Zhou, Y., Qiu, T., Pan, S., et al. (2013). A structure-activity relationship study of flavonoids as inhibitors of *E.coli* by membrane interaction effect. *Biochim. Biophys. Acta* 1828, 2751–2756. doi: 10.1016/j.bbamem.2013.07.029

Xia, T., Kovochich, M., Liong, M., Mädler, L., Gilbert, B., Shi, H., et al. (2008). Comparison of the mechanism of toxicity of zinc oxide and cerium oxide nanoparticles based on dissolution and oxidative stress properties. *ACS Nano* 2, 2121–2134. doi: 10.1021/nn800511k

Yugal, K. M., Panda, S. K., Bastia1, A. K., and Tapan, K. M. (2017). Biosynthesis of silver nanoparticles from *Protium serratum* and investigation of their potential impacts on food safety and control. *Front. Microbiol.* 8:626. doi: 10.3389/fmicb.2017.00626

Zhang, X. F., Liu, Z. G., Shen, W., and Gurunathan, S. (2016). Silver nanoparticles: synthesis, characterization, properties, applications, and therapeutic approaches. *Int. J. Mol. Sci.* 17:1534. doi: 10.3390/ijms17091534

Zulfa, Z., Chia, C. T., and Rukayadi, Y. (2016) In vitro antimicrobial activity of *Cymbopogon citratus* (lemongrass) extracts against selected food borne pathogens. *IFRJ* 23, 1262–1267.

Conflict of Interest Statement: The authors declare that the research was conducted in the absence of any commercial or financial relationships that could be construed as a potential conflict of interest.

frontiers
in Microbiology

ORIGINAL RESEARCH
published: 24 April 2019
doi: 10.3389/fmicb.2019.00824

Biogenic Silver Nanoparticles as a Post-surgical Treatment for *Corynebacterium pseudotuberculosis* Infection in Small Ruminants

Laerte Marlon Santos[1]†, Danijela Stanisic[2]†, Ulisses José Menezes[1], Marcos Antônio Mendonça[1], Thiago Doria Barral[1], Núbia Seyffert[3], Vasco Azevedo[4], Nelson Durán[5], Roberto Meyer[1], Ljubica Tasic[2] and Ricardo Wagner Portela[1]*

[1] Laboratório de Imunologia e Biologia Molecular, Instituto de Ciências da Saúde, Universidade Federal da Bahia, Salvador, Brazil, [2] Laboratório de Química Biológica, Departamento de Química Orgânica, Instituto de Química, Universidade Estadual de Campinas, Campinas, Brazil, [3] Programa de Pós-Graduação em Microbiologia, Instituto de Biologia, Universidade Federal da Bahia, Salvador, Brazil, [4] Laboratório de Genética Celular e Molecular, Instituto de Ciências Biológicas, Universidade Federal de Minas Gerais, Belo Horizonte, Brazil, [5] Laboratório de Biologia Estrutural e Funcional, Instituto de Biologia, Universidade Estadual de Campinas, Campinas, Brazil

OPEN ACCESS

Edited by:
Renata Katsuko Takayama Kobayashi,
State University of Londrina, Brazil

Reviewed by:
Luis Carlos Guimarães,
Universidade Federal do Pará, Brazil
Flavia Figueira Aburjaile,
Federal University of Pernambuco, Brazil

Correspondence:
Ricardo Wagner Portela
rwportela@gmail.com

† These authors have contributed equally to this work

Specialty section:
This article was submitted to Antimicrobials, Resistance and Chemotherapy, a section of the journal Frontiers in Microbiology

Received: *01 December 2018*
Accepted: *01 April 2019*
Published: *24 April 2019*

Citation:
Santos LM, Stanisic D, Menezes UJ, Mendonça MA, Barral TD, Seyffert N, Azevedo V, Durán N, Meyer R, Tasic L and Portela RW (2019) Biogenic Silver Nanoparticles as a Post-surgical Treatment for Corynebacterium pseudotuberculosis Infection in Small Ruminants. Front. Microbiol. 10:824. doi: 10.3389/fmicb.2019.00824

Caseous lymphadenitis (CL) is an infectious and zoonotic disease characterized by the development of granulomas in the lymph nodes and internal organs of small ruminants. The etiological agent of this disease is *Corynebacterium pseudotuberculosis*, a Gram-positive and facultative intracellular bacterium. The conventional treatment for CL consists of drainage and chemical cauterization of the lesions using a 10% iodine solution. However, this type of treatment is not effective, due to iodine's cytotoxic profile and low antibacterial activity. Currently, silver nanoparticles (AgNPs) can be seen as an alternative treatment for CL due to their antimicrobial activity and wound healing effects. Therefore, the present study aimed to evaluate AgNPs as a post-surgical treatment for CL. Twenty-nine goats and sheep with clinical signs of CL were selected. Surgical intervention was performed to excise the caseous lesions. To treat the lesions, an ointment formulation based on AgNP mixed with natural waxes and oils was used in the experimental group, and the conventional treatment with 10% iodine was used in the control group. Bacteria were isolated from the excised caseous material. The animals were observed for 8 weeks after the surgical treatment, and blood samples were taken weekly. The surgical wounds of sheep treated with AgNP healed faster, and the surgical wound area was smaller during the observation period; the latter effect was also observed in goats. AgNP-treated animals also had less purulent discharge and less moisture in the surgical wounds. The AgNP-treated animals had lower leukocyte counts and lower titers of anti-*C. pseudotuberculosis* antibodies. There was no statistically significant difference between the groups with regard to the hemogram results. The results of the susceptibility testing of *C. pseudotuberculosis* strains (T1, 1002, FRC41, and VD57 strains) and clinical isolates to AgNPs showed growth inhibition, even at low concentrations. It can be concluded that post-surgical treatment of CL using the AgNP-based ointment may be a promising tool in the control of CL, through faster healing, decreased wound contamination, and no apparent toxic effects.

Keywords: antimicrobials, caseous lymphadenitis, nanotechnology, small ruminants, wound healing

INTRODUCTION

Caseous lymphadenitis (CL), an infectious disease caused by the bacterium *Corynebacterium pseudotuberculosis* that affects small ruminants, has a chronic and debilitating profile and a zoonotic potential. CL is characterized by the development of granulomas in the lymph nodes and in organs such as the spleen, lungs, liver, and kidneys (Dorella et al., 2006). The disease is associated with a decrease in the production of wool and meat, as well as a high cost of treatment (Santiago et al., 2013).

A definitive diagnosis of CL is made through the isolation of the etiologic agent from caseous material retrieved from lesions. The only possible treatment currently conducted in sheep and goat farms is drainage of the lesions with an application of a 10% iodine solution for chemical cauterization (de Farias et al., 2018), a procedure that can hinder the healing process due to the histotoxic profile of iodine (Punjataewakupt et al., 2019). The secretion from the operatory wounds pose a potential risk for environmental contamination since *C. pseudotuberculosis* can survive for long periods in the soil at sheep and goat farms (Spier et al., 2012).

The inappropriate use of antimicrobials has been a cause of multidrug-resistant bacteria development. In response, conventional antibiotics are being substituted by new alternative technologies such as nanotechnology, which has broad potential use in human and veterinary medicine (Rudramurthy et al., 2016). Silver nanoparticles (AgNPs) are seen as a good option among nanoparticles with antimicrobial activity because, besides having a marked antibacterial profile, they also contribute to wound healing, are durable and efficacious, and are relatively inexpensive to produce (Lee et al., 2007; Zang et al., 2008).

It is necessary that new compounds be developed for the post-surgical treatment of CL. Given the antibacterial activity and wound healing effects of AgNP, this study aimed to verify the efficacy of a biogenic AgNP topical ointment in the treatment of sheep and goats who underwent extraction of CL lesions.

MATERIALS AND METHODS

Animals and Ethical Aspects

This study was carried out in a sheep and goat breeding farm in the municipality of Capim Grosso, Bahia State, Brazil. Twenty-nine mixed breed animals with clinical signs of CL were selected. These animals had a complete surgical removal of the CL lesions with a standardized incision size and were divided into four groups: group CP (10 goats treated with AgNP ointment); group CI (10 goats treated with 10% iodine solution); group OP (5 sheep treated with the AgNP-based ointment); and group OI (4 sheep treated with 10% iodine solution). All the animals were treated at the time of the CL lesion excision. The clinical, serological, hematological, and biochemical follow-up was carried out shortly before the surgical procedure and within 8 weeks after the surgical procedure. This study was approved by the Committee on the Use of Animals in Scientific Experimentation of the School of Veterinary Medicine of the Federal University of Bahia (protocol number 35/2017).

Biogenic AgNP Synthesis

The synthesis of the AgNPs was performed following the procedure described by Ballottin et al. (2017). Briefly, *Fusarium oxysporum* fungus was grown in a solid culture medium consisting of 0.5% yeast extract, 2% malt, 2% agar and distilled water, and kept at 28°C for 1 week. After growth, sterilized distilled water was added to the culture under constant stirring until reaching a protein concentration of 0.1 g/mL and kept under stirring for 72 h. A vacuum filtration was performed and then 0.01 mol/L of $AgNO_3$ was added to the supernatant. The solution was maintained at 28°C and sealed with aluminum foil until the formation of the nanoparticles. The AgNPs were characterized and showed sizes of 28.0 ± 13.1 nm, polydispersity of 0.231, zeta potential of -31.7 ± 2.8 mV, and were spherical in form (Stanisic et al., 2018).

AgNP Ointment Production

For the post-surgical treatment of CL, an ointment based on AgNPs, natural waxes, and oils was made, as described by Stanisic et al. (2018). In the first step of ointment production, the oils and waxes (31% solid vaseline, 20% lanoline, 10% liquid vaseline, 9.0% cera alba, 8.0% cetostearyl alcohol, and 2.0% cholesterol) were blended and heated at 60°C until the mixture was homogeneous, and all of the ingredients were fused. Then, the emulsion was cooled to room temperature (25°C), while constantly mixing to maintain its homogeneity. In the second step of ointment production, 20% part-to-part of a 12.8 mg/mL colloidal solution of biogenic AgNPs was added gradually to the mixture at room temperature under constant stirring (Stanisic et al., 2018). The final ointment was a gray oil/water cream that was easy to apply and left an oily film when applied to the skin surface.

Bacterial Strains

For the *in vitro* analysis of bacterial susceptibility to AgNPs, we used four *C. pseudotuberculosis* strains: the 1002 strain, which is used as a reference in the genome project of the bacteria (Mariano et al., 2016) and has already had its whole genome sequenced (GenBank CP001809.2); the VD57 strain, which is a highly virulent strain isolated from a goat CL lesion

(Almeida et al., 2016) that has a sequenced genome (GenBank CP009927.1); the FRC41 strain, which was isolated from a human case of lymphadenitis in France (Join-Lambert et al., 2006), and also has a sequenced genome (GenBank CP013146.1); and the T1 strain, which is an attenuated strain used as a CL vaccine model (Moura-Costa et al., 2008), and also has a sequenced genome (GenBank CP015100.1). All the *C. pseudotuberculosis* strains herein used belong to the biovar *ovis*.

Isolation of *C. pseudotuberculosis* From Caseous Lesions

For the isolation of *C. pseudotuberculosis* from the granuloma material, caseous samples collected from the animals that underwent the CL lesion excision were inoculated into Brain and Heart Infusion agar (HIMEDIA, Mumbai, India) and supplemented with 5% sheep blood. After inoculation, the plates were incubated for 48 h at 37°C. The isolated colonies were macroscopically characterized, stained using the Gram method, and subjected to biochemical tests. Colonies that were Gram-positive, exhibited catalase production, demonstrated positive reactions in the glucose, maltose, sucrose, and urea tests, and negative reactions in the lactose, trealose, salicin, and motility tests were identified as *C. pseudotuberculosis* (Moura-Costa et al., 2008).

Determination of *C. pseudotuberculosis* Laboratorial Strains and Clinical Isolates Susceptibility/Resistance to AgNP Profile

The broth microdilution methodology was performed according to Norman et al. (2014), with modifications. The AgNP solution was diluted in sterile milliQ water in concentrations ranging from 7.5 to 0.02 mg/mL. The strains were inoculated in BHI broth (HIMEDIA, Mumbai, India) Tween 80 0.1% for 12 h prior to the assay. After incubation, the strains were diluted in 2 × BHI to achieve an optical density of 0.08–0.10 at 600 nm, which contains 3×10^6 CFU/mL of *C. pseudotuberculosis*. Subsequently, these suspensions were diluted in BHI broth to obtain a concentration of 1×10^6 CFU/mL. One hundred μL of the inoculum and 100 μL of the AgNP colloidal solution were placed in each well. Two controls were used for each dilution, one positive (bacterial suspension without AgNPs) and one negative (AgNP colloidal solution without bacterial inoculation). Plates were then incubated for 48 h at 37°C. Analysis was performed in a spectrophotometer at the wavelength of 600 nm and the minimal concentration that inhibited 100% of the bacterial growth (MIC_{100}) was established. Then, 20 μL of each well was removed and inoculated into BHI agar plates, which were incubated for 48 h at 37°C. Minimal bactericidal concentration (MBC_{100}) was defined as the lowest concentration capable of killing all bacteria.

Surgical Procedure

Before the surgical incision, the hair in the skin above the CL-affected lymph node was shaved, followed by a 70% alcohol asepsis. For the surgical treatment, a 2 cm long standard incision was made with a #4 scalpel blade on the CL lesions with subsequent drainage of all the caseous material. This material was collected in sterile containers and sent to the laboratory to confirm the presence of *C. pseudotuberculosis* through microbiological assays. In CI and OI groups, a commercial 10% iodine solution was used in the surgical wound. In the CP and OP groups, the AgNP ointment was added to the surgical lesion, filling all space left by the drainage of the caseous lesion (**Supplementary Figure S1**). The clinical, hematological and serological follow-up of the animals were performed immediately before and after the surgical procedure, and within 8 weeks after the surgery, with a 1-week interval between observations and collections. The animals' cardiac and respiratory rate, rectal temperature, body score, and skin turgor return time were evaluated during the observation period.

Lesion drainage occurred in a location the herd could not access, and, in order to reduce environmental contamination, treated animals only returned to the herd after the lesion had completely healed. Jugular venipuncture was performed just before the surgery and weekly for 8 weeks following surgery. Blood was collected (10 mL) in a Vacutainer®-type tube without anticoagulant. Samples were then centrifuged at 4000 × *g* for 10 min and the serum was obtained. These samples were used in the serological tests. Also, blood samples (10 mL) were collected in Vacutainer® tubes with ethylenediaminetetraacetic acid (EDTA) anticoagulant to perform blood cells counts using an automatized counter. The area of open the surgical wounds were measured using a caliper over the course of the 8 weeks of post-surgical follow-up.

Immunological Assay

To detect *C. pseudotuberculosis*-specific antibodies in the animals' serum samples, it was used serum samples collected from the animals during the observation period. The serum samples were analyzed using the indirect ELISAs developed by Rebouças et al. (2013) for sheep and by Seyffert et al. (2010) for goats.

Statistical Analysis

The statistical analyses were conducted using SPSS 18 (IBM, United States). The unpaired Student *t*-test was used to compare blood cell counts, open wound areas, body and hydration scores, and ELISA results between groups. Data from animals that had moisture and purulent secretion in their surgical wounds and the presence of lymph node enlargement were compared using the chi square test. The curves of bacterial growth inhibition by AgNPs, as well as the surgical wounds healing, were compared using the Wilcoxon signed rank test. Values with $p < 0.05$ were considered statistically significant.

RESULTS

Susceptibility of *C. pseudotuberculosis* Strains and Clinical Isolates to AgNP

Evaluation of the *C. pseudotuberculosis* standard strain's susceptibility to AgNP using the broth microdilution method

TABLE 1 | Susceptibility of *C. pseudotuberculosis* strains to AgNP.

Host	Strain	MIC_{100} (mg/mL)	MBC_{100} (mg/mL)
Goat	1002	0.625	0.625
Human	FRC41	0.625	1.25
Goat	T1	0.625	1.25
Goat	VD57	7.5	>7.5

A microdilution in broth assay was carried out with different AgNP dilutions (0.02–7.5 mg/ml). MIC_{100} is defined as the AgNP concentration where there was inhibition of 100% of bacterial growth, and MBC_{100} as the AgNP concentration where there was 100% of bactericidal action, in mg/ml.

(Norman et al., 2014) indicated a 100% inhibition of the growth of T1, 1002, and FRC41 strains at a 0.625 mg/mL concentration of AgNP. The virulent strain VD57 showed MIC_{100} only at an AgNP dilution of 7.5 mg/mL. Similar results were observed for the minimal bactericide concentration values, with a MBC_{100} of 1.25 to 0.625 mg/mL for the 1002, FRC41, and T1 strains. We observed no bactericidal action for VD57 in the AgNP concentrations used in this experiment (**Table 1**). When comparing the growth inhibition curves, the 1002, T1, and FRC41 strains demonstrated a similar pattern of inhibition, but were statistically different from the VD57 curve on the Wilcoxon signed rank test (**Figure 1**).

As for the clinical isolates obtained from the animals included in this study, the AgNP concentration of 0.156 mg/mL inhibited 100% of the growth of 11 isolates. Two isolates showed a high susceptibility to AgNP, with 100% inhibition of growth up to the AgNP concentration of 0.02 mg/mL. The concentrations of 0.040 mg/mL and 0.080 mg/mL together demonstrated MIC_{100} for six isolates. Eight clinical isolates showed less susceptibility, with inhibition of 100% growth at a concentration of 0.312 mg/mL AgNP. Two isolates demonstrated MIC_{100} at a concentration of 0.625 mg/mL AgNP. The MBC_{100} ranged from 0.020 to 0.625 mg/mL, and only three isolates demonstrated the maximum MBC_{100} of 0.625 mg/mL (**Supplementary Tables S1**, **S2**).

Evaluation of Surgical Wounds

As shown in **Figure 2**, surgical wounds of sheep treated with AgNP ointment took an average of 16.3 days to completely heal, while those treated with 10% iodine took an average of 24.5 days. *Post hoc* analysis revealed that this difference was significant ($p < 0.05$). The surgical wounds of nanoparticle-treated goats took approximately 18 days to completely heal, and those of 10% iodine-treated goats took an average of 23 days to completely heal. This result was not significantly different at $p < 0.05$. Associated with the faster wound healing, it could also be observed that the hair around the surgical wounds in the AgNP-treated animals grew faster (**Supplementary Figure S2**).

Regarding the area of the surgical wounds (**Figure 3**), AgNP-treated goats presented a significant difference when compared to those treated with 10% iodine 1 and 4 weeks after the surgical procedure. The areas of the wounds were also smaller. The AgNP-treated sheep presented significant differences in surgical wound areas 4 and 5 weeks after removal of the caseous material when compared to those treated with 10% iodine ($p < 0.05$). The healing curve of AgNP-treated sheep was also significantly different from that of animals treated with 10% iodine at the Wilcoxon signed rank test ($p < 0.05$).

Regarding the presence of purulent secretion in surgical wounds, **Figure 4A** expresses the number of events observed during 8 weeks after the surgical procedure. Goats treated with iodine demonstrated purulent secretion in their wounds in

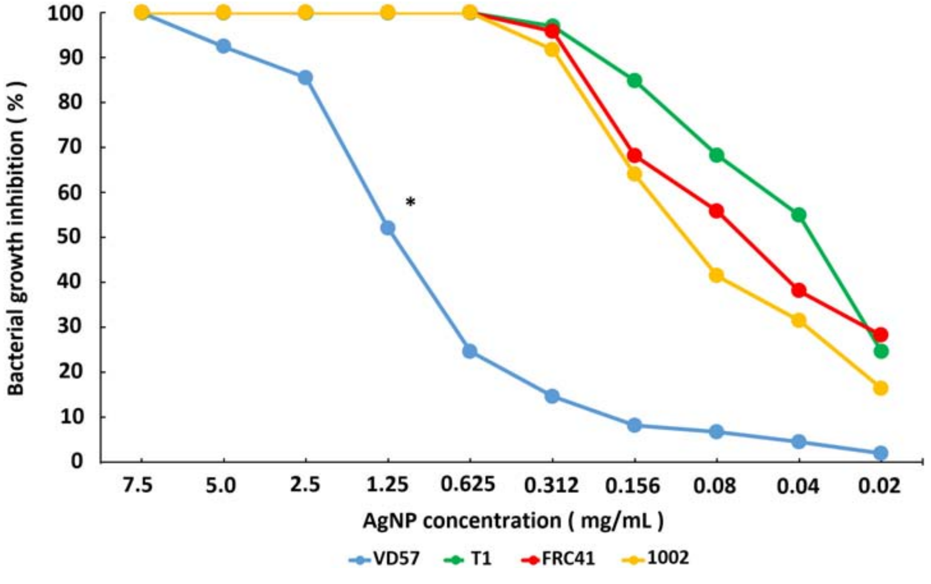

FIGURE 1 | Inhibition of *C. pseudotuberculosis* strains growth by different concentrations of AgNP. The results are expressed as the means of three different experiments. The curves of inhibition were statistically compared using the Wilcoxon signed-rank test, and the symbol "*" indicates statistical difference with $p < 0.05$.

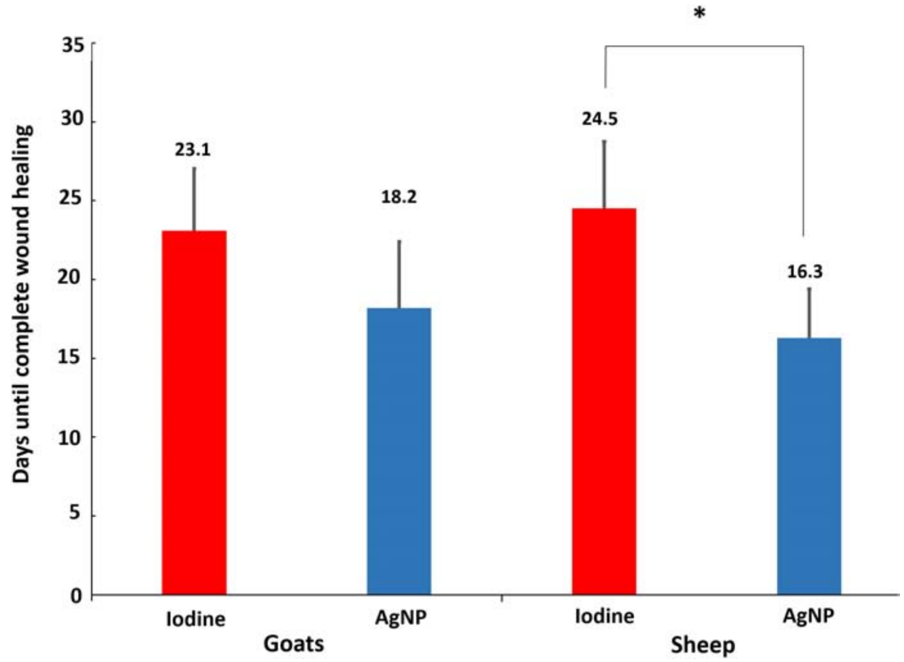

FIGURE 2 | Average number of days needed for complete wound healing after the surgical procedure for the treatment of caseous lymphadenitis (CL). Twenty goats were used (10 treated with 10% iodine solution and 10 with AgNP ointment) and 9 sheep (four treated with 10% iodine solution and five with AgNP). The symbol "*" indicates statistical difference with a $p < 0.05$ using the unpaired Student *t*-test.

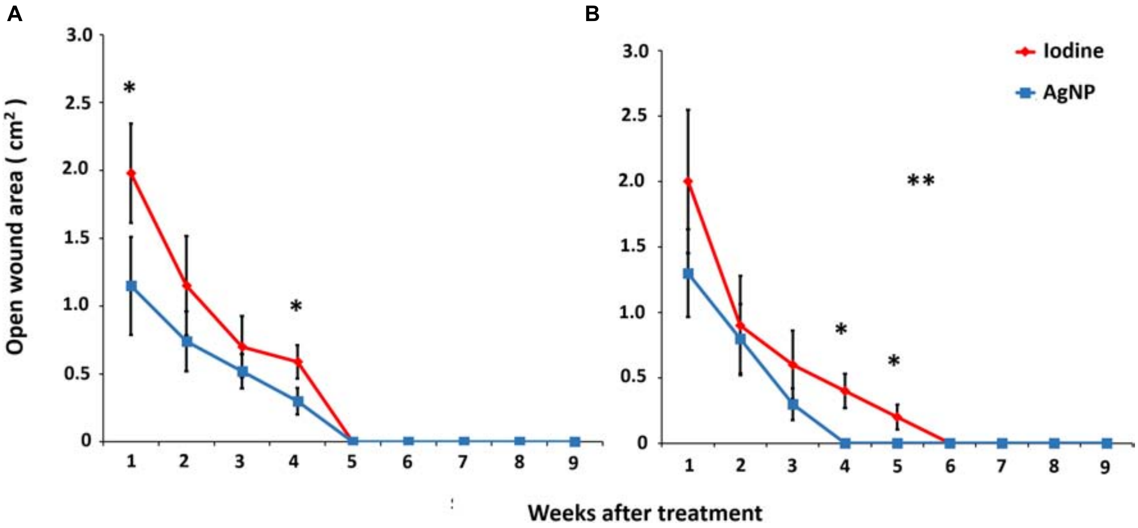

FIGURE 3 | Areas of open surgical wounds in **(A)** 20 goats, 10 treated with 10% iodine solution and 10 with nanoparticle ointment, and **(B)** 9 sheep, 4 treated with 10% iodine solution, and five with AgNP ointment, after the CL surgical treatment. The means of each point were statistically compared using the unpaired *t* test and the "*" symbol indicates statistical difference at $p < 0$. The healing curves are compared using the Wilcoxon signed rank and the symbol "**" indicates statistical difference between the curves at $p < 0.05$.

significantly more observations (20%) than those treated with the ointment (5%). In sheep, we observed pruritic discharges in the wounds of iodine-treated animals in 28% observations, whereas, in AgNP-treated sheep, this discharge was only observed once (2.5%). This difference was significantly different at the chi square test ($p < 0.05$).

Regarding the presence of moisture in the surgical wounds (**Figure 4B**), in both goats and sheep treated with AgNPs, humid wounds were observed in 6.25 and 2.5% of the observations, respectively. This was significantly different compared to animals treated with 10% iodine. Lymph node enlargement in goats treated with AgNPs was detected in 17.5% of the

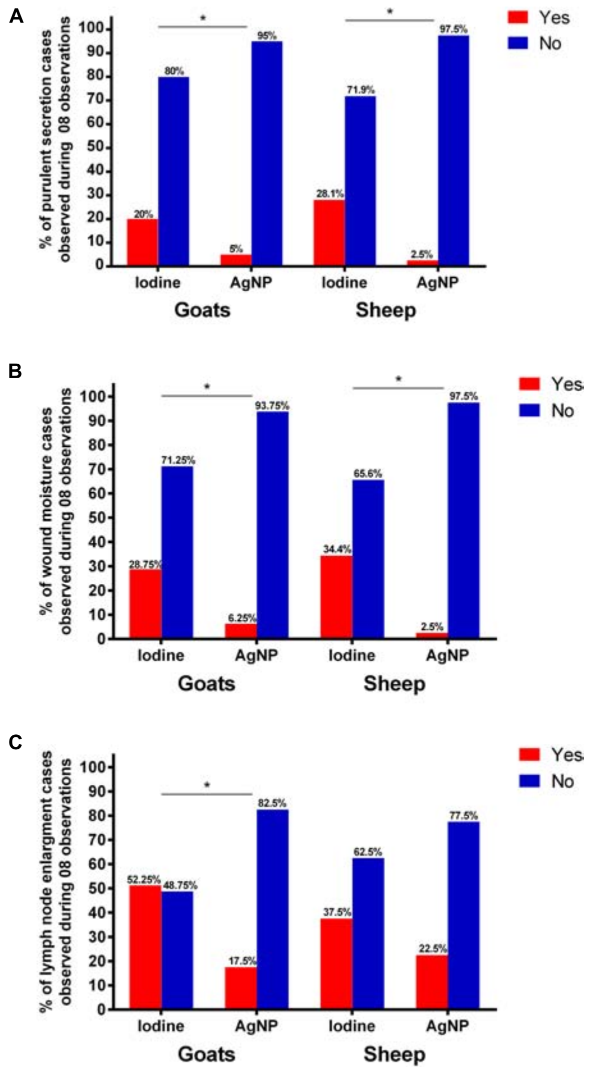

FIGURE 4 | Presence of **(A)** purulent secretion and **(B)** moisture in surgical wounds an **(C)** detection of lymph node enlargement in animals treated with iodine or AgNP ointment after removal of CL lesions. The data express the number of events observed over the course of 8 weeks after the surgical procedure. The symbol "*" stands for statistical difference between the iodine group and the group treated with nanoparticles at $p < 0.05$ using the chi square test.

observations, while iodine-treated animals demonstrated lymph node enlargement in 52.25% of the observations, which was significantly different at the chi square test at $p < 0.05$ (**Figure 4C**). In sheep, there was no statistical difference in the occurrence of lymph node enlargement cases when the two treatments were compared.

Clinical Post-surgical Evaluation of the Animals Treated With the AgNP Ointment and Iodine 10%

The animals of this study were evaluated over a 2-month period, between May and July of 2017, in the municipality of Capim Grosso, Bahia State, Brazil. The average temperature in this location during this time of year is 28°C. The ambient temperature was constant during the course of this experiment. **Figure 5** shows that, throughout the experiment, cardiac, and respiratory rate and rectal temperature presented little variation and there was no statistical significance between the two experimental groups at any time. Regarding the mean body scores, there was no statistical difference between the groups. Mean hydration levels, measured using the skin return time following the skin turgor test, were within normal limits, and no statistical difference was found between the two treatment groups (**Figure 6**). It is noteworthy to state that no clinical sign of dermatitis, photosensitivity or hypersensitivity was observed in animals treated with the AgNP ointment.

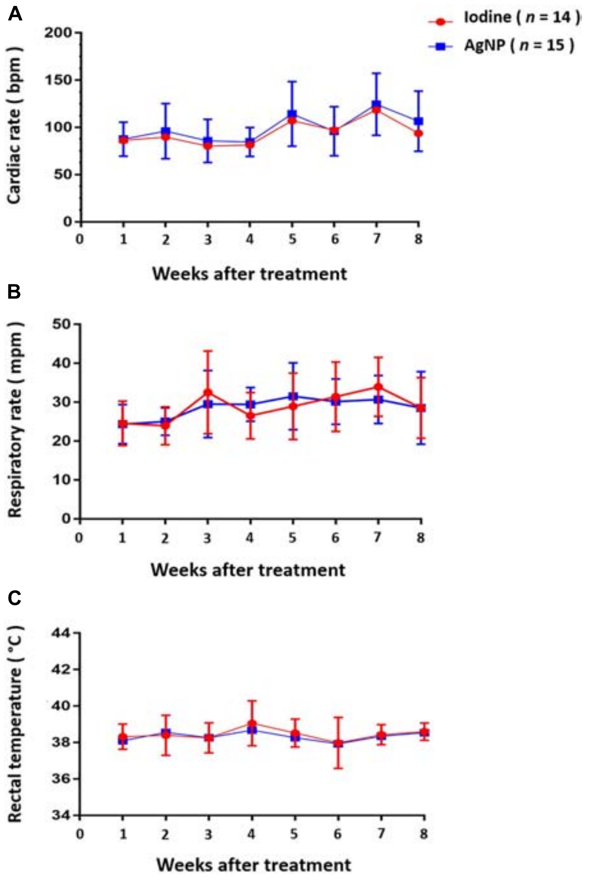

FIGURE 5 | Clinical parameters of the animals that underwent the surgical procedure for CL lesions and treatment with iodine or AgNP. It were assessed the **(A)** cardiac rate (expressed in beats per minute), **(B)** respiratory rate (expressed in movements per minute), and **(C)** the rectal temperature (expressed in Celsius grades). The data are presented as the means of the groups at each moment of observation, and no statistical differences were seen between the groups at any evaluation point using the unpaired Student *t*-test ($p < 0.05$).

Blood Cell Counts

In the evaluation of hemogram results (quantification of red blood cells, hemoglobin, globular volume, and mean globular

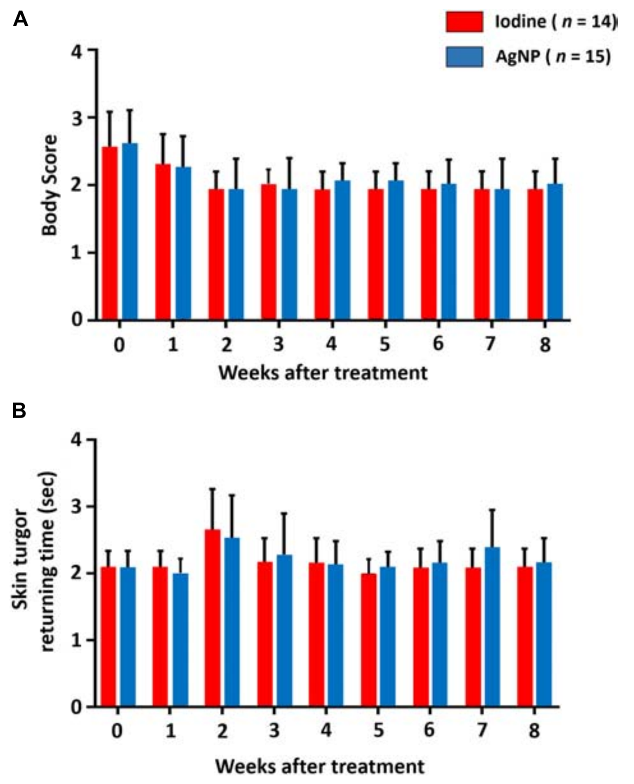

FIGURE 6 | Determination of the **(A)** body score and the **(B)** skin turgor return time of animals treated with iodine or AgNP ointment. Results are presented as the means of each observation time for each group and the bars indicate their respective standard deviations. No statistical differences were seen between the groups at any evaluation point using the unpaired Student *t*-test.

volume), there was no statistically significant difference in either goats or sheep treated with AgNPs compared to those treated with iodine, and the values remained within the reference values described for small ruminants (Weiss and Wardrop, 2016). In the leukogram, the leukocyte count in iodine-treated goats was statistically higher than goats treated with AgNPs 5 to 8 weeks after the surgical treatment, with a statistical significance at the seventh and 8 week ($p < 0.05$). For sheep, the leukocyte count of iodine-treated animals was statistically higher from 4 weeks after the surgical procedure until the end of the observation period, as demonstrated in **Figure 7**.

Immunological Assay

The detection of IgG immunoglobulins specific for *C. pseudotuberculosis* (**Figure 8**) demonstrated that, for both sheep and goats, production of specific antibodies peaked soon after the surgical intervention, but these levels normalized during the experiment. For goats, there was a higher production of *C. pseudotuberculosis* specific antibodies in the iodine-treated group in the first week, which was statistically different when compared to the AgNP-treated group. In sheep, differences between treatment groups occurred during the first 2 weeks after the surgical procedure, with specific antibody levels in the iodine-treated group higher than the AgNP-treated group, when values were compared by the unpaired Student *t*-test ($p < 0.05$).

DISCUSSION

The present study examines the effectiveness of AgNP-ointment as an alternative post-surgical treatment of CL in small ruminants. For a more complete verification of this application, verification of the clinical parameters of the treated animals, in addition to bacteriological tests, were conducted with standard strains, and clinical isolates of the bacterium.

The results of the broth microdilution susceptibility test confirmed that AgNPs demonstrated high efficacy in inhibiting the growth of three standard strains of *C. pseudotuberculosis* (T1, 1002, and FRC41) and clinical isolates collected from

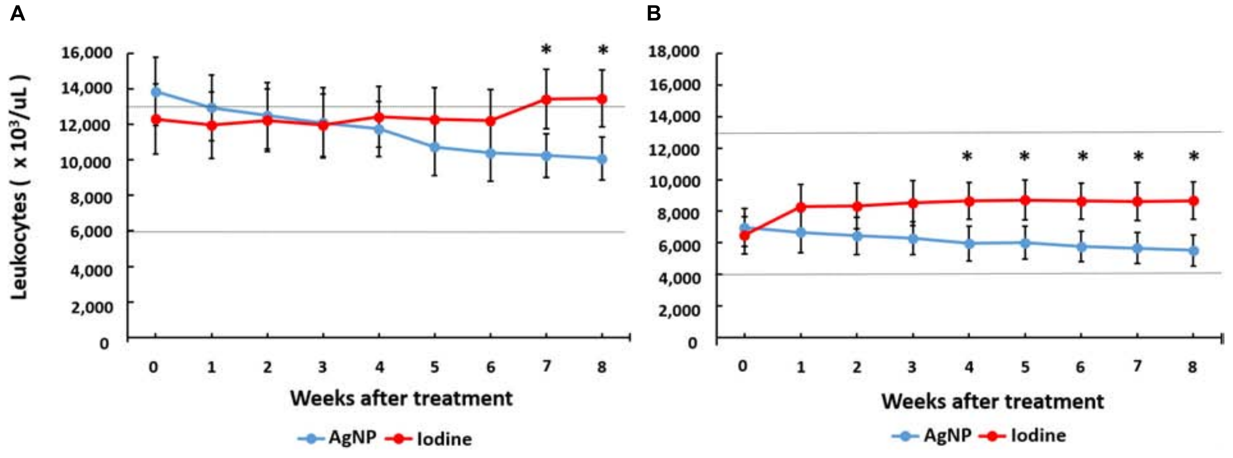

FIGURE 7 | Total leukocyte counts of iodine or AgNP-treated goats **(A)** and sheep **(B)** after surgical removal of CL lesions. The means of each group at each point were compared using the unpaired Student *t*-test. The symbol "*" represents a statistical difference at $p < 0.05$. The internal lines of each graph represent the lower and upper values of the reference value according to Weiss and Wardrop (2016).

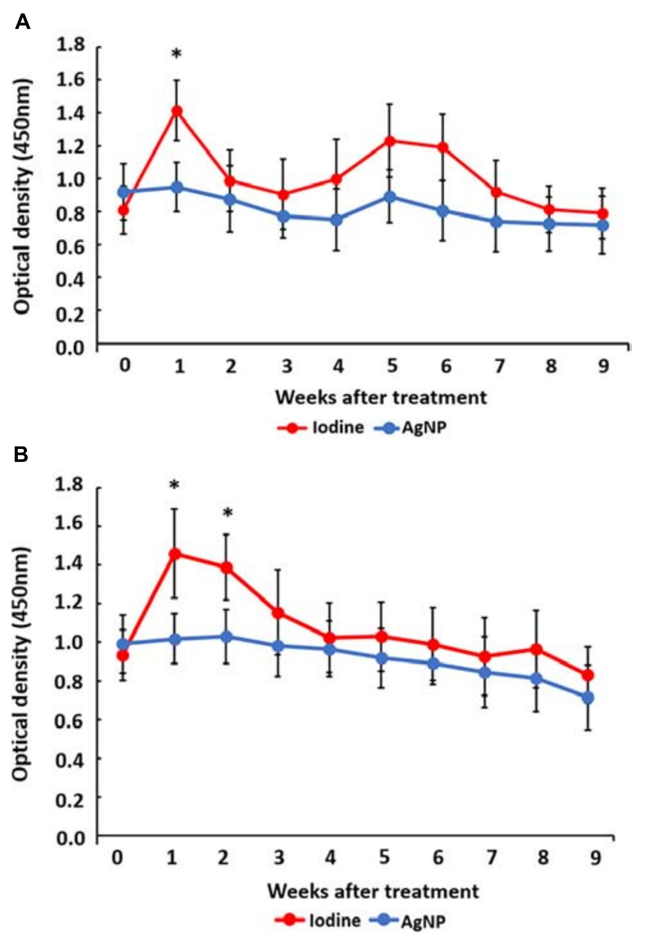

FIGURE 8 | Detection of anti-*C. pseudotuberculosis*-specific antibodies in **(A)** goats and **(B)** sheep after surgical removal of CL lesions and treatment with iodine or AgNP ointment. The results are expressed as the means of optical densities per group by collection point. The bars represent the standard deviations. The means of each group at each point were compared using the unpaired Student *t*-test. The symbol "*" represents a statistical difference at $p < 0.05$.

animals with caseous lesions, even at high dilutions. This finding agrees with studies showing the effectiveness of AgNPs against other bacteria, such as *Pseudomonas aeruginosa*, *Escherichia coli,* and *Salmonella* Typhi (Franci et al., 2015). Singh et al. (2013) tested bacterial strains of *Staphylococcus aureus* and *Streptococcus mutans* that exhibited resistance to β-lactam antibiotics and showed that the addition of AgNP reduced the minimal inhibitory concentration to the antibiotics and made the bacteria more susceptible to antibiotic treatment. In addition, it has been shown that AgNPs can be used as a topical drug owing to its high stability and low toxicity (Singh et al., 2013).

Regarding the lower susceptibility of the VD57 strain, it should be taken into account that VD57 is a highly virulent strain with a high replication rate and is well adapted to the culture conditions due to its long isolation time (Moura-Costa et al., 2008; Almeida et al., 2016). Although the relationship between virulence and susceptibility of *Corynebacteria* to antibiotics is not described, this relationship was observed in *Mycobacterium tuberculosis* (Rastogi et al., 1996), and in *Klebsiella pneumoniae* (Padilla et al., 2010).

It should be noted that, even though *in vitro* results demonstrated significant AgNP antimicrobial activity, *in vivo* CL treatment is difficult, because several characteristics of *C. pseudotuberculosis* infection and CL pathogenesis hamper the contact of drugs with the pathogen and provide some protection against certain antibiotics commonly used in the treatment of the disease. Among these factors, the presence of a thick fibrous capsule around the typical lesions, the caseous characteristic of the lesion, and even the intracellular nature of the organism during parts of the disease cycle can be seen (Williamson, 2001; Baird and Fontaine, 2007). Therefore, surgical excision of granulomatous lesions is still the most feasible option compared to systemic treatment with antimicrobial agents. Antibiotic drugs would be of greater importance in post-surgical treatment of the disease, since they inhibit environmental contamination (if the procedure is not done well and the lesion material continues to be released) or limit the spread of the pathogen in the animal after the lesion is broken. Thus, AgNP-containing ointment is possibly an effective treatment against CL, as it has good antimicrobial activity, a significant effect against bacteria resistant to antimicrobial agents, and its action is more concentrated on the physical aspects of the membrane, and therefore, is less likely to induce resistance (Apte et al., 2013; Rahisuddin et al., 2015; El-Batal et al., 2016; Halbus et al., 2017).

AgNP-treated animals demonstrated faster healing with a smaller area of the surgical lesion. It is worth noting that the wound healing process is complex and involves inflammation, granulation tissue formation, re-epithelization, and extracellular matrix remodeling (Chu et al., 2012; Heydarnejad et al., 2013; Chai et al., 2018). The clinical treatment of wounds remains a challenge in surgical procedures as the selected treatment should facilitate the healing process without producing harmful side-effects. Wound disinfection with 10% iodine solution is routinely used as the post-surgical treatment of LC but has several drawbacks; it is histotoxic and can disrupt the cicatrizing process (Burd et al., 2007; Santiago et al., 2013). This situation was observed in this study, as animals treated with iodine required a longer time for wound healing in both sheep and goats.

Recent studies have described the topical application of AgNPs for wound healing. Naraginti et al. (2016), who compared AgNPs with 1% soframycin, found that the healing time in rats, treated with gold nanoparticles, and AgNPs, was an average of 14 days after experimental surgery, whereas the group treated with 1% soframycin presented a delayed healing. Stojkovska et al. (2018) compared wound healing under AgNP treatment with commercial silver sulfadiazine cream and found that the AgNP-treated wounds took approximately 19 days to resolve, while the silver sulfadiazine-treated group took 21 days. Another recent study, described by Chai et al. (2018), observed, in humans, the resolution of AgNP-treated wounds in 17 days, 9 days sooner than the control treatment. The results obtained in the aforementioned studies align with the findings in the current study for both goats (18 days) and sheep (16 days).

Naraginti et al. (2016) also verified that the healing action of the nanoparticles in their study was most notable during the initial stages of wound healing, which resulted in a substantial reduction of open wound areas in the entire healing period. This effect was also observed in the current experiment; within the first week after the surgical procedure, the wound size in AgNP-treated animals was smaller than in the iodine-treated animals. This finding may be due to the fact that AgNPs present pronounced antimicrobial activity (Halbus et al., 2017). Their use in managing difficult-to-heal wounds can reduce the time required for tissue repair through anti-inflammatory effects and the prevention of wound colonization by opportunistic agents (Sandri et al., 2012; Stojkovska et al., 2018). Another study conducted by Silva et al. (2017) described that AgNPs induced a greater reduction in wound area by contraction, had low cytotoxicity, and promoted the growth of hair on the surface of the wound in a manner similar to that seen on the skin near the incision area. In our study, we were able to observe that wounds in animals treated with AgNPs not only healed faster, but also presented a faster hair growth.

Several studies report the healing potential of AgNPs, such as Galandáková et al. (2016), which demonstrated that AgNPs induce the release of a series of pro-inflammatory markers in several cell types, which accelerate healing. Stojkovska et al. (2018) stated that the decrease in wound area depends on contraction, as evidenced by Adibhesami et al. (2017) who found that AgNPs revert the inflammatory process in less time compared to antibiotics. In this study, not only did animals treated with iodine demonstrate more cases of pruritic exudate, but their wounds also maintained a moist environment ideal for bacterial growth. The increased purulent secretion observed in animals treated with iodine may be justified not only by the fact that iodine does not have an overall bactericidal action, but also because its use as an antiseptic has some disadvantages such as dermal irritation and a greater tendency to prolong inflammation (Iwasawa and Nakamura, 2003). It should be noted that animals in this study have not been treated for possible new CL lesions because it is believed that this would interfere with the immunological and hematological data of the animals. This non-isolation of the bacterium in new cases of lymphadenomegaly prevents the affirmation that further lymph node enlargement cases in animals treated with AgNPs may be due to *C. pseudotuberculosis* itself, however, it can be speculated that there was an inhibition of new infections by several bacterial agents that are sensitive to the AgNPs.

Several studies have shown that the temperature increase in different seasons may influence clinical parameters, such as cardiac and respiratory rates and rectal temperature (Marai et al., 2007). In our study, the temperature was constant for the duration of the experimental period, reducing environmental influences on these parameters. Similar values for the clinical parameters were observed across groups during the study period, and these parameters remained within the normal ranges (Riedi et al., 2018). This result reflects the fact that the treatment with AgNP-based ointment did not induce side-effects that would result in changes in these parameters. There were also no statistically significant differences in body and skin turgor return time scores. These findings indicate that the AgNP ointment did not induce physical side-effects, such as the development of hypersensitivity reactions, fever, or dermatitis. Pulit et al. (2011) cited that the contact of humans with AgNPs may cause adverse effects, and these different results may have been due to the different composition and thickness of the skin of small ruminants and humans. Another aspect to be considered is the size of the AgNPs, since Kang et al. (2017) described that 5 nm AgNPs amplify the clinical features of atopic dermatitis, and Park et al. (2011) found that 4 nm AgNPs presented a higher cytotoxic effect than AgNPs at high concentrations with 20 and 70 nm sizes. The AgNPs studied herein have an average size of 28 nm, and this characteristic can then be associated with a lower occurrence of adverse effects.

The results of the hemogram for both goats and sheep treated with AgNPs were within normal range, demonstrating that there were no toxic effects that could be expressed in hematological constituents. Similar results were observed in rabbits (Karavana et al., 2012), and humans (Chai et al., 2018), in which AgNPs showed low cytotoxicity. The higher leukocyte counts found in the animals treated with iodine, compared to those treated with AgNPs, are possibly due to iodine-related increases in levels of inflammation in ruminants due to tissue toxicity, and possibly due to fact that the topical application of nanoparticles are more effective in the suppression of inflammation (Naraginti et al., 2016). This has a consequent reduction of the presence of secondary bacterial infection in the small ruminants.

Immunity to *C. pseudotuberculosis* is attributed to humoral and cellular mechanisms (Lan et al., 1998). Humoral immunity is important in the fight against *C. pseudotuberculosis* since antibodies neutralize bacterial exotoxins, avoiding their dissemination in the host (Vale et al., 2016). The results obtained in this study regarding the detection of anti-*C pseudotuberculosis* specific antibodies, for both sheep and goats, demonstrated a higher production of these antibodies in the iodine-treated group of animals than in the AgNP-treated animals during the initial period of analysis. Goats and sheep that do not receive treatment after infection by *C. pseudotuberculosis* have a high humoral immune response for 70 days with peaks in the first weeks following removal of the lesions, and antibody titers beginning to decline after this period (Solanet et al., 2011). The lower titers of antibodies may be related to the absorption of AgNPs by the damaged skin, preventing the occurrence of antigenic stimuli by disseminated bacteria at the time of the surgical procedure. This absorption effect has already been described (Salomoni et al., 2017; Galbiati et al., 2018). Therefore, a lower infectious post-treatment load may warrant the lower titer of antibodies.

ETHICS STATEMENT

This study was approved by the Committee on the Use of Animals in Scientific Experimentation of the School of

Veterinary Medicine of the Federal University of Bahia (protocol number 35/2017).

AUTHOR CONTRIBUTIONS

DS, UM, LS, MM, TB, NS, and ND performed the experiments. UM, LS, and MM performed the data analysis. VA, LT, RM, and RP designed the experiments. RP, UM, and NS wrote the manuscript. VA, RM, and LT critically reviewed the manuscript. All authors contributed to manuscript revision, read and approved the submitted version.

FUNDING

This work was funded by Fundação de Apoio à Pesquisa e à Extensão (FAPEX). UM is a Master fellow from Coordenação de Aperfeiçoamento de Pessoal de Nível Superior (CAPES). LS is a Ph.D. fellow from CAPES. VA is a research fellow from Conselho Nacional de Desenvolvimento Científico e Tecnológico (CNPq). DS is a Ph.D. fellow from CNPq.

ACKNOWLEDGMENTS

We would like to thank Francisca Soares (LABIMUNO-UFBA) for technical assistance.

SUPPLEMENTARY MATERIAL

The Supplementary Material for this article can be found online at: https://www.frontiersin.org/articles/10.3389/fmicb.2019.00824/full#supplementary-material

REFERENCES

Adibhesami, M., Ahmadi, M., Farshid, A. A., Rezaei, F. S. B., and Naghadeh, D. (2017). Effects of silver nanoparticles on *Staphylococcus aureus* contaminated open wound healing in mice: an experimental study. *Vet. Res. Forum.* 8, 23–28.

Almeida, S., Tiwari, S., Mariano, D., Souza, F., Jamal, S. B., Coimbra, N., et al. (2016). The genome anatomy of *Corynebacterium pseudotuberculosis* VD57 a highly virulent strain causing caseous lymphadenitis. *Stand. Genomic. Sci.* 11:29. doi: 10.1186/s40793-016-0149-7

Apte, M., Sambre, D., Gaikawad, S., Joshi, S., Bankar, A., Kumar, A. R., et al. (2013). Psychrotrophic yeast *Yarrowia lipolytica* NCYC 789 mediates the synthesis of antimicrobial silver nanoparticles via cell-associated melanin. *AMB Express.* 3:32. doi: 10.1186/2191-0855-3-32

Baird, G. J., and Fontaine, M. C. (2007). *Corynebacterium pseudotuberculosis* and its role in ovine caseous lymphadenitis. *J. Comp. Pathol.* 137, 179–210. doi: 10.1016/j.jcpa.2007.07.002

Ballottin, D., Fulaz, S., Cabrini, F., Tsukamoto, J., Durán, N., Alves, O. L., et al. (2017). Antimicrobial textiles: biogenic silver nanoparticles against Candida and Xanthomonas. *Mater. Sci. Eng. C Mater. Biol. Appl.* 75, 582–589. doi: 10.1016/j.msec.2017.02.110

Burd, A., Kwok, C. H., Hung, S. C., Chan, H., Gu, H., Lam, W. K., et al. (2007). A comparative study of the cytotoxicity of silver-based dressings in monolayer cell, tissue explant, and animal models. *Wound Repair Regen.* 15, 94–104. doi: 10.1111/j.1524-475X.2006.00190.x

Chai, S. H., Wang, Y., Qiao, Y., Wang, P., Li, Q., Xia, C., et al. (2018). Bio fabrication of silver nanoparticles as an effective wound healing agent in the wound care after anorectal surgery. *J. Photochem. Photobiol. B* 178, 457–462. doi: 10.1016/j.jphotobiol.2017.10.024

Chu, C. Y., Peng, F. C., Chiu, Y. F., Lee, H. C., Chen, C. W., Wei, J. C., et al. (2012). Nanohybrids of silver particles immobilized on silicate platelet for infected wound healing. *PLoS One* 7:1371. doi: 10.1371/journal.pone.0038360

de Farias, A. E. M., Alves, J. R. A., Alves, F. S. F., Pinheiro, R. R., Faccioli-Martins, P. Y., Lima, A. M. C., et al. (2018). Seroepidemiological characterization and risk factors associated with seroconversion to *Corynebacterium pseudotuberculosis* in goats from Northeastern Brazil. *Trop. Anim. Health Prod.* doi: 10.1007/s11250-018-1748-7 [Epub ahead of print].

Dorella, F. A., Pacheco, L. G., Oliveira, S. C., Miyoshi, A., and Azevedo, V. (2006). *Corynebacterium pseudotuberculosis*: microbiology, biochemical properties, pathogenesis and molecular studies of virulence. *Vet. Res.* 2006, 201–218. doi: 10.1051/vetres:2005056

El-Batal, A. I., Gharib, F. A. E., Ghazi, S. M., Hegazi, A. Z., and El-Hafz, A. G. M. A. (2016). Physiological responses of two varieties of common bean (*Phaseolus vulgaris* L.) to foliar application of silver nanoparticles. *Nanomater. Nanotechno.* 6:13. doi: 10.5772/62202

Franci, G., Falanga, A., Galdiero, S., Palomba, L., Rai, M., Morelli, G., et al. (2015). Silver nanoparticles as potential antibacterial agents. *Molecules* 20, 8856–8874. doi: 10.3390/molecules20058856

Galandáková, A., Frankova, J., Ambrozova, N., Habartova, K., Pivodova, V., Zalesak, B., et al. (2016). Effects of silver nanoparticles on human dermal fibroblasts and epidermal keratinocytes. *Hum. Exp. Toxicol.* 35, 946–957. doi: 10.1177/0960327115611969

Galbiati, V., Cornaghi, L., Gianazza, E., Potenza, M. A., Donetti, E., Marinovicha, M., et al. (2018). In vitro assessment of silver nanoparticles immunotoxicity. *Food Chem. Toxicol.* 112, 363–374. doi: 10.1016/j.fct.2017.12.023

Halbus, A. F., Horozov, T. S., and Paunov, V. N. (2017). Colloid particle formulations for antimicrobial applications. *Adv. Colloid Interface Sci.* 249, 134–148. doi: 10.1016/j.cis.2017.05.012

Heydarnejad, M. S., Rahnama, S., Dehkordi, M. M., Yarmohammadi, P., and Aslnai, H. (2013). Silver nanoparticles accelerate skin wound healing in mice (*musmusculus*) through suppression of innate immune system. *Nanomed. J.* 1, 79–87. doi: 10.7508/NMJ.2014.02.003

Iwasawa, A., and Nakamura, Y. (2003). Cytotoxic effect and influence of povidone-iodine on wounds in guinea pig. *J. Jap. Ass. Infect. Dis.* 77, 948–956.

Join-Lambert, O. F., Ouache, M., Canioni, D., Beretti, J. L., Blanche, S., Berche, P., et al. (2006). *Corynebacterium pseudotuberculosis* necrotizing lymphadenitis in a twelve-year-old patient. *J. Pediatr. Infect. Dis. J.* 25, 848–851. doi: 10.1097/01.inf.0000234071.93044.77

Kang, H., Kim, S., Lee, K. H., Jin, S., Kim, S. H., Lee, K., et al. (2017). 5 nm silver nanoparticles amplify clinical features of atopic dermatitis in mice by activating mast cells. *Small* 13:1602363. doi: 10.1002/smll.201602363

Karavana, S. Y., Gokçe, E. H., Rençber, S., Özbal, S., Pekçetin, Ç., Guneri, P., et al. (2012). A new approach to the treatment of recurrent aphthous stomatitis with bioadhesive gels containing cyclosporine a solid lipid nanoparticle: *in vivo*/*in vitro* examinations. *Int. J. Nanomed.* 7:5693. doi: 10.2147/IJN.S36883

Lan, D. B., Taniguchi, S., Makino, S., Shirahata, T., and Nakane, A. (1998). Role of endogenous tumor necrosis factor alpha and gamma interferon in resistance to *Corynebacterium pseudotuberculosis* infection in mice. *Microbiol. Immunol.* 42, 863–870. doi: 10.1111/j.1348-0421.1998.tb02362.x

Lee, H. Y., Chattopadhyay, H. K., Lee, Y. M., Kim, K., and Park, S. B. (2007). A practical procedure for producing silver nanocoated fabric and its antibacterial evaluation for biomedical applications. *RSC Adv.* 28, 2959–2961. doi: 10.1039/B703034G

Marai, I. F. M., El-Darawany, A. A., Fadiel, A., and Abdel-Hafez, M. (2007). Physiological traits as affected by heat stress in sheep - A review. *Small Ruminant Res.* 71, 1–12. doi: 10.1016/j.smallrumres.2006.10.003

Mariano, D. C., Sousa, T. D. J., Pereira, F. L., Aburjaile, F., Barh, D., Rocha, F., et al. (2016). Whole-genome optical mapping reveals a mis-assembly between two rRNA operons of *Corynebacterium pseudotuberculosis* strain 1002. *BMC Genomics* 30:315. doi: 10.1186/s12864-016-2673-7

Moura-Costa, L. F., Bahia, R. C., Carminati, R., Vale, V. L., Paule, B. J., Portela, R. W., et al. (2008). Evaluation of the humoral and cellular immune response to different antigens of *Corynebacterium pseudotuberculosis* in Canindé goats and their potential protection against caseous lymphadenitis. *Vet. Immunol. Immunopathol.* 126, 131–141. doi: 10.1016/j.vetimm.2008.06.013

Naraginti, S., Kumari, P. L., Sivakumar, R. K., Das, C. A., Patil, S. H. D., and Andhalkar, V. V. (2016). Amelioration of excision wounds by tropical application of green synthesized, formulated silver and gold nanoparticles in albino Wistar rats. *Mater. Sci. Eng.* 62, 293–300. doi: 10.1016/j.msec.2016.01.069

Norman, E., Batista, M., Lawhon, S., Zhang, S., Kuskie, K., Swinford, K., et al. (2014). *In vitro* susceptibility of equine-obtained isolates of *Corynebacterium pseudotuberculosis* to gallium maltolate and 20 other antimicrobial agents. *J. Clin. Microbiol.* 52, 2684–2685. doi: 10.1128/JCM.01252-14

Padilla, E., Llobert, E., Sánchez, A. D., Martinez, L. M., Bengoechea, J. A., and Alberti, S. (2010). *Klebsiella pneumoniae* AcrAB efflux pump contributes to antimicrobial resistance and virulence. *Antimicrob. Agents Chemother.* 54, 177–183. doi: 10.1128/AAC.00715-09

Park, J., Lim, D. H., Lim, H. J., Kwon, T., Choi, J. S., Jeong, S., et al. (2011). Size dependent macrophage responses and toxicological effects of Ag nanoparticles. *Chem. Commun.* 47, 4382–4384. doi: 10.1039/c1cc10357a

Pulit, J., Banach, M., and Kowaski, Z. E. (2011). Nanosilver - making difficult decision. *Ecol. Chem. Eng.* 18, 185–195.

Punjataewakupt, A., Napavichayanun, S., and Aramwit, P. (2019). The downside of antimicrobial agents for wound healing. *Eur. J. Clin. Microbiol. Infect. Dis.* 38, 39–51. doi: 10.1007/s10096-018-3393-5

Rahisuddin, A., Khan, Z., and Manzoor, N. (2015). Biosynthesis of silver nanoparticles and its antibacterial and antifungal activities towards Gram-positive, Gram-negative bacterial strains and different species of Candida fungus. *Bioprocess Biosyst. Eng.* 38, 1773–1781. doi: 10.1007/s00449-015-1418-3

Rastogi, N., Labrousse, V., and Goh, K. S. (1996). *In vitro* activities of fourteen antimicrobial agents against drug susceptible and resistant clinical isolates of *Mycobacterium tuberculosis* and comparative intracellular activities against the virulent H37Rv strain in human macrophages. *Curr. Microbiol.* 33, 167–175. doi: 10.1007/s002849900095

Rebouças, M. F., Loureiro, D., Bastos, B. L., Moura-Costa, L. F., Hanna, S. A., Azevedo, V., et al. (2013). Development of an indirect ELISA to detect *Corynebacterium pseudotuberculosis* specific antibodies in sheep employing T1 strain culture supernatant as antigen. *Pesq. Vet. Bras.* 33, 1296–1302. doi: 10.1590/S0100-736X2013001100002

Riedi, A. K., Knubben-Schweizer, G., and Meylan, M. (2018). Clinical findings and diagnostic procedures in 270 small ruminants with obstructive urolithiasis. *J. Vet. Intern. Med.* 32, 1274–1282. doi: 10.1111/jvim.15128

Rudramurthy, G. R., Swamy, M. K., Sinniah, U. R., and Ghasemzadeh, A. (2016). Nanoparticles: alternatives against drug-resistant pathogenic microbes. *Molecules* 21:836. doi: 10.3390/molecules21070836

Salomoni, R., Léo, P., Montemor, A. F., Rinaldi, B. G., and Rodrigues, M. F. A. (2017). Antibacterial effect of silver nanoparticles in *Pseudomonas aeruginosa*. *Nanotechnol. Sci. Appl.* 10:115. doi: 10.2147/NSA.S133415

Sandri, G., Bonferoni, M. C. A., D'autilia, F., Rossi, S., Ferrari, F., Grisoli, P., et al. (2012). Wound dressings toxiced on silver sulfadiazine solid lipid nanoparticles for tissue repairing. *Eur. J. Pharm. Biopharm.* 84, 84–90. doi: 10.1016/j.ejpb.2012.11.022

Santiago, L. B., Pinheiro, R. R., Alves, F. S. F., Dos Santos, V. W. S., Rodrigues, A. D. S., Lima, A. M. C., et al. (2013). *In vivo* evaluation of antiseptics and disinfectants on control of Caseous Lymphadenitis: clinical, haematological, serological and microbiological monitoring. *Arq. Inst. Biol.* 80, 273–280. doi: 10.1590/S1808-16572013000300003

Seyffert, N., Guimarães, A. S., Pacheco, L. G. C., Portela, R. W., Bastos, B. L., Dorella, F. A., et al. (2010). High seroprevalence of caseous lymphadenitis in Brazilian goat herds revealed by *Corynebacterium pseudotuberculosis* secreted proteins-based ELISA. *Res. Vet. Sci.* 88, 50–55. doi: 10.1016/j.rvsc.2009.07.002

Silva, M. M. P., Aguiar, M. I. F., Rodrigues, A. B., Miranda, M. D. C., Araújo, M. A. M., Rolim, I. L. T. P., et al. (2017). The use of nanoparticles in wound treatment: a systematic review. *Rev. Esc. Enferm. USP.* 51:e03272. doi: 10.1590/S1980-220X2016043503272

Singh, R., Wagh, P., Wadhwani, S., Gaidhani, S., Kumbhar, A., and Bellare, J. (2013). Synthesis, optimization, and characterization of silver nanoparticles from *Acinetobacter calcoaceticus* and their enhanced antibacterial activity when combined with antibiotics. *Int. J. Nanomed.* 8:4277. doi: 10.2147/IJN.S48913

Solanet, J. J., Malena, R., Estein, S. M., and Belchior, S. E. (2011). Desarrollo de uma puebra de ELISA para detectar anticuerpos em carneros vacunados o infectado con *Corynebacterium pseudotuberculosis*. *Rev. Argent. Microbiol.* 43, 9–17.

Spier, S. J., Toth, B., Edman, J., Quave, A., Habasha, F., Garrick, M., et al. (2012). Survival of *Corynebacterium pseudotuberculosis* biovar equi in soil. *Vet. Rec.* 170:180. doi: 10.1136/vr.100543

Stanisic, D., Fregonesi, N. L., Barros, C. H. N., Pontes, J. G. M., Fulaz, S., Menezes, U. J., et al. (2018). NMR insights on Nano silver post-surgical treatment of superficial caseous lymphadenitis in small ruminants. *RSC Adv.* 8, 40778–40786. doi: 10.1039/c8ra08218a

Stojkovska, J., Djurdjevic, Z., Jancic, I., Bufan, B., Milenkovic, M., Jankovic, R., et al. (2018). Comparative *in vivo* evaluation of novel formulations based on alginate and silver nanoparticles for wound treatments. *J. Biomater. Appl.* 32, 1197–1211. doi: 10.1177/0885328218759564

Vale, V. L. C., Silva, M. C., Souza, A. P., Trindade, S. C., Moura-Costa, L. F., Lima, E. K. N. S., et al. (2016). Humoral and cellular immune responses in mice against secreted and somatic antigens from a *Corynebacterium pseudotuberculosis* attenuated strain: immune response against a *C. pseudotuberculosis strain*. *BMC Vet. Res.* 12:195. doi: 10.1186/s12917-016-0811-8

Weiss, D. J., and Wardrop, K. J. (2016). *Schalmś Veterinary Hematology*. Hoboken: Wiley-Blackwell.

Williamson, L. H. (2001). Caseous lymphadenitis in small ruminants. *Vet. Clin. North Am. Food Anim. Pract.* 17, 359–371. doi: 10.1016/S0749-0720(15)30033-5

Zang, Y., Peng, H., Huang, W., Zhou, Y., and Yan, D. (2008). Facile preparation and characterization of highly antimicrobial colloid Ag or Au nanoparticles. *J. Colloid Interface Sci.* 325, 371–376. doi: 10.1016/j.jcis.2008.05.063

Conflict of Interest Statement: The authors declare that the research was conducted in the absence of any commercial or financial relationships that could be construed as a potential conflict of interest.

frontiers
in Microbiology

ORIGINAL RESEARCH
published: 26 April 2019
doi: 10.3389/fmicb.2019.00820

Biogenic Synthesis of Silver Nanoparticles Using *Phyllanthus emblica* Fruit Extract and Its Inhibitory Action Against the Pathogen *Acidovorax oryzae* Strain RS-2 of Rice Bacterial Brown Stripe

Md. Mahidul Islam Masum[1,2], Mst. Mahfuja Siddiqa[3], Khattak Arif Ali[1], Yang Zhang[1], Yasmine Abdallah[1], Ezzeldin Ibrahim[1], Wen Qiu[1]*, Chenqi Yan[4] and Bin Li[1]*

[1] State Key Laboratory of Rice Biology and Key Lab of Molecular Biology of Crop Pathogens and Insects, Institute of Biotechnology, Zhejiang University, Hangzhou, China, [2] Department of Plant Pathology, Bangabandhu Sheikh Mujibur Rahman Agricultural University, Gazipur, Bangladesh, [3] Department of Botany, Jagannath University, Dhaka, Bangladesh, [4] Institute of Biotechnology, Ningbo Academy of Agricultural Sciences, Ningbo, China

OPEN ACCESS

Edited by:
Gerson Nakazato,
State University of Londrina, Brazil

Reviewed by:
M. Oves,
King Abdulaziz University,
Saudi Arabia
Ram Prasad,
Amity University, India

****Correspondence:***
Wen Qiu
wqiu2015@zju.edu.cn
Bin Li
libin0571@zju.edu.cn

Specialty section:
This article was submitted to Antimicrobials, Resistance and Chemotherapy, a section of the journal Frontiers in Microbiology

Received: *03 February 2019*
Accepted: *01 April 2019*
Published: *26 April 2019*

Citation:
Masum MMI, Siddiqa MM, Ali KA, Zhang Y, Abdallah Y, Ibrahim E, Qiu W, Yan C and Li B (2019) Biogenic Synthesis of Silver Nanoparticles Using Phyllanthus emblica Fruit Extract and Its Inhibitory Action Against the Pathogen Acidovorax oryzae Strain RS-2 of Rice Bacterial Brown Stripe. Front. Microbiol. 10:820. doi: 10.3389/fmicb.2019.00820

Biogenic synthesis of silver nanoparticles (AgNPs) using plants has become a promising substitute to the conventional chemical synthesis method. In this study, we report low-cost, green synthesis of AgNPs using fresh fruit extract of *Phyllanthus emblica*. The biosynthesized AgNPs was confirmed and characterized by analysis of spectroscopy profile of the UV-visible and Energy dispersive spectrophotometer, Fourier transform infrared, X-ray diffraction pattern, and electron microscopy images examination. UV-visible spectra showed a surface resonance peak of 430 nm corresponding to the formation of AgNPs, and FTIR spectra confirmed the involvement of biological molecules in AgNPs synthesis. In spherical AgNPs, the particle size ranged from 19.8 to 92.8 nm and the average diameter was 39 nm. Synthesized nanoparticles at 20 μg/ml showed remarkable antimicrobial activity *in vitro* against the pathogen *Acidovorax oryzae* strain RS-2 of rice bacterial brown stripe, while 62.41% reduction in OD_{600} value was observed compared to the control. Moreover, the inhibitory efficiency of AgNPs increased with the increase of incubation time. Furthermore, AgNPs not only disturbed biofilm formation and swarming ability but also increased the secretion of effector Hcp in strain RS-2, resulting from damage to the cell membrane, which was substantiated by TEM images and live/dead cell staining result. Overall, this study suggested that AgNPs can be an attractive and eco-friendly candidate to control rice bacterial disease.

Keywords: *Phyllanthus emblica*, green synthesis, nanoparticles, characterization, antibacterial activity

INTRODUCTION

In recent decades, the development of new and effective antimicrobials against infections caused by antibiotic-resistant bacteria has been increasingly interested. Several studies have reported that nanoparticles made up of different noble metals like Ag, Cu, and Au, which can be applied to kill both resistant and nonresistant bacteria (Bindhu and Umadevi, 2014; Chidurala et al., 2016;

Escárcega-González et al., 2018). In recent years, silver nanoparticles (AgNPs) have received a great deal of attention from many researchers working on multiple disciplines due to their unique features and a wide spectrum of applications (Sharma et al., 2009; Galdiero et al., 2011), for instance, in food science, medical, agriculture, and agricultural technologies (Kumar et al., 2008; Lü et al., 2009; Sastry et al., 2010; Oves et al., 2013; Aziz et al., 2015). Previous studies have demonstrated that AgNPs have potential antimicrobial activities against *Escherichia coli*, *Staphylococcus aureus*, and *Serratia marcescens* (Kim et al., 2007; Oves et al., 2013; Aziz et al., 2016). It also shows anti-nematodes (Mahmoud et al., 2016), anti-viral (Galdiero et al., 2011; Oves et al., 2013; Elbeshehy et al., 2015), anti-cancer (Oves et al., 2018; Aziz et al., 2019), and anti-inflammatory effects (Manikandan et al., 2017).

Several methods have been described for the synthesis of AgNPs, such as chemical reduction, microemulsions, radiation, hybrid methods, photochemical reduction and sonoelectrochemical, microwave-based systems and recently green synthesis route (Socol et al., 2002; Solanki and Murthy, 2010; Nadagouda et al., 2011; Iravani et al., 2014). However, these physiochemical methods, although some are durable and technically viable, are highly restricted in large-scale application due to the use of hazardous chemicals, high cost, high energy and time consuming, and difficulty in waste purification (Kowshik et al., 2003). Therefore, there is a growing need to use economical and environmentally safe and green synthesis routes that use non-toxic chemicals in the synthesis protocol of nanosilver. Alternatively, green synthesis route of AgNPs using several microorganisms, plants, and algae is natural, biocompatible, and environmentally safe methods (Bhattacharya and Gupta, 2005; Mohanpuria et al., 2008; Aziz et al., 2015).

Indeed, the use of plant materials can be more beneficial for nanosilver synthesis than bacterial and chemical methods because of no threat of bacterial and dangerous chemical contamination and less energy utilization with wider implications and easiness. Moreover, the green synthesis of AgNPs based on plant extract mechanisms alleviates the metal ions (Rai and Ingle, 2012) due to the presence of functional molecules such as phenol, terpenoids, ketones, carboxylic acids, aldehydes, enzymes, amides, and flavones (Prabhu and Poulose, 2012). Recent research reported that AgNPs have been synthesized using a variety of natural plants such as fruit extract of *Emblica officinalis* (Ankamwar et al., 2005), leaves extract of *Citrus limon* (Vankar and Shukla, 2012), green tea (*Camellia sinensis*) (Nakhjavani et al., 2017), *Coffea Arabica* (Dhand et al., 2016), neem (*Azadirachta indica*) (Ahmed et al., 2016), *Acalypha indica* (Krishnaraj et al., 2012), *Aloe vera* plant extract (Tippayawat et al., 2016), latex of *Jatropha gossypifolia* (Borase et al., 2014), root extract of *Morinda citrifolia* (Suman et al., 2013), *Phoenix dactylifera* (Oves et al., 2018), inflorescence extract of *Mangifera indica* (Qayyum et al., 2017), etc.

In this perception, *Phyllanthus emblica* L. (Family: Phyllanthaceae) commonly known as emblica/amla exhibits a striking assortment of shapes of development such as herbs and bushes, pachycaulous succulents, climbers, and drifting aquatics. The fruits of *Phyllanthus* spp. are widely used in preparation of traditional medicines in Southeast Asia due to unique properties such as rich antioxidant activity, anti-aging, antipuretic, and anti-inflammatory (Dang et al., 2011; Pientaweeratch et al., 2016; Manikandan et al., 2017). Moreover, this selection was provoked by the opportunity of inducing shape control of nanoparticles due to the potential sources of naturally occurring phytochemcals, (especially polyphenols, tannnis, ascorbic acides, flavonoids) in the fruit extract (Ramesh et al., 2015; Manikandan et al., 2017). Although many pharmacognosy and phytochemistry investigations have been successfully conducted in this plant, its opportunity as biocompatible materials for the production of AgNPs is still to be fully scanned. Therefore, we have used the *P. emblica* fruit extract to provide a biodegradable, natural product nanosilver without any risk of chemical toxicity, while the natural reserves will remain unaffected. In addition, there is no report on the inhibitory effect of AgNPs mediated by plants against rice pathogenic bacteria *Acidovorax oryzae* (Ao).

The Gram-negative bacteria Ao has wide host ranges within economically important monocotyledon plants such as cereal grain crops, and sugar crops (Hayward, 1960; Song et al., 2004; Masum et al., 2017). In particular, the individual strains of this pathogen can cause bacterial brown strip disease in rice, which has recently attracted considerable interest in China, for which contaminated seeds are the main sources for the spread of the disease to new plants over long distances (Shakya et al., 1985; Xie et al., 2011; Tian et al., 2015). Currently, bactericide is manily used to prevent and control bacterial diseases. However, the necessity for developing novel prevention and control strategies is increasing due to serious environmental pollution and bacterial resistance by the excessive use of chemicals in rice-growing countries across the world. Application of biosynthesized AgNPs is considerable interest in the field of agriculture because of their antioxidant and wide spectrum of antimicrobial activity along with their eco-friendly, biocompatible, and cost-effective nature. The nanoparticles are not only reported for improving plant improvement but exhibits different bactericidal mechanisms (Oves et al., 2013; Aziz et al., 2016; Qayyum et al., 2017; Mahawar and Prasanna, 2018). It is therefore of keen interest to scrutinize the inhibitory effect of synthesized AgNPs against Ao, which can be used in the field of nanotechnology as a cost-efficient, environmentally friendly and safe strategy.

Therefore, we aim to synthesize AgNPs using fresh fruit extract of *P. emblica* and evaluate their antibacterial efficacy against pathogen Ao strain RS-2 of rice bacterial brown stripe.

MATERIALS AND METHODS

Materials

In order to obtain biosynthesized AgNPs, fresh fruits of *Phyllanthus emblica* were procured from the supermarket in Kunming City, Yunnan Province, China, and stored before use at 4°C. We acquired silver nitrate ($AgNO_3$) from a company Sinopharm Chemical Reagent Co., Ltd. (Shanghai, China). Ao strain RS-2 previously isolated from natural diseased rice plants was collected from Plant Bacteriology Laboratory in Zhejiang

University. The bacterial strain was routinely grown in Luria-Bertani (LB) medium consisting of tryptone 10 g, yeast extract 5 g, NaCl 10 g, ddH_2O to 1000 ml and with/without agar 15 g, pH 7.0) at 30°C as described by Masum et al. (2017).

Preparation of Extract From *P. emblica* Fresh Fruit

The fresh fruit extract of *P. emblica* fruit extract has been prepared following a procedure reported earlier (Ramesh et al., 2015; Manikandan et al., 2017) with slight modification. Briefly, the fresh fruits were carefully clean with sterilized double deionized water (ddH_2O) and then chopped into small pieces and removed seeds. The sliced fruits were then finely macerated by a blender through sterile ddH_2O to obtain 10% (w/v) fruit broth. The resulting extract was passed through a muslin cloth and then filter by Whatman No. 1 filters paper and kept at 4°C until use.

Biosynthesis of AgNPs Using *P. emblica* Fruit Extract

In the biosynthesis process of AgNPs, the effects of the quantity of fruit extract were assessed to intensify the synthesis route producing the metal nanoparticles. In a 100 ml aqueous solution $AgNO_3$ (1 mM), various concentrations of aqueous fruit extract (2.5, 5, 10, and 15 ml) were added and boiled (65°C) for 20 min and then kept at room temperature under dark condition. To confirm that the synthesis of AgNPs was mediated by phytochemicals of *P. emblica* fruits, control flasks containing the mixture of aqueous solution of $AgNO_3$ and sterile ddH_2O were used. The reduction of silver ions was thus observed by changing the optical color in dark brown an taking into account the complete bio-reduction of $Ag+$, overnight samples of synthesized AgNPs were measured using UV-2550 Shimadzu Spectrophotometer (Shimadzu Corporation, Kyoto, Japan). The rapidly formed biosynthesized AgNPs were obtained by centrifugation at 10,000 rpm for 10 min in a centrifuge machine (JEOL, JEM-200EX; Tokyo, Japan) followed by carefully washed with sterile ddH_2O and freeze-dried following the instruction of Alpha 1-2 LDplus (GmbH, Germany) and then stored at −80°C. Based on the fast reduction of $AgNO_3$ into AgNPs, only the capable AgNPs sample prepared from 15 ml of fruit extract was used for further characterization using several methods including Fourier transform infrared spectroscopy (FTIR), X-ray diffraction (XRD), transmission electron microscopy (TEM), scanning electron microscopy (SEM), and energy dispersive X-ray (EDX) spectroscopy. All steps are shown sequentially in **Figure 1**.

Characterization of the Synthesized AgNPs

Biosynthesized AgNPs due to the reduction of silver metal ions with aqueous *P. emblica* fruit extract was observed by UV-2550 Shimadzu Spectrophotometer (Shimadzu Corporation, Kyoto, Japan) operated with 1 nm resolution and wavelength of 200-800 nm. The dried sample's FTIR spectrum was documented by the FTIR machine (Vector 22, Bruker, Germany) using ranges between 450 and 4000 cm^{-1} with a resolution of 4 cm^{-1}. XRD pattern of the dried nanoparticles was obtained using Powder X-ray Diffractometer (Siemens D5000, Germany) as described in the instructions. In addition, X-MaxN Energy dispersive spectroscopy (EDS, Oxford Instruments, Oxford, United Kingdom) confirmed the presence of nanosilver elements at 20 keV. Scanning Electron microscopy (SEM) (SU8010, Hitachi, Japan) was used to characterize the shape of AgNPs. On the carbon-coated copper grid, a thin film of the dried samples was made by simply placing a little sample followed by drying for 5 min under the mercury lamp. A Field-Emission Scanning Electron Microscope (FE-SEM) images were used to study the size and morphology of AgNPs. Moreover, AgNPs have been structurally characterized in high resolution mode (HR-TEM) using FEI Technai F20 TEM instrument. To prepare a thin coat of the sample, a drop of silver solution was placed on the grid for 1 min, followed by solvent evaporation under vacuum and then placed sequentially in a grid box.

In vitro Antibacterial Activity of AgNPs

Antimicrobial activity of synthesized AgNPs was evaluated against the pathogen Ao strain RS-2 of rice bacterial brown stripe by agar well diffusion technique as described by Elbeshehy et al. (2015) with little change. Briefly, 200 ml of bacterial suspension (approximately ∼1 × 10^8 CFU/ml), previously overnight cultivated in LB broth at 30°C, was spread with 5 ml of LB agar medium on the top of solid LB agar medium in a Petri dish plate. Once the upper inoculated agar medium was air-dried, 40 μl of the final concentration of AgNPs from 5 to 30 μg/ml were loaded at the same distance on agar well (6 mm) and grown for 24 h at 30°C. The same amount of filter-sterilized *P. emblica* fruit extract was used as a control. Antibacterial activity was determined by averaging the diameter of inhibition zone formed around the center of each well. To determine the antibacterial activity, the diameter of the inhibition zone was measured around the whole. Two repeated experiment has been done following complete randomized design with three replications.

Minimum Inhibitory Concentration (MIC) of AgNPs

The 5 ml AgNPs solutions have been adjusted by adding the stock of AgNPs to the half-strength LB broth in order to obtain a final concentration of AgNPs of 5, 10, 20, and 30 μg/ml, respectively. The MIC of AgNPs was determined by inoculating the 100 μl of bacteria cells of Ao strain RS-2 (∼approximately 1 × 10^8 CFU/ml) into AgNPs solution of different concentrations, while the control was only sterile ddH_2O (without AgNPs). The samples were then incubated at 30°C for 12 h at 180 rpm. The bacterial numbers in the samples were computed by reading the absorbance value at 600 nm using a ThermoMultiskan EX Microplate Photometer (Thermo Fisher Scientific, Waltham, MA, United States). With six replicates for each treatment, this experiment was repeated three times.

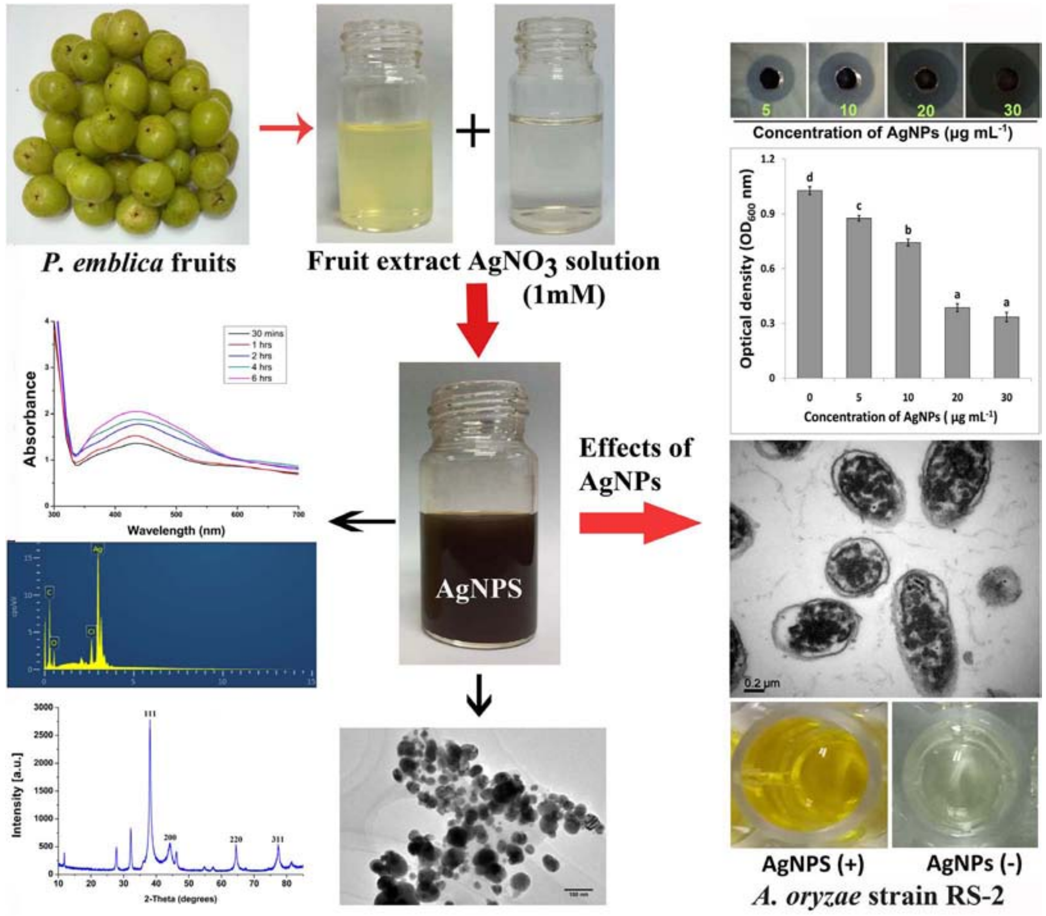

FIGURE 1 | Schematic diagram for biosynthesis of AgNPs using fruit extract of *Phyllanthus emblica* and its inhibitory effect on Ao strain RS-2.

Effect of Contact Time of AgNPs on Cell Survival of Ao Strain RS-2

The effect of incubation time of Ao strain RS-2 treated with AgNPs was evaluated by counting the viable cell spread on LB agar plates (Lou et al., 2011). In this procedure, AgNPs solutions were prepared by diluting the AgNPs stock (2 mg/ml) with sterile ddH$_2$O to provide a final concentration of 20 μg/ml AgNPs, which has been listed as MIC against strain RS-2 by comparison with the other AgNPs concentrations tested. In order to achieve a final bacterial concentration of approximately 10^8 CFU/ml, a newly prepared bacterial solution was supplemented with 5 ml of AgNPs solution; while in the control treatment, AgNPs was replaced with sterile ddH$_2$O and then incubated for 3, 6, and 12 h in a shaker at 30°C. The bacterial suspensions were withdrawn from inoculated samples and diluted serially with sterilized ddH$_2$O. A 100 μl of diluted samples were spread on LB agar plates and cultured at 30°C at 48 h. After incubation, the number of colony forming units (CFU) was enumerated to determine the cell survival activity while the average number of CFU was noted at the lowest dilution (Lou et al., 2011; Li et al., 2013). There were six replicates in each treatment and the experiment was done two times.

Swarming Motility Assay

The effect of AgNPs on Ao strain RS-2 swarming motility was assayed on LB plates supplemented by 0.7 percent (w/v) agar as previously described by Dong et al., 2016). In the center of each swarming plate containing AgNPs (20 μg/ml), 5 μl of strain RS-2 suspension (approximately 1 × 10^8 CFU/ml) were dropped, while the plate without AgNPs was served as control and then incubated for 3 days at 30°C. To evaluate the swarming motility, the colony diameter of strain RS-2 was assessed as reported in our previous study (Masum et al., 2017). The motility assay was repeated three times with six replications.

Biofilm Inhibition Assay

The inhibitions of bacterial biofilm formation by AgNPs were performed using the 96-well microtitre plate method as described Masum et al. (2018) with slight modification. Briefly, the overnight cell suspension of Ao strain RS-2 was re-cultured into a fresh LB broth at shaker to obtain the mid-exponential growth. Thereafter, 100 μl of bacterial cells (approximately ~1 × 10^8 CFU/ml) was inoculated onto each well with AgNPs concentration of 20 μg/ml, while sterile ddH$_2$O were used as a control. The plates were kept without agitation at 30°C for 24 h of adhesion. Culture media from each well were then removed and washed gently with sterile ddH_2O. At room temperature, 100 μl solution of crystal violet (0.1%, w/v) was added to stain the biofilm in the well of plate and incubate for 45 min. The unattached violet crystal solution was discarded three times from the plate with sterile ddH_2O. Bacterial biofilm was determined by measuring the absorbance at 570 nm after dissolving the CV stain with 125 μl of acetic acid (33%, v/v) using a SPECTRAmax®PLUS384 Microplate Spectrophotometer. With 12 replications for each treatment, this experiment was repeated three times independently.

Live/Dead Cell Staining

To observe damage and intact membranes in bacterial cells exposed to 20 μg/ml AgNPs, live/dead staining technique was used following the protocol of BacLight bacterial viability kit (Invitrogen). There are two nucleic acid stains in the kit namely (i) a red-fluorescent (propidium iodide stain), and (ii) a green-fluorescent (SYTO 9 stain). To verify the validity of the kit, live bacteria as a negative control, and the dead bacteria samples treated by isopropanol were stained, respectively, according to the description of the kit's protocol. Fluorescence in the sample was then detected using the Olympus inverted confocal microscope as described previously (Cui et al., 2014).

Transmission Electron Microscopy (TEM) Analysis

For TEM analysis, Ao strainRS-2 has been prepared as mentioned in the previous studies (Li et al., 2013; Dong et al., 2016). Briefly, 1000 μl suspension of Ao strainRS-2 (approximately 1×10^8 CFU/ml) was inoculated with AgNPs, to a final 20 μg/ml of AgNPs. The treated sample was incubated at rotary 160 rpm shaking at 30°C for 8 h. The bacterial suspension without AgNPs served as control. The bacterial cells were washed twice after centrifugation with a solution containing 0.1 mol/l phosphate-buffered saline (PBS) (pH 7.2) and fixed in glutaraldehyde [2.5% (v/v) in 0.1 M PBS]. The samples were then post-fixed with osmium tetroxide [1% (w/v) in 0.1 M PBS] for 1 h at room temperature and rinsed with the 0.1 M PBS buffer three times, followed by dehydration with a series of ethanol solutions including 50, 70, 80, 90, 95, and 100%. A low-viscosity medium of Spurr resin was used to embed the specimen which has been incised with a diamond knife on Supernova Ultramicrotome (Astria). The section stained with uranyl acetate and alkaline lead citrate was monitored in TEM of Model JEM-1230 (Japan) following the standard procedures.

Secretion of Effectors Protein Hcp (Hemolysin Coregulated Protein)

The secreted Hcp protein of Ao strain RS-2were measured by Enzyme-linked immune sorbent assay (ELISA) experiment as described in our previous studies (Li et al., 2014; Masum et al., 2017). The ELISA was conducted in a standard 96 microtiter plate (Corning-Costar Corp., Corning, NY, United States) as described by Slutzki et al. (2012). Briefly, 150 μl of filtered antigen was pipetted to coat the microtiter plates and incubated overnight at 4°C followed by washing with wash buffer. After blocking the plates with a blocking buffer of 175 μl/well, it was kept at 37°C for 1 h and decanted. In order to detect Hcp protein of Ao strainRS-2 treated with or without AgNPs at 30 μg/ml, the Hrp-conjugated Goat Anti-Rabbit IgG polyclonal antibody was used at a dilution of 1:5000. The value of optical density (OD_{450}) was registered using a microplate reader (Multiscan microtiter plate reader) set at 450 nm.

Statistical Analysis

The experimental data were analyzed using the SPSS software package SPSS 21 (United States) and the mean values of the treatments were grouped by selecting the LSD (least significant difference) tools. Data are represented as the average values with standard error of at least three values of each independent experiment.

RESULTS

Synthesis and Characterization of the Synthesized Nanoparticles

In order to standardize the nanoparticles synthesis route, different quantities of *P. emblica* fruit extract varied from 2.5, 5, 10, 15 ml with 100 ml aqueous solution of $AgNO_3$ (1 mM) were tested in this study. After 30 min, the dissolution of the 15 ml fruit extract caused the rapid change in color from light yellowish to dark brown, indicating the fast reduction of Ag^+ to Ag^0 in $AgNO_3$ solution (**Figure 2A**), while the color in other samples was changed after incubation for 2–8 h in a dark room and the control sample remained colorless. Furthermore, the synthesis of AgNPs in the solution was confirmed by the results of UV-visible spectrophotometers, which exhibited a spectrum of surface plasmon resonance (SRP) ranging from 430 to 436 nm of absorption band (**Figure 2B**). However, it could be noted that AgNPs was also synthesized with 2.5 ml of fruit extract in 100 ml $AgNO_3$ solution. Indeed, the SPR spectra of AgNPs derived from the higher concentration of fruit extract showed a sharper and strong absorption band at 430 nm (**Figure 2B**). Moreover, the UV-vis spectra results showed an increase in the absorbance intensity of the reaction mixture with time and the solution was stable after 24 h of incubation, which indicates the completion of nanoparticles formation in solution. Therefore, the AgNPs mediated by the mixture of 15 ml fruit extract and 100 ml $AgNO_3$ solution was freeze-dried and used for further studies.

In addition, **Figure 3** shows the FTIR spectra of biogenic AgNPs derived from *P. emblica* fruit extract after reaction with $AgNO_3$ and fruit extract control without $AgNO_3$. The FTIR data indicates the marginal shift in the peak position of spectra as depicted in **Figure 3**. The spectral analysis reveals the number of functional biological group responsible for stabilization of nanoparticles, which acts as capping or stabilizing agents. FTIR measurement based on AgNPs mediated by fruit extract revealed different absorption peaks at 3404, 2923, 2852, 1637, 1535, 1384, 1219, 1160, 1061, and 519 cm^{-1}. In case of AgNPs, a very strong absorption peak shifted toward a lower

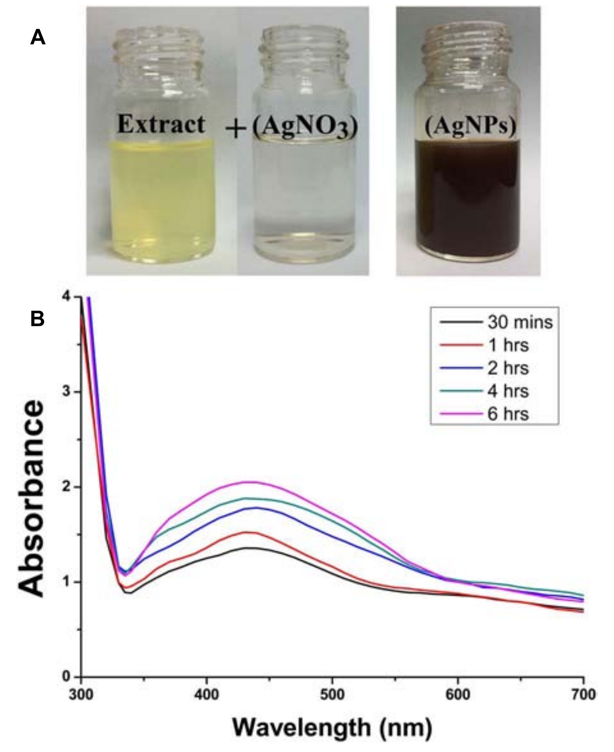

FIGURE 2 | Confirmation of biosynthesized silver nanoparticles (AgNPs). **(A)** Color changes in the *Phyllanthus emblica* fruit extract (PFE) after addition of silver nitrate (1 mM aqueous solution of $AgNO_3$) for nanoparticles synthesis; **(B)** UV–visible spectrum of AgNPs synthesized by phytochemical agents in the PFE. The peak at 430 nm corresponds to the surface plasmon resonance of AgNPs.

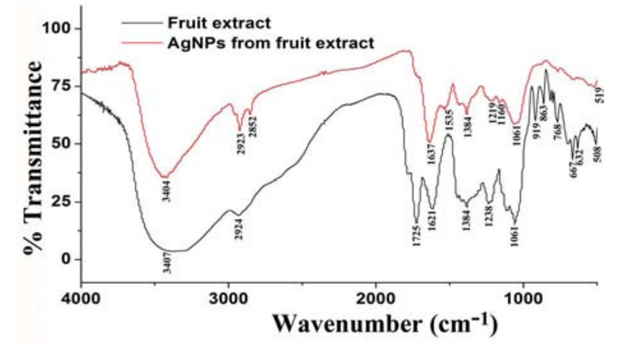

FIGURE 3 | Fourier-transform infrared spectrum of biosynthesized AgNPs (up) and fruit extract of *Phyllanthus emblica* (down) after 24 h of incubation.

wave number was observed at 3404 cm^{-1}, which indicates the binding of silver ion (Ag^+) with hydroxyl and or amine groups in the *P. emblica* fruit extract. Other bands figured at about 2923 and 2852 cm^{-1}, are also remarkable because of the stretching vibration of hydrocarbon (C–H) bonded of alkenes, while the peak at 1637 cm^{-1} is also predominant and represents the involvement of amide-I bond (–C = O) of proteins as a capping agent and stabilization of AgNPs. Moreover, the band at 1621 cm^{-1} in fruit extraction was due to the presence of amide I vibrations, which was shifted to 1535 cm^{-1} in AgNPs due to the proteins that may have been linked to AgNPs by the amine groups. The peak observed around 1384 cm^{-1} in AgNPs spectra extract that could be assigned to C–H symmetric vibrations and same peak was also observed in fruit extract. The spectral peak at 1238 cm^{-1} in extract (shifted to 1219 cm^{-1} in AgNPs) was found by the C–C stretching vibration (**Figure 3**).

Furthermore, XRD analysis confirmed the crystalline nature of mediated AgNPs based on the emission peaks of $2\theta = 38.178$, 44.428, 64.583, and 77.639°, corresponding to the silver crystal planes (111), (200), (220), and (311), respectively, (**Figure 4F**). The TEM images clearly showed that most AgNPs were highly mono-dispersed in spherical shapes (**Figures 4A,B**),which was in conformity with the SEM image (**Figure 5A**). Moreover, the HR-TEM images (**Figures 4C,D**) of a biosynthesized silver nanoparticle revealed crystalline nature of the particles showing the lattice fringe quite clearly. The bright circular spots in SAED pattern (**Figure 4E**) demonstrated the (111), (200), and (220) planes, which also revealed the crystalline nature of the particles formed. These data are in lines with the XRD results obtained. The size distributions of the AgNPs varied between 19.8 and 92.8 nm with a mean value of 39.1 nm (**Figure 5A**). EDX instrument furthermore confirmed the existence of the silver element in the synthesized AgNPs (**Figure 5B**).

In vitro Antimicrobial Activity of AgNPs

The biosynthesized AgNPs exhibited good sensitivity response at the four different concentrations against Ao strain RS-2 compared to *P. emblica* fruit extract (PFE) after 24 h of incubation in the agar media (**Figure 6**). The inhibition zone diameter increased by increasing the concentration of AgNPs against strain RS-2, which varied from 1.27 to 1.96 cm (**Figure 6B**). The largest inhibition zone was achieved by a concentration of 30 μg/ml, followed by 20 μg/mlof AgNPs (**Figure 6A**). In contrast, the control PFE showed the smallest inhibition zone (1.05 cm) compared to the addition of AgNPs treatments (**Figure 6A**). Although antibacterial activity was detected in the control containing only $AgNO_3$ (data not shown), it was significantly increased by the addition of AgNPs. Taken together, these results suggested that the synthesized AgNPs showed an excellent antimicrobial activity against strain RS-2.

Minimum Inhibitory Concentration (MIC) of AgNPs Against Ao Strain RS-2

Compared to the control, the results of this study showed that AgNPs had a noticeable antimicrobial activity against Ao strainRS-2 after 12 h of incubation (**Figure 7**).The antimicrobial activity was varied at different levels of AgNPs. In general, the biosynthesized AgNPs concentrations of 5, 10, 20, and 30 μg/ml caused 14.70, 27.65, 62.41, and 67.43% reduction in the OD_{600} values, respectively, while a maximum value of OD_{600} (1.027) was observed in strain RS-2 in the absence of AgNPs (**Figure 7**). However, there was no significant difference

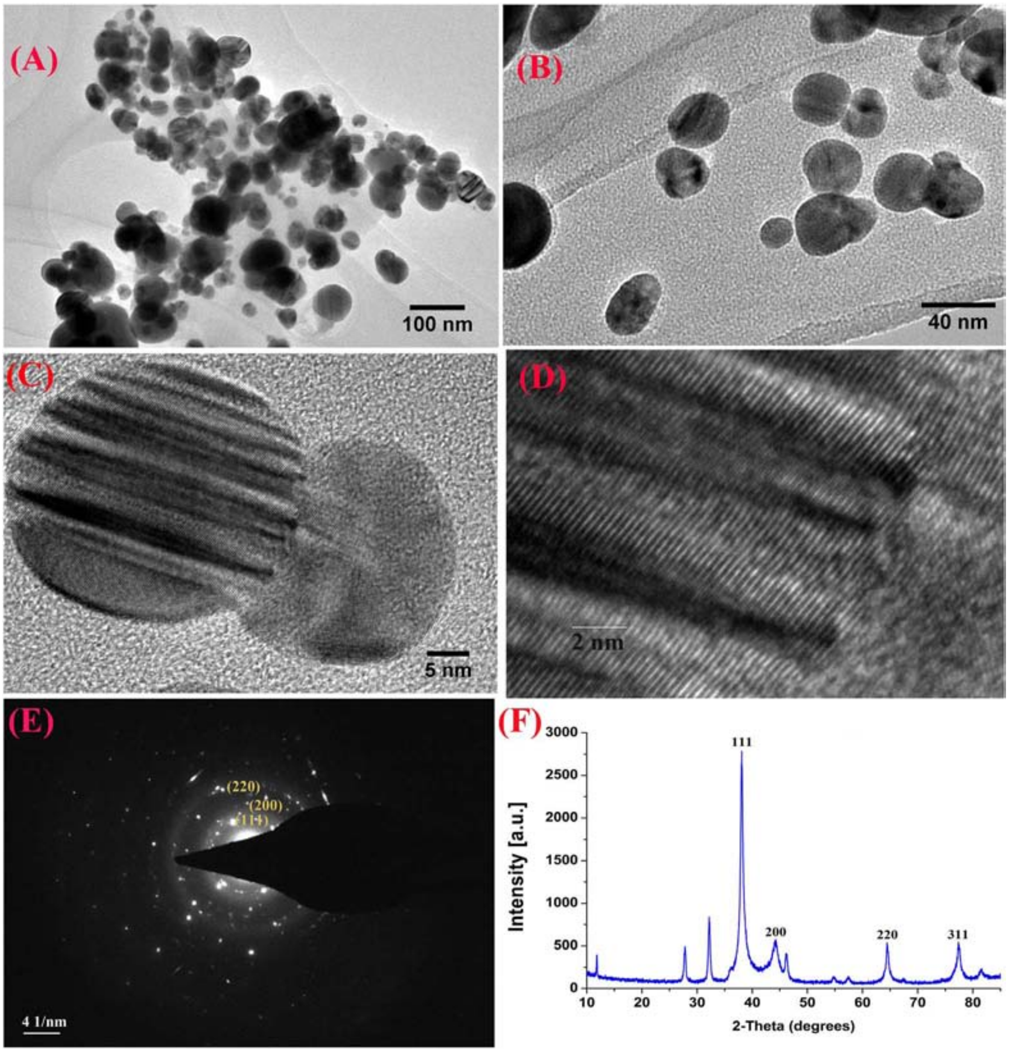

FIGURE 4 | TEM images of the biosynthesized silver nanoparticles (AgNPs) **(A,B)**; HRTEM image with lattice fringe **(C,D)**; corresponding SAED pattern **(E)**; and X-ray diffraction patterns of synthesized AgNPs **(F)**.

between the concentration of 20 and 30 μg/ml in the antibacterial activities of AgNPs, which indicated that Ao strain RS-2 is highly susceptible to both AgNPs concentrations.

Effect of Contact Time of AgNPs on Cell Survival of Ao Strain RS-2

To investigate whether the incubation time affects the antimicrobial activity of AgNPs; an experiment was conducted by enumerating the surviving cell of Ao strain RS-2 at different incubation period up to 12 h. Results showed that the initial bacterial survival of strain RS-2 in sterile ddH$_2$O was 8.19 log CFU/ml as a control, while the bacterial survival remained stable with the increase in the contact time (**Table 1**). However, in the AgNPs treatments (20 μg/ml), the cell survival of strain RS-2 decreased by 1.40, 3.65, 4.09, and 4.97 log CFU/ml as compared with the corresponding control after 1.5, 3.0, 6.0, or 12.0 h of contact time, respectively. Obviously, in the presence of AgNPs, cell survival was decreased with the increase in contact time (**Table 1**).

Swarming Motility

The effects of AgNPs on the bacterial movement were examined by evaluating the diameter of vicinity covered by Ao strain RS-2 on LB agar plates supplied with AgNPs (20 μg/ml). Results of experiment showed that colonies measurement of strain RS-2 were 11.4, 16.0, and 22.7 mm in the absence of AgNPs after incubation of 24, 48, and 72 h (**Figure 8A**). Interestingly, the swarming ability of strain RS-2 was significantly inhibited by the incubation with AgNPs at different time (**Figure 8B**). As a result, the colony diameter of strain RS-2 were 8.7, 10.6, and 15.1 mm after 24, 48, and 72 h of incubation with AgNPs, which were decreased by 23.68, 33.66, and 33.67%, respectively, compared with the corresponding control (**Figure 8**). These results showed that the AgNPs had a significant effect on the swarming motility

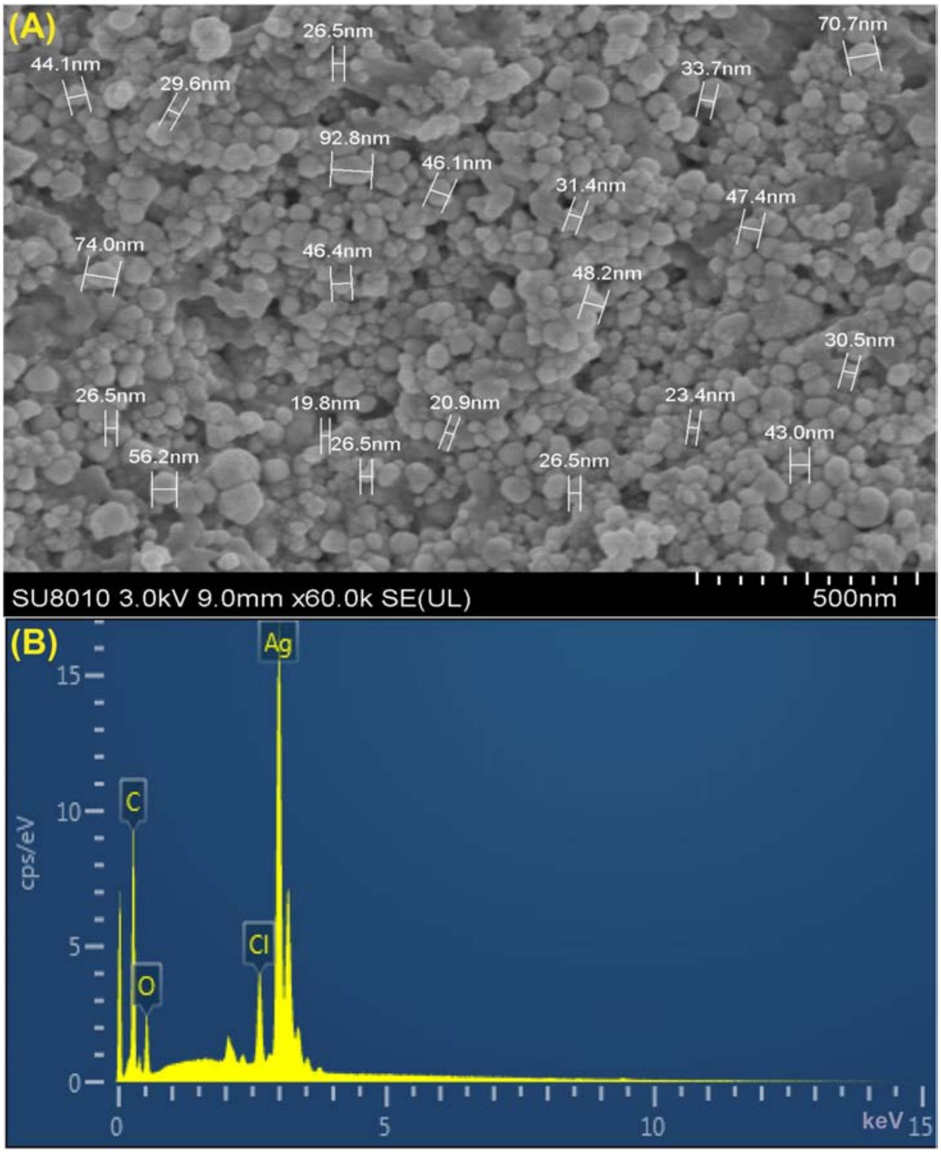

FIGURE 5 | (A) SEM image of silver nanoparticles (AgNPs) synthesized by reducing 1 mM $AgNO_3$ using fresh fruit extract of *Phyllanthus emblica*. A representative SEM image recorded from a thin film of synthesized AgNPs prepared on carbon-coated copper grid and estimation of nanoparticles diameter. **(B)** Energy Dispersive Spectroscopy (EDS) patterns of synthesized AgNPs; EDS spectra recorded from a film of synthesized AgNPs with different X-ray emission peaks labeled.

of Ao strain RS-2 at a concentration of 20 μg/ml regardless of the incubation period.

Biofilm Formation

After 1 day's incubation at 30°C without stirring, the biofilm formation of strain RS-2 was quantified and displayed a significant inhibition effect when we exposed a concentration of 20 μg/ml of AgNPs in microtitre plates, compared with control (**Figure 9**). Indeed, the OD_{570} value of Ao strain RS-2 was 0.129 without AgNPs, while the strain RS-2 treated with AgNPs had a lower OD_{570} value (0.043). In general, the biosynthesized AgNPs caused 66.64% reduction in the OD_{570} value of Ao strains RS-2 as compared to the control (**Figure 9**).

Live/Dead Cell Staining

In order to clarify the antimicrobial mechanism of AgNPs, the live/dead bacterial cells of Ao strain RS-2 were stained after 8 h of treatment. Without AgNPs, staining results in live bacteria clearly showed intact membranes, which can be induced from fluoresce green (**Figure 10A**), while fluoresce red dead cells were detected after heated the bacteria (**Figure 10B**). Interestingly, after exposing the strain RS-2 to AgNPs (20 μg/ml), some bacterial cells were monitored to fluoresce green (**Figure 10C**). But, when AgNPs was treated, the number of green fluorescent cells of strain RS-2 decreased significantly, suggesting an inhibition of bacterial growth and replication. Taken together, these results indicate that AgNPs had a bactericidal effect on strain RS-2.

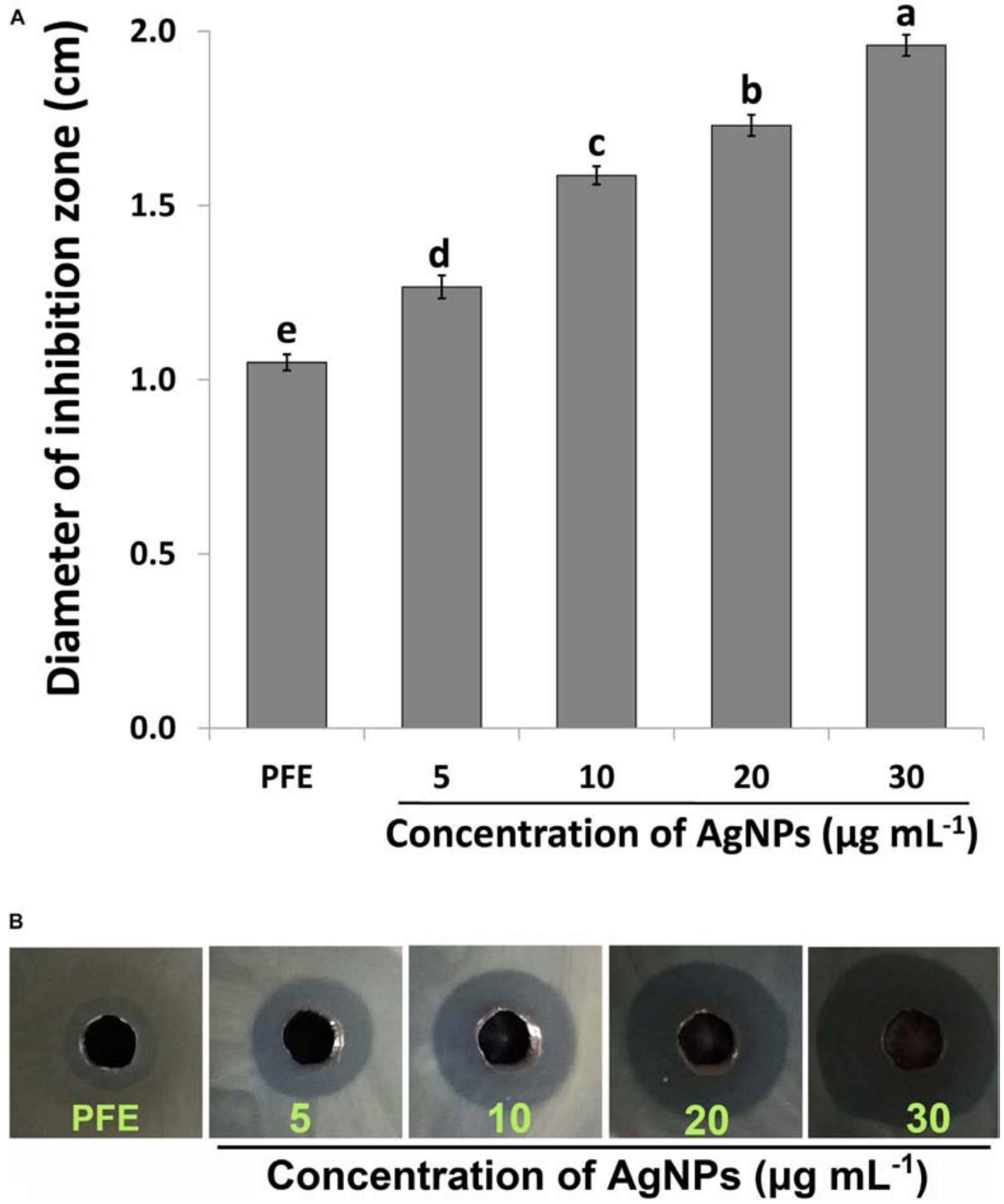

FIGURE 6 | *In vitro* inhibitory effect of silver nanoparticles (AgNPs) synthesized by *Phyllanthus emblica* fruit extract (PFE) against *Acidovorax oryzae* strain RS-2. **(A)** Diameter of bacterial growth inhibition (cm) caused by PFE and different concentration of AgNPs; Vertical bars represent standard errors of the means ($n = 3$). Bars followed by the same letter(s) are not significantly different ($P \leq 0.05$). **(B)** Bacterial growth inhibition zone achieved in agar well diffusion method by PFE and concentration of AgNPs at 5, 10, 20, and 30 µg/ml.

Damage of Bacterial Cells by the Synthesized AgNPs

TEM analysis of Ao strain RS-2 was used to study the effect of AgNPs on the major structural damage of bacterial cells. TEM results of strain RS-2 indicated that the membranes of untreated cells were intact with uniformly distributed cytochylema and electron-dense material throughout the bacterial cytoplasm (**Figures 11A,C**). After treatment with AgNPs, however, the cell wall and cytoplasmic membrane of strain RS-2 became wrinkle and abnormal (**Figures 11B,D**). Besides, the synthesized AgNPs badly ruptured the part of the cell wall, therefore, leading to leaching out of nutrient and nucleic material swollen cell structure and caused the death of the bacterium, and there was evidence of dead cells in live/dead staining images.

Secretion of Effector Protein Hcp

Effects of AgNPs on effector protein Hcp secretion in Ao strain RS-2 were studied on the basis of an experiment with ELISA using Hcp effector protein polyclonal antibody. Based on the optical density measurement of Hcp protein (OD_{540}) using

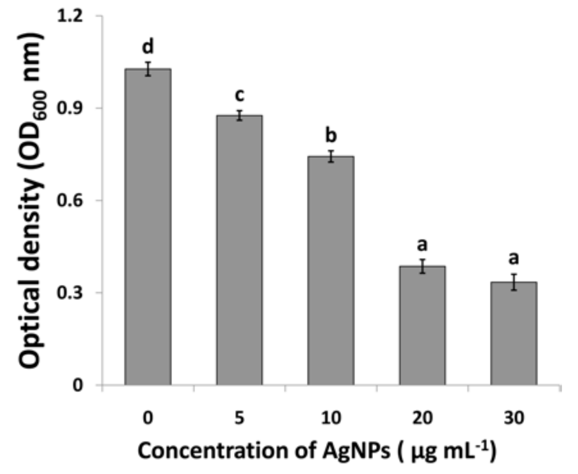

FIGURE 7 | Determination of minimum inhibition concentration of silver nanoparticles (AgNPs) mediated by *Phyllanthus emblica* fruit extract against *Acidovorax oryzae* strain RS-2. Vertical bars represent standard errors of the means (n = 6). Bars followed by the same letter(s) are not significantly different ($P \leq 0.05$).

TABLE 1 | Effect of contact time of AgNPs on the antibacterial activity against *Acidovorax oryzae* strain RS-2.

Contact time (h)	Bacterial survival ($\log_{10}$ CFU/ml)	
	Control	AgNPs[a]
0.0	8.19 ± 0.010 a[b]	8.19 ± 0.010 e
1.5	8.18 ± 0.013 a	6.78 ± 0.089 d
3.0	8.16 ± 0.012 a	4.51 ± 0.056 c
6.0	8.12 ± 0.022 a	4.03 ± 0.024 b
12.0	8.09 ± 0.027 a	3.12 ± 0.041 a

[a] *Concentration of AgNPs solution was 20 µg/ml.* [b] *Data from the two repeated experiments with six replications were pooled because there was no significant difference between repeat experiments. Means in a column followed by the same letter are not significantly different according to the LSD test ($P \leq 0.05$).*

an indirect ELISA experiment, the drawn standard curve for Hcp protein represented in this study as $y = 110.4x + 0.027$ showed a high coefficient of correlation (R^2 = 0.999) for its reliability (**Figure 12B**). The supernatant of strain RS-2 showed a strong positive ELISA reaction when we used AgNPs at a concentration of 20 µg/ml, however, there was a negative reaction (P/N ≤ 1.5) in the absence of AgNPs for the culture broth of strain RS-2 (**Figure 12C**). According to a standard curve, colorimetric analysis showed that the concentration of Hcp in the sample treated with AgNPs and positive control was 0.015 and 0.012 mg/ml, respectively. Obviously, these data indicated that AgNPs had an effect on the secretion of Hcp proteins in strain RS-2.

DISCUSSION

Biologically synthesized AgNPs have been reported to be promising therapeutic molecules with significant antimicrobial and antiviral activities (Kim et al., 2007; Rogers et al., 2008; Galdiero et al., 2011; Oves et al., 2013; Bhuyan et al., 2015; Aziz et al., 2016; Zhang et al., 2016). Although many nanoparticles have been successfully synthesized using microorganisms and plants, searching new nanoparticles with precise biological, physical, and chemical features is still at the cutting edge of nanoscience research. *Phyllanthus* has a noteworthy variety of forms of growth and the fruits are widely used in several preparations of traditional medicine due to its rich antioxidant, anti-aging, antipuretic, and anti-inflammatory properties and the potential sources of naturally occurring phytochemcals in the fruit extract (Ramesh et al., 2015; Manikandan et al., 2017). In this study, synthesis and characterization of AgNPs from *P. emblica* fruit extract is reported, which may benefit from ecological and economical aspects. Additionally, synthesized AgNPs have greatly affected the growth of bacteria, integrity of cell, biofilm production, swarming motility and the secretion of Hcp effectors of Ao strain RS-2. Overall, this study reported green-synthesized AgNPs mediated by *P. emblica* plant extract and demonstrated its antibacterial activity and mechanism against the pathogen of bacterial rice brown stripe.

It has been well described that biosynthesis of nanoparticles employing the use of plant extract is a noble strategy for biosynthesis reaction because of their nontoxic properties and thus provide natural capping agents (Sharma et al., 2009; Rai and Ingle, 2012; Oves et al., 2013, 2018; Prasad, 2014; Aziz et al., 2016, 2019; Qayyum et al., 2017). Results here showed that synthesis of AgNPs occurred after exposing silver nitrate to *P. emblica* fruit extract even at different ratios and hence, the change in dark brown color was observed due to the succession of nanoparticles formation, which has been further justified by ultraviolet–visible spectroscopy. Biosynthesized AgNPs had a strong band of absorption at 430 nm, due to its SRP attributes. Here, the intensity of the color change from light yellowish to dark brown is directly related to the quantity of the extract and incubation period, and this is probably because of the stimulation of longitudinal plasmon vibrations and $AgNO_3$ reduction (Kumar and Mamidyala, 2011; Yamal et al., 2013; Manikandan et al., 2017). Therefore, in agreement with earlier reports (Sosa et al., 2003; Tran et al., 2013; Manikandan et al., 2017),increasing the absorption point with an increase extract ratio is a reliable criterion, thus indicating the synthesis of symmetrical nanoparticles. With the intention to identify the key factors for the silver ions (Ag^+) reduction into AgNPs (Ag^0) in the aqueous extract of *P. emblica* fruits, FTIR analyses have been carried out. In case of AgNPs, a shift in the absorbance peak with variable band intensity was observed at different points when compared with control fruit extract. *P. emblica* fruit extract based AgNPs spectra revealed different absorption bands ranging from 519 to 3404 cm^{-1}. This predicts the presence of possible biomolecules that are involved in reduction and stabilization of silver ions (Ag^+) to AgNPs (Ag^0) present in aqueous fruit extract. In agreement with previous reports, the FTIR spectrum analysis in this study detected several absorption peaks, specifically for N–H stretching vibrations, indicating strong hydrogen bonding, and C = O extension vibrations

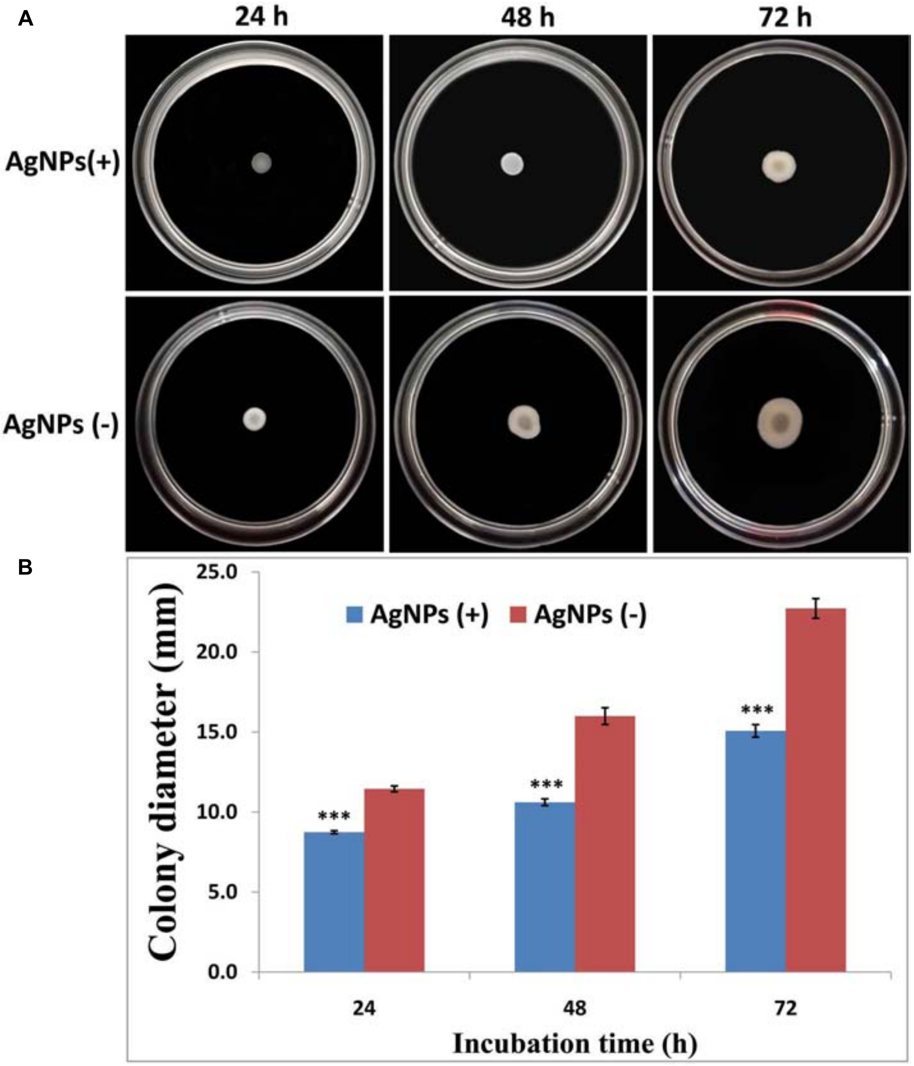

FIGURE 8 | Effect of silver nanoparticles (AgNPs) mediated *Phyllanthus emblica* fruit extract on the swarming motility of *Acidovorax oryzae* strain RS-2. The concentration of AgNPs is 20 μg/ml. $^{***}P < 0.001$. Error bars represent the standard error of the mean (n = 6). **(A)** Bacterial swarming motility was determined by measuring the diameters of bacterial colony on the plates from three independent experiments; **(B)** Colony diameter at different incubation time.

attributed to carboxylic acids, ketones, and aldehydes, which were linked to the silver ions reduction leading to nanoparticles stabilization because of oxidizing the hydroxyl radical (Selvi et al., 2016; Manikandan et al., 2017; Qayyum et al., 2017; Oves et al., 2018; Aziz et al., 2019). Different peaks at two–theta value in XRD results revealed the presence of AgNPs having varied face-centered cubic (fcc) silver planes, while the peaks at 2Θ value of 38 degrees was the sharpest and the (111) plane therefore appears to be preferentially similar to the supporting substratum surface. Similar results were also shown in other studies (Mahmoud et al., 2016; Manikandan et al., 2017; Oves et al., 2018; Aziz et al., 2019). The TEM and HRTEM images of biosynthesized AgNPs showed that most of the particles were nearly spherical in shape and crystalline in nature, particularly, the HRTEM images showed the presence of lattice fringe corresponds to Ag plane (Soman and Ray, 2016). In our study, we have observed a few traces of AgNPs clusters that may contribute to particle size variation. On close observation, we can clearly see that the clusters have been formed when the individual particles have clustered together. Various sizes of spherical AgNPs with crystallization of bio-organic compounds were reported by previous studies by TEM and SEM analysis (Elbeshehy et al., 2015; Mahmoud et al., 2016; Ghiuță et al., 2018; Oves et al., 2018; Aziz et al., 2019). Moreover, the corresponding SAED pattern of the synthesized AgNPs depicted the crystalline structure of the particles, which was again confirmed by the energy dispersive X-ray analysis (EDX) results obtained. The EDX signals confirmed an existence of the silver element in the synthesized AgNPs with a peak optical absorption range, which has been observed in the biosynthesized AgNPs using *P. acidus* and *Solanum xanthocarpum* fruit extract (Amin et al., 2012; Manikandan et al., 2017). Metallic silver nanocrystals generally

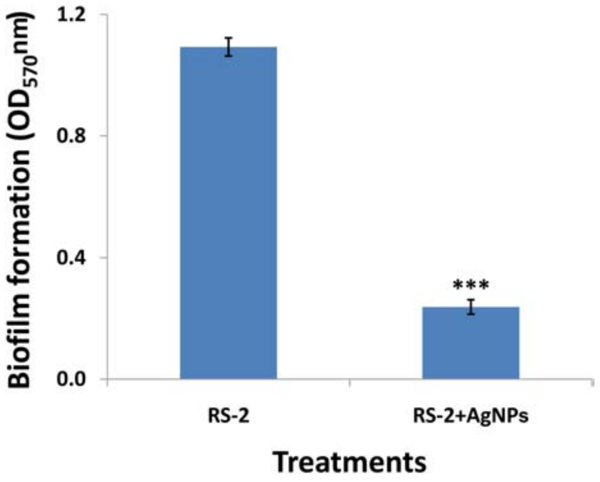

FIGURE 9 | Effect of silver nanoparticles (AgNPs) mediated *Phyllanthus emblica* fruit extract on biofilm formation of *Acidovorax oryzae* strain RS-2 after 24 h incubation at 30°C for 24 h without agitation. Vertical bars represent standard errors of the means (n = 6). The concentration of AgNPs is 20 μg/ml. ***P < 0.001.

show typical EDX signals, which is typical for the absorption of metalic silver (Park et al., 2007). EDX peaks from C, O, and Cl may be caused due to the carbon coated copper grid or by the emission of X- rays from proteins and enzymes of fruit extract (Manikandan et al., 2017), while the nanoparticles can be adhered to either by free amino groups or cysteine residues (Mandal et al., 2005).

Synthesized AgNPs using plants or microorganisms are well-known approach for the development of safe and competent control strategies against resistant bacteria (Kim et al., 2007; Oves et al., 2013; Elbeshehy et al., 2015; Aziz et al., 2016; Zhang et al., 2016; Manikandan et al., 2017). *In vitro* results showed that AgNPs synthesized by the fruit extract of *P. emblica* had effective antibacterial activity against strain RS-2 with the inhibition zone of 27–1.96 cm, while the growth of Ao strain RS-2 was dependent on the concentration of nanoparticles. In addition, significant *in vitro* inhibition of bacterial growth (OD_{600} value) using the dosages of 20 and 30 μg/ml AgNPs were observed and the difference was not obvious, suggesting a MIC of 20 μg/ml AgNPs against strain RS-2. Earlier reports also showed that AgNPs have a concentration-dependent inhibitory effect on a wide range of pathogenic bacteria (Aziz et al., 2016; Mahmoud et al., 2016; Qayyum et al., 2017; Oves et al., 2018). These results are also partly explained due to the smallest AgNPs (having an average diameter of 39 nm), which has been shown a strong inhibitory effect against many Gram-negative bacteria elsewhere (Pal et al., 2007; Singh et al., 2015). Furthermore, similar to previous reports (Lara et al., 2010; Zarei et al., 2014; Qayyum et al., 2017; Oves et al., 2018), this report also showed that bacterial survival in AgNPs solution was affected by the incubation time, while after 6 h exposing, AgNPs concentration of 20 μg/ml had an about 4 log reduction in the viable population of Ao strain RS-2 compared with control.

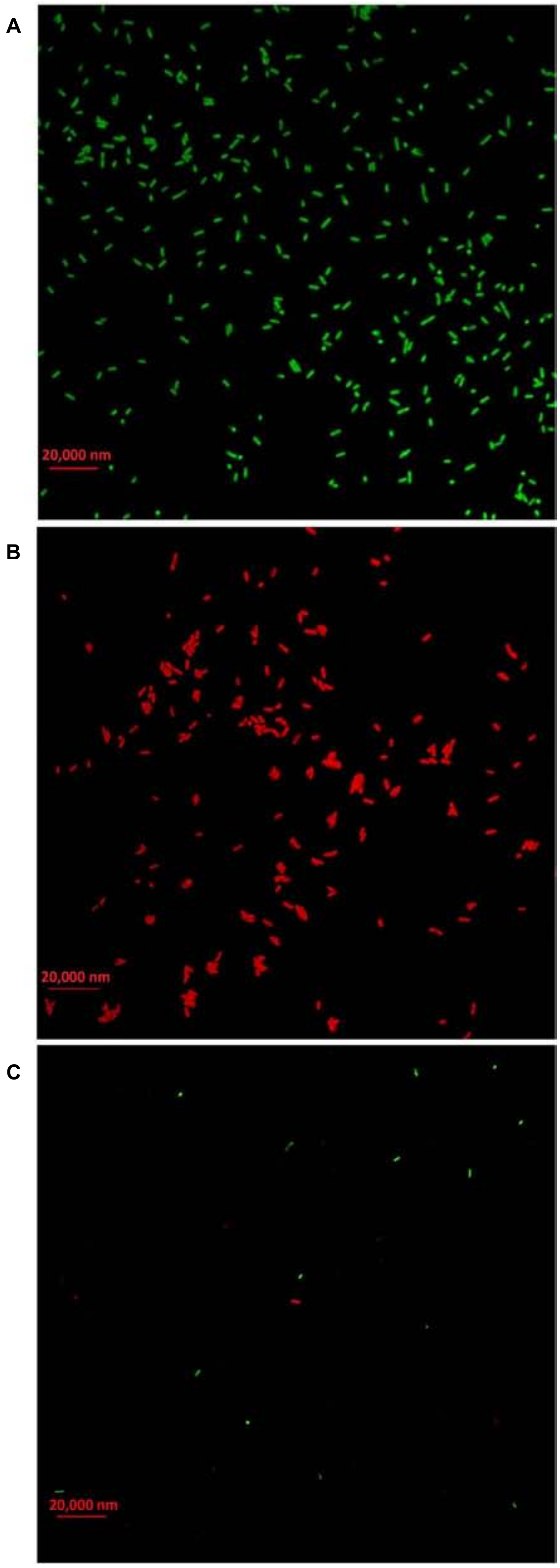

FIGURE 10 | Live/dead cell staining analysis of *Acidovorax oryzae* strain RS-2 cells exposed to 20 μg/ml of silver nanoparticles (AgNPs) for 6 h.

(Continued)

FIGURE 10 | Continued
Staining were carried out using live/dead BacLight bacterial viability kit (Invitrogen, Carlsbad, CA, United States), and visualized by fluorescence microscopy. Green fluorescence is representative of live bacteria with intact membranes, while red fluorescence is representative of dead bacteria. **(A)** Live bacteria in negative control (without AgNPs); **(B)** Dead bacteria in negative control (Heat); **(C)** Bacteria in AgNPs treatment.

In addition, TEM micrographs have also shown the different morphological changes that occurred in Ao strain RS-2 upon exposure of AgNPs (20 μg/ml). It has been reported that green nanoparticles have the ability to attach the bacterial cell membrane more quickly and strongly compared to chemically synthesized nanoparticles that support its better antibacterial action (Parashar et al., 2011). Therefore, TEM was used to see how AgNPs interact with bacterial cells. With the addition of the synthesized AgNPs, the reduction of bacterial numbers and further bacterial death could be caused by the damage of bacterial cell integrity and leakage of cytoplasm. The bacteriostatic effect of AgNPs can be justified by the analysis of bacterial live/dead cell staining results. According to the previous studies, AgNPs directly altered cellular processes, including permeability, transport of electron, osmoregulation, and respiration, perhaps because of the attachment of Ag^+ ions with the negatively charged cell-surface. Consequently, it causes the release of bacterial DNA (Marambio-Jones and Hoek, 2010; Rajeshkumar and Malarkodi, 2014), which was clearly revealed from the TEM figures. Qayyum et al. (2017) has been demonstrated that AgNPs interaction with bacterial cells led to the production of ROS, which might be partially justified the distortion of bacterial membranes or lysis of bacterial cells that ultimately led to death of cells. Therefore, it is reasonable to assume that antimicrobial activity of AgNPs can be attributed, at least in part, to the damage of the membrane and cytoplasm of Ao.

A noticeable finding of this study is that AgNPs inhibited the swarming motility and biofilm formation of Ao strain RS-2 in comparison with control, indicating that inhibitory effect of AgNPs is partly due to the disruption of flagella and interference with the biofilm formation. Moreover, it has been reported that green AgNPs interact with bacterial cells and produced ROS, which causes protein denaturation and other macromolecules damage and improper expression of the bacterial virulence factor, including inhibition of biofilm (Qayyum et al., 2017). Previous studies demonstrated that bacterial movement was directly linked to the growth of bacteria, biofilm formation and pathogenesis (Bahar et al., 2010; Liu et al., 2012). Swarming ability of bacteria has indeed been shown to be a decisive

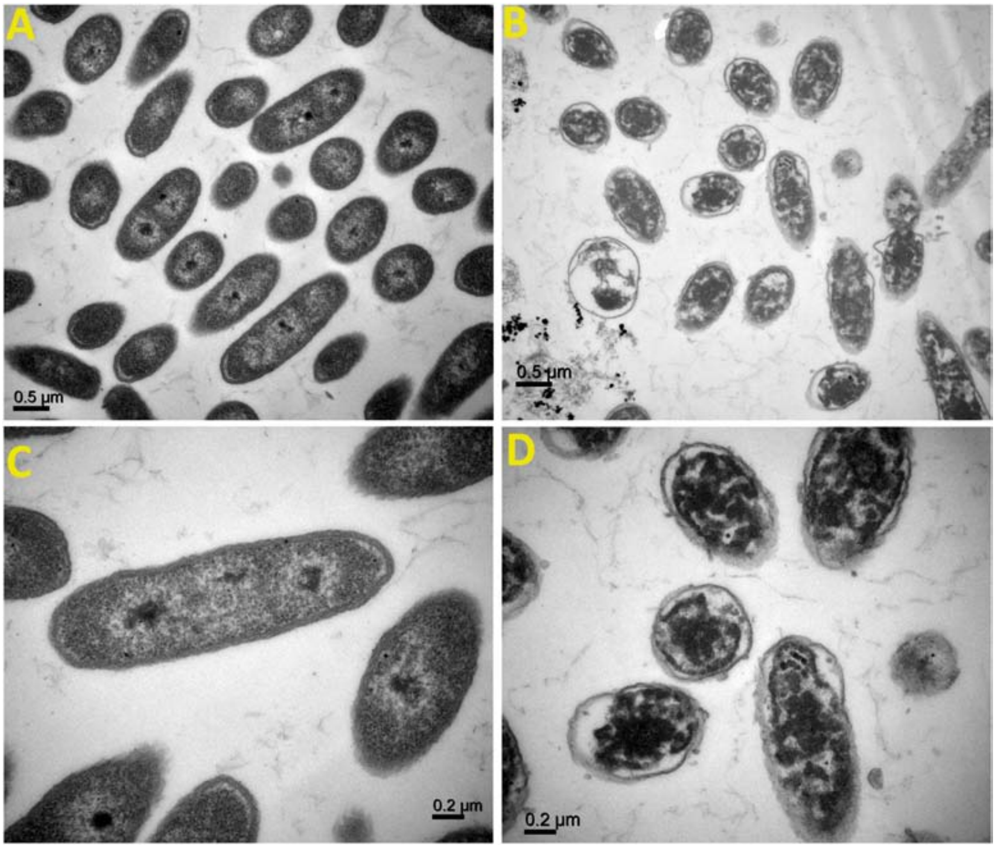

FIGURE 11 | Transmission electron microscopic observation of *Acidovorax oryzae* strain RS-2 treated without **(A,C)** and with **(B,D)** biosynthesized silver nanoparticles (AgNPs)at 20 μg/ml. Scale bar in **(A,B)** = 0.5 μm; in **(C,D)** = 0.2 μm.

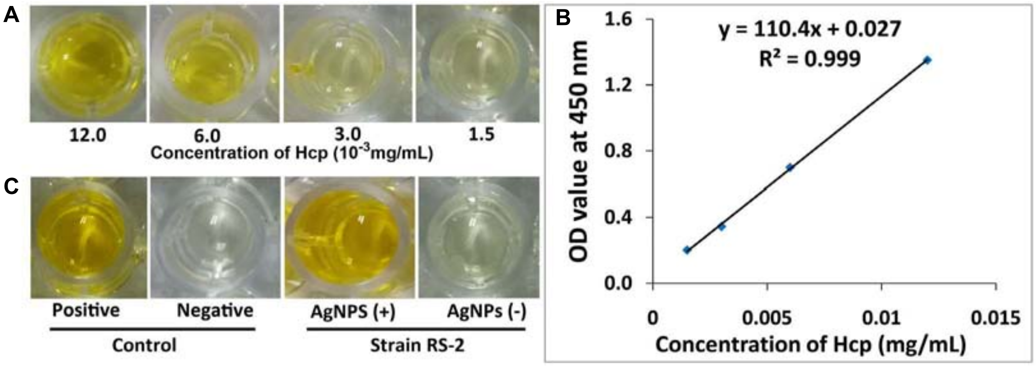

FIGURE 12 | Effect of silver nanoparticles (AgNPs) mediated *Phyllanthus emblica* fruit extract on the secretion of Hcp protein in *Acidovorax oryzae* strain RS-2. **(A)** ELISA of Hcp protein at different concentrations; **(B)** Standard curve, the negative reaction (P/N value < 1.5); **(C)** ELISA measurement of Hcp secreted by strain RS-2. The positive reaction (P/N value ≥ 1.5); The purified Hcp-His fusion protein and His protein were used as the positive and the negative control, respectively. The experiment was conducted three times with three replicates.

factor in colonizing the host for successful infection through attachment and chemotaxis via type IV pili (Liu et al., 2012; Ogunyemi et al., 2019). Besides, biofilm formation was thought to play a vital role in the virulence of plant pathogenic bacteria by employing several mechanisms such as (i) increasing the potential to survive in hazardous conditions and limited nutrient availability, (ii) emerging resistance to plant-derived antibacterial compounds and/or, (iii) stimulating colonization of the host (Mansfield et al., 2012; Bogino et al., 2013). Moreover, swarming is crucial for the various phages of biofilm development, such as hunting for a favorable locale, surface adherence, structural disassembly, and discharge from the matrix of biofilm (Klausen et al., 2003). Additionally, our previous study found that the production of exopolysaccharide (EPS), a key component of the biofilm complex is strongly associated with virulence factors in Ao strain RS-1 (Zhang et al., 2017). According to the findings here, several studies have also been shown that AgNPs was able to affect the swarming ability and biofilm formation, resulting in less virulence (Vyshnava et al., 2016; Qayyum et al., 2017; Alavi and Karimi, 2018).

Results of the ELISA showed that Ao strain RS-2 treated with AgNPs caused increased secretion of Hcp protein as compared to the control (without AgNPs).These results are pretty congruent with the observations of Dong et al., 2016), who reported that camptothecin, a monoterpenoid indole alkaloid antimicrobial compound, caused the up-regulated expression of *hcp* and the increased secretion of Hcp in live Ao strain RS-2 detected on ELISA analysis. Indeed, Hcp are thought to be the components or effectors proteins as T6SS-hallmark components in many Gram-negative bacteria (Mougous et al., 2006; Wu et al., 2008; Masum et al., 2017). Moreover, recent studies have also reported that T6SS play a key function in several virulence-related attributes such as growth of bacteria, production of biofilm and extracellular polymeric substances, EPS production, survival, and rigidity to a variety of stimuli (Burtnick and Brett, 2013; Cui et al., 2015; Masum et al., 2017; Hu et al., 2018). Additionally, according to the results achieved in this study, Ho et al. (2013) also observed that T6SS activity was strongly induced due to damaged membrane, therefore, it is reasonably to infer that the increased secretion of Hcp effectors proteins in strain RS-2 could be partly attributed to membrane disruption.

The use of biogenic AgNPs in the protection of crop diseases offers an excellent promise in insect and pathogens management as an alternative to chemically produced pesticides. AgNPs are remarkably effective against phytopathogens with low toxicity and lead to broad spectrum of applicability such as in pesticidal, antiviral, antifungal, antibacterial as well as nematicidal activities (Gupta et al., 2018). It opens up a new tool for disease management, rapid disease detection and reducing nutrient losses in fertilization by an optimized nutrient management. Moreover, AgNPs can be used as a foliar spray to halt the growth of fungi, molds, rot and several other plant diseases due to its quite stable and highly dispersive in water solution. However, they may have some limitations of its bactericidal nature able to kill beneficial microbes or it may be no effect on the beneficial microbes. Research on the application of nanoparticles in agriculture is still in the early stages, especially with regard to their interventions with microorganisms that are beneficial for agriculture. Because of the lack of effective environmental safety protocols, only *in vitro* studies have been reported so far and *in vivo* studies are still not adequately documented. Preliminary we tested the impact of AgNPs on plant growth promoting bacteria (PGPBs), including *Bacillus amyloliquefaciens* strain D16 isolated from rice and *Paneabacillus polymyxa* strain SX3 from cotton in our laboratory, and hence, we did not observe a significant effect on PGPBs upon exposure the concentration of 5–20 μg/mL (data not shown). Nonetheless, other studies demonstrated that PGPBs are inhibited upon exposure to AgNPs but the toxic effects above a certain concentration (mostly ≥ 100ppm) (Gupta et al., 2018; Mahawar and Prasanna, 2018). However, extrapolation of our observations to more general cases is limited because of *in vitro* evaluation. On the other hand, it has been reported that low dose of AgNPs can up-regulate the nitrogen fixation genes and increases the functioning of arbuscular mycorrhizal fungi in the plant rhizosphere (Mahawar and Prasanna, 2018).

In general, the effect of nanoparticles (NP) interactions with plants or microbes is largely depended on "nano-specific" (type, size, surface charge), doses, species of plant or microbe, and media. Furthermore, there is immense research scope in this unexplored, promising and challenging area and hence, a clear picture of the agro-ecological consequences of AgNPs would necessitate more in-depth perceptive studies in interaction of plant-microbe-nanoparticle systems.

CONCLUSION

In conclusion, this study clearly provides an economical, environmental friendly, and straightforward reproducible approach in AgNPs synthesis employing *P. Emblica* fruit extracts as a reducing, stabilizing, and capping agent. The biosynthesized AgNPs were characterized thoroughly by UV-Visible and Energy Dispersive X-Ray Spectroscopy, X-Ray diffraction, FTIR, TEM, HRTEM and SEM. The FTIR results found several phytochemicals responsible for the rapid reduction of ions, leading to AgNPs formation. Especially, hydroxyl groups oxidation of hydrolysate, which likely stimulated the formation of nanoparticles. In the reaction mixture, biosynthesized AgNPs have been detected as mono-dispersed, rather stable, of comparatively smaller in shape and were adhered with an organic layer, in which proteins participated. Furthermore, this study clearly demonstrated that bacterial growths of Ao strain RS-2 were inhibited by the synthesized AgNPs, while effects varied with the period of incubation and applied concentration. Hence, it is noticeably observed that the MIC of AgNPs at 20 μg/ml was able to affect bacterial growth, cell survival, biofilm formation, and swarming ability. ELISA experiment demonstrated that AgNPs resulted in increased secretion of Hcp proteins in Ao strain RS-2, which might be justified by the damaged membrane in reference to TEM images and results of live/dead cell staining assays. The bacteriostatic effect of AgNPs is generally achieved due to direct interaction between AgNPs and bacterial cells, which caused the destruction of biofilm and cell membrane and released intracellular materials from bacteria. In addition, until now, only *in vitro* studies have been reported and *in vivo* studies are not yet adequately documented, because of the lack of effective environmental safety protocols. However, our results could be used in the future to detect and catalog AgNPs with antibacterial properties to protect crops. Altogether, this project clearly showed the antimicrobial potential of biosynthesized AgNPs to control the pathogen of rice bacterial brown stripe.

AUTHOR CONTRIBUTIONS

MMM, MMS, and BL each made significant contributions to the design of the experiments. MMM, YZ, and KA participated to perform the experiments. MMM, MMS, KA, and YA contributed appreciably to the collection and analysis of data. YA, EI, CY, and BL provided chemicals, materials, and tools for analysis. MMM, BL, and WQ had substantial contributions to the interpretation of data and preparing the manuscript. All authors reviewed and approved final manuscript.

FUNDING

The authors would like to thank the National Natural Science Foundation of China (31872017, 31571971, 31371904, and 31801787), Zhejiang Provincial Natural Science Foundation of China (LZ19C140002), Zhejiang Provincial Project (2017C02002 and 2019C02006), National Key Research and Development Program of China (2017YFD0201104), Shanghai Agricultural Basic Research Project (2014:7-3-1), Key Scientific Technological Project of Ningbo (2016C11017), the Fundamental Research Funds for the Central Universities, Dabeinong Funds for Discipline Development and Talent Training in Zhejiang University, Key Subject Construction Program of Zhejiang for Modern Agricultural Biotechnology and Crop Disease Control (2010DS700124), China Postdoctoral Science Special Foundation (517000-X91803), and Zhejiang Provincial Postdoctoral Foundation (517000-X81802) for providing financial supports.

REFERENCES

Ahmed, S., Saifullah, Ahmad, M., Swami, B. L., and Ikram, S. (2016). Green synthesis of silver nanoparticles using *Azadirachta indica* aqueous leaf extract. *J. Rad. Res. Appl. Sci.* 9, 1–7. doi: 10.1016/j.jrras.2015.06.006

Alavi, M., and Karimi, N. (2018). Antiplanktonic, antibiofilm, antiswarming motility and antiquorum sensing activities of green synthesized Ag-TiO2, TiO2-Ag, Ag-Cu and Cu-Ag nanocomposites against multi-drug-resistant bacteria. *Artif. Cells Nanomed. Biotechnol.* 46(Suppl. 3), S399–S413. doi: 10.1080/21691401.2018.1496923

Amin, M., Anwar, F., Janjua, M. R., Iqbal, M. A., and Rashid, U. (2012). Green synthesis of silver nanoparticles through reduction with *Solanum xanthocarpum* L. berry extract: characterization, antimicrobial and urease inhibitory activities against helicobacter pylori. I. *J. Mol. Sci.* 13, 9923–9941. doi: 10.3390/ijms13089923

Ankamwar, B., Damle, C., Ahmad, A., and Sastry, M. (2005). Biosynthesis of gold and silver nanoparticles using *Emblica officinalis* fruit extract, their phase transfer and transmetallation in an organic solution. *J. Nanosci. Nanotechnol.* 5, 1665–1671. doi: 10.1166/jnn.2005.184

Aziz, N., Faraz, M., Pandey, R., Shakir, M., Fatma, T., Varma, A., et al. (2015). Facile algae-derived route to biogenic silver nanoparticles: synthesis, antibacterial, and photocatalytic properties. *Langmuir* 31, 11605–11612. doi: 10.1021/acs.langmuir.5b03081

Aziz, N., Pandey, R., Barman, I., and Prasad, R. (2016). Leveraging the attributes of mucor hiemalis-derived silver nanoparticles for a synergistic broad-spectrum antimicrobial platform. *Front. Microbiol.* 7:1984. doi: 10.3389/fmicb.2016.01984

Aziz, N., Sherwani, A., Faraz, M., Fatma, T., and Prasad, R. (2019). Illuminating the anticancerous efficacy of a new fungal chassis for silver nanoparticle synthesis. *Front. Chem.* 7:65. doi: 10.3389/fchem.2019.00065

Bahar, O., De La Fuente, L., and Burdman, S. (2010). Assessing adhesion, biofilm formation and motility of *Acidovorax citrulli* using microfluidic flow chambers. *FEMS Microbiol. Lett.* 312, 33–39. doi: 10.1111/j.1574-6968.2010.02094.x

Bhattacharya, D., and Gupta, R. K. (2005). Nanotechnology and potential of microorganisms. *Crit. Rev. Biotechnol.* 25, 199–204. doi: 10.1080/07388550500361994

Bhuyan, T., Mishra, K., Khanuja, M., Prasad, R., and Varma, A. (2015). Biosynthesis of zinc oxide nanoparticles from *Azadirachta indica* for antibacterial and photocatalytic applications. *Mat. Sci. Semicon. Proc.* 32, 55–61. doi: 10.1016/j.mssp.2014.12.053

Bindhu, M. R., and Umadevi, M. (2014). Antibacterial activities of green synthesized gold nanoparticles. *Mater. Lett.* 120, 122–125. doi: 10.1016/j.matlet.2014.01.108

Bogino, P. C., Oliva Mde, L., Sorroche, F. G., and Giordano, W. (2013). The role of bacterial biofilms and surface components in plant-bacterial associations. *Int. J. Mol. Sci.* 14, 15838–15859. doi: 10.3390/ijms140815838

Borase, H. P., Patil, C. D., Salunkhe, R. B., Suryawanshi, R. K., Salunke, B. K., and Patil, S. V. (2014). Transformation of aromatic dyes using green synthesized silver nanoparticles. *Bioprocess Biosyst. Eng.* 37, 1695–1705. doi: 10.1007/s00449-014-1142-4

Burtnick, M. N., and Brett, P. J. (2013). *Burkholderia mallei* and *Burkholderia pseudomallei* cluster 1 type VI secretion system gene expression is negatively regulated by iron and zinc. *PLoS One* 8:e76767. doi: 10.1371/journal.pone.0076767

Chidurala, S. C., Kalagadda, V. R., and Tambur, P. (2016). Antimicrobial activity of pure Cu nano particles synthesized by surfactant varied chemical reduction method. *Environ. Nanotechnol. Monit. Manag.* 6, 88–94. doi: 10.1016/j.enmm.2016.06.004

Cui, Z., Ibrahim, M., Yang, C., Fang, Y., Annam, H., Li, B., et al. (2014). Susceptibility of opportunistic *Burkholderia glumae* to copper surfaces following wet or dry surface contact. *Molecules* 19, 9975–9985. doi: 10.3390/molecules19079975

Cui, Z., Jin, G., Li, B., Kakar, K., Ojaghian, M., Wang, Y., et al. (2015). Gene expression of type VI secretion system associated with environmental survival in *Acidovorax avenae* subsp. avenae by principle component analysis. *Int. J. Mol. Sci.* 16, 22008–22026. doi: 10.3390/ijms160922008

Dang, G. K., Parekar, R. R., Kamat, S. K., Scindia, A. M., and Rege, N. N. (2011). Antiinflammatory activity of *Phyllanthus emblica*, *Plumbago zeylanica* and *Cyperus rotundus* in acute models of inflammation. *Phytother. Res.* 25, 904–908. doi: 10.1002/ptr.3345

Dhand, V., Soumya, L., Bharadwaj, S., Chakra, S., Bhatt, D., and Sreedhar, B. (2016). Green synthesis of silver nanoparticles using *Coffea arabica* seed extract and its antibacterial activity. *Mater. Sci. Eng. C. Mater. Biol. Appl.* 58, 36–43. doi: 10.1016/j.msec.2015.08.018

Dong, Q., Luo, J., Qiu, W., Cai, L., Anjum, S. I., Li, B., et al. (2016). Inhibitory effect of camptothecin against rice bacterial brown stripe pathogen *Acidovorax avenae* subsp. avenae RS-2. *Molecules* 21:E978. doi: 10.3390/molecules21080978

Elbeshehy, E. K. F., Elazzazy, A. M., and Aggelis, G. (2015). Silver nanoparticles synthesis mediated by new isolates of *Bacillus* spp., nanoparticle characterization and their activity against bean yellow mosaic virus and human pathogens. *Front. Microbiol.* 6:453. doi: 10.3389/fmicb.2015.00453

Escárcega-González, C. E., Garza-Cervantes, J. A., Vázquez-Rodríguez, A., Montelongo-Peralta, L. Z., Treviño-González, M. T., Díaz Barriga Castro, E., et al. (2018). In vivo antimicrobial activity of silver nanoparticles produced via a green chemistry synthesis using *Acacia rigidula* as a reducing and capping agent. *Int. J. Nanomed.* 13, 2349–2363. doi: 10.2147/IJN.S160605

Galdiero, S., Falanga, A., Vitiello, M., Cantisani, M., Marra, V., and Galdiero, M. (2011). Silver nanoparticles as potential antiviral agents. *Molecules* 16, 8894–8918. doi: 10.3390/molecules16108894

Ghiuţă, I., Cristea, D., Croitoru, C., Kost, J., Wenkert, R., Vyrides, I., et al. (2018). Characterization and antimicrobial activity of silver nanoparticles, biosynthesized using *Bacillus* species. *Appl. Surf. Sci.* 438, 66–73. doi: 10.1016/j.apsusc.2017.09.163

Gupta, N., Upadhyaya, C. P., Singh, A., Abd-Elsalam, K. A., and Prasad, R. (2018). "Applications of silver nanoparticles in plant protection," in *Nanobiotechnology Applications in Plant Protection*, eds K. A. Abd-Elsalam and R. Prasad (Berlin: Springer), 247–265. doi: 10.1007/978-3-319-91161-8_9

Hayward, A. C. (1960). A method for characterizing *Pseudomonas solanacearum*. *Nature* 186, 405–406. doi: 10.1038/186405a0

Ho, B. T., Basler, M., and Mekalanos, J. J. (2013). Type 6 secretion system-mediated immunity to type 4 secretion system-mediated gene transfer. *Science* 342, 250–253. doi: 10.1126/science.1243745

Hu, Y.-Y., Liu, C.-X., Liu, P., Wu, Z.-Y., Zhang, Y.-D., Xiong, X.-S., et al. (2018). Regulation of gene expression of hcp, a core gene of the type VI secretion system in *Acinetobacter baumannii* causing respiratory tract infection. *J. Med. Microbiol.* 67, 945–951. doi: 10.1099/jmm.0.000753

Iravani, S., Korbekandi, H., Mirmohammadi, S. V., and Zolfaghari, B. (2014). Synthesis of silver nanoparticles: chemical, physical and biological methods. *Res. Pharm. Sci.* 9, 385–406.

Kim, J. S., Kuk, E., Yu, K. N., Kim, J. H., Park, S. J., Lee, H. J., et al. (2007). Antimicrobial effects of silver nanoparticles. *Nanomed. Nanotechnol.* 3, 95–101. doi: 10.1016/j.nano.2006.12.001

Klausen, M., Heydorn, A., Ragas, P., Lambertsen, L., Aaes-Jørgensen, A., Molin, S., et al. (2003). Biofilm formation by *Pseudomonas aeruginosa* wild type, flagella and type IV pili mutants. *Mol. Microbiol.* 48, 1511–1524. doi: 10.1046/j.1365-2958.2003.03525.x

Kowshik, M., Ashtaputre, S., Kharrazi, S., Vogel, W., Urban, J., Kulkarni, S. K., et al. (2003). Extracellular synthesis of silver nanoparticles by a silver-tolerant yeast strain MKY3. *Nanotechnology* 14:95. doi: 10.1088/0957-4484/14/1/321

Krishnaraj, C., Ramachandran, R., Mohan, K., and Kalaichelvan, P. T. (2012). Optimization for rapid synthesis of silver nanoparticles and its effect on phytopathogenic fungi. *Spectrochim. Acta A Mol. Biomol. Spectrosc.* 93, 95–99. doi: 10.1016/j.saa.2012.03.002

Kumar, A., Vemula, P. K., Ajayan, P. M., and John, G. (2008). Silver-nanoparticle-embedded antimicrobial paints based on vegetable oil. *Nat. Mat.* 7, 236–241. doi: 10.1038/nmat2099

Kumar, C. G., and Mamidyala, S. K. (2011). Extracellular synthesis of silver nanoparticles using culture supernatant of *Pseudomonas aeruginosa*. *Colloids Surf. B Biointerfaces* 84, 462–466. doi: 10.1016/j.colsurfb.2011.01.042

Lara, H. H., Ayala-Núñez, N. V., Ixtepan Turrent, L. D. C., and Padilla, R. C. (2010). Bactericidal effect of silver nanoparticles against multidrug-resistant bacteria. *World J. Microbiol. Biotechnol.* 26, 615–621. doi: 10.1007/s11274-009-0211-3

Li, B., Ibrahim, M., Ge, M., Cui, Z., Sun, G., Xu, F., et al. (2014). Transcriptome analysis of *Acidovorax avenae* subsp. avenae cultivated in vivo and co-culture with Burkholderia seminalis. *Sci. Rep.* 4:5698. doi: 10.1038/srep05698

Li, B., Liu, B., Shan, C., Ibrahim, M., Lou, Y., Wang, Y., et al. (2013). Antibacterial activity of two chitosan solutions and their effect on rice bacterial leaf blight and leaf streak. *Pest Manag. Sci.* 69, 312–320. doi: 10.1002/ps.3399

Liu, H., Tian, W.-X., Ibrahim, M., Li, B., Zhang, G.-Q., Zhu, B., et al. (2012). Characterization of pilP, a gene required for twitching motility, pathogenicity, and biofilm formation of *Acidovorax avenae* subsp. avenae RS-1. *Eur. J. Plant Pathol.* 134, 551–560. doi: 10.1007/s10658-012-0038-x

Lou, M. M., Zhu, B., Muhammad, I., Li, B., Xie, G. L., Wang, Y. L., et al. (2011). Antibacterial activity and mechanism of action of chitosan solutions against apricot fruit rot pathogen *Burkholderia seminalis*. *Carbohyd. Res.* 346, 1294–1301. doi: 10.1016/j.carres.2011.04.042

Lü, J.-M., Wang, X., Marin-Muller, C., Wang, H., Lin, P. H., Yao, Q., et al. (2009). Current advances in research and clinical applications of PLGA-based nanotechnology. *Expert Rev. Mol. Diagn.* 9, 325–341. doi: 10.1586/erm.09.15

Mahawar, H., and Prasanna, R. (2018). Prospecting the interactions of nanoparticles with beneficial microorganisms for developing green technologies for agriculture. *Environ. Nanotech. Monitor Manage* 10, 477–485. doi: 10.1016/j.enmm.2018.09.004

Mahmoud, W. M., Abdelmoneim, T. S., and Elazzazy, A. M. (2016). The impact of silver nanoparticles produced by *Bacillus pumilus* as antimicrobial and nematicide. *Front. Microbiol.* 7:1746. doi: 10.3389/fmicb.2016.01746

Mandal, S., Phadtare, S., and Sastry, M. (2005). Interfacing biology with nanoparticles. *Curr. Appl. Phys.* 5, 118–127. doi: 10.1016/j.cap.2004.06.006

Manikandan, R., Beulaja, M., Thiagarajan, R., Palanisamy, S., Goutham, G., Koodalingam, A., et al. (2017). Biosynthesis of silver nanoparticles using aqueous extract of *Phyllanthus acidus* L. fruits and characterization of its anti-inflammatory effect against h2o2 exposed rat peritoneal macrophages. *Proc. Biochem.* 55, 172–181. doi: 10.1016/j.procbio.2017.01.023

Mansfield, J., Genin, S., Magori, S., Citovsky, V., Sriariyanum, M., Ronald, P., et al. (2012). Top 10 plant pathogenic bacteria in molecular plant pathology. *Mol. Plant. Pathol.* 13, 614–629. doi: 10.1111/j.1364-3703.2012.00804.x

Marambio-Jones, C., and Hoek, E. M. V. (2010). A review of the antibacterial effects of silver nanomaterials and potential implications for human health and the environment. *J. Nanopart. Res.* 12, 1531–1551. doi: 10.1007/s11051-010-9900-y

Masum, M. M. I., Liu, L., Yang, M., Hossain, M. M., Siddiqa, M. M., Supty, M. E., et al. (2018). Halotolerant bacteria belonging to operational group *Bacillus amyloliquefaciens* in biocontrol of the rice brown stripe pathogen *Acidovorax oryzae*. *J. Appl. Microbiol.* doi: 10.1111/jam.14088 [Epub ahead of print].

Masum, M. M. I., Yang, Y., Li, B., Olaitan, O. S., Chen, J., Zhang, Y., et al. (2017). Role of the genes of type VI secretion system in virulence of rice bacterial brown stripe pathogen *Acidovorax avenae* subsp. avenae Strain RS-2. *Int. J. Mol. Sci.* 18, E2024. doi: 10.3390/ijms18102024

Mohanpuria, P., Rana, N. K., and Yadav, S. K. (2008). Biosynthesis of nanoparticles: technological concepts and future applications. *J. Nanopart. Res.* 10, 507–517. doi: 10.1007/s11051-007-9275-x

Mougous, J. D., Cuff, M. E., Raunser, S., Shen, A., Zhou, M., Gifford, C. A., et al. (2006). A virulence locus of *Pseudomonas aeruginosa* encodes a protein secretion apparatus. *Science* 312, 1526–1530. doi: 10.1126/science.1128393

Nadagouda, M. N., Speth, T. F., and Varma, R. S. (2011). Microwave-assisted green synthesis of silver nanostructures. *Acc. Chem. Res.* 44, 469–478. doi: 10.1021/ar1001457

Nakhjavani, M., Mohsen Sarafraz, M., Nikkhah, V., Shoja, S., and Sarafraz, M. (2017). Green synthesis of silver nanoparticles using green tea leaves: experimental study on the morphological, rheological and antibacterial behaviour. *Heat Mass Transfer* 53, 3201–3209. doi: 10.1007/s00231-017-2065-9

Ogunyemi, S. O., Fang, Y., Qiu, W., Li, B., Chen, J., Yang, M., et al. (2019). Role of type IV secretion system genes in virulence of rice bacterial brown stripe pathogen *Acidovorax oryzae* strain RS-2. *Microb. Pathog.* 126, 343–350. doi: 10.1016/j.micpath.2018.11.017

Oves, M., Aslam, M., Rauf, M. A., Qayyum, S., Qari, H. A., Khan, M. S., et al. (2018). Antimicrobial and anticancer activities of silver nanoparticles synthesized from the root hair extract of *Phoenix dactylifera*. *Mater. Sci. Eng. C Mater. Biol. Appl.* 89, 429–443. doi: 10.1016/j.msec.2018.03.035

Oves, M., Khan, M. S., Zaidi, A., Ahmed, A. S., Ahmed, F., Ahmad, E., et al. (2013). Antibacterial and cytotoxic efficacy of extracellular silver nanoparticles biofabricated from chromium reducing novel OS4 strain of *Stenotrophomonas maltophilia*. *PLoS One* 8:e59140. doi: 10.1371/journal.pone.0059140

Pal, S., Tak, Y. K., and Song, J. M. (2007). Does the antibacterial activity of silver nanoparticles depend on the shape of the nanoparticle? A study of the Gram-negative bacterium *Escherichia coli*. *Appl. Environ. Microbiol.* 73, 1712–1720. doi: 10.1128/AEM.02218-06

Parashar, U. K., Kumar, V., Bera, T., Saxena, P. S., Nath, G., Srivastava, S. K., et al. (2011). Study of mechanism of enhanced antibacterial activity by green synthesis of silver nanoparticles. *Nanotechnology* 22:415104. doi: 10.1088/0957-4484/22/41/415104

Park, J., Joo, J., Kwon, S. G., Jang, Y., and Hyeon, T. (2007). Synthesis of monodisperse spherical nanocrystals. *Angew. Chem. Int. Ed. Engl.* 46, 4630–4660. doi: 10.1002/anie.200603148

Pientaweeratch, S., Panapisal, V., and Tansirikongkol, A. (2016). Antioxidant, anti-collagenase and anti-elastase activities of *Phyllanthus emblica*, *Manilkara zapota* and silymarin: an in vitro comparative study for anti-aging applications. *Pharm. Biol.* 54, 1865–1872. doi: 10.3109/13880209.2015.1133658

Prabhu, S., and Poulose, E. K. (2012). Silver nanoparticles: mechanism of antimicrobial action, synthesis, medical applications, and toxicity effects. *Int. Nano Lett.* 2:32. doi: 10.1186/2228-5326-2-32

Prasad, R. (2014). Synthesis of Silver Nanoparticles in Photosynthetic Plants. *J. Nanopart.* 2014:8. doi: 10.1155/2014/963961

Qayyum, S., Oves, M., and Khan, A. U. (2017). Obliteration of bacterial growth and biofilm through ROS generation by facilely synthesized green silver nanoparticles. *PLoS One* 12:e0181363. doi: 10.1371/journal.pone.0181363

Rai, M., and Ingle, A. (2012). Role of nanotechnology in agriculture with special reference to management of insect pests. *Appl. Microbiol. Biotechnol.* 94, 287–293. doi: 10.1007/s00253-012-3969-4

Rajeshkumar, S., and Malarkodi, C. (2014). In vitro antibacterial activity and mechanism of silver nanoparticles against foodborne pathogens. *Bioinorg. Chem. Appl.* 2014:581890. doi: 10.1155/2014/581890

Ramesh, P. S., Kokila, T., and Geetha, D. (2015). Plant mediated green synthesis and antibacterial activity of silver nanoparticles using *Emblica officinalis* fruit extract. *Spectrochim. Acta A* 142, 339–343. doi: 10.1016/j.saa.2015.01.062

Rogers, J. V., Parkinson, C. V., Choi, Y. W., Speshock, J. L., and Hussain, S. M. (2008). A preliminary assessment of silver nanoparticle inhibition of monkeypox virus plaque formation. *Nanoscale Res. Lett.* 3:129. doi: 10.1007/s11671-008-9128-2

Sastry, R. K., Rashmi, H. B., Rao, N. H., and Ilyas, S. M. (2010). Integrating nanotechnology into agri-food systems research in India: a conceptual framework. *Technol. Forecast. Soc.* 77, 639–648. doi: 10.1016/j.techfore.2009.11.008

Selvi, B. C. G., Madhavan, J., and Santhanam, A. (2016). Cytotoxic effect of silver nanoparticles synthesized fromPadina tetrastromaticaon breast cancer cell line. *Adv. Nat. Sci.: Nanosci. Nanotechnol.* 7:035015. doi: 10.1088/2043-6262/7/3/035015

Shakya, D. D., Vinther, F., and Mathur, S. B. (1985). World wide distribution of a bacterial stripe pathogen of rice identified as *Pseudomonas avenae*. *J. Phytopathol.* 114, 256–259. doi: 10.1111/j.1439-0434.1985.tb00850.x

Sharma, V. K., Yngard, R. A., and Lin, Y. (2009). Silver nanoparticles: green synthesis and their antimicrobial activities. *Adv. Colloid. Interfac.* 145, 83–96. doi: 10.1016/j.cis.2008.09.002

Singh, S., Bharti, A., and Meena, V. K. (2015). Green synthesis of multi-shaped silver nanoparticles: optical, morphological and antibacterial properties. *J. Mater. Sci. Mater. Electron.* 26, 3638–3648. doi: 10.1007/s10854-015-2881-y

Slutzki, M., Barak, Y., Reshef, D., Schueler-Furman, O., Lamed, R., and Bayer, E. A. (2012). Indirect ELISA-based approach for comparative measurement of high-affinity cohesin-dockerin interactions. *J. Mol. Recognit.* 25, 616–622. doi: 10.1002/jmr.2178

Socol, Y., Abramson, O., Gedanken, A., Meshorer, Y., Berenstein, L., and Zaban, A. (2002). Suspensive electrode formation in pulsed sonoelectrochemical synthesis of silver nanoparticles. *Langmuir* 18, 4736–4740. doi: 10.1021/la015689f

Solanki, J. N., and Murthy, Z. V. P. (2010). Highly monodisperse and sub-nano silver particles synthesis via microemulsion technique. *Colloids Surfaces A Physicochem. Eng. Aspects* 359, 31–38. doi: 10.1016/j.colsurfa.2010.01.058

Soman, S., and Ray, J. G. (2016). Silver nanoparticles synthesized using aqueous leaf extract of *Ziziphus oenoplia* (L.) Mill: characterization and assessment of antibacterial activity. *J. Photochem. Photobiol. B Biol.* 163, 391–402. doi: 10.1016/j.jphotobiol.2016.08.033

Song, W. Y., Kim, H. M., Hwang, C. Y., and Schaad, N. W. (2004). Detection of *Acidovorax avenae* ssp. avenae in Rice Seeds Using BIO-PCR. *J. Phytopathol.* 152, 667–676. doi: 10.1111/j.1439-0434.2004.00914.x

Sosa, I. O., Noguez, C., and Barrera, R. G. (2003). Optical properties of metal nanoparticles with arbitrary shapes. *J. Phys. Chem. B* 107, 6269–6275. doi: 10.1021/jp0274076

Suman, T. Y., Radhika Rajasree, S. R., Kanchana, A., and Elizabeth, S. B. (2013). Biosynthesis, characterization and cytotoxic effect of plant mediated silver nanoparticles using *Morinda citrifolia* root extract. *Colloids Surf B. Biointerfaces* 106, 74–78. doi: 10.1016/j.colsurfb.2013.01.037

Tian, Y., Zhao, Y., Wu, X., Liu, F., Hu, B., and Walcott, R. R. (2015). The type VI protein secretion system contributes to biofilm formation and seed-to-seedling transmission of *Acidovorax citrulli* on melon. *Mol. Plant Pathol.* 16, 38–47. doi: 10.1111/mpp.12159

Tippayawat, P., Phromviyo, N., Boueroy, P., and Chompoosor, A. (2016). Green synthesis of silver nanoparticles in *Aloe vera* plant extract prepared by a hydrothermal method and their synergistic antibacterial activity. *PeerJ* 4:e2589. doi: 10.7717/peerj.2589

Tran, T. T. T., Vu, T. T. H., and Nguyen, T. H. (2013). Biosynthesis of silver nanoparticles using *Tithonia diversifolia* leaf extract and their antimicrobial activity. *Material. Lett.* 105, 220–223. doi: 10.1016/j.matlet.2013.04.021

Vankar, P. S., and Shukla, D. (2012). Biosynthesis of silver nanoparticles using lemon leaves extract and its application for antimicrobial finish on fabric. *Appl. Nanosci.* 2, 163–168. doi: 10.1007/s13204-011-0051-y

Vyshnava, S. S., Kanderi, D. K., Panjala, S. P., Pandian, K., Bontha, R. R., Goukanapalle, P. K. R., et al. (2016). Effect of silver nanoparticles against the formation of biofilm by *Pseudomonas aeruginosa* an in silico approach. *Appl. Biochem. Biotech.* 180, 426–437. doi: 10.1007/s12010-016-2107-7

Wu, H. Y., Chung, P. C., Shih, H. W., Wen, S. R., and Lai, E. M. (2008). Secretome analysis uncovers an Hcp-family protein secreted via a type VI secretion system in *Agrobacterium tumefaciens*. *J. Bacteriol.* 190, 2841–2850. doi: 10.1128/JB.01775-07

Xie, G. L., Zhang, G. Q., Liu, H., Lou, M. M., Tian, W. X., Li, B., et al. (2011). Genome sequence of the rice-pathogenic bacterium *Acidovorax avenae* subsp. avenae RS-1. *J. Bacteriol.* 193, 5013–5014. doi: 10.1128/JB.05594-11

Yamal, G., Sharmila, P., Rao, K. S., and Pardha-Saradhi, P. (2013). Inbuilt potential of YEM medium and its constituents to generate Ag/Ag(2)O nanoparticles. *PLoS One* 8:e61750. doi: 10.1371/journal.pone.0061750

Zarei, M., Jamnejad, A., and Khajehali, E. (2014). Antibacterial effect of silver nanoparticles against four foodborne pathogens. *Jundishapur J. Microbiol.* 7:e8720. doi: 10.5812/jjm.8720

Zhang, X. F., Liu, Z. G., Shen, W., and Gurunathan, S. (2016). Silver nanoparticles: synthesis, characterization, properties, applications, and therapeutic approaches. *Int. J. Mol. Sci.* 17:E1534. doi: 10.3390/ijms17091534

Zhang, Y., Zhang, F., Li, B., Yang, Y. Z., Ibrahim, M., Fang, Y. S., et al. (2017). Characterization and functional analysis of clpB gene from *Acidovorax avenae* subsp. avenae RS-1. *Plant Pathol.* 66, 1369–1379. doi: 10.1111/ppa.12685

Conflict of Interest Statement: The authors declare that the research was conducted in the absence of any commercial or financial relationships that could be construed as a potential conflict of interest.

frontiers
in Microbiology

ORIGINAL RESEARCH
published: 30 April 2019
doi: 10.3389/fmicb.2019.00931

Phytofabrication of Selenium Nanoparticles From *Emblica officinalis* Fruit Extract and Exploring Its Biopotential Applications: Antioxidant, Antimicrobial, and Biocompatibility

Lokanadhan Gunti[1], Regina Sharmila Dass[1]* and Naveen Kumar Kalagatur[2,3]

[1] Molecular Fungal Genetics and Mycotoxicology Research Unit, Department of Microbiology, Pondicherry University, Puducherry, India, [2] Food Microbiology Division, Defence Food Research Laboratory, Mysuru, India, [3] Immunology and Toxicology Division, DRDO-BU Center for Life Sciences, Coimbatore, India

OPEN ACCESS

Edited by:
Gerson Nakazato,
State University of Londrina, Brazil

Reviewed by:
Ren-You Gan,
Shanghai Jiao Tong University, China
Venkataramana M.,
Lorven Biologics Private Limited, India

***Correspondence:**
Regina Sharmila Dass
reginadass@gmail.com

Specialty section:
This article was submitted to Antimicrobials, Resistance and Chemotherapy, a section of the journal Frontiers in Microbiology

Received: *30 January 2019*
Accepted: *12 April 2019*
Published: *30 April 2019*

Citation:
Gunti L, Dass RS and Kalagatur NK (2019) Phytofabrication of Selenium Nanoparticles From Emblica officinalis Fruit Extract and Exploring Its Biopotential Applications: Antioxidant, Antimicrobial, and Biocompatibility. Front. Microbiol. 10:931. doi: 10.3389/fmicb.2019.00931

In the present study, phytofabricated selenium nanoparticles (PF-SeNPs) were prepared from aqueous fruit extract of *Emblica officinalis* in a facile, green, economic, tactic and eco-friendly way. The aqueous fruit extract of *E. officinalis* was found to be rich with various secondary metabolites including phenolics (59.18 ± 2.91 mg gallic acid equivalents/g), flavonoids (38.50 ± 2.84 mg catechin equivalents/g), and tannins (44.28 ± 3.09 mg tannic acid equivalents/g) and determined that highly appropriate for the biosynthesis of nanoparticles. The facile phytofabrication of PF-SeNPs was confirmed by UV-visible and FTIR spectroscopic analysis. The XRD pattern and Raman spectroscopy showed that synthesized PF-SeNPs were amorphous in nature. The Zeta potential analysis confirmed that PF-SeNPs were negatively charged (−24.4 mV). The DLS analysis revealed that PF-SeNPs were in nano size and less aggregated with poly-dispersity index of less than 0.2. The SEM images depicted that PF-SeNPs were spherical in shape. The EDX analysis revealed that PF-SeNPs were constituted with Se (61.60%), C (29.96%), and O (4.41%). The HR-TEM analysis determined that PF-SeNPs were in nano size with an average diameter of 15–40 nm. The PF-SeNPs have offered fascinating bio-potential applications, such as antioxidant, antimicrobial and biocompatibility. They have also exhibited dose-dependent free radical scavenging activity, and EC50 was determined as 15.67 ± 1.41 and 18.84 ± 1.02 μg/mL for DPPH and ABTS assays, respectively. The PF-SeNPs has also shown the wide range of antimicrobial activity on foodborne pathogens, and it was found to be highly efficient on fungi followed by Gram-positive and Gram-negative bacteria. The biocompatibility of PF-SeNPs was assessed in N2a cells with much higher IC50 value (dose required to inhibit 50% of cell viability) compared to sodium selenite. Also, mitochondrial membrane potential (MMP) and caspase-3 were much less altered on treatment of PF-SeNPs related to sodium selenite. The cytotoxic studies clearly determined that PF-SeNPs was much less toxic and safer related to sodium selenite. Thus, PF-SeNPs could find suitable application as antioxidant and antimicrobial agent in food, biomedical, and pharmaceutical industry.

Keywords: phytofabrication, selenium nanoparticles, *Emblica officinalis*, antioxidant activity, antimicrobial activity, biocompatibility

INTRODUCTION

Antibiotic resistance and food safety have become two of the major health apprehensions for the public, government, and regulatory agencies in the last two decades (Sundararaj et al., 2019). The infectious diseases are the primary causes of deaths that occur worldwide. Ever since the advent of antibiotics, morbidity, and mortality rate of infectious diseases are being mitigated. However, nowadays, there is an upsurge in antibiotic-resistant microorganisms, which is an emerging utmost concern. Also, Food and Agriculture Organization (FAO) of the United Nations estimate a loss of 25% of the agronomic products worldwide owed to fungal infestation and is measured as major threat to food industry (Bryden, 2007; Kalagatur et al., 2018c,d). Particularly, fungal secondary metabolites (mycotoxins) are highly poisonous and could cause a variety of ailments in humans and farm animals (Mudili et al., 2014). Further, the use of synthetic food additives is one of the foremost concerns in food industries because of their ability to incite digestive disorders and carcinogenicity (El-Wahab and Moram, 2013). Thus, there is a necessity to design substitutive compounds with antioxidant and antimicrobial properties that do not induce antimicrobial resistance and detrimental effects on human and animal health and can be used by the food industries in compliance to food safety.

The recent boom in nanotechnology has fortunately provided us an indefinite range of applications in biomedicine and food science. Particularly, nanoparticles have the extensive range of applications in biological sciences, i.e., pharmaceuticals, medical diagnosis, cosmetics, agriculture and food industry, etc. (Kalagatur et al., 2018a; Siddaiah et al., 2018). In the last decade, several pharmaceutical companies have obtained the consent of nano-formulation based drugs and diagnostics from the Food and Drug Administration (FDA) and World Health Organization (WHO) (Mittal et al., 2014). Furthermore, nanomaterials have also found an appropriate role in the agro-food-feed sectors; for example, crop production, nutritional properties, enhancement of water quality, food packaging, etc.

The most routinely synthesized nano-antimicrobials are made up of silver, gold, titanium, zinc, cadmium, gadolinium, selenium, copper, etc. However, due to the high cost of silver, gold and copper metals, their use in biomedical and food sciences is limited. Also, cadmium, titanium, gadolinium, and zinc are unacceptable due to their high toxic nature (Zuverza-Mena et al., 2017; Sohal et al., 2018). Among the nanomaterials, selenium nanoparticles (SeNPs) have drawn attention and are widely accepted in biomedicine and food science due to their low toxicity and high biocompatibility (Tran et al., 2015). Captivatingly, selenium is a key factor in the formation of selenoproteins, which are vital antioxidants like thioredoxin reductase, glutathione peroxidase, and deiodinase (Rotruck et al., 1973). Selenium is one of the trace minerals, which is essential for the maintenance of human health, with approximately 40–300 mg as daily nutritional supplement for an adult (Rayman, 2005). Further, SeNPs have potent free radicals scavenging effects, both in *in vitro* as well as *in vivo* conditions and protect DNA from oxidative damage (Battin et al., 2011). Along with the aforementioned properties, several studies have reported that the SeNPs possess anti-carcinogenic activity against several types of cancers (Huang et al., 2013). Also, SeNPs show unique antimicrobial activities against *Candida albicans* (Kheradmand et al., 2014), *Proteus mirabilis* and *Pseudomonas aeruginosa* (Shakibaie et al., 2015). Accordingly, SeNPs are highly acceptable and recommended for use in biomedical and food science.

Selenium nanoparticles can be synthesized by physical, chemical, and biological approaches. The chemical and physical methods need high thermal conditions, hazardous chemicals and acidic pH, which is extremely toxic and unsafe for biological applications (Iranifam et al., 2013). Whereas, biological synthesis of SeNPs is safe, eco-friendly, inexpensive and non-toxic (Wadhwani et al., 2016). Moreover, biologically made SeNPs are more stable due to the natural coating of organic materials over the surface, which do not allow nanoparticles to be aggregated with the time period (Park et al., 2011). The use of plant extracts for the synthesis of nanoparticles might be beneficial over microbial synthesis by eliminating the extravagant procedures for maintaining cultures. Despite the fact, that a large number of plants are reported for nanoparticle synthesis, only few reports are available on phytogenic synthesis of SeNPs. These studies include synthesis using leaf extract of *Capsicum annuum* (Li et al., 2007), seed extract of fenugreek (Ramamurthy et al., 2013), leaf extract of lemon (Prasad et al., 2013), dried fruit extract of *Vitis vinifera* (Sharma et al., 2014), leaf extract of *Terminalia arjuna* (Prasad and Selvaraj, 2014), flower extracts of *Bougainvillea spectabilis* (Deepa and Ganesan, 2014), leaf extract of *Leucas lavandulifolia* (Kirupagaran et al., 2016), leaf extract of *Clausena dentate* (Sowndarya et al., 2017), aqueous extract of *Allium sativum* (Anu et al., 2017), leaf extracts of *Diospyros montana* (Kokila et al., 2017), leaf extracts of *Psidium guajava* (Alam et al., 2018), polysaccharides from *Lycium barbarum* and green tea extracts (Zhang et al., 2018). In this study, we report for the first time, a quick synthesis of phytofabricated selenium nanoparticles (PF-SeNPs) from fruit extract of *Emblica officinalis* and establishment of biocompatibility of PF-SeNPs relating with cytotoxicity of precursor sodium selenite.

Emblica officinalis is also known as *Phyllanthus emblica*, which belongs to the family Phyllanthaceae and genus *Phyllanthus*, whose edible fruits are widely used in Indian Ayurvedic medicine (Dharmananda, 2003). There are abundant benefits of *E. officinalis,* which include, antibacterial (Philip et al., 2012), antifungal (Mehmood et al., 1999), antioxidant and cardioprotective activities (Golechha et al., 2012). The *E. officinalis* fruits are a rich source of hydrolyzable phenolics, flavonoids, and tannins that play a key role in reducing and regulating the shape of nanoparticles (Ankamwar et al., 2005).

In the present study, phytofabricated-SeNPs (PF-SeNPs) were synthesized using aqueous fruit extracts of *E. officinalis* by green, low-cost and simple reduction method. The as-synthesized PF-SeNPs were preliminarily characterized and confirmed by UV–visible spectroscopy. The particle sizes of PF-SeNPs were determined by dynamic light scattering (DLS) analysis. The nature of PF-SeNPs was confirmed by Fourier transform infrared spectroscopy (FTIR), Raman spectroscopy, and X-ray diffraction (XRD) analysis. The shape, size, and chemical composition of PF-SeNPs were determined by scanning electron microscopy (SEM), high-resolution transmission electron microscopy (HR-TEM), and energy dispersive X-ray analysis (EDX) analysis, respectively. In conclusion, potential biological applications of PF-SeNPs were explored by antibacterial, antifungal, antioxidant and biocompatibility assays.

MATERIALS AND METHODS

Chemicals and Reagents

Sodium selenite (98%), 2,2-diphenyl-1-picrylhydrazyl (DPPH), 3-(4,5-dimethylthiazol-2-yl)-2,5-diphenyltetrazolium bromide) (MTT), Tween 80, methanol, acetate buffer, tetracycline, nystatin, rhodamine 123, caspase-3 kit, Dulbecco's modified Eagle media (DMEM), Folin-Ciocalteu reagent, 2,2-azinobis-(3-ethylbenzothiazoline-6-sulfonate) (ABTS), Dulbecco's phosphate buffered saline pH 7.4 (DPBS) and fetal bovine serum (FBS) were obtained from Sigma-Aldrich (Bengaluru, India). The microbial culture media, including Muller Hinton Broth (MHB), Muller Hinton Agar (MHA), brain heart infusion (BHI) broth, sabouraud dextrose agar (SDA), and sabouraud dextrose broth (SDB) were obtained from HiMedia (Mumbai, India). The live/dead dual staining assay kit was purchased from Thermo Fisher Scientific (Bengaluru, India). The plastic and glassware were obtained from Nunc and Borosil, respectively (Bengaluru, India). The other chemicals used in the study were belonged to analytical grade and were obtained from Merck Millipore (Bengaluru, India).

Collection and Preparation of *E. officinalis* Fruit Aqueous Extract

The fresh fruits of *E. officinalis* were collected from the local agriculture market, Pondicherry, India. They were washed thoroughly with distilled water, deseeded using a sterile knife and the edible part of the fruit was used to prepare fruit extract. Briefly, 100 g of edible fruit was ground well in a mortar using water (w/v, 1:2). The solution obtained was filtered through Whatman No. 1 filter paper, stored at 4°C and further used for chemical profile analysis and nanoparticle preparation.

Chemical Profile of Aqueous Fruit Extract of *E. officinalis*

Plants and its sources contain a wide range of secondary metabolites, and these were considered as potential reducing substances for biogenic production of nanoparticles (Akhtar et al., 2013). The total phenolic, flavonoid and tannin contents of *E. officinalis* fruit extract were determined in order to evaluate its suitability in biogenic production of nanoparticles.

Estimation of Total Phenolics

The total phenolic content of *E. officinalis* fruit extract was determined by Folin-Ciocalteu assay (Kalagatur et al., 2018b). Gallic acid was considered as a reference phenolic compound and the obtained result was stated as mg of gallic acid equivalents per g of *E. officinalis* fruit extract (mg GAE/g). Briefly, 0.5 mL of fruit extract was diluted thrice with distilled water and blended with 0.5 mL of 7.5% sodium carbonate solution and 0.25 mL of Folin-Ciocalteu reagent. The obtained blend was incubated for 30 min at 27 ± 2°C under dark and absorbance was recorded at 765 nm using a plate reader (Synergy H1, BioTek, United States).

Estimation of Total Flavonoids

The total flavonoid content of *E. officinalis* fruit extract was determined by aluminum chloride colorimetric assay (Kalagatur et al., 2018b). Catechin was considered as a reference flavonoid compound and the obtained result was stated as mg of catechin equivalents per g of *E. officinalis* fruit extract (mg CE/g). Briefly, 0.5 mL of fruit extract was blended with 70 μL of sodium nitrite solution (5%) and incubated at 27 ± 2°C for 5 min. Later, the mixture was blended with 0.5 mL of sodium hydroxide (1 M), 0.15 mL of aluminum chloride (10%) and 1.3 mL of deionized water. The reaction mixture was incubated for 5 min at 27 ± 2°C and absorbance was measured at 415 nm using a plate reader (Synergy H1, BioTek, United States).

Estimation of Total Tannins

Total tannin content was estimated spectrophotometrically as per procedure of Price and Butler (1977). Tannic acid was considered as reference tannin compound and the obtained result was stated as mg of tannic acid equivalents per g of *E. officinalis* fruit extract (mg TAE/g). Briefly, 4 mL of fruit extract was blended with 3 mL of 0.1 M $FeCl_3$ in 0.1 N HCl and 3 mL of 0.008 M $K_3Fe(CN)$ and incubated in the dark for 15 min at 27 ± 2°C. Later, the optical density was measured at 720 nm using a multimode reader (Synergy H1, BioTek, United States).

Synthesis of Phytofabricated Selenium Nanoparticles (PF-SeNPs)

Briefly, 2 mL of aqueous fruit extract of *E. officinalis* was added dropwise into 10 mL of 10 mM sodium selenite under magnetic stirring condition. Next, reaction mixture was allowed for reduction in dark condition at 27 ± 2°C and 120 rpm on orbital shaker for 24 h and observed for color change.

Characterization of Biogenic PF-SeNPs

UV–Visible Spectroscopy

The bio-reduction of sodium selenite by aqueous fruit extract of *E. officinalis* was monitored by observing the color change. After the formation of brick-red color, absorbance of the nanoparticles was measured at wavelength ranging between 200 and 800 nm with 1 nm wavelength intervals using UV–visible spectrophotometer (Agilent-Cary 60, United States).

Fourier Transform Infrared (FTIR) Spectroscopic Analysis

Fourier Transform Infrared spectrum was used in order to confirm the presence of various reducing and stabilizing functional groups of metabolites in aqueous fruit extract of *E. officinalis* and to detect their possible role in fabrication of PF-SeNPs. Briefly, PF-SeNPs solution was dried out and ground into a homogeneous powder, and spectra were attained at 400–4,000 cm^{-1} wavenumbers against potassium bromide background using the spectrophotometer (Thermo Nicolet 6700, United States).

X-Ray Diffraction Analysis

The phase structure of PF-SeNPs was observed by XRD analysis using X'Pert PRO diffractometer in Debye-Scherrer configuration (PANalytical, Spectris Technologies Pvt. Ltd., India) attached with Cu anode as a source of X-rays and Ni filter was used to attenuate pipeline of Cu Kβ. The Cu Kα radiation was generated at a wavelength of 1.5406 Å by operating the instrument at 40 kV and 40 mA. The measurement was recorded by using a 0.5 mm glass capillary over a 2θ range of 10–80° with a scanning rate of 0.05° at a time interval of 1 s. The Scherrer equation was applied to calculate the average dimension (L_a) of crystalline domains,

$$L_a = \frac{K\lambda}{\beta\cos(\theta_{Bragg})}$$

Where, L_a was the average dimension of crystalline domains, K was the non-dimensional shape factor and usually considered as 0.9, β was the full width at half maximum (FWHM) in 2θ value, and λ was the wavelength at which Cu $K\alpha$ radiation was generated.

Raman Spectroscopic Analysis

Raman spectroscopy was used to explore the nature of nanomaterials, which is recognized as a perfect technique that even detects slight variations. Briefly, dried PF-SeNPs were placed as a thin film on aluminum foil and spectra were recorded at 785 nm excitation and spectral range of 150–1,200 cm^{-1} with an interval of 10 s using Renishaw's in Via Raman microscope (Renishaw, India).

Dynamic Light Scattering and Zeta-Potential Analysis

This technique was used to determine the hydrodynamic size of particles by focusing a monochromatic light on to the solution, which causes a Doppler shift. Once the laser light hits the moving particles, it changes the wavelength of the incoming light and scatters the light at an angle. This angle of scattered light is inversely propositional to the size of the particle. The size distribution of PF-SeNPs was monitored at 27 ± 2°C using Zetasizer (Nano ZS, Malvern Instrument, United Kingdom). The Zeta-potential of the nanoparticles was measured to find the surface charge on it.

Scanning Electron Microscopic and Energy-Dispersive X-Ray Analysis

Scanning electron microscopy was carried to know the shape, surface morphology and size of the nanoparticles. Briefly, PF-SeNPs suspension was air dried before loading them to sample holders. Later, PF-SeNPs were coated with gold using sputter coater in a vacuum and further, images were taken at 20 kV and different magnifications using SEM (Icon Analytical, Quanta 250, FEI, United States). Energy-dispersive X-ray (EDX) analysis was performed at 20 kV in order to know the elemental compositions of nanoparticles. The PF-SeNPs were dissolved in absolute ethanol and one drop of the suspension was placed on a sample loading grid, evenly dried and element analysis was performed.

High-Resolution Transmission Electron Microscopy Analysis

The shape and size of PF-SeNPs was determined by HR-TEM analysis. Briefly, one mg of PF-SeNPs was suspended in 1 mL of ethanol and subjected to sonication for 15 min. Subsequently, a drop of supernatant dispersion was collected and placed on the copper grid, and images were captured at different magnifications using HR-TEM (JEM-2100, JEOL Ltd., Tokyo, Japan).

Biopotential Applications of PF-SeNPs

Antioxidant Assay

Free radical scavenging activity of PF-SeNPs was determined by DPPH and ABTS radical scavenging assays as per earlier reported methods (Kumar et al., 2016; Sellamani et al., 2016).

In DPPH radical scavenging assay, various concentrations of PF-SeNPs (up to 100 μg) was blended with 0.5 mL of DPPH solution (250 μM in methanol) and 1 mL of 0.1 M acetate buffer and final volume was made up to 3 mL with methanol. The reaction mixture was shaken thoroughly and left in the dark for 30 min at 27 ± 2°C. Then the absorbance was measured at 517 nm using UV-Visible spectrophotometer (Agilent-Cary 60, United States). The reaction mixture without PF-SeNPs was used as control and ascorbic acid was used as standard.

In ABTS radical scavenging assay, ABTS radical solution was produced by reaction between 7 mM of ABTS and 2.45 mM of potassium persulfate (1:1) in water and incubated at 27 ± 2°C under the dark for 12 h. Further, the optical density of ABTS radical solution was adjusted to 0.7 at 734 nm by diluting with methanol. Subsequently, various concentration of PF-SeNPs (up to 100 μg) was added to 3 mL of ABTS solution (0.7 optical density) and incubated at 27 ± 2°C for 6 min under dark and optical density was measured at 734 nm using UV-visible spectrophotometer (Agilent-Cary 60, United States). The ABTS solution without test sample was used as control and ascorbic acid was used as standard.

The DPPH and ABTS radical scavenging activity of the test sample was calculated using the formula,

$$\text{DPPH (or) ABTS radical scavenging activity (\%)} = \frac{(1 - A_{TS})}{A_C} \times 100$$

Where, A_{TS} and A_{C} were absorbance of the test sample and control, respectively.

Antimicrobial Activity

Microbial culture maintenance

Antimicrobial activity of PF-SeNPs was carried out on foodborne pathogens, including bacteria (*Escherichia coli* MTCC 41, *Listeria monocytogenes* MTCC 657, *Staphylococcus aureus* MTCC 96, and *Enterococcus faecalis* MTCC 439) and fungi (*Aspergillus brasiliensis* MTCC 1344, *A. flavus* MTCC 1883, *A. oryzae* MTCC 634, *A. ochraceus* MTCC 10276, *Fusarium anthophilum* MTCC 10129, and *Rhizopus stolonifer* MTCC 4886). Bacteria were grown in BHI broth for 24 h at 37°C and optical density was determined at 600 nm using the UV-visible spectrophotometer (Agilent-Cary 60, United States). The optical density (OD) of the broth was adjusted to 0.5 McFarland standard with sterile phosphate-buffered saline, pH 7.4 (PBS) and used in further studies. Similarly, the fungal isolates were grown in SDA Petri plates for 7 days at 28°C and fungal spores were collected in sterile peptone broth containing 0.001% Tween 80 by using a soft scraper. The spore count was determined by hemocytometer, and its count was adjusted to 1×10^6 per mL and used in further studies.

Micro-well dilution method

Antimicrobial activity of PF-SeNPs on foodborne pathogens was determined by micro-well dilution technique as per instructions of Clinical and Laboratory Standards Institute (CLSI) (Kalagatur et al., 2015).

For antibacterial activity, different concentrations of PF-SeNPs and 10 μL of active bacterial culture of 0.5 McFarland standards were added to the wells of 96-well plate, and final volume was adjusted to 100 μL with MHB. The plates were incubated at 37°C for 24 h and OD at 600 nm was determined using the spectrophotometer. The concentration of PF-SeNPs at which no increase in OD was noticed as minimum inhibitory concentration (MIC). Further, 10 μL of sample was collected from the wells and spread plated on MHA Petri plates and incubated for 24 h at 37°C. The concentration of PF-SeNPs at which complete bacterial growth was not observed, was defined as minimum bactericidal concentration (MBC). Tetracycline was used as a standard antibacterial agent.

For antifungal activity, different concentrations of PF-SeNPs and 10 μL of fungal spores (1×10^6 per mL) were added to wells of 96-well plate, and final volume was adjusted to 100 μL with SDB and incubated at 28°C for 3 days. The concentration of PF-SeNPs, at which no visible fungal growth was observed, served as MIC. Further, 10 μL of sample was collected from the wells and inoculated on SDA Petri plates and incubated for 3 days at 28°C. The concentration of PF-SeNPs at which no fungal growth was observed, served as minimum fungicidal concentration (MFC). Nystatin was used as a standard antifungal agent.

Biocompatibility Assay

Finally, biocompatibility of PF-SeNPs was assessed by relating with the precursor (sodium selenite) in *in vitro* cell line model by various cytotoxicity assays, including MTT, live/dead dual staining, mitochondrial membrane potential (MMP), and caspase-3 assays. The toxic effect of sodium selenite and PF-SeNPs on cell viability was studied by MTT and live/dead dual staining assays (Kalagatur et al., 2017, 2018b). The MMP was crucial for ATP synthesis and maintaining the other functionalities of cells. The effect of sodium selenite and PF-SeNPs on MMP of cells was studied by rhodamine 123 staining assay (Kalagatur et al., 2017). Caspase-3 is caspase protein, and its activation by both extrinsic (death ligand) and intrinsic (mitochondrial) pathways leads to apoptotic cell death. The caspase-3 activity was determined using caspase-3 assay kit (Kalagatur et al., 2018b).

Cell culture and treatments

The cell line, N2a (*Mus musculus* neuroblastoma) was obtained from National Centre for Cell Sciences (NCCS), Pune, India. The cells were sub-cultured in DMEM supplemented with 10% FBS, 50 μg/mL of streptomycin and 50 mU/mL of penicillin in humidified incubator at 5% CO_2 and 37°C. The cells were grown in 75 cm^2 cell culture flask, and confluent cells were used in further experiments. The stock solution of sodium selenite and PF-SeNPs were prepared in DMSO (0.5%). Further, working concentration of sodium selenite and PF-SeNPs were made in DMEM devoid of FBS and concentration of DMSO was maintained at <0.01% throughout the study.

Approximately, 1.5×10^4 confluent cells were seeded in 96-well cell culture plates and allowed to adhere for overnight. Then, the cells were treated distinctly with different concentrations of sodium selenite and PF-SeNPs in DMEM medium devoid of FBS for 24 h. The cells treated alone with DMEM devoid of FBS was considered as control. The cells treated with H_2O_2 was considered as a positive control. Subsequently, plates were distinctly used for MTT, live/dead, MMP, and caspase-3 assays.

MTT assay

Succeeding, treatments and incubation were as detailed in section "Cell Culture and Treatments." The media was replaced with 10 μL of MTT dye (5 mg/mL) and 90 μL of DMEM devoid of FBS and incubated for 4 h at 37°C. Finally, the medium containing MTT was aspirated and substituted with DMSO for 30 min to solubilize the formazan crystals and absorbance was measured at 570 nm using multiplate reader (Synergy H1, BioTek, United States). The cell viability was expressed with respect to control (100%).

Live/dead cell assay

Succeeding, treatments and incubation were as detailed in section "Cell Culture and Treatments." The cells were washed for twice with DPBS and stained with dual staining dyes (4 μM of ethidium homodimer-1 and 2 μM of calcein AM) and cell viability were determined as per methodology of Kalagatur et al. (2017). Also, images were captured using an inverted fluorescence microscope (EVOS, Thermo Fisher Scientific, United States).

MMP assay

Succeeding, treatments and incubation were as detailed in section "Cell Culture and Treatments." The cells were washed for twice with DPBS and stained with rhodamine 123 (5 μM) in DPBS for 15 min. The fluorescent images were captured under GFP filter of an inverted fluorescence microscope (EVOS, Thermo Fisher Scientific, United States) and optical density was recorded at excitation of 511 nm and emission of 534 nm using multiplate reader (Synergy H1, BioTek, United States). The results were expressed with respect to control (100%).

Caspase-3 assay

Succeeding, treatments and incubation were as detailed in section "Cell Culture and Treatments." The cells were washed twice with DPBS and treated with caspase-3 kit as per manufacturer's instructions and absorbance was measured at an excitation of 360 nm and emission of 460 nm using a plate reader (Synergy H1, BioTek, United States). The results were expressed with respect to control (100%).

Statistical Analysis

All the experiments were done independently in triplicates, and results were expressed as mean ± SD. The data were processed by one-way ANOVA and the statistical difference were estimated by Tukey's multiple comparison test using software GraphPad Prism trial version 7 (San Diego, United States). The *p*-value was considered as a significant at ≤ 0.05.

RESULTS AND DISCUSSION

Chemical Profile of *E. officinalis* Fruit Extract

Generally, plant sources are eco-friendly, non-toxic, and highly esteemed based on their utility in bio-medicine and food sciences. Especially, plant secondary metabolites are highly appreciated and have already been reported in prodigious claims, i.e., antioxidant, antimicrobial, anticancer properties, etc. (Golechha et al., 2012; Philip et al., 2012; George et al., 2016; Muniyandi et al., 2017). Also, plant secondary metabolites are reported as potential candidates for biogenic production of nanoparticles and the method was highly satisfactory and being termed as green synthesis tactic (Akhtar et al., 2013). In the present study, *in vitro* assays for total phenolic, flavonoid and tannin contents of *E. officinalis* fruit extract are shown in **Figure 1**. The results revealed that *E. officinalis* fruit extract contain decent amount of phenolics (59.18 ± 2.91 mg GAE/g), flavonoids (38.50 ± 2.84 mg CE/g), and tannins (44.28 ± 3.09 mg TAE/g).

In support of our results, Liu et al. (2008a) have determined 62.5 ± 0.7, 203.5 ± 2.1, 269.3 ± 0.4, and 439.9 ± 1.3 mg GAE/g of total phenolic contents in aqueous, butanol, ethyl acetate, and ethyl ether extracts of amla fruit, respectively. Additionally, Liu et al. (2008b) have assessed the phenolic and flavonoid contents of methanolic extracts of amla fruit from six different regions of China and determined in the range from 81.5 to 120.9 mg GAE/g and 20.3 to 38.7 mg quercetin equivalents (QE)/g, respectively. Similarly, Pientaweeratch et al. (2016) from Thailand have determined total phenolic content of 362.43 ± 11.2 mg GAE/g and total flavonoid content of 21.04 ± 0.67 mg QE/g in ethanolic extract of amla. Further, Nambiar et al. (2015) carried out experiments to compare the phytochemical analysis of methanolic extracts of fruit, pulp and seeds of *E. officinalis,* where they determined the total phenolic content, flavonoid content and tannin content in the range of 6.00 ± 0.01–6.50 ± 0.10 μg GAE/mg of dry weight, 71.28 ± 1.00–72.35 ± 0.04 μg QE/mg of dry weight and 6.06 ± 0.01–111.26 ± 0.01 μg TAE/mg, respectively. However, insufficient reports are available in support of our study, especially on tannin content of *E. officinalis*. Typically, secondary metabolites of plants depend on various factors, i.e., genetics of plant, weather and harvesting conditions, nutrition availability, extraction technique, etc. (Verma et al., 2018). Therefore, obtained the quantity of phenolics, flavonoids and tannins in the present study was quite dissimilar with earlier reports. Overall, the present as well as earlier reports accomplish that *E. officinalis* fruit extract is rich with phenolics, flavonoids, and tannins, and it could be the potential contender for reduction and stabilization of metal ions and green synthesis of nanoparticles (Akhtar et al., 2013).

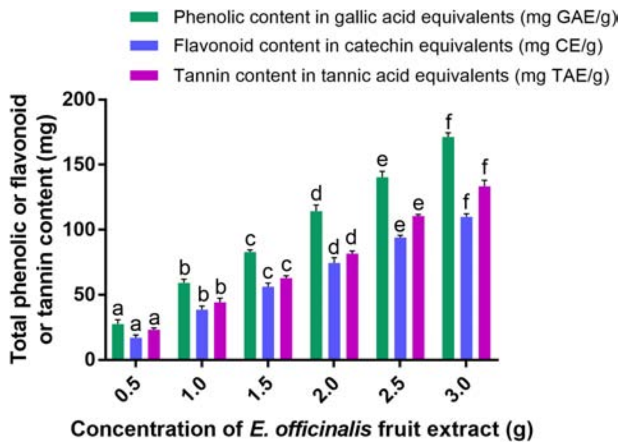

FIGURE 1 | Total phenolic, flavonoid, and tannin contents in aqueous fruit extract of *E. officinalis*. The experiments were executed independently in triplicates and data was expressed as mean ± SD. The statistical difference between the test samples were assessed by Tukey's multiple comparison test and $p \leq 0.05$ was considered as a significant. The bar graphs with different alphabetic letters within the respective study were significant.

Biogenic Synthesis and Characterization of PF-SeNPs

Originally, sodium selenite solution was colorless. The color of sodium selenite turned into brick-red with the addition of *E. officinalis* fruit extract after 24 h (**Figure 2A**). The formation of brick-red solution was due to the excitation of the surface plasmon resonance and it was an indication for reduction of sodium selenite into elemental selenium. The

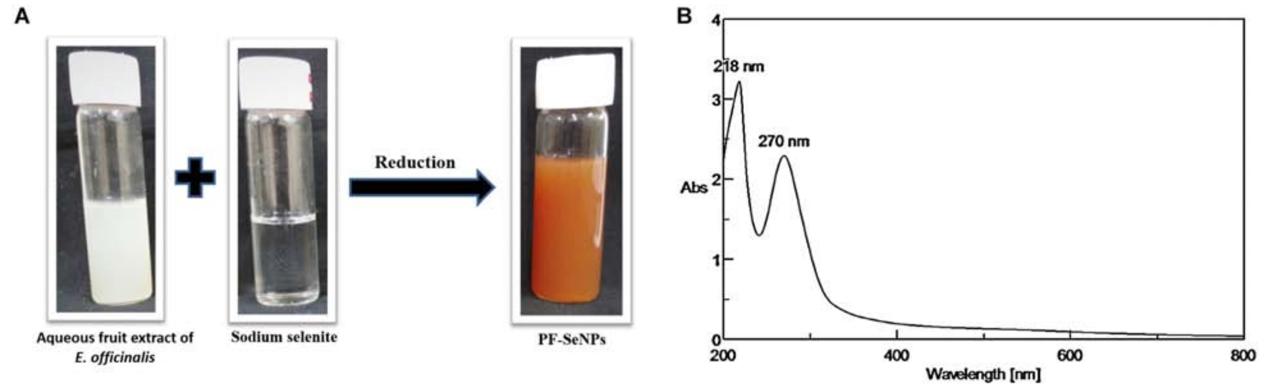

FIGURE 2 | (A) Reduction of sodium selenite by aqueous fruit extract of *E. officinalis* to form phytofabricated selenium nanoparticles (PF-SeNPs). **(B)** UV-visible spectra of biogenic PF-SeNPs.

reduction of sodium selenite into PF-SeNPs can occur by the action of phenolics, flavonoids, and tannins of *E. officinalis* (Ankamwar et al., 2005). The preliminary confirmation of PF-SeNPs formation was concluded by plasmon resonance using UV-Visible spectroscopy. The absorption maximum was observed at 270 nm, which indicate that plant material has reduced and stabilized the PF-SeNPs formation (**Figure 2B**). The UV-visible absorption maximum in the present study was found to be in agreement with earlier reports. Kokila et al. (2017) have prepared SeNPs from *Diospyros montana* leaf extract by green synthesis approach and observed UV-visible absorption maximum at 261 nm. Similarly, Anu et al. (2017) have green-synthesized SeNPs from *Allium sativum* and noticed UV-visible maximum at 260 nm. Likewise, Fesharaki et al. (2010) have observed UV-visible maximum at 218 and 248 nm (located between 200 and 300 nm) for *Klebsiella pneumoniae* mediated bio-synthesized SeNPs. On the other hand, Shah et al. (2010) have synthesized polyvinyl alcohol-stabilized SeNPs by wet chemical method involving a reaction of acetone and noticed UV-visible maximum at 270 nm. The study concluded that sodium selenite was successfully converted into PF-SeNPs by reduction action of aqueous fruit extract of *E. officinalis*.

Further, FTIR spectroscopic analysis was performed to confirm the feasible role of *E. officinalis* fruit extract in the bio-synthesis of PF-SeNPs. FTIR allows the determination of the functional groups that exist on the surface of nanoparticles by measuring the vibrational frequencies of chemical bonds. The obtained molecular data facilitates to establish structural and conformational changes of the co-ordinating self-assembled functional groups on the surface of nanoparticles (Movasaghi et al., 2008). In the present study, FTIR spectra of aqueous fruit extract of *E. officinalis* and PF-SeNPs have been detailed in **Figure 3**. FTIR spectrum of aqueous fruit extract of *E. officinalis* has presented multiple intense peaks at 3,382, 2,926, 2,854, 1,718, 1,651, 1,448, 1,350, 1,211, 1,050, 879 and 572 cm^{-1}, which corresponds to attendance of –OH group, stretching vibration of aliphatic C–H, carboxylic acid O–H, carbonyl C=O stretch, amide I vibrations, C=C aromatic, CH_3 C–H bending in alkyls, R–O–R (ether), superposition in the plane of C–H bending of polysaccharide, C–C stretching vibration and OH bending of the phenolic groups, respectively (Ankamwar et al., 2005; Movasaghi et al., 2008). Whereas, during PF-SeNPs biosynthesis course, broad intense peak at 3,382 cm^{-1} of aqueous fruit extract of *E. officinalis* was shifted to 3,348 cm^{-1} of PF-SeNPs, which suggested that selenium has interacted with the hydroxyl group from aqueous fruit extract of *E. officinalis* through hydrogen bonding and facilitated biosynthesis of PF-SeNPs. Likewise, prominent peak at 1,718 cm^{-1} (carbonyl C=O stretch) of aqueous fruit extract of *E. officinalis* has disappeared in PF-SeNPs, which specify that carbonyl C=O stretch has enabled the synthesis of PF-SeNPs (Ankamwar et al., 2005). Similarly, peak at 1,651 cm^{-1} (amide I vibrations) in aqueous fruit extract of *E. officinalis* was shifted to higher frequencies 1,662 cm^{-1} in PF-SeNPs biosynthesis, which shows the interaction of proteins of aqueous fruit extract of *E. officinalis* with selenium through the amine groups. The large and intense peak at 1,050 cm^{-1} in aqueous fruit extract of *E. officinalis* was shifted to 1,042 cm^{-1} in PF-SeNPs, which represents the characteristic Se–O stretching vibration, according to the report of Kannan et al. (2014) and accomplishes the successful biosynthesis of PF-SeNPs. According to Kimura et al. (2005), peaks at 1,050 cm^{-1} (C-O), 1,540 cm^{-1} (C-N-H) and 1,660 cm^{-1} (HN-H) are indicative of carbohydrate and protein character, respectively. FTIR analysis indicated that proteins and carbohydrates were dominant on the surface of PF-SeNPs. The aforementioned variations at the peaks show that secondary metabolites of aqueous fruit extract of *E. officinalis* have successfully facilitated the biosynthesis of PF-SeNPs by reduction process and could aid in protection of PF-SeNPs from aggregation and thereby retain their long-term stability (Park et al., 2011).

The nature of the synthesized PF-SeNPs was assessed by XRD and Raman spectroscopic analysis. The XRD pattern of PF-SeNPs has been depicted in **Figure 4A**, which shows broader peak without any sharp Bragg's peaks and thus, it specifies that synthesized red elemental PF-SeNPs is certainly amorphous in nature, which is in agreement with previous reports. Li et al. (2007) and Yang et al. (2012) have phyto-synthesized

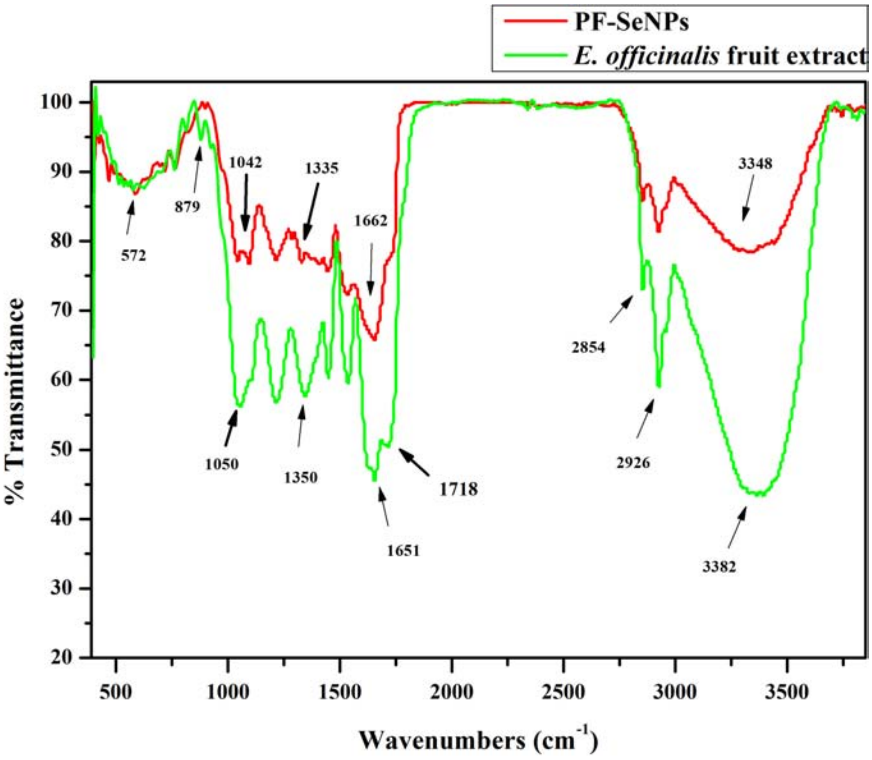

FIGURE 3 | Fourier transform infrared spectroscopy (FTIR) of aqueous fruit extract of *E. officinalis* and phytofabricated selenium nanoparticles (PF-SeNPs).

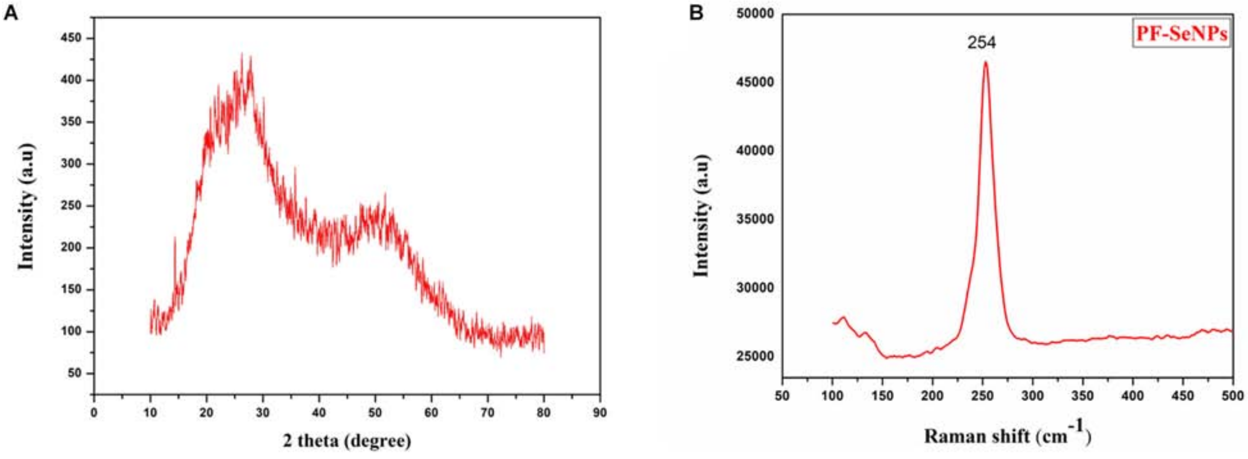

FIGURE 4 | (A) X-ray diffraction (XRD) pattern and **(B)** Raman spectroscopy of phytofabricated selenium nanoparticles (PF-SeNPs).

SeNPs correspondingly from *Capsicum annuum* leaf extract and *Spirulina* polysaccharide and reported its nature as amorphous. The attained XRD results were further evaluated by Raman spectroscopic analysis. Raman spectroscopy provides the unique feature of detecting vibrational characteristics of the synthesized nanomaterials, which are amorphous or crystalline in nature and it also has been proven to be a powerful tool to analyze the phase of nanoparticles (Baganich et al., 1991). In the present study, characteristic resonance peak was observed at 254 cm^{-1} (**Figure 4B**), and it could be attributed to amorphous selenium as a consequence of irregularly and arrayed selenium atoms as disordered chains (Li et al., 2010).

The stability and hydrodynamic size of PF-SeNPs were assessed by Zeta potential and DLS analysis. Zeta potential is the measure of an effective electric charge on the surface of nanoparticles. The magnitude of the Zeta potential delivers information on particle stability. The nanoparticles with higher magnitude of Zeta potential exhibits increased stability due to greater electrostatic repulsion between nanoparticles. In the present study, the sharp peak of Zeta potential for PF-SeNPs was noticed at −24.4 mV, and it was concluded that surface of PF-SeNPs is negatively charged (**Figure 5A**). The negative charged potential value was imparted to PF-SeNPs because of reducing agents (phenolics, flavonoids, and tannins) of aqueous fruit extract of *E. officinalis*. Also, the attendance of negative electrostatic forces between PF-SeNPs favors to exist in dispersion form (Kokila et al., 2017). Further, the DLS pattern reveals that the optimized SeNPs synthesized by this method have a size ranging from 20 to 60 nm and display a narrow peak (**Figure 5B**), which indicates nanoparticles are monodispersed and having polydispersity index less than 0.2, which shows the lesser aggregation of particles (Bhattacharjee, 2016).

The morphology of SeNPs was confirmed by SEM analysis and was found to be spherical (**Figure 6A**). The existence of three strong peaks at 1.5 keV of EDX spectrum confirm the presence of elemental Se (61.60%), C (29.96%) and O (4.41%) (**Figure 6B**). The shape and size of PF-SeNPs were confirmed by HR-TEM analysis, and it was found to be spherical shape with an average diameter of 15–40 nm (**Figure 6C**). The obtained HR-TEM results were in accordance with DLS and SEM assessments of PF-SeNPs. However, the sizes of the PF-SeNPs were slightly higher in DLS related to HR-TEM analysis, and it could be

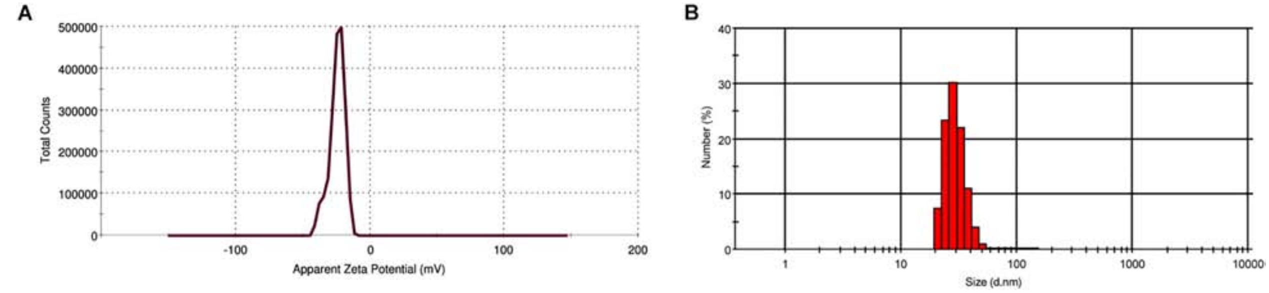

FIGURE 5 | (A) Zeta potential (mV) and **(B)** size distribution (d.nm) of phytofabricated selenium nanoparticles (PF-SeNPs).

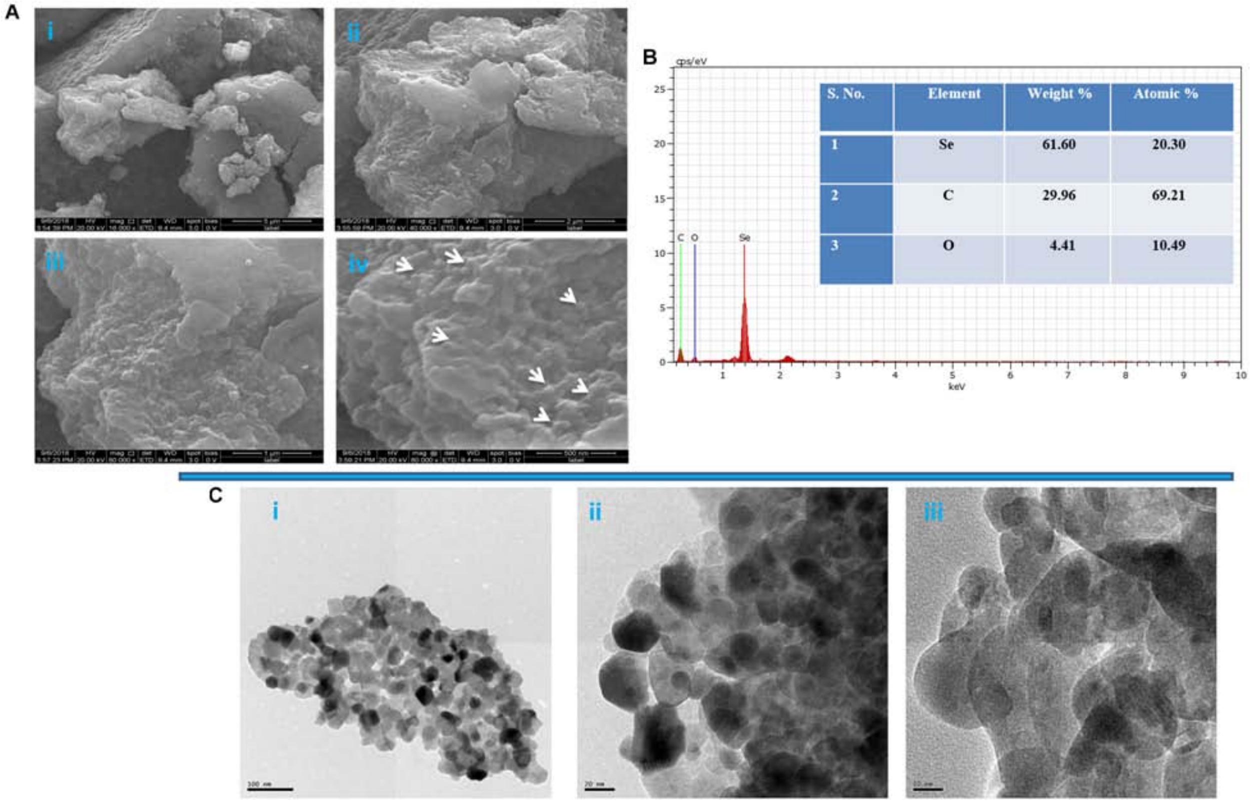

S. No.	Element	Weight %	Atomic %
1	Se	61.60	20.30
2	C	29.96	69.21
3	O	4.41	10.49

FIGURE 6 | (A) Scanning electron microscopic image of phytofabricated selenium nanoparticles (PF-SeNPs) at magnification of (i) 5 μm, (ii) 2 μm, (iii) 1 μm, and (iv) 500 nm. **(B)** Energy-dispersive X-ray analysis of PF-SeNPs. **(C)** Transmission electron microscopic images of PF-SeNPs at (i) 100 nm, (ii) 20 nm, and (iii) 10 nm.

due to hydrodynamic coating of water molecules around PF-SeNPs (Eaton et al., 2017). In support of our study, Li et al. (2007), Yang et al. (2012), Ramamurthy et al. (2013), Kong et al. (2014), Sharma et al. (2014) and have bio-synthesized SeNPs from *Capsicum annuum* L. extract, *Spirulina* polysaccharide, fenugreek seed extract, Arabic gum, *Vitis vinifera* dried fruit extract, and observed optimum size of SeNPs as 80, 90–550, 50–150, 34 and 3–18 nm, respectively. The size of bio-synthesized nanoparticles relies on chemical constituents of the biomaterial employed (Akhtar et al., 2013). Therefore, the size of PF-SeNPs in our study was quite diverse related to earlier reports.

Bio-Potentials of PF-SeNPs

Antioxidant Activity

Antioxidant activity of PF-SeNPs was assessed by DPPH and ABTS free radical scavenging assays. The PF-SeNPs has shown potent DPPH and ABTS radical scavenging activity and it was exhibited in dose-dependent manner (**Figures 7A,B**). It shows that antioxidant activity was directly proportional to the concentration of PF-SeNPs. The EC50 (effective concentration required to inhibit 50% of free radicals) of PF-SeNPs was determined as 15.67 ± 1.41 and 18.84 ± 1.02 μg/mL for DPPH and ABTS radical scavenging activity, respectively. Whereas, EC50 value of ascorbic acid (reference standard) was noticed as 19.21 ± 2.63 and 21.69 ± 1.77 μg/mL for DPPH and ABTS radical scavenging activity, respectively. The PF-SeNPs has exhibited potent antioxidant activity compared to ascorbic acid. Our results were in line and comparable with the reports of phyto-synthesized SeNPs. Recently, Kokila et al. (2017) have phyto-synthesized SeNPs of 16 nm size and noticed their EC50 value as 22.5 μg/mL. In another report, Qiu et al. (2018) have synthesized pectin decorated SeNPs of 41 nm and quantified its EC50 value as 500 μg/mL. The aforementioned studies strongly support that the antioxidant activity of PF-SeNPs is dependent not only on size and but also on surface functional moieties of nanoparticles that are occupied by secondary metabolites of *E. officinalis* fruit extract (Zhang et al., 2004; Singh et al., 2018).

The higher antioxidant property of PF-SeNPs could be due to selenium as well, which plays a key role in an upturn of selenoenzymes like glutathione peroxidase and assist in protecting the cells and tissue under *in vivo* conditions from free radicals (Rotruck et al., 1973). Consequently, the physicians and nutritionists routinely recommend to consume Se-rich food sources (nuts, cereals and mushrooms) for keeping the individual fit (Combs and Combs, 1986). Therefore, preparation of nanoparticles with Se and augmentation of their bio-functions by phytofabrication is much anticipated and accepted by the consumer, government, and regulatory agencies (El-Ramady et al., 2014). Therefore, bio-synthesized PF-SeNPs could be considered as highly biocompatible, and it could find a potential role in substituting the synthetic antioxidants and could be used as an natural antioxidant embedding agent in food packaging material (Vera et al., 2016; Wadhwani et al., 2016).

Antimicrobial Activity

Selenium is considered as potent antimicrobial agents, and its derivative substance like selenium sulfide is widely used in medicine to treat infections of *Malassezia* and *Tinea versicolor* (Pierard et al., 1997). However, excess use of selenium causes toxic effects and leads to selenosis (Spallholz, 1994). Consequently, contemporary research has focused on diminishing the toxicity and improving the bio-functional aspects of selenium. In turn, nanotechnology has provided the safe strategy to reduce the toxicity and improve the bio-functionality of selenium through biosynthesis.

In the present study, the antimicrobial activity of biosynthesized PF-SeNPs was tested against foodborne pathogens by micro-well dilution technique as per instructions of CLSI. To the best of our knowledge, previous studies were mostly focused on an evaluation of the MIC activity of bio-synthesized PF-SeNPs. Only a few studies were focused on the evaluation of

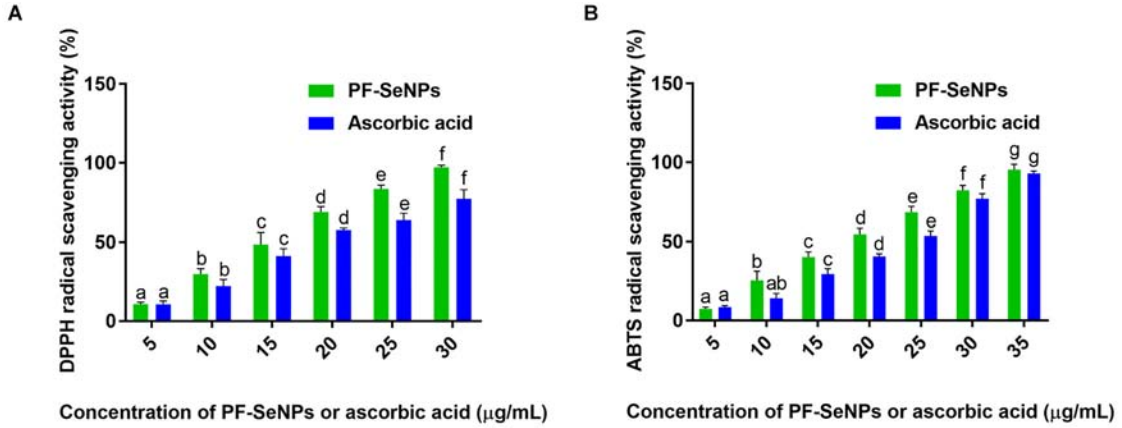

FIGURE 7 | Determination of dose-dependent antioxidant potential of phytofabricated selenium nanoparticles (PF-SeNPs) and ascorbic acid by **(A)** DPPH and **(B)** ABTS radical scavenging assays. The experiment was executed independently in triplicates and data was expressed as mean ± SD. The statistical difference between the test samples were assessed by Tukey's multiple comparison test and $p \leq 0.05$ was considered as a significant. The bar graphs with different alphabetic letters within the respective study were significant.

MBC and MFC value of biosynthesized PF-SeNPs. In medical microbiology, determination of MBCs and MFCs has been encouraged for the treatment of serious microbial infections (i.e., endocarditis) or treatment of immunosuppressed patients (Sykes, 2013).

The biogenic PF-SeNPs have presented potent antimicrobial activity on both bacterial and fungal pathogens (**Table 1**). In the case of antibacterial activity, MIC and MBC values of PF-SeNPs were in the range of 09.16 ± 0.76–59.83 ± 2.56 and 19.83 ± 1.25–97.50 ± 3.27 μg/mL, respectively. The lowest MIC and MBC values of PF-SeNPs were correspondingly noticed as 09.16 ± 0.76 and 19.83 ± 1.25 μg/mL against *S. aureus* MTCC 96. While, highest MIC and MBC values of PF-SeNPs were correspondingly noticed as 59.83 ± 2.56 and 97.50 ± 3.27 μg/mL against *E. coli* MTCC 41. Together, the potent antibacterial activity of PF-SeNPs was observed against Gram-positive bacteria (*S. aureus* MTCC 96, *E. faecalis* MTCC 439 and *L. monocytogenes* MTCC 657) compared to Gram-negative bacteria (*E. coli* MTCC 4). On the other hand, PF-SeNPs exhibited potent antifungal activity compared to antibacterial activity. The MIC and MFC values of PF-SeNPs on fungi were observed in the range of 07.50 ± 1.32–25.50 ± 2.78 and 10.67 ± 1.04–38.17 ± 1.75 μg/mL, respectively. The least MIC and MFC of PF-SeNPs were correspondingly observed as 07.50 ± 1.32 and 10.67 ± 1.04 μg/mL against *R. stolonifer* MTCC 4886. The highest MIC and MFC of PF-SeNPs were correspondingly observed as 25.50 ± 2.78 and 38.17 ± 1.75 μg/mL against *A. oryzae* MTCC 634.

In support of our study, reports are scarce on antimicrobial activity of biosynthesized SeNPs using plant extracts. Kokila et al. (2017) have biosynthesized SeNPs using leaf extract and reported their antimicrobial activity in the form of zone of inhibition as 08, 07, and 08 mm against *S. aureus*, *E. coli,* and *A. niger*, respectively. Alternatively, few reports are available on the exploration of biosynthesized SeNPs using microbial sources. Zonaro et al. (2015) have biosynthesized SeNPs from *Stenotrophomonas maltophilia* and noticed MIC values of 125 mg/L against *E. coli* JM109 and *E. coli* ATCC 25922, and 250 mg/L against *P. aeruginosa* PAO1, *P. aeruginosa* ATCC 27853 and *S. aureus* ATCC 25923. In case of antifungal activity, Shahverdi et al. (2010) have synthesized SeNPs from *Klebsiella pneumonia* and observed complete inhibition of visible fungal growth in the range of 10–260 μg/mL against *M. sympodialis, M. furfur,* and *A. terreus*. In the same way, Kazempour et al. (2013) have biosynthesized SeNPs from *Klebsiella pneumonia* and estimated their MIC values as 250 and 2,000 μg/mL toward *A. brasiliensis* and *Candida albicans*, respectively.

TABLE 1 | Antimicrobial effect of phytofabricated selenium nanoparticles (PF-SeNPs) from *E. officinalis* fruit extract on various foodborne pathogens determined by micro-well dilution technique.

Microbial culture	MIC$^{@}$ (μg/mL)	MBC$^{\#}$/MFC$^{\$}$ (μg/mL)
Bacteria		
Escherichia coli MTCC 41	59.83 ± 2.56^{a}	97.50 ± 3.27^{a}
Listeria monocytogenes MTCC 657	33.17 ± 2.84^{b}	53.50 ± 3.04^{b}
Staphylococcus aureus MTCC 96	09.16 ± 0.76^{c}	19.83 ± 1.25^{c}
Enterococcus faecalis MTCC 439	16.17 ± 2.02^{d}	33.17 ± 3.32^{d}
Fungi		
Aspergillus brasiliensis MTCC 1344	07.66 ± 1.52^{a}	11.83 ± 0.76^{a}
A. flavus MTCC 1883	13.50 ± 1.32^{b}	20.50 ± 2.29^{b}
A. oryzae MTCC 634	25.50 ± 2.78^{c}	38.17 ± 1.75^{c}
A. ochraceus MTCC 10276	13.33 ± 1.89^{bd}	21.00 ± 1.32^{bd}
Fusarium anthophilum MTCC 10129	11.83 ± 0.28^{abde}	22.17 ± 1.60^{bde}
Rhizopus stolonifer MTCC 4886	07.50 ± 1.32^{aef}	10.67 ± 1.04^{af}

$^{@}$MIC, minimum inhibitory concentration; $^{\#}$MBC, minimum bactericidal concentration; $^{\$}$MFC, minimum fungicidal concentration. The statistical difference between the test samples within MIC and MBC/MFC of the bacteria and fungi were assessed by Tukey's multiple comparison test. The $p \leq 0.05$ was considered as significant. The different alphabetic letters within MIC and MBC/MFC of the bacteria and fungi were significant.

In earlier reports, researchers have established that biosynthesized nanoparticles elicit antimicrobial effects through different ways. The antimicrobial activity depends on the size of nanoparticles. The small size of nanoparticles can effortlessly cross the cell wall and membrane and induce cell lysis. It further, interferes with respiratory sequence and ATP synthesis, and stops cell division and induce the microbial cell death (Zonaro et al., 2015).

Our study has shown potent antimicrobial activity against Gram-positive bacteria compared to Gram-negative bacteria. To explain this, Tran et al. (2015) have assessed the antibacterial mechanism of SeNPs in Gram-positive and Gram-negative bacteria and concluded that SeNPs have strong electrostatic repulsion toward the lipopolysaccharide and membrane of Gram-negative bacteria, which is highly negative in nature. Whereas, Gram-positive bacteria have considerably less negative charge than Gram-negative bacteria. So, there is a possibility of higher deposition of SeNPs on the surface of Gram-positive bacteria to induce bacterial death. Therefore, Gram-negative bacteria tend to show resistance to PF-SeNPs. Interestingly, PF-SeNPs have presented potent antimicrobial activity against fungi rather than bacteria. The selenium is considered as the strong antifungal agent rather than antibacterial, and hence, it is highly used in anti-dandruff shampoo to treat fungal infections (Pierard et al., 1997). Therefore, in our study, strong antifungal activities of PF-SeNPs were noticed. Until date, the exact mechanism involved in an antifungal activity of selenium is unknown.

Biocompatibility Assay

Biocompatibility of synthesized PF-SeNPs was appraised by comparing with the cytotoxicity aspects of sodium selenite in N2a cells, and it was done by cell viability, MMP and caspase-3 assays.

The cell viability was considered by MTT and live/dead dual staining assays. The MTT assay measure the cell viability as a function of redox potential of cell and metabolically active cells convert MTT reagent to purple formazan crystals and its strength is directly proportional to viable cells (Kalagatur et al., 2018b). The other assay, live/dead dual staining is an advanced cell viability technique and it consists of two staining reagents, i.e., calcein AM and ethidium homodimer-1. The calcein AM is used to stain live cells and it actively passes through cellular membrane and emits green fluorescence at an excitation of 495 nm and emission of 515 nm by action of ubiquitous intracellular esterases of live cells. The other dye, ethidium homodimer-1 is specific for dead cells and it cross only through compromised cellular membrane and strongly binds to nuclear material of cell and emits red fluorescence at an excitation of 495 nm and emission of 635 nm (Kalagatur et al., 2018b). In the present study, MTT and live/dead dual staining assays concluded that sodium selenite and PF-SeNPs

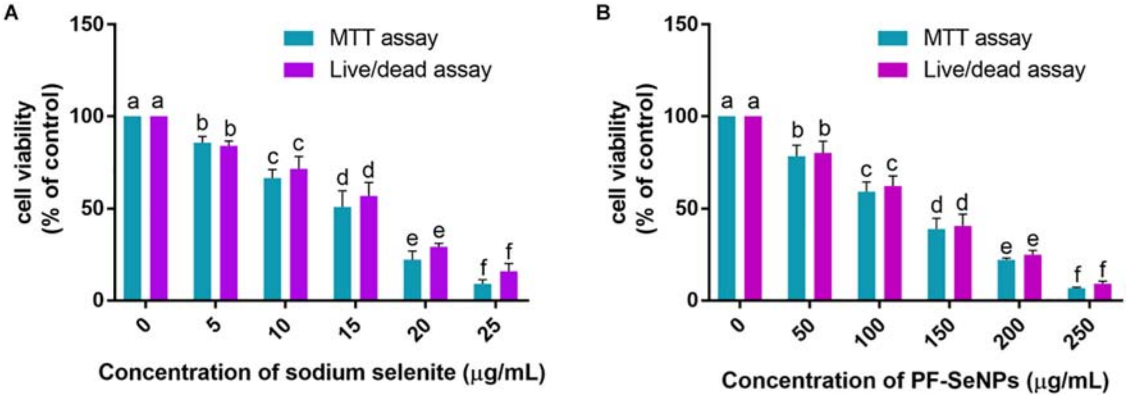

FIGURE 8 | Determination of dose-dependent inhibitory effect of **(A)** sodium selenite and **(B)** phytofabricated selenium nanoparticles (PF-SeNPs) on cell viability of N2a cells for 24 h by MTT and live/dead dual staining assays. The experiments were executed independently in triplicates and data was expressed as mean ± SD. The statistical difference between the test samples were assessed by Tukey's multiple comparison test and $p \leq 0.05$ was considered as a significant. The bar graphs with different alphabetic letters within the respective study were significant.

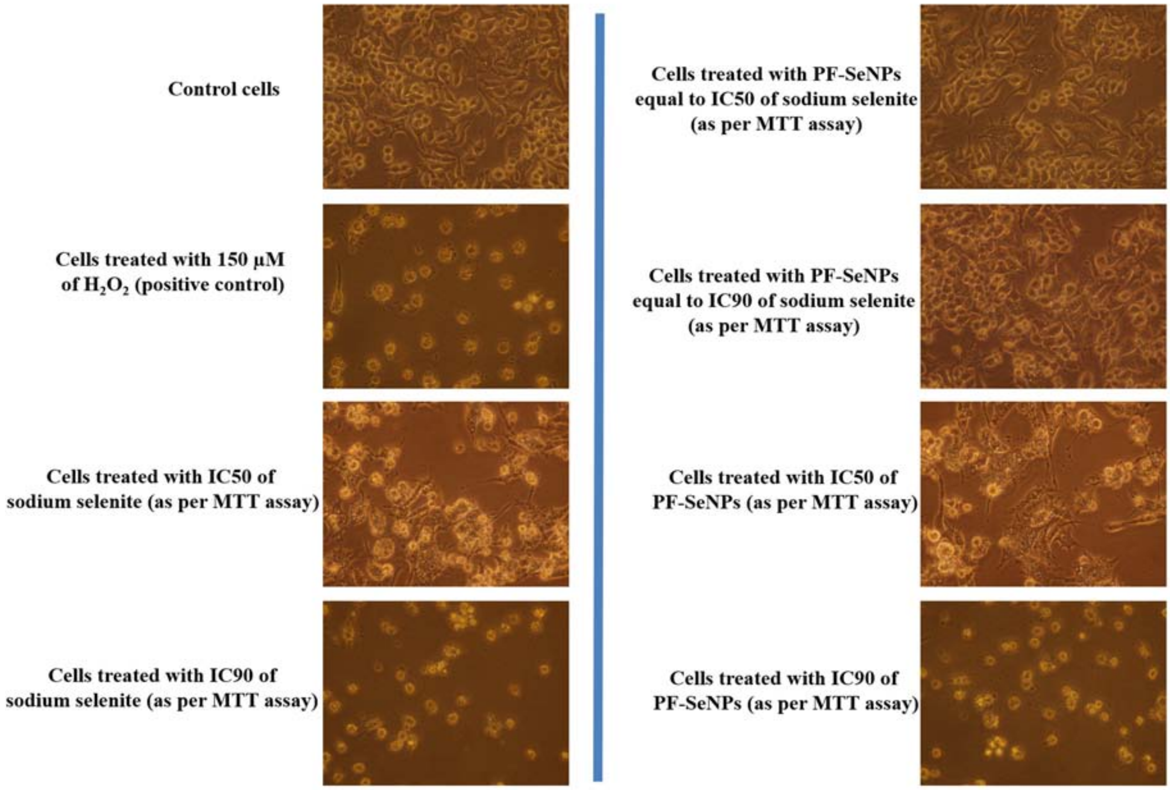

FIGURE 9 | Bright-field microscopic images of N2a cells treated with 150 μM of H_2O_2 and different concentrations of sodium selenite and phytofabricated selenium nanoparticles (PF-SeNPs) for 24 h. All images were captured at magnification of 400×.

have inhibited the cell viability in dose-dependent way (**Figure 8**). However, sodium selenite has inhibited cell viability at much lower concentration compared to PF-SeNPs. The IC50 (dose required to inhibit 50% of cell viability) and IC90 (dose required to inhibit 90% of cell viability) values were calculated to assess the cytotoxicity of sodium selenite and PF-SeNPs. In MTT assay, IC50 and IC90 values for sodium selenite and PF-SeNPs were observed as 14.01 ± 1.88 and 24.60 ± 2.19 μg/mL, 127.28 ± 3.73 and 234.41 ± 5.57 μg/mL, respectively. In live/dead dual staining assay, IC50 and IC90 values for sodium selenite and PF-SeNPs were noticed as 15.30 ± 2.08 and 27.11 ± 1.92 μg/mL, 132.66 ± 4.02 and 241.83 ± 4.79 μg/mL, respectively. Meanwhile, 150 μM of H_2O_2 inhibited 92.38 ± 2.91% of cell viability as determined by MTT assay (graph not shown) and was considered as positive control. The observed inhibitory concentrations of sodium selenite and PF-SeNPs were much like in both MTT and live/dead dual staining assays. The IC50 and IC90 values of PF-SeNPs was much higher compared to sodium selenite and concluded that PF-SeNPs was less toxic than sodium selenite. To assess further, bright-field and live/dead fluorescent microscopic images were depicted in **Figures 9**, **10**, respectively. The bright-field images have clearly showed cellular membrane rupture and apoptotic bodies in cells treated with IC50 values of sodium selenite and PF-SeNPs. Relatively, massive cellular membrane damage and high apoptotic bodies formation were noticed

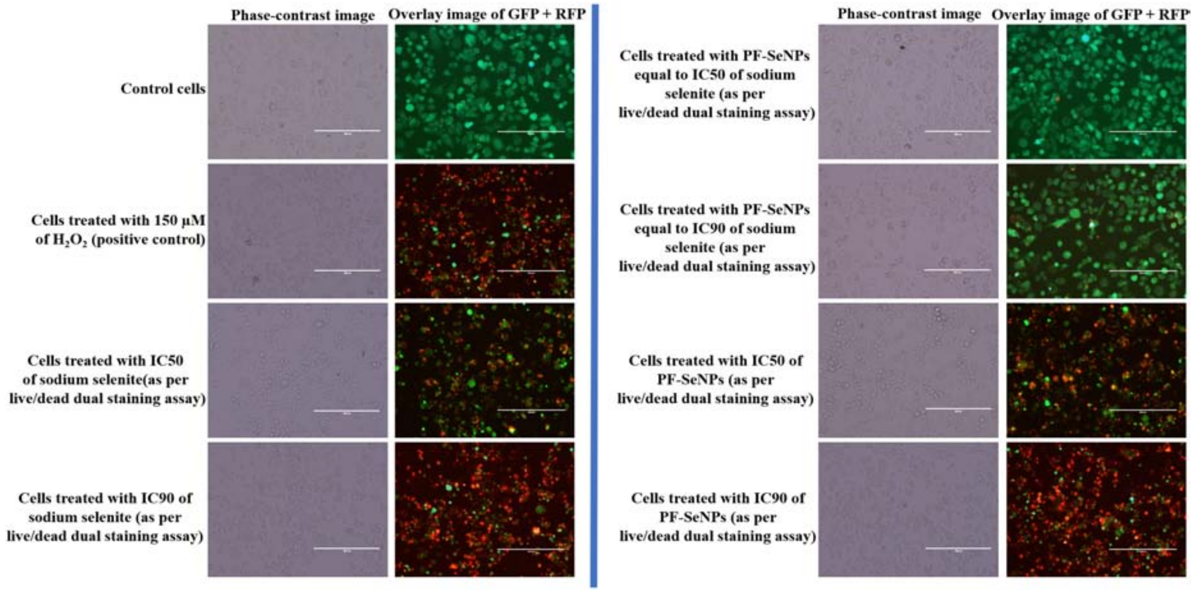

FIGURE 10 | Live/dead dual staining images of N2a cells treated with 150 μM of H_2O_2 and different concentrations of sodium selenite and phytofabricated selenium nanoparticles (PF-SeNPs) for 24 h. The scale bar is 200 μm.

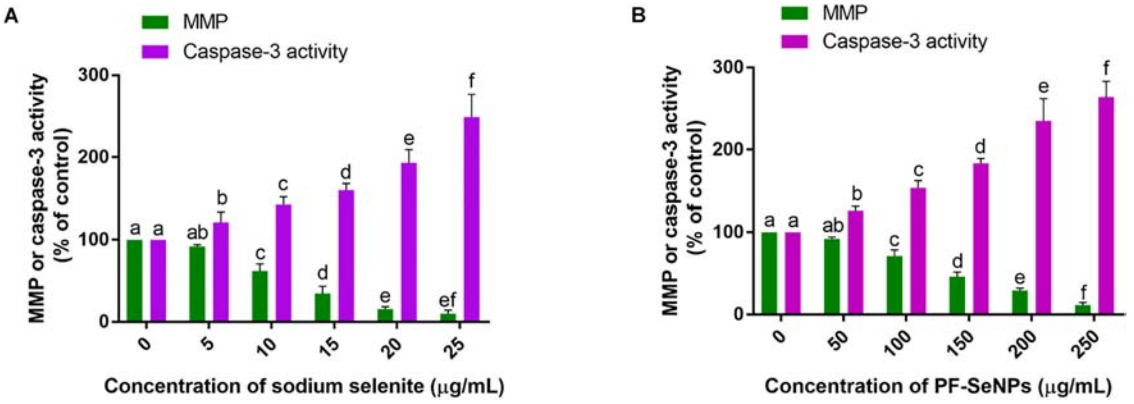

FIGURE 11 | Effect of different concentration of **(A)** sodium selenite and **(B)** phytofabricated selenium nanoparticles (PF-SeNPs) on mitochondrial membrane potential (MMP) and caspase-3 activity of N2a cells for 24 h. The experiments were executed independently in triplicates and data was expressed as mean ± SD. The statistical difference between the test samples were assessed by Tukey's multiple comparison test and $p \leq 0.05$ was considered as a significant. The bar graphs with different alphabetic letters within the respective study were significant.

at IC90 values of sodium selenite and PF-SeNPs (**Figure 9**). Similarly, live/dead dual staining assay has also determined comparable pattern of results with bright-field microscopic images. At IC50 dose of sodium selenite and PF-SeNPs, about half live (green) and dead (red) cells were noticed and as usually quite higher number of dead (red) cells was noticed at IC90 concentrations of sodium selenite and PF-SeNPs (**Figure 10**). Interestingly, cells treated with PF-SeNPs equal to IC50 and IC90 doses of sodium selenite has shown negligible changes in bright-field and live/dead fluorescent images compared to control cells (**Figures 9**, **10**). Thus, cell viability assays concluded that PF-SeNPs was less toxic and much safer compared to sodium selenite. Our results were well supported by earlier reports, Anu et al. (2017) has compared the cytotoxic effects of chemically synthesized and green-synthesized of SeNPs using *Allium sativum* on Vero cells and reported that green-synthesized SeNPs were less toxic than chemically synthesized SeNPs. Similarly, Forootanfar et al. (2014) have biosynthesized SeNPs from marine bacterial isolate *Bacillus* sp. MSh-1 and noticed lower cytotoxic effect in MCF-7 cells related to selenium dioxide.

The molecular mechanisms involved in the cytotoxicity was revealed by MMP and caspase-3 assays. Upholding the MMP is crucial for ATP synthesis and other cellular functions, and its

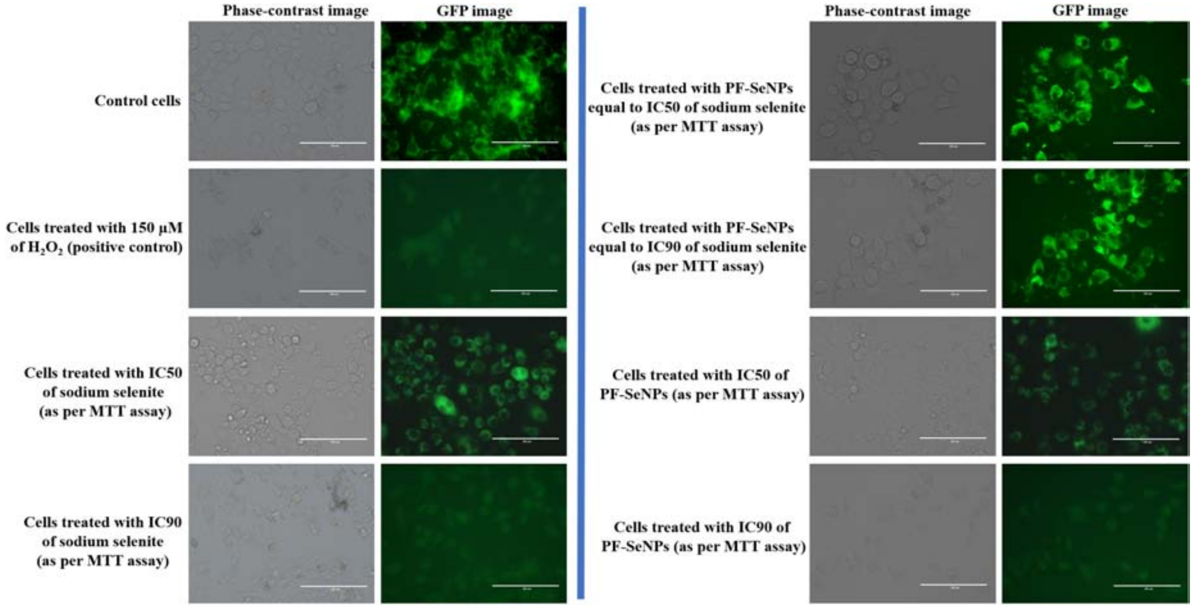

FIGURE 12 | Rhodamine 123 stained images depicting mitochondrial membrane potential (MMP) of N2a cells treated with 150 µM of H_2O_2 and different dose of sodium selenite and phytofabricated selenium nanoparticles (PF-SeNPs) for 24 h. The scale bar is 100 µm.

TABLE 2 | Overview of *in vitro* cytotoxicity of selenium nanoparticles (SeNPs) on different cell lines.

S. No.	Precursor	Reducing agent	Stabilizing agent	Cell line	IC50 value	References
1	Sodium selenite	*Psidium guajava* leaf extract	–	CHO pro (hamster ovary)	88 ± 2.1 µg/mL	Alam et al., 2018
2	Sodium selenite	Ascorbic acid	Dextrin	NIH-3T3 (mouse embryonic fibroblast)	149 ± 60.5 µg/mL	Malhotra et al., 2016
3	Sodium selenite	Ascorbic acid	*Ganoderma lucidum* polysaccharides	Raw 264.7 (mouse macrophage)	5–100 µg/mL	Wang et al., 2014
4	Sodium selenite	*Halococcus salifodinae* BK18	–	HaCat (human skin)	150 µg/mL	Srivastava et al., 2014
5	Sodium selenite	*Gracilaria lemaneiformis* polysaccharides	–	Chem-5 (human brain glial)	159.9 ± 9.73 µM	Jiang et al., 2014
1.				HK-2 (human kidney)	79.5 ± 4.26 µM	
0.				L02 (human liver)	95.6 ± 7.68 µM	
6	Selenium dioxide	*Bacillus* sp. MSh-1	–	MCF-7 (human mammary gland)	41.5 ± 0.9 µg/mL	Forootanfar et al., 2014
7	Selenous acid	Ascorbic acid	Chitosan	HK-2 (human kidney)	98.29 µM	Yu et al., 2012
8	Selenium dioxide	Ascorbic acid	Sialic acid	HK-2 (human kidney)	40 µg/mL	Zheng et al., 2011
9	Sodium selenite	Ascorbic acid	*Undaria pinnatifida* polysaccharides	Hs68 (human skin fibroblast)	67.9 µM	Chen et al., 2008

depletion induces the cell death. The level of MMP is routinely assessed by rhodamine 123 staining and its fluorescence strength is considered as directly proportional to the level of MMP (Kalagatur et al., 2017). On the other hand, caspase-3 is a caspase protein and its activation induce the cell death by apoptosis process (Porter and Jänicke, 1999). In the present study, sodium selenite and PF-SeNPs have depleted the MMP and elevated the caspase-3 activity in dose-dependent manner (**Figure 11**). The study concluded that sodium selenite and PF-SeNPs induce the cytotoxicity by apoptosis process through depleting MMP levels. However, sodium selenite has depleted the MMP and elevated the caspase-3 activity at much lower levels compared to PF-SeNPs and these results were in accordance the outcome of cell viability assays. Most importantly, cells treated with PF-SeNPs of IC50 and IC90 values of sodium selenite have not shown much reduction in fluorescence (MMP) compared to control (**Figure 12**). The obtained cytotoxicity of PF-SeNPs was found to be comparable with earlier reports (**Table 2**). Thus, biocompatibility study concluded that biosynthesized PF-SeNPs were much less toxic and safer in comparison to sodium selenite.

CONCLUSION

The present study shows phytofabrication of SeNPs from aqueous fruit extract of *E. officinalis* by facile, green, economic, and eco-friendly approach. The aqueous fruit extract of *E. officinalis* was rich with phenolics, flavonoids, and tannins, and was found appropriate for biosynthesis of nanoparticles. The synthesized PF-SeNPs exhibited highly stable, negative charge, amorphous nature, spherical shape and nano-size. The PF-SeNPs has presented efficient bio-potential applications, i.e., antioxidant, antimicrobial, and biocompatibility. The PF-SeNPs has shown potent free radical scavenging activity and it was found highly efficient than standard antioxidant ascorbic acid. Also, PF-SeNPs shown potent antimicrobial activity on wide range of foodborne pathogens and it was found highly efficient on fungi followed by Gram-positive and Gram-negative bacteria. The PF-SeNPs have exhibited lesser toxicity on N2a cells compared to sodium selenite, rendering them highly safer and biocompatible. Therefore, with these bio-potential impacts, the PF-SeNPs have a tremendous application to be applied in the pharmaceutical, biomedical and food industries, and exclusively as an antimicrobial and antioxidant agent.

AUTHOR CONTRIBUTIONS

LG and RD have designed the work. LG, RD, and NK executed the experiments, drafted the results, and approved the final version of the manuscript.

ACKNOWLEDGMENTS

The facilities provided by Central Instrumentation Facility, Pondicherry University is acknowledged. LG is grateful to Pondicherry University for providing Non-NET University Fellowship. NK is thankful to CSIR, Government of India for providing Research Associateship (HRDG sanction letter no/File no: 09/1202(001)/2018-EMR-I).

REFERENCES

Akhtar, M. S., Panwar, J., and Yun, Y. S. (2013). Biogenic synthesis of metallic nanoparticles by plant extracts. *ACS Sustain. Chem. Eng.* 1, 591–602. doi: 10.1021/sc300118u

Alam, H., Khatoon, N., Raza, M., Ghosh, P. C., and Sardar, M. (2018). Synthesis and characterization of nano selenium using plant biomolecules and their potential applications. *BioNanoScience* 9, 96–104. doi: 10.1007/s12668-018-0569-5

Ankamwar, B., Damle, C., Ahmad, A., and Sastry, M. (2005). Biosynthesis of gold and silver nanoparticles using *Emblica officinalis* fruit extract, their phase transfer and transmetallation in an organic solution. *J. Nanosci. Nanotechnol.* 5, 1665–1671. doi: 10.1166/jnn.2005.184

Anu, K., Singaravelu, G., Murugan, K., and Benelli, G. (2017). Green-synthesis of selenium nanoparticles using garlic cloves (*Allium sativum*): biophysical characterization and cytotoxicity on vero cells. *J. Cluster Sci.* 28, 551–563. doi: 10.1007/s10876-016-1123-7

Baganich, A. A., Mikla, V. I., Semak, D. G., Sokolov, A. P., and Shebanin, A. P. (1991). Raman scattering in amorphous selenium molecular structure and photoinduced crystallization. *Phys. Status Solidi* 166, 297–302. doi: 10.1002/pssb.2221660133

Battin, E. E., Zimmerman, M. T., Ramoutar, R. R., Quarles, C. E., and Brumaghim, J. L. (2011). Preventing metal-mediated oxidative DNA damage with selenium compounds. *Metallomics* 3, 503–512. doi: 10.1039/c0mt00063a

Bhattacharjee, S. (2016). DLS and zeta potential–What they are and what they are not? *J. Control. Release* 235, 337–351. doi: 10.1016/j.jconrel.2016.06.017

Bryden, W. L. (2007). Mycotoxins in the food chain: human health implications. *Asia Pac. J. Clin. Nutr.* 16, 95–101.

Chen, T., Wong, Y. S., Zheng, W., Bai, Y., and Huang, L. (2008). Selenium nanoparticles fabricated in *Undaria pinnatifida* polysaccharide solutions induce mitochondria-mediated apoptosis in A375 human melanoma cells. *Colloids Sur. B Biointerfaces* 67, 26–31. doi: 10.1016/j.colsurfb.2008.07.010

Combs, G. F., and Combs, S. B. (1986). *The Role of Selenium in Nutrition*. Orlando, FL: Academic Press, Inc.

Deepa, B., and Ganesan, V. (2014). Bioinspiredsynthesis of selenium nanoparticles using flowers of *Catharanthus roseus* (L.) *G. Don*. and Peltophorum pterocarpum (DC.) backer ex Heyne–a comparison. *Int. J. Chem. Tech. Res.* 2015:2.

Dharmananda, S. (2003). *Emblic Myrobalans: AMLA Key Herb of Ayurvedic Medicine. ITM*.

Eaton, P., Quaresma, P., Soares, C., Neves, C., de Almeida, M. P., Pereira, E., et al. (2017). A direct comparison of experimental methods to measure dimensions of synthetic nanoparticles. *Ultramicroscopy* 182, 179–190. doi: 10.1016/j.ultramic.2017.07.001

El-Ramady, H. R., Domokos-Szabolcsy, É, Abdalla, N. A., Alshaal, T. A., Shalaby, T. A., Sztrik, A., et al. (2014). Selenium and nano-selenium in agroecosystems. *Environ. Chem. Lett.* 12, 495–510. doi: 10.1007/s10311-014-0476-0

El-Wahab, H. M. F. A., and Moram, G. S. E. D. (2013). Toxic effects of some synthetic food colorants and/or flavor additives on male rats. *Toxicol. Ind. Health* 29, 224–232. doi: 10.1177/0748233711433935

Fesharaki, P. J., Nazari, P., Shakibaie, M., Rezaie, S., Banoee, M., Abdollahi, M., et al. (2010). Biosynthesis of selenium nanoparticles using *Klebsiella pneumoniae* and their recovery by a simple sterilization process. *Braz. J. Microbiol.* 41, 461–466. doi: 10.1590/S1517-838220100002000028

Forootanfar, H., Adeli-Sardou, M., Nikkhoo, M., Mehrabani, M., Amir-Heidari, B., Shahverdi, A. R., et al. (2014). Antioxidant and cytotoxic effect of biologically synthesized selenium nanoparticles in comparison to selenium dioxide. *J. Trace Elem. Med. Biol.* 28, 75–79. doi: 10.1016/j.jtemb.2013.07.005

George, E., Kasipandi, M., Vekataramana, M., Kumar, K. N., Allen, J. A., Parimelazhagan, T., et al. (2016). In vitro anti-oxidant and cytotoxic analysis of pogostemon mollis benth. *Bangladesh J. Pharmacol.* 11, 148–158.

Golechha, M., Bhatia, J., and Singh Arya, D. (2012). Studies on effects of *Emblica officinalis* (Amla) on oxidative stress and cholinergic function in scopolamine induced amnesia in mice. *J. Environ. Biol.* 33:95.

Huang, Y., He, L., Liu, W., Fan, C., Zheng, W., Wong, Y. S., et al. (2013). Selective cellular uptake and induction of apoptosis of cancer-targeted selenium nanoparticles. *Biomaterials* 34, 7106–7116. doi: 10.1016/j.biomaterials.2013.04.067

Iranifam, M., Fathinia, M., Rad, T. S., Hanifehpour, Y., Khataee, A. R., and Joo, S. W. (2013). A novel selenium nanoparticles-enhanced chemiluminescence system for determination of dinitrobutylphenol. *Talanta* 107, 263–269. doi: 10.1016/j.talanta.2012.12.043

Jiang, W., Fu, Y., Yang, F., Yang, Y., Liu, T., Zheng, W., et al. (2014). *Gracilaria lemaneiformis* polysaccharide as integrin-targeting surface decorator of selenium nanoparticles to achieve enhanced anticancer efficacy. *ACS Appl. Materials Interfaces* 6, 13738–13748. doi: 10.1021/am5031962

Kalagatur, N. K., Ghosh, O. S. N., Sundararaj, N., and Mudili, V. (2018a). Antifungal activity of chitosan nanoparticles encapsulated with *Cymbopogon martinii* essential oil on plant pathogenic fungi *Fusarium graminearum*. *Front. Pharmacol.* 9:610. doi: 10.3389/fphar.2018.00610

Kalagatur, N. K., Kamasani, J. R., and Mudili, V. (2018b). Assessment of detoxification efficacy of irradiation on zearalenone mycotoxin in various fruit juices by response surface methodology and elucidation of its in-vitro toxicity. *Front. Microbiol.* 9:2937. doi: 10.3389/fmicb.2018.02937

Kalagatur, N. K., Kamasani, J. R., Siddaiah, C., Gupta, V. K., Krishna, K., and Mudili, V. (2018c). Combinational inhibitory action of *Hedychium spicatum* L. essential oil and γ-radiation on growth rate and mycotoxins content of Fusarium graminearum in maize: response surface methodology. *Front. Microbiol.* 9:1511. doi: 10.3389/fmicb.2018.01511

Kalagatur, N. K., Mudili, V., Kamasani, J. R., and Siddaiah, C. (2018d). Discrete and combined effects of Ylang-Ylang (*Cananga odorata*) essential oil and gamma irradiation on growth and mycotoxins production by *Fusarium graminearum* in maize. *Food Control* 94, 276–283. doi: 10.1016/j.foodcont.2018.07.030

Kalagatur, N. K., Karthick, K., Allen, J. A., Ghosh, N., Sivaraman, O., Chandranayaka, S., et al. (2017). Application of activated carbon derived from seed shells of *Jatropha curcas* for decontamination of zearalenone mycotoxin. *Front. Pharmacol.* 8:760. doi: 10.3389/fphar.2017.00760

Kalagatur, N. K., Mudili, V., Siddaiah, C., Gupta, V. K., Natarajan, G., Sreepathi, M. H., et al. (2015). Antagonistic activity of *Ocimum sanctum* L. essential oil on growth and zearalenone production by Fusarium graminearum in maize grains. *Front. Microbiol.* 6:892. doi: 10.3389/fmicb.2015.00892

Kannan, S., Mohanraj, K., Prabhu, K., Barathan, S., and Sivakumar, G. (2014). Synthesis of selenium nanorods with assistance of biomolecule. *Bull. Materials Sci.* 37, 1631–1635. doi: 10.1007/s12034-014-0712-z

Kazempour, Z. B., Yazdi, M. H., Rafii, F., and Shahverdi, A. R. (2013). Sub-inhibitory concentration of biogenic selenium nanoparticles lacks post antifungal effect for *Aspergillus niger* and *Candida albicans* and stimulates the growth of *Aspergillus niger*. *Iran. J. Microbiol.* 5:81.

Kheradmand, E., Rafii, F., Yazdi, M. H., Sepahi, A. A., Shahverdi, A. R., and Oveisi, M. R. (2014). The antimicrobial effects of selenium nanoparticle-enriched probiotics and their fermented broth against *Candida albicans*. *DARU J. Pharm. Sci.* 22:48. doi: 10.1186/2008-2231-22-48

Kimura, K., Hane, Y., and Watanabe, Y. (2005). Effect of pre-coagulation on mitigating irreversible fouling during ultrafiltration of a surface water. *Water Sci. Technol.* 51, 93–100. doi: 10.2166/wst.2005.0626

Kirupagaran, R., Saritha, A., and Bhuvaneswari, S. (2016). Green synthesis of selenium nanoparticles from leaf and stem extract of leucas lavandulifolia sm. and their application. *J. Nanosci. Technol.* 2, 224–226.

Kokila, K., Elavarasan, N., and Sujatha, V. (2017). *Diospyros montana* leaf extract-mediated synthesis of selenium nanoparticles and their biological applications. *New J. Chem.* 41, 7481–7490. doi: 10.1039/c7nj01124e

Kong, H., Yang, J., Zhang, Y., Fang, Y., Nishinari, K., and Phillips, G. O. (2014). Synthesis and antioxidant properties of gum arabic-stabilized selenium nanoparticles. *Int. J. Biol. Macromol.* 65, 155–162. doi: 10.1016/j.ijbiomac.2014.01.011

Kumar, K. N., Venkataramana, M., Allen, J. A., Chandranayaka, S., Murali, H. S., and Batra, H. V. (2016). Role of *Curcuma longa* L. essential oil in controlling the growth and zearalenone production of Fusarium graminearum. *LWT Food Sci. Technol.* 69, 522–528. doi: 10.1016/j.lwt.2016.02.005

Li, S., Shen, Y., Xie, A., Yu, X., Zhang, X., Yang, L., et al. (2007). Rapid, room-temperature synthesis of amorphous selenium/protein composites using *Capsicum annuum* L extract. *Nanotechnology* 18:405101. doi: 10.1088/0957-4484/18/40/405101

Li, W. R., Xie, X. B., Shi, Q. S., Zeng, H. Y., You-Sheng, O. Y., and Chen, Y. B. (2010). Antibacterial activity and mechanism of silver nanoparticles on *Escherichia coli*. *Appl. Microbiol. Biotechnol.* 85, 1115–1122. doi: 10.1007/s00253-009-2159-5

Liu, X., Cui, C., Zhao, M., Wang, J., Luo, W., Yang, B., et al. (2008a). Identification of phenolics in the fruit of emblica (*Phyllanthus emblica* L.) and their antioxidant activities. *Food Chem.* 109, 909–915. doi: 10.1016/j.foodchem.2008.01.071

Liu, X., Zhao, M., Wang, J., Yang, B., and Jiang, Y. (2008b). Antioxidant activity of methanolic extract of emblica fruit (*Phyllanthus emblica* L.) from six regions in China. *J. Food Compost. Anal.* 21, 219–228. doi: 10.1016/j.jfca.2007.10.001

Malhotra, S., Welling, M. N., Mantri, S. B., and Desai, K. (2016). In vitro and in vivo antioxidant, cytotoxic, and anti-chronic inflammatory arthritic effect of selenium nanoparticles. *J. Biomed. Mater. Res. B Appl. Biomater.* 104, 993–1003. doi: 10.1002/jbm.b.33448

Mehmood, Z., Ahmad, I., Mohammad, F., and Ahmad, S. (1999). Indian medicinal plants: a potential source for anticandidal drugs. *Pharm. Biol.* 37, 237–242. doi: 10.1076/phbi.37.3.237.6296

Mittal, A. K., Kumar, S., and Banerjee, U. C. (2014). Quercetin and gallic acid mediated synthesis of bimetallic (silver and selenium) nanoparticles and their antitumor and antimicrobial potential. *J. Colloid Interface Sci.* 431, 194–199. doi: 10.1016/j.jcis.2014.06.030

Movasaghi, Z., Rehman, S., and Rehman, D. I. (2008). Fourier transform infrared (FTIR) spectroscopy of biological tissues. *Appl. Spectr. Rev.* 43, 134–179. doi: 10.1080/05704920701829043

Mudili, V., Siddaih, C. N., Nagesh, M., Garapati, P., Naveen Kumar, K., Murali, H. S., et al. (2014). Mould incidence and mycotoxin contamination in freshly harvested maize kernels originated from India. *J. Sci. Food Agric.* 94, 2674–2683. doi: 10.1002/jsfa.6608

Muniyandi, K., George, E., Mudili, V., Kalagatur, N. K., Anthuvan, A. J., Krishna, K., et al. (2017). Antioxidant and anticancer activities of Plectranthus stocksii Hook. f. leaf and stem extracts. *Agric. Nat. Resour.* 51, 63–73. doi: 10.1016/j.anres.2016.07.007

Nambiar, S. S., Paramesha, M., and Shetty, N. P. (2015). Comparative analysis of phytochemical profile, antioxidant activities and foam prevention abilities of whole fruit, pulp and seeds of *Emblica officinalis*. *J. Food Sci. Technol.* 52, 7254–7262. doi: 10.1007/s13197-015-1844-x

Park, Y., Hong, Y. N., Weyers, A., Kim, Y. S., and Linhardt, R. J. (2011). Polysaccharides and phytochemicals: a natural reservoir for the green synthesis of gold and silver nanoparticles. *IET Nanobiotechnol.* 5, 69–78. doi: 10.1049/iet-nbt.2010.0033

Philip, J., John, S., and Iyer, P. (2012). Antimicrobial activity of *Aloevera barbedensis*, *Daucus carota*, *Emblica officinalis*, honey and *Punica granatum* and formulation of a health drink and salad. *Malays J. Microbiol.* 8, 141–147.

Pientaweeratch, S., Panapisal, V., and Tansirikongkol, A. (2016). Antioxidant, anti-collagenase and anti-elastase activities of *Phyllanthus emblica*, *Manilkara zapota* and silymarin: an in vitro comparative study for anti-aging applications. *Pharm. Biol.* 54, 1865–1872. doi: 10.3109/13880209.2015.1133658

Pierard, G. E., Arrese, J. E., Piérard-Franchimont, C., and De Doncker, P. (1997). Prolonged effects of antidandruff shampoos-time to recurrence of *Malassezia ovalis* colonization of skin. *Int. J. Cosmetic Sci.* 19, 111–117. doi: 10.1046/j.1467-2494.1997.171706.x

Porter, A. G., and Jänicke, R. U. (1999). Emerging roles of caspase-3 in apoptosis. *Cell Death Differ.* 6:99. doi: 10.1038/sj.cdd.4400476

Prasad, K. S., Patel, H., Patel, T., Patel, K., and Selvaraj, K. (2013). Biosynthesis of Se nanoparticles and its effect on UV-induced DNA damage. *Colloids Sur. B Biointerfaces* 103, 261–266. doi: 10.1016/j.colsurfb.2012.10.029

Prasad, K. S., and Selvaraj, K. (2014). Biogenic synthesis of selenium nanoparticles and their effect on As (III)-induced toxicity on human lymphocytes. *Biol. Trace Elem. Res.* 157, 275–283. doi: 10.1007/s12011-014-9891-0

Price, M. L., and Butler, L. G. (1977). Rapid visual estimation and spectrophotometric determination of tannin content of sorghum grain. *J. Agric. Food Chem.* 25, 1268–1273. doi: 10.1021/jf60214a034

Qiu, W. Y., Wang, Y. Y., Wang, M., and Yan, J. K. (2018). Construction, stability, and enhanced antioxidant activity of pectin-decorated selenium nanoparticles. *Colloids Sur. B Biointerfaces* 170, 692–700. doi: 10.1016/j.colsurfb.2018.07.003

Ramamurthy, C. H., Sampath, K. S., Arunkumar, P., Kumar, M. S., Sujatha, V., Premkumar, K., et al. (2013). Green synthesis and characterization of selenium nanoparticles and its augmented cytotoxicity with doxorubicin on cancer cells. *Bioprocess Biosyst. Eng.* 36, 1131–1139. doi: 10.1007/s00449-012-0867-1

Rayman, M. P. (2005). Selenium in cancer prevention: a review of the evidence and mechanism of action. *Proc. Nutr. Soc.* 64, 527–542. doi: 10.1079/pns2005467

Rotruck, J. T., Pope, A. L., Ganther, H. E., Swanson, A. B., Hafeman, D. G., and Hoekstra, W. (1973). Selenium: biochemical role as a component of glutathione peroxidase. *Science* 179, 588–590. doi: 10.1126/science.179.4073.588

Sellamani, M., Kalagatur, N. K., Siddaiah, C., Mudili, V., Krishna, K., Natarajan, G., et al. (2016). Antifungal and zearalenone inhibitory activity of *Pediococcus pentosaceus* isolated from dairy products on *Fusarium graminearum*. *Front. Microbiol.* 7:890. doi: 10.3389/fmicb.2016.00890

Shah, C. P., Dwivedi, C., Singh, K. K., Kumar, M., and Bajaj, P. N. (2010). Riley oxidation: a forgotten name reaction for synthesis of selenium nanoparticles. *Mater. Res. Bull.* 45, 1213–1217. doi: 10.1016/j.materresbull.2010.05.013

Shahverdi, A. R., Fakhimi, A., Mosavat, G., Jafari-Fesharaki, P., Rezaie, S., and Rezayat, S. M. (2010). Antifungal activity of biogenic selenium nanoparticles. *World Appl. Sci. J.* 10, 918–922.

Shakibaie, M., Forootanfar, H., Golkari, Y., Mohammadi-Khorsand, T., and Shakibaie, M. R. (2015). Anti-biofilm activity of biogenic selenium nanoparticles and selenium dioxide against clinical isolates of *Staphylococcus aureus*, *Pseudomonas aeruginosa*, and *Proteus mirabilis*. *J. Trace Elem. Med. Biol.* 29, 235–241. doi: 10.1016/j.jtemb.2014.07.020

Sharma, G., Sharma, A. R., Bhavesh, R., Park, J., Ganbold, B., Nam, J. S., et al. (2014). Biomolecule-mediated synthesis of selenium nanoparticles using dried *Vitis vinifera* (raisin) extract. *Molecules* 19, 2761–2770. doi: 10.3390/molecules19032761

Siddaiah, C. N., Prasanth, K. V. H., Satyanarayana, N. R., Mudili, V., Gupta, V. K., Kalagatur, N. K., et al. (2018). Chitosan nanoparticles having higher degree of acetylation induce resistance against pearl millet downy mildew through nitric oxide generation. *Sci. Rep.* 8:2485. doi: 10.1038/s41598-017-19016-z

Singh, M., Sharma, N., Paras, H. S., Hans, N. S., Singh, N. P., and Sarin, A. (2018). Antioxidative potential of *Phyllanthus emblica* for oxidation stability of biodiesels. *Environ. Progress Sustain. Energy* 38, 721–726. doi: 10.1002/ep.13006

Sohal, I. S., O'Fallon, K. S., Gaines, P., Demokritou, P., and Bello, D. (2018). Ingested engineered nanomaterials: state of science in nanotoxicity testing and future research needs. *Particle Fibre Toxicol.* 15:29. doi: 10.1186/s12989-018-0265-1

Sowndarya, P., Ramkumar, G., and Shivakumar, M. S. (2017). Green synthesis of selenium nanoparticles conjugated *Clausena dentata* plant leaf extract and their insecticidal potential against mosquito vectors. *Artif. Cells Nanomed. Biotechnol.* 45, 1490–1495. doi: 10.1080/21691401.2016.1252383

Spallholz, J. E. (1994). On the nature of selenium toxicity and carcinostatic activity. *Free Radic. Biol. Med.* 17, 45–64. doi: 10.1016/0891-5849(94)90007-8

Srivastava, P., Braganca, J. M., and Kowshik, M. (2014). In vivo synthesis of selenium nanoparticles by *Halococcus salifodinae* BK18 and their anti-proliferative properties against HeLa cell line. *Biotechnol. Progress* 30, 1480–1487. doi: 10.1002/btpr.1992

Sundararaj, N., Kalagatur, N. K., Mudili, V., Krishna, K., and Antonysamy, M. (2019). Isolation and identification of enterotoxigenic *Staphylococcus aureus* isolates from Indian food samples: evaluation of in-house developed aptamer linked sandwich ELISA (ALISA) method. *J. Food Sci. Technol.* 56, 1016–1026. doi: 10.1007/s13197-019-03568-1

Sykes, J. E. (2013). *Canine and Feline Infectious Diseases-E-BOOK*. Amsterdam: Elsevier Health Sciences.

Tran, P. A., O'Brien-Simpson, N., Reynolds, E. C., Pantarat, N., Biswas, D. P., and O'Connor, A. J. (2015). Low cytotoxic trace element selenium nanoparticles and their differential antimicrobial properties against *S. aureus* and *E. coli*. *Nanotechnology* 27:045101. doi: 10.1088/0957-4484/27/4/045101

Vera, P., Echegoyen, Y., Canellas, E., Nerín, C., Palomo, M., Madrid, Y., et al. (2016). Nano selenium as antioxidant agent in a multilayer food packaging material. *Anal. Bioanal. Chem.* 408, 6659–6670. doi: 10.1007/s00216-016-9780-9

Verma, M., Rai, G. K., and Kaur, D. (2018). Effect of extraction solvents on phenolic content and antioxidant activities of Indian gooseberry and guava. *Int. Food Res. J.* 25, 762–768.

Wadhwani, S. A., Shedbalkar, U. U., Singh, R., and Chopade, B. A. (2016). Biogenic selenium nanoparticles: current status and future prospects. *Appl. Microbiol. Biotechnol.* 100, 2555–2566. doi: 10.1007/s00253-016-7300-7

Wang, J., Zhang, Y., Yuan, Y., and Yue, T. (2014). Immunomodulatory of selenium nano-particles decorated by sulfated *Ganoderma lucidum* polysaccharides. *Food Chem. Toxicol.* 68, 183–189. doi: 10.1016/j.fct.2014.03.003

Yang, F., Tang, Q., Zhong, X., Bai, Y., Chen, T., Zhang, Y., et al. (2012). Surface decoration by Spirulina polysaccharide enhances the cellular uptake and anticancer efficacy of selenium nanoparticles. *Int. J. Nanomed.* 7:835. doi: 10.2147/IJN.S28278

Yu, B., Zhang, Y., Zheng, W., Fan, C., and Chen, T. (2012). Positive surface charge enhances selective cellular uptake and anticancer efficacy of selenium nanoparticles. *Inorg. Chem.* 51, 8956–8963. doi: 10.1021/ic301050v

Zhang, W., Zhang, J., Ding, D., Zhang, L., Muehlmann, L. A., Deng, S. E., et al. (2018). Synthesis and antioxidant properties of *Lycium barbarum* polysaccharides capped selenium nanoparticles using tea extract. *Artif. Cells Nanomed. Biotechnol.* 46, 1463–1470. doi: 10.1080/21691401.2017.1373657

Zhang, S.-Y., Zhang, J., Wang, H.-Y., and Chen, H.-Y. (2004). Synthesis of selenium nanoparticles in the presence of polysaccharides. *Mat. Let.* 58, 2590–2594. doi: 10.1016/j.matlet.2004.03.031

Zheng, J. S., Zheng, S. Y., Zhang, Y. B., Yu, B., Zheng, W., Yang, F., et al. (2011). Sialic acid surface decoration enhances cellular uptake and apoptosis-inducing activity of selenium nanoparticles. *Colloids Sur. B Biointerfaces* 83, 183–187. doi: 10.1016/j.colsurfb.2010.11.023

Zonaro, E., Lampis, S., Turner, R. J., Qazi, S. J. S., and Vallini, G. (2015). Biogenic selenium and tellurium nanoparticles synthesized by environmental microbial isolates efficaciously inhibit bacterial planktonic cultures and biofilms. *Front. Microbiol.* 6:584. doi: 10.3389/fmicb.2015.00584

Zuverza-Mena, N., Martinez-Fernandez, D., Du, W., Hernandez-Viezcas, J. A., Bonilla-Bird, N., Lopez-Moreno, M. L., et al. (2017). Exposure of engineered nanomaterials to plants: insights into the physiological and biochemical responses-A review. *Plant Physiol. Biochem.* 110, 236–264. doi: 10.1016/j.plaphy.2016.05.037

Conflict of Interest Statement: The authors declare that the research was conducted in the absence of any commercial or financial relationships that could be construed as a potential conflict of interest.

frontiers
in Microbiology

ORIGINAL RESEARCH
published: 24 May 2019
doi: 10.3389/fmicb.2019.01141

Vancomycin-Loaded Nanoparticles Enhance Sporicidal and Antibacterial Efficacy for *Clostridium difficile* Infection

Yi-Hsuan Chen[1,2], Tsung-Ju Li[3], Bo-Yang Tsai[3], Liang-Kuei Chen[4], Yi-Hsin Lai[3], Meng-Jia Li[4], Cheng-Yang Tsai[2], Pei-Jane Tsai[3,4,5]* and Dar-Bin Shieh[2,3,6,7]*

[1] Department of Medicine, College of Medicine, National Cheng Kung University, Tainan, Taiwan, [2] Institute of Oral Medicine and Department of Stomatology, National Cheng Kung University Hospital, College of Medicine, National Cheng Kung University, Tainan, Taiwan, [3] Institute of Basic Medical Sciences, College of Medicine, National Cheng Kung University, Tainan, Taiwan, [4] Department of Medical Laboratory Science and Biotechnology, National Cheng Kung University, Tainan, Taiwan, [5] Center of Infectious Disease and Signaling Research, National Cheng Kung University, Tainan, Taiwan, [6] Advanced Optoelectronic Technology Center, National Cheng Kung University, Tainan, Taiwan, [7] Center for Micro/Nano Science and Technology, National Cheng Kung University, Tainan, Taiwan

Edited by:
Renata Katsuko Takayama Kobayashi,
State University of Londrina, Brazil

Reviewed by:
Meera Unnikrishnan,
University of Warwick,
United Kingdom
Jianhua Wang,
Feed Research Institute, Chinese Academy of Agricultural Sciences,
China

***Correspondence:**
Pei-Jane Tsai
peijtsai@mail.ncku.edu.tw;
pjtsai219@gmail.com
Dar-Bin Shieh
dbshieh@mail.ncku.edu.tw;
darbinshieh@gmail.com

Specialty section:
This article was submitted to
Antimicrobials, Resistance
and Chemotherapy,
a section of the journal
Frontiers in Microbiology

Received: 31 January 2019
Accepted: 06 May 2019
Published: 24 May 2019

Citation:
Chen Y-H, Li T-J, Tsai B-Y, Chen L-K, Lai Y-H, Li M-J, Tsai C-Y, Tsai P-J and Shieh D-B (2019) Vancomycin-Loaded Nanoparticles Enhance Sporicidal and Antibacterial Efficacy for Clostridium difficile Infection. Front. Microbiol. 10:1141. doi: 10.3389/fmicb.2019.01141

Current antibiotic treatments fail to eliminate the *Clostridium difficile* (*C. difficile*) spores and induce dysbiosis and intestinal inflammation via off-target effect, which causes refractory *C. difficile* infection raise an unmet need for a spore-specific antimicrobial treatment. We developed a sporicidal and antimicrobial vancomycin-loaded spore-targeting iron oxide nanoparticle (van-IONP) that selectively binds to *C. difficile* spores. Cryo-electron microscopy showed that vancomycin-loaded nanoparticles can target and completely cover spore surfaces. They not only successfully delayed the germination of the spores but also inhibited ∼50% of vegetative cell outgrowth after 48 h of incubation. The van-IONPs also inhibited the interaction of spores with HT-29 intestinal mucosal cells *in vitro*. In a murine model of C. difficile infection, the van-IONP significantly protected the mice from infected by *C. difficile* infection, reducing intestinal inflammation, and facilitated superior mucosal viability compared with equal doses of free vancomycin. This dual-function targeted delivery therapy showed advantages over traditional therapeutics in treating *C. difficile* infection.

Keywords: *Clostridium difficile*, spore, nanoparticle, target therapeutics, antibiotics

INTRODUCTION

Clostridium difficile (*C. difficile*) infection (CDI), the clinical manifestations of which (e.g., severe or bloody diarrhea, PMC, and toxic megacolon) are usually dangerous and fatal. *C. difficile* caused almost half a million infections in the United States in 2011, and an estimated 83,000 of the patients had at least one recurrence. Approximately 29,000 died within 30 days after the initial diagnosis (Bouwknegt et al., 2015). CDI is one of the most common healthcare-acquired infections associated with the rising use of antibiotics (Johnson et al., 1999). *C. difficile*, transmitted in humans through the fecal-oral route, is an anaerobic Gram-positive, spore-forming bacillus that produces toxins, including TcdA and TcdB, two large-molecules that damage intestinal mucosa and induce neutrophilic colitis and pseudomembranous colitis (PMC) (Leffler and Lamont, 2015). Moreover, more-virulent strains like BI/NAP1/027, an additional binary toxin composed of two subunits CdtA and CdtB, which increase the adherence of bacteria to the intestinal mucosa (Gerding et al., 2014).

The risk of *C. difficile* recurrence ranges from 20% after an initial episode to 60% after multiple recurrences. The healthcare costs associated with recurrent infection are usually much higher than are those from primary infections (Leffler and Lamont, 2015). Recurrences are primarily attributed to the dysbiosis and intestinal inflammation caused by current antibiotics like vancomycin (Gómez et al., 2017). Spore formation is also important for transmitting CDI because spores can withstand harsh environments, including radiation, high temperature, extreme freezing, and chemical disinfectants (Lawley et al., 2010; Deakin et al., 2012). Spores can re-activate themselves to the vegetative state via germination when the environment becomes favorable. Therefore, inactivating spores, increasing excretion of spores from GI tract, and inhibiting spore germination are the current unmet needs in CDI prevention and therapy.

To effectively prevent the transmission and recurrence of CDI, inactivation of spores is critical. Many nanoparticle types – silver, zinc oxide, and magnesium oxide – can inhibit spore dormancy and reactivation (Gopinath et al., 2015; Wagner et al., 2016). However, current sporicidal mechanisms rely on the release of the metal ions of the nanoparticles, which might be absorbed by the intestine. Therefore, an ideal sporicidal nanomaterial should target a specific spore but not release potentially toxic metal ions.

Furthermore, using antibiotics to eliminate newly germinated vegetative cells can reduce the infection rate of CDI. One approach for increasing the antimicrobial efficacy of antibiotics without raising the overall dose is to increase the local targeting concentration, particularly by conjugating antibiotics with pathogen-targeting delivery systems like nanoparticles. The targeting therapy concept originally comes from and is widely used in anticancer therapy (Sugahara et al., 2010; Simón-Gracia et al., 2016). This concept was gradually shifted to the antimicrobial field. In the regime of infectious disease, nanoparticles are conjugated with pathogen-targeting peptides or they act as pathogen-targeting materials themselves. For example, a *Staphylococcus aureus*-targeting peptide was conjugated to a nanoparticle platform loaded with antibiotics to treat difficult-to-manage infections in a mouse model (Kwon et al., 2017). The conjugation increases the local concentration of the antibiotics and reduces the off-target side effects. More important, the nanoparticle delivery platform appears to accumulate in the target site for longer period and able to penetrate deeper into infected tissue, which might also increase its antibacterial effects (Hussain et al., 2018).

We previously reported (Lee et al., 2017) that single-crystal non-stoichiometric $Fe_{3-\delta}O_4$ magnetite nanoparticles (IONP) was sporicidal and was uniquely spore-binding. However, those nanoparticles were unable to inhibit *C. difficile* vegetative cells. On the other hand, vancomycin alone was unable to eradicate *C. difficile* spores; thus, outcomes were often relapses of the disease. In this study, we developed vancomycin-loaded $Fe_{3-\delta}O_4$ magnetite nanoparticles (van-IONPs) to target and inhibit both the vegetative cells and the spores of *C. difficile*. We then comprehensively evaluated these van-IONPs *in vitro* and in a mouse *in vivo* disease model. We also explored the mechanisms of these synergistic inhibitory functions.

MATERIALS AND METHODS

Preparation of the $Fe_{3-\delta}O_4$ Iron Oxide Nanoparticles

$Fe_{3-\delta}O_4$ iron oxide nanoparticles (IONPs) were synthesized using thermal decomposition, as previously described (Huang et al., 2011). Briefly, 1.42 g of iron acetylacetonate was mixed with 0.57 mL of oleic acid and 20 mL of trioctylamine (all 3: Sigma-Aldrich, St. Louis, MO, United States). The solution was refluxed at 325°C in an argon environment for 30 min. The solution was then cooled to room temperature and washed with a toluene-ethanol solution. A magnet was used to concentrate and collect the NPs, which were then transferred to chloroform solutions (Merck, Whitehouse Station, NJ, United States) and mixed with 0.4 mg/mL of prostate specific membrane antigen (PSMA) (Sigma-Aldrich) for 6 h at 55°C. Finally, the PSMA-coated NPs were collected and washed 3 times with high purity water (MQ water, 18.2 MΩ cm, Milli-Q; Merck Ltd., Taipei, Taiwan).

Surface Modification of Nanoparticles With Vancomycin

The IONPs (6×10^{15} particles) were dissolved in 0.1 mL of 0.1 M 2-ethanesulfonic acid (MES) buffer with 0.5 M sodium chloride. The solution was then charged with 2 mg of carbodiimide (EDC) and 2.5 mg of N-hydroxysuccinimide (NHS) (all: 2 Sigma-Aldrich, St. Louis, MO) and mixed for 30 min at 4°C to activate the functional group for conjugation. After the reaction with EDC/NHS, the IONPs were attracted by a magnet and washed 3 times with MES buffer to remove residual EDC/NHS. The activated IONPs were then conjugated with 0.5 mg of vancomycin in 0.1 mL of MES buffer and stirred for 3 h at room temperature. The resulting vancomycin-loaded IONPs (van-IONPs) were centrifuged at 15,500 × *g* and the supernatant was collected for the free vancomycin quantification. The pellets were washed 3 times with 0.1 mL of MES buffer and finally dispersed in 0.05 mL of MES (concentration: 500 μg/mL) and stored at 4°C.

Confirmation of Vancomycin-Modified Nanoparticles by Fourier Transform Infrared Spectroscopy

Fourier transform infrared spectroscopy (FTIR) was used to confirm that the vancomycin had been successfully conjugated on the surfaces of IONPs. The data were collected using the synchrotron radiation (SR-FTIR) spectromicroscopy facility at the National Synchrotron Radiation Research Center (NSRRC) beamline 14A1 (BL14A1) in Taiwan. An FTIR spectrometer (Thermo Nicolet 6700; Thermo Fisher Scientific, Waltham, MA, United States) and continuum infrared microscope were used to record the data (resolution: 4 cm^{-1}, step size: 15 μm, aperture size: 30 μm, and 128 scans).

Quantification of Vancomycin Loaded on Nanoparticles

Microplate readers (SpectraMax M2/M2e; Molecular Devices, San Jose, CA, United States) were used to measure the fluorescence emission spectra of vancomycin hydrochloride (Sigma-Aldrich) solutions. To plot the standard curve of vancomycin concentration, a 96-well plate was loaded with solutions (0.1 mL at vancomycin concentrations of 0, 0.0625, 0.125, 0.25, and 0.5 mg/mL). Fluorescence was measured using a 280 nm excitation wavelength and a 380 nm emission wavelength. 0.1 mL supernatants collected from the conjugation step were moved to a 96-well plate to measure fluorescence. The final concentrations of the supernatants were compared with the initial concentrations to calculate the binding amount of vancomycin on the van-IONPs.

Bacterial Culture and Spore Purification

C. difficile CCUG 37780 (tcdA−, tcdB−) and BAA-1805 (tcdA+, tcdB+) were purchased from the Culture Collections of the University of Göteborg (Göteborg, Sweden), and from American Type Culture Collection (Manassas, VA, United States), respectively. All strains were incubated in brain-heart infusion medium (BHIS; BD Difco, Franklin Lakes, NJ, United States), which supplemented with 0.5% yeast extract (BD Difco) and 0.1% L-cysteine (Amresco, Solon, OH, United States), at 37°C under anaerobic conditions. The spores were prepared with modifications and then purified as previously described (Sorg and Sonenshein, 2010). Briefly, 0.2 mL of *C. difficile* in BHIS medium was spread on 6-well dishes with BHIS, and then the dish was incubated at 37°C in an anaerobic chamber for 7 days. After the incubation, the 6-well dishes were washed with 200 μL of ice-cold water to separate the cells on the dishes; the cells were resuspended in 3 mL of ddH_2O. To further separate the spores with the residual vegetative cells, 100 μL of the suspension was spread on top of the 1 mL 50% Nycodenz® solution in an Eppendorf tube, and then centrifuged at 15,500 × *g* for 30 min to separate spores from vegetative cells. The pellets were washed and centrifuged 5 times with ice-cold ddH_2O to remove the Nycodenz, and then stored at 4°C.

Spore Germination Assay

The stock solutions containing the spores were incubated at 60°C for 30 min and then the supernatant had been removed, the BHIS was added to a final spore concentration (15,500 × g) of OD600 0.2. Two microliters of solution were dispensed into each Eppendorf tube, which was then centrifuged at 15,500 × g to remove the BHIS. The pellets were resuspended in 100 μL of ddH_2O test medium for the following groups: (1) free vancomycin (18 mg/mL), (2) bare IONPs (500 μg/mL), (3) the van-IONPs (IONP: 500 μg/mL; Equivalent vancomycin on such concentration of IONPs: 18 mg/mL), (4) 3% bleach (Wako, Osaka, Japan), and (5) ddH_2O alone (negative control). After 20 min of incubation, each tube was centrifuged at 15,500 × *g*, washed 3 times with ddH_2O, and then resuspended in 180 μL of BHIS. A 90 μL solution from each test sample was then transferred to a 96-well plate that contained 10 μL of taurocholic acid (TA)(Sigma-Aldrich) to the final concentration 10 mM to induce spore germination. The germination process was analyzed for 12 min at a wavelength of 600 nm (an optical density of 600: OD600) determined at 1 min intervals using a spectrophotometer (Tecan Austria GmbH, Grödig, Austria) at room temperature. The Tn and T0 denote the OD values at time n and time 0. Untreated spores were used as negative controls. Spore germination induction and analyses were modified from previously described protocols (Sorg and Sonenshein, 2010).

Spore Viability Analysis

After the germination assay, 100 μL of solution was removed from the 96-well plate, serially diluted, and spread evenly on the BHIS dishes. The plate-counts (CFU/mL) were done after 48 h of incubation in an anaerobic tank at 37°C.

Nanoparticle-Spore Binding Efficiency Assay

C. difficile BAA-1805 spores at a concentration of OD600 2.0 were incubated with 100 μL van-IONPs (75, 150, 300, 500, 700 μg/mL) in ddH_2O in tubes for 20 min. The spore samples treated with ddH_2O were mock controls. The samples were then placed next to a magnet for 20 min to transfer all the supernatant to clean tubes. The OD600 of the supernatants were measured and compared with the control. The binding efficiency was calculated as followed.

$$\text{Efficiency} = \left(1 - \frac{\text{OD600 of supernatant of experiment group}}{\text{OD600 of supernatant of mock control}}\right) \times 100\%$$

Then, the magnet-concentrated fractions were washed 3 times with ddH_2O to remove the residual supernatant and resuspended in 100 μL of ddH_2O. The spores were lysed via heating the van-IONP pellet-spore complex in 95 Celsius degree for 15 min to extract the DNA from spores (Rose et al., 2011). A polymerase chain reaction (PCR) was used to measure 1 μL of magnetically-concentrated fractions and of supernatants for the presence of the *TPI* gene, a *C. difficile* housekeeping gene. Images of spores and of van-IONP pellets in the supernatant were captured using a transmission electron microscope (TEM) (JEM-1400; JEOL, Tokyo, Japan).

Spore Adhesion Assay

To assess the ability of our van-IONPs to reduce the adherence of spores to the intestinal epithelial cells, we used *in vitro* human intestinal epithelial cells (HT29). We adapted and modified the method previously described to assay the adherence of spores to the intestinal epithelial cells (Mora-Uribe et al., 2016). In brief, HT29 cells were incubated in the 24-well plate (1.8×10^5 cells/well). *C. difficile* BAA-1805 spores (1.8×10^6; MOI 10) were treated with FM 4-64 fluorescent dye, coincubated with van-IONPs for 20 min, and then added to the plate. The spores were added to the wells to infect the HT29 cells. The spore-infected cells were incubated for 3 h for spore adherence. After they had been incubated, the spores unbound to cells were washed away 3 times with PBS, and the HT29 cells remaining on the plate were examined under a fluorescence microscope. The fluorescence intensity was measured by ImageJ and the relative fluorescence was calculated by setting intensity of spore alone group as one.

In vivo Analysis of the Efficacy of Vancomycin-Conjugated Nanoparticles

Animal studies were approved by the Laboratory Animal Center of the National Cheng Kung University Medical College (IRB #: NCKU-IACUC-105-182) and performed according to the local guidelines. To evaluate the *in vivo* efficacy of the targeted therapy, an infected mouse model was used. The protocol was adapted and modified from previous report (Hung et al., 2015). Briefly, the mice were given an antibiotic cocktail (0.4 mg/mL of kanamycin, 0.035 mg/mL of gentamicin, and 0.057 mg/mL of colistin) in their drinking water for 48 h, and then they were given an oral 200 μL proton pump inhibitor (PPI) (2 mg/mL) every 12 h for 2 days before they were infected with *C. difficile* spores. All the mice were pre-gavaged with a 50 μL PPI (2 mg/mL) and then intraperitoneally (i.p.) injected with clindamycin (4 mg/kg). *C. difficile* BAA-1805 spores (2×10^6 CFU) were then coincubated with 0.1 mL 500 μg/ml van-IONPs, 0.1 mL 500 μg/ml IONP, 0.1 mL 18 mg/ml vancomycin and 0.1 mL ddH_2O as spore alone group for 20 min to enable attachment of van-IONPs to the spores. before the mice were fed with sample solution through oral route. The antibiotic cocktail water was replaced with normal water after the *C. difficile* infection symptoms (e.g., diarrhea, weight loss, hunched posture, and death) were monitored. All mice were anesthetized with isoflurane with oxygen and their colon tissue was harvested 72 h later. TRIzol reagent (Sigma-Aldrich) was used to extract colon tissue RNA. The levels of inflammatory gene expression were estimated using a real-time PCR assay (StepOnePlus; Applied Biosystems). Histopathology was used to evaluate the damage caused by CDI to the intestinal mucosa. The colon samples were fixed in 4% formaldehyde buffered with PBS and then embedded in paraffin. Deparaffinized 6 μm-thick sections were stained with hematoxylin and eosin (H&E) and Periodic acid-Schiff (PAS) stains. The results were captured using an optical microscopy.

Statistics

All data were expressed as the mean ± standard deviations and statistical comparisons among the groups were analyzed by Student's *t*-test. Multiple intergroup comparisons were assessed by one-way ANOVA, followed by post hoc Tukey's test with GraphPad Prism version 6.0. Statistical significance was set at $P < 0.05$.

RESULTS

Clostridium difficile Spore Germination Assay of Free Vancomycin

To show whether the free vancomycin can target spores and inhibit the spore germination as well as the following vegetative cells growth, an optical density-based spore germination assay was done. The CCUG 37780 spores after vancomycin treatment were washed 3 times with ddH_2O and activated in 10 mM of taurocholic acid (TA) solution. Spore germination was not significantly inhibited after vancomycin treatment at 18 mg/mL concentration (**Figure 1A**). Colony-forming unit (CFU) assay showed no significant inhibition of spore germination 48 h after they had been treated with vancomycin at 18 mg/mL concentration (**Figure 1B**). The results suggest the vancomycin cannot specifically target to spores and to exert antibacterial effect ($n = 4$).

Targeting the Efficacy of Vancomycin-Loaded $Fe_{3-\delta}O_4$ Nanoparticles on *C. difficile* Spores

FTIR analysis (**Supplementary Figure 1**) and fluorescence spectroscopy confirmed the conjugation and loading capacity of the vancomycin and the IONPs ($n = 5$). Vancomycin has a fluorescence emission peak of 350 nm when excited by 280 nm photons (Zarkan et al., 2016). We obtained a standard curve and estimated that there were 5.8 ± 1.5 molecules of vancomycin on each IONP.

To estimate the dose dependence of van-IONP in spore binding, we perform the nanoparticle-spore binding efficiency assay ($n = 4$). The results showed that nanoparticles targeted to the spores were dose-dependent and reached a plateau at concentration of 500 μg/mL (**Figure 1C**). Furthermore, to confirm the spores were successfully captured by the van-IONP, PCR analysis was performed, and the result confirmed the presence of *C. difficile* spores on the surface of the van-IONPs. The band of the *TPI* gene, which is the housekeeping gene of *C. difficile*, showed that the van-IONPs captured the spores (**Figure 1D**). Based on the binding efficiency assay which showed a plateau after 500 μg/mL, we chose 500 μg/mL as our standard concentration of van-IONPs in the following experiments. The concentration of vancomycin on van-IONP was estimated to be 18 mg/mL.

The specific targeting effect of the van-IONPs on the *C. difficile* spores was also assayed using a transmission electron microscope (TEM). TEM images showed that spores treated with 500 μg/mL van-IONPs were fully surrounded by the IONPs (**Figure 1E**).

In vitro Assay of the Therapeutic Potential of Vancomycin-Conjugated Nanoparticles

To investigate whether van-IONPs have inhibitory effect on spore germination, an optical density-based spore germination assay was done ($n = 4$). The spore germination was significantly inhibited by both van-IONP and IONP (**Figure 1F**). After

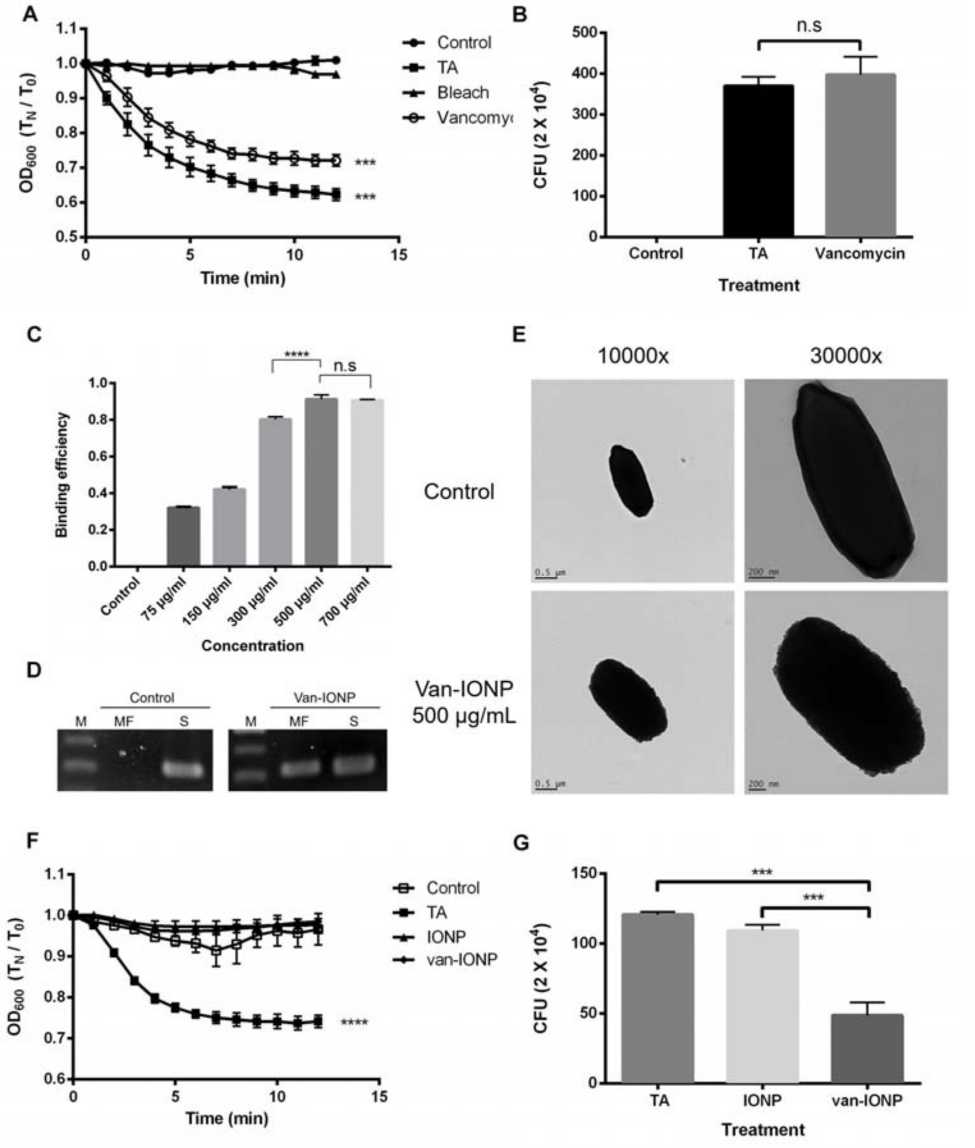

FIGURE 1 | *In vitro* assay of the targeting property and therapeutic potential of van-IONPs. **(A)** The vancomycin treatment at 18 mg/mL did not significantly inhibit spore germination in the 12-min germination induction analysis. **(B)** There was no significant difference in the CFU count between the 18 mg/mL vancomycin-treated group and the 10 mM TA-treated group after 48 h of incubation. The result of both 12 min germination induction analysis and 48 h incubation showed that the free vancomycin was unable to specifically target the spores and to exert prolonged antibacterial effect on vegetative cell outgrowth. **(C)** The OD_{600} binding test shows the binding efficiency of van-IONPs to spores reach a plateau after 500 μg/mL. **(D)** The PCR assay of magnetically-concentrated fraction showed the presence of *TPI* gene, a housekeep gene of *C. difficile* spores, on the van-IONPs. (MF, magnetically-concentrated fraction; S, supernatant). **(E)** The upper TEM image shows that native spores have a smooth coat; the lower TEM images show accumulated van-IONPs on spore surfaces with rough surface after incubation and that the spores were completely covered with 500 μg/mL van-IONPs. **(F)** The van-IONP treatment can significantly inhibit the germination of spores in the 12 min germination induction analysis **(G)** The CFU of the vegetative cell outgrowth was counted by plating and incubating them on BHIS for 48 h and showed van-IONP is efficacious in inhibition the vegetative cell outgrowth. ***$P < 0.001$, ****$P < 0.0001$.

germination, the spores were plated for the CFU assay. The CFU assay showed that after 48 h of incubation, the vancomycin on the van-IONPs had bound to the spores and that the growth of newly germinated vegetative cells had been inhibited (**Figure 1G**) The CFU assay showed that the vancomycin was brought to the surface of spores via van-IONP to inhibit the outgrowth of the vegetative cells.

To further illustrate the protective effect of van-IONP to the intestinal mucosa, a spore adhesion assay ($n = 4$) was conducted and showed that spores treated with van-IONPs had fewer adherence with intestinal mucosal comparing with the control group (spore-only) (**Figure 2A**). The fluorescence intensity was measured by ImageJ and the control group was significantly higher than that of the van-IONP-treated group (**Figure 2B**). The

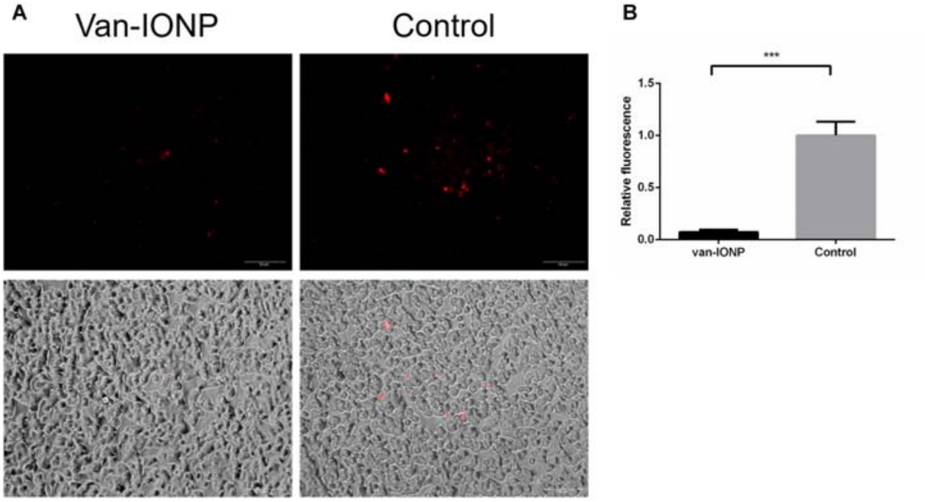

FIGURE 2 | *In vitro* assay of intestinal protective potential of van-IONPs. **(A)** Fluorescence (upper) and light-overlaid (lower) micrographs of adhered fluorescent-labeled *C. difficile* spores (red) to monolayers of HT29 cells. The amount adhered to spores was lower in the van-IONP-treated group than in the control group. **(B)** The fluorescence intensity was counted using ImageJ software; the intensity was significantly higher in the control group than in the van-IONP-treated group ($n = 5$). ***$P < 0.001$.

result implied the van-IONPs can reduce the binding affinity of spores to the intestinal cells.

In vivo Assay of Therapeutic Effects of Vancomycin-Conjugated Nanoparticles

To investigate the potential of the targeted therapy of van-IONPs in clinical translation, we compared the therapeutic effects of the free vancomycin, which is widely used to treat CDI, with vancomycin-conjugated nanoparticles. In our infection model ($n = 6$), the mice were orally infected by the toxigenic *C. difficile* BAA-1805 spores, resulting in 17% mortality after 3 days from infection without treatment. The inflammatory signal peaked 3 days after *C. difficile* infection had been induced (Lee et al., 2017). Thus, in our *in vivo* mice experiment, the mice were sacrificed 3 days after infection for analysis. A real-time reverse transcription quantitative polymerase chain reaction (RT-qPCR) was used to determine the gene expression of the proinflammatory cytokines TNF-α and IFN-γ. The inflammation level in van-IONP is significantly lower than spore alone, vancomycin, and INOP group. To note that, the expression level of TNF-α and IFN-γ in free vancomycin group is significantly higher than van-IONP group, suggesting that a high dose of free vancomycin can further increase inflammation level in CDI mice (**Figures 3A,B**). In the clinical outcome, both body weight loss and cecum weight have no difference between free vancomycin, IONP and van-IONP group (**Figures 3C**,**D**). The histopathological image showed lower neutrophil infiltration in van-IONP group compared to spore alone and IONP group (**Figure 3F**). The mucosal cells of free vancomycin showed more erosion than van-IONPs group (**Figure 3F**) and the PAS stain also showed more mucosal cell viability in mucus production in van-IONP comparing to free vancomycin group (**Figure 3G**). The pathological scores measured by the inflammatory cell infiltrate, epithelial changes and mucosal architectures in 6 random fields of tissue sections according to the suggested guideline (Erben et al., 2014). The result of van-IONP showed significantly lower score than other groups which indicate the therapeutic effects of van-IONP *in vivo* (**Figure 3E**).

DISCUSSION

C. difficile is a major cause of healthcare-acquired life-threatening diarrhea, which is associated with substantial mortality around the world (Ananthakrishnan, 2011). The traditional treatments of choice include the use of antibiotics metronidazole and vancomycin. However, the off-target effect of the traditional antibiotics can contribute to intestinal dysbiosis (aka: dysbacteriosis) and result in recurrent infection (Hopkins and Wilson, 2018). To reduce the off-target effect, one on the paradigms is to deliver the therapeutics via targeting vehicles. Antibiotics-loaded nanoparticles have been widely used in combating other strains of bacteria, such as e.g., *Staphylococcus aureus* (Alvarez et al., 2014; Kavruk et al., 2015; Hussain et al., 2018), and *Pseudomonas aeruginosa* (Kwon et al., 2017), to provide sustained and targeted delivery to enhance the increase therapeutic efficacy. However, the carrier nanoparticles of those delivery systems do not possess any therapeutic efficacy.

The interaction of *C. difficile* spores to the intestinal mucosa plays a significant role in many stages of the CDI infection: the initial stage of infection, the persistence of *C. difficile* spores in healthy individuals and the CDI relapse (Paredes-Sabja and Sarker, 2012). While vancomycin is highly active against vegetative cells, there is no evidence to show it has antispore activity (Baines et al., 2009); and although new antibiotics, fidaxomicin, was reported to inhibit sporulation, its inhibitory effect on preexisting spores is unclear (Babakhani et al., 2012).

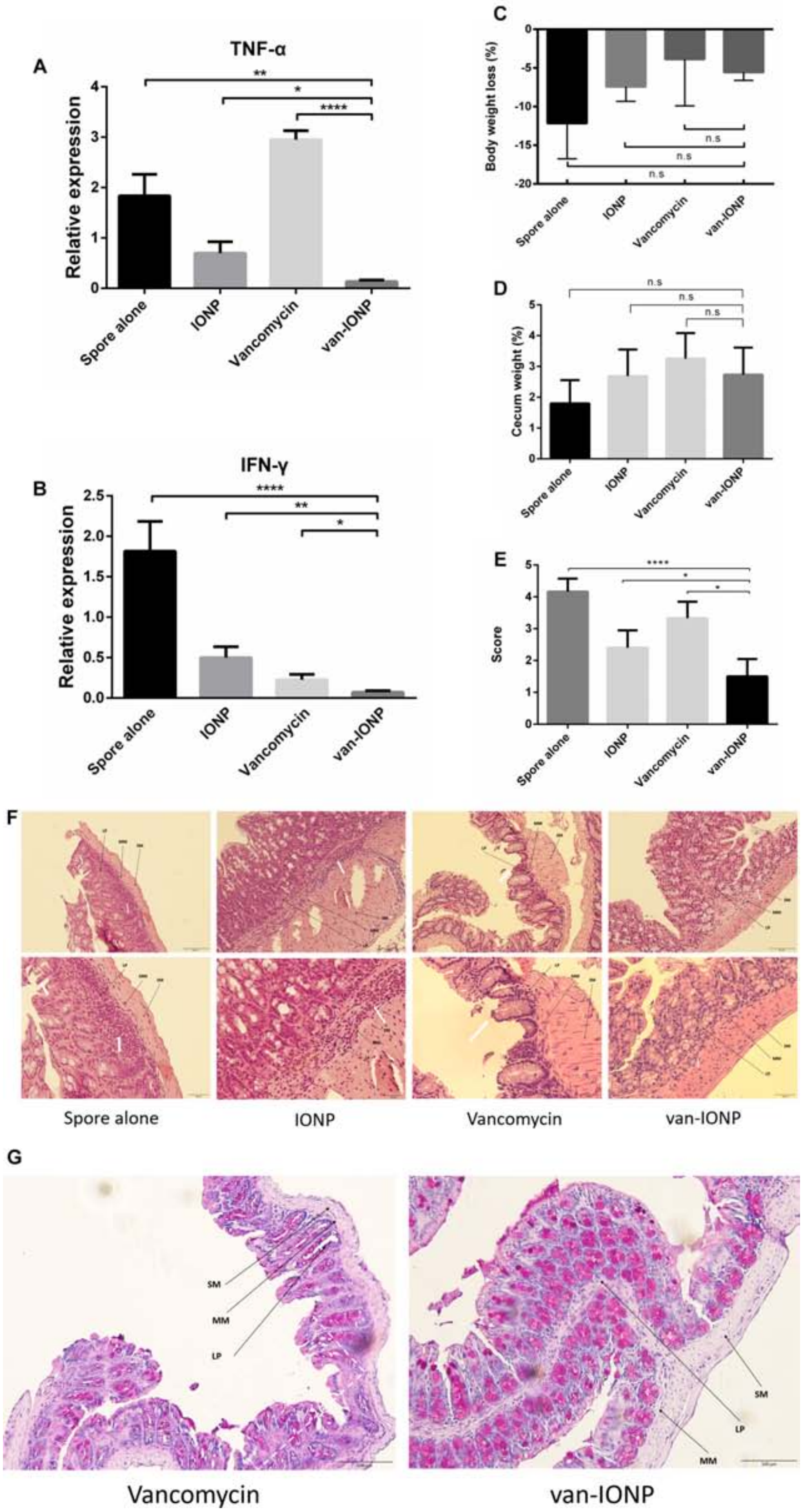

FIGURE 3 | *In vivo* assay of therapeutic effects of van-IONPs in mice ($n = 6$). **(A)** The TNF-α expression level of the van-IONP was significantly lower than spore alone, free vancomycin and IONP group. TNF-α expression is highest in free vancomycin group which suggests the intestinal cell damage caused by free vancomycin. **(B)** The IFN-γ expression level was significantly lower than spore alone, free vancomycin and IONP group **(C)** The cecum weight of the mice was not significantly different between each group. **(D)** The body weight loss of the mice was not significantly different between each group **(E)** The pathological scores were

(Continued)

FIGURE 3 | Continued
measured by 6 randomly selected sections of intestinal tissue and the van-IONP group is significantly lower than other groups **(F)** Histopathological images showed lower neutrophil infiltration in the lamina propria (LP) and submucosa (SM) of van-IONP group compared to spore alone and IONP group. The mucosal layers of the free vancomycin group showed greater erosion than the van-IONP group. **(G)** PAS staining shows the decreased mucosal cell viability damaged by free vancomycin. (LP, lamina propria; MM, muscularis mucosae; SM, submucosa; white arrow, lesion site) $^*P < 0.05$, $^{**}P < 0.01$, $^{****}P < 0.0001$.

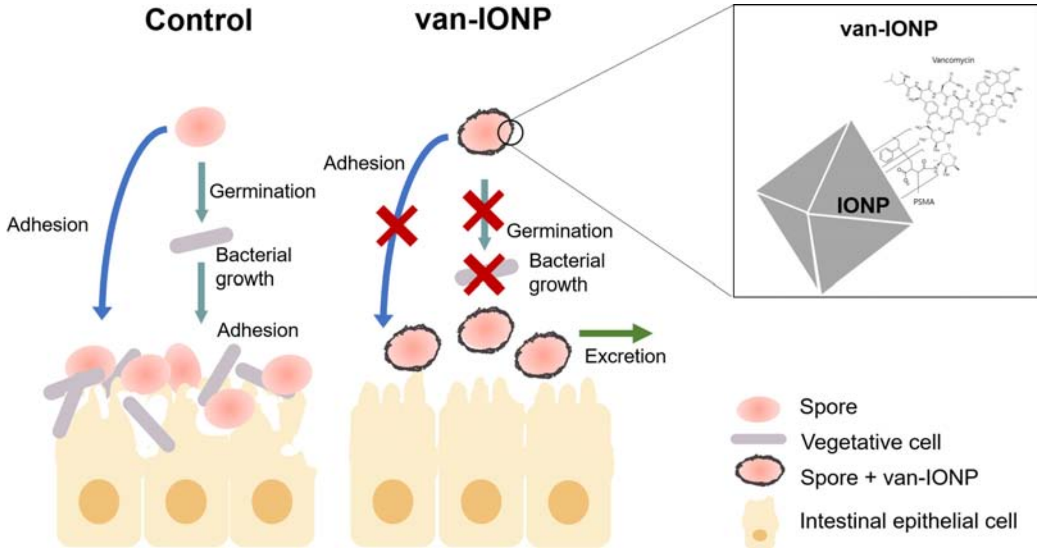

FIGURE 4 | Schematic illustration of the potential mechanisms that underlay the dual-function efficacy of van-IONPs to *C. difficile* infection. Van-IONPs bound to spores and inhibited their germination and adhesion to intestinal mucosa, which increased clearance of the spores from the mucosa surface. The bounded van-IONP can also eliminate the newly germinated vegetative cells. This was enabled by conjugating vancomycin to the surface of IONPs (Box: top right) and creating a locally concentrated dosage of vancomycin around spores.

Because *C. difficile* infection contains spore germination phase and vegetative outgrowth phase, we developed a dual-function targeted therapy using van-IONPs by conjugating IOPNs with vancomycin to inhibit germination as well as outgrowth. We firstly confirmed that IONPs have spore-specific binding properties that make them useful for the targeted delivery of synergistic therapeutics. TEM images showed that our van-IONPs had surrounded the spores even after they had been rigorously washed, which indicated the strong binding affinity. The mechanism by which the van-IONP can possess strong binding affinity to the spores is still not very well understood. It is probably due to the hydrophobic interaction between the exosporium and the nanoparticles (Joshi et al., 2012; Knowles et al., 2018). The van-IONP also showed inhibitory effect on the spore germination in the germination assay. One of the possible mechanisms is the interference of the CspC receptor pathway caused by surrounded nanoparticles that are needed in the spore germination, which is a bile salt sensitive receptor and plays an important role in initiating the spore germination (Francis et al., 2013).

Moreover, several studies report that immobilization of antibiotics on nanocarriers can be a general strategy for enhancing the concentration and potentiate the antimicrobial effect to the surface of pathogens (Hassan et al., 2017; Hussain et al., 2018). In our study, the van-IONPs and the conjugated vancomycin surround the spore very densely under the TEM images. The bioavailability of conjugation of vancomycin to the surface of nanocarriers through EDC/NHS reaction has been shown in past studies and the vancomycin can still preserved the functional groups to form specific hydrogen bonding toward gram-positive *C. difficile* vegetative cells at the terminal d-alanyl-d-alanine moieties (Gu et al., 2003; Kell et al., 2008). We found that the van-IONPs significantly inhibited the outgrowth of germinated spores after 48 h of incubation whereas the IONPs and free vancomycin cannot. The result showed vancomycin can be brought to the surface of spores by our spore-targeting van-IONPs. This local aggregation of van-IONP around spores may concentrate the vancomycin dosage around the spores (Qi et al., 2013; Hassan et al., 2017). We also observed that under the same concentration, the van-IONP can inhibit outgrowth of vegetative cells and IONP cannot (**Supplementary Figure 2**). Thus, our van-IONPs not only inhibit spore germination, but also enable vancomycin to accumulate on the spore surface, which optimizes its antibacterial efficacy to outgrowth of vegetative cells. This dual-function design is necessary to solve the unmet needs in current CDI therapy, which cannot deal with the spores.

Studies showed the outer layer of the *C. difficile* spores contain enterocytic-surface-specific ligands and receptor that provide specific adherence to the intestinal mucosal cells. The hydrophobicity of the intact exosporium of the spores also contribute to stronger attachments to the cells. The alternation to the ultrastructure of the exosporium reduced the hydrophobicity and adherence (Joshi et al., 2012; Paredes-Sabja and Sarker, 2012; Mora-Uribe et al., 2016). We hypothesized the coating of the van-IONPs around the spores can interfere with the ligand-receptor and hydrophobic interactions between the exosporium and the intestinal mucosal cells and significantly reduce the number of residual spores in the gut. In our study, after three rounds of washing with buffer, lower amount of residual fluorescence of dyed spores was observed in the HT29 cells in van-IONP treated group. We found that vancomycin does not affect the IONP adherence to spore and can significantly reduce spore adherence to mucosal cells, which indicate the vancomycin is not important for reducing spore adherence (**Supplementary Figure 3**). In the present study, van-IONP can significantly reduce adherence of spores to the HT29 and show potentially protective effect to the intestinal mucosa.

The 22 nm IONP has been shown to have high biocompatibility in previous report (Lee et al., 2017) and conjugation of vancomycin through EDC/NHS reaction to nanoparticle won't increase its toxicity (Qi et al., 2013). The vancomycin on van-IONP was also stable in the acidic environment of the mouse digestive tract. To evaluate the therapeutic effect and the benefit of specific targeting provided by our van-IONP, we analyzed the clinical severity and the inflammation levels in the mouse intestines. 500 μg/mL van-IONPs can significantly reduce severity of infection in inflammatory characteristic and pathological outcome comparing to other groups. However, there were no significant differences in total body weight loss or cecum weight between the groups. This might be associated with many confounding factors such as the uncontrollable intake of food and water of each mouse. The expression of interferon gamma (IFN-γ) and tumor necrosis factor alpha (TNF-α) is significantly lower in van-IONP group than in other groups, which showed the potential for van-IONPs as an effective therapeutic agent. The surge of necrosis factor alpha (TNF-α), which mediates the necrotic cell death pathway of the most cells (Morgan et al., 2008), in free vancomycin group suggested the excessive concentration of antibiotics might create reactive oxidative stress to the cells and induce mitochondrial dysfunction to initiate cell death (Kalghatgi et al., 2013). This is consistent with reports (Sekirov et al., 2008) that vancomycin might induce tissue damage, disrupt intestinal microbiota, and result in a more severe inflammation. Though vancomycin was effective in suppressing acute infection but the perturbation of antibiotics to the intestinal tissues lead to more susceptible to infection (Warren et al., 2013). The histopathologic analysis of the colon tissue showed more mucosal cell shedding in H&E stain in free vancomycin group and PAS staining also confirmed that mucus secretion was lower in the free vancomycin-treated CDI mice than in the van-IONPs-treated group, which indicated profound damage to the intestinal mucosa.

CONCLUSION

In conclusion, we developed a vancomycin-targeted delivery system against CDI in which the nanocarrier also inhibited spore germination. The underlying mechanisms that our van-IONPs utilized were shown in **Figure 4** and include: (1) the van-IONPs strongly bind to *Clostridium difficile* spores and reduce their adherence to the intestinal mucosa; (2) biocompatible van-IONPs with a high loading capacity aggregates vancomycin around the pathogens; (3) the van-IONPs also inhibited spore germination. Finally, the van-IONPs could be scaled up using green synthesis processing at a significantly lower cost than current antimicrobial targeting biologics. Furthermore, the intriguing mechanisms underlying the specific interaction between van-IONPs and *Clostridium difficile* spores warrant additional investigation, which might lead to new prophylactic or therapeutic to a wide spectrum of other spore-generating pathogens in human and livestock diseases.

ETHICS STATEMENT

This study was carried out in accordance with the recommendations of Laboratory Animal Center of the National Cheng Kung University Medical College (IRB #: NCKU-IACUC-105-182). The protocol was approved by the Laboratory Animal Center of the National Cheng Kung University Medical College.

AUTHOR CONTRIBUTIONS

Y-HC, P-JT, and D-BS designed the experiments. Y-HC, L-KC, Y-HL, C-YT, and M-JL conducted the experiments. Y-HC, T-JL, B-YT, and L-KC analyzed the data. Y-HC, T-JL, and B-YT prepared the manuscript.

FUNDING

This work was financially supported by the Center of Applied Nanomedicine, National Cheng Kung University from The Featured Areas Research Center Program within the framework of the Higher Education Sprout Project by the Ministry of Education (MOE) in Taiwan and also supported by the grants from Ministry of Science and Technology (MOST 108-2321-B-006-004, MOST 107-2321-B-006-010, MOST 107-2321-B-006-019, MOST 107-2314-B-006-02) and Ministry of Health and Welfare (MOHW107-TDU-B-211-123003).

ACKNOWLEDGMENTS

We thank the technical assistance provided by the lab members of P-JT and D-BS.

SUPPLEMENTARY MATERIAL

The Supplementary Material for this article can be found online at: https://www.frontiersin.org/articles/10.3389/fmicb.2019.01141/full#supplementary-material

REFERENCES

Alvarez, G. S., Hélary, C., Mebert, A. M., Wang, X., Coradin, T., and Desimone, M. F. (2014). Antibiotic-loaded silica nanoparticle–collagen composite hydrogels with prolonged antimicrobial activity for wound infection prevention. *J. Mater. Chem. B* 2, 4660–4670. doi: 10.1039/c4tb00327f

Ananthakrishnan, A. N. (2011). *Clostridium difficile* infection: epidemiology, risk factors and management. *Nat. Rev. Gastroenterol. Hepatol.* 8, 17–26. doi: 10.1038/nrgastro.2010.190

Babakhani, F., Bouillaut, L., Gomez, A., Sears, P., Nguyen, L., and Sonenshein, A. L. (2012). Fidaxomicin inhibits spore production in *Clostridium difficile*. *Clin. Infect. Dis.* 55(Suppl. 2), S162–S169. doi: 10.1093/cid/cis453

Baines, S. D., O'Connor, R., Saxton, K., Freeman, J., and Wilcox, M. H. (2009). Activity of vancomycin against epidemic *Clostridium difficile* strains in a human gut model. *J. Antimicrob. Chemother.* 63, 520–525. doi: 10.1093/jac/dkn502

Bouwknegt, M., van Dorp, S., and Kuijper, E. (2015). Burden of *Clostridium difficile* infection in the United States. *N. Engl. J. Med.* 372, 2368–2370. doi: 10.1056/NEJMc1505190

Deakin, L. J., Clare, S., Fagan, R. P., Dawson, L. F., Pickard, D. J., West, M. R., et al. (2012). The *Clostridium difficile* Spo0A gene is a persistence and transmission factor. *Infect. Immun.* 80, 2704–2711. doi: 10.1128/IAI.00147-12

Erben, U., Loddenkemper, C., Doerfel, K., Spieckermann, S., Haller, D., Heimesaat, M. M., et al. (2014). A guide to histomorphological evaluation of intestinal inflammation in mouse models. *Int. J. Clin. Exp. Pathol.* 7, 4557–4576.

Francis, M. B., Allen, C. A., Shrestha, R., and Sorg, J. A. (2013). Bile acid recognition by the *Clostridium difficile* germinant receptor, CspC, is important for establishing infection. *PLoS Pathog.* 9:e1003356. doi: 10.1371/journal.ppat.1003356

Gerding, D. N., Johnson, S., Rupnik, M., and Aktories, K. (2014). *Clostridium difficile* binary toxin CDT: mechanism, epidemiology, and potential clinical importance. *Gut Microbes* 5, 15–27. doi: 10.4161/gmic.26854

Gómez, S., Chaves, F., and Orellana, M. A. (2017). Clinical, epidemiological and microbiological characteristics of relapse and re-infection in *Clostridium difficile* infection. *Anaerobe* 48, 147–151. doi: 10.1016/j.anaerobe.2017.08.012

Gopinath, P. M., Dhanasekaran, D., Ranjani, A., Thajuddin, N., Akbarsha, M. A., Velmurugan, M., et al. (2015). Optimization of sporicidal activity and environmental *Bacillus* endospores decontamination by biogenic silver nanoparticle. *Future Microbiol.* 10, 725–741. doi: 10.2217/fmb.14.150

Gu, H., Ho, P. L., Tong, E., Wang, L., and Xu, B. (2003). Presenting vancomycin on nanoparticles to enhance antimicrobial activities. *Nano Lett.* 3, 1261–1263. doi: 10.1021/nl034396z

Hassan, M. M., Ranzoni, A., Phetsang, W., Blaskovich, M. A. T., and Cooper, M. A. (2017). Surface ligand density of antibiotic-nanoparticle conjugates enhances target avidity and membrane permeabilization of vancomycin-resistant bacteria. *Bioconjug. Chem.* 28, 353–361. doi: 10.1021/acs.bioconjchem.6b00494

Hopkins, R. J., and Wilson, R. B. (2018). Treatment of recurrent colitis: a narrative review. *Gastroenterol. Rep.* 6, 21–28. doi: 10.1093/gastro/gox041

Huang, C.-C., Chuang, K.-Y., Chou, C.-P., Wu, M.-T., Sheu, H.-S., Shieh, D.-B., et al. (2011). Size-control synthesis of structure deficient truncated octahedral Fe3-δO4 nanoparticles: high magnetization magnetites as effective hepatic contrast agents. *J. Mater. Chem.* 21, 7472–7479. doi: 10.1039/c1jm10325c

Hung, Y.-P., Ko, W.-C., Chou, P.-H., Chen, Y.-H., Lin, H.-J., Liu, Y.-H., et al. (2015). Proton-pump inhibitor exposure aggravates *Clostridium difficile*-associated colitis: evidence from a mouse model. *J. Infect. Dis.* 212, 654–663. doi: 10.1093/infdis/jiv184

Hussain, S., Joo, J., Kang, J., Kim, B., Braun, G. B., She, Z.-G., et al. (2018). Antibiotic-loaded nanoparticles targeted to the site of infection enhance antibacterial efficacy. *Nat. Biomed. Eng.* 2, 95–103. doi: 10.1038/s41551-017-0187-5

Johnson, S., Samore, M. H., Farrow, K. A., Killgore, G. E., Tenover, F. C., Lyras, D., et al. (1999). Epidemics of diarrhea caused by a clindamycin-resistant strain of *Clostridium difficile* in four hospitals. *N. Engl. J. Med.* 341, 1645–1651. doi: 10.1056/NEJM199911253412203

Joshi, L. T., Phillips, D. S., Williams, C. F., Alyousef, A., and Baillie, L. (2012). Contribution of spores to the ability of *Clostridium difficile* to adhere to surfaces. *Appl. Environ. Microbiol.* 78, 7671–7679. doi: 10.1128/AEM.01862-12

Kalghatgi, S., Spina, C. S., Costello, J. C., Liesa, M., Morones-Ramirez, J. R., Slomovic, S., et al. (2013). Bactericidal antibiotics induce mitochondrial dysfunction and oxidative damage in Mammalian cells. *Sci. Transl. Med.* 5:192ra85. doi: 10.1126/scitranslmed.3006055

Kavruk, M., Celikbicak, O., Ozalp, V. C., Borsa, B. A., Hernandez, F. J., Bayramoglu, G., et al. (2015). Antibiotic loaded nanocapsules functionalized with aptamer gates for targeted destruction of pathogens. *Chem. Commun.* 51, 8492–8495. doi: 10.1039/c5cc01869b

Kell, A. J., Stewart, G., Ryan, S., Peytavi, R., Boissinot, M., Huletsky, A., et al. (2008). Vancomycin-modified nanoparticles for efficient targeting and preconcentration of Gram-positive and Gram-negative bacteria. *ACS Nano* 2, 1777–1788. doi: 10.1021/nn700183g

Knowles, B. R., Yang, D., Wagner, P., Maclaughlin, S., Higgins, M. J., and Molino, P. J. (2018). Zwitterion functionalized silica nanoparticle coatings: the effect of particle size on protein, bacteria, and fungal spore adhesion. *Langmuir* 35, 1335–1345. doi: 10.1021/acs.langmuir.8b01550

Kwon, E. J., Skalak, M., Bertucci, A., Braun, G., Ricci, F., Ruoslahti, E., et al. (2017). Porous silicon nanoparticle delivery of tandem peptide anti-infectives for the treatment of *Pseudomonas aeruginosa* lung infections. *Adv. Mater.* 29. doi: 10.1002/adma.201701527

Lawley, T. D., Clare, S., Deakin, L. J., Goulding, D., Yen, J. L., Raisen, C., et al. (2010). Use of purified *Clostridium difficile* spores to facilitate evaluation of health care disinfection regimens. *Appl. Environ. Microbiol.* 76, 6895–6900. doi: 10.1128/AEM.00718-10

Lee, W.-T., Wu, Y.-N., Chen, Y.-H., Wu, S.-R., Shih, T.-M., Li, T.-J., et al. (2017). Octahedron iron oxide nanocrystals prohibited *Clostridium difficile* spore germination and attenuated local and systemic inflammation. *Sci. Rep.* 7:8124. doi: 10.1038/s41598-017-08387-y

Leffler, D. A., and Lamont, J. T. (2015). *Clostridium difficile* infection. *N. Engl. J. Med.* 372, 1539–1548. doi: 10.1056/NEJMra1403772

Mora-Uribe, P., Miranda-Cárdenas, C., Castro-Córdova, P., Gil, F., Calderón, I., Fuentes, J. A., et al. (2016). Characterization of the adherence of spores: the integrity of the outermost layer affects adherence properties of spores of the epidemic strain R20291 to components of the intestinal mucosa. *Front. Cell. Infect. Microbiol.* 6:99. doi: 10.3389/fcimb.2016.00099

Morgan, M. J., Kim, Y.-S., and Liu, Z. (2008). TNFalpha and reactive oxygen species in necrotic cell death. *Cell Res.* 18, 343–349. doi: 10.1038/cr.2008.31

Paredes-Sabja, D., and Sarker, M. R. (2012). Adherence of *Clostridium difficile* spores to Caco-2 cells in culture. *J. Med. Microbiol.* 61, 1208–1218. doi: 10.1099/jmm.0.043687-0

Qi, G., Li, L., Yu, F., and Wang, H. (2013). Vancomycin-modified mesoporous silica nanoparticles for selective recognition and killing of pathogenic gram-positive bacteria over macrophage-like cells. *ACS Appl. Mater. Interfaces* 5, 10874–10881. doi: 10.1021/am403940d

Rose, H. L., Dewey, C. A., Ely, M. S., Willoughby, S. L., Parsons, T. M., Cox, V., et al. (2011). Comparison of eight methods for the extraction of *Bacillus atrophaeus* spore DNA from eleven common interferents and a common swab. *PLoS One* 6:e22668. doi: 10.1371/journal.pone.0022668

Sekirov, I., Tam, N. M., Jogova, M., Robertson, M. L., Li, Y., Lupp, C., et al. (2008). Antibiotic-induced perturbations of the intestinal microbiota alter host susceptibility to enteric infection. *Infect. Immun.* 76, 4726–4736. doi: 10.1128/IAI.00319-08

Simón-Gracia, L., Hunt, H., Scodeller, P., Gaitzsch, J., Kotamraju, V. R., Sugahara, K. N., et al. (2016). iRGD peptide conjugation potentiates intraperitoneal tumor delivery of paclitaxel with polymersomes. *Biomaterials* 104, 247–257. doi: 10.1016/j.biomaterials.2016.07.023

Sorg, J. A., and Sonenshein, A. L. (2010). Inhibiting the initiation of *Clostridium difficile* spore germination using analogs of chenodeoxycholic acid, a bile acid. *J. Bacteriol.* 192, 4983–4990. doi: 10.1128/JB.00610-10

Sugahara, K. N., Teesalu, T., Karmali, P. P., Kotamraju, V. R., Agemy, L., Greenwald, D. R., et al. (2010). Coadministration of a tumor-penetrating peptide enhances the efficacy of cancer drugs. *Science* 328, 1031–1035. doi: 10.1126/science.1183057

Wagner, G., Korenkov, V., Judy, J. D., and Bertsch, P. M. (2016). Nanoparticles composed of Zn and ZnO inhibit spore germination and infectivity on tobacco leaves. *Nanomater* 6:E50. doi: 10.3390/nano6030050

Warren, C. A., van Opstal, E. J., Riggins, M. S., Li, Y., Moore, J. H., Kolling, G. L., et al. (2013). Vancomycin treatment's association with delayed intestinal tissue injury, clostridial overgrowth, and recurrence of *Clostridium difficile* infection in mice. *Antimicrob. Agents Chemother.* 57, 689–696. doi: 10.1128/aac.00877-12

Zarkan, A., Macklyne, H.-R., Truman, A. W., Hesketh, A. R., and Hong, H.-J. (2016). The frontline antibiotic vancomycin induces a zinc starvation response in bacteria by binding to Zn(II). *Sci. Rep.* 6:19602. doi: 10.1038/srep19602

Conflict of Interest Statement: The authors declare that the research was conducted in the absence of any commercial or financial relationships that could be construed as a potential conflict of interest.

frontiers in Microbiology

ORIGINAL RESEARCH
published: 12 June 2019
doi: 10.3389/fmicb.2019.01244

Biofabrication of Zinc Oxide Nanoparticles With *Syzygium aromaticum* Flower Buds Extract and Finding Its Novel Application in Controlling the Growth and Mycotoxins of *Fusarium graminearum*

Thimappa Ramachandrappa Lakshmeesha[1], Naveen Kumar Kalagatur[2,3], Venkataramana Mudili[3], Chakrabhavi Dhananjaya Mohan[4], Shobith Rangappa[5], Bangari Daruka Prasad[6], Bagepalli Shivaram Ashwini[7], Abeer Hashem[8,9], Abdulaziz A. Alqarawi[10], Jahangir Ahmad Malik[10], Elsayed Fathi Abd_Allah[10], Vijai Kumar Gupta[11], Chandra Nayaka Siddaiah[1]* and Siddapura Ramachandrappa Niranjana[1]*

[1] Department of Studies in Biotechnology, University of Mysore, Mysore, India, [2] Microbiology Division, Defence Food Research Laboratory, Mysore, India, [3] Toxicology and Immunology Division, DRDO-BU-Centre for Life Sciences, Bharathiar University, Coimbatore, India, [4] Department of Studies in Molecular Biology, University of Mysore, Mysore, India, [5] Adichunchanagiri Institute for Molecular Medicine, Mandya, India, [6] Department of Physics, BMS Institute of Technology and Management, Bengaluru, India, [7] East Point College of Medical Sciences and Research Centre, Bengaluru, India, [8] Botany and Microbiology Department, College of Science, King Saud University, Riyadh, Saudi Arabia, [9] Mycology and Plant Disease Survey Department, Plant Pathology Research Institute, Agriculture Research Center (ARC), Giza, Egypt, [10] Department of Plant Production, College of Food and Agricultural Sciences, King Saud University, Riyadh, Saudi Arabia, [11] Department of Chemistry and Biotechnology, Tallinn University of Technology, Tallinn, Estonia

Edited by:
Gerson Nakazato,
State University of Londrina, Brazil

Reviewed by:
Vivek K. Bajpai,
Dongguk University, South Korea
Esther Garcia-Cela,
Cranfield University, United Kingdom
Marcia Regina Salvadori,
University of São Paulo, Brazil

***Correspondence:**
Chandra Nayaka Siddaiah
moonnayak@gmail.com
Siddapura Ramachandrappa Niranjana
srn@appbot.uni-mysore.ac.in

Specialty section:
This article was submitted to Antimicrobials, Resistance and Chemotherapy, a section of the journal Frontiers in Microbiology

Received: 01 December 2018
Accepted: 20 May 2019
Published: 12 June 2019

Citation:
Lakshmeesha TR, Kalagatur NK, Mudili V, Mohan CD, Rangappa S, Prasad BD, Ashwini BS, Hashem A, Alqarawi AA, Malik JA, Abd_Allah EF, Gupta VK, Siddaiah CN and Niranjana SR (2019) Biofabrication of Zinc Oxide Nanoparticles With Syzygium aromaticum Flower Buds Extract and Finding Its Novel Application in Controlling the Growth and Mycotoxins of Fusarium graminearum. Front. Microbiol. 10:1244. doi: 10.3389/fmicb.2019.01244

Fusarium graminearum is a leading plant pathogen that causes Fusarium head blight, stalk rot, and Gibberella ear rot diseases in cereals and posing the immense threat to the microbiological safety of the food. Herein, we report the green synthesis of zinc oxide nanoparticles from *Syzygium aromaticum* (SaZnO NPs) flower bud extract by combustion method and investigated their application for controlling of growth and mycotoxins of *F. graminearum*. Formation of SaZnO NPs was confirmed by spectroscopic methods. The electron microscopic (SEM and TEM) analysis revealed the formation of triangular and hexagonal shaped SaZnO NPs with size range 30–40 nm. The synthesized SaZnO NPs reduced the growth and production of deoxynivalenol and zearalenone of *F. graminearum* in broth culture. Further analysis revealed that treatment of mycelia with SaZnO NPs resulted in the accumulation of ROS in the dose-dependent manner. Also, SaZnO NPs treatment enhanced lipid peroxidation, depleted ergosterol content, and caused detrimental damage to the membrane integrity of fungi. Moreover, SEM observations revealed that the presence of diverged micro-morphology (wrinkled, rough and shrank surface) in the macroconidia treated with SaZnO NPs. Taken together, SaZnO NPs may find a potential application in agriculture and food industries due to their potent antifungal activity.

Keywords: green synthesis, zinc oxide nanoparticles, mycotoxin, deoxynivalenol, zearalenone

INTRODUCTION

The world population is estimated to reach about 10.5 billion by 2050, and accessibility of food needs to rise about 60% to accomplish the food security (Alexandratos and Bruinsma, 2012). The food security could be improved through production and minimizing the food losses. In the interim, agriculture is facing climate change and limitation in land and water, and therefore, hard to increase food production (Aulakh and Regmi, 2013). As per FAO, about 1300 million tons of food are wasted per annum worldwide due to inappropriate post-harvesting practices (FAO, 2012). Thus, saving the food loss at a post-harvesting session could be the greatest resolve to improve the food security (Gustavsson et al., 2011). In this context, particularly fungal infestations are the foremost accountable for food loss, and FAO estimated that about 25% of agricultural commodities were contaminated with fungi (Smith et al., 2016). The fungal infestation brings unacceptable features in color, texture, flavor, and taste of food and introduces hazardous mycotoxins in food (Kumar et al., 2016).

The major mycotoxigenic fungal species liable for infestations are *Aspergillus*, *Alternaria*, *Claviceps*, *Fusarium*, *Penicillium*, and *Stachybotrys* (Richard, 2007). Among these mycotoxigenic species, *Fusarium graminearum* is one of the most accountable for food waste and food safety worldwide. The *F. graminearum* is devastating plant pathogen and causes FHB, stalk rot, and Gibberella ear rot diseases in cereals and accountable for loss of billion dollars worldwide (Pasquali et al., 2016). It is also liable for production of hazardous mycotoxins, including DON, NIV, and ZEA (Mudili et al., 2014). These mycotoxins classified as the group 3 carcinogens and cause a variety of toxic effects, such as neurotoxicity, hepatotoxicity, immunotoxicity, reproductive and developmental toxicity, nephrotoxicity, etc. (Richard, 2007; Venkataramana et al., 2014; Escrivá et al., 2015; Kalagatur et al., 2017, 2018b). Consequently, *F. graminearum* is posing the immense threat to the microbiological safety of food. Since last decade, microbiologists and food technologists have given greatest attention toward *F. graminearum* infestations and proposed variety of combat methods (Kalagatur et al., 2015, 2018c,d,e; Kumar et al., 2016; Sellamani et al., 2016). Unfortunately, most of the approaches have limitations and not acceptable. The application of synthetic fungicidal agents is not satisfactory due to its hazardous nature and development of fungicide-resistant fungi. Though, irradiation and high-pressure processing decontamination techniques are still not wide-spread owing to the prerequisite of high-cost equipment and skilled workers. The plant-based antifungal materials, i.e., crude extracts, essential oils, and phytocompounds are biodegradable and not cause side-effects (George et al., 2016; Kalagatur et al., 2018d,e). Therefore, there is a huge demand for the plant-based antifungals. Hence, plant-based synthesis of antifungal nanoparticles could be the novel, promising, and satisfactory tactic.

At present, nanotechnology has created an enormous revolution in the researchers. Zinc oxide nanoparticles (ZnO NPs) have roused a considerable interest among scientists due to their environment-friendly and potential applications in the field nanomedicine, biosensors, antibacterial, antifungal, and photochemical activities (Zhang P. et al., 2017; Zheng et al., 2017; Zhu L. et al., 2017). ZnO is a semiconductor material (II–VI), having a wide band gap of $E_g = 3.37$ eV semiconductor material with an extensive exciton binding energy of 60 meV at room temperature (Iorgu et al., 2013). In recent years, the interest in ZnO NPs applications for microbial control have grown considerably due to development of multidrug resistance among microbes (Kadiyala et al., 2018). Green synthesis of ZnO NPs is preferred over chemical and physical method as it is an eco-friendly and cost-effective method without use of high temperature, pressure toxic chemicals, and eliminates the generation of hazardous substances (Basnet et al., 2018). Among the green mediated synthesis of ZnO NPs, plant-mediated biofabrication of ZnO NPs has gained popularity over another method as its easily available in large quantity, it contains secondary metabolites, it reduces the processing time in maintaining bacterial and fungal cultures and cross-contamination is negligible among plant extracts (Ahmed et al., 2017; Vijayakumar et al., 2017).

The *Syzygium aromaticum* L. (clove) is an evergreen tree that rises to a height ranging from 7 to 13 m, which produces a flower bud that has numerous medicinal properties. The main constituents of the clove buds are eugenol, carvacrol, thymol, and cinnamaldehyde (Chen et al., 2016). The health benefits of cloves have been known for centuries such as an effective remedy for a headache, indigestion problem, cough, nausea, hypertension, etc. (Kheawfu et al., 2017). Clove buds extracts have been used in Ayurveda as a source of antimicrobial agents against oral microorganisms that are generally connected with dental caries and also finds use in fragrance and flavoring industries (Hamed et al., 2012; Chatterjee and Bhattacharjee, 2015).

To the best of our knowledge, for the first time an attempt has been made to report the inhibition of *F. graminearum* growth and mycotoxins production from SaZnO NPs, synthesized from *S. aromaticum* flower bud extracts, no such study has been reported, so far.

MATERIALS AND METHODS

Chemicals and Reagents

Zinc nitrate hexahydrate ($Zn(NO_3)_2.6H_2O$), DON (purity 98% TLC and CAS number: 51481-10-8), Dulbecco's phosphate buffer saline pH 7.4 (DPBS), lipid peroxidation assay kit, and ZEA (purity 99% HPLC and CAS number: 17924-92-4) were purchased from Sigma-Aldrich, India. Peptone, Tween 80, CZA, CZB, PI, sterile gauze, DCFH-DA, syringe filters (0.45 μm),

---

Abbreviations: ANOVA, analysis of variance; CZA, czapek dox agar; CZB, czapek dox broth; DCFH-DA, dichloro-dihydro-fluorescein diacetate; DON, deoxynivalenol; DPBS, dulbecco's phosphate-buffered saline; EDX, energy dispersive X-ray diffractive; FAO, Food and Agriculture Organization; FHB, fusarium head blight; FTIR, fourier-transform infrared spectroscopy; GC-MS, gas chromatography-mass spectroscopy; GFP, green fluorescent protein; HPLC, high-performance liquid chromatography; MDA, malondialdehyde; NIV, nivalenol; PI, propidium iodide; ROS, reactive oxygen species; SaZnO NPs, *Syzygium aromaticum* zinc oxide nanoparticles; SEM, scanning electron microscope; TEM, transmission electron microscopy; UV, ultraviolet; XRD, X-ray diffraction; ZEA, zearalenone; ZnO, zinc oxide.

double-layered muslin cloth, and Whatman no.1 filter papers were obtained from HiMedia, India. Immuno-affinity columns specific for DON and ZEA were obtained from Vicam, Waters, United States. All other chemicals and reagents were of AR grade and purchased from Merck Millipore, India. The plastic ware was purchased from Nunc, India. Glassware used were washed with 2% sodium hypochlorite solution and maintained in sterile condition.

Preparation of *Syzygium aromaticum* Extract

Syzygium aromaticum flower buds were collected from the local market, Mysore, and the voucher was identified and safeguarded in Department of studies in Biotechnology, University of Mysore, India.

Flower buds (10 g) were rinsed 2–3 times in de-ionized water, shade dried for 144 h and powdered utilizing a clean electric blender and put away in sterile polyethylene test sacks before utilize. The powder obtained was macerated with solvent hexane at the ratio of 1:6 (w/v) in a glass screw cap reagent bottle and was kept for 96 h. Subsequently, the supernatant was filtered through twofold layered muslin fabric, and the supernatant was recovered by centrifugation at 4000 rpm for 10 min. The supernatant was sieved through Whatman No. 1 filter paper and achieved filtrate was considered as mother extract and kept aseptically in a darker screw capped bottle at 4°C for additionally utilize (Cansian et al., 2016).

GC-MS Analysis of *S. aromaticum* Extract

To determine chemical constituents of *S. aromaticum* flower bud, the extract which served as a mother extract was subjected to gas chromatography (GC) and mass spectrophotometer (MS) analyses using Clarus 680 GC equipped with Elite-5MS (95% dimethylpolysiloxane, 5% biphenyl, ID $\times$ 250 μm df, 30 m $\times$ 0.25 mm) and the components were separated using Helium gas as a transporter gas at a steady flow of 1 mL/min. A quantity of 1 μL *S. aromaticum* extract was injected into the instrument, and the oven temperature was maintained as per the following: 60°C for 2 min and elevated till it reaches 300°C at the rate of 10°C min^{-1} where it was seized for 6 min. Mass detector conditions were as follows: ionization mode electron impact at 70 eV and ion source temperature 240°C with a scan interval of 0.1 to 0.2 s. The spectrums of the obtained constituents were equated with the database of known spectrum constituents from the GC-MS NIST (2008) library (Bhuiyan, 2012; Ali et al., 2014).

Biosynthesis of SaZnO NPs

Zinc nitrate ($Zn(NO_3)_2 6H_2O$) was used as the substrate, and *S. aromaticum* extract was used as fuel at the ratio of 1:5 (*w/v*) and mixed to form a solution. The solution was transferred to China dish and mixed in magnetic stirrer for $\sim$ 5–10 min and then placed in a preheated muffle furnace maintained at 400 $\pm$ 10°C. The entire combustion process was completed in less than 4 min (Lakshmeesha et al., 2014). The final product as-synthesized SaZnO NPs was off-white color.

Characterization of SaZnO NPs

UV-Vis spectroscopic absorption measurements were carried out at room temperature using a UV–Vis spectrophotometer Beckman Coulter, (DU739, Germany) over the range of 200–800 nm. Fourier transform infrared (FTIR) transmittance was carried out with a PerkinElmer Spectrum 1000, (Shimadzu-8400S) in the range of 450–4000 cm^{-1}. The crystallinity and phase purity of SaZnO NPs were characterized by XRD using a Rigaku Desktop MiniFlex II X-ray powder diffractometer with Cu kα radiation at an angle 2θ (λ = 0.15418 nm). The particle size was determined by Scherrer equation.

$$D = \frac{0.89\lambda}{\beta \cos\theta}$$

Where λ is the wavelength (Cu Kα) of X-Rays, β is the full width at half- maximum (FWHM) of the peak, and θ is the diffraction angle. The XRD pattern of SaZnO NPs was analyzed with the ICDD Powder Diffraction File database (International Centre for Diffraction Data) using Crystallographica Search-Match Version 2, 1, 1, 1. The surface morphology of SaZnO NPs samples is studied using SEM HITACHI (S-3400 N, Japan). The size of SaZnO NPs was studied using TEM (Tecnai G2 Spirit Bio-TWIN Transmission Electron Microscope).

Antifungal and Antimycotoxin Activity of SaZnO NPs on *F. graminearum*

Fungi Cultural Conditions

Fusarium graminearum isolated from maize kernels in our previous study (Mudili et al., 2014) were grown for 14 days at 28°C in CZA plates. The fungal spores were collected in peptone water containing 0.01% Tween 80 and mycelium debris was separated from the suspension by filtering through sterile gauze. The spore number was estimated by hemocytometer and fixed approximately to 10^6 spores/mL and used in further studies.

Treatment of SaZnO NPs

Different concentrations of SaZnO NPs (25, 50, 75, 100, 125, and 140 μg/mL) were added to 250 mL of Erlenmeyer flask that contained 100 mL of sterile CZB. The flasks were inoculated with 10 μL of fungal spore suspension (10^6 spores/mL) and incubated at 28°C for 14 days with 12 h of light per day. The flasks not contain SaZnO NPs and inoculated with fungi was considered as a control. Following the incubation period, the fungal mycelium was separated from the broth by sieving through Whatman no.1 filter paper. The fungal mycelium and filtrate were used for determination of fungal biomass (growth) and mycotoxins, respectively.

Determination of Fungal Growth (Biomass)

Subsequently, attained fungal mycelium was washed with deionized water for twice and packed in pre-weighed Whatman no.1 filter paper. The sample was subjected to drying at 60°C employing hot-air oven and weighed.

Quantification of Mycotoxins

Briefly, the attained filtrate was blended with acetonitrile (1:1, v/v) at 120 rpm for 30 min and 15 mL of the blend was discretely passed through immunoaffinity columns of DON and

ZEA mycotoxins at speed of 3 – 4 drops per sec as per the guidance of the manufacturer, Vicam, United States. Following, mycotoxins were eluted in 5 mL of acetonitrile and dried out at 60°C using a water bath. Next, the final residue was re-dissolved in 1 mL of acetonitrile and used for detection of DON and ZEA mycotoxins. The quantification of DON and ZEA was done using HPLC (Shimadzu, Japan) equipped with C18 column (5 μm, 250 × 4.6 mm) and a fluorescence detector. The analysis was carried out in reverse phase, and mobile phase was acetonitrile and water (1:1, v/v) with a flow rate of 1 mL/min, and an injection volume of sample was 25 μL. The excitation and emission of the detector were set to 365 and 455 nm for DON, and 334 and 450 nm for ZEA, respectively. The quantification of DON and ZEA was determined from their corresponding standard calibration curves. For the construction of calibration curves, stock solutions of DON and ZEA were prepared separately in acetonitrile (1 mg/mL) and different concentrations were made in distilled water and used for HPLC quantification. The retention time and limit of detection for DON and ZEA were noticed as 7.31 and 12.06 min, and 24 and 21 ng/mL, respectively. The calibration curves of mycotoxins were constructed with peak area versus concentration.

Assessment of Antifungal Mechanism of SaZnO NPs on *F. graminearum*

The antifungal mechanism of SaZnO NPs on *F. graminearum* was assessed by determining the intracellular ROS, lipid peroxidation, ergosterol content, membrane integrity, and micromorphology of macroconidia.

Estimation of ROS Generation

A quantity of 10 μL of fungal spore suspension was aseptically inoculated to 1 mL of CZB in 12-well plate and allowed to grow for 3 days at 28°C. Following, different concentration of SaZnO NPs (25, 50, 75, 100, 125, and 140 μg/mL) was added and further incubated at 160 rpm (rotary shaker) and 28°C for 24 h with 12 h light per day. The CZB contained only fungal inoculum and not treated SaZnO NPs was referred as a control. Following, samples were stained with 5 μM of DCFH-DA and washed for twice with DPBS. The optical density was measured at excitation of 495 nm and emission of 550 nm using the plate reader (Synergy H1, BioTek, United States) and results was expressed in percentage of ROS release with respect to control. The standard curve of ROS released versus hydrogen peroxide was constructed and used for quantification of ROS release. In addition, phase-contrast and fluorescent images were also captured using the inverted fluorescence microscope (EVOS, Thermo Scientific, United States).

Estimation of Lipid Peroxidation

A quantity of 1 mL CZB was inoculated with 10 μL of fungal spore suspension (10^6 spores/mL) in 12-well plate and incubated at 28°C for 3 days. Following, fungi were treated with different doses of SaZnO NPs (25, 50, 75, 100, 125, and 140 μg/mL) and incubated at 160 rpm (rotary shaker) and 28°C for 24 h with 12 h light. The fungal sample not treated with SaZnO NPs was denoted as a control. The MDA, the end product of lipid peroxidation was quantified using lipid-peroxidation assay kit as per instructions from the manufacturer (Sigma-Aldrich). The results were expressed with respect to control.

Estimation of Ergosterol Content

A volume of 10 μL of fungal spore suspension (10^6 spores/mL) and different concentration of SaZnO NPs (25, 50, 75, 100, 125, and 140 μg/mL) were added to 100 mL of CZB in 250 mL Erlenmeyer flask and incubated at 28°C and 160 rpm (rotary shaker) for 7 days with 12 h light per day. Following, 50 mg of fungal mycelia was recovered and washed with distilled water for twice and used for determination of ergosterol. The extraction and HPLC quantification of ergosterol were done as per our previous reported methodology of Sellamani et al. (2016).

Assessment of Membrane Integrity of Spores

A quantity of 1 mL of seven-day-old fungal spore suspension (10^6/mL) was treated with different concentration of SaZnO NPs (25, 50, 75, 100, 125, and 140 μg/mL) in 2 mL Eppendorf and incubated at 160 rpm (rotary shaker) and 28°C for 24 h with 12 h of light. The spore suspension not treated with SaZnO NPs was considered as control. Following spore suspension was stained with 5 μM of PI for 15 min and washed for twice with DPBS by centrifugation at 5000 rpm for 5 min. The PI stained spores were measured at excitation of 490 nm and emission of 635 nm using the flow cytometry (Beckman Coulter) and results was expressed in percentage with respect to control. The phase-contrast and fluorescent images of spores were captured under an inverted fluorescence microscope (EVOS, Thermo Scientific, United States).

Observation of Micromorphology of Macroconidia

The fungi were grown at 28°C for 7 days with 12 h light per day on CZA plate and 1 cm^2 of mycelia was collected under aseptic condition. The CZA slides were prepared with different concentrations of SaZnO NPs (100, 125, and 140 μg/mL) and inoculated with 7-days old fungal mycelium (1 cm^2) and incubated in the sterile humid atmospheric chamber at 28°C for 3 days with 12 h light per day. The CZA slide not contains SaZnO NPs and inoculated with fungi was control. Following, mycelium mat was recovered and attached to dual adhesive carbon tape and micrographs of macroconidia were captured under SEM (FEI Quanta 200, United States) in an environmental mode at 20 KV.

Statistical Analysis

The studies were performed independently for six times, and results were expressed as mean ± SD. The data were analyzed by one-way ANOVA and statistical difference between experimental groups was compared by Tukey's test using GraphPad Prism trial version 7. The *p*-value was stated as a significant at ≤ 0.05.

RESULTS

GC-MS of *S. aromaticum* Extract and Characterization of SaZnO NPs

The *S. aromaticum* hexane extract subjected for GC-MS revealed the presence of eugenol ($C_{10}H_{10}O_2$), beta-caryophyllene

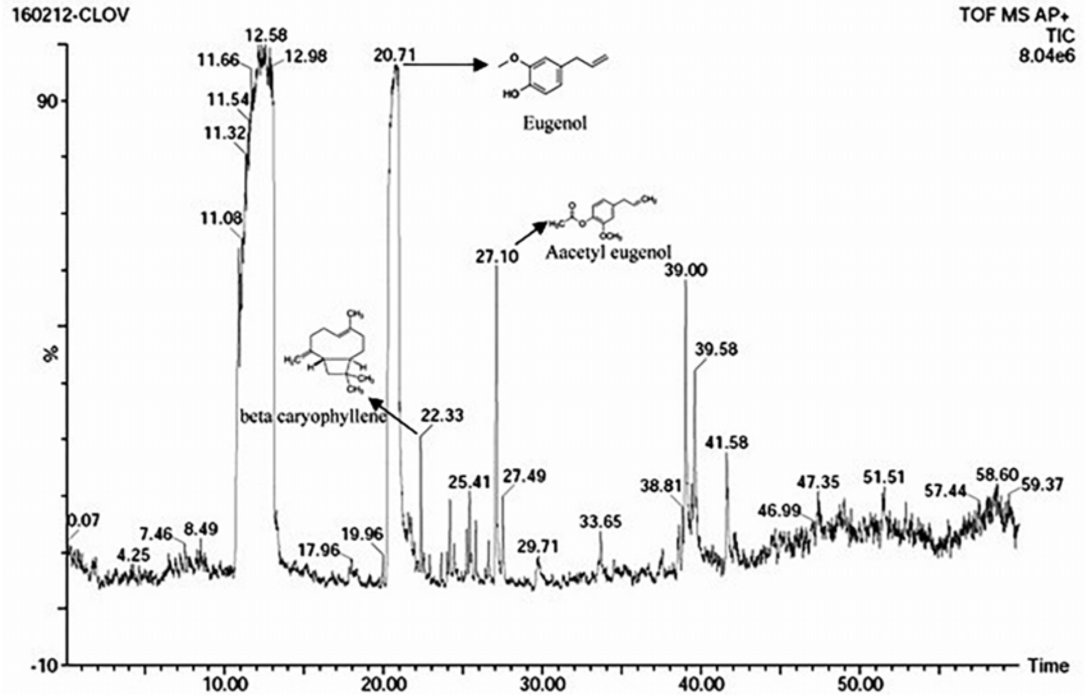

FIGURE 1 | GC-MS chromatogram of *S. aromaticum* flower buds hexane extract.

($C_{15}H_{24}$), acetyl eugenol ($C_{12}H_{14}O_3$), and many other compound types (**Figure 1** and **Table 1**). The results were in agreement with the earlier studies (Ali et al., 2014; Sheweita et al., 2016; Chen et al., 2017a,b). Eugenol was regarded as the major component of *S. aromaticum* (Kovács et al., 2016), the probable mechanism of formation of SaZnO NPs may be attributed to repeating structural units of eugenol participating in intermolecular cross-linking with ZnO to form a stable SaZnO NPs structure. UV–visible spectra of SaZnO NPs are shown in **Figure 2A**. It can be observed that there is a maximum absorption peak in the UV region of ∼378 nm, which is a characteristic band for the wurtzite hexagonal pure SaZnO (Reddy et al., 2011). **Figure 2B** shows the FTIR spectrum of SaZnO NPs acquired in the range of 400–4000 cm^{-1}. The appearance of peaks in the region of 406 cm^{-1} is ascribed to the formation of metal-oxygen bond (Kavyashree et al., 2015). The SEM micrographs (**Figure 2C**) shows the SaZnO NPs formed are of highly agglomerated, to form a well-defined triangular to nearly hexagonal shape in nature, which can be attributed to wurtzite structure of ZnO NPs which is in accordance with recent findings (Velmurugan et al., 2016; Ahmed et al., 2017).

TABLE 1 | Major components of *S. aromaticum* flower buds hexane extract.

Component	Eugenol	Beta caryophyllene	Acetyl eugenol
Retention time	20.71	22.33	27.10
Molecular formula	$C_{10}H_{10}O_2$	$C_{15}H_{24}$	$C_{12}H_{14}O_3$
Molecular weight	164.2	204.36	206.24

The EDX (**Figure 2D**) study was carried out for the synthesized SaZnO NPs showed the peaks corresponded to zinc yield (82.96%) and oxygen elements (12.64%) of the ZnO NPs which indicates that the SaZnO NPs synthesized is of pure form (Chen et al., 2017b). The XRD pattern of the synthesized SaZnO NPs as seen in **Figure 2E**. The appearance of all diffraction peaks corresponds to (100), (002), (101), (102), (110), (103), (200), (112), (201), (004), (202), (104), and (203) planes are indicated to hexagonal wurtzite structure of ZnO and could be readily indexed to (JCPDS Card No. 75-576). The Miller indices (100), (002), and (101) XRD peaks correspond to Bragg angles 31.8, 34.5, and 36.4°, respectively (Reddy et al., 2011) which indicates that the ZnO NPs are of good crystalline in nature. The (hkl) standard intensity plane was taken from JCPDS data. All the diffraction peaks can be fit to the hexagonal wurtzite phase ZnO with cell constants of a = 3.25 A° and c = 5.21 A° (Suresh et al., 2015). No other additional diffraction peaks from impurities were observed in the spectrum confirms the phase purity of ZnO NPs. The average grain size (D) of ZnO samples calculated from the Scherrer's equation (Prashanth et al., 2018) using the sharpest reflection was 35.69 nm. The TEM image (**Figure 2F**) supported the SEM results of SaZnO NPs which are hexagonal in shape and having an average size in the range of 30–40 nm.

Effect of SaZnO NPs on Fungal Growth and Mycotoxins Production of *F. graminearum*

In the present study, the inhibitory effect of SaZnO NPs on fungal growth (fungal biomass) and mycotoxins (DON and ZEA)

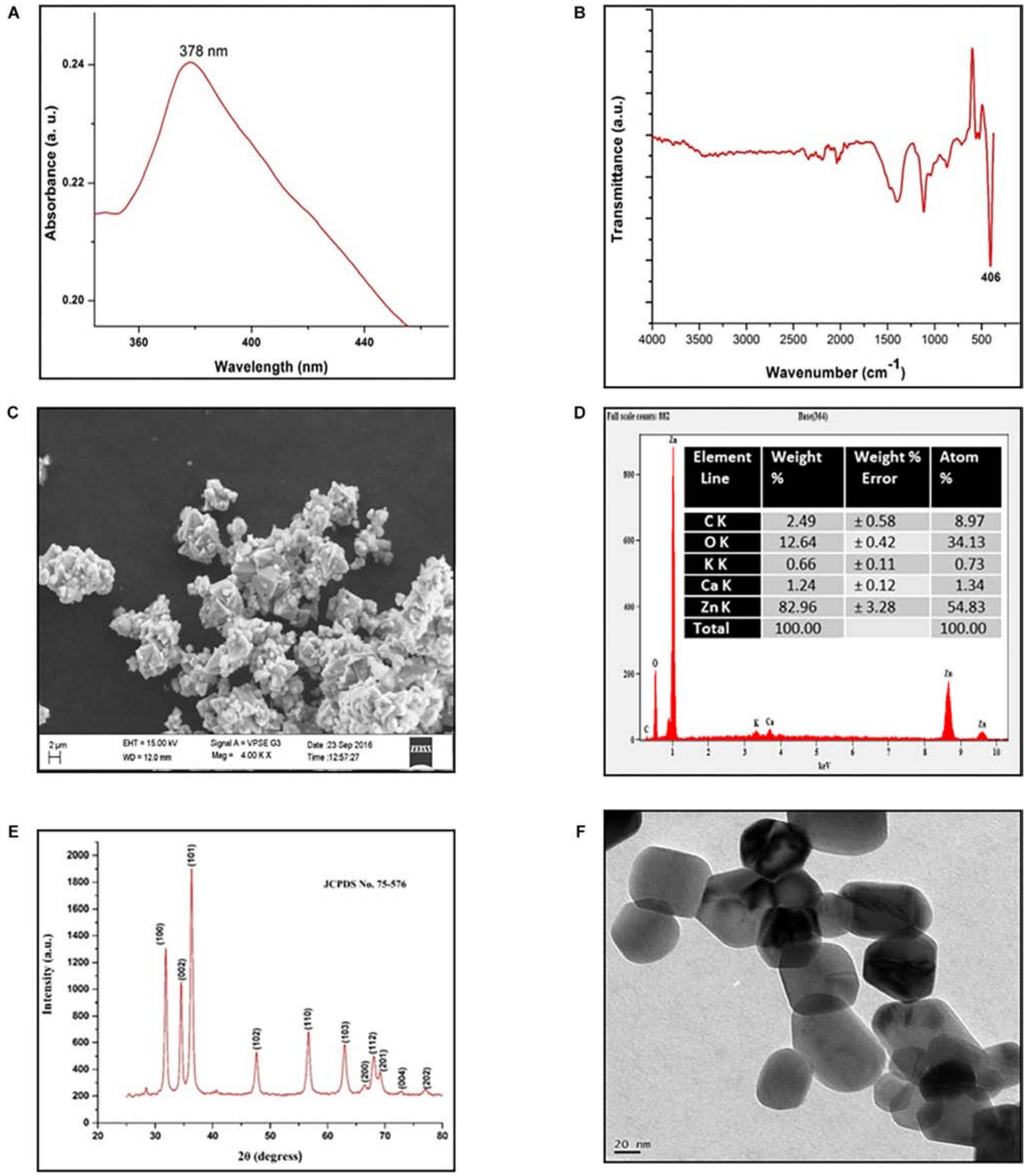

Element Line	Weight %	Weight % Error	Atom %
C K	2.49	±0.58	8.97
O K	12.64	±0.42	34.13
K K	0.66	±0.11	0.73
Ca K	1.24	±0.12	1.34
Zn K	82.96	±3.28	54.83
Total	100.00		100.00

FIGURE 2 | Characterization of SaZnO-NPs. **(A)** UV-Visible spectrum of SaZnO NPs, **(B)** FTIR spectrum of SaZnO NPs, **(C)** SEM micrograph of SaZnO NPs, **(D)** EDX pattern of SaZnO NPs **(E)** XRD pattern of SaZnO NPs, **(F)** TEM micrograph of SaZnO NPs.

production of *F. graminearum* was determined in broth culture. The SaZnO NPs has successfully decreased the fungus growth and mycotoxins production in broth culture (**Figure 3**). A quantity of 47.98 ± 3.61 mg of fungal biomass, 520.5 ± 28.46 μg of DON, and 678.8 ± 29.40 of ZEA were noticed in 100 mL of control broth culture (SaZnO NPs untreated). Whereas, the SaZnO NPs

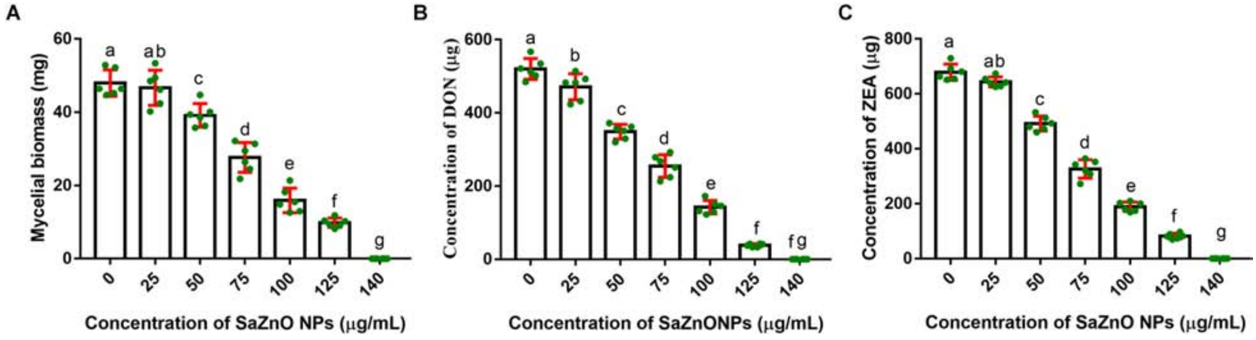

FIGURE 3 | Dose-dependent inhibitory effect of SaZnO NPs on **(A)** mycelial biomass (fungal growth), **(B)** deoxynivalenol (DON), and **(C)** zearalenone (ZEA) of *F. graminearum* in broth culture. The data was analyzed by one-way ANOVA according to Tukey's multiple comparison test and experimental clusters denoted with different alphabetic letters were significant ($p < 0.05$).

treated test samples were exhibited the lower levels of fungal growth and mycotoxins compared to control. The complete eliminations of fungal growth and mycotoxins were noticed at 140 μg/mL of SaZnO NPs. The inhibitory effects of SaZnO NPs on fungal growth and mycotoxins were assessed by constructing linear regression curves (**Supplementary Figure S1**). The linear regression curves have exhibited goodness of fit (R^2) of 0.9703, 0.9938, and 0.9872 for fungal biomass, DON, and ZEA, respectively (**Supplementary Table S1**). The regression models have confirmed that effect of SaZnO NPs on fungal growth and mycotoxins production was effective and dose-dependent.

Antifungal Mechanism of SaZnO NPs

Analysis of ROS Generation and Lipid Peroxidation

The effect of SaZnO NPs on ROS generation and lipid peroxidation was determined by DCFH-DA staining and MDA analysis, respectively. The phase-contrast and GFP images of control and SaZnO NPs treated fungal samples of ROS investigation were depicted in **Figure 4A**. The accumulation of ROS molecules was significantly ($P < 0.05$) high in SaZnO NPs treated samples compared to control (**Figure 4B**). The results determined that accumulation of ROS molecules was directly proportional to the dose of SaZnO NPs and it shows the dose-dependent manner. Likewise, lipid peroxidation was also highly influenced by SaZnO NPs and MDA levels were increased in fungi with the treatment of SaZnO NPs (**Figure 5A**). Furthermore, the accumulation of MDA levels was directly proportional to SaZnO NPs and it was dose-dependent and in accordance with the results of ROS analysis.

Analysis of Ergosterol Content and Membrane Integrity

Ergosterol is a key sterol component in the cell membrane of fungi and helpful for guarding the permeability and fluidity of membrane through interactions with phospholipids and other components of the membrane. The ergot is present only in fungi and yeast, and it is absent in animals. Therefore, disruption of ergot biosynthesis is considered as one of the particulars focuses for the advancement of new antifungal agents (Ahmad et al., 2010). The effect of SaZnO NPs on the ergosterol biosynthesis of *F. graminearum* was depicted in **Figure 5B**. A quantity of 42.7 ± 3.10 μg of ergosterol was measured in SaZnO NPs untreated control sample. Whereas, biosynthesis of ergosterol was reduced with treatment of SaZnO NPs and showed the dose-dependent mode of decrease. The fungal growth was absent at 140 μg/mL of SaZnO NPs and ergosterol was not determined.

Sustaining the membrane integrity is most necessary for viable cells and therefore, is often used as an index of living cells. The loss of membrane structure and integrity release cytochrome c and activate the death of cells by the apoptosis process. The membrane integrity of fungal spores is generally estimated by a fluorometric method using PI staining. The PI is a fluorescent stain that intensely binds to DNA and is incapable to enter the membrane of viable cells, and however, it uniquely stains DNA of non-viable cells by crossing the damaged cell membrane. Phase-contrast images and its corresponding RFP images of control and SaZnO NPs treated fungal spores were depicted in **Figure 6A**. The fluorescence intensity of fungal spores was enhanced on the treatment of SaZnO NPs related to untreated control. The percentage PI stained spores were recorded by flow cytometry and their number was increased with the dose of SaZnO NPs (**Figure 6B**). The results evidently proved that SaZnO NPs induces the detriments in membrane integrity of fungal spores and thereby promotes the death of fungi in a dose-dependent fashion.

Assessment of Micromorphology of Macroconidia

The micromorphology of fungal macroconidia was observed using SEM under environmental mode (**Figure 7**). The macroconidia in the control sample have exhibited healthy morphological characters, such as smooth, turgid, and regular. Whereas, SaZnO NPs treated macroconidia have shown detrimental micromorphological features, including irregular, wrinkled, disrupted, shrunk, and blebs. Captivatingly, severe detrimental micromorphological changes in fungal macroconidia were noticed at the high dose of SaZnO NPs related lower doses and control (**Figures 7A–D**). The study decided that fungicidal action of SaZnO NPs is due to detrimental damage of macroconidia, and it could be due to the surge of intracellular ROS and

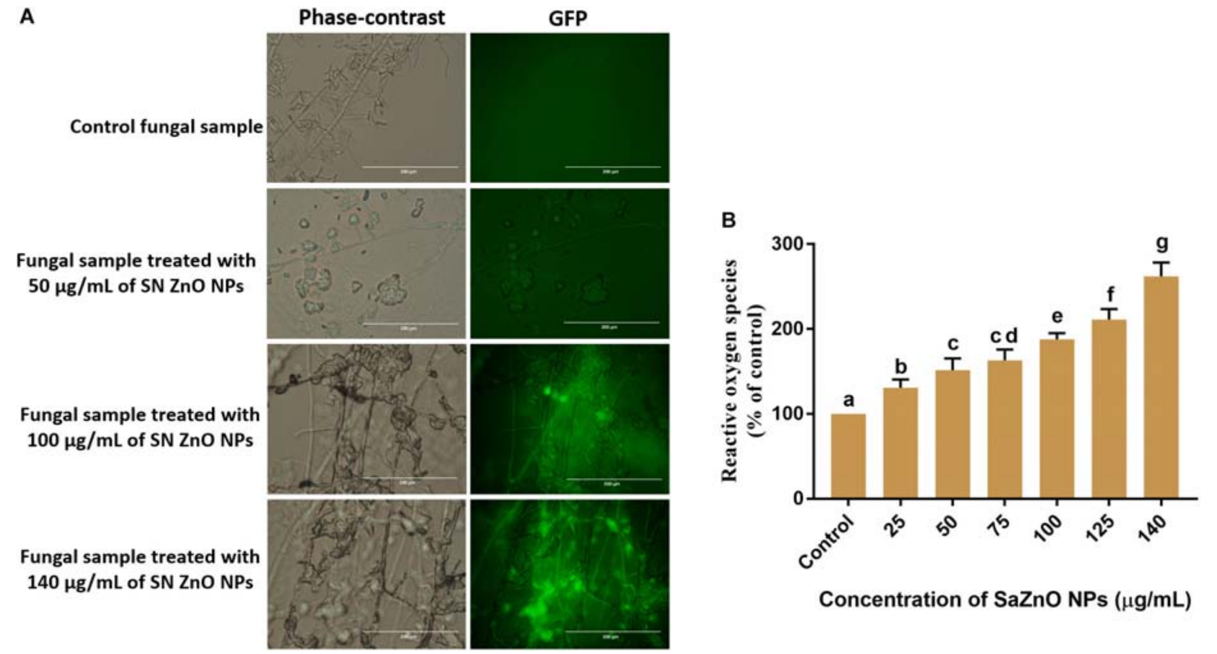

FIGURE 4 | Assessment of different concentration of SaZnO NPs on generation of intracellular reactive oxygen species (ROS). **(A)** phase-contrast and green fluorescent protein (GFP) images of control and SaZnO NPs treated fungal samples. **(B)** Dose-dependent effect of SaZnO NPs on accumulation of ROS in fungi. The data was analyzed by one-way ANOVA according to Tukey's multiple comparison test and experimental clusters denoted with different alphabetic letters were significant ($p < 0.05$).

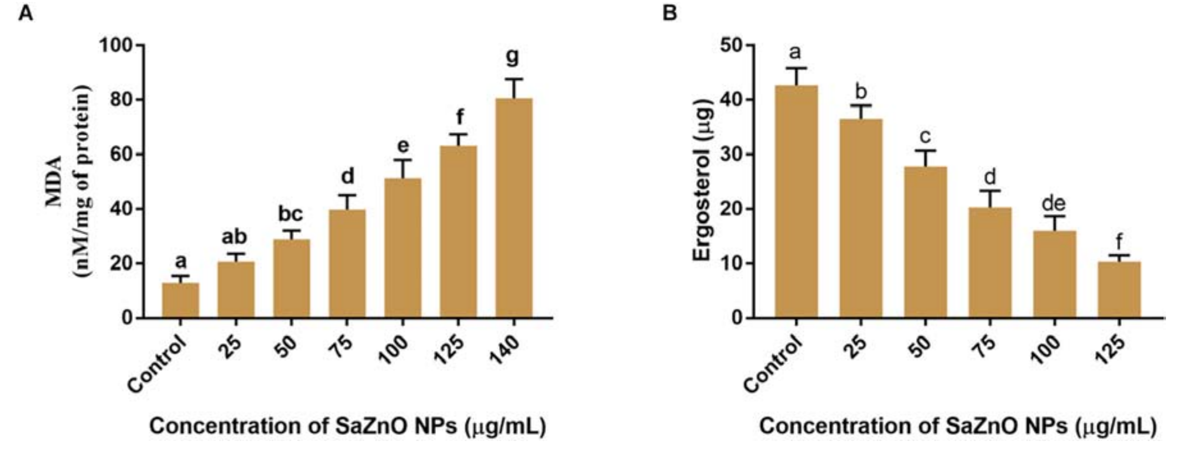

FIGURE 5 | (A) Effect of different concentration of SaZnO NPs on fungal lipid peroxidation (MDA release). **(B)** Effect of different concentration of SaZnO NPs on fungal ergosterol content. The data was analyzed by one-way ANOVA according to Tukey's multiple comparison test and experimental clusters denoted with different alphabetic letters were significant ($p < 0.05$).

lipid peroxidation, and the collapse of ergosterol content and membrane integrity.

DISCUSSION

Since last decade, nanotechnology has offered various beneficial assistances to the agriculture and food industry. Which include antimicrobial agents, nanobiosensors, food packaging material, catalysts, etc. (Zhu and Deng, 2017; Zhu H. et al., 2017; Zhu L. et al., 2017; Siddaiah et al., 2018; Kalagatur et al., 2018a; Gunti et al., 2019). As of now, the contagious pervasion and mycotoxin pollution of nourishment is one of the principals stresses of agribusiness and sustenance industry (Adeyeye, 2016). Right now, microbiologists have given extraordinary significance to seek novel antifungal and antimycotoxin mixes, which ought to be unique in relation to as of now accessible antifungal and antimycotoxin substances or ought to have productive

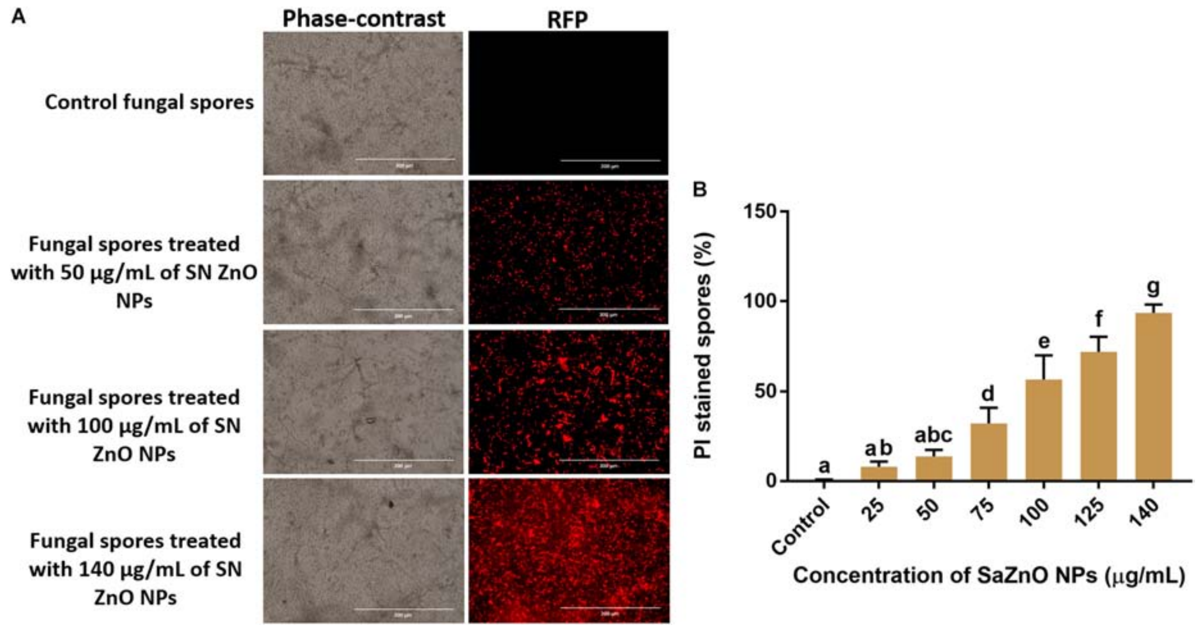

FIGURE 6 | Assessment of different concentration of SaZnO NPs on membrane integrity of fungal spores. **(A)** phase-contrast and red fluorescent protein (RFP) images of control and SaZnO NPs treated fungal spore samples. **(B)** Flowcytometric estimation of percentage of propidium iodide (PI) stained fungal spores. The data was analyzed by one-way ANOVA according to Tukey's multiple comparison test and experimental clusters denoted with different alphabetic letters were significant ($p < 0.05$).

antifungal and antimycotoxin movement. Be that as it may, best of our insight utilization of nanomaterials for controlling development and creation of mycotoxins in rare. In this way, an exertion made to investigate the biosynthesized SaZnO NPs for controlling of development and mycotoxins of wrecking plant pathogen *F. graminearum*.

The antifungal mechanism of SaZnO NPs on *F. graminearum* was unveiled by evaluating the aggregation of ROS, lipid peroxidation, ergosterol content, membrane integrity, and micromorphology of macroconidia. The antimicrobial activity of ZnO NPs directly correlated to detrimental action of radicals such as $^{\bullet}OH$, H^+, $HO_2^{\bullet}$ and H_2O_2 on cell wall and other cellular constituents. The ZnO NPs with deformities can be enacted by both UV and noticeable light electron-gap sets (e^-h^+). Initially, protons and electrons generate from SaZnO NPs by action of light energy. Following, protons react with water molecules and form $^{\bullet}OH$ and electrons react with O_2 and generate $^{\bullet}O_2$. Next, combination of $^{\bullet}OH$ and $^{\bullet}O_2$ generates $HO_2^{\bullet}$ and succeeding, $HO_2^{\bullet}$ recombines with proton and electron and generate H_2O_2 (Zhang et al., 2007; Padmavathy and Vijayaraghavan, 2008). The overall generation of radicals is represented in below reaction.

$$\mathrm{ZnO} + \text{light} \longrightarrow \text{proton } (h^+) + \text{electron } (e^-)$$

$$h^+ + H_2O \longrightarrow OH^{\bullet} + H^+ : e^+ + O_2 \longrightarrow {}^{\bullet}O_2$$

$$OH^{\bullet} + {}^{\bullet}O_2 \longrightarrow HO_2^{\bullet}$$

$$HO_2^{\bullet} + H^+ + e^- \longrightarrow H_2O_2$$

The microorganisms on their cell wall bear a negative charge while SaZnO NPs carry a positive charge along these lines this cooperation makes an electromagnetic fascination between the organisms and nanoparticles. As SaZnO NPs on coming into contact with the surface of microbes produce ROS by action of light. Antifungal mechanisms of SaZnO NPs might be credited to the ROS such as hydroxyl radicals ($OH^{\bullet}$) superoxides ($^{\bullet}O_2$) and hydrogen peroxide (H_2O_2) (Prasanna and Vijayaraghavan, 2017; Wang et al., 2017; Youssef et al., 2017).

In a biological context, intracellular ROS assume an unequivocal part as couriers in quality articulation and cell flagging and expressly starts oxidative pressure intervened apoptosis (Simon et al., 2000). The ROS molecules are formed as byproducts in mitochondrial electron transport by various inward and outer pressure factors, for example, radiations, warm treatment, supplement lack, drugs, anti-infection agents, antimicrobial peptides, nanoparticles, saltiness, microbial poisons, metals, and so on (Matai et al., 2014; Zhang Z.-Z. et al., 2017; Kalagatur et al., 2018d,e). The elevated ROS molecules attack the lipid molecules comprising of carbon-carbon double bonds in polyunsaturated fatty acids and fetch lipid peroxidation (Sebaaly et al., 2016). Furthermore, elevation of ROS levels eventually impairments the proteins, lipids, and nucleic acids, and triggers oxidative-stress mediated apoptosis by releasing mitochondrial cytochrome c and death receptors.

Antifungal and antimycotoxin activities of SaZnO NPs might be due to an elevation of ROS and thus, it could induce death of fungi by oxidative-stress mediated apoptosis. In support of the present study, several studies have evidenced that nanoparticles (Mitra et al., 2017), physical agents (Calado et al., 2014; Kalagatur et al., 2018d,e), synthetic fungicides (Delattin et al., 2014) and bio-fungicides (Sebaaly et al., 2016; Sellamani et al., 2016)

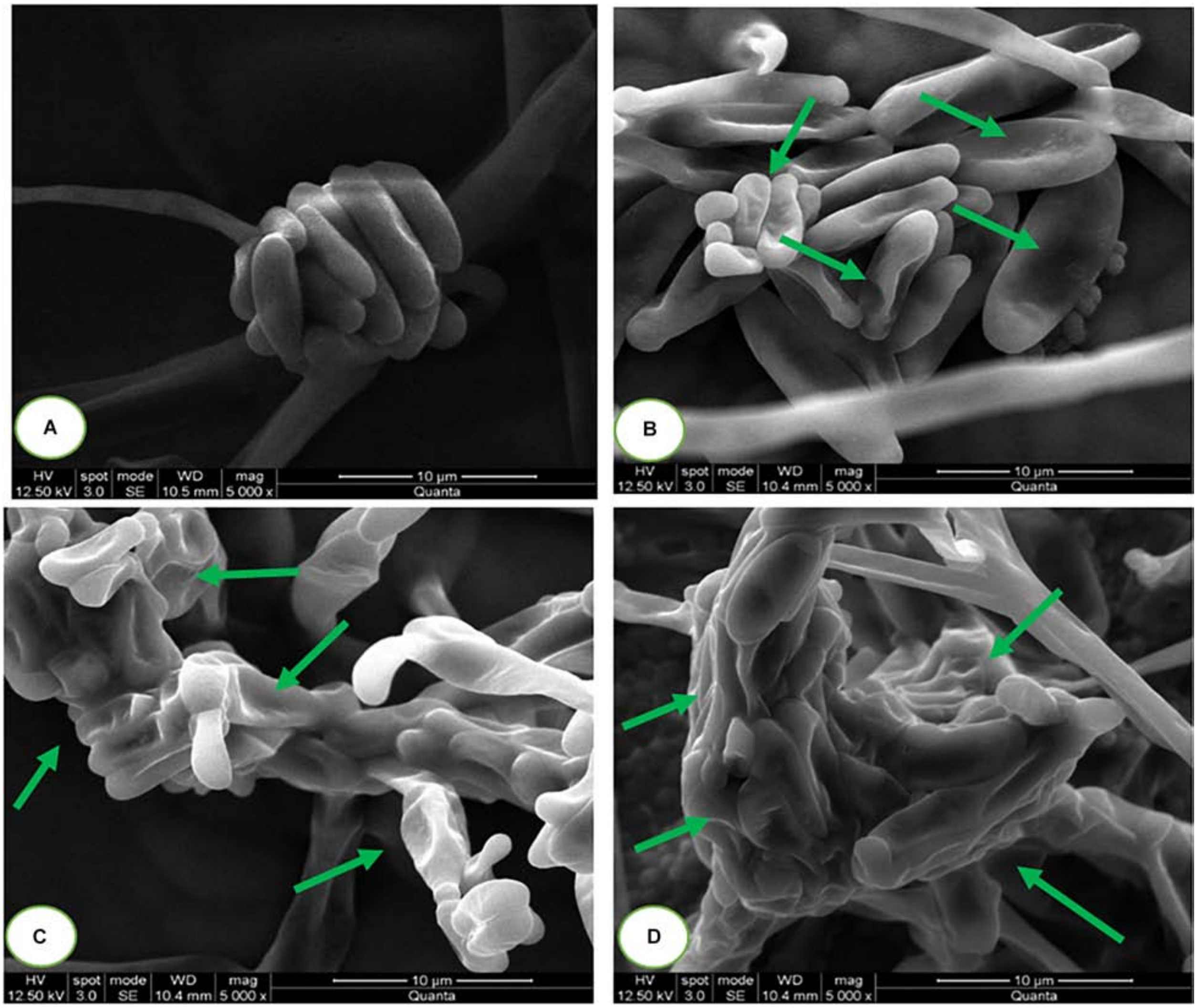

FIGURE 7 | Scanning electron microscopic images of fungal macroconidia at **(A)** 0 (Control), **(B)** 100, **(C)** 125, and **(D)** 140 µg/mL of SaZnO NPs.

could induce the death of fungi through oxidative-stress mediated apoptosis by elevation of ROS. Specifically concerning to nanomaterials, few reports were available on antifungal and antimycotoxin capabilities of nanomaterials. Best of our knowledge, until the date, no report is available on antifungal and antimycotoxin abilities of biofabricated ZnO NPs on *F. graminearum* and present study is first report. Most recently, Hernández-Meléndez et al. (2018) reported that flower-shaped ZnO inhibit the growth and aflatoxin production of *A. flavus* by multiple degenerative alterations in fungi via ROS generation. Besides, Savi et al. (2013) proved that zinc compounds could generate intracellular ROS and exhibit strong inhibitory activity on growth and fumonisin mycotoxin production of *F. verticillioides* by detrimental action on hyphae and conidia. Captivatingly, Mitra et al. (2017) reported that citrate decorated silver nanoparticles independently inhibit the fungal growth and aflatoxin production in *A. parasiticus* and revealed that silver nanoparticles inhibit aflatoxin production by downregulating the aflatoxin biosynthesis genes at its below the lethal dose.

In addition, our study revealed that SaZnO NPs might exhibit potent fungicidal activity on *F. graminearum* through inhibition of ergosterol biosynthesis and disrupting the membrane integrity. In support of the present result, Sellamani et al. (2016) demonstrated that *Pediococcus pentosaceus* isolated from dairy products has exhibited potent antifungal activity on *F. graminearum* by inhibiting the ergosterol biosynthesis. Ahmad et al. (2010) have proven that the antifungal activity of thymol and carvacrol is due to disruption of ergosterol biosynthesis and membrane integrity. In the same way, Prasher et al. (2018) have confirmed that green synthesized silver nanoparticles exhibit the potent antifungal activity through disturbing ergosterol biosynthesis and membrane integrity. However, molecular mechanism involved in inhibition of growth and mycotoxins production of fungi by nanomaterials is unclear and exhaustive studies are needed.

CONCLUSION

In conclusion, we have synthesized a highly facile, non-toxic and inexpensive approach to the green synthesis of SaZnO NPs. The SaZnO NPs has presented potent inhibitory activity against growth and mycotoxin production of *F. graminearum*. Furthermore, the antifungal mechanism of SaZnO NPs on *F. graminearum* was established by assessing the membrane integrity, ROS generation, lipid peroxidation, ergosterol content, and micromorphology of macroconidia. These studies demonstrated that SaZnO NPs has upraised the ROS levels and lipid peroxidation, and depleted the ergosterol content, and detrimentally altered the membrane integrity and micromorphology of macroconidia. The proposed antifungal mode suggested that SaZnO NPs could efficiently restrain the growth and mycotoxin production of devastating plant pathogen *F. graminearum* and could be used in novel fungicide formulations as the potent substitute of synthetic fungicides for agriculture and food industry.

AUTHOR CONTRIBUTIONS

TL and CS designed the experiments. TL and NK performed the experiments. TL, CS, CM, VG, and NK wrote the manuscript. TL, CM, CS, SN, VM, BA, AH, EA_A, AA, and BP reviewed and finalized the manuscript. All authors read and approved the final version of this manuscript.

ACKNOWLEDGMENTS

TL would like to acknowledge the UGC (University Grants Commission), New Delhi, India for providing the financial support under UGC Post-Doctoral Fellowship for SC/ST Candidates (2015/16) (No. F/PDFSS-2015-17-KAR-11458). The authors acknowledge the recognition of University of Mysore as an Institution of Excellence and financial support from the Ministry of Human Resource Development, Government of India through the University Grants Commission, New Delhi, India. They would like to extend their sincere appreciation to the Deanship of Scientific Research at King Saud University for its funding to the Research Group number (RG-1435-014).

SUPPLEMENTARY MATERIAL

The Supplementary Material for this article can be found online at: https://www.frontiersin.org/articles/10.3389/fmicb.2019.01244/full#supplementary-material

FIGURE S1 | Linear regression curves for inhibitory effect of SaZnO NPs on **(A)** mycelial biomass, **(B)** deoxynivalenol (DON), and **(C)** zearalenone (ZEA) of *F. graminearum*.

TABLE S1 | Linear regression curve fit for dose-dependent inhibitory effect of SaZnO NPs on fungal growth (mycelial biomass), deoxynivalenol (DON), and zearalenone (ZEA) of *F. graminearum* in broth culture.

REFERENCES

Adeyeye, S. A. O. (2016). Fungal mycotoxins in foods: a review. *Cogent. Food Agric.* 2:1213127. doi: 10.1080/23311932.2016.1213127

Ahmad, A., Khan, A., Manzoor, N., and Khan, L. A. (2010). Evolution of ergosterol biosynthesis inhibitors as fungicidal against Candida. *Microb. Pathog.* 48, 35–41. doi: 10.1016/j.micpath.2009.10.001

Ahmed, S., Annu Chaudhry, S. A., and Ikram, S. (2017). A review on biogenic synthesis of ZnO nanoparticles using plant extracts and microbes: a prospect towards green chemistry. *J. Photochem. Photobiol. B.* 166, 272–284. doi: 10.1016/j.jphotobiol.2016.12.011

Alexandratos, N., and Bruinsma, J. (2012). *World Agriculture Towards 2030/2050: the 2012 Revision*. Rome: FAO.

Ali, S., Prasad, R., Mahmood, A., Routray, I., Shinkafi, T. S., Sahin, K., et al. (2014). Eugenol-rich fraction of syzygium aromaticum (Clove) reverses biochemical and histopathological changes in liver cirrhosis and inhibits hepatic cell proliferation. *J. Cancer Prev.* 19, 288–300. doi: 10.15430/JCP.2014.19.4.288

Aulakh, J., and Regmi, A. (2013). *Post-Harvest Food Losses Estimation-Development of Consistent Methodology*. Rome: FAO.

Basnet, P., Inakhunbi Chanu, T., Samanta, D., and Chatterjee, S. (2018). A review on bio-synthesized zinc oxide nanoparticles using plant extracts as reductants and stabilizing agents. *J. Photochem. Photobiol. B.* 183, 201–221. doi: 10.1016/j.jphotobiol.2018.04.036

Bhuiyan, M. N. I. (2012). Constituents of the essential oil from leaves and buds of clove (*Syzigium caryophyllatum* (L.) Alston). *Afr. J. Pharm. Pharmaco.* 6, 1260–1263. doi: 10.5897/AJPP10.004

Calado, T., Venâncio, A., and Abrunhosa, L. (2014). Irradiation for mold and mycotoxin control: a review. *Compr. Rev. Food Sci. Food Saf.* 13, 1049–1061. doi: 10.1111/1541-4337.12095

Cansian, R. L., Vanin, A. B., Orlando, T., Piazza, S. P., Puton, B. M. S., Cardoso, R. I., et al. (2016). Toxicity of clove essential oil and its ester eugenyl acetate against *Artemia salina*. *Braz. J. Biol.* 77, 155–161. doi: 10.1590/1519-6984.12215

Chatterjee, D., and Bhattacharjee, P. (2015). Use of eugenol-lean clove extract as a flavoring agent and natural antioxidant in mayonnaise: product characterization and storage study. *J. Food Sci. Technol.* 52, 4945–4954. doi: 10.1007/s13197-014-1573-6

Chen, H., Diao, J., Li, Y., Chen, Q., and Kong, B. (2016). The effectiveness of clove extracts in the inhibition of hydroxyl radical oxidation-induced structural and rheological changes in porcine myofibrillar protein. *Meat Sci.* 111, 60–66. doi: 10.1016/j.meatsci.2015.08.017

Chen, X., Ren, L., Li, M., Qian, J., Fan, J., and Du, B. (2017a). Effects of clove essential oil and eugenol on quality and browning control of fresh-cut lettuce. *Food Chem.* 214, 432–439. doi: 10.1016/j.foodchem.2016.07.101

Chen, X., Wu, Z., Liu, D., and Gao, Z. (2017b). Preparation of ZnO photocatalyst for the efficient and rapid photocatalytic degradation of azo dyes. *Nanoscale Res. Lett.* 12, 143–153. doi: 10.1186/s11671-017-1904-4

Delattin, N., Cammue, B. P., and Thevissen, K. (2014). Reactive oxygen species-inducing antifungal agents and their activity against fungal biofilms. *Future Med. Chem.* 6, 77–90. doi: 10.4155/fmc.13.189

Escrivá, L., Font, G., and Manyes, L. (2015). In vivo toxicity studies of fusarium mycotoxins in the last decade: a review. *Food Chem. Toxicol.* 78, 185–206. doi: 10.1016/j.fct.2015.02.005

FAO (2012). *The State of Food Insecurity in the World 2012. Economic Growth is Necessary but not Sufficient to Accelerate Reduction of Hunger and Malnutrition*. Rome: FAO.

George, E., Kasipandi, M., Vekataramana, M., Kumar, K. N., Allen, J. A., Parimelazhagan, T., et al. (2016). In vitro anti-oxidant and cytotoxic analysis of Pogostemon mollis Benth. *Bangladesh J. Pharmacol.* 11, 148–158. doi: 10.3329/bjp.v11i1.24157

Gunti, L., Dass, R. S., and Kalagatur, N. K. (2019). Phytofabrication of Selenium Nanoparticles from Emblica officinalis fruit extract and exploring its biopotential applications: antioxidant. Antimicrobial, and Biocompatibility. *Front. Microbiol.* 10:931. doi: 10.3389/fmicb.2019.00931

Gustavsson, J., Cederberg, C., Sonesson, U., van Otterdijk, R., and Meybeck, A. (2011). *Global Food Losses and Food Waste*. Rome: FAO.

Hamed, S. F., Sadek, Z., and Edris, A. (2012). Antioxidant and antimicrobial activities of clove cud essential oil and eugenol nanoparticles in alcohol-free microemulsion. *J. Oleo Sci.* 61, 641–648. doi: 10.5650/jos.61.641

Hernández-Meléndez, D., Salas-Téllez, E., Zavala-Franco, A., Téllez, G., Méndez-Albores, A., and Vázquez-Durán, A. (2018). Inhibitory effect of flower-shaped zinc oxide nanostructures on the growth and aflatoxin production of a highly toxigenic strain of aspergillus flavus link. *Materials* 11:1265. doi: 10.3390/ma11081265

Iorgu, A. I., Berger, D., Alexandrescu, L., Vasile, B. S., and Matei, C. (2013). Synthesis of photoluminescent pure and doped cadmium sulfide by reverse microemulsion method. *Chalcogenide Lett.* 10, 525–531.

Kadiyala, U., Turali-Emre, E. S., Bahng, J. H., Kotov, N. A., and VanEpps, J. S. (2018). Unexpected insights into antibacterial activity of zinc oxide nanoparticles against methicillin resistant *Staphylococcus aureus* (MRSA). *Nanoscale* 10, 4927–4939. doi: 10.1039/C7NR08499D

Kalagatur, N. K., Ghosh, O. S. N., Sundararaj, N., and Mudili, V. (2018a). Antifungal activity of chitosan nanoparticles encapsulated with *Cymbopogon martinii* essential oil on plant pathogenic fungi Fusarium graminearum. *Front. Pharmacol.* 9:610. doi: 10.3389/fphar.2018.00610

Kalagatur, N. K., Kamasani, J. R., and Mudili, V. (2018b). Assessment of detoxification efficacy of irradiation on zearalenone mycotoxin in various fruit juices by response surface methodology and elucidation of its in-vitro toxicity. *Front. Microbiol.* 9:2937. doi: 10.3389/fmicb.2018.02937

Kalagatur, N. K., Kamasani, J. R., Mudili, V., Krishna, K., Chauhan, O. P., and Sreepathi, M. H. (2018c). Effect of high pressure processing on growth and mycotoxin production of Fusarium graminearum in maize. *Food Biosci.* 21, 53–59. doi: 10.1016/j.fbio.2017.11.005

Kalagatur, N. K., Kamasani, J. R., Siddaiah, C., Gupta, V. K., Krishna, K., and Mudili, V. (2018d). Combinational inhibitory action of *Hedychium spicatum* L. essential oil and γ-radiation on growth rate and mycotoxins content of *Fusarium graminearum* in maize: response surface methodology. *Front. Microbiol.* 9:1511. doi: 10.3389/fmicb.2018.01511

Kalagatur, N. K., Mudili, V., Kamasani, J. R., and Siddaiah, C. (2018e). Discrete and combined effects of Ylang-Ylang (*Cananga odorata*) essential oil and gamma irradiation on growth and mycotoxins production by *Fusarium graminearum* in maize. *Food Control* 94, 276–283. doi: 10.1016/j.foodcont.2018.07.030

Kalagatur, N. K., Karthick, K., Allen, J. A., Ghosh, N., Sivaraman, O., Chandranayaka, S., et al. (2017). Application of activated carbon derived from seed shells of *Jatropha curcas* for decontamination of zearalenone mycotoxin. *Front. Pharmacol.* 8:760. doi: 10.3389/fphar.2017.00760

Kalagatur, N. K., Mudili, V., Siddaiah, C., Gupta, V. K., Natarajan, G., Sreepathi, M. H., et al. (2015). Antagonistic activity of Ocimum sanctum L. essential oil on growth and zearalenone production by Fusarium graminearum in maize grains. *Front. Microbiol.* 6:892. doi: 10.3389/fmicb.2015.00892

Kavyashree, D., Shilpa, C. J., Nagabhushana, H., Daruka Prasad, B., Sreelatha, G. L., Sharma, S. C., et al. (2015). ZnO superstructures as an antifungal for effective control of malassezia furfur, dermatologically prevalent yeast: prepared by Aloe vera assisted combustion method. *ACS Sustain. Chem. Eng.* 3, 1066–1080. doi: 10.1021/sc500784p

Kheawfu, K., Pikulkaew, S., Hamamoto, H., Sekimizu, K., and Okonogi, S. (2017). Influence of clove oil and eugenol on muscle contraction of silkworm (*Bombyx mori*). *Drug Discov. Ther.* 11, 64–69. doi: 10.5582/ddt.2017.01012

Kovács, J. K., Felsõ, P., Makszin, L., Pápai, Z., Horváth, G., Ábrahám, H., et al. (2016). Antimicrobial and virulence-modulating effects of clove essential oil on the foodborne pathogen *Campylobacter jejuni*. *Appl. Environ. Microbiol.* 82, 6158–6166. doi: 10.1128/AEM.01221-16

Kumar, K. N., Venkataramana, M., Allen, J. A., Chandranayaka, S., Murali, H. S., and Batra, H. V. (2016). Role of *Curcuma longa* L. essential oil in controlling the growth and zearalenone production of *Fusarium graminearum*. *LWT-Food Sci. Technol.* 69, 522–528. doi: 10.1016/j.lwt.2016.02.005

Lakshmeesha, T. R., Sateesh, M. K., Prasad, B. D., Sharma, S. C., Kavyashree, D., Chandrasekhar, M., et al. (2014). Reactivity of crystalline ZnO superstructures against fungi and bacterial pathogens: synthesized using Nerium oleander leaf extract. *Cryst. Growth Des.* 14, 4068–4079. doi: 10.1021/cg500699z

Matai, I., Sachdev, A., Dubey, P., Uday Kumar, S., Bhushan, B., and Gopinath, P. (2014). Antibacterial activity and mechanism of Ag-ZnO nanocomposite on S. aureus and GFP-expressing antibiotic resistant E. coli. *Colloids Surf. B Biointer.* 115, 359–367. doi: 10.1016/j.colsurfb.2013.12.005

Mitra, C., Gummadidala, P. M., Afshinnia, K., Merrifield, R. C., Baalousha, M., Lead, J. R., et al. (2017). Citrate-coated silver nanoparticles growth-independently inhibit aflatoxin synthesis in *Aspergillus parasiticus*. *Environ. Sci. Technol.* 51, 8085–8093. doi: 10.1021/acs.est.7b01230

Mudili, V., Siddaih, C. N., Nagesh, M., Garapati, P., Kumar, N. K., Murali, H. S., et al. (2014). Mould incidence and mycotoxin contamination in freshly harvested maize kernels originated from India. *J. Sci. Food Agric.* 94, 2674–2683. doi: 10.1002/jsfa.6608

Padmavathy, N., and Vijayaraghavan, R. (2008). Enhanced bioactivity of ZnO nanoparticles-an antimicrobial study. *Sci. Technol. Adv. Mater.* 9, 35004–35011. doi: 10.1088/1468-6996/9/3/035004

Pasquali, M., Beyer, M., Logrieco, A., Audenaert, K., Balmas, V., Basler, R., et al. (2016). A European database of *Fusarium graminearum* and *F. culmorum* trichothecene genotypes. *Front. Microbiol.* 7:406. doi: 10.3389/fmicb.2016.00406

Prasanna, L. V., and Vijayaraghavan, R. (2017). Chemical manipulation of oxygen vacancy and antibacterial activity in ZnO. *Mater. Sci. Eng. C* 77, 1027–1034. doi: 10.1016/j.msec.2017.03.280

Prashanth, G. K., Prashanth, P. A., Nagabhushana, B. M., Ananda, S., Krishnaiah, G. M., Nagendra, H. G., et al. (2018). Comparison of anticancer activity of biocompatible ZnO nanoparticles prepared by solution combustion synthesis using aqueous leaf extracts of *Abutilon indicum*. Melia azedarach and Indigofera tinctoria as biofuels. *Artif. Cells Nanomed. Biotechnol.* 46, 968–979. doi: 10.1080/21691401.2017.1351982

Prasher, P., Singh, M., and Mudila, H. (2018). Green synthesis of silver nanoparticles and their antifungal properties. *Bionanoscience* 8, 254–263. doi: 10.1007/s12668-017-0481-4

Reddy, A. J., Kokila, M. K., Nagabhushana, H., Rao, J. L., Shivakumara, C., Nagabhushana, B. M., et al. (2011). Combustion synthesis, characterization and raman studies of ZnO nanopowders. *Spectrochim. Acta A Mol. Biomol. Spectrosc.* 81, 53–58. doi: 10.1016/j.saa.2011.05.043

Richard, J. L. (2007). Some major mycotoxins and their mycotoxicoses-An overview. *Int. J. Food Microbiol.* 119, 3–10. doi: 10.1016/j.ijfoodmicro.2007.07.019

Savi, G. D., Vitorino, V., Bortoluzzi, A. J., and Scussel, V. M. (2013). Effect of zinc compounds on Fusarium verticillioides growth, hyphae alterations, conidia, and fumonisin production. *J. Sci. Food Agric.* 93, 3395–3402. doi: 10.1002/jsfa.6271

Sebaaly, C., Charcosset, C., Stainmesse, S., Fessi, H., and Greige-Gerges, H. (2016). Clove essential oil-in-cyclodextrin-in-liposomes in the aqueous and lyophilized states: from laboratory to large scale using a membrane contactor. *Carbohyd. Polym.* 138, 75–85. doi: 10.1016/j.carbpol.2015.11.053

Sellamani, M., Kalagatur, N. K., Siddaiah, C., Mudili, V., Krishna, K., Natarajan, G., et al. (2016). Antifungal and zearalenone inhibitory activity of *Pediococcus pentosaceus* isolated from dairy products on Fusarium graminearum. *Front. Microbiol.* 7:890. doi: 10.3389/fmicb.2016.00890

Sheweita, S. A., El-Hosseiny, L. S., and Nashashibi, M. A. (2016). Protective effects of essential oils as natural antioxidants against hepatotoxicity induced by cyclophosphamide in mice. *PLoS One* 11:e0165667. doi: 10.1371/journal.pone.0165667

Siddaiah, C. N., Prasanth, K. V. H., Satyanarayana, N. R., Mudili, V., Gupta, V. K., Kalagatur, N. K., et al. (2018). Chitosan nanoparticles having higher degree of acetylation induce resistance against pearl millet downy mildew through nitric oxide generation. *Sci. Rep.* 8:2485. doi: 10.1038/s41598-017-19016-z

Simon, H. U., Haj-Yehia, A., and Levi-Schaffer, F. (2000). Role of reactive oxygen species (ROS) in apoptosis induction. *Apoptosis* 5, 415–418. doi: 10.1023/A:1009616228304

Smith, M. C., Madec, S., Coton, E., and Hymery, N. (2016). Natural co-occurrence of mycotoxins in foods and feeds and their in vitro combined toxicological effects. *Toxins* 8:94. doi: 10.3390/toxins8040094

Suresh, D., Shobharani, R. M., Nethravathi, P. C., Pavan Kumar, M. A., Nagabhushana, H., and Sharma, S. C. (2015). Artocarpus gomezianus aided green synthesis of ZnO nanoparticles: luminescence, photocatalytic and antioxidant properties. *Spectrochim. Acta A Mol. Biomol. Spectrosc.* 141, 128–134. doi: 10.1016/j.saa.2015.01.048

Velmurugan, P., Park, J. H., Lee, S. M., Yi, Y. J., Cho, M., Jang, J. S., et al. (2016). Eco-friendly approach towards green synthesis of zinc oxide nanocrystals and its potential applications. *Artif. Cells Nanomed. Biotechnol.* 44, 1537–1543. doi: 10.3109/21691401.2015.1059840

Venkataramana, M., Nayaka, S. C., Anand, T., Rajesh, R., Aiyaz, M., Divakara, S. T., et al. (2014). Zearalenone induced toxicity in SHSY-5Y cells: the role of oxidative stress evidenced by N-acetyl cysteine. *Food Chem. Toxicol.* 65, 335–342. doi: 10.1016/j.fct.2013.12.042

Vijayakumar, S., Malaikozhundan, B., Shanthi, S., Vaseeharan, B., and Thajuddin, N. (2017). Control of biofilm forming clinically important bacteria by green synthesized ZnO nanoparticles and its ecotoxicity on Ceriodaphnia cornuta. *Microb. Pathog.* 107, 88–97. doi: 10.1016/j.micpath.2017.03.019

Wang, Z., Zhang, L., Liu, Z., Sang, L., Yang, L., and Chen, Q. (2017). The antibacterial polyamide 6-ZnO hierarchical nanofibers fabricated by atomic layer deposition and hydrothermal growth. *Nanoscale Res. Lett.* 12, 421–429. doi: 10.1186/s11671-017-2162-1

Youssef, A. M., El-Nahrawy, A. M., and Abou Hammad, A. B. (2017). Sol-gel synthesis and characterizations of hybrid chitosan-PEG/calcium silicate nanocomposite modified with ZnO-NPs and (E102) for optical and antibacterial applications. *Int. J. Biol. Macromol.* 97, 561–567. doi: 10.1016/j.ijbiomac.2017.01.059

Zhang, P., Zhang, W., Wang, J., Jiang, K., Zhang, J., Li, W., et al. (2017). The electro-optic mechanism and infrared switching dynamic of the hybrid multilayer VO_2/Al:ZnO heterojunctions. *Sci. Rep.* 7, 4425–4439. doi: 10.1038/s41598-017-04660-2

Zhang, Z.-Z., Xu, J.-J., Shi, Z.-J., Cheng, Y.-F., Ji, Z.-Q., Deng, R., et al. (2017). Short-term impacts of Cu, CuO, ZnO and Ag nanoparticles (NPs) on anammox sludge CuNPs make a difference. *Bioresour. Technol.* 235, 281–291. doi: 10.1016/j.biortech.2017.03.135

Zhang, Y. G., Ma, L. L., Li, J. L., and Yu, Y. (2007). In situ Fenton reagent generated from TiO2/Cu2O composite film: a new way to utilize TiO2 under visible light irradiation. *Environ. Sci. Technol.* 41, 6264–6269. doi: 10.1021/es070345i

Zheng, L., Wan, Y., Qi, P., Sun, Y., Zhang, D., and Yu, L. (2017). Lectin functionalized ZnO nanoarrays as a 3D nano-biointerface for bacterial detection. *Talanta* 167, 600–606. doi: 10.1016/j.talanta.2017.03.007

Zhu, H., Xu, X., Tian, X., Tang, J., Liang, H., Chen, L., et al. (2017). A thresholdless tunable raman nanolaser using a ZnO-graphene superlattice. *Adv. Mater.* 29:1604351. doi: 10.1002/adma.201604351

Zhu, L., Wang, L., Xue, F., Chen, L., Fu, J., Feng, X., et al. (2017). Piezo-phototronic effect enhanced flexible solar cells based on n-ZnO/p-SnS core–shell nanowire array. *Adv. Sci.* 4, 1600185–1600192. doi: 10.1002/advs.201600185

Zhu, J., and Deng, D. (2017). Ammonia-assisted wet-chemical synthesis of ZnO microrod arrays on substrates for microdroplet transfer. *Langmuir* 33, 6143–6150. doi: 10.1021/acs.langmuir.7b00921

Conflict of Interest Statement: The authors declare that the research was conducted in the absence of any commercial or financial relationships that could be construed as a potential conflict of interest.

frontiers
in Microbiology

METHODS
published: 30 July 2019
doi: 10.3389/fmicb.2019.01667

A Novel Antifungal System With Potential for Prolonged Delivery of Histatin 5 to Limit Growth of *Candida albicans*

Carolina R. Zambom[1]*, Fauller H. da Fonseca[1], Edson Crusca Jr.[1], Patrícia B. da Silva[2], Fernando R. Pavan[3], Marlus Chorilli[2] and Saulo S. Garrido[1]*

[1]Department of Biochemistry and Chemical Technology, Institute of Chemistry, UNESP – São Paulo State University, Araraquara, Brazil, [2]Department of Drugs and Medicines, School of Pharmaceutical Sciences of Araraquara, UNESP – São Paulo State University, Araraquara, Brazil, [3]Department of Biological Sciences, School of Pharmaceutical Sciences of Araraquara, UNESP – São Paulo State University, Araraquara, Brazil

Edited by:
Renata Katsuko Takayama Kobayashi,
State University of Londrina, Brazil

Reviewed by:
Terezinha Inez Svidzinski,
State University of Maringá, Brazil
Sumant Puri,
Temple University, United States

***Correspondence:**
Carolina R. Zambom
carolinarz@gmail.com
Saulo S. Garrido
saulo.santesso@unesp.br

Specialty section:
This article was submitted to Antimicrobials, Resistance and Chemotherapy, a section of the journal Frontiers in Microbiology

Received: 13 December 2018
Accepted: 04 July 2019
Published: 30 July 2019

Citation:
Zambom CR, da Fonseca FH, Crusca E Jr, da Silva PB, Pavan FR, Chorilli M and Garrido SS (2019) A Novel Antifungal System With Potential for Prolonged Delivery of Histatin 5 to Limit Growth of Candida albicans. Front. Microbiol. 10:1667. doi: 10.3389/fmicb.2019.01667

Currently 75–88% of fungal infections are caused by *Candida* species, and *Candida albicans* is the main microorganism that causes these infections, especially oral candidiasis. An option for treatment involves the use of the antifungal peptide Histatin 5 (Hst 5), which is naturally found in human saliva but undergoes rapid degradation when present in the oral cavity, its site of action. For this reason, it is important to develop a way of applying this peptide to the oral lesions, which promotes the gradual release of the peptide. In the present study, we have evaluated the development of liposomes of different lipid compositions, loaded with the peptide as a way to promote its release slowly and gradually, preserving its antifungal potential. For this, the peptide 0WHistatin 5, an analog of the peptide Hst 5, was synthesized, which contains the amino acid tryptophan in its sequence. The solid phase synthesis method was used, followed by cleavage and purification. The liposomes were produced by thin film hydration technique in three different lipid compositions, F1, F2, and F3 and were submitted to an extrusion and sonication process to standardize the size and study the best technique for their production. The liposomes were characterized by dynamic light scattering, and tests were performed to determine the encapsulation efficiency, release kinetics, stability, and evaluation of antifungal activity. The extruded liposomes presented average size in the range of 100 nm, while sonicated liposomes presented a smaller size in the range of 80 nm. The encapsulation efficiency was higher for the sonicated liposomes, being 34.5% for F1. The sonicated F3 presented better stability when stored for 60 days at 4°C. The liposomes showed the ability to release the peptide for the total time of 96 h, with the first peak after 5 h, and a further increase of the released after 30 h. Time-kill assay showed that the liposomes were able to control yeast growth for 72 h. The data suggest that the liposomes loaded with 0WHistatin 5 maintained the action of the peptide and were able to limit the growth of *C. albicans*, being a suitable system for use in the treatment of oral candidiasis.

Keywords: antifungal system, oral candidiasis, *Candida albicans*, Histatin 5, liposomes

INTRODUCTION

In recent decades, there has been an increase in mortality caused by fungal infections which have gone from isolated and rare cases to one of the greatest global public health problems especially among immunocompromised individuals (Robbins et al., 2016). This fact is related to medical interventions such as chemotherapy for cancer treatment, immunosuppression for transplantation, and the high prevalence of HIV infections (Berkow and Lockhart, 2017). This has allowed the appearance of prevalent fungal infections among which the main pathogens are *Candida albicans*, *Cryptococcus neoformans*, and *Aspergillus fumigatus* (Robbins et al., 2016). These pathogens cause the death of more than 1 million people annually in the world with 75–88% of fungal infections being caused by *Candida* species, which generated a cost of $ 1.7 billion for public health in the US and the increase of severe cases of hospital infections (Berkow and Lockhart, 2017).

C. albicans exists as a commensal microorganism of the skin, mouth, and gastrointestinal tract. Its spread is controlled by coexistence with the normal human microbiota and also by the processes of defense related to immune system. However, when there is suppression of the immune response against *C. albicans*, colonization of the tissue occurs establishing the infection, more commonly manifested as candidiasis and oropharyngeal candidiasis (Robbins et al., 2016).

Because it is a polymorphic microorganism, *C. albicans* is able to transition between the yeast and hypha lifestyles. The hypha has greater resistance and greater invasive capacity in tissues compared to the yeast. For this reason, this species demonstrates resistance to the most common antifungals, such as polyenes (nystatin and amphotericin B) or azoles (itraconazole, miconazole, and fluconazole) (Hawser and Douglas, 1995).

An alternative treatment is the use of fluconazole and amphotericin B, which are more effective but have higher levels of toxicity and should not be used in constant or routine doses (Johnson et al., 1995; Cannon et al., 2007). For this reason, the search for new treatment options and new drugs are constantly developing mainly in the biotechnology field. An example of this is the biologically active peptides naturally found in living organisms such as the antimicrobial peptides (AMPs) of Histatin class.

One of these AMPs, that is, the focus of this data is Histatin 5 (Hst 5), one of the peptides of the Histatin class naturally present in human saliva and potentially active against pathogenic yeast such as *C. albicans* (Helmerhorst et al., 1999; Baev et al., 2002). Hst 5 is a peptide of about 3 kDa composed of a linear sequence of 24 amino acid residues, has a positive charge at physiological pH, assumes α-helix structure in DMSO (dimethylsulfoxide) and TFE (trifluorethanol)/water, and in water preferably takes on a random structure (Seo et al., 2012).

Recent studies have demonstrated that Hst 5 is able to inhibit *C. albicans* growth in concentrations ranging from 25 to 800 μg ml^{-1} (Moffa et al., 2015b) with MIC of 25 μg ml^{-1} (Konopka et al., 2010). Another feature of this peptide is its ability to protect the oral epithelium from *C. albicans* infection, proven in *in vitro* studies with gingival fibroblast cells, in which at a concentration of 50 μg ml^{-1}, there was no invasion of the cells by the microorganism (Moffa et al., 2015b).

However, we have reported that Hst 5 undergoes rapid degradation, and the proteolysis has been the major focus aimed at explaining that degradation causes the reduction or even loss of its antifungal activity (Moffa et al., 2015a). Another problem observed was that Hst 5 can interact with other proteins present in saliva, such as amylase, resulting in a complex free of antifungal activity (Moffa et al., 2015a).

One way to overcome this problem would be the use of nanocarriers, such as liposomes, that can incorporate the peptide and increase its availability at the site of action. Liposomes have been used in therapeutics for more than 40 years, presenting many advantages, including biocompatibility, because they are constituted by phospholipids, such as the biological membranes of the cells (Chorilli et al., 2013).

The liposome advantage is related to a longer duration of the therapeutic effect of the drug (De Araújo et al., 2003), prolonging its action and allowing larger doses to be administered without the risks of toxicity (Frézard et al., 2005). Thus, there are a lower number of drug administrations throughout the treatment, as demonstrated by studies with liposome-encapsulated LL-37 peptide which showed improved bioactivity and reduced toxicity for treatment of HSV-1. The studies carried out indicated the LL-37 liposomal formulation as an effective system for carrying and delivering the peptide to the action target (Ron-Doitch et al., 2016).

Liposomes are also effective in promoting protection against external degradation by enzymes or by proteolytic degradation (Voltan et al., 2016). For this reason, they are used for encapsulation of peptides and proteins. Liposomes encapsulated with peptide ghrelin, used to treat cachexia, characterized as extreme weakness in patients afflicted with chronic diseases, showed that liposomes were able to protect the peptide from the attack of trypsin and carboxylesterase enzymes by 20 and 81%, respectively (Salade et al., 2017).

Thus, these positive aspects about the use of liposomes motivated us to elaborate a system to apply Histatin 5, with the main interest in increasing peptide availability at the site of action, causing its fungicidal effect to be preserved and intensified over a longer period, thus optimizing treatment against *C. albicans*.

MATERIALS AND METHODS

Chemicals and Microorganisms

Reagents N-α-fluorenylmethyloxycarbonyl-amino acids (Fmoc-amino acid) and Fmoc-tyr-wang resin were purchased from Novabiochem®. N-hydroxybenzotriazole (HOBt), N,N′-diisopropylcarbodiimide (DIC), dichloromethane (DCM), dimethylformamide (DMF), and trifluoroacetic acid (TFA) were purchased from Fluka®. Ethanedithiol (EDT), glacial acetic acid, dimethylformamide (DMF), dimethyl sulfoxide (DMSO), chloroform, and grade HPLC acetonitrile (ACN) were purchased from Merck®. The microorganism *C. albicans* (ATCC 90028) was donated by the National Institute of Quality Control in

Health (INCQS – Fundação Oswaldo Cruz Brazil). All lipids were purchased from Sigma®.

Peptide Synthesis

The peptide was synthesized manually according to the Fmoc chemistry (Merrifield, 1963). In each synthetic cycle, the deprotection of the α-amino group deprotection was performed with 20% piperidine in DMF for 20 min. The coupling reactions were performed with a threefold excess of DIC component and HoBt in DMF/DCM (1:1, v:v). After approximately 2 h of coupling, the ninhydrin test was performed to confirm the occurrence of the reaction. Final cleavage of the peptide from the resins and the deprotection of the side-chain protector groups were done by treatment with a solution containing TFA (94.5%), deionized water (2.5%), EDT (2.5%), and TIS (0.5%) at 25°C for 3 h. After the cleavage procedure, the crude peptides were precipitated with ethyl ether, separated from the soluble non-peptidic contents by centrifugation, extracted into 10% acetic acid in water and lyophilized.

The analog peptide 0WHistatin 5 (0WHst 5) was synthesized with the addition of the amino acid tryptophan (W) in amino terminal extremity, as can be seen in **Table 1**. Because it is a fluorescent amino acid, with excitation at the wavelength of 280 nm and emission of fluorescence at the wavelength of 360 nm, its addition allowed its monitoring by fluorescence technique, with greater sensitivity as can be seen in the following sections.

The purification process of the crude peptides was performed in semi-preparative HPLC with a Zorbax Eclipse XDB C18 reverse phase column (9.4 mm × 250 mm and 5 μm). The qualitative analysis was performed analytically using a Shimadzu LC-10A/C-47A separation system coupled to a Shimadzu LC-10A/C-47A UV/Vis detector with a Waters Symmetry C18 column (2.1 mm × 150 mm and 5 μm). The chromatographic conditions in the semi-preparative mode were: solvents A (0.045% $TFA.H_2O$) and B (0.036% TFA. ACN), gradient of 0.33%/min solvent B over 90 min, flow rate of 5 ml/min, and detection wavelength at 220 nm. For the analytical mode, the conditions were: solvents A (0.045% $TFA.H_2O$) and B (0.036% TFA.ACN), gradient from 5 to 95% solvent B in 30 min, flow rate of 0.6 ml/min, and detection wavelength at 220 nm. After the purification procedure of the peptide, the molecule characterization was done using mass spectrometry. The analysis of pure peptides was performed by HPLC coupled to mass spectrometer operated in electrospray positive mode (LC/ESI-MS+) in a Bruker® type Ion Trap Amazon SL mass spectrometer. This procedure allowed to determine the quality and identity of the sample simultaneously.

TABLE 1 | Amino acid sequence of Histatin 5 and the synthesized 0WHistatin 5 analog peptide.

Peptide	Amino acid sequence
Histatin 5	DSHAKRHHGYKRKFHEKHHSHRGY
0WHistatin 5	**W**DSHAKRHHGYKRKFHEKHHSHRGY

Preparation of Liposomes

Three different liposome formulations were produced by the thin film hydration technique. The lipid film was composed of soy dipalmitoyl phosphatidylcholine (DPPC), cholesterol (Chol), polyethylene glycol (PEG), and 1-palmitoyl-2-oleoyl-sn-glycero-3-phospho-rac-1-glycerol (POPG). The lipid mixtures were dissolved in chloroform and then were evaporated under nitrogen flow, to form a thin lipid film in tube wall. For resuspension of the lipid film, solutions with or without the peptides solubilized in a 10 mM Tris HCl buffer, pH 7.4, was used. A suspension of large multilamellar vesicles (MLV's) was obtained and submitted to two different techniques for homogenization: extrusion, using Avanti Polar Lipids® extruder equipped with Nuclepore® polycarbonate membrane, GE Healthcare Life Science, with pores of 100 nm, and sonication, using titanium tip sonicator (QSonica® Q700).

Physical Characterization of Liposomes

Determination of the Mean Hydrodynamic Diameter, Polydispersity Index, and Zeta Potential

The mean hydrodynamic diameter (Z-Ave or d.nm) and polydispersity index (PDI) were determined by dynamic light scattering (DLS, Zetasizer Nano NS, Malvern Instruments®, Malvern, UK). The zeta potential (ZP) of the liposomes was evaluated by the electrophoretic mobility of the particles according to the Helmholtz-Smoluchowski equation and processed using the Zetasizer Nano NS equipment software (Malvern Instruments). The suspensions of empty and loaded liposomes were diluted in 10 mM Tris HCl buffer, pH 7.4, in a 1:10 ratio. All experiments were run in triplicate at 25°C.

Encapsulation Efficiency

The unencapsulated peptide separation was performed by molecular exclusion chromatography technique, using a Sephadex® G-50 column, with 10 mM Tris HCl buffer, 150 mM NaCl, pH 7.4.

The fractions with liposomes were frozen in liquid nitrogen and lyophilized for 48 h. Then 3 ml of methanol were added to the samples, an aliquot of this solution was diluted in methanol and analyzed in spectrofluorometer to quantify the encapsulated peptide. Once the encapsulated peptide concentration was determined, the encapsulation efficiency, EE, was calculated using Equation 1.

$$\mathrm{EE}\left(\%\right) = \frac{\text{Encapsulated peptide}}{\text{Total added peptide}} \times 100 \tag{1}$$

Formulation Stability

The produced formulations, F1, F2, and F3, were stored at 8°C and at 37°C. The mean size, polydispersity index, and zeta potential were analyzed after 1, 5, 10, 15, 30, 45, and 60 days of storage.

In vitro Release Study

The release kinetics of the encapsulated peptide was performed using the fluorescence technique, since the inserted tryptophan (W) provides fluorescence to the molecule. Spectrofluorometer Varian® CaryEclipse coupled to a circulation system of the solution 10 mM Tris HCl, pH 7.4, was used. About 1 ml of the solution of liposome and 0WHst 5 was added to a cellulose acetate dialysis membrane (Sigma-Aldrich® cut-off 14,000 kDa).

The peptide that permeated the dialysis tube and exited into the buffer solution was monitored by the Kinetics Varian® CaryEclipse software, with maximum fluorescence emission at 360 nm for 96 h. The maximum fluorescence was plotted against the time and, by the use of the standard curve, the total peptide released by the system was evaluated by the plot of the maximum released concentration against the time.

Time-Kill Curve Studies

For the preparation of the standardized suspensions of *C. albicans* (ATCC 90028), an inoculum size of 1.10^5 CFU ml^{-1} was used. Nine milliliters of Sabouraud Dextrose Broth (SDB) prepared with the microorganism were added in an Erlenmeyer for the growth control, 512 μg ml^{-1} of fluconazole was used for the positive control (cell death) and for testing the systems produced 1 ml of the liposomal system encapsulated or not with 0WHst 5 was added. The Erlenmeyers were then incubated at 37°C, under constant stirring, and aliquots of 100 μl were withdrawn and serially diluted every 3 h for 12 h. After this period, the aliquots were withdrawn and serial diluted every 12 h for 60 h. About 100 μl of each dilution were transferred to a plate with SDA and incubated for 48 h. The colonies in each plate were then counted.

Statistical Analysis

t-Student test was used to verify the statistical difference between the last points of the time kill test curves. The level of significance was 90%. The growth control and fluconazole curves were performed in duplicate.

RESULTS AND DISCUSSION

Preparation of Liposomes

In this work, three liposomal formulations were used according to the amounts shown in **Table 2**. The amounts are represented in mass. The peptide used was successfully obtained with high purity (>95%) and loaded into the liposomes as described in the methodology section.

TABLE 2 | Lipid composition of the liposomes.

Formulation	DPPC	Chol	PEG	POPG
F1	40	2	–	–
F2	40	2	1	–
F3	40	2	–	1

To determine the amount of extrusion cycles and sonication time required for the formation of the liposomes, periodic measurements were made in a spectrophotometer (Chorilli et al., 2013). The results shown in **Figure 1** indicates that there is a decrease in absorbance at 410 nm as a function of sonication time and amount of extrusion cycles, respectively, for all formulations developed.

All the formulations produced required 15 extrusion cycles to be formed, thus, the addition of PEG in F2 and POPG in F3 did not promote differences in the number of extrusion cycles observed for F1 which does not have any of these components. When PEG and POPG were added to the formulation of these liposomes, the main objective was to promote better features like fluidity and stability to vesicles. For the sonication technique, monitoring was performed after every 2 min, as seen in **Figure 1B**, and the stabilization of the absorbance values was achieved in the time of 4 min for all formulations. As in the extrusion, the addition of PEG and POPG in F2 and F3 did not affect the minimum time of 2 min of sonication observed for formulation F1 that does not contain these components.

Physical Characterization of Liposomal Formulation

The mean size, zeta potential, and polydispersity index (PDI) for empty and loaded liposomes with 0WHst 5, can be seen in **Tables 3** and **4**.

The mean size of the empty and sonicated liposomes was lower than for the empty liposomes obtained by extrusion. This can be observed by comparing the sizes for the empty liposomes obtained by extrusion and sonication seen in **Tables 3** and **4**.

This fact is related to the technique of obtaining the liposomes. The 100 nm pores of the polycarbonate membrane used in the extruder, ensures final sizes closer to 100 nm. In sonication, there is no way to control or predict the final mean size of the liposomes, which may vary as the amplitude, sonication time, and potency of the equipment change.

There was an increase in the mean size of loaded liposomes when compared to empty liposomes and this was observed for all formulations obtained by both techniques. According to **Table 3**, the empty F2 size was 97.2 nm, and after the addition of 0WHst 5, it had a size of 119.2 nm. For sonicated F3, the mean size before loading of the peptide was 82.2 nm, rising to 133.6 nm with 0WHst 5. The same can be observed sonicated F1, which after addition of 0WHst 5 presented a 144.3 nm, against 88.1 nm when empty. We observed an increase in size for liposomes after peptides had been encapsulated, and this indicates that 0WHst 5 was incorporated into the liposomes, probably in the inner aqueous compartment because it is a water-soluble molecule (Nii and Ishii, 2005; Mohan et al., 2016). These data are interesting from the point of view of the intended application, which aims to stabilize the peptide and promote a better availability of it at the site of action.

The zeta potential of the produced liposomes is negative for all formulations prepared. The zeta potential value became less negative for all sonicated formulations after incorporation of the peptide. 0WHst 5 is a positively charged peptide

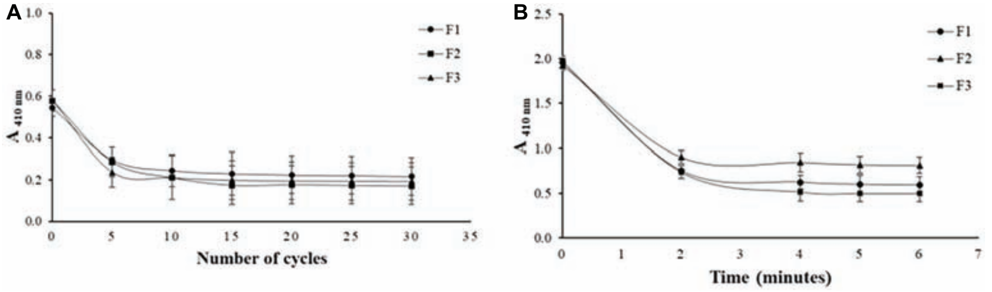

FIGURE 1 | Effect of the amount of extrusion cycles on different liposome compositions **(A)** and effect of sonication time on different liposome compositions **(B)**.

TABLE 3 | Size, PDI, and zeta potential for empty and loaded F1, F2, and F3 liposomes, obtained by extrusion.

Formulation	Size (nm)	PDI	Zeta potential (mV)
F1	106.1 ± 1.70	0.128 ± 0.06	−49.8 ± 1.17
F1/0WHst 5	116.6 ± 0.30	0.081 ± 0.10	−43.0 ± 0.50
F2	97.1 ± 1.77	0.099 ± 0.04	−38.5 ± 2.29
F2/0WHst 5	119.2 ± 0.80	0.087 ± 0.08	−42.2 ± 0.90
F3	105.1 ± 0.70	0.113 ± 0.06	−42.7 ± 1.89
F3/0WHst 5	112.6 ± 0.50	0.068 ± 0.08	−47.4 ± 0.50

TABLE 4 | Size, PDI, and zeta potential for empty and loaded F1, F2, and F3 liposomes, obtained by sonication.

Formulation	Size (nm)	PDI	Zeta potential (mV)
F1	88.1 ± 8.03	0.371 ± 0.01	−51.4 ± 8.94
F1/0WHst 5	144.3 ± 0.35	0.255 ± 0.01	−48.6 ± 0.21
F2	96.4 ± 10.41	0.382 ± 0.05	−56.4 ± 2.28
F2/0WHst 5	147.4 ± 1.45	0.124 ± 0.09	−51.5 ± 1.79
F3	82.2 ± 4.77	0.287 ± 0.02	−56.5 ± 3.78
F3/0WHst 5	133.6 ± 0.82	0.241 ± 0.01	−52.3 ± 8.17

TABLE 5 | Efficiency of encapsulation for the formulations F1, F2, and F3.

Formulation	Extrusion (%)	Sonication (%)
F1	17.7	34.5
F2	9.5	12.2
F3	12.7	14.2

(net charge at pH 7: +5.7) that interferes with the final charge of the liposomes, making them less negative. The POPG lipid used in the F3 formulation is anionic and confers a greater amount of negative charges to the external lipid bilayer which may be less influenced by the positive charge of 0WHst 5. The standard zeta potential value used for this is ±30 mV (Ebrahimi et al., 2015; Berbel Manaia et al., 2017; Sato et al., 2017). The sonicated and extruded encapsulated F1, F2, and F3 formulations have zeta potential in the range of −30 to −50 mV, indicating that all formulations are stable.

PDI values in the range of 0.07 to 0.09 were found for all extruded formulations containing 0WHst 5, as can be seen in **Table 3**. Thus, it can be stated that there is a monodispersion. For sonication, PDI values of 0.371, 0.382, and 0.287 were found for empty F1, F2, and F3, respectively, indicating homogeneity of the analyzed sample. However, there are vesicles in other size ranges, characterizing a polydispersity.

The PDI values fell to 0.255, 0.124, and 0.241, respectively, when 0WHst 5 was loaded into the liposomes prepared by sonication. Addition of the peptide to the formulations made them more homogeneous. The same effect was also observed for the liposomes obtained by extrusion, with 0.128 of PDI for empty and 0.081 for loaded F1 formulation.

Encapsulation Efficiency

The encapsulation efficiency (EE) for the 0WHst 5 is below 40%, as seen in **Table 5**. Addition of cholesterol to all formulations may have hindered encapsulation. This component prevents the phase transition of the lipid bilayers and always maintains them in a state of intermediate fluidity, tending to be more rigid, which hinders the incorporation of molecules (Roy et al., 2016).

However, EE was higher for formulations produced by sonication, with the highest value of 34.5% for F1. This formulation also showed the highest efficiency among the formulations obtained by extrusion, with a value of 17.7%. F1 is composed of DPPC and cholesterol, DPPC has T_m (phase transition temperature) of 42°C, with a room temperature of 25°C bilayer is in its gel phase and rigid. Even so, it is the formulation that incorporated the largest amount of the peptide for the two techniques used.

The absence of other components contributed to the incorporation of the peptide according to this methodology. The presence of PEG in F2 and POPG in F3 made it difficult to incorporate 0WHst 5 into the liposomes. The encapsulation efficiency for F3 was little higher when compared to F2. The presence of POPG in this formulation aims to favor the crystalline liquid phase of the bilayer and grant more fluidity, since this lipid has T_m of −2°C, contributing the incorporation of the peptide. The lower EE was for F2, which has PEG in its composition. However, the presence of this component increases the physical-chemical stability of the liposomes, as will be seen in the following results. The increase in stability prolongs their presence in the human organism, by decreasing the uptake of the vesicles by the cells of the immune system and favors adherence in mucous membranes (Ron-Doitch et al., 2016; Jøraholmen et al., 2017), which may be a desirable characteristic for the intended application.

Stability Studies

According to **Figure 2A**, there were slight changes in average size and PDI for the sonicated F1 stored at 4°C. For this reason, sonication produced liposomes with better stability than the extrusion, maintaining the formulation stable during 60 days at 4°C. Storage at 37°C was more damaging to all formulations, providing many variations on mean size and PDI over time, which was also observed by Çelik et al. (2017).

The temperature of 4°C favors the storage of liposomes obtained by both techniques. It can be observed that for F2 (**Figures 2A,B**) up to 30 days, the average size and PDI did not show great variations, and after 45 days, a small variation of average size, from approximately 160 to 130 nm for sonication and from 160 to 110 nm for extrusion, with increase of PDI. Sonicated F1 and F2 presented better parameters and better stability when stored at 4°C. F2 has PEG in its composition, which according to some studies favors the maintenance of vesicle stability as also observed by Rai et al. (2008). Even though it does not favor encapsulation efficiency, as discussed previously, this component helps to maintain the stability of the formulation, which remains intact for longer when stored at 4°C.

Sonicated F3 is the most stable formulation compared to F1 and F2, according to the graphs of **Figures 2A** and **3A**.

In general, the best storage temperature is 4°C for all formulations. The technique that presents better stability is sonication. The lipids used in the liposomes may influence the stability, since the best stability was for F3, which has POPG in its composition. This component provides a more fluidity to the lipid bilayer, which can generate better adaptation throughout the storage period. POPG also confers a greater

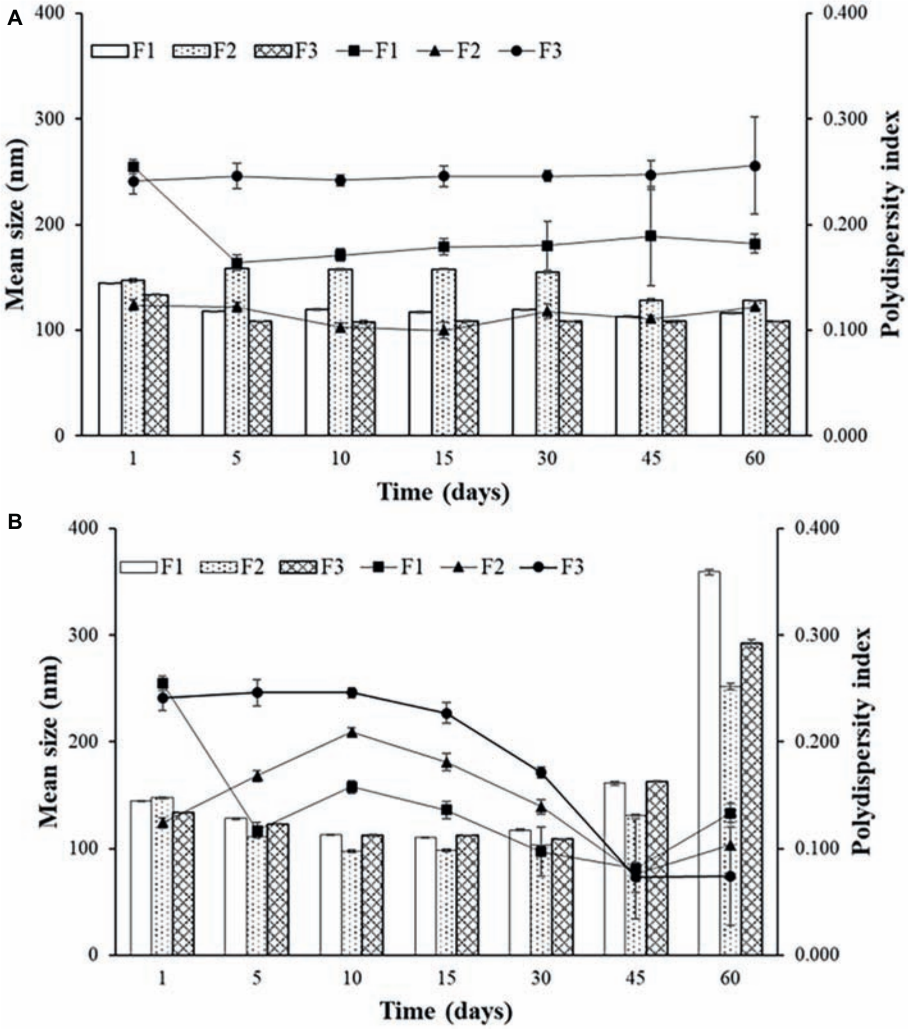

FIGURE 2 | Mean size and polydispersity index (PDI) for F1, F2, and F3 obtained by sonication stored at 4°C **(A)** and at 37°C **(B)**.

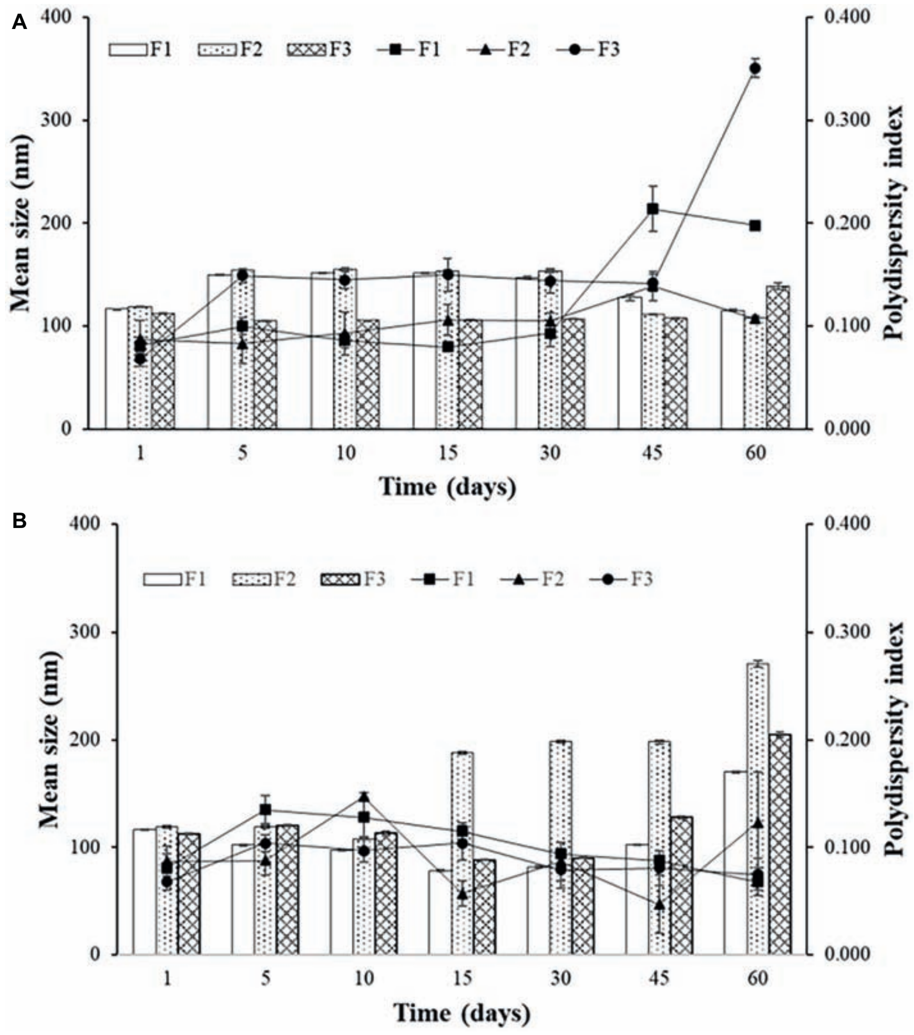

FIGURE 3 | Mean size and polydispersity index (PDI) for F1, F2, and F3 obtained by extrusion stored at 4°C **(A)** and at 37°C **(B)**.

amount of negative charges to the bilayer, which difficult the aggregation of the liposomes. F2, which contains PEG, also showed better stability than F1, which has only DPPC and cholesterol. The addition of different lipids to the liposomes has made peptide encapsulation more difficult as previously seen, but may improve stability, as seen in these results.

In vitro Release Study

Graph A of **Figure 4** represents the crossing of the unencapsulated peptide over the dialysis membrane. This test was performed as a control for the release experiments of the developed liposomal system. Thus, it was possible to know the time required for the non-encapsulated peptide to leave the dialysis membrane, once the peptide encapsulated in the liposomes would only come out after its rupture, which would take a longer time. The total crossing over of the unencapsulated peptide occurs after 5 h. For F1, F2, and F3 (**Figures 4B–D**), a 5-h time release peak is observed, similar to the unencapsulated peptide release profile.

The release profile indicates the occurrence of burst effect, which is characterized by the large amount of drug that is released in the first 24 h (Huang and Brazel, 2001). This effect is advantageous since the release of a large amount of 0WHst 5 in a short period of time can be used as the dose of attack to inhibit the growth of microorganisms moments after its application at the site of action. Because it is a release system that is intended for topical application for the treatment of oral lesions caused by *C. albicans*, a rapid release directly at the site of action would rapidly inhibit the proliferation of the microorganism (Huang and Brazel, 2001).

For all formulations, the profiles observed for extrusion and sonication were similar, and the use of distinct techniques for the production of liposomes does not interfere with their release kinetics. The burst effect observed in the first 5 h indicates that the released content is not encapsulated in the liposomes, or that it may be interacting with its outer surface, as also observed by Calienni et al. (2017). Thus, the release process for these liposomes occurs in two steps, initially there is a rapid release,

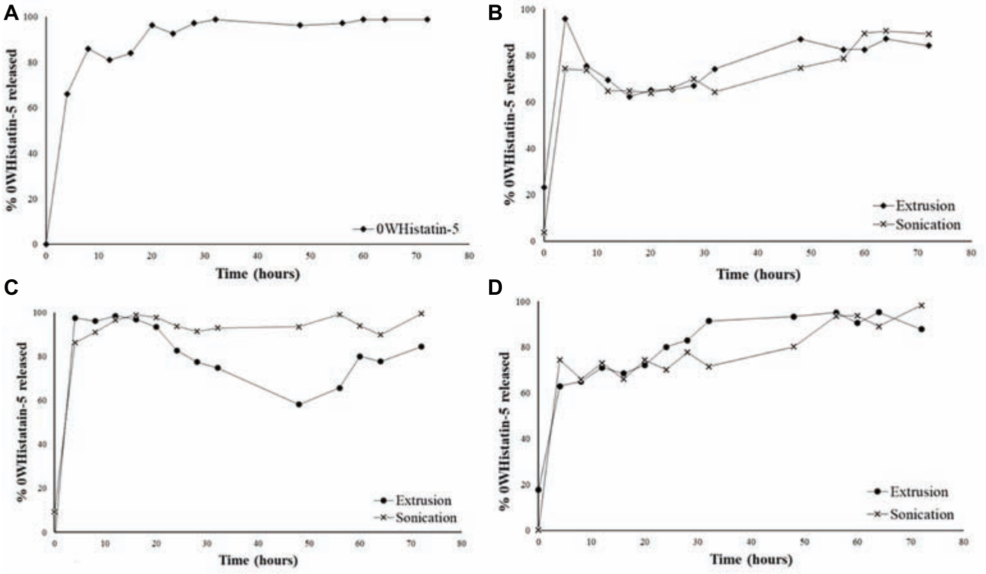

FIGURE 4 | Release profile for: free 0WHistatin 5 **(A)**; F1 **(B)**; F2 **(C)**; and F3 **(D)**, loaded with 0WHistatin 5.

followed by a drop indicating the dialysis system's equilibrium due to osmotic forces. In a second moment, release of the remaining amount of the peptide occurs slowly for 80 h. The slow release step is related to disruption of the liposomes, which thereby releases the peptide contained therein (Lopes et al., 2012).

The release kinetics for nanocarriers is related to their encapsulation efficiency (EE) and stability. A higher EE will certainly result in a higher release peak, especially if burst effect occurs (Luan et al., 2006). Thus, in general, the formulations obtained by sonication, which have higher EE, also show greater increase in their second moment in the release profile.

Killing Curve Studies

The experimental points shown in the graphs were calculated according to Equation 2, where *F* is the dilution factor, *C* is the colony forming unit count, and *V* is the volume of the portion used in the final dilution. The uncertainty of each experimental point was calculated from the standard uncertainty values and expanded uncertainty according to Corry et al. (2007) and Niemi and Niemelä (2001). The error bars do not appear in the graphs presented, since the expanded uncertainties presented results of one to two orders of magnitude lower than the experimental values.

$$y\left(UFC/ml\right) = F \cdot \frac{C}{V} \tag{2}$$

ATCC 90028 was used in this test because it is considered a standard strain for screening tests for new antifungal agents. Besides, this study is based on the proposal of developing a liposomal system capable of prolonging the release of the antifungal peptide Histatin 5. The idea emerged from two studies of our research group involving this peptide for the treatment and prevention of oral candidiasis, mainly caused by *C. albicans* (Moffa et al., 2015a,b).

Previously, MIC assay was performed, and the values found for this strain were 128 μg ml^{-1} for fluconazole and 257.8 μg ml^{-1} for Histatin 5, as well as for the analog peptide 0WHistatin 5. The concentration of 512 μg ml^{-1} for fluconazole in the time kill assay represents four times the MIC value, since the intention was to visualize the cell death caused by the drug, which was used as a positive control. For the peptide, the MIC value was used since it was also the value used to prepare the liposomes and perform the encapsulation efficiency tests.

MIC assay was performed following the M27-A3 methodology of the Clinical and Laboratory Standards Institute Manual with the peptides 0WHistatin 5 and Histatin 5 using SB medium. This medium was chosen to provide enough nutrients to the microorganism during the 72 h of the time kill assay. It was necessary that there was enough amount of nutrients in the medium to promote the microorganism growth for the total time, because the developed system showed release for more than 60 h. Therefore, the observed death effect would be caused by the action of the peptide 0WHistatin 5 and not due to lack of nutrients.

The obtained result is consistent with the literature, and the MIC value for Histatin 5 and 0WHistatin 5 was 64.45 μg ml^{-1}. Thus, the use of the SB medium did not interfere with the antifungal activity of the peptide and indicated that it can be used to perform time kill assays.

To determine MIC for the liposomal preparations is not possible, because the encapsulated peptide is in the liposome internal aqueous compartment, and, when serial dilutions are made, only the number of liposomes present in solution is diluted, while their internal concentration is not.

The internal concentration was determined by calculating the encapsulation efficiency. Therefore, performing a serial dilution test, such as the MIC, would not give us an enlightening result regarding the concentration of liposomal system to

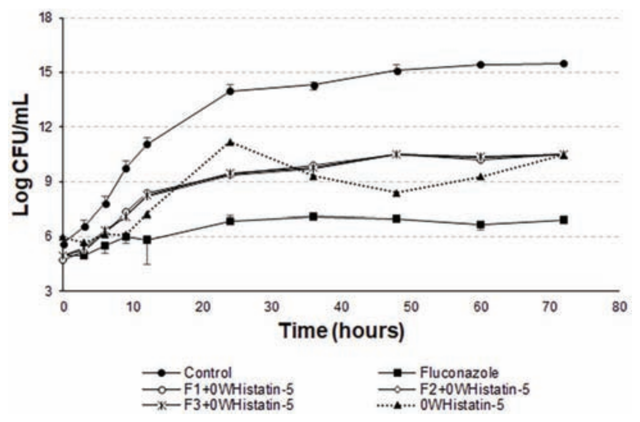

FIGURE 5 | Time-kill curves for *C. albicans* (ATCC 90028) treated with extruded F1, F2, and F3 loaded with 0WHistatin 5. The lines referring to F1 + 0WHistatin 5, F2 + 0WHistatin 5, and F3 + 0WHistatin 5 systems are overlapping because the number of counted colonies were close.

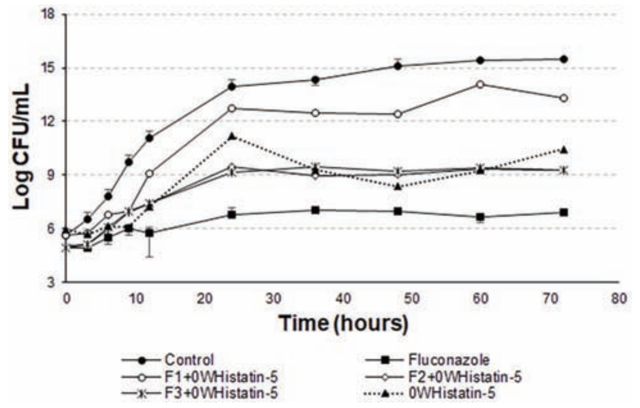

FIGURE 6 | Time-kill curves for *C. albicans* (ATCC 90028) treated with sonicated F1, F2, and F3 loaded with 0WHistatin 5. The lines referring to F2 + 0WHistatin 5and F3 + 0WHistatin 5 systems are overlapping because the number of counted colonies was close.

be used. Thus, it was determined 1 ml of liposomal system for use in the tests to make it possible to apply the value obtained in the encapsulation efficiency tests to estimate the concentration of the encapsulated peptide.

Data of the time-kill assay (**Figure 5**) show that for 12 h the peptide inhibited the growth of the microorganism the same way that fluconazole. A dose of 257.8 μg ml^{-1} of 0WHst 5 and a dose of 512 μg ml^{-1} of fluconazole were used, demonstrating that 0WHst 5 in a lower dosage is capable of performing the same inhibition. This result is in agreement with Moffa et al. (2015b), which found inhibition in the range of 800–25 μg ml^{-1} for Hst 5. When incubating the peptide with *C. albicans* for only 1.5 h, Moffa et al. (2015b) obtained an approximate 2-log reduction in the CFU ml^{-1}. As shown in the graph of **Figure 5**, after 12 h at 4-log reduction in CFU ml^{-1} was observed.

The *t*-student test showed that the means of the last point of the growth control curve and the last point of the curves F1 + 0WHistatin 5, F2 + 0WHistatin 5, F3 + 0WHistatin 5, and 0WHistatin 5 were statistically different, at the level of significance of 90%. This occurred for the systems produced by extrusion and sonication and showed that the produced liposomal system was effective in controlling the growth of *C. albicans*. This demonstrates that with prolonged treatment with 0WHst 5, it is possible to further reduce the growth of the microorganism.

However, Moffa et al. (2015a) proves that Hst 5 undergoes proteolytic action when present in human saliva, in addition to complexing with the enzyme salivary amylase, which leads to a decrease in the antifungal action of the peptide. These two effects occur rapidly as soon as the peptide is mixed with the total human saliva content. Encapsulating this peptide in liposomes is an attempt to protect it from these actions, allowing it to act for an extended period when added to its site of action. The data for the liposomal systems developed in this work (**Figures 5** and **6**) demonstrated prolonged activity for all the produced formulations, as well as the peptide 0WHistatin 5. This proves that the encapsulated peptide does not lose its action and maintains its antifungal potential. In addition, encapsulating the peptide in the

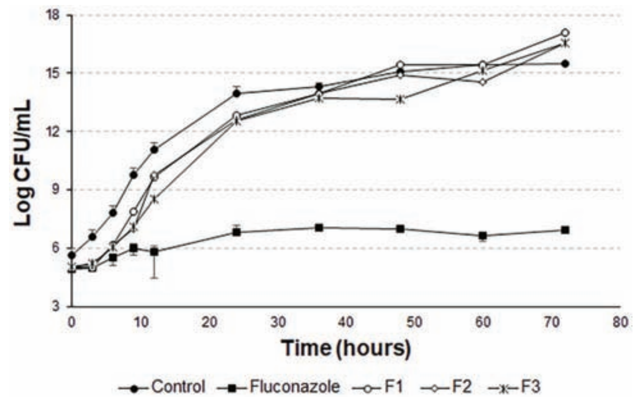

FIGURE 7 | Time-kill curves for *C. albicans* (ATCC 90028) treated with sonicated and empty F1, F2, and F3.

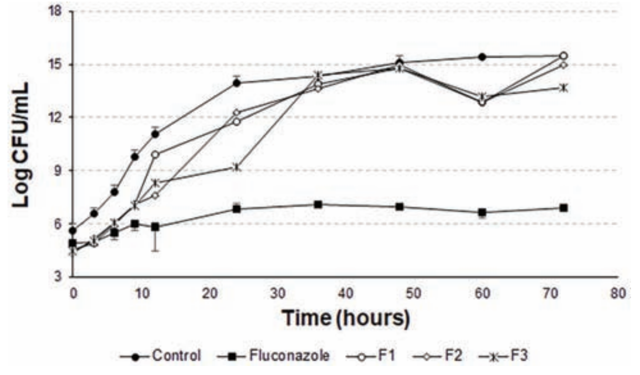

FIGURE 8 | Time-kill curves for *C. albicans* (ATCC 90028) treated with extruded and empty F1, F2, and F3.

liposomes improves the growth limitation, as it becomes more stable than for the non-encapsulated peptide. In **Figure 5**, after 24 h of incubation, there was a 3-log reduction in CFU ml^{-1}, which remained constant during the 72-h test, reaching a reduction of 4 logs in CFU ml^{-1} at the end. For liposomes obtained by sonication (**Figure 6**), after 24 h incubation, the reduction was 4 logs for F2 and F3 and 2 logs for F1. This reduction was also maintained over the 72-h test period. For F2 and F3, the reduction was 6 logs at 72 h.

Han et al. (2016) inhibited close to 100% of *C. albicans* cells by treating them with 16 μg ml^{-1} Hst 5, after a total time of 1 h. This demonstrates that this peptide acts very well in the first few moments after addition to the medium. Thus, this study demonstrates that the use of a nanocarrier, such as liposomes, is able to prolong the time of peptide action, inhibiting the growth of the microorganism for 72 h.

The *t*-student test was applied to compare the last points of the F1, F2, and F3 curves with the last point of the growth control curve. For F1, the means compared are statistically equal. For F2 and F3, the means are statistically different. However, it can be noted from **Figure 8** that there is no pronounced cell death as in **Figures 5** and **6**.

In **Figure 7**, the means of the last points of F1, F2, F3, and growth control are statistically different. There is also no pronounced cell death, as in **Figure 8**. This demonstrates that the liposomal system without the peptide 0WHst 5 does not affect the growth of *C. albicans*, with 0WHst 5 being responsible for the effect discussed above.

CONCLUSION

The results obtained in this work indicate that the extruded liposomes are more homogeneous while the sonicated liposomes have a greater polydispersity. However, encapsulation efficiency values were higher for sonicated liposomes, which also produced more stable liposomes during storage at 4°C, among which F3 was the most stable. The results observed in the release kinetics studies indicate that there is a relationship between the stability of the liposome formulation and the release profile over time, the liposomes exhibit good stability, which controlled and prolonged release of the peptide. The time-kill results using ATCC 90028 showed that the liposomal systems preserved the antifungal activity of the peptide and were able to limit yeast growth for 72 h. As the results were promising and demonstrated to limit the growth of this microorganism, the intent of the research group is testing the systems for other strains, including clinical isolates and resistant strains of *C. albicans*. We can conclude that the liposomal system produced has the potential to limit the growth of the microorganism. Complementary tests, such as system degradation in human saliva and *in vivo* tests are the future steps off this work.

AUTHOR CONTRIBUTIONS

CZ performed all the experiments and wrote the manuscript. FF assisted in the time kill test and collaborated with the manuscript correction. EJ carried out the purification and characterization by mass spectroscopy of the peptide and critically reviewed the manuscript. PS characterized liposomes and assisted in the discussion of these results. FP elaborated, analyzed the data, and contributed to the discussion of time kill tests. MC and SG supervised the project and did the final revision of the manuscript.

FUNDING

This work was supported by grants from FAPESP (proc. 2013/19370-2 and 2018/03018-1).

ACKNOWLEDGMENTS

CZ and FF thank CAPES and CNPq foundations for Ph.D. and Master fellowship, respectively.

REFERENCES

Baev, D., Li, X. S., Dong, J., Keng, P., and Edgerton, M. (2002). Human salivary Histatin 5 causes disordered volume regulation and cell cycle arrest in *Candida albicans*. *Infect. Immun.* 70, 4777–4784. doi: 10.1128/IAI.70.9.4777-4784.2002

Berbel Manaia, E., Paiva Abuçafy, M., Chiari-Andréo, B. G., Lallo Silva, B., Oshiro-Júnior, J. A., and Chiavacci, L. (2017). Physicochemical characterization of drug nanocarriers. *Int. J. Nanomedicine* 12, 4991–5011. doi: 10.2147/IJN.S133832

Berkow, E., and Lockhart, S. (2017). Fluconazole resistance in *Candida* species: a current perspective. *Infect. Drug Resist.* 10, 237–245. doi: 10.2147/IDR.S118892

Calienni, M. N., Temprana, C. F., Prieto, M. J., Paolino, D., Fresta, M., Tekinay, A. B., et al. (2017). Nano-formulation for topical treatment of precancerous lesions: skin penetration, in vitro, and in vivo toxicological evaluation. *Drug Deliv. Transl. Res.* 8, 1–19. doi: 10.1007/s13346-017-0469-1

Cannon, R. D., Lamping, E., Holmes, A. R., Niimi, K., Tanabe, K., Niimi, M., et al. (2007). *Candida albicans* drug resistance another way to cope with stress. *Microbiology* 153, 3211–3217. doi: 10.1099/mic.0.2007/010405-0

Çelik, B., Sağıroğlu, A. A., and Özdemir, S. (2017). Design, optimization and characterization of coenzyme Q10- and D-panthenyl triacetate-loaded liposomes. *Int. J. Nanomedicine* 12, 4869–4878. doi: 10.2147/IJN.S140835

Chorilli, M., Calixto, G., Rimério, T. C., and Scarpa, M. V. (2013). Caffeine encapsulated in small unilamellar liposomes: characterization and in vitro release profile. *J. Dispers. Sci. Technol.* 34, 1465–1470. doi: 10.1080/01932691.2012.739535

Corry, J. E., Jarvis, B., Passmore, S., and Hedges, A. (2007). A critical review of measurement uncertainty in the enumeration of food micro-organisms. *Food Microbiol.* 24, 230–253. doi: 10.1016/j.fm.2006.05.003

De Araújo, D. R., Pinto, L. D. M. A., Braga, A. D. F. D. A., and de Paula, E. (2003). Formulações de anestésicos locais de liberação controlada: aplicações terapêuticas. *Rev. Bras. Anestesiol.* 53, 663–671. doi: 10.1590/S0034-70942003000500014

Ebrahimi, H. A., Javadzadeh, Y., Hamidi, M., and Jalali, M. B. (2015). Repaglinide-loaded solid lipid nanoparticles: effect of using different surfactants/stabilizers on physicochemical properties of nanoparticles. *DARU J. Pharm. Sci.* 23:46. doi: 10.1186/s40199-015-0128-3

Frézard, F., Schettini, D. A., Rocha, O. G. F., and Demicheli, C. (2005). Lipossomas: propriedades físico-químicas e farmacológicas, aplicações na quimioterapia à base de antimônio. *Quim Nova* 28, 511–518. doi: 10.1590/S0100-40422005000300025

Han, J., Jyoti, M. A., Song, H.-Y., and Jang, W. S. (2016). Antifungal activity and action mechanism of Histatin 5-halocidin hybrid peptides against *Candida* ssp. *PLoS One* 11:e0150196. doi: 10.1371/journal.pone.0150196

Hawser, S. P., and Douglas, L. J. (1995). Resistance of *Candida albicans* biofilms to antifungal agents in vitro. *Antimicrob. Agents Chemother.* 39, 2128–2131. doi: 10.1128/AAC.39.9.2128

Helmerhorst, E. J., Breeuwer, P., van 't Hof, W., Walgreen-Weterings, E., Oomen, L. C. J. M., Veerman, E. C. I., et al. (1999). The cellular target of Histatin 5 on *Candida albicans* is the energized mitochondrion. *J. Biol. Chem.* 274, 7286–7291. doi: 10.1074/jbc.274.11.7286

Huang, X., and Brazel, C. S. (2001). On the importance and mechanisms of burst release in matrix-controlled drug delivery systems. *J. Control. Release* 73, 121–136. doi: 10.1016/S0168-3659(01)00248-6

Johnson, E. M., Warnock, D. W., Luker, J., and Porter, S. R. (1995). Emergence of azole drug resistance in *Candida* species from HIV-infected patients receiving prolonged fluconazole therapy for oral candidosis. *J. Antimicrob. Chemother.* 35, 103–114. doi: 10.1093/jac/35.1.103

Jøraholmen, M. W., Basnet, P., Acharya, G., and Škalko-Basnet, N. (2017). PEGylated liposomes for topical vaginal therapy improve delivery of interferon alpha. *Eur. J. Pharm. Biopharm.* 113, 132–139. doi: 10.1016/j.ejpb.2016.12.029

Konopka, K., Dorocka-Bobkowska, B., Gebremedhin, S., and Düzgüneş, N. (2010). Susceptibility of *Candida* biofilms to H 5 and fluconazole. *Antonie Van Leeuwenhoek* 97, 413–417. doi: 10.1007/s10482-010-9417-5

Lopes, S., Simeonova, M., Gameiro, P., Rangel, M., and Ivanova, G. (2012). Interaction of 5-fluorouracil loaded nanoparticles with 1,2-dimyristoyl-sn-glycero-3-phosphocholine liposomes used as a cellular membrane model. *J. Phys. Chem. B* 116, 667–675. doi: 10.1021/jp210088n

Luan, X., Skupin, M., Siepmann, J., and Bodmeier, R. (2006). Key parameters affecting the initial release (burst) and encapsulation efficiency of peptide-containing poly(lactide-co-glycolide) microparticles. *Int. J. Pharm.* 324, 168–175. doi: 10.1016/j.ijpharm.2006.06.004

Merrifield, R. B. (1963). Solid phase peptide synthesis. I. The synthesis of a tetrapeptide. *J. Am. Chem. Soc.* 85, 2149–2154. doi: 10.1021/ja00897a025

Moffa, E. B., Machado, M. A. A. M., Mussi, M. C. M., Xiao, Y., Garrido, S. S., Giampaolo, E. T., et al. (2015a). In vitro identification of Histatin 5 salivary complexes. *PLoS One* 10, 1–13. doi: 10.1371/journal.pone.0142517

Moffa, E. B., Mussi, M. C. M., Xiao, Y., Garrido, S. S., Machado, M. A. A. M., Giampaolo, E. T., et al. (2015b). Histatin 5 inhibits adhesion of *C. albicans* to reconstructed human oral epithelium. *Front. Microbiol.* 6, 1–7. doi: 10.3389/fmicb.2015.00885

Mohan, A., McClements, D. J., and Udenigwe, C. C. (2016). Encapsulation of bioactive whey peptides in soy lecithin-derived nanoliposomes: influence of peptide molecular weight. *Food Chem.* 213, 143–148. doi: 10.1016/j.foodchem.2016.06.075

Niemi, R. M., and Niemelä, S. I. (2001). Measurement uncertainty in microbiological cultivation methods. *Accred. Qual. Assur.* 6, 372–375. doi: 10.1007/s007690100360

Nii, T., and Ishii, F. (2005). Encapsulation efficiency of water-soluble and insoluble drugs in liposomes prepared by the microencapsulation vesicle method. *Int. J. Pharm.* 298, 198–205. doi: 10.1016/j.ijpharm.2005.04.029

Rai, P., Vance, D., Poon, V., Mogridge, J., and Kane, R. S. (2008). Stable and potent polyvalent anthrax toxin inhibitors: raft-inspired domain formation in liposomes that contain PEGylated lipids. *Chem. Eur. J.* 14, 7748–7751. doi: 10.1002/chem.200801097

Robbins, N., Wright, G. D., and Cowen, L. E. (2016). "Antifungal drugs: the current armamentarium and development of new agents" in *Microbiology Spectrum 4* (American Society of Microbiology), 903–922. doi: 10.1128/microbiolspec.Funk-0002-2016

Ron-Doitch, S., Sawodny, B., Kühbacher, A., David, M. M. N., Samanta, A., Phopase, J., et al. (2016). Reduced cytotoxicity and enhanced bioactivity of cationic antimicrobial peptides liposomes in cell cultures and 3D epidermis model against HSV. *J. Control. Release* 229, 163–171. doi: 10.1016/j.jconrel.2016.03.025

Roy, B., Guha, P., Bhattarai, R., Nahak, P., Karmakar, G., Chettri, P., et al. (2016). Influence of lipid composition, pH, and temperature on physicochemical properties of liposomes with curcumin as model drug. *J. Oleo Sci.* 65, 399–411. doi: 10.5650/jos.ess15229

Salade, L., Wauthoz, N., Deleu, M., Vermeersch, M., De Vriese, C., Amighi, K., et al. (2017). Development of coated liposomes loaded with ghrelin for nose-to-brain delivery for the treatment of cachexia. *Int. J. Nanomedicine* 12, 8531–8543. doi: 10.2147/IJN.S147650

Sato, M. R., Oshiro Junior, J. A., Machado, R. T. A., de Souza, P. C., Campos, D. L., Pavan, F., et al. (2017). Nanostructured lipid carriers for incorporation of copper(II) complexes to be used against *Mycobacterium tuberculosis*. *Drug Des. Devel. Ther.* 11, 909–921. doi: 10.2147/DDDT.S127048

Seo, M.-D., Won, H.-S., Kim, J.-H., Mishig-Ochir, T., and Lee, B.-J. (2012). Antimicrobial peptides for therapeutic applications: a review. *Molecules* 17, 12276–12286. doi: 10.3390/molecules171012276

Voltan, A., Quindós, G., Alarcón, K., Fusco-Almeida, A. M., Mendes-Giannini, M. J., and Chorilli, M. (2016). Fungal diseases: could nanostructured drug delivery systems be a novel paradigm for therapy? *Int. J. Nanomedicine* 11, 3715–3730. doi: 10.2147/IJN.S93105

Conflict of Interest Statement: The authors declare that the research was conducted in the absence of any commercial or financial relationships that could be construed as a potential conflict of interest.

frontiers
in Microbiology

ORIGINAL RESEARCH
published: 07 August 2019
doi: 10.3389/fmicb.2019.01757

Presentation of Antibacterial and Therapeutic Anti-inflammatory Potentials to Hydroxyapatite *via* Biomimetic With *Azadirachta indica*: An *in vitro* Anti-inflammatory Assessment in Contradiction of LPS-Induced Stress in RAW 264.7 Cells

Anusuya Nagaraj and Suja Samiappan*

Department of Biochemistry, Bharathiar University, Coimbatore, India

OPEN ACCESS

Edited by:
Gerson Nakazato,
State University of Londrina, Brazil

Reviewed by:
Venkataramana M.,
Independent Researcher,
Andhra Pradesh, India
Bing Tian,
Zhejiang University,
China

Correspondence:
Suja Samiappan
sujaramalingam08@gmail.com

Specialty section:
This article was submitted to
Antimicrobials, Resistance and
Chemotherapy,
a section of the journal
Frontiers in Microbiology

Received: *07 April 2019*
Accepted: *16 July 2019*
Published: *07 August 2019*

Citation:
Nagaraj A and Samiappan S (2019) Presentation of Antibacterial and Therapeutic Anti-inflammatory Potentials to Hydroxyapatite via Biomimetic With Azadirachta indica: An in vitro Anti-inflammatory Assessment in Contradiction of LPS-Induced Stress in RAW 264.7 Cells. Front. Microbiol. 10:1757. doi: 10.3389/fmicb.2019.01757

In the present study, for the first time, biomimetization of hydroxyapatite (HA) with *Azadirachta indica* (AI) was proposed and established its antioxidant, antibacterial, and anti-inflammatory potential on lipopolysaccharide (LPS). The ethanolic extract of AI was found rich with phenolics and flavonoids, and determined their concentration as 8.98 ± 1.41 mg gallic acid equivalents/g and 5.46 ± 0.84 mg catechin equivalents/g, respectively. The HA was prepared by sol-gel method from calcium nitrate tetrahydrate and orthophosphoric acid, and successfully biomimetization was performed with ethanolic extract of AI. The FTIR analysis settled that as-synthesized HA-AI composite was comprised of both HA and AI. The XRD pattern and Zeta potential revealed that the HA-AI composite was crystalline and negative in charge (–24.0 mV). The average-size distribution, shape, and size of the HA-AI composite was determined as 238.90 d.nm, spherical, and 117.90 nm from size distribution, SEM, and HR-TEM analysis, respectively. The SEM-EDX concluded that the HA-AI composite was comprised of elements of HA as well as AI. The HA-AI composite presented potential antioxidant activity and its EC50 values (dose required to inhibit about half of the radicals) for ABTS and DPPH assays were determined as 115.72 ± 2.33 and 128.51 ± 1.04 μg/ml, respectively. The HA-AI composite showed potent antibacterial activity, and minimum inhibitory concentration (MIC) and minimum bactericidal concentration (MBC) towards *S. aureus* (ATCC 700699) and *E. coli* (ATCC 10536) were correspondingly determined as 266.7 ± 28.87 and 600.0 ± 50.0 μg/ml, and 400.0 ± 86.6 and 816.7 ± 76.38 μg/ml. Most importantly, HA-AI composite presented the potential anti-inflammatory response toward lipopolysaccharide (LPS) in RAW 264.7 cells. The dose of 250 μg/ml of HA-AI composite has shown optimum protection against LPS-induced stress (1 μg/ml) by scavenging oxidants and regulating mitochondrial membrane potential (MMP), inflammatory and apoptotic factors. Thus, this study concluded that the impartation of potential biofunctional features to HA from plant sources through biomimetic approach is much beneficial and could find potential application in dentistry and orthopedic.

Keywords: biomimetic, hydroxyapatite, *Azadirachta indica*, antioxidant, antibacterial, anti-inflammation

INTRODUCTION

The earth is an affluent source of biominerals, such as calcium carbonates, calcium phosphates, iron hydroxides, and iron oxyhydroxides of unicellular and multicellular organisms that occur in the form of shell, ivory, teeth, magnetic crystals, etc. (Driessens and Verbeeck, 1990; Dhami et al., 2013). The biominerals possess excellent strength, fracture toughness, highly smooth finish of surface, are non-toxic and eco-friendly, and have the potential to be used as implanting agents in the dental and orthopedic fields (Cao et al., 2010). Particularly, the group of calcium apatite known as hydroxyapatite (HA) is the principal biomineral constituent and takes over 70% of weight in the bone and tooth enamel and exists in trace amount in the pineal gland and corpora arenacea (Shetty and Kundabala, 2013). HA owns great mechanical strength, biocompatibility, low resorbability, osteoconductivity, etc. Thus, HA is extensively used in orthopedic and dentistry as metallic implant coating and cavity filling material and also, as the key constituent in toothpaste and mouthwashes to remineralize artificial carious lesions (Pepla et al., 2014).

Regrettably, HA is highly biocompatible and apposite for prevalence bacterial biofilm and endotoxins (Zablotsky et al., 1992). Endotoxins, also known as lipoglycans and lipopolysaccharides (LPS), consist of lipid and polysaccharide O-antigen, and are exclusively present in the outer membrane of Gram-negative bacteria (Raetz and Whitfield, 2002). LPS induces the bulk release of inflammatory cytokines, which may result in septic shock, systemic inflammatory response syndrome, severe tissue damage, and multiple organ dysfunction (Lamping et al., 1998). With the advent of nanotechnology, the proficiency of HA as an implant in orthopedic and dentistry has been greatly boosted by doping it with chemical elements such as titanium, cobalt, magnesium, zinc, silver, and gold (Lin et al., 2007; Mo et al., 2008; Nirmala et al., 2011; Kramer et al., 2014; Gayathri et al., 2018; Sathiskumar et al., 2018). However, these chemical elements detrimentally interact with blood cells, including erythrocytes, leukocytes, platelets, and macrophages due to the generation of oxidative stress and inflammatory response (Asharani et al., 2010; Chen et al., 2015). Typically, these chemical elements form fibrous local pseudocapsules interacting with fibroblasts and deposit in the local tissues and organs. Also, these chemical substances translocate and disseminate into the key organs such as liver, spleen, lung, and kidney *via* blood circulation and constitute a health risk (Kim et al., 2010; Khan et al., 2012; Wang et al., 2016). Insight of the aforementioned demerits, biomimetic of HA composite with potent antibacterial and anti-inflammatory bioresources could be highly preferred and recommended over chemical substances for orthopedic implants. In the current scenario, plant sources are highly preferred due to their non-toxicity and eco-friendliness (Kalaiselvi et al., 2018; Phatai et al., 2019). Therefore, the biomimetic of HA with plant sources could be highly appropriate and satisfactory.

To the best of our knowledge, the therapeutic potential of the biomimetic HA composite with plant sources on inflammatory response has not been documented so far, so this would be the first investigation. In the present study, HA was prepared by sol-gel method from calcium nitrate tetrahydrate and orthophosphoric acid. Furthermore, biomimetic of HA with ethanolic extract of *Azadirachta indica* (AI) was undertaken. AI is an ancient herbal medicinal plant that belongs to the *Meliaceae* family and is widely recommended in a variety of biological uses such as anti-allergic, antimicrobial, antimalarial, antiulcer, antitumor, insecticide, and pesticide (Biswas et al., 2002; Pankaj et al., 2011; Alzohairy, 2016).

The synthesized HA and biomimetic HA-AI composite were characterized by FTIR, XRD, Zeta potential and size distribution, SEM with EDX, and HR-TEM analysis. The *in vitro* radical scavenging potential of HA-AI composite was studied by DPPH and ABTS assays. The *in vitro* antibacterial activity of the HA-AI composite against pathogenic bacteria was determined in minimum inhibitory concentration (MIC) and minimum bactericidal concentration (MBC) by micro-well dilution technique. Furthermore, detrimental micro-morphological changes induced in pathogenic bacteria by the HA-AI composite were registered by SEM observation. The *in vitro* anti-inflammatory response of the HA-AI composite against endotoxin LPS was assessed in macrophages (RAW 264.7 cells) by determining cell viability, oxidative and mitochondrial stress, inflammatory, and caspase-3 levels.

MATERIALS AND METHODS

Chemicals and Reagents

Ethanol (99.80%), 2,2-diphenyl-1-picrylhydrazyl (DPPH), Muller-Hinton agar (MHA), Muller-Hinton broth (MHB), 2,2′-azino-bis (3-ethylbenzothiazoline-6-sulphonic acid) (ABTS), and fetal bovine serum (FBS) were received from HiMedia, Mumbai, India. Calcium nitrate tetrahydrate, orthophosphoric acid, gallic acid, catechin, rutin, Dulbecco's modified Eagle's medium (DMEM), antibiotic and antimycotic solution, lipid peroxidation kit, Griess reagent, caspases kits (3/7, 8, and 9), antioxidant enzyme kits (SOD, CAT, and GSH), ELISA kits (TNF-α and IL-6), primer sequences (TNF-α, IL-6, iNOS, COX-2, and β-actin), dichloro-dihydro-fluorescein diacetate (DCFH-DA), TRI reagent, rhodamine 123, and 4′,6-diamidino-2-phenylindole (DAPI) were purchased from Sigma-Aldrich, Bengaluru, India. The live/dead dual staining kit was purchased from Thermo Fisher Scientific and iScript One-Step RT-PCR kit with SYBR green was obtained from Bio-Rad, Bengaluru, India.

Collection, Preparation, and Phytochemical Analysis of Plant Material

AI was collected from Bharathiar University Campus, Coimbatore, India. The voucher was authenticated in Department of Botany, Bharathiar University, and safeguarded. The stem was detached and washed twice with double distilled water and dried under shade at room temperature for 2 weeks. Following, 500 g was ground to a fine powder by electrical blender, and active components were extracted by ethanol solution following cold maceration technique (Pandey et al., 2014). The attained ethanolic extract was concentrated by lyophilization (−39°C) and stored in a screw-capped amber glass vial at 4°C for further use.

Determination of Total Phenolics

The total phenolics of AI extract were determined by Folin-Ciocalteu assay (Kalagatur et al., 2018). In brief, different concentrations of AI extract were supplemented to 0.5 ml of 7.5% sodium carbonate solution and 0.25 ml of Folin-Ciocalteu reagent and incubated in the dark at room temperature for 30 min. Subsequently, optical density (OD) was monitored at 765 nm using the multimode plate reader (Synergy H1, BioTek, USA). Gallic acid (GA) was considered as the reference standard and the calibration curve was constructed. The total phenolics of AI extract were derived from the calibration curve of GA and the result was expressed as milligrams of GA equivalents per gram of AI extract (mg GAE/g).

Determination of Total Flavonoids

The determination of total flavonoids of AI extract was undertaken by aluminum chloride colorimetric method (Kalagatur et al., 2018). Briefly, different concentrations of AI extract were supplemented to 70 μl of sodium nitrite solution (5%) and allowed to rest for 5 min before being combined with 1.3 ml of distilled water, 0.5 ml of sodium hydroxide (1 M), and 0.15 ml of aluminum chloride (10%) and kept at room temperature for 5 min. Ensuing, OD was monitored at 415 nm using a multimode plate reader (Synergy H1, BioTek, USA). Catechin (CC) was considered as the reference standard and a calibration curve was constructed. The total flavonoids of AI extract were derived from the calibration curve of CC and the result was expressed as milligrams of CC equivalents per gram of AI extract (mg CCE/g).

Preparation of Hydroxyapatite

HA was prepared by sol-gel process as described before (Sanosh et al., 2009) with minor modifications. Calcium nitrate tetrahydrate (CNT) and orthophosphoric acid (PA) were used as the precursors. A solution of PA (0.25 M) was prepared in distilled water and ammonia was added by continuous stirring until the pH adjusted to 10. The ratio of Ca/P was maintained at ~1.67 by adding CNT solution (1 M in distilled water) and the solution was vigorously stirred at 200 rpm for 1 h. The solution was subjected to aging for overnight and dried at 65°C in a hot air oven.

The obtained powder was washed repeatedly with distilled water to remove NH_4 and NO_3 and calcined in the electrical furnace at 800°C for 1 h. The HA powder was packed in amber glass vial and stored at room temperature for further purposes.

The following reactions occur in the formation of HA during sol-gel preparation,

$$H_3PO_4 + 3NH_4OH \rightarrow (NH_4)_3PO_4 + 3H_2O \qquad (1)$$

$$6(NH_4)_3PO_4 + 10Ca(NO_3)_2 \cdot 4H_2O \rightarrow Ca_{10}(PO_4)_6(OH)_2 + 20NH_4NO_3 \qquad (2)$$

Preparation and Characterization of HA-AI Composite

The biomimetic of HA with AI, and thus the preparation of HA-AI composite, was done previously described (Bismayer et al., 2005) with slight modifications. The ethanolic extracts of AI and HA were blended (400:400 mg, w/w) in 40 ml of ethanol, incubated overnight at 120 rpm, and dried out in hot air oven at 25–30°C. The prepared HA-AI composite was stored in an amber glass vial at 4°C in a dry place and used for further studies.

The physicochemical analysis of the prepared HA and HA-AI composite was assessed by various techniques, including Fourier transform infrared spectroscopy (FTIR), X-ray diffraction (XRD), Zeta potential and size distribution, scanning electron microscope-energy dispersive X-ray (SEM-EDX), and high-resolution transmission electron microscopy (HR-TEM) analysis. The FTIR analysis was performed to confirm the successful frame-up of the HA-AI composite. The samples were pelletized with KBr and IR transmission spectra were recorded in attenuated total reflectance mode (ATR) from 4,000 to 400 cm^{-1} at a data acquisition rate of 2 cm^{-1} using FTIR 84005 (Shimadzu, Tokyo, Japan). The XRD analysis was done to understand the nature of the HA and HA-AI composite using Ultima IV diffractometer (Rigaku, USA) with Cu Kα radiation (λ = 1.541 Å) in 2θ range of 10°–80° with scan rate of 3°/min. The crystallite pattern of HA and HA-AI composite was calculated from the standard XRD pattern of the International Centre for Diffraction Data (ICDD). The surface charge and size distribution of the HA and HA-AI composite were measured using Zeta Sizer ZS 90 (Malvern Instruments, Germany) with He-Ne laser beam at 532 nm wavelength in backscattering mode. The surface microstructure and elemental composition of HA and HA-AI composite were examined using SEM-EDX (FEI, Quanta 200, Thermo Fisher Scientific, USA). The shape and size of the HA and HA-AI composite were confirmed by HR-TEM.

Antioxidant Potential of HA-AI Composite

The radical scavenging potential of the HA-AI composite was assessed by DPPH and ABTS radical scavenging activity (Kumar et al., 2016). In case of DPPH assay, a stable DPPH radical solution was prepared by dissolving 2.4 mg of DPPH in 100 ml of methanol. For ABTS assay, an ABTS radical solution was prepared by incubating the reaction mixture of 7 mM ABTS in water and 2.45 mM potassium persulfate in water (1:1, v/v) for 12–16 h in the dark at room temperature. The ABTS radical solution was diluted with methanol to attain the optical density (OD) of 0.70 at 734 nm. Following, different concentrations of the HA-AI composite were prepared in methanol and 100 μl was added to 2.9 ml of DPPH and 3.9 ml of ABTS radical solution. The blend was shaken vigorously and incubated for 30 min in the dark at room temperature. The ODs of DPPH and ABTS blends were determined using multiplate reader (Synergy H1, BioTek, USA) at 517 and 734 nm, respectively. The radical solution alone was considered as control and rutin was used as standard antioxidant compound. The percentage of radical scavenging activity was estimated using the formula

$$\text{DPPH or ABTS radical scavenging activity}\,(\%) = \frac{A_t}{A_c} \times 100$$

where A_c and A_t were absorbance of control and test sample, respectively.

Microbicidal Activity of HA-AI Composite

The microbicidal activity of the HA-AI composite was determined by micro-well dilution method as per the Clinical & Laboratory Standards Institute (CLSI) (Qaiyumi, 2007). The selected pathogenic bacteria, *Staphylococcus aureus* (ATCC 700699) and *Escherichia coli* (ATCC 10536), were obtained from the American Type Culture Collection (ATCC), USA. The bacteria were grown overnight in MHB at 37°C, and OD was determined at 600 nm using a microplate reader (Synergy H1, BioTek, USA) and OD of broth culture was adjusted to 0.5 McFarland standard with sterile PBS pH 7.4. A quantity of 10 μl broth culture (0.5 McFarland standard) and different concentrations of HA-AI composite were added to the wells of the microtiter plate and the final volume was adjusted to 100 μl with MHB and incubated for 24 h at 37°C. The wells containing only bacteria without HA-AI composite were considered as control and tetracycline was used as a reference standard. Following the incubation period, OD was measured at 600 nm and the concentration of the HA-AI composite, at which an increase in OD (bacterial growth) is not registered, was stated as minimum inhibitory concentration (MIC). Subsequently, a volume of 10 μl was collected from each well of the microtiter plate and spread plated on MHA Petri plates and incubated for 24 h at 37°C. The concentration of HA-AI composite at which bacterial growth did not reoccur was specified as MBC.

Concurrently, 10 μl of control and test bacterial samples were collected from microtiter plate and heat fixed to the glass slide. The bacterial samples were fixed with the gradient solutions of glutaraldehyde (5, 10, and 15%) and sputter coated with gold-palladium as per the technique described by Kalagatur et al. (2015). The micro-morphology of bacteria was photographed using SEM (FEI, Quanta 200, Thermo Fisher Scientific, USA) at 20 kV in environmental mode.

Therapeutic Potential of HA-AI Composite on LPS-Induced Inflammatory Stress

Cell Culture and Treatments

The therapeutic potential of the HA-AI composite on LPS-induced inflammatory stress was revealed in RAW 264.7 cells (macrophages) of *Mus musculus*. The RAW 264.7 cells were acquired from the National Centre for Cell Science (NCCS, Pune, India) and maintained in DMEM supplemented with 10% FBS, penicillin (100 U/ml), and streptomycin (100 μg/ml) in humidified atmospheric conditions of 5% CO_2 and 95% air at 37°C. The cells were grown in 75 cm^2 cell culture flasks, and media was regularly changed on alternate days, and confluent cells were utilized for the experiments. The stock solution of the HA-AI composite was prepared in dimethyl sulfoxide (DMSO) and the final concentration of DMSO in the experimental sample was not higher than 0.01%.

To test the anti-inflammatory effect of HA-AI composite on LPS-induced stress, 1.5×10^4 cells were seeded in 96-well cell culture plates and allowed to settle overnight. The cells were pre-treated with different concentrations of the HA-AI composite for 12 h and exposed to 1 μg/ml of LPS for 24 h in DMEM devoid of FBS. In literature, several studies prominently produced inflammatory response in *in vitro* cell line model with 1 μg/ml of LPS (Alvarez-Suarez et al., 2017; Gasparrini et al., 2017). Therefore, in the present study, 1 μg/ml of LPS was used to stimulate the inflammatory response in RAW 264.7 cells. The cells were treated with the same concentration of DMSO in which the HA-AI composite prepared was considered as control. Following, plates were distinctly employed for cell viability, oxidative and inflammatory stress, mitochondrial membrane potential (MMP), and apoptosis analysis.

Most importantly, before undertaking a detailed assessment of oxidative and inflammatory stresses, MMP, and apoptosis. The cytotoxic effect of different concentrations of HA and HA-AI composite on cell viability for 24 h were judged by MTT assay. Following, the protective efficacy of HA and HA-AI composite on LPS (1 μg/ml) induced cell death were distinctively studied by cell viability assays (MTT and live/dead) and superlative protective demonstrative on LPS-induced cell death was chosen for detailed investigations.

Cell Viability Analysis

MTT Assay

MTT assay measures the cell viability based on the redox potential of the cell. Following the cell culture and treatments stage, media were replaced with 100 μl of MTT reagent (5 mg/ml in DPBS) and incubated for 3 h at room temperature. Next, the MTT reagent was substituted with 100 μl of DMSO and kept for 30 min to solubilize the formazan crystals. The OD was measured at 570 nm using multiplate reader (Synergy H1, BioTek, USA). The results were stated with respect to control (100%) (Venkataramana et al., 2014).

Live/Dead Dual Staining Assay

The percentage of live and dead cells was determined by the live/dual staining technique consisting of calcein AM and ethidium homodimer-1. The calcein AM reacts with intracellular esterases of live cells and appears green in color. Whereas, ethidium homodimer crosses through damaged cellular membrane of dead cells and binds with the nuclei to produce red color (Haugland et al., 1994). After the cell culture and treatment stage, cells were washed with DPBS and stained with 2 μM of calcein AM and 4 μM of ethidium homodimer-1 for 15 min and washed with DPBS twice. The OD was recorded using multiplate reader (Synergy H1, BioTek, USA) as per instructions from the manufacturer. The percentage of live/dead cells was computed using a technique previously described (Kalagatur et al., 2017). Furthermore, images were captured using the inverted fluorescence microscope (EVOS FLC, Thermo Fisher Scientific, USA).

Analysis of Oxidative and Inflammatory Stress

Estimation of Reactive Oxygen Species

The contents of intracellular reactive oxygen species (ROS) were determined by DCFH-DA staining (LeBel et al., 1992; Kalagatur et al., 2017). After the cell culture and treatment phase, cells were incubated with 5 μM of DCFH-DA for 15 min and washed twice with DPBS. The fluorescence intensity was recorded at an excitation of 495 nm and an emission of 550 nm using the microplate reader (Synergy H1, BioTek, USA). The standard curve for ROS released versus H_2O_2 constructed and used to express the amount of ROS released. The results were expressed with respect to control (100%). Moreover, microscopic images of cells were captured using phase contrast and green fluorescent protein (GFP) filters of an inverted fluorescence microscope (EVOS FLC, Thermo Fisher Scientific, USA).

Estimation of Nitrite

The nitrite (NO) content was determined using Griess reagent. After the cell culture and treatments phase, 100 μl of the cell culture supernatant was collected and added to an equal volume of Griess reagent according to the instructions from the manufacturer. The absorbance was monitored at 550 nm using a multiplate reader (Synergy H1, BioTek, USA). The standard curve of sodium nitrite ($NaNO_2$) constructed and amount of NO released were expressed as μM of $NaNO_2$ (Giustarini et al., 2008).

Estimation of Lipid Peroxidation

After cell culture and treatments, cells were lysed and absorbance of malondialdehyde (MDA), an indicator of lipid peroxidation, was measured at 532 nm using a multiplate reader (Synergy H1, BioTek, USA) as per instructions from the manufacturer. The standard curve for MDA was constructed and the amount of MDA released was expressed as nM MDA (Gaweł et al., 2004).

Estimation of Antioxidant Enzymes

After cell culture and treatments, cells were lysed using the cell lysis buffer and supernatant was collected by centrifugation at 12,000× *g* for 10 min at 4°C and used for estimation of antioxidant enzymes (SOD, CAT, and GSH) using enzyme analysis kits (Sigma-Aldrich). The methodology was performed as manufacturer's instruction (Djordjevic et al., 2004).

Estimation of TNF-α and IL-6

The inflammatory markers, TNF-α and IL-6, were measured using ELISA kits. After "cell culture and treatments", supernatant was collected and treated with reagents of TNF-α and IL-6 of ELISA kits as per manufacturer's instructions and OD was measured at 450 nm using multiplate reader (Synergy H1, BioTek, USA) (Bienvenu et al., 1993).

Real-Time PCR Analysis

The inflammatory regulatory genes, TNF-α, IL-6, iNOS, and COX-2, were quantified by RT-PCR analysis. The β-actin was used as reference gene (**Supplementary Table S1**). Following cell culture and treatments, total RNA was extracted from cells using TRI reagent as per manufacturer's instructions and RNA purity and quantity were determined measuring OD at 260/280 nm using NanoDrop 8,000 Spectrophotometer (Thermo Fisher Scientific, USA). The RT-PCR analysis was carried out using iScript One-Step RT-PCR kit as per manufacturer's instructions employing Light cycler 480 (Roche, USA). Briefly, the total reaction mixture of 50 μl consisted of 1 μl of primer (450 nM) and template RNA (100 ng), 1 μl of iScript reverse transcriptase for one-step RT-PCR, 25 μl of 2X SYBR Green RT-PCR reaction mix, and 22 μl of nuclease-free water (PCR grade). The RT-PCR analysis consists of 10 min of cDNA synthesis at 50°C for one cycle, 5 min of polymerase activation at 95°C and followed by 35 cycles of PCR at 95°C for 10 s, and finally 60°C for 30 s for combined annealing and extension. The relative fold expression of test genes was measured with respect to the normalized reference gene (Tellman and Olivier, 2006).

Estimation of Mitochondrial Membrane Potential

The MMP was determined by rhodamine 123 staining technique. After cell culture and treatments, cells were stained with rhodamine 123 for 15 min and washed with DPBS twice, and fluorescence intensity was recorded at excitation of 511 nm and emission of 534 nm under a microplate reader (Synergy H1, BioTek, USA) (Emaus et al., 1986; Kalagatur et al., 2018). The microscopic images of cells were captured using phase contrast and GFP filters of an inverted fluorescence microscope (EVOS FLC, Thermo Fisher Scientific, USA).

Analysis of Apoptosis

DAPI Staining

The nuclear content of cells was observed by DAPI staining. After cell culture and treatments, cells were stained with 1 μM of DAPI for 15 min and washed twice with DPBS. The images were captured under DAPI filter using the inverted fluorescence microscope (EVOS FLC, Thermo Fisher Scientific, USA). At least 1,000 cells were considered for apoptotic analysis in 10 different microscopic fields and results were expressed as apoptotic bodies/100 cells (Tan et al., 2006; Kalagatur et al., 2018).

Caspase-3/7, 8, and 9 Analysis

After cell culture and treatments, cells were individually treated with fluorimetric reagents of caspase-3/7, 8, and 9 analysis kits as per manufacturer's instructions and optical density was recorded at excitation of 360 nm and emission of 460 nm using a multiplate reader (Synergy H1, BioTek, USA) (Cohen, 1997; Tan et al., 2006; Kalagatur et al., 2018).

Statistical Analysis

The phytochemical, antioxidant, antimicrobial, and anti-inflammatory analyses were performed individually in six replicates and the achieved results were stated as mean ± standard deviation. The data were statistically evaluated by one-way ANOVA following Tukey's *post hoc* multiple comparison test. The statistical variance among the experimental groups was measured as significant at $p < 0.05$.

RESULTS AND DISCUSSION

Phytochemical Analysis of AI Extract

The successful biomimetic of nanomaterials with plant extract depends on their secondary metabolites, i.e., phenolics and flavonoids. The phenolics and flavonoids assist in reducing and stabilizing agents in biomimetic of nanomaterials (Ahmed et al., 2016). Hence, in the present study, phenolics and flavonoids were estimated. The obtained ethanolic stem extract of AI was found affluent with phenolics and flavonoids, and their concentrations were noted as 8.98 ± 1.41 mg GAE/g and 5.46 ± 0.84 mg CCE/g, respectively (**Figure 1**). These results were in accordance with previous documented literature. However, the concentrations of phenolics and flavonoids in our study were quite varied compared to existing literature. Al-Jadidi and Hossain (2016) determined total phenolics and flavonoids in AI stem extract to be in the range of 20.80–107.29 mg/100 g and 136.50–484.50 mg/100 g, respectively. Furthermore, Choudhary and Swarnkar (2011) determined total phenolics and flavonoids in stem bark to be 42.12 ± 1.08 mg GAE/g and 08.08 ± 0.62 mg quercetin equivalents (QE)/g, respectively. By contrast, Choudhary and Swarnkar (2011) have documented quite diverse quantities of total phenolics and flavonoids in leaves extract and determined them to be 08.83 ± 0.35 mg GAE/g and 07.82 ± 0.39 mg QE/g. In another study, Sultana et al. (2007) used different solvent extraction techniques (ethanol, methanol, and acetone) and determined the total phenolics and flavonoids in AI bark in the range of 9.30 ± 0.37–12.0 ± 0.36 mg GAE/g and 2.52 ± 0.10–3.31 ± 0.16 mg CCE/g, respectively. The quality and quantity of secondary metabolites of plant depend on genome, part of the plant (leaves, stem, flower, fruit, and root), climatic conditions, nutrients, and as well extraction technique (Sultana et al., 2007; Choudhary and Swarnkar, 2011). Hence, might be the concentration of phenolics and flavonoids were varied in our study. To conclude, the obtained ethanolic stem extract of AI was highly suitable for biomimetic of nanomaterials.

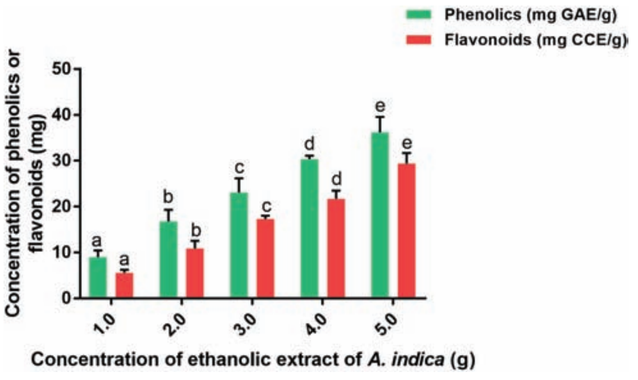

FIGURE 1 | Total phenolics (mg GAE/g) and flavonoids (mg CCE/g) in ethanolic extract of *A. indica* (AI). The experiments were performed individually in six replicates and achieved results were stated as mean ± standard deviation. The data were statistically evaluated by one-way ANOVA following Tukey's *post hoc* multiple comparison test. The statistical variance among the experimental groups was measured as significant at $p < 0.05$. The columns with different alphabets were significant within the respective study.

Physicochemical Characterization of HA-AI Composite

In the present study, HA was successfully synthesized by sol-gel approach using CNT and PA as precursors. The synthesized HA was washed thoroughly with distilled water to get rid of NH_4 and NO_3 and effectively calcined at 800°C. Furthermore, biomimetization of HA with AI was undertaken and attained combination was dried at 25–30°C and used in further determinations.

FTIR spectrum was recorded in the range of 4,000–400 cm^{-1} and the infrared peaks of HA, AI, and HA-AI composite were depicted in **Figure 2**. In HA, peaks at 558.291, 606.503, 696.177, 879.381, and 1,037.52 cm^{-1} show the characteristic presence of the phosphate group of HA. Furthermore, C=C stretching of alkene group was present at 1,639 cm^{-1} and the peak at 2,047.07 cm^{-1} corresponds to carbonyl stretch. The broad peaks which subsist between 2,856.06 and 3,448.1 cm^{-1} conform to the presence of OH (**Figure 2A**; Sanosh et al., 2009; Kramer et al., 2014), while AI had exhibited characteristic peaks at 1,046.19, 1,246.75, 1,328.71, 1,375.96, 1,512.88, 1,619.91, 1,735.62, 2,925.48, and 3,396.99 cm^{-1}, which corresponds to amines, carboxylic acids, aromatic compounds, phenols, nitro compounds, alkenes, aldehydes, alkanes, and alcohol of phytochemical constituents of AI stem extract (**Figure 2B**). Whereas, the HA-AI composite presented characteristic functional groups of both HA and AI and concluded the successful formation of the HA-AI composite (**Figure 2C**).

The XRD pattern of the synthesized HA and HA-AI composite was given in **Figures 2D,E**. The majority of the diffraction peaks for HA appeared at 2θ values of 17.25, 22.49, 25.85, 28.10, 31.46, 32.97, 34.45, 40.10, 46.81, 53.15, and 59.91 were assigned to corresponding planes of 110, 111, 002, 102, 211, 300, 202, 221, 222, 004, and 420 (**Figure 2D**). The presence of a sharp peak at 31.46 caused by 211 plane confirmed the formation of HA with pure crystalline phase. The obtained planes were well-matched with the standard ICDD File no: 09-169 and 09-432 (Kaygili et al., 2014; Atak et al., 2017; Gayathri et al., 2018). Whereas, the HA-AI composite exhibited slight shifting in the diffraction peaks at 2θ values of 26.22, 28.47, 31.46, 34.81, 47.55, 53.52, and 59.82. The observed shifting could be due to the accumulation of AI within HA (**Figure 2E**). The XRD pattern of the HA-AI composite clinched that no noticeable change was observed in crystallinity of HA due to the accumulation of AI. However, the intensity of the diffraction peaks was reduced in HA-AI composite compared to HA due to the accumulation of phytochemical constituents of AI. In support of the present study, and earlier report (Gopi et al., 2013) concluded that the biomimetic of HA composites with plant extracts does not change the crystallinity of HA.

Zeta potential measurement is carried out to determine the colloidal long-term stability and surface charge of the particles and results were depicted in **Figure 3**. The Zeta potentials of HA and HA-AI composite in ethanol were determined as −5.87 and −24.0 mV, respectively, and concluded that the HA-AI composite was highly stable than HA (**Figures 3A,B**). The HA-AI composite with negative Zeta potential could be a highly appropriate implanted material intended for the maintenance of viable cells in biological systems (Chen et al., 2009). Next, dynamic light scattering (DLS) pattern revealed the average size distribution of HA and HA-AI composite were at 186.54 and 238.90 d.nm, respectively (**Figures 3C,D**). The polydispersity index of 0.130 and 0.227 were correspondingly noticed for HA and HA-AI composite, which was recognized as the lesser agglomeration.

Figure 4 shows the morphology and size of HA and HA-AI composite. The SEM showed that the size of HA and HA-AI composite was in the range of 306–320 nm and 320–496 nm, respectively (**Figures 4A,B**). The shape of HA and HA-AI composite was a characteristic slight agglomerated nanosphere shape, and the result was in accordance with the polydispersity index of HA and HA-AI composite. The result showed that incorporation of AI into HA increased the size of the HA-AI composite related to HA and however, does not affect the morphology. The HR-TEM analysis also confirmed that the HA and HA-AI composites were spherical in shape and their size were 106.21 and 177.90 nm, respectively (**Figures 4C,D**). The elemental composition of HA, AI, and HA-AI composite was determined by SEM-EDX and results were depicted in **Figures 4E–G**.

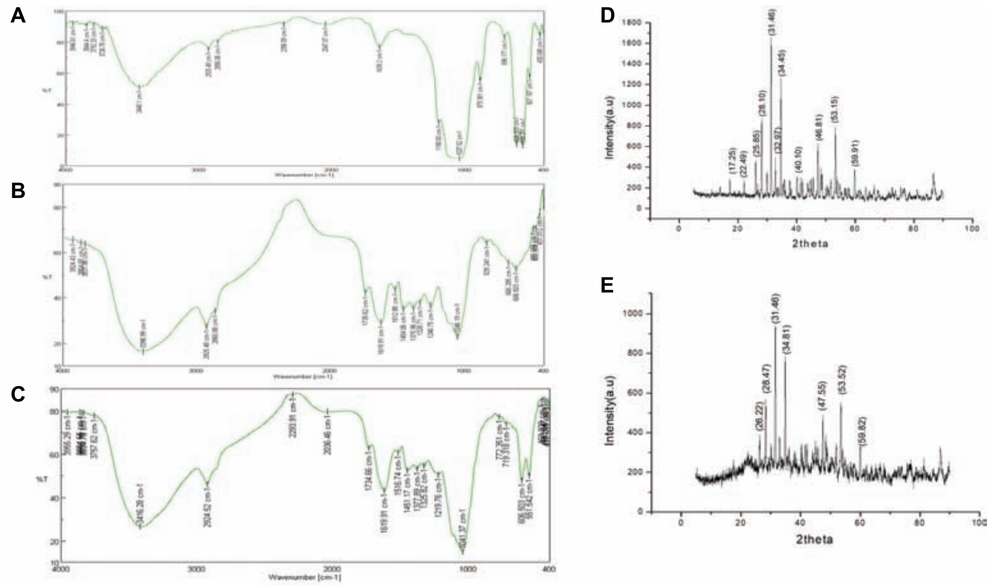

FIGURE 2 | FT-IR spectrum of **(A)** hydroxyapatite (HA), **(B)** ethanolic extract of *A. indica* (AI), and **(C)** hydroxyapatite–*A. indica* (HA-AI) composite. XRD pattern of **(D)** HA and **(E)** HA-AI composite.

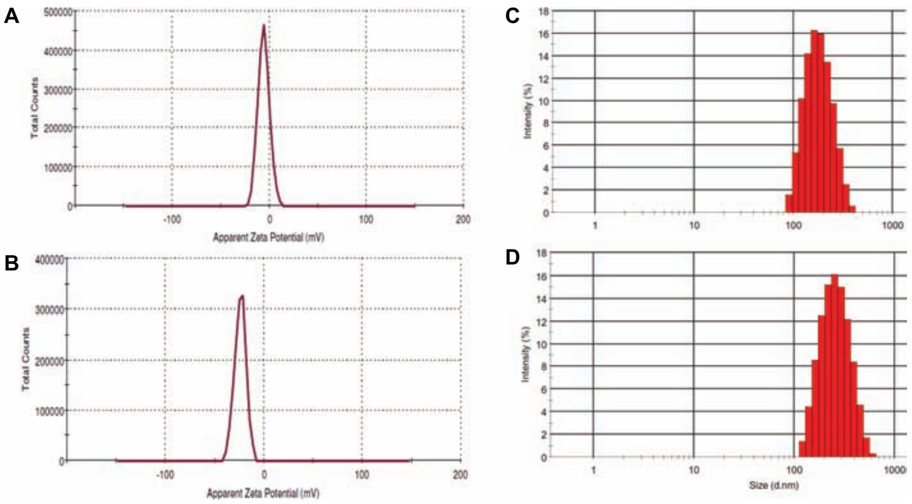

FIGURE 3 | Zeta potential of **(A)** hydroxyapatite (HA) and **(B)** hydroxyapatite–*A. indica* (HA-AI) composite. DLS pattern of **(C)** HA and **(D)** HA-AI composite.

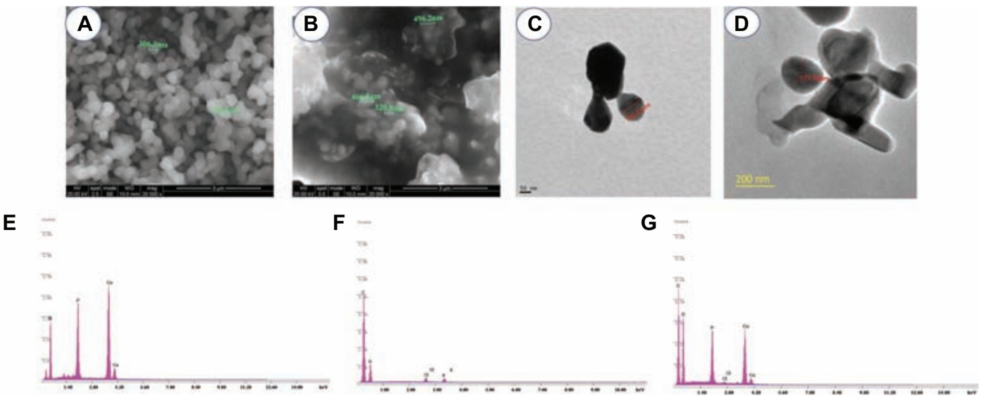

FIGURE 4 | SEM images of **(A)** hydroxyapatite (HA) and **(B)** hydroxyapatite–*A. indica* (HA-AI) composite. HR-TEM image of **(C)** HA and **(D)** HA-AI composite. SEM-EDX pattern of **(E)** HA, **(F)** AI, and **(G)** HA-AI composite.

TABLE 1 | Elemental analysis of hydroxyapatite (HA), *A. indica* (AI), and HA-AI composite by SEM-EDX.

Elements	HA	AI	HA-AI composite
Ca (%)	46.91	–	34.70
P (%)	32.14	–	28.88
O (%)	19.52	11.07	14.19
C (%)	–	83.64	19.31
Cl (%)	–	2.41	1.07
K (%)	–	1.09	
Total (%)	98.57	98.21	98.15

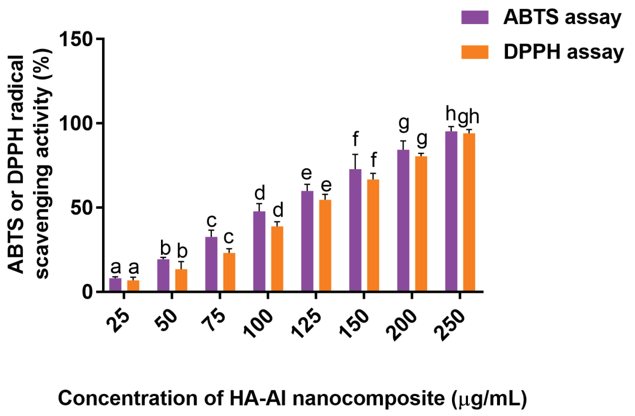

FIGURE 5 | ABTS and DPPH radical scavenging potentials of hydroxyapatite–*A. indica* (HA-AI) composite. The experiments were performed individually in six replicates and achieved results were stated as mean ± standard deviation. The data were statistically evaluated by one-way ANOVA following Tukey's *post hoc* multiple comparison test. The statistical variance among the experimental groups was measured as significant at $p < 0.05$. The columns with different alphabets were significant within the respective study.

The HA was found to be constituted of elements Ca (46.91%), P (32.14%), and O (19.52%), and AI was constituted of elements O (11.07%), C (83.64%), Cl (2.41%), and K (1.09%). The HA-AI composite found consists of both elemental constituents of HA and AI, which comprise of Ca (34.70%) P (28.88%), O (14.19%), C (19.31%), and Cl (1.07%). Thus, SEM-EDX analysis concluded that HA was successfully composed of constituents of AI (**Table 1**).

Antioxidant Potential of HA-AI Composite

The radical scavenging potential of the HA-AI composite was determined by ABTS and DPPH radical scavenging assays and obtained results were shown in **Figure 5**. The HA-AI composite exhibited dose-dependent radical scavenging activity and EC50 values (dose required to inhibit about half of radicals) for ABTS and DPPH assays were determined as 115.72 ± 2.33 and 128.51 ± 1.04 μg/ml, respectively. In support of our study, most recently, Sumathra et al. (2018) loaded plant compound 6-gingerol into phosphorylated chitosan armed HA composite and noticed DPPH radical scavenging activity up to 76.16% and reported its biocompatibility for advancing activity on osteoblast and osteosarcoma cells. In our study, a relevant antioxidant activity of the HA-AI composite was noticed, and it could be due to phenolics and flavonoids of AI (Sultana et al., 2007; Choudhary and Swarnkar, 2011). Mostly, environmental pollutants and microbial toxins exhibit toxic effects through the generation of oxidative stress (Zablotsky et al., 1992; Nason et al., 2009). Therefore, the developed HA-AI composite could be highly applicable as an antioxidant in orthopedic and dental implants (Ramakrishnan et al., 2010).

Microbicidal Activity of HA-AI Composite

The antimicrobial activity of the developed HA-AI composite was tested on selected pathogenic bacteria by micro-well dilution assay as per approved technique of CLSI. The MIC and MBC of HA-AI composite on *S. aureus* (ATCC 700699) and *E. coli* (ATCC 10536) were correspondingly determined as 266.7 ± 28.87 and 600.0 ± 50.0 μg/ml, and 400.0 ± 86.6 and 816.7 ± 76.38 μg/ml. In the interim, MIC and MBC values of standard antibacterial agent tetracycline on *S. aureus* (ATCC 700699) and *E. coli* (ATCC 10536) were determined as 10.32 ± 0.88 and 16.06 ± 1.02 μg/ml, and 22.90 ± 2.40 and 38.32 ± 2.04 μg/ml, respectively. The determined antibacterial activity of HA-AI composite was lower compared to standard tetracycline.

Furthermore, the antimicrobial potential of the HA-AI composite on the micromorphology of bacteria was confirmed by SEM (**Figure 6**). The HA-AI composite untreated (control) bacteria exhibited characteristic healthy morphology, i.e., smooth and regular surface, whereas bacteria treated with MIC and MBC of HA-AI composite showed detrimental changes in micromorphology, i.e., irregular surface, vesicles, and cellular debris. The evidential detrimental changes in the micromorphology of bacteria were noticed at MBC related to MIC.

In support of our study, Kalaiselvi et al. (2018) synthesized HA nanorods using the flower extract of *Moringa oleifera* and observed the potent antibacterial activity on Gram-positive bacteria (*Bacillus subtilis*, *Monococcus luteus*, and *S. aureus*) and Gram-negative bacteria (*Klebsiella pneumoniae*, *Pseudomonas aeruginosa*, and *Salmonella paratyphi*). Likewise, Scatolini et al. (2018) tested biomimetic HA with different Brazilian propolis and noticed potent antibacterial activity on *S. aureus* ATCC 25923 in the range of >12.5 to >100 μg/ml for MIC and >206.7–800 μg/ml for MBC. Gopi et al. (2013) also synthesized green template assisted HA nanorods using tartaric acid from sources such as banana, grape, and tamarind, and showed a potent antibacterial activity against *E. coli* and *Klebsiella* sp. at a concentration of 100 μl. Similarly, Lakshmeesha et al. (2019) biofabricated zinc oxide nanoparticles with flower bud extract of *Syzygium aromaticum* and demonstrated a potent antifungal and antimycotoxin activity on *F. graminearum*, and Gunti et al. (2019) phytofabricated selenium nanoparticles with fruit extract of *Emblica officinalis* and showed their potent antibacterial activity on foodborne pathogens including bacteria (*E. coli, L. monocytogenes*, *S. aureus*, and *E. faecalis*) and fungi (*A. brasiliensis, A. flavus*, *A. oryzae*, *A. ochraceus*, *F. anthophilum*, and *R. stolonifer*).

The HA is highly biocompatible and will not have antimicrobial property (Zablotsky et al., 1992). In our study, HA-AI composite exhibited potent antimicrobial activity and it could be by phytochemical constituents of AI. Correspondingly, several reports evidently demonstrated the antimicrobial activity of phytoconstituents of AI (Almas, 1999; Thakurta et al., 2007; Joshi et al., 2011). Our study suggests that HA successfully gained antimicrobial activity from AI through biomimetic and, thereby, could find a potential role as an antimicrobial agent in orthopedic and dental implants.

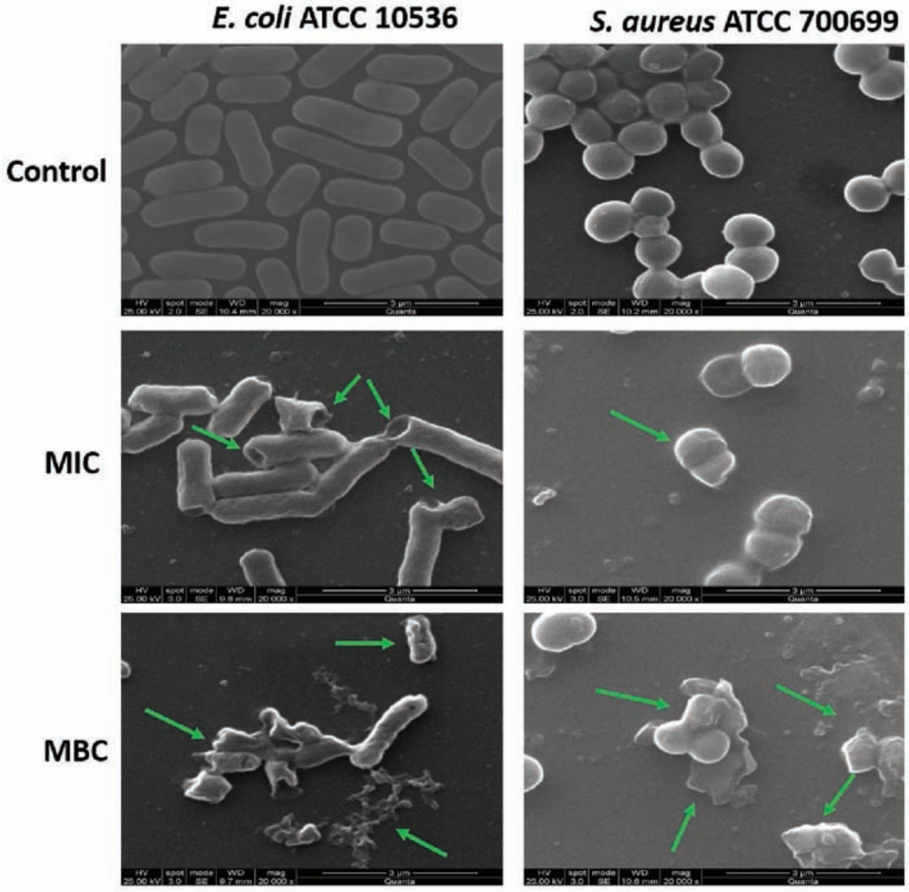

FIGURE 6 | SEM images of *S. aureus* (ATCC 700699) and *E. coli* (ATCC 10536) as untreated (control) and treated with minimum inhibitory concentration (MIC) and minimum bactericidal concentration (MBC) of hydroxyapatite–*A. indica* (HA-AI) composite.

Therapeutic Potential of HA-AI Composite on LPS-Induced Inflammatory Stress

At first, the effects of different concentrations of HA and HA-AI composite on *via*bility of RAW 264.7 cells were assessed by cell viability assay, i.e., MTT assay. Both HA and HA-AI composite were found to be highly biocompatible, and HA and HA-AI composite correspondingly exhibited a significant cytotoxicity after 2.50 and 1.00 mg/ml related to control (**Figures 7A,B**).

The LPS-induced inflammatory response was attenuated with pre-treatment of RAW 264.7 cells with different concentrations of HA and HA-AI composite. Thus, ≤3 and 1 mg/ml of HA and HA-AI composite were chosen to assess their therapeutic potential towards the inflammatory response of LPS (1 μg/ml). The cells pre-treated with HA (up to 3 mg/ml) were not found to be cytoprotective against LPS-induced cell death (**Figures 7C,D**). Whereas, cells pre-treated with the HA-AI composite showed an attenuated response against LPS-induced cell death. The cell viability assays, i.e., MTT and live/dead cell dual staining assays revealed that the HA-AI composite was effective in protecting the cells from LPS-induced inflammatory death, and this characteristic was determined to be dose-dependent (**Figures 7E,F**). The superlative protective activity of HA-AI composite was noticed at 250 μg/ml. The bright-field microscopic images of cells were depicted in **Figure 7G**, and images evidently showed that cells treated with LPS (1 μg/ml) produced detrimental morphological changes, i.e., disruption of characteristic cell morphology, disruption of cell membrane, and formation of apoptotic bodies and cellular debris. Whereas cells pre-treated with HA-AI composite survived from the LPS-induced death and optimum protection was noticed at 250 μg/ml of HA-AI composite. The other cell viability assay, live/dead dual staining cell images were depicted in **Figure 7H**. The cells treated only with LPS (1 μg/ml) evidently showed a greater number of dead cells (red) related to control, whereas cells pre-treated with HA-AI composite survived from LPS-induced death and a greater number of live cells (green) were perceived to be related to LPS-treated cells. In accordance to bright-field microscopic images, optimum protection of HA-AI composite against LPS-induced death was noticed at 250 μg/ml. In conclusion, cell viability assays determined that the HA-AI composite was effective in protecting the cells from LPS-induced death and while HA does not have cytoprotective activity. Thus, we can conclude that AI has successfully imparted protective efficacy to HA *via* biomimetic.

Next, the protective efficacy of the HA-AI composite on oxidative and inflammatory stress induced by LPS is depicted

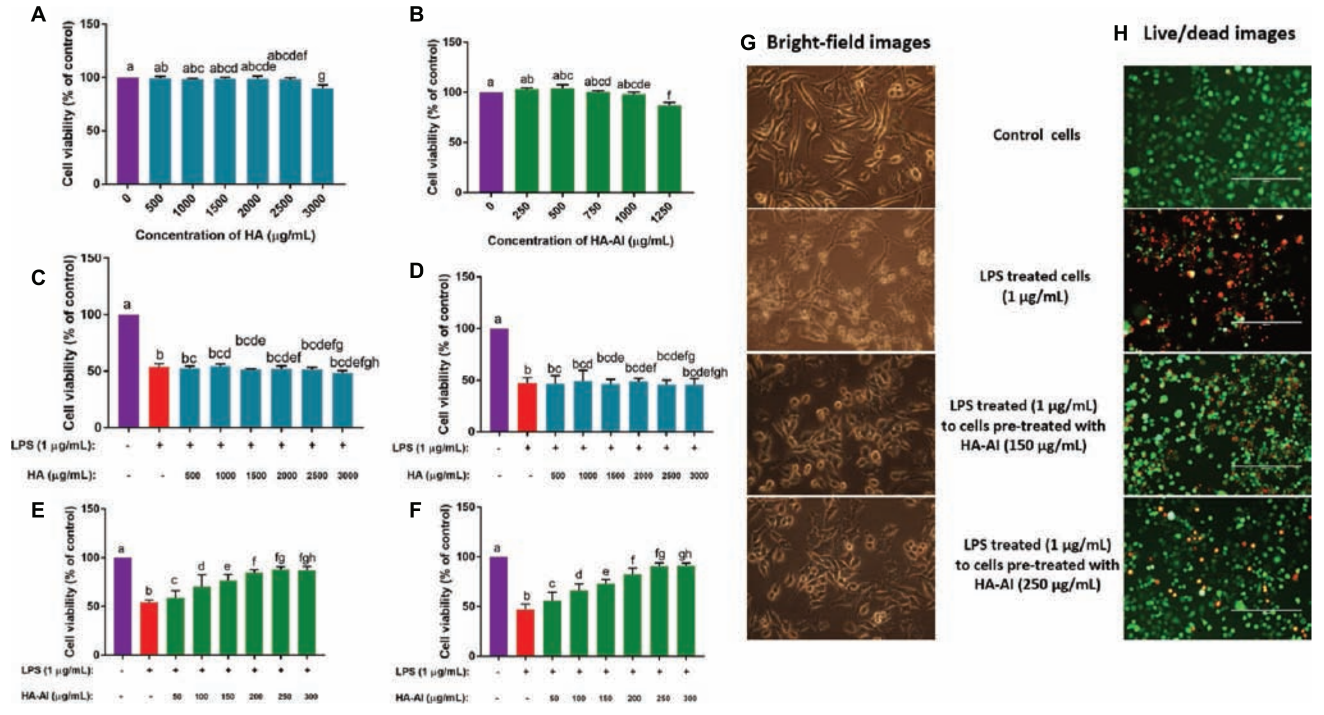

FIGURE 7 | Assessment of protective efficacy of hydroxyapatite (HA) and hydroxyapatite–*A. indica* (HA-AI) composite on LPS-induced death of RAW 264.7 cells by cell viability assays. Biocompatibility of **(A)** HA and **(B)** HA-AI composite on cell viability determined by MTT assay. Protective efficacy of HA against LPS-induced cell death determined by **(C)** MTT and **(D)** live/dead dual staining assays. Protective efficacy of HA-AI composite against LPS-induced cell death determined by **(E)** MTT and **(F)** live/dead dual staining assays. **(G)** Bright-fielding microscopic images representing the protective efficacy of HA-AI composite on LPS-induced cell death. The images were taken at magnification of 400×. **(H)** Live/dead dual staining microscopic images representing the protective efficacy of HA-AI composite on LPS-induced cell death. The scale bar is 200 μm. Green and red colors represent the live and dead cells, respectively. The experiments were performed individually in six replicates and achieved results were stated as mean ± standard deviation. The data were statistically evaluated by one-way ANOVA following Tukey's *post hoc* multiple comparison test. The statistical variance among the experimental groups was measured as significant at $p < 0.05$. The columns with different alphabets were significant within the respective study.

in **Figure 8**. The HA-AI composite exhibited dose-dependent protective character against intracellular ROS molecules generated by LPS (**Figure 8A**). The phase-contrast and fluorescent microscopic images of cells exhibiting the protective efficacy of HA-AI composite on LPS-induced oxidative stress is shown in **Figure 8B**. The images evidently showed higher intensity (fluorescence) of oxidative stress in LPS-treated cells related to control. Whereas cells pre-treated with HA-AI composite showed an attenuated response towards oxidative stress generated by LPS related to cells treated alone with LPS and greater protective efficacy of HA-AI composite against LPS was noticed at 250 μg/ml. Likewise, the HA-AI composite exhibited dose-dependent protective efficacy against nitrite generation and lipid peroxidation induced by LPS (**Figures 8C,D**). Moreover, HA-AI composite effectively protected the antioxidant enzymes (SOD, GSH, and CAT) from LPS-induced detrimental effects, and it was also found to be dose dependent (**Figures 8E–G**). Thus, HA-AI composite successfully protected the cells from oxidative stress induced by LPS through safeguarding the antioxidant enzymes. Next, the inflammatory regulatory factors, TNF-α and IL-6, were quantified by ELISA. The results showed that the cells pre-treated with HA-AI composite attenuated generation of TNF-α and IL-6 induced by LPS related to cells treated alone with LPS and was found to be dose-dependent in accordance with the outcomes of oxidative stress (**Figures 8H,I**). Furthermore, RT-PCR analysis concluded that HA-AI composite successfully down-regulated the expression of inflammatory regulatory genes (TNF-α, IL-6, iNOS, and COX-2) induced by LPS (**Figures 8J–M**). Thus, oxidative and inflammatory studies concluded that the HA-AI composite protected the cells from LPS-induced inflammatory stress.

In another study, LPS has significantly depleted the MMP levels of cells related to control and, thus, concluded that LPS might induce cell death through depletion of MMP and obstruction of ATP synthesis. Whereas cells pre-treated with HA-AI composite protected the cells from depletion of MMP induced by LPS, and were also found dose-dependent on results of cell viability, and oxidative and inflammatory assays (**Figure 9A**). The phase-contrast and fluorescent microscopic images of MMP assay were depicted in **Figure 9B**. The images evidently showed the restoration of fluorescence (MMP) in cells pre-treated with HA-AI composite related to cells treated alone with LPS. Thus, assays concluded that the HA-AI composite aided in protecting the cells from LPS-induced cell death.

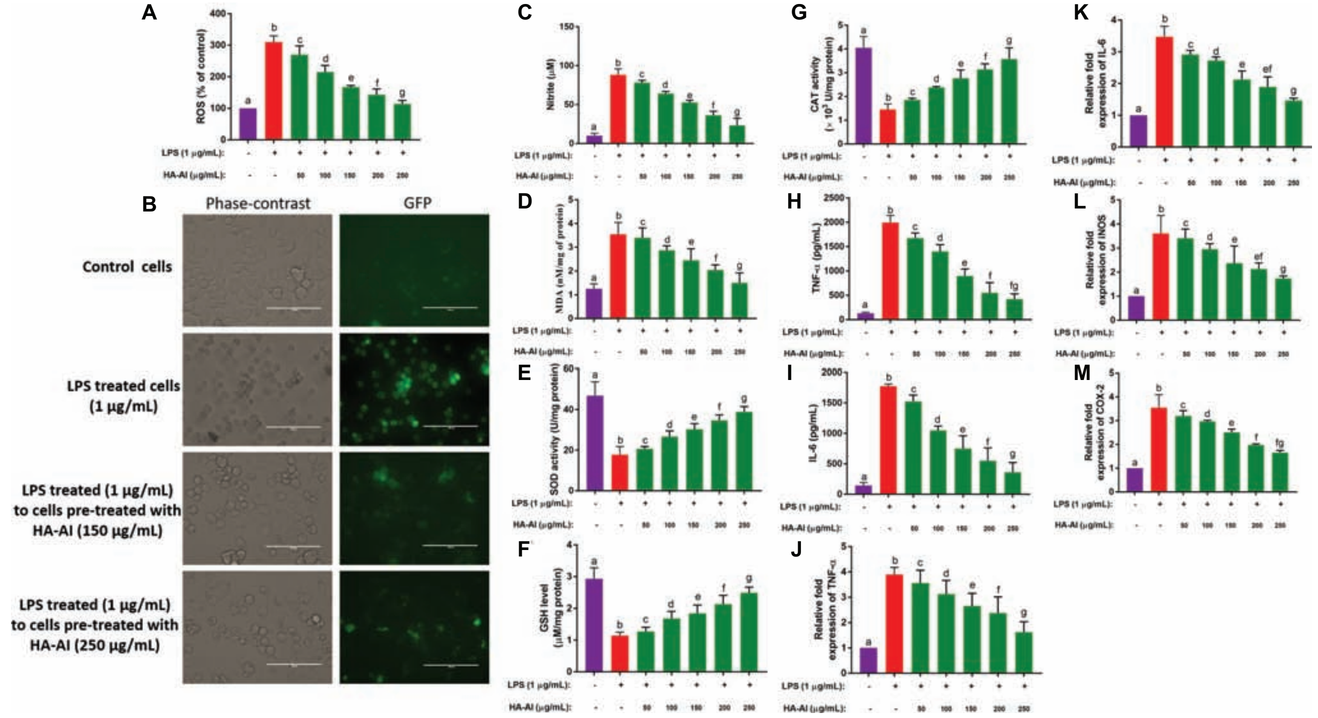

FIGURE 8 | Assessment of protective efficacy of hydroxyapatite–*A. indica* (HA-AI) composite on LPS-induced oxidative and inflammatory stress in RAW 264.7 cells. **(A)** Dose-dependent protective efficacy of HA-AI composite on LPS-induced intracellular ROS generation by DCFH-DA staining. **(B)** Phase contrast and fluorescent microscopic images depicting the protective efficacy of HA-AI composite on LPS-induced intracellular ROS generation by DCFH-DA staining. The scale bar is 100 μm. **(C)** Dose-dependent protective efficacy of HA-AI composite on LPS-induced nitrite generation. **(D)** Dose-dependent protective efficacy of HA-AI composite on LPS-induced lipid peroxidation. **(E–G)** Dose-dependent protective efficacy of HA-AI composite on LPS-induced detrimental effect on antioxidant enzymes, i.e. SOD, GSH, and CAT. **(H,I)** Dose-dependent protective efficacy of HA-AI composite on LPS-induced inflammatory cytokines (TNF-α and IL-6) by ELISA. **(J–M)** Dose-dependent protective efficacy of HA-AI composite on LPS-induced inflammation regulatory genes (TNF-α, IL-6, iNOS, and COX-2) by real-time PCR analysis. The experiments were performed individually in six replicates and achieved results were stated as mean ± standard deviation. The data were statistically evaluated by one-way ANOVA following Tukey's *post hoc* multiple comparison test. The statistical variance among the experimental groups was measured as significant at $p < 0.05$. The columns with different alphabets were significant within the respective study.

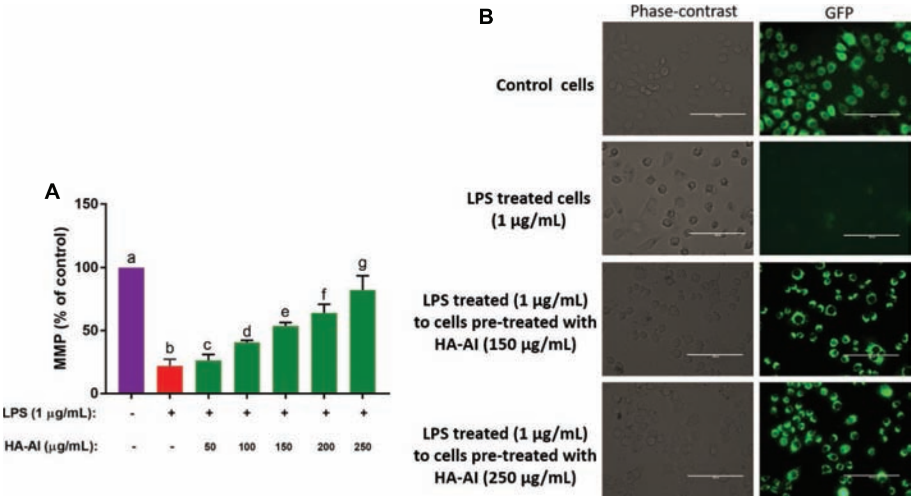

FIGURE 9 | Assessment of restoring efficacy of hydroxyapatite–*A. indica* (HA-AI) composite on LPS-induced depletion of mitochondrial membrane potential (MMP) in RAW 264.7 cells by rhodamine 123 staining. **(A)** Dose-dependent restoring efficacy of HA-AI composite on LPS-induced depletion of MMP. **(B)** Phase contrast and fluorescent microscopic images depicting the restoring efficacy of HA-AI composite on LPS-induced depletion of MMP. The scale bar is 100 µm. The experiments were performed individually in six replicates and achieved results were stated as mean ± standard deviation. The data were statistically evaluated by one-way ANOVA following Tukey's *post hoc* multiple comparison test. The statistical variance among the experimental groups was measured as significant at $p < 0.05$. The columns with different alphabets were significant within the respective study.

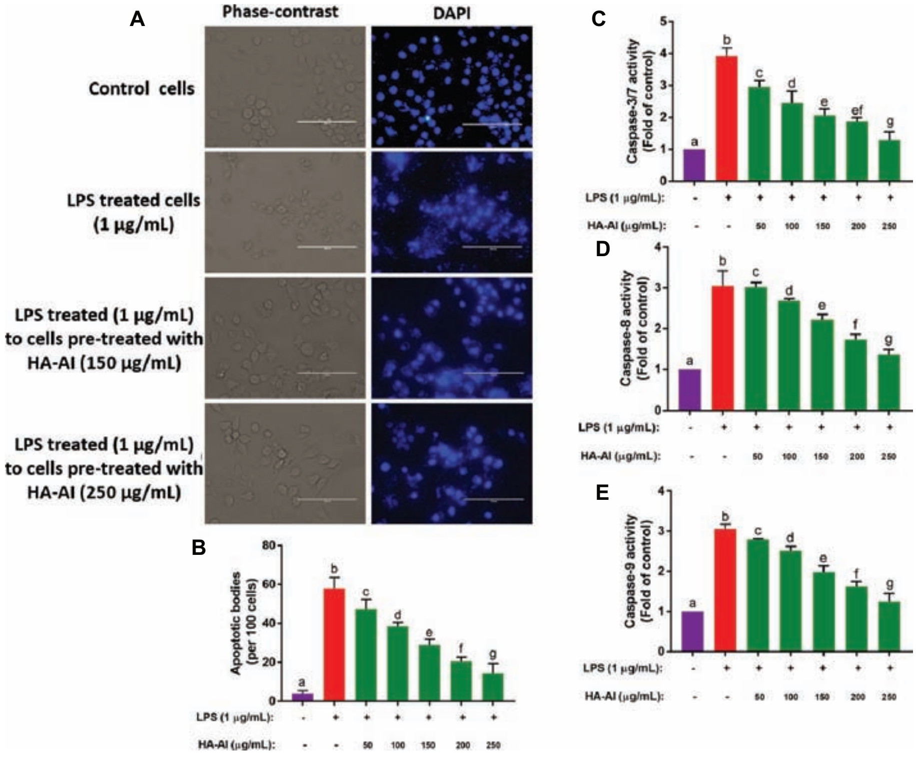

FIGURE 10 | Assessment of protective efficacy of hydroxyapatite–*A. indica* (HA-AI) composite on LPS-induced nuclear damage and apoptosis in RAW 264.7 cells. **(A)** Phase contrast and fluorescent microscopic images depicting the protective efficacy of HA-AI composite on LPS-induced nuclear damage by DAPI staining. **(B)** Dose-dependent protective efficacy of HA-AI composite on LPS-induced apoptosis by DAPI staining. **(C–E)** Dose-dependent restoring efficacy of HA-AI composite on LPS-induced depletion of caspases (3/7, 8, and 9). The experiments were performed individually in six replicates and achieved results were stated as mean ± standard deviation. The data were statistically evaluated by one-way ANOVA following Tukey's *post hoc* multiple comparison test. The statistical variance among the experimental groups was measured as significant at $p < 0.05$. The columns with different alphabets were significant within the respective study.

In the final study, the protective efficacy of the HA-AI composite on nuclear damage and apoptosis induced by LPS was evaluated by DAPI staining and measurement of caspases 3/7, 8, and 9 (**Figure 10**). In **Figure 10A**, LPS detrimentally effaced the nuclear material of cell, resulting in the fragmentation and leakage of nuclear material from nucleus. Whereas cells pre-treated with HA-AI composite protected the cells from nuclear damage induced by LPS. Furthermore, a number of apoptotic bodies were high in LPS-treated cells related to control. On the other hand, fewer apoptotic bodies were noticed in cells pre-treated with HA-AI composite related to cells treated alone with LPS (**Figure 10B**). Moreover, LPS treated to cells pre-treated with HA-AI composite exhibited significantly low levels of caspases (3/7, 8, and 9) related to cells treated alone with LPS (**Figures 10C–E**). Thus, overall studies determined that HA-AI composite protected the nuclear material of cells from LPS-induced stress and regulate the apoptotic death through maintenance of caspase levels.

To the best of our knowledge, our study is first report that demonstrated the anti-inflammatory activity of biomimetic HA. However, earlier reports evidently proved the anti-inflammatory activity of various extracts of AI. The researchers reported that phenolics and flavonoids of AI were significantly inhibiting the functions of TNF-α, IL-6, iNOS, COX-2, and NFκB of macrophages and neutrophils relevant to the inflammatory response. The major phenolics and flavonoids responsible for anti-inflammatory responses are nimbin, nimbidin, azadirachtin, quercetin, salannin, gallic acid, catechin, and epicatechin (Atawodi and Atawodi, 2009; Schumacher et al., 2011; Alzohairy, 2016). Moreover, in support of our study, researchers proved that phenolics and flavonoids of other plant extracts were highly efficient in contrasting inflammatory responses (Kalaiselvi et al., 2013; Alvarez-Suarez et al., 2017; Gasparrini et al., 2017). In our study, HA alone did not show protective effectiveness against LPS-induced inflammatory stress. Whereas, the HA-AI composite presented potent anti-inflammatory activity against LPS-induced stress. It can be concluded that the observed anti-inflammatory activity of HA-AI composite could be due to phenolics and flavonoids of AI. In conclusion, our study demonstrated that antioxidant, antibacterial, and anti-inflammatory proficiency could be presented to HA *via* biomimetic with plant sources.

CONCLUSION

Ethanolic extract of AI was found rich with phenolics and flavonoids, and determined to be a potential contender for biomimetic of nanomaterials. The HA was synthesized by sol-gel method and HA was biomimetic with AI to form HA-AI composite. The FTIR concluded that the as-synthesized HA-AI composite was successfully comprised of constituents of HA and AI. The XRD pattern and Zeta potential determined that the HA-AI composite was in crystalline phase, has negative charge and could be highly suitable for biological purposes. The SEM showed that the HA-AI composite was spherical in shape, and furthermore, TEM concluded that the HA-AI composite was nano in size. The SEM-EDX concluded that the HA-AI composite comprised elements of HA and AI. The as-synthesized HA-AI composite has presented potential antioxidant, antibacterial, and anti-inflammatory activities against LPS which could be due to phenolics and flavonoids of AI. The HA-AI composite protected the RAW 264.7 cells from LPS-induced cell death through scavenging oxidants, restoring MMP, and upholding inflammatory and apoptotic factors. The study showed that potential beneficial activities were imparted to HA from AI through biomimetic. Thus, the HA-AI composite could be highly applicable as an antibacterial and anti-inflammatory substitute in dentistry and orthopedic.

DATA AVAILABILITY

The raw data supporting the conclusions of this manuscript will be made available by the authors, without undue reservation, to any qualified researcher.

AUTHOR CONTRIBUTIONS

AN and SS have designed the work, executed the experiments, drafted the results, and approved the final version of the manuscript.

ACKNOWLEDGMENTS

The first author AN was thankful to Bharathiar University for providing the opportunity to pursue Ph.D. Also, AN was thankful to DST-PURSE and Bharathiar University for providing the support and instrumentation facility. The authors were grateful to Dr. K. Kadirvelu, Scientist "F," Joint Director and OIC, DRDO-BU Centre for Life Sciences for providing instrumentation facility and encouragement.

SUPPLEMENTARY MATERIAL

The Supplementary Material for this article can be found online at: https://www.frontiersin.org/articles/10.3389/fmicb.2019.01757/full#supplementary-material

REFERENCES

Ahmed, S., Ahmad, M., Swami, B. L., and Ikram, S. (2016). A review on plants extract mediated synthesis of silver nanoparticles for antimicrobial applications: a green expertise. *J. Adv. Res.* 7, 17–28. doi: 10.1016/j.jare.2015.02.007

Al-Jadidi, H. S. K., and Hossain, M. A. (2016). Determination of the total phenols, flavonoids and antimicrobial activity of the crude extracts from locally grown neem stem. *Asian Pac. J. Trop. Dis.* 6, 376–379. doi: 10.1016/S2222-1808(15)61051-9

Almas, K. (1999). The antimicrobial effects of extracts of *Azadirachta indica* (Neem) and *Salvadora persica* (Arak) chewing sticks. *Indian J. Dent. Res.* 10, 23–26.

Alvarez-Suarez, J. M., Carrillo-Perdomo, E., Aller, A., Giampieri, F., Gasparrini, M., González-Pérez, L., et al. (2017). Anti-inflammatory effect of Capuli cherry against LPS-induced cytotoxic damage in RAW 264.7 macrophages. *Food Chem. Toxicol.* 102, 46–52. doi: 10.1016/j.fct.2017.01.024

Alzohairy, M. A. (2016). Therapeutics role of *Azadirachta indica* (Neem) and their active constituents in diseases prevention and treatment. *Evid. Based Complement. Alternat. Med.* 2016. doi: 10.1155/2016/7382506

Asharani, P. V., Sethu, S., Vadukumpully, S., Zhong, S., Lim, C. T., Hande, M. P., et al. (2010). Investigations on the structural damage in human erythrocytes exposed to silver, gold, and platinum nanoparticles. *Adv. Funct. Mater.* 20, 1233–1242. doi: 10.1002/adfm.200901846

Atak, B. H., Buyuk, B., Huysal, M., Isik, S., Senel, M., Metzger, W., et al. (2017). Preparation and characterization of amine functional nano-hydroxyapatite/chitosan bionanocomposite for bone tissue engineering applications. *Carbohydr. Polym.* 164, 200–213. doi: 10.1016/j.carbpol.2017.01.100

Atawodi, S. E., and Atawodi, J. C. (2009). *Azadirachta indica* (Neem): a plant of multiple biological and pharmacological activities. *Phytochem. Rev.* 8, 601–620. doi: 10.1007/s11101-009-9144-6

Bienvenu, J., Coulon, L., Doche, C., Gutowski, M. C., and Grau, G. E. (1993). Analytical performances of commercial ELISA-kits for IL-2, IL-6 and TNF-alpha. A WHO study. *Eur. Cytokine Netw.* 4, 447–451.

Bismayer, U., Shi, J., Klocke, A., Gierlotka, S., and Palosz, B. F. (2005). From dental enamel to synthetic hydroxyapaptite-metal composites. *Key Eng. Mater*. 288, 561–564.

Biswas, K., Chattopadhyay, I., Banerjee, R. K., and Bandyopadhyay, U. (2002). Biological activities and medicinal properties of neem (Azadirachta indica). *CURRENT SCIENCE-BANGALORE-*, 82, 1336–1345.

Cao, H., Zhang, L., Zheng, H., and Wang, Z. (2010). Hydroxyapatite nanocrystals for biomedical applications. *J. Phys. Chem. C* 114, 18352–18357. doi: 10.1021/jp106078b

Chen, L. Q., Fang, L., Ling, J., Ding, C. Z., Kang, B., and Huang, C. Z. (2015). Nanotoxicity of silver nanoparticles to red blood cells: size dependent adsorption, uptake, and hemolytic activity. *Chem. Res. Toxicol.* 28, 501–509. doi: 10.1021/tx500479m

Chen, Y. M., Ogawa, R., Kakugo, A., Osada, Y., and Gong, J. P. (2009). Dynamic cell behavior on synthetic hydrogels with different charge densities. *Soft Matter* 5, 1804–1811. doi: 10.1039/b818586g

Choudhary, R. K., and Swarnkar, P. L. (2011). Antioxidant activity of phenolic and flavonoid compounds in some medicinal plants of India. *Nat. Prod. Res.* 25, 1101–1109. doi: 10.1080/14786419.2010.498372

Cohen, G. M. (1997). Caspases: the executioners of apoptosis. *Biochem. J.* 326, 1–16. doi: 10.1042/bj3260001

Dhami, K. N., Reddy, M. S., and Mukherjee, A. (2013). Biomineralization of calcium carbonates and their engineered applications: a review. *Front. Microbiol.* 4:314. doi: 10.3389/fmicb.2013.00314

Djordjevic, A., Spasic, S., Jovanovic-Galovic, A., Djordjevic, R., and Grubor-Lajsic, G. (2004). Oxidative stress in diabetic pregnancy: SOD, CAT and GSH-Px activity and lipid peroxidation products. *J. Matern. Fetal Neonatal Med.* 16, 367–372. doi: 10.1080/14767050400018270

Driessens, F. C., and Verbeeck, R. K. (1990). *Biominerals*. Boca Raton: CRC Press.

Emaus, R. K., Grunwald, R., and Lemasters, J. J. (1986). Rhodamine 123 as a probe of transmembrane potential in isolated rat-liver mitochondria: spectral and metabolic properties. *Biochim. Biophys. Acta Bioenerg.* 850, 436–448. doi: 10.1016/0005-2728(86)90112-X

Gasparrini, M., Forbes-Hernandez, T. Y., Giampieri, F., Afrin, S., Alvarez-Suarez, J. M., Mazzoni, L., et al. (2017). Anti-inflammatory effect of strawberry extract against LPS-induced stress in RAW 264.7 macrophages. *Food Chem. Toxicol.* 102, 1–10. doi: 10.1016/j.fct.2017.01.018

Gaweł, S., Wardas, M., Niedworok, E., and Wardas, P. (2004). Malondialdehyde (MDA) as a lipid peroxidation marker. *Wiad. Lek.* 57, 453–455.

Gayathri, B., Muthukumarasamy, N., Velauthapillai, D., and Santhosh, S. B. (2018). Magnesium incorporated hydroxyapatite nanoparticles: preparation, characterization, antibacterial and larvicidal activity. *Arab. J. Chem.* 11, 645–654. doi: 10.1016/j.arabjc.2016.05.010

Giustarini, D., Rossi, R., Milzani, A., and Dalle-Donne, I. (2008). Nitrite and nitrate measurement by Griess reagent in human plasma: evaluation of interferences and standardization. *Methods Enzymol.* 440, 361–380. doi: 10.1016/S0076-6879(07)00823-3

Gopi, D., Bhuvaneshwari, N., Indira, J., Kanimozhi, K., and Kavitha, L. (2013). A novel green template assisted synthesis of hydroxyapatite nanorods and their spectral characterization. *Spectrochim. Acta A Mol. Biomol. Spectrosc.* 107, 196–202. doi: 10.1016/j.saa.2013.01.052

Gunti, L., Dass, R. S., and Kalagatur, N. K. (2019). Phytofabrication of selenium nanoparticles from *Emblica officinalis* fruit extract and exploring its biopotential applications: antioxidant, antimicrobial, and biocompatibility. *Front. Microbiol.* 10:931. doi: 10.3389/fmicb.2019.00931

Haugland, R. P., MacCoubrey, I. C., and Moore, P. L. (1994). U.S. Patent No. 5,314,805. Washington, DC: U.S. Patent and Trademark Office.

Joshi, B., Sah, G. P., Basnet, B. B., Bhatt, M. R., Sharma, D., Subedi, K., et al. (2011). Phytochemical extraction and antimicrobial properties of different medicinal plants: *Ocimum sanctum* (Tulsi), *Eugenia caryophyllata* (Clove), *Achyranthes bidentata* (Datiwan) and *Azadirachta indica* (Neem). *J. Microbiol. Antimicrob.* 3, 1–7.

Kalagatur, N. K., Kamasani, J. R., and Mudili, V. (2018). Assessment of detoxification efficacy of irradiation on zearalenone mycotoxin in various fruit juices by response surface methodology and elucidation of its in-vitro toxicity. *Front. Microbiol.* 9:2937. doi: 10.3389/fmicb.2018.02937

Kalagatur, N. K., Karthick, K., Allen, J. A., Ghosh, N., Sivaraman, O., Chandranayaka, S., et al. (2017). Application of activated carbon derived from seed shells of *Jatropha curcas* for decontamination of zearalenone mycotoxin. *Front. Pharmacol.* 8:760. doi: 10.3389/fphar.2017.00760

Kalagatur, N. K., Mudili, V., Siddaiah, C., Gupta, V. K., Natarajan, G., Sreepathi, M. H., et al. (2015). Antagonistic activity of *Ocimum sanctum* L. essential oil on growth and zearalenone production by *Fusarium graminearum* in maize grains. *Front. Microbiol.* 6:892. doi: 10.3389/fmicb.2015.00892

Kalaiselvi, V., Mathammal, R., Vijayakumar, S., and Vaseeharan, B. (2018). Microwave assisted green synthesis of hydroxyapatite nanorods using *Moringa oleifera* flower extract and its antimicrobial applications. *Int. J. Vet. Sci. Med.* 6, 286–295. doi: 10.1016/j.ijvsm.2018.08.003

Kalaiselvi, P., Rajashree, K., Priya, L. B., and Padma, V. V. (2013). Cytoprotective effect of epigallocatechin-3-gallate against deoxynivalenol-induced toxicity through anti-oxidative and anti-inflammatory mechanisms in HT-29 cells. *Food Chem. Toxicol.* 56, 110–118. doi: 10.1016/j.fct.2013.01.042

Kaygili, O., Dorozhkin, S. V., and Keser, S. (2014). Synthesis and characterization of Ce-substituted hydroxyapatite by sol–gel method. *Mater. Sci. Eng. C* 42, 78–82. doi: 10.1016/j.msec.2014.05.024

Khan, H. A., Abdelhalim, M. A. K., Al-Ayed, M. S., and Alhomida, A. S. (2012). Effect of gold nanoparticles on glutathione and malondialdehyde levels in liver, lung and heart of rats. *Saudi J. Biol. Sci.* 19, 461–464. doi: 10.1016/j.sjbs.2012.06.005

Kim, Y. S., Song, M. Y., Park, J. D., Song, K. S., Ryu, H. R., Chung, Y. H., et al. (2010). Subchronic oral toxicity of silver nanoparticles. *Part. Fibre Toxicol.* 7:20. doi: 10.1186/1743-8977-7-20

Kramer, E., Itzkowitz, E., and Wei, M. (2014). Synthesis and characterization of cobalt-substituted hydroxyapatite powders. *Ceram. Int.* 40, 13471–13480. doi: 10.1016/j.ceramint.2014.05.072

Kumar, K. N., Venkataramana, M., Allen, J. A., Chandranayaka, S., Murali, H. S., and Batra, H. V. (2016). Role of *Curcuma longa* L. essential oil in controlling the growth and zearalenone production of *Fusarium graminearum*. *LWT Food Sci. Technol.* 69, 522–528. doi: 10.1016/j.lwt.2016.02.005

Lakshmeesha, T. R., Kalagatur, N. K., Mudili, V., Mohan, C. D., Rangappa, S., Prasad, B. D., et al. (2019). Biofabrication of zinc oxide nanoparticles with *Syzygium aromaticum* flower buds extract and finding its novel application in controlling the growth and mycotoxins of *Fusarium graminearum*. *Front. Microbiol.* 10:1244. doi: 10.3389/fmicb.2019.01244

Lamping, N., Dettmer, R., Schröder, N. W., Pfeil, D., Hallatschek, W., Burger, R., et al. (1998). LPS-binding protein protects mice from septic shock caused by LPS or gram-negative bacteria. *J. Clin. Invest.* 101, 2065–2071.

LeBel, C. P., Ischiropoulos, H., and Bondy, S. C. (1992). Evaluation of the probe 2′, 7′-dichlorofluorescin as an indicator of reactive oxygen species formation and oxidative stress. *Chem. Res. Toxicol.* 5, 227–231. doi: 10.1021/tx00026a012

Lin, Y., Yang, Z., and Cheng, J. (2007). Preparation, characterization and antibacterial property of cerium substituted hydroxyapatite nanoparticles. *J. Rare Earths* 25, 452–456. doi: 10.1016/S1002-0721(07)60455-4

Mo, A., Liao, J., Xu, W., Xian, S., Li, Y., and Bai, S. (2008). Preparation and antibacterial effect of silver–hydroxyapatite/titania nanocomposite thin film on titanium. *Appl. Surf. Sci.* 255, 435–438.

Nason, R., Jung, J. Y., and Chole, R. A. (2009). Lipopolysaccharide-induced osteoclastogenesis from mononuclear precursors: a mechanism for osteolysis in chronic otitis. *J. Assoc. Res. Otolaryngol.* 10, 151–160. doi: 10.1007/s10162-008-0153-8

Nirmala, R., Park, H. M., Kalpana, D., Kang, H. S., Navamathavan, R., Lee, Y. S., et al. (2011). Bactericidal activity and in vitro cytotoxicity assessment of hydroxyapatite containing gold nanoparticles. *J. Biomed Nanotechnol.* 7, 342–350.

Pandey, G., Verma, K. K., and Singh, M. (2014). Evaluation of phytochemical, antibacterial and free radical scavenging properties of Azadirachta indica (neem) leaves. *Int. J. Pharm. Pharm. Sci.*, 6, 444–447.

Pankaj, S., Lokeshwar, T., Mukesh, B., and Vishnu, B. (2011). Review on neem (Azadirachta indica): thousand problems one solution. *Int. Res. J. Pharm.* 2, 97–102.

Pepla, E., Besharat, L. K., Palaia, G., Tenore, G., and Migliau, G. (2014). Nano-hydroxyapatite and its applications in preventive, restorative and regenerative dentistry: a review of literature. *Ann. Stomatol.* 5, 108–114. doi: 10.11138/ads/2014.5.3.108

Phatai, P., Futalan, C. M., Kamonwannasit, S., and Khemthong, P. (2019). Structural characterization and antibacterial activity of hydroxyapatite synthesized via sol-gel method using glutinous rice as a template. *J. Sol-Gel Sci. Technol.* 89, 1–12. doi: 10.1007/s10971-018-4910-9

Qaiyumi, S. (2007). "Macro-and microdilution methods of antimicrobial susceptibility testing" in *Antimicrobial susceptibility testing protocols*. eds. R. Schwalbe, L. Steele-Moore and A. C. Goodwin (Boca Raton: Taylor & Francis), 75–79.

Raetz, C. R., and Whitfield, C. (2002). Lipopolysaccharide endotoxins. *Annu. Rev. Biochem.* 71, 635–700. doi: 10.1146/annurev.biochem.71.110601.135414

Ramakrishnan, P., Hecht, B. A., Pedersen, D. R., Lavery, M. R., Maynard, J., Buckwalter, J. A., et al. (2010). Oxidant conditioning protects cartilage from mechanically induced damage. *J. Orthop. Res.* 28, 914–920. doi: 10.1002/jor.21072

Sanosh, K. P., Chu, M. C., Balakrishnan, A., Kim, T. N., and Cho, S. J. (2009). Preparation and characterization of nano-hydroxyapatite powder using sol-gel technique. *Bull. Mater. Sci.* 32, 465–470. doi: 10.1007/s12034-009-0069-x

Sathiskumar, S., Vanaraj, S., Sabarinathan, D., and Preethi, K. (2018). Evaluation of antibacterial and antibiofilm activity of synthesized zinc-hydroxyapatite biocomposites from Labeo rohita fish scale waste. *Mater. Res. Express* 5:025407.

Scatolini, A. M., Pugine, S. M. P., de Oliveira Vercik, L. C., de Melo, M. P., and da Silva Rigo, E. C. (2018). Evaluation of the antimicrobial activity and cytotoxic effect of hydroxyapatite containing Brazilian propolis. *Biomed. Mater.* 13:025010. doi: 10.1088/1748-605X/aa9a84

Schumacher, M., Cerella, C., Reuter, S., Dicato, M., and Diederich, M. (2011). Anti-inflammatory, pro-apoptotic, and anti-proliferative effects of a methanolic neem (*Azadirachta indica*) leaf extract are mediated via modulation of the nuclear factor-κB pathway. *Genes Nutr.* 6, 149–160. doi: 10.1007/s12263-010-0194-6

Shetty, N., and Kundabala, M. (2013). Biominerals in restorative dentistry. *J. Interdiscip. Dent.* 3, 64–70. doi: 10.4103/2229-5194.126858

Sultana, B., Anwar, F., and Przybylski, R. (2007). Antioxidant activity of phenolic components present in barks of *Azadirachta indica*, *Terminalia arjuna*, *Acacia nilotica*, and *Eugenia jambolana* lam. Trees. *Food Chem.* 104, 1106–1114. doi: 10.1016/j.foodchem.2007.01.019

Sumathra, M., Rajan, M., and Munusamy, M. A. (2018). A phosphorylated chitosan armed hydroxyapatite nanocomposite for advancing activity on osteoblast and osteosarcoma cells. *New J. Chem.* 42, 12457–12466. doi: 10.1039/C8NJ01316K

Tan, T. W., Tsai, H. R., Lu, H. F., Lin, H. L., Tsou, M. F., Lin, Y. T., et al. (2006). Curcumin-induced cell cycle arrest and apoptosis in human acute promyelocytic leukemia HL-60 cells via MMP changes and caspase-3 activation. *Anticancer Res.* 26, 4361–4371.

Tellman, G., and Olivier, G. (2006). Light cycler 480 real time PCR system; innovative solutions for relative quantification. *Biochemica* 4, 16–18.

Thakurta, P., Bhowmik, P., Mukherjee, S., Hajra, T. K., Patra, A., and Bag, P. K. (2007). Antibacterial, antisecretory and antihemorrhagic activity of *Azadirachta indica* used to treat cholera and diarrhea in India. *J. Ethnopharmacol.* 111, 607–612. doi: 10.1016/j.jep.2007.01.022

Venkataramana, M., Nayaka, S. C., Anand, T., Rajesh, R., Aiyaz, M., Divakara, S. T., et al. (2014). Zearalenone induced toxicity in SHSY-5Y cells: the role of oxidative stress evidenced by N-acetyl cysteine. *Food Chem. Toxicol.* 65, 335–342. doi: 10.1016/j.fct.2013.12.042

Wang, J., Wang, L., and Fan, Y. (2016). Adverse biological effect of TiO_2 and hydroxyapatite nanoparticles used in bone repair and replacement. *Int. J. Mol. Sci.* 17:798.

Zablotsky, M. H., Diedrich, D. L., and Meffert, R. M. (1992). Detoxification of endotoxin-contaminated titanium and hydroxyapatite-coated surfaces utilizing various chemotherapeutic and mechanical modalities. *Implant. Dent.* 1, 154–158. doi: 10.1097/00008505-199205000-00009

Conflict of Interest Statement: The authors declare that the research was conducted in the absence of any commercial or financial relationships that could be construed as a potential conflict of interest.

Advantages of publishing in Frontiers

OPEN ACCESS
Articles are free to read
for greatest visibility
and readership

FAST PUBLICATION
Around 90 days
from submission
to decision

HIGH QUALITY PEER-REVIEW
Rigorous, collaborative,
and constructive
peer-review

TRANSPARENT PEER-REVIEW
Editors and reviewers
acknowledged by name
on published articles

Frontiers
Avenue du Tribunal-Fédéral 34
1005 Lausanne | Switzerland

Visit us: www.frontiersin.org
Contact us: info@frontiersin.org | +41 21 510 17 00

REPRODUCIBILITY OF RESEARCH
Support open data
and methods to enhance
research reproducibility

DIGITAL PUBLISHING
Articles designed
for optimal readership
across devices

FOLLOW US
@frontiersin

IMPACT METRICS
Advanced article metrics
track visibility across
digital media

EXTENSIVE PROMOTION
Marketing
and promotion
of impactful research

LOOP RESEARCH NETWORK
Our network
increases your
article's readership